Marcel G. Friedrich

Vibrational Spectroscopic and Electrochemical Investigations of Multi-centered Heme Proteins in Biomimetic Membrane Architectures

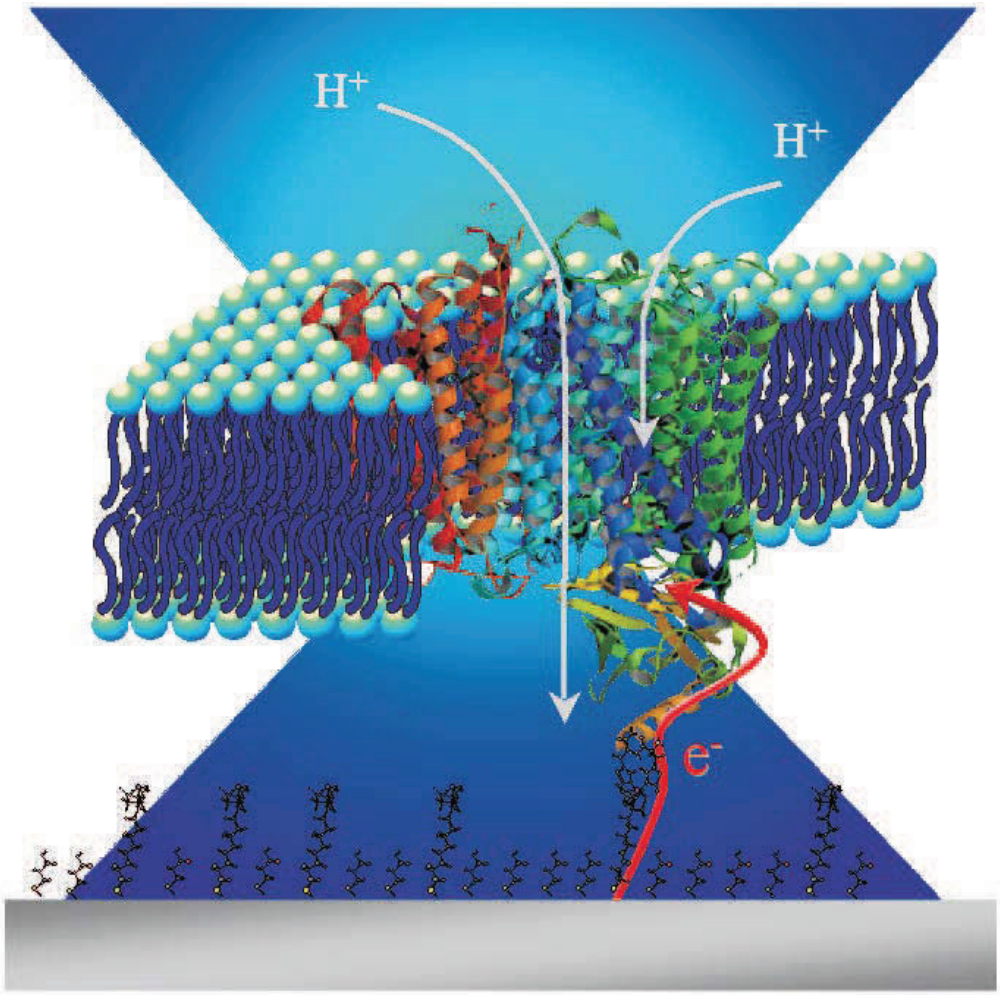

Mainz 2007

Vibrational Spectroscopic and Electrochemical Investigations of Multi-centered Heme Proteins in Biomimetic Membrane Architectures

---

Dissertation

zur Erlangung des akademischen Grades
"'Doktor der Naturwissenschaften"' (Dr. rer. nat)
am Fachbereich Chemie und Pharmazie
der Johannes Gutenberg-Universität Mainz

Vorgelegt von:

Marcel Günther Friedrich

geboren in Dernbach

Mainz, March 2007

Damit das **M**ögliche entsteht,
muss **i**mmer wieder das **U**nmögliche versucht werden.

Hermann Hesse

To create the **P**ossible,
you have to **c**ontinue trying the **i**mpossible.

Hermann Hesse

Diese Doktorarbeit ist meinen Eltern gewidmet,
für ihre immerwährende Unterstützung
und den grossartigen Rückhalt, den sie immer
darstellten.

This doctoral thesis is dedicated to my parents,
for their marvellous and neverending support.

Erklärung

Alle wesentlichen Tätigkeiten zur Diplomarbeit wurden am Max-Planck-Institut für Polymerforschung in Mainz durchgeführt.

Ich versichere, dass ich meine Dissertation selbstständig verfaßt und keine anderen als die angegebenen Quellen und Hilfsmittel benutzt habe.

Mainz, den 5th March 2007

Marcel Friedrich

Abstract

Membrane proteins play a major role in every living cell. They are the key factors in the cell's metabolism and in other functions, for example in cell-cell interaction, signal transduction, and transport of ions and nutrients. Cytochrome c oxidase (CcO), as one of the membrane proteins of the respiratory chain, plays a significant role in the energy transformation of higher organisms. CcO is a multi centered heme protein, utilizing redox energy to actively transport protons across the mitochondrial membrane. One aim of this dissertation is to investigate single steps in the mechanism of the ion transfer process coupled to electron transfer, which are not fully understood. The protein-tethered bilayer lipid membrane is a general approach to immobilize membrane proteins in an oriented fashion on a planar electrode embedded in a biomimetic membrane. This system enables the combination of electrochemical techniques with surface enhanced resonance Raman (SERRS), surface enhanced reflection absorption infrared (SEIRAS), and surface plasmon spectroscopy to study protein mediated electron and ion transport processes.

The orientation of the enzymes within the surface confined architecture can be controlled by specific site-mutations, i.e. the insertion of a poly-histidine tag to different subunits of the enzyme. CcO can, thus, be oriented uniformly with its natural electron pathway entry pointing either towards or away from the electrode surface. The first orientation allows an ultra-fast direct electron transfer(ET) into the protein, not provided by conventional systems, which can be leveraged to study intrinsic charge transfer processes. The second orientation permits to study the interaction with its natural electron donor cytochrome c.

Electrochemical and SERR measurements show conclusively that the redox site structure and the activity of the surface confined enzyme are preserved. Therefore, this biomimetic system offers a unique platform to study the kinetics of the ET processes in order to clarify mechanistic properties of the enzyme. Highly sensitive and ultra fast electrochemical techniques allow the separation of ET steps between all four redox centres including the determination of ET rates. Furthermore, proton transfer coupled to ET could be directly measured and discriminated from other ion transfer processes, revealing novel mechanistic information of the proton transfer mechanism of cytochrome c oxidase. In order to study the kinetics of the ET inside the protein, including the catalytic center, time resolved SEIRAS and SERRS measurements were performed to gain more insight into the structural and coordination changes of the heme environment.

The electrical behaviour of tethered membrane systems and membrane intrinsic proteins as well as related charge transfer processes were simulated by solving the respective sets of differential equations, utilizing a software package called SPICE. This helps to understand charge transfer processes across membranes and to develop models that can help to elucidate mechanisms of complex enzymatic processes.

Membranproteine spielen eine zentrale Rolle in jeder lebenden Zelle. Sie haben eine Schlüsselfunktion in vielen Prozessen, wie beispielsweise im Metabolismus von Zellen, der Zell-Zell Interaktion, der Signal Übermittlung und dem Transport von Ionen und Nährstoffen.

Cytochrome c Oxidase ist eines der Membranproteine in der Atmungskette und spielt eine wichtige Rolle bei der Energie-Transformation in höher entwickelten Organismen. Es ist ein Häm-Protein mit mehrere Redox Zentren, das die Energie der Redox Prozesse zum aktiven Transport von Protonen über die Mitochondrienmembrane nutzt. Ein Ziel dieser Arbeit ist die Untersuchung des Mechanismus einzelner Schritte des Protonentransfers, die an Eletronentransferprozesse innerhalb des Proteins gekoppelt sind.

Die sogenannte 'Protein-tethered Bilayer Lipid Membrane' ist ein universeller Ansatz zur Immobilisierung von Membranproteinen auf Oberflächen, eingebettet in einer vorgegebenen Orientierung und in ein biomimetisches Membransystem. Dieses System erlaubt die kombinierte Anwendung von elektrochemischen Techniken mit oberflächen-verstärkter resonanter Raman (SERRS), oberflächen-verstärkter Reflektions-Absorptions Infrarot (SEIRAS) und Oberflächenplasmonen Spektroskopie, um Elektronen- und Ionentransferprozesse von Proteinen zu untersuchen. Die homogen orientierte Immobilisierung der Proteine in dieser Oberflächen-gebundenen Architektur kann durch spezifische Mutationen, d.h. die Insertion eines Poly-Histidine Ankers an jeweils verschiedenen Untereinheiten des Enzyms, kontrolliert werden. Damit kann die Cytochrome c Oxidase entweder mit ihrer natürlichen Elektronenakzeptorseite zur Elektrode hin oder von ihr weg orientiert werden. Die erstgenannte Orientierung ermöglicht einen sehr schnellen Elektronentransfer (ET) zum Protein, der mit herkömmlichen Systemen so nicht möglich ist. Somit ist es möglich, intrinsische Prozesse des Proteins zu untersuchen. Die zweite Orientierung hingegen ermöglicht die Interaktion des Enzyms mit dem natürlichen Elektronenüberträger, Cytochrome c, zu untersuchen.

Elektrochemische und SERR Messungen zeigen eindrucksvoll, dass die Strukturen der redox-aktiven Zentren wie auch die Aktivität des Systems auf der Oberfläche nach dem Immobilisieren erhalten bleiben. Damit stellt dieses biomimetische System eine einzigartige Plattform da, mit deren Hilfe man die Kinetik von ET -Prozessen und die Mechanistischen Eigenschaften von Enzymen untersuchen kann. Elektrochemische Techniken erlauben die einzelnen ET -Schritte zwischen den vier Redox-Zentren der Oxidase aufzulösen und deren Geschwindigkeitskonstanten zu bestimmen. Des Weiteren konnte der Protonentransfer, der mit dem Elektronentransfer gekoppelt ist, direkt unabhängig gemessen werden. Damit war es möglich neue Informationen über den Mechanismus der Protonentranslokation der Cytochrome c Oxidase zu erlangen. Um die Kinetik des ET innerhalb des Proteins bis zum des katalytischen Zentrum zu untersuchen, wurden zeitaufgelöste SEIRAS und SERRS Messungen durchgeführt, um einen tieferen Einblick in die zeitabhängigen Veränderungen von Struktur und Koordination der Hämumgebung zu erhalten.

Das elektrische Verhalten von Oberflächenverankerten Membransystemen und der eingelagerten Membranproteine, wie auch die damit zusammenhängenden Ladungstransferprozesse, konnten simuliert werden. Dies war möglich durch eine numerische Lösung der Differentialgleichungen der genannten Prozesse mittels des Software-Paketes SPICE. Dies ist insbesondere für das bessere Verständnis dieser Prozesse hilfreich und auch um Modelle zu entwickeln, die dabei helfen können die Mechanismen von komplexen enzymatischen Prozessen aufzuklären.

Included Paper

This dissertation is based on the following eight scientific publications and manuscripts, which derived from the results obtained during my Ph.D. work. Copies of these papers are included in the appendix at the end of this thesis.

Paper 1

Frank Giess, **Marcel G. Friedrich**, Joachim Heberle, Renate L. Naumann, and Wolfgang Knoll
The Protein-Tethered Lipid Bilayer: A Novel Mimic of the Biological Membrane
Biophys. J., 87, 3213, (2004)

Paper 2

Marcel G. Friedrich, Frank Gieß, Renate Naumann, Wolfgang Knoll, Kenichi Ataka, Joachim Heberle, Jana Hrabakova, Daniel H. Murgida and Peter Hildebrandt
Active site structure and redox processes of cytochrome c oxidase immobilised in a novel biomimetic lipid membrane
Chem. Comm., 21, 2376, (2004)

Paper 3

Marcel G. Friedrich, Joseph W. F. Robertson, Dieter Walz, Wolfgang Knoll and Renate Naumann
Electronic Wiring of Membrane Proteins: A Kinetic Study of Cytochrome c Oxidase
Accepted by Biophys. J.

Paper 4

Marcel G. Friedrich, Markus Plum, Vinzenz Kirste, Bernd Ludwig, WolfgangK noll, Renate L. C. Naumann
In-situ Monitoring of the Catalytic Turnover of Cytochrome c Oxidase in a Biomimetic Architecture
Submitted to Biophys. J. (2007)

Paper 5

Marcel G. Friedrich, Vinzenz Kirste, Jiapeng Zhi, Robert B. Gennis, Wolfgang Knoll, Renate L. C. Naumann
Activity of Membrane Proteins Immobilized on Surfaces as a Function of Packing Density
Biophys. J. under review (2007)

Paper 6

Joseph W. F. Robertson*, **Marcel G. Friedrich***, Dieter Walz, Wolfgang Knoll and Renate Naumann
(*J.W.F. Roberston and M.G. Friedrich contributed equally to this publication*)
Modelling Ion Transport in Tethered Bilayer Lipid Membranes.
1. Passive Ion Permeation
Submitted to J. Phys. Chem. B (2007)

Paper 7

Vinzenz Kirste, **Marcel G. Friedrich**, Jiapeng Zhu, Robert B. Gennis, Wolfgang Knoll and Renate L. C. Naumann
Time-resolved Surface Enhanced Infrared Reflection Absorption Spectroscopy into electrochemically induced Electron Transfer to Cytochrome c Oxidase
In preparation

Paper 8

Marcel G. Friedrich, Wolfgang Knoll, Renate L. C. Naumann
Orientational Control of Direct Electron Transfer to Cytochrome c Oxidase monitored by surface enhanced resonance Raman (SERR) spectroscopy
In preparation

Contents

1 Introduction

Membrane proteins play central roles in the physiology of living cells. With the advances in genomic mapping, it has been revealed that ca. 20-30% of the genes of an organism encode for membrane proteins [1, 2]. These proteins are the key factors in the cell's metabolism, for example in cell-cell interaction, signal transduction, and transport of ions and nutrients [3]. Additionally, membrane proteins account for the two key reactions of biochemistry: respiration and photosynthesis [3, 4, 5]. Due to this important function, they are a preferred target for pharmaceuticals (currently more than 60% of consumed drugs). [6, 7, 8, 9] In fact, many hereditary and acquiring diseases have been attributed to defects in the functionality of membrane proteins.

Contrary to the fundamental role in biology, the experimental accessibility of membrane proteins remains challenging. Structural as well as functional characterization of membrane proteins is difficult due to their amphiphilic properties that interfere with crystallization necessary for X-ray crystallography. Although the first complete X-ray crystallographic analysis of an integral membrane protein was successfully carried out a number of years ago by Deisenhofer, Huber and Michel [10], the number of membrane proteins whose X-ray crystal structures are known is still very small and represents only 0.2% of all solved protein structures [11, 12, 13]. The limitation of solution-state NMR experiments to low-molecular-weight particles forces investigators to use organic solvents or detergent solutions rather than lipid bilayer systems. Obviously, all of these structural methods are unable to reflect the importance of the membrane water interface for the structural and functional properties of membrane proteins [14, 15].

Various model systems of the biological membrane address this issue. Reconstitution of membrane proteins into a lipid bilayer is a powerful tool for the analysis of functions as well as structures of membrane proteins. Solubilized membrane proteins are purified and reconstituted, i.e. reintegrated into an (artificial) lipid bilayer, which mimics their native environment in the plasma membrane. Membrane-related processes have attracted an enormous interest, but systematic studies of such complex systems are difficult and limited to only a few examples. The incorporation of purified membrane proteins into the classical liposomal or vesicular systems forms a so-called proteoliposome. This lipid bilayer encloses an inner cavity that allows the investigation of transport and/or catalytic properties of any membrane protein without interference by other membrane components. However, reconstitution into functional proteoliposomes has been an empirical domain and experimental difficulties arise when there is a need to control contents or solute concentrations of the inner compartment. The same holds for the application of a homogeneous transmembrane

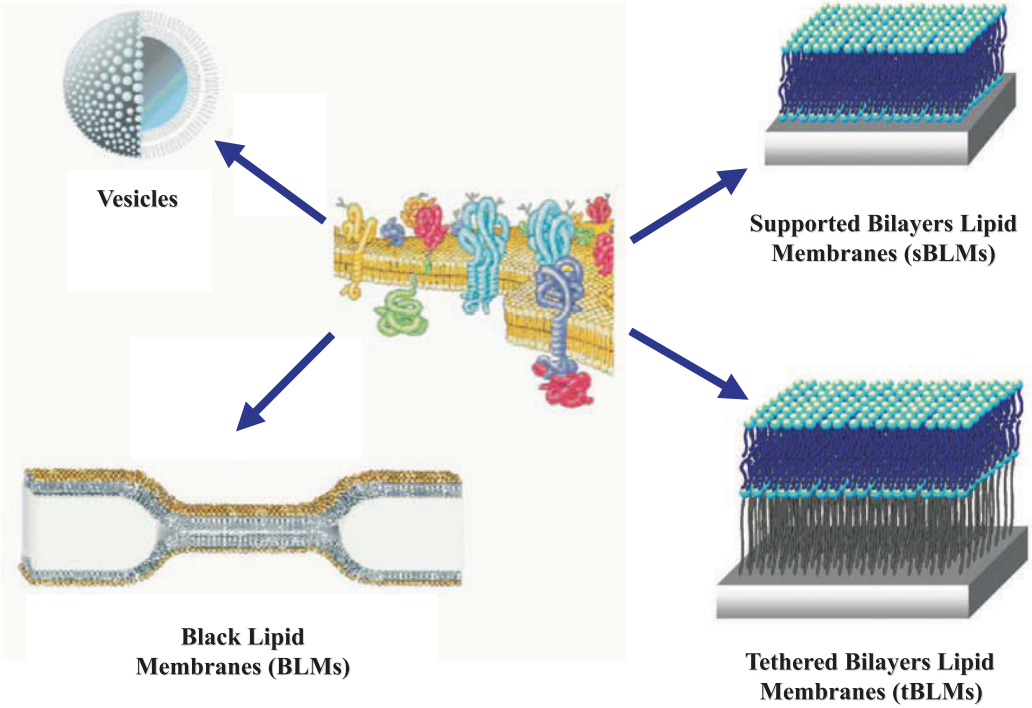

Figure 1.1: Biomimetic membrane systems

potential that is limited to the generation of a diffusion potential by the usage of ionspecific ionophores [16]. These problems do not arise when using black lipid membranes (BLMs) that provide equal access to both sides of a membrane. However, BLMs lack mechanical stability [17], which render this systems impractical for many applications, e.g. for biosenors. The incorporation of bigger membrane proteins, such as cytochrome c oxidase, is especially delicate in the case of BLMs. For all of these systems, it is impossible to apply surface-sensitive techniques such as ATR-FTIR, SERS, AFM, SPR, or QCM, and may never evolve to a routinely used and/or large-scale technology for biosensing or lab-on-a chip applications.

To overcome these problems and to provide a suitable platform for biosensing applications, the concept of solid-supported bilayer lipid membranes (sBLMs) has been proposed [18, 19]. In this concept, a lipid bilayer is directly placed on top of a solid support. If this support is an electrode, electrical characterization of the membrane is possible. The disadvantage of this system is the limited space between the membrane and the support, which is seldom sufficient to serve as an ion reservoir, needed for transport of ions to occur through the embedded membrane proteins. Moreover, proteins with large extramembrane domains cannot be incorporated without the risk of denaturation. In order to circumvent these limitations, new strategies for model membranes were developed, starting with hybrid-membranes, polymer-supported and tethered bilayer lipid membranes (tBLMs) [20].

tBLMs address the necessity of a submembraneous space providing both an ionic reservoir as well as adequate space for the incorporated membrane proteins [21, 22, 23, 24, 25, 26, 27, 28, 29]. The most demanding problem in tBLMs is to achieve electrical properties that are competitive with BLMs, i.e., show a capacitance of $0.5\ \mu F/cm^2$ and resistances $>1\ M\Omega cm^2$ [30, 25, 31, 28]. However, the tethering molecules inevitably apply diffusional constraints to the lipid molecules of the tBLM so as to prevent the membrane protein from diffusing freely and/or from undergoing conformational changes necessary for its biological activity. Furthermore, the tethering portion may not be compatible with bulky extramembraneous domains. Ion carriers and channel peptides were successfully incorporated into tBLMs. However, large complex membrane proteins proved difficult to insert in a functionally active form. Moreover, there is no possibility to control the orientation during reconstitution, which is a prerequisit for the study of vectorial charge transfer. Thus, membrane proteins display full activity only when they are inserted into a lipid bilayer in a defined orientation. As a consequence, none of the attempts made so far to incorporate membrane proteins into a tBLM have ever evolved into a system, permits quantitative assessment of their activity.

To address these chellanges a biomimetic membrane architecture was developed, the protein-tethered bilayer lipid membrane (ptBLM), which was designed to immobilize complex transmembrane proteins in strict orientations. The ptBLM is based on an nitrilo-tri-acetic acid (NTA)-functionalized surface, which, after chelation with Ni^{2+} or Cu^{2+} ions, reversibly binds proteins genetically engineered with histine(His)-tags. A lipid bilayer is then reconstituted *in-situ* around the bound proteins. In this novel approach, the transmembrane protein itself is attached to the support serving at the same time as a scaffold for a surrounding lipid bilayer membrane. Due to the protein-tethering architecture, this concept also provides, similar to the tBLM, an interstitial aqueous layer between the protein/lipid layer and the electrode. This interstitial space prevents the protein from interacting with the surface, and at the same time serves as a reservoir for ions.

2 Motivation

The aim of the present work is to study a complex membrane protein, such as cytochrome c oxidase in a functionally active state and on a quantitative basis. For this purpose, the protein had first to be immobilized in a biomimetic membrane system.

The protein-tethered bilayer lipid membrane, specially designed for this purpose, accounts for three key issues: 1) the orientational control due to the position of the introduced His-tag at the protein, 2) the submembrane space as an reservoir for ions and 3) the possibility to apply defined electric fields across the surface confined membrane. All of these conditions qualify the ptBLM to obtain quantitative information about charge transfer processes and conformational transitions in membrane proteins. One of the main objectives was to investigate electron transfer processes coupled to proton translocation, accompanied by structural changes within the active sites of redox-active membrane proteins. Cytochrome c Oxidase (CcO) serves as a model system for a multi-redox centered transmembrane protein (chapter 3). It is the final complex of the respiratory chain in mitochondria and bacterial cells. It catalyzes the 4-electron reduction of O_2 to 2 H_2O, and utilizes the considerable free energy of this reaction to generate a proton motive force across the membrane. For each molecule of O_2 reduced, 8 protons are taken up from the anodic side of the membrane, e.g. the cytoplasm in bacteria or the matrix of mitochondria, 4 of these protons are used to form H_2O and 4 protons are pumped across the membrane. Considering the significance of respiration for life science, this enzyme has been the subject of intense research for many years (for a review see ref. [32]). However, the mechanism of how electron transfer is coupled to the proton translocation is not yet completely understood.

In order to gain new insights into these processes, a bioelectronic coupling of CcO would be highly desirable. Direct electron transfer (ET) from the electrode to the enzyme would give information about ET pathways inside the protein up to the catalytic center. Such processes have been investigated in the case of soluble redox proteins [33, 34, 35, 36], using electrochemical methods, but these investigations have not been possible with membrane proteins so far. Electrochemical methods could be directly applied to CcO, provided the protein could be immobilized so as to selectively communicate with the electrode. This could be realized by immobilizing CcO in the ptBLM in different orientations. Site-specific mutations offer the possibility to introduce poly-histidine(His)-tag to different positions in the protein, which consequently allows an orientation of the natural electron entry either towards the electrode surface or away into the solution. The first case provides the possibility to access the redox centers of the protein by a direct (ET) from the electrode (chapter 5.4.1), triggering the redox state of the enzyme. This would permit the study of

electron transfer processes without the kinetic limitation of slow diffusion processes arising when soluble redox couples or mediators are used (chapter 5.6). Apart from the ET, the proton transfer associated with redox transitions could also be investigated. The inverted orientation will be used to study the interaction with soluble electron donors in the bulk solution (chapter 5.8). Both concepts are expected to provide complementary information about the mechanism of proton transfer CcO.

Various well-established and powerful electrochemical techniques are available for the determination of kinetic parameters of redox reactions [37] (chapter 4.1). However, the principle disadvantage of these approaches is that such purely electrical measurements lack molecular specificity. The electrochemical response indicates ET rates, but it provides no direct information about the identity of reaction products, intermediates, or structural changes during electron transfer processes. Important structural changes are associated with electron transfer and proton pumping, such as redox-linked changes in the heme structure or in amino acid side-chains [38].

Vibrational spectroscopies, such as Raman or infrared are techniques that provide such information. Vibrational modes reveal information about redox, coordination and ligation states of metal complexes, present in most redox active membrane proteins, such as heme proteins. X-ray crystallographic data help for the interpretation of these results. Infrared spectroscopy allows to probe conformational changes during the enzymatic activity of amino acids in close proximity to the active sites or along the electron and proton pathways in the protein. Raman spectroscopy with a resonant enhancement of the iron porphyrin system is able to study selectively the structural changes of the heme centers in the enzyme during catalytic activity.

Direct ET between electrode and enzymes requires a surface confinement of the system of interest. The ptBLM represent as a monolayer of proteins attached to the surface. The main disadvantage of vibrational spectroscopy is its low sensitivity as compared for example to other spectroscopic techniques, such as fluorescence, thus, requiring a high analyte concentration. To be able to reach a sufficient sensitivity to study a monolayer of protein, several enhancement effects, such as surface and resonant enhancement, have to be utilized to increase the signal. By applying surface-enhanced resonance Raman spectroscopy (SERRS) or surface enhanced infrared reflection absorption spectroscopy (SEIRAS), it is possible to to achieve the sensitivity required to effectively monitor the spectroscopic response of the interfacial region.

These spezialized spectroelectrochemical investigations require special equipments dedicated to the purpose described above. Therefore, different experimental setups have to be established, to combine both *in-situ* surface-enhanced resonance Raman spectroscopy (SERRS) or surface-enhanced infrared reflection-absorption spectroscopy (SEIRAS) with electrochemical measurements (chapters 5.2 and 5.7.2). Complementary information can be expected to be characteristic for redox linked changes in the enzymes immobilized in a

ptBLM. The possibility of direct electrochemical triggering of the enzymatic redox states would further open the way to perform time resolved spectroscopy. This could give insight into structural changes of the active sites of electron and proton transfer pathways. These spectroelectrochemical measurements in a time resolved regime could therefore contribute to the ongoing debate about the mechansim of CcO.

3 Cytochrome c oxidase

Cytochrome c oxidase (CcO) is the terminal complex of the respiratory chain of mitochondria and many bacteria. In many species, including mammalian mitochondria, CcO contains two prosthetic heme a groups, for that reason it is also called cytochrome aa_3. Being responsible for catalyzing more than 95% of the oxygen taken up by aerobically growing higher organisms, CcO is an efficient energy-transducer. However, despite a long history of investigation the mechanism of charge transfer of this enzyme is not completely understood yet [39, 40] . It acts as a redox-driven proton pump, which couples the free energy of the catalysed reduction of oxygen into water to the generation of a transmembrane difference in electrochemical potentials of protons ($\Delta\tilde{\mu}_{H^+}$). The energy of the proton translocation processes is given by:

$$\Delta_R G = -n \cdot (\Delta\mu_{H^+} + F\Delta\Psi) = -n \cdot \Delta\tilde{\mu}_{H^+} \tag{3.1}$$

with $\Delta_R G$ being the free reaction enthalpy of the redox process, transfered into a electrochemical potential of the protons ($\Delta\tilde{\mu}_{H^+}$), μ_{H^+} the free enthalpy of the proton, $\Delta\Psi$ the transmembrane potential, F the Faraday constant and n the net number of translocated protons.

The resulting energy of the proton translocation processes, that is transfered into the electrochemical potential difference, drives the ATP syntethase in order to transform ADP into ATP, the energy currency in every living organism. The complexity of cytochrome c oxidase is reflected by its subunit structure and energy transduction pathways. The diversity of bacterial enzymes has fostered the notion of a large family of heme-copper terminal oxidases that utilize the same strategy by preserving the same pathway for electrons and protons through the enzyme. This chapter summarizes the state of the knowledge about the structure, the function as well as the enzymatic cycle of CcO. The enzymatic cycle is controversially discussed in the literature and the aim of this thesis is to provide further insight into this mechanistic processes.

3.1 The Repiratory Chain

The main function of the respiratory chain in every living organism is to transfer the energy of oxygen reduction by NADH, a strong reductant, into a highly energetic compound, namely ATP [1], that drives all the essential processes in the organism, such as muscle con-

[1] The process performed by the respiratory chain is also known as oxidative phosphorylation, which refers to the energy transfer of the electron transfer (ET) process to oxygen, which is reduced to water, the

traction, nerve excitation as well as transport of ions and nutrients [3]. NADH in turn is formed in a sequence of metabolic reactions from glucose and other nutrients in the citric acid cycle which are thus consumed to form ATP.
The overall process of aerobic breakdown of nutrients yields more energy than the breakdown with any other available oxidant. However, the problem with oxygen as an oxidant is that it forms during its reduction oxygen radicals that are extremely toxic and dangerous for the organism. Therefore, specialized enzymes have been evolved during evolution to catalyse the complete O_2 reduction in a controlled fashion, without releasing dangerous intermediates of O_2 breakdown. These enzymes comprise the so-called respiratory chain [3].

The mitochondrial respiratory chain[2] 3.1, is composed of energy-transducing, multi-subunit transmembrane proteins, designated complex I-IV and mobile electron carriers, which shuttle electrons between the complexes [41]. In eukaryotes, these enzymes are located in the inner membrane of the mitochondria. In bacteria and archaea, they are found in the cytoplasmic membrane. The membranes which house these enzymes are composed of lipid bilayers that are highly impermeable to charged molecules.

In the citric acid cycle the redox energy of carbohydrates, amino acids or fatty acids, provided by food uptake and their digestion, is transformed and stored in highly energetic redox compounds, such as NADH or FADH [3], which have a strong potential for donating electrons.

The respiratory enzymes control with their electron transport chain the passage of electrons from these compounds across the membrane and mediate the reaction of the electrons with O_2. Electron transfer from NADH to molecular oxygen is highly exergonic, so that a large amount of energy is gained when electrons are transported along the respiratory chain from NADH to dioxygen.The enzymes of the respiratory chain conserve this energy by translocating protons across the membrane thereby generatig a difference of electrochemical potential of the protons. This difference, $\Delta\tilde{\mu}_{H^+}$, consists of a chemical part, $\Delta\mu_{H^+}$, or the pH difference, and an electrical part, $\Delta\Psi$, being the potential difference across the membrane. Hence, the membrane plays a crucial role in this system in which the proton concentration gradient can be established. The redox reactions proceed downhill the redox potentials, these exergonic reations ($\Delta_R G < 0$), thus, providing the required energy to transfer the protons across the membrane. The stored energy is further utilized to drive ATP synthesis in the ATP syntethase. The theory, comprising the principle of coupling ET processes to the generation of the stored energy $\Delta_R G\Delta = -n \cdot \tilde{\mu}_{H^+}$, which is used to drive the ATP synthesis, was first proposed by Peter Mitchell and is called chemiosmotic theory [42].

The first complex in the respiratory chain (Fig. 3.1) is complex I, the NADH-ubiquinone

energy that drives the phsosphorylation of ADP into ATP.
[2]The respiratory chain is located in the cristae of the inner membrane

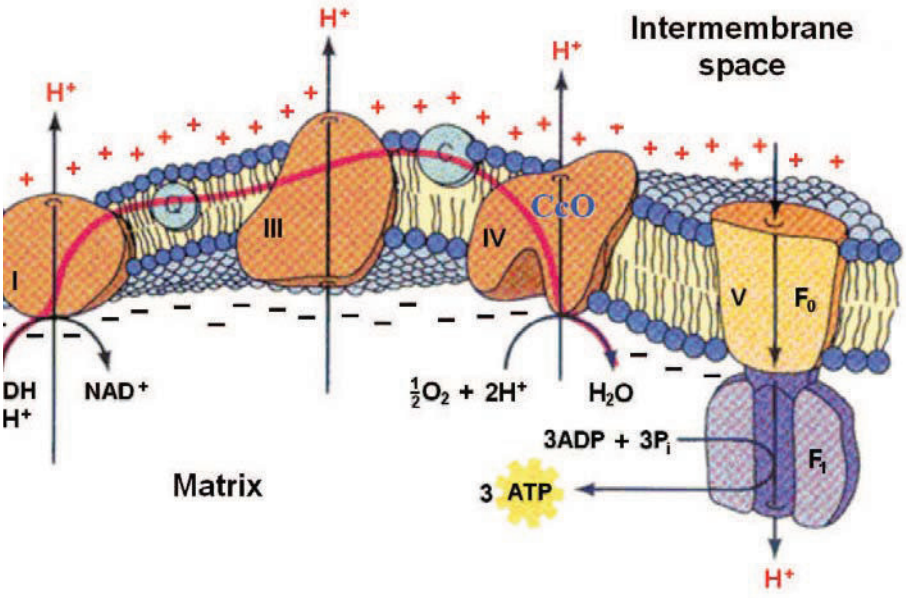

Figure 3.1: The respitory chain in Mitochondria [3].

oxidoreductase, which transfers electrons from NADH to ubiquinone (UQ) and couples this redox reaction to translocation of protons across the membrane [3]. Complex II, the succinate-ubiquinone reductase, is also a component of the citric acid cycle. It catalyzes the ET from succinate to ubiquinone. The enzyme is anchored in the membrane but does not contribute directly to the formation of a concentration difference of protons across the (mitochondrial) membrane ($\Delta\tilde{\mu}_{H^+}$). Complex III, the ubiquinol-cytochrome c oxidoreductase, is commonly referred to as the cytochrome bc_1 complex. The cytochrome bc_1 complex translocates one proton per electron transfered to cytochrome c across the membrane . The mechanism by which this enzyme couples ET to proton translocation is called the protonmotive Q cycle [3, 43].
Complex IV, the cytochrome c oxidase, is the last enzyme of the mitochondrial respiratory chain. This cytochrome aa_3 type of oxidase catalyzes the reduction of dioxygen to water. Furthermore, it couples this redox reaction to the translocation of one proton across the mitochondrial membrane per each electron transported to dioxygen [44, 3, 45].

In the mitochondrial and bacterial respiratory chain there are two mobile electron carriers, the ubiquinone and cytochrome c. Ubiquinone is a small, hydrophobic, two-electron and two-proton carrier present in the lipid membrane. Due to its small size and hydrophobicity, it is freely diffusible within the lipid bilayer and can shuttle reducing equivalents between the less mobile enzyme complexes. It is composed of a benzoquinone ring, which is directly involved in the redox reactions, and a highly hydrophobic isoprenoid tail, which accounts for its hydrophobic nature. The number of isoprene units present in the native ubiquinone molecule varies with species. The ubiquinone molecule can accept or donate either one or two electrons. When a proton and an electron are transferred to the fully

oxidized ubiquinone (UQ), the neutral half-reduced semiquinone ($UQH\bullet$) is formed. The fully reduced ubiquinol (UQH_2), carries two electrons and two protons. Ubiquinol is able to act between two electron donor and one-electron acceptor systems.

Cytochrome *c* (cyt c) is a small soluble protein with a covalently attached prosthetic heme *c*. It is a one-electron carrier that is found in the mitochondrial intermembrane space or periplasm of bacteria and transfers electrons between the cytochrome bc_1 complex and cytochrome *c* oxidase. Cyt c diffuses between these complexes and alternately binds to both enzymes during ET. Positively charged lysine residues surround the heme crevice on the surface of cytochrome. These interact with anionic residues on the two enzymes, complex III and IV, to direct cyt c while binding it in order to receive or to donate an electron.

3.2 Structure and Function

Crystallization and X-ray diffraction analysis of several bacterial Cytochrome *c* oxidases have led to a better understanding of the complex function of this enzyme. Until today the structures of five different CcO types have been solved [46, 47, 48, 49, 50, 51, 52] down to a resolution of about 2.8 $\mathring{A}$, revealing a striking degree of similarity among them. The enzymes from *Paracoccus denitrificans* and *Rhodobacter sphaeroides* may be viewed as simple bacterial model systems that perfectly match the mitochondrial enzyme, at least in all the basic enzymatic functions [38].

Cytochrome *c* Oxidases generally have a common two-subunit (SU) core which corresponds to the two mitochondrially encoded subunits of the eukaryotic cytochrome *c* oxidase [54, 55]. Bacterial CcO has usually only one additional subunit contrary to the eukaryotic CcO that has a more complicated structure. For example, cytochrome *c* oxidase from bovine heart mitochondria has ten subunits in addition to the three subunit core. Despite their simpler structure, bacterial enzymes function similarly to the mitochondrial enzyme. To date, site-specific mutagenesis of bacterial oxidases combined with a variety of spectroscopic methods has provided a wealth of information about the structure and function of these enzymes [56]. The elucidation of the crystal structures of cytochrome *c* oxidases from both bovine heart mitochondria and *P. denitrificans* improved the structural understanding of these enzymes and provided a better basis for functional studies [46, 47, 48]. The studies in the framework of this thesis employ the smaller bacterial versions (125 kD) of cytochrome *c* oxidase from cell membranes of bacteria, e.g. *Rhodobacter sphaeroides* [57] or *Paracoccus denitrificans* [58] as model systems of the 500 kD large CcO complex located in the inner mitochondrial membrane of higher organisms [47]. According to X-ray crystallography [38, 47, 57, 58] , all of these versions are identical with respect to the structure and function of their electron and proton translocation pathways. The similarity between mitochondrial and bacterial CcO originates in their close evolutionary relationship [59, 60].

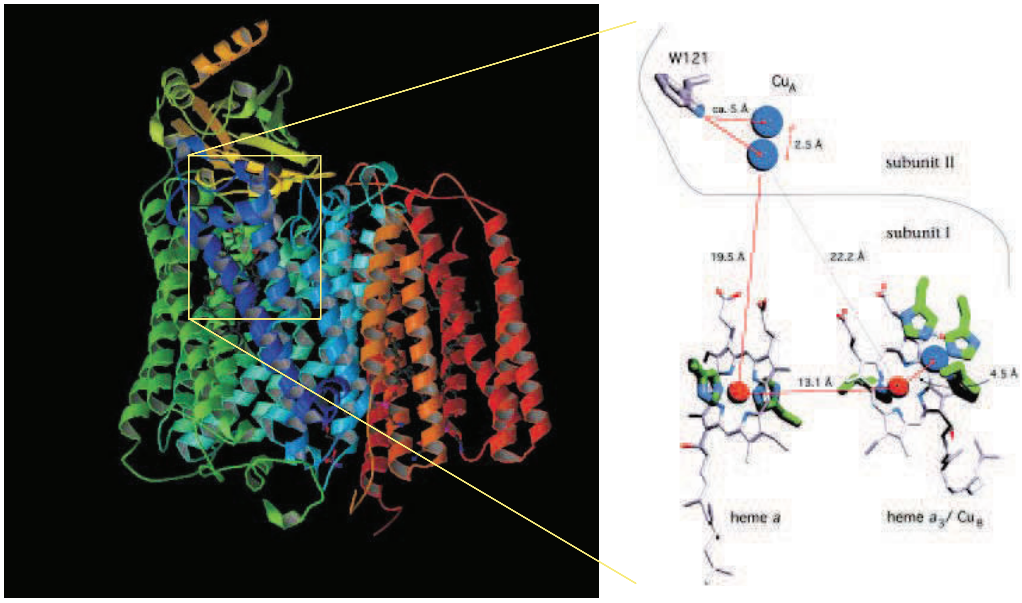

Figure 3.2: Cytochrome c oxidase from *Paracoccus denitrificans*. The enzyme consists of three subunit (SUs), whereas SU I and SU II embedd the four redox centers (Cu_A, heme a, heme a_3 and Cu_B) [53]

.

Subunit I (SUI) is largely embedded in the membrane and contains three of the four redox centers of the enzyme, two a-type hemes and Cu_B. They are liganded by amino acid side chains of this subunit and are located at about one third of the membrane depth from the periplasmic surface (Fig. 3.2). Two histidines provide the axial ligands to the low-spin heme a, whereas a histidine and a presumed hydroxyl or a water molecule provide ligands to the high-spin heme a_3 moiety. Both hemes are oriented perpendicular to the membrane plane with an edge to edge distance of 4.7 $\AA$ to 13.2 $\AA$, depending on the kind of oxidase, between both iron atoms [38]. Heme a_3, together with a copper ion (Cu_B) in its immediate vicinity forms the binuclear center where oxygen binding and reduction take place. Both in the oxidized and the reduced form of the enzymes, the copper ion is chelated by three histidines, with a distance of 4.5 - 5.2 $\AA$. Subunit II is L-shaped and is composed of two Cu ions in a mixed-valence state (Cu^{1+}/Cu^{2+}) with an median distance of 2.6 $\AA$ [38]. Subunit III is fully embedded in the membrane and in both bacterial and eukaryotic CcO, SU III does not contain any prosthetic group so that its importance for the enzyme is largely unkown. The lone standing subunits I and II from *P. denitrificans*, for example, have been shown to be fully active and able to translocate protons [38]. However, based on gene deletion studies it was proposed that SU III is needed for the correct assembly of the enzyme and it may also stabilize the mature oxidase [61, 38]. In addition to the three mitochondrially-encoded subunits, CcO from bovine heart mitochondria has ten nuclear-encoded subunits. The importance of these subunits for the eukaryotic oxidases is not known but it has been suggested that they have stabilizing and regulatory functions [38, 62].

Based on a large variety of spectroscopic and kinetic data [63, 64, 65, 66] it is generally accepted that the internal ET in the enzyme proceeds in four repective steps form the Cu_A center located in SU II to the three redox sites in SU I, heme a and then to the binuclear center composed of heme a_3 and Cu_B, where the reduction of O_2 to water is catalyzed. The reaction catalysed by cytochrome c oxidase can be summarized as follows:

$$O_2 + 4e^- + 8H^+_{cytoplasm} \xrightarrow{CcO} 2H_2O + 4H^+_{periplasm} \tag{3.2}$$

For the catalysed reaction, i.e. the reduction of one oxygen molecule to water, four electrons are consumed from the outer side of the membrane and eight protons from the inner side, leading to a charge separation of eight charges per turnover across the mitochondrial membrane. This gives rise to bring about a membrane potential of $\sim$ 50 mV [67] and a proton gradient across the membrane of up to 4 pH units in the mitochondria [3]. The main feature of CcO is that it functions as a proton pump, which translocates one proton across the membrane per each electron transported to dioxygen [3, 64].

For water formation, four electrons and four protons are required. However, when catalyzed by CcO, four additional protons are translocated from the inner cytoplasmic to the outer periplasmic side of the membrane [68, 69]. The enzyme thus contributes to the electrochemical potential difference by removing four negative charges from the outer side and eight positive charges from the inner side, releasing four of the positive charges to the outer side. The net charge translocation is eight positive charges from the inner to the outer side. The four protons, that are used for the water formation, must be transported over approximately 30 $\AA$ to the active site, whereas the pumped protons must be driven over the entire distance of 50 $\AA$ across the membrane [70]. Electron transfer from the periplasm initiates the catalytic cycle. The complete turnover, i.e. the conversion of an oxygen molecule, is completed in approximately 4 ms [71].
In order to accomplish a turnover, specific changes at the active site must trigger chemical and physical changes throughout the protein, including alterations in amino acid side chain orientations, hydrogen bond lengths, and protonation states. These structural changes must occur in a carefully controlled, coordinated and sequential fashion. Neither of these structural changes nor their precise sequence is known. This sequence of structural changes constitutes the mechanism. It is believed that the principal aspects of the mechanism are the same for every member of the enzymatic family to which CcO belongs [72]. Furthermore, it is likely that aspects of CcO´s proton pumping mechanism can be universally found in other proton translocating enzymes.

The stoichiometry in equation (3.2) was first determined by Wikstroem in 1977 through experiments on intact mitochondria [68]. Since then, with the advances of techniques in molecular biology and biophysics, the focus has shifted from studying CcO within whole organelles to direct molecular approaches. What remains unknown, however, is how, on a molecular level, the redox reactions of the respiratory chain, in particular of CcO, are cou-

pled to the generation of a transmembrane gradient, which is one of the issues of this thesis.

The heme a is coordinated by two histidines and resides approximately 13 $\mathring{A}$ from the periplasmic membrane surface at an angle of about 35 $\mathring{A}$ with respect to the membrane normal. ET from Cu_A to heme a contributes to the transmembrane potential [73]. The heme a_3 is a high-spin heme, which is coordinated by a single histidine. Heme a_3 is at equal depth to heme a within the membrane, i.e. also 13 $\mathring{A}$ from the periplasmic membrane surface. The heme porphyrin planes face each other at an angle of 104°, with heme ions separated by about 14 $\mathring{A}$ and an edge-to-edge distance of only 4.5 $\mathring{A}$. Electron at heme a_3, laterally within the membrane, does not contribute to the transmembrane potential, since only charge transfer across a dielectrica, here the membrane, contributes to the establishment of a potential difference. Heme a_3 together with Cu_B comprises the binuclear center, the site at which O_2 is bound and converted to water [74, 70]. The iron of heme a_3 [75] is ligated by two histidines in SUI. The coordination of iron porphyrine centers with histidines is a general principle in all oxidase analogas [59].

3.3 The Electron Pathway

The initial step of the catalytic/enzymatic process is the binding of cytochrome c at SU II of cytochrome c oxidase, close to the Cu_A center at the intermembrane side in the mitochondrea or the periplasmic site in bacteria [76, 43]. This binding is accompanied by ET to CcO. Mutations have shown, that the electrons exclusively enter via the Cu_A center of the mitochondrial as well as that of the bacterial oxidase [38]. cyt c is directed via a long-range electrostatic attraction and preorientation between the cyt c, which has a large number of positively charged lysine residues around the heme crevice, and CcO that has an accummulation of acidic and negatively charged amino acids on the surface of SU II close to the Cu_A site [77, 78, 4, 79]. This preorientation, which was confirmed by differenent mutation experiments [38, 77, 78, 79], is required for an efficient ET after the binding step. It was shown by a series of specific mutation experiments [80, 77, 78, 79] that the electron entry site of CcO is a tryptophan residue at the docking side of cyt c which leads the electron to the first redox site, the Cu_A center. This center is located at a distance of about 5 $\mathring{A}$ from the binding side [38]. The further path leads from the reduced Cu_A center to the low-spin heme a iron in SUI, which has a distance of about 19.5 $\mathring{A}$ [38], is a fast ET process of about 100 μs and an exchange rate of about 10^4 s^{-1} [81]. The big advantage of hemes in ET processes it that an electron can be delocalized over the conjugated porphyrin ring system, stabilizing the presence of the charge in the low dielectric protein environment [82].

The electron transfer cascade within the enzyme is followed by a reduction of the binuclear site, comprised by a high-spin heme a_3 and Cu_B, via the heme a center. Both heme sites are separated by a distance of only 4.5 $\mathring{A}$. It is not known to what extent specific bonds in the protein are used as ET pathways [83, 84] or whether electrons tunnel between the redox centers [85, 86]. In either case, amino acid side chains may facilitate the ET process.

The observed ET time constants, between Cu_A and heme a in CcO, are 50-120 μs [87, 88] and from heme a to heme a_3 about 3-50 μs [89, 90, 91, 88]. These ET processes are coupled to slow events, e.g. proton uptake and/or structural changes, which limit the rate of ET [86, 92]. The coupling of ET to proton uptake implies that it is the proton uptake events, which are the rate-limiting steps that control O_2 catalysis [93].

3.4 The Enzymatic Cycle

The catalytic cycle of cytochrome c oxidase is divided into two phases. The first phase is a 'reductive phase', reductive with respect to the enzyme. This part of the catalytic cycle fills the redox sites with electrons. A second so-called 'oxidative phase' follows, where oxygen is bound and reduced (Fig.3.3 and 3.4) [44, 56, 45, 94]. The reduction of O_2 begins when the two-electron reduced binuclear site binds O_2. Dioxygen enters the binuclear site by first binding transiently to Cu_B and after that to Fe_{a3} [38]. The initial ferrous heme-oxy intermediate A was first observed by Chance *et al.* [95] using low temperature kinetic methods. The initial binding of dioxygen to Fe_{a3} is weak [95, 38]. However, in the next redox step dioxygen is trapped kinetically by an extremely fast ET from Fe_a to dioxygen-bound Fe_{a3} [38]. The resulting intermediate, state P, was initially proposed to be a ferric peroxy $O-O$ form of the binuclear center [38]. However, recent resonance Raman spectroscopic studies [44, 96] and mass spectrometric work [97] have shown that the $O-O$ bond is already broken in this intermediate. The next step, the oxy ferryl intermediate F is formed [38]. Finally the fourth electron moves to the binuclear site and the fully oxidized enzyme (O-state) is generated [56, 44].

A total of four protons are needed to complete the reduction of O_2 to two water molecules, which provides the driving force for the pumping of four protons. There is an ongoing controversy [98, 99, 100, 101, 82] about the definitive assignement of proton pumping to particular steps of the catalytic cycle, impeding identification of the source of the driving force needed to pump protons [102, 99].
The catalytic cycle can be divided into a set of spectroscopically observable intermediates [103, 74]. A scheme of the catalytic cycle, based on that of Ref. [94], is shown in Figure 3.3. The six transitions described correspond to the entry of the four electrons from cytrochrome c, the binding of O_2, and the cleavage of the O=O bond. The nomenclature of all these states has not yet been standardized, but O, E, R_2, A, P, and F are used here. The names and identities are correlated below. These six states display distinct characteristic visible absorbance changes when the metal cofactors undergo changes in valence, spin and ligation [74, 104]. In addition, these visible absorbance changes have been correlated to characteristic resonance Raman spectra of the oxygen adducts to heme a_3 [105]. Figure 3.3 depicts some of the changes at the active site, including the valence states of the metal centers, during the transitions between these six states. The state O, when all metal centers being oxidized, serves as a spectroscopic reference. It is not clear what adducts are bound to the binuclear center. The delivery of the first electron, passed from

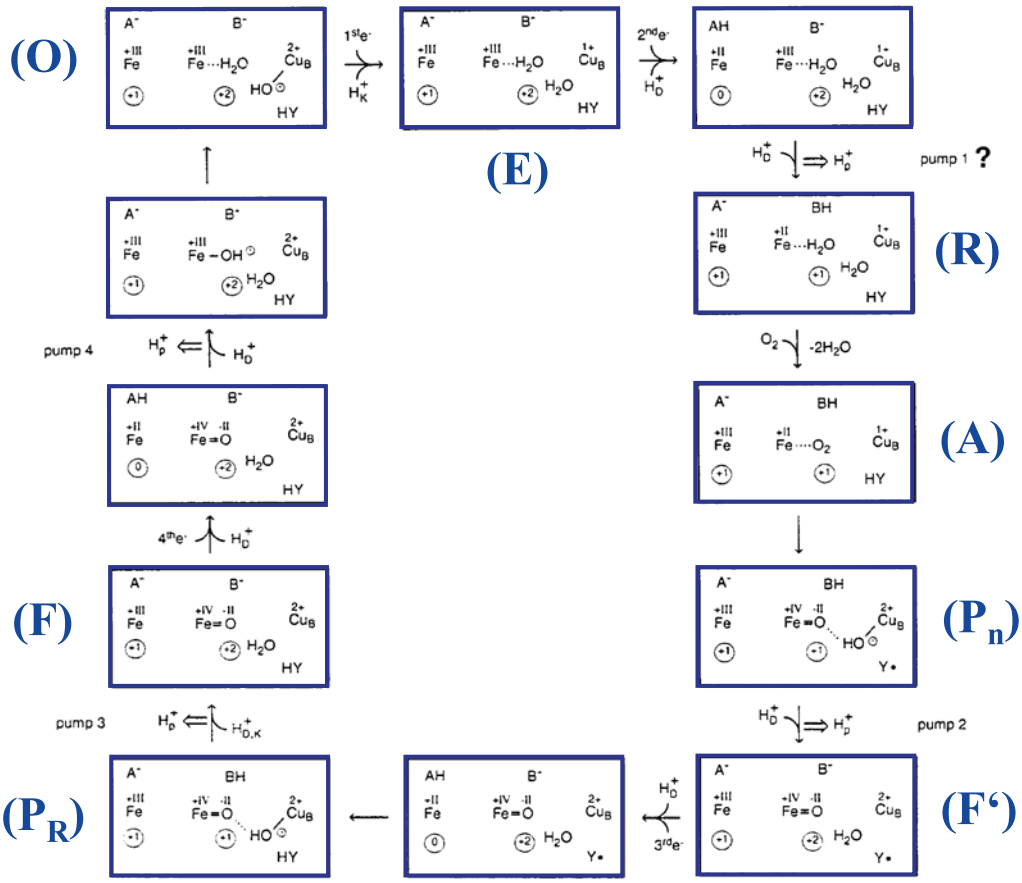

Figure 3.3: Proposed reaction scheme of the catalytic center during enzymatic activity. The single states are coloured in blue. (Modified from [94])

Cu_A along the electron pathway, reduces the binuclear center. This state is the E-state, the one-electron reduced state. The ET, in particular the ET step from Cu_A to heme a [106] or from heme a to heme a_3, is rate-limited by the uptake of a proton through the K pathway [107], manifested as a transfer rate that is inversely proportional to the solution pH [108]. Although depicted in Figure 3.3 as residing on Cu_B, in reality this electron is probably shared by Fe_{a3} and Cu_B [109, 110, 102]. In addition to equilibration of the electron, equilibration of the hydroxide adduct, a switch from Cu_B to Fe_{a3} is assumed [110].

E is one of the states mostly examined by backflow experiments [111, 112], i.e. by driving the two-electron state back to the one-electron state. This is achieved by binding carbon monoxide (CO) to the iron of the reduced heme a_3, where O_{2s} usually binds. In the two-electron reduced enzyme, heme a_3 is reduced while heme a is oxidized. The dissociation of CO from heme a_3 results in a transient change in the heme a_3 redox potential, which initiates the backflow of electrons from heme a_3 to heme a. CO binds to CcO at heme a_3,

the physiological location of binding. The combination of a laser pulse to dissociate the Fe-CO bond and time-resolving spectroscopy makes it possible to follow the changes in and around the binuclear center that are caused by CO photolysis. In this case, the reduction potential of heme a is higher relative to that of heme a_3 after dissociation of CO from heme a_3. First, an electron is transferred from heme a_3 to heme a, i.e. the opposite direction to that of the from physiological ET. This ET has a time constant of approximately 3 μs [112]. The ET proceeds further backwards to Cu_A with a time constant of approximately 35 μs [112]. A multitude of CO-photolysis experiments have been performed using visible, infrared and Raman spectroscopy under various conditions [91]. E can also be formed by chemical treatment, i.e. sequential exposure of protein solution in O_2 to H_2O_2 and then CO [113], although the resulting E population can be rather unstable [102].

After the uptake of the second electron and a proton, the enzyme reaches a two-electron reduced state, R_2. (The D- and K-pathway are both likely to be involved in this step [102, 114, 110]. Proton pumping occurs during this transition [99, 115, 102], although it remains unclear whether or not the energy of a previous turnover is used to accomplish the translocation. The intermediate E is also termed 'mixed-valence', because the valence of the four metal centers are mixed: Cu_A and heme a oxidized but heme a_3 and Cu_B reduced, i.e. metal center valences (Cu_A^{2+}) , heme a_3^+, heme a_3^{2+} and Cu_B^{1+}. In the T state, CcO is able to bind CO to the iron of the reduced heme a_3, producing R_2CO, also termed the 'CO-mixed-valence' state. The $Fe_{a3} - CO$ bond can be photolyzed, initiating electron backflow to heme a. In the absence of O_2, photolysis of the R_2CO enzyme results in E. In the presence of O_2, photolysis of R_2CO initiates the reaction of R_2 with O_2.

The physiological R_2 state is often modeled by the fully-reduced state, R_4. This state is created by supplying O with four electrons in the absence of O_2, e.g. by using chemical reductants such as sodium dithionite ($Na_2S_2O_4$). This fully-reduced state (R_4) has a valence configuration of $(Cu_A)_2^{1.5+}$, Fe_{a2}^+, Fe_{a3}^{2+}, and Cu_B^{1+}. A variety of adducts can be bound to Fe_{a3} in R_2 or R_4 , including CO and CN-. R_4 is more stable than R_2 and easier to create homogeneously. CO photolysis from Fe_{a3} R_4CO does not result in electron backflow, but certainly causes a cascade of structural changes. In the presence of O_2, photolysis of R_4CO liberates R_4 for reactions with O_2.
After the uptake of two electrons, associated with an uptake of one proton, oxygen can bind to the binuclear center, forming the A intermediate, which because of the ferrous-oxa Fe_{a3} has also been termed 'oxy' [74, 116]. A characteristic Raman band at $571cm^{-1}$ has been assigned to the $O = O$ vibration of $Fe_{a3}^{3+} - O = O$ in A [117, 105].

Once O_2 is bound to heme a_3, the $O = O$ bond is rapidly split and the resulting intermediate is called P. This intermediate has an oxoferryl configuration for heme a_3, i.e. $Fe_{a3}^{4+} = O_2$- [97]. The name P, which has also been called compound C [95], origninates from the incorrect speculation that this intermediate had an peroxy structure, i.e. $Fe_{a3} - O - O$. The transition from A (Fe_{a3}^{3+}-O=O-Cu_B^+) to P ($Fe_{a3}^{4+} = O_2 - Cu_B^{2+}$) requires more electrons than the two electrons externally injected in the catalytic cycle before. The third electron

is thought to be provided from an internal electron rearrangement, i.e. from somewhere within the protein. The donor of this electron remains unknown. It is considered highly unlikely that heme a_3 or Cu_B supply the electron. It is speculated that the source is the histidine-tyrosince active site pair [118]. Neither proton uptake nor proton translocation are speculated to occur during the transition from A to the P state.

There are three forms of P, namely PM, PR and PH, distinguished by the methods of generating the intermediates. From the reaction with O_2 of the R_2 and R_4 forms, PM and PR result, respectively [119]. pH can be generated by exposing a solution of the enzyme in O to a buffer solution containing a low concentration of H_2O_2 [116, 120, 121]. PH seems indistigushable from PM by visible absorbance and resonance Raman spectroscopy [96, 105], while PM and PR exhibit subtle differences in visible absorbance kinetics in the reaction with oxygen upon CO-photolysis [122]. Specific structural differences between PM and PR are not yet known. It is, however, speculated that they differ by the protonation of the tyrosine that is envolved in the ET process and located close to the binuclear center. After accepting a third electron by the external donor, such as cyt c, and the uptake of another proton, the F state is formed. Similar to the P state, the F state has an oxoferryl structure, i.e. $Fe^{4+}_{a3} = O_2$, with a characteristic $Fe - a3^{4+}$=O vibration mode at $786cm^{-1}$ [123, 105]. P and F both have a $Fe^{4+}_{a3} = O_2$- structure, however, their Raman and visible absorbance spectra differ considerably. The externally donated electron is thought to resolve the radical at the histidine-tyrosine pair [124, 125]. In addition, at least one proton is pumped in the P to F transition [103, 82, 98] and hence there is much interest in identifying the aspects of structural differences between P an F that reflect proton pumping [125, 118, 82, 126].

As with P, there are multiple forms of F with spectroscopic variations depending on how the state is created. F can be observed transiently in the reaction with O_2 following photolysis of R_2CO or R_4CO, resulting in FM and FR, respectively, each with subtle differences in visible absorbance kinetics [122].

The last step of the catalytic cycle is the receiving of a final externally donated electron and the uptake of a proton. The heme a_3 adduct is reduced and lost as a water molecule, at least one proton is pumped, O is regenerated and the cycle is completed.

Protons are taken up from the cytoplasm and transported to the binuclear center, buried deep within the protein interior, where protons are needed for the catalytic reaction, however, the mechanism of proton pumping is poorly understood. It is assumed that the transferred protons are proceeding via a a so-called Grotthus-type hopping mechanism through the enzyme [129, 130], along hydrogen bonds provided by a chain of water molecules and certain amino acid residues of the enzyme. Molecular dynamics simulation have been carried out and could demonstrate plenty of water embedded inside CcO, in particular along the pathway that is assigned to the proton translocation, in accordance to X-ray crystallographic findings. [131].

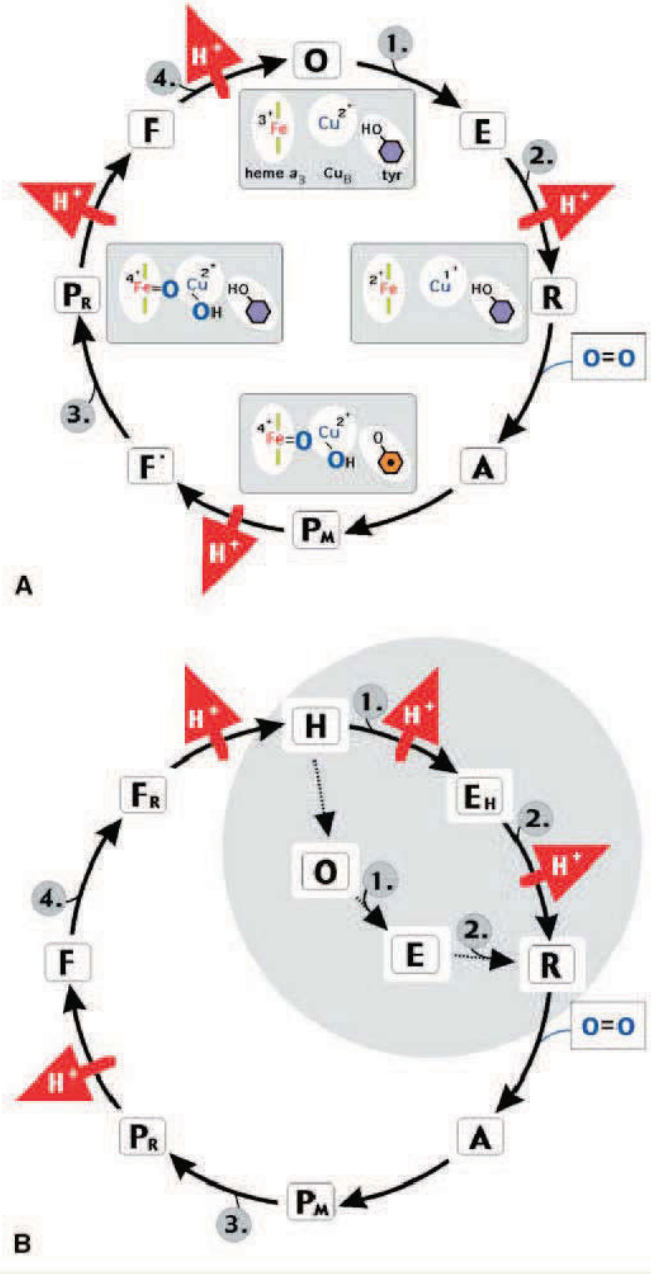

Figure 3.4: Enzymatic cycle of cytochrome c oxidase proposed by (a) Michel et al. [98, 115, 100] and (b) modified cycle proposed by Wikstroem et al. [127, 128]. The intermediate states are displayed with their electronic configuration at the binuclear center (gray boxes). The four electron entry steps (gray circles) are numbered, and transmembrane proton translocation steps highlighted by red arrowheads. For further details, see text. Figure is reproduced from ref. [38].

Both a direct and an indirect coupling mechanism have been proposed for redox-linked proton translocation in cytochrome *c* oxidase (Krab1987,Morgan1994). In the direct coupling system one of the redox-active prosthetic groups is directly involved in proton pumping. In the indirect coupling mechanism, the energy from the redox chemistry is transmitted by conformational changes of the proteon structure allowing the pump element to be located at some distance from the redox center.

Recently, Rich *et al.* [132] proposed a general model for direct energy coupling in the heme-copper oxidases, which they called the 'glutamate trap'. This model is based on the principle of electroneutrality, where all electron transfers to the binuclear site are made electroneutral by protonation changes [133]. When electrons are transported to the binuclear site protons are taken up into the 'trap' from the proton-input side of the membrane to maintain electroneutrality. The chemical transformation of dioxygen and subsequent uptake of protons for water formation provides a driving force in the form of electrostatic repulsion, to eject protons from the "trap". The unidirectional proton trafficking follows two different pathways that are called the K- and the D-pathway, located in SU I. The names are derived from two highly conserved residues at each entrance side, a lysine ($K362$) and an aspartate ($D132$) [134, 135]. First it was believed that the $K-$channel exclusively transported the protons required for the reduction of O_2 to water, while the $D-$channel would transport the pumped protons [136, 45]. Further experimental results gave rise to the assumption that the $K-$channel provided all protons for the first half of the catalytic cycle, while the $D-$channel provided all protons for the remaining steps [116, 107]. However, both hypothesis could not hold. Today it is emerging that both pathways participate throughout the whole catalytic cycle. In any case, it is clear that the pathways have distinct roles in passing protons to the binuclear center during specific steps of the catalytic cycle. The $D-$channel conducts both the protons to be translocated and the protons needed for dioxygen chemistry during the oxidative phase of the reaction cycle [88, 107]. It is also possible that the $D-$channel participates in proton uptake during the reductive phase of the catalytic cycle [64] Currently it is believed that the $D-$channel transports all of the pumped protons, since mutations of some D-pathway residues eliminate proton pumping or even decouples proton pumping from oxygen chemistry [137, 138, 139, 140]. The $K-$channel may be preferentially used for proton uptake only during the reductive phase of the catalytic cycle [38, 141, 88]. It was shown that one of the first two protons required for the O_2 reduction is uptaken through the K-pathway [107]. Assignment of the remaining distinct roles, however, is so far unkown. There is an ongoing controversy about the function of the $K-$channel.
Alternatively, it has been suggested that the $K-$channel is not a proton conducting pathway at all but may function as a "dielectric well", which would provide transient charge compensation to charge uncompensated intermediate reaction states [38, 120]. Rottenberg [142] pointed out the possibility that the $K-$channel could be a "hydroxyl ion wire", facilitating movement of hydroxyl anions instead of protons.

At the external side of the binuclear center, there is a highly hydrophilic domain, containing several charged and polar amino acid residues as well as several water molecules, providing the proton exit pathway. This hydrophilic region is also connected to a structure that could serve as a water channel for remove of water produced at the binuclear site [48]. This possible water channel, which is lined with hydrophilic residues, extends from the external side of heme a_3 along the SU I and II interface to the outside surface of the enzyme [48].

A notion central for understanding processes proceeding at the membrane-embedded heme-copper site is the electroneutrality principle [133]. Stabilizing a charge introduced into a well-insulated membrane environment is only feasible in a thermodynamically compatible way by concominant charge compensation , i.e. an electron transferred to a heme site should immediately pull in a proton, via one of its respective pathways.

The exact occurrence of proton pumping throughout the catalytic cycle is, however, unknown till today. There is an ongoing and controversy debate about the exact mechanism of the proton translocation. Wikstroem *et al.* showed that proton pumping is linked to the oxidative phase. By time-resolved measurements for the generation of an electrical membrane potential combined with parallel optical detection, it was shown that in the fully reduced enzyme the main proton translocation events occur during the transition from the P to the F and further to the O state. This means only after the uptake and transfer of the third and fourth electron along the ET pathway [38]. These two steps were suggested to be coupled to translocation of two protons each [143, 38]. Thus, the four ET steps needed to complete the reduction of dioxygen to water are not equal with respect to coupling to proton translocation. Recently, Verkhovsky *et al.* [144, 128] observed that translocation of four protons occurs only if re-reduction of the enzyme immediately follows the oxidative phase of the catalytic cycle.

However, Michel *et al.* proposed a contrary model based on crystallographic and re-evaluation of the mentioned published results [145]. This model comprises a transport mechanism that includes proton pumping also in the reductive phase, suggesting that the transition from the F to the O state is coupled to the pumping of only one proton and translocation of one proton is mechanistically and energetically coupled to the reductive phase of the catalytic cycle. Experimental observations from other groups, however, are inconsistent with this model [135, 110, 146].

They reported a charge translocation corresponding to pumping of one proton induced by the second electron transferred into the enzyme [147]. This was shown by measuring the generation of the electric potential across the membrane of a proteoliposome containing CcO, via capacitive coupling of the vesicular system to an free spanning BLM.

The further steps in the ocidative part of the reaction cycle, from the PM state to the O state (Fig. 3.4) require two more electron input to reduce the tyrosine side chain radical, leading to the F state, and the ferryl state of the high-spin heme, completing the oxygen

cycle. Three more proton translocation events are assumed to occur during these steps [38], but an alternative scheme has been put forward by Wikstroem [140, 128](see Fig. 3.4B).

Untill now, the exact molecular mechanism of proton translocation is poorly understood. It is not known which of the ET steps exactly drives the proton translocation, how the concerted action of proton pumping and its vectorial character is achieved or how the proton pathway ensures, that no back-leak occurs.

4 Combination of Electrochemical and Vibrational Spectroscopic Techniques

In this chapter the different electrochemical and surface enhanced vibrational spectroscopic methods that are applied to the investigation of the mechanism of cytochrome c oxidase are presented. The theoretical and experimental background is discussed, which is necessary for the understanding of the experiments and results presented in Chapter 5.

4.1 Electrochemical Techniques

Electrochemical techniques are essential for the investigation of redox active species on a conducting electrode (in most cases metals). They are design to study electron transfer processes from the metal surface to solubilized or surface confined species.

In this chapter the necessary basement for the understanding of the applied techniques as well as the fundamentals for the determination of rate constans of electron transfer (ET) processes, such as cyclic voltammetry and differential pulse voltammetry, or for the determination of the electrical properties of a dielectric layer, such electrochemical impedance spectroscopy, are discussed. For further details about the theoretical background or experimental applications the reader is refered to standard text books [37, 148].

4.1.1 Theory

Cyclic Voltammetry (CV) has become a very popular technique for initial electrochemical studies of new systems and has proven very useful in obtaining information about fairly complicated electrode reactions. Cyclic voltammetry is (nowadays) the most widely used technique for acquiring qualitative information about electrochemical reactions [37, 149, 150]. The power of CV results from its ability to rapidly provide considerable information on the thermodynamics of redox processes and the kinetics of heterogeneous electron-transfer reactions, and on coupled chemical reactions or adsorption processes.
Over the past couple of decades potential sweep techniques, such as CV, have been applied to an ever increasing range of systems, and at the same time the mathematical description of these techniques has been developed sufficiently to enable kinetic parameters to be determined for a wide variety of mechanisms. It is, however, in the area of preliminary mechanistic investigations that sweep techniques, in particular cyclic voltammetry, are probably most useful. An 'electrochemical spectrum' indicating the potentials at which processes occur can be rapidly obtained, while from the sweep rate dependence the involve-

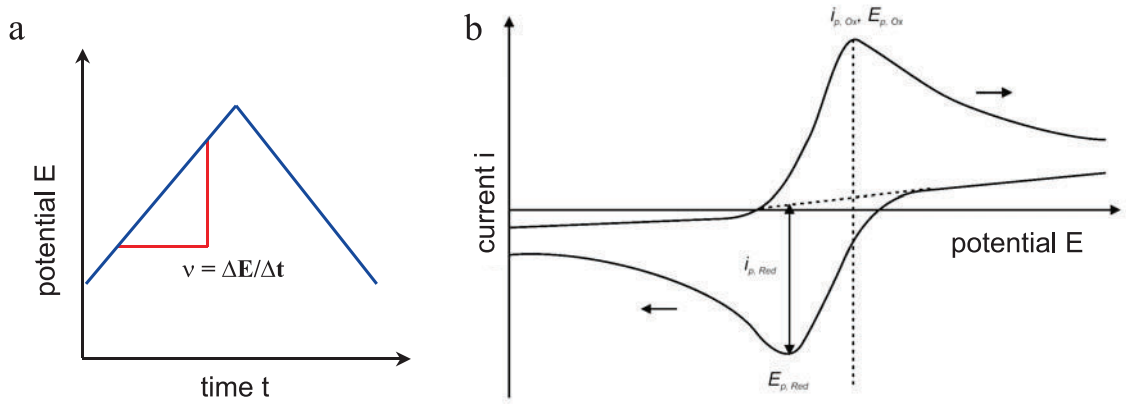

Figure 4.1: (a)Complex wave form composed of two isosceles triangles, used in cyclic voltammetry. The voltage is first held at the initial potential where no electrolysis occurs and hence no Faradaic current flows. As the voltage is scanned in the positive direction, so the reduced compound is oxidised at the electrode surface. At a particular set value the scan direction is reversed and the material that was oxidised in the outward excursion is then reduced. The scan rate $\nu = dE/dt$ can be calculated from the slope of the potential increase. (b) The data is plotted as current i vs. potential E. The characteristics of the CV features depend on the the rate of the ET reaction, the chemical reactivity of the electroactive species and of the scan rate ν.

ment of coupled homogeneous reactions is readily identified, and other complications such as adsorption can be recognised. In view of these capabilities, CV is nearly always the technique of choice when studying a system for the first time.

The potential-time waveforms used for sweep measurements are shown in Fig. 4.1 The potential is normally, starting from an starting or equilibrium potential E_{start}, swept between two different potentials E_1 and E_2 at a known sweep rate, ν, before reversing the sweep back to the initial potential E_{start}. One measurement can comprise several sweeps between E_1 and E_2.

The sweep rates used in conventional experiments range from a few mVs^{-1} up to a few hundred Vs^{-1}. Rates up to several thousand Vs^{-1} have been used, but such high values introduce considerable experimental difficulties, e.g. double layer charging and i_R drop effects due to uncompensated resistances, which generally restrict their application. CV is an powerful tool for the determination of formal redox potentials, detection of electrochemical reactions and evaluation of electron transfer kinetics. Another essential benefit is the possibility to determine the surface coverage of redox active species adsorbed to the electrode surface.

Fundamental to all electrochemical methods is the study of charge transfer processes at the electrode/solution interface. In principle we can distinguish two different types of redox species: solubilized or surface confined redox species. In the following context both cases

will be discussed. The simplest electrochemical redox reaction is described by equation 4.1

$$Ox + ne^- \rightleftharpoons Red \tag{4.1}$$

with Ox and Red as the oxidised and reduced form of the redox species, respectively, and n the number of electrons (e^-) transferred during the redox process. The cyclic voltammetric response (for a $1e^-$ transfer reaction) of a solubilized species following this redox equation is shown in Fig. 4.1. The electrolyte solution initially contains only the reduced but not the oxidized species. After the establishement of the initial set potential, which has to be substantially more negative than the reduction potential of the redox pair, a non-Faradaic charging current flows, which charges the electric double layer at the electrode/ electrolyte interface. As the voltage is scanned at a constant rate in the positive direction, reaching the vicinity of the oxidizing potential E_{ox} of the species, the reduced compound is oxidised at the electrode surface and an anodic, Faradaic current flows. As the potential continues to grow more positive, the surface concentration must decrease. Hence, the flux to the surface and therefore the current increases. As the potential moves past E_{ox} the surface concentration nearly drops to zero, mass transfer of the redox species to the surface reaches a maximum rate, and then it declines as the depletion effect dominates. The observation is therefore a peaked current-potential curve like that depicted in Fig 4.1. At a particular set value the scan direction is reversed and the material that was oxidised is then again reduced, following the same process as described before.

The scan starts at a potential well positive of E^0 for the reduction and when the electrode potential reaches the vicinity of E^0, the reduction begins and current starts to increase. As the potential continues to grow more negative, the surface concentration of the oxidized species must drop; hence the flux to the surface and the current increases exponentially with potential. As the potential moves past E^0, the surface concentration drops nearly to zero, aand concentration gradient is set up for both Red and Ox. The mass transfer to the surface reaches a maximum rate and diffusion occurs down these concentration gradients. As a result the current declines as the depletion effect sets in and since the current now depends upon the rate of mass transfer to the electrode surface the time dependence of the current is proportional to $\sqrt{t}$. The observation is therefore an asymmetric peaked current-potential curve like that depicted in Fig 4.3. When the scanned potential approaches the oxidation potential of Red the anodic current increases exponentially. The anodic peak of the curve corresponds to the point when all reduced molecules at the surface are immediately converted into their oxidised form and diffusion controls the current, which decreases as concentration gradients for Red and Ox are established. Upon reversal of the scan the same processes occur in the cathodic part of the voltammogram.

A cyclic voltammogram can be characterized by different characteristic quantities. The most important are the peak currents i_{Ox} and i_{Red} as well as the respective peak potentials E_{Ox} and E_{Red}. From these peak potentials the so-called mid-potential

$$E_{1/2} = \frac{E_{p,Ox} + E_{p,Red}}{2} \tag{4.2}$$

can be determined, which is very close/ equivalent to the thermodynamic redox potential E^0. As already mentioned, two different types of current, non-Faradaic and Faradaic, can be distinguished in general. Non-Faradaic currents are solely of an electrostatic nature and are not connected to an electrochemical reaction but rather result from the reorientation of ions in the electrolyte at the electrode interface. The charging of the so-called Helmholtz double layer is such an example. Faradaic currents arise from electron transfer processes. According to Faraday's law the electric current flowing through the electrode due to the application of a potential is related stoichiometrically to the amount of reactant consumed or produced by the electrochemical reaction. In the example mentioned above, the Faradaic current is controlled by the heterogeneous electron transfer across the interface and the material transported to and from the surface. In general material transport is controlled by the three mechanisms difusion, migration, and convection. Migration (movement of particles along a potential gradient) however can be minimised by an appropriate cell construction and the addition of sufficient electrolyte salt. The influence of convection can also be substantially reduced when restricting to short experiments at constant temperature and negligible mechanic agitation. The only contribution to mass transport is then diffusion that is described by Fick's laws. The heterogeneous electron transfer is given by the Butler-Volmer equation:

$$i = nFAk_0 \left[c_{Ox} \cdot e^{[-\frac{\alpha nF}{RT}(E-E^0)]} - c_{Red} \cdot e^{[-\frac{(1-\alpha)nF}{RT}(E-E^0)]} \right] \tag{4.3}$$

where k_0 is the standard rate constant, α is an transfer coefficient. R is the molar gas constant. F is the Faraday constant, and E^0 is the standard potential. The difference E - E^0 is referred to as the overpotential (η). Depending on the relative magnitude of the rate constants of the mass transport k_{MT} and the heterogeneous rate of charge transfer k_{CT} one distinguishes:

$k_{CT} \gg k_{MT}$: Processes where the charge transfer is much faster than the mass transport so that the system remains in equilibrium throughout the potential scan, are called reversible. They are diffusion controlled and if the system is in equilibrium ($i = 0$) the Butler-Volmer equation simplifies to the Nernst equation:

$$E = E^0 + \frac{RT}{nF} ln \left(\frac{c_{Ox}}{c_{Red}} \right) \tag{4.4}$$

A system is considered to be at equilibrium, when equation 4.4 holds throughout a CV (or

any other electrochemical experiment). The system is then reversible.

The following parameters characterise the cyclic voltammogram of reversible processes:

- The peak potential separation $E_{Ox} - E_{Red}$ is equal to 59/n mV at 25 °C where n is the number of electron equivalents transferred during the redox process.
- The peak width is equal to 28.5/n mV for all scan rates. With increasing number of electrons the peak becomes more and more narrow. In simple one-step redox reactions, as depicted in equation 4.1, it is therefore possible to determine the number of envolved electrons. It is more reliable to use the peak width, since the peak separation can be easily distracted by irreversible effects of the system or increasing scan rates.
- The area covered by the redox peak is proportional to the transferred charge of the redox process:
  with
  $$\frac{E \cdot i}{\nu} = E \cdot \left(\frac{dQ}{dt}\right) / \left(\frac{dE}{dt}\right) = Q \tag{4.5}$$
- The ratio of the peak current i_{Ox}/i_{Red} of an ideal reversible system is equal to unity for all scan rates.
- The peak current of a reversible redox couple increases linearly as a function of the square root of the scan rate ν and is given by the Randles-Sevcik equation
  $$i_p = (2.69 \cdot 10^5) \cdot n^{3/2} A c_O \cdot \sqrt{D}\sqrt{\nu} \tag{4.6}$$
  where D is the diffusion coefficient.
- The peak potential E does not depend on the sweep rate ν.

For irreversible processes, the individual peaks are reduced in size and widely separated. Totally irreversible systems are characterized by a shift of the peak potential with the scan rate. The peak potential occurs at potentials higher than E^0, with an additional over-potential so that the voltammogram becomes more drawn-out, characteristic for irreversible processes.

The reversible case arises when the couple O/R has sufficiently fast kinetics that the electron transfer process at the surface appears to be in equilibrium. When either a reaction with poorer kinetics is investigated or the potential scan rate is increased so that the rate of non-steady state diffusion is high enough that the electron transfer reaction cannot remain in equilibrium, the kinetics of the electron transfer reaction must be considered. Slow electron transfer reactions must be driven by the application of an overpotential, according to eq. 4.3. Hence, the peak for an oxidation process is shifted to more positive potentials

and that for a reduction to more negative potentials. The peak separation will therefore increase above that for a reversible process. Furthermore, the shapes of the peaks will change. They will become more drawn out as the over-potential must increase with the current density. On the other hand, at high overpotentials the electrode reaction will still be diffusion controlled.

In practice, complete Nernstian systems are difficult to find as electron transfer between all electrode and a redox-active molecule is often quite slow. The experiments can be made more Nernstian, though, by reducing the scan rate. Moreover, a peak separation of 59/n mV is often hard to achieve as it depends strongly on the electrode preparation.

The difference (ΔE_p) between anodic ($E_{p,ox}$) and cathodic peak potential ($E_{p,Red}$) is a useful diagnostic test of Nernstian reaction and is in the case of solubilized redox species close to 2.3 $\frac{RT}{nF}$ or 59/n mV at 25°C.

In a slow voltage scan the diffusion layer will grow much further away from the electrode in comparison to a fast scan. Consequently the flux to the electrode surface is considerably smaller at slow scan rates than it is at faster rates. As the current is proportional to the flux towards the electrode the magnitude of the current will increase with the scan rates.

For reactions that are 'slow' (so called irreversible ET reactions) the voltage applied will not result in the generation of the concentrations at the electrode surface predicted by the Nernst equation (eq. 4.4). This happens because the kinetics of the reaction are 'slow' and thus the equilibria are not established rapidly in comparison to the voltage scan rate. In these cases the peak separation is no longer fixed but varies as a function of the square root of the scan rate. By analysing the variation of peak position as a function of scan rate it is possible to gain an estimate for the ET rate constant.

4.1.2 Surface Confined Processes

So far the discussion of cyclic voltammetry has assumed that all the reactants and products are freely soluble in the solution and that surface processes, such as phase formation and removal and reactant or product adsorption need not be considered. The electrochemical response, e.g cyclic voltammograms, for the electrode redox reaction can be affected quite significantly by the adsorption or attachment of the redox couple onto the electrode [151, 152]. The reason is that in the case of surface confined redox species there is no longer a diffusion limited mass transport to the electrode.

Fig 4.2 shows a cyclic voltammogram of a surface confined reversible redox species.

The major differences when compared to a voltammogram for a reaction in which both product and reactant are dissolved in solution is that the peaks are sharp and symmetrical,

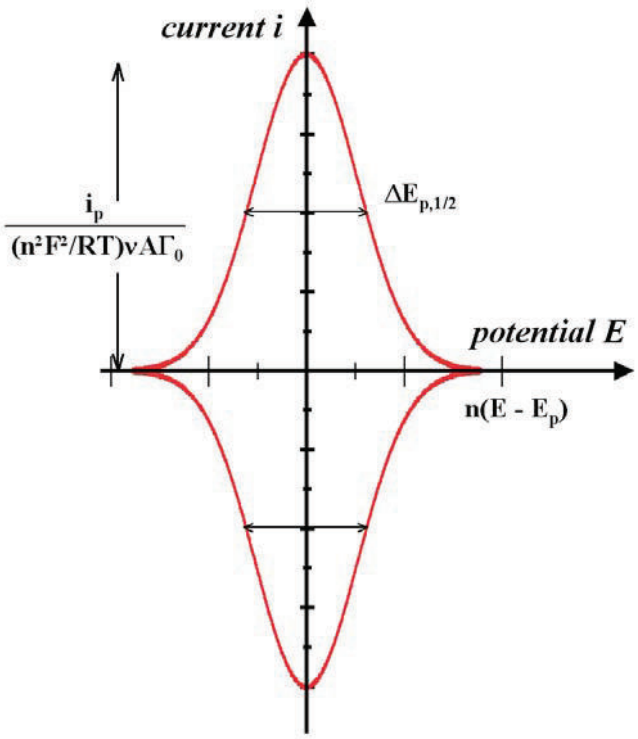

Figure 4.2: Cyclic voltammogram for reduction and oxidation of a surface confined redox couple (corrected for charging current). The reduction and oxidation peaks of surface confined ET reactions can be represented as gaussian curves.

following a perfect Gaussian curve [37], due to the lack of mass transport. The charges associated with anodic and cathodic processes are equal, also due to the fixed amount of reactant on the surface.

The current rises from essentially zero to a peak value and then falling again to zero with theoretically no peak separation. Is the surface confined couple separated by a dielectric layer, the capacitance of this layer can cause, according to the discussion above, a capacitive current, so that the redox peaks are offset by a constant current, the charging current.
In the case of a totally reversible surface confined redox species the peak separation is zero, $E_{p,Red} = E_{p,Ox}$ and the peak current is given by [37]

$$i_p = \frac{n^2F^2}{4RT}\nu A\Gamma \tag{4.7}$$

where Γ is the surface coverage of the redox species, which is constant over time, $\Gamma_R(t) + \Gamma_O(t) = \Gamma_T$. The derivation of this formular is described in the literature [37, 153, 152].

This equation shows first that the current and therefore the amount of reactions is determined by the number of redox sites on the electrode surface. Furthermore, it shows that the peak current is proportional to the potential scan rate, ν, in contrast to the $\sqrt{\nu}$ dependence observed for Nernstian waves of diffusing species. The peak width, presented by the half-height of either cathodic or anodic wave is given by $\Delta E_{p,1/2} = 90.6/n$ mV at 25°C.

Under normal experimental conditions even with expected reversible systems there is always a small peak separation, caused by nonidealities [154, 155]. When their peak position is still unchanged for a wide scan rate range, these redox systems are called quasi-reversible. The area comprised by the cathodic or anodic peak corresponds to the charge Q associated with the reduction of oxidation of the surface confined redox active layer. Thus the surface coverage Γ_T is determined by:

$$\Gamma_T = \left| \frac{Q}{nF} \right| \tag{4.8}$$

For non-Nernstian systems the shape of the cyclic voltammogram changes. For the irreversible case the forward peak ceases to be symmetric with absence of a reverse peak.

4.1.3 Protein Film Voltammetry

Electron-transfer (ET) is an important subject in in bioenergetics, in particular protein-mediated electron transfer plays a key role in almost all reactions of photosynthesis and respiration. In a series of well-controlled ET reactions, the energy of the redox reactions is converted into a trans-membrane gradient of protons. In nature, redox-active membrane proteins are arranged in a sequence in which the electrons are transported between and within the enzymes, from one redox center to the next (compare Chapter 3). In these enzymes the redox properties of transition metals embedded in their active sites, have been exploited to perform some of the most sophisticated chemistry known. Research is in particular focused on the mechanisms by which ET is coupled to protein-mediated ion transport or chemical reactions. Usually, the ET process drives ligand or substrate binding, ion transfer, and conformational changes in proteins, while in turn ET can also be controlled by these processes. However, the exact mechanisms are difficult to determine.

Common techniques to study electron transfer processes in proteins[1] utilize a defined laser pulse to initialize ET by generation of a certain activated redox state of a protein-attached electron donator, a so-called caged compound [156, 157, 158, 159, 160, 161, 162, 147]. Depending on the efficiency of the caged compound a portion of these electron donators, which is usually a few percent, can readily inject electrons into the protein. The elucidation

[1] in most cases solubilized or present as proteoliposoms

of kinetic data is a non-trivial affair, since the experimental results are often complicated by diffusion processes or due to their capacitive coupling to e.g. BLM-layers [147].

An alternative way to investigate mechanisms of ET processes, is to utilize electrochemical techniques, such as voltammetry [163, 164, 165]. These methods offer an dynamical control of the driving force, i.e. the applied potential, and can be effectively combined with spectroscopic methods to study redox-induced structural changes of active structures in the enzymes. [166, 167, 168]. Electrochemical techniques can induce ET to and into redox active proteins. By varying the potential, electrons are driven in and out of the active sites, resulting in diagnostically useful current signals. Thus electrochemistry provides a much higher degree of control over the protein reactivity. It is also possible to resolve complex reactions over a wide dynamic range, e.g. catalysis of enzymes can be measured in a wide frequency window, to reveal processes that are mechanistically informative.

Particularly interesting is to study ET kinetics between the electrode and the adsorbed proteins, by using direct ET. In this case the use of mediators can be avoided. When the proteins are immobilized on the electrode surface, problems of slower diffusion processes complicating the ET process do not arise. It therefore becomes possible to exploit the unique abilities of dynamic electrochemical methods, such as cyclic voltammetry, to control, detect and quantify the complex redox-coupled chemical reactions that occur at the active sites. This kind of voltammetry of surface confined protein systems is called protein film voltammetry [163, 169, 170, 171, 172, 173, 164, 165].

Dynamic electrochemical techniques that allow control of the driving force, i.e. the applied potential, in a time-resolved manner, enable measurement and analysis of ET rates. Advantages over conventional methods, using freely diffusing molecules, include the abilities to study fast reactions not complicated by slow diffusion processes and the attainment of high sensitivity with extremely small quantities of protein samples. The amount of sample required is typically in the range or 10^{-12} to 10^{-11} mol cm^{-2} [174, 163, 154]. Ultimately, the aim would be that the protein-electrode interface can mimic the protein-protein or protein-membrane interactions in biology [167], e.g. by utilizing tethered lipid bilayer architectures embedding the enzyme, as utilized in the present work.

The advantage of cyclic voltammetry is the possibility to vary the potential in a time-resolved manner, by changing the velocity of the potential sweep, the so-called scan rate (ν). By introducing a new time related parameter, i.e. the variability of the scan rate, it is possible to obtain kinetic information of an ET reaction. Thus, a scan rate study of cyclic voltammograms, provides a powerful tool to measure and analyze ET rates, particularly when the redox system is immobilized on the electrode surface [163, 170, 174, 164, 165]. The theoretical framework for the electrochemistry of adsorbed species was developed primarily by E. Laviron in the 70s [34, 153, 175, 176]. Laviron´s methods, based on Butler-Volmer type kinetics, are commonly used to determine rate constants of ET reactions.

This paragraph will give a brief overview of how kinetic data of a surface confined ET reaction can be determined according to the method developed by E. Laviron in 1979 [34].

We consider the simple one-electron redox reaction

$$O + e^- \rightleftharpoons R \tag{4.9}$$

at the electrode surface. Then the rate for the forward reaction (k_f) and the backward reaction (k_b) as a function of the applied potential is given by

$$k_f = k_0 e^{-\alpha \frac{F}{RT}(E-E^0)} \tag{4.10}$$

$$k_b = k_0 e^{(1-\alpha) \frac{F}{RT}(E-E^0)} \tag{4.11}$$

with T being the temperature, F the Faradaic constant and R the molar gas constant. E^0 is the standard potential of the redox couple, the potential where the rate constant of the forward reaction equals the rate constant of the backward reaction , $k_f = k_b$. k^0 is the standard rate constant[2] [177], which is the exchange rate at the formal reduction potential E^0. It is a measure of the kinetic properties of a redox couple. The higher k^0 the faster the ET reaction, reaching an equilibrium on a short time scale. Note that k_f and k_b can be made quite large, even if k^0 is small, by applying a sufficiently high potential relative to E^0. Therefore k^0 is a better way to represent kinetics of ET processes being an intrinsic rate constant independent from the applied potential. α is the so-called transfer coefficient, which is a measure of the symmetry of the energy barrier of the redox reaction (Fig.4.3) and can vary from zero to unity.

With Γ_O and Γ_R being the surface concentration of O and R and with Γ_T as the constant sum

$$\Gamma_T = \Gamma_O + \Gamma_R = const. \tag{4.12}$$

The current response as a function of the applied potential is given by the Butler-Volmer equation for electrode kinetics:

$$i = FAk^0[\Gamma_O(t)e^{-\alpha \frac{F}{RT}(E-E^0)} - \Gamma_R(t)e^{(1-\alpha) \frac{F}{RT}(E-E^0)}] \tag{4.13}$$

with A being the electro-active area.

[2] also called intrinsic rate constant

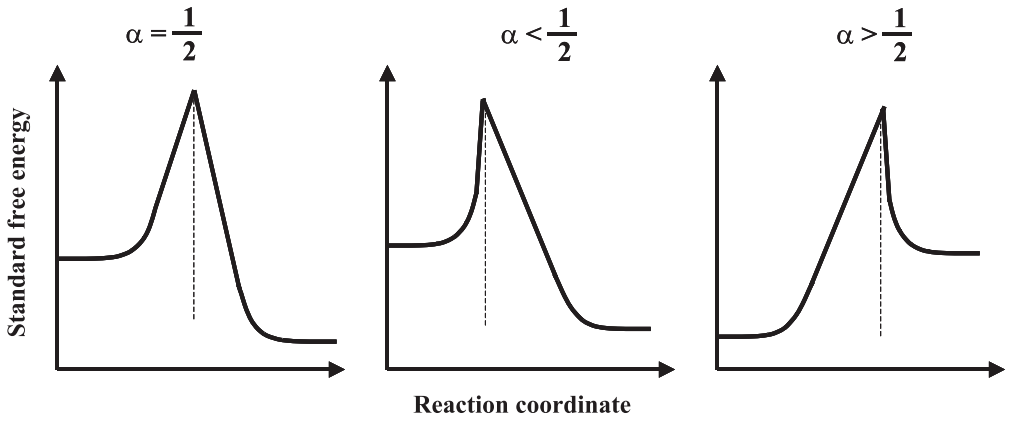

Figure 4.3: The transfer coefficient α is an indicator of the symmetry of the energy barrier of an electrochemical redox reaction. α can vary from zero to unity and is in most cases, in particular for reversible systems equal to 0,5.

The difference E - E^0 is referred to as the overpotential, which is defined as the deviation of the potential from the equilibrium potential for the couple Ox/Red. The use of the overpotential has the effect of transposing the experimental potential from a scale dependent on an arbitray choice of reference electrode to an intrinsic potential scale dependent only on the chemistry of the couple under study.

The Butler-Volmer model [37] for electrochemical kinetics predicts that increasing the driving force, i.e. the over-potential, should raise the rate of the electron transfer exponentially.

After conducting a scan rate dependent cyclic voltammetry study of the system, information about the kinetics of ET can be obtained when plotting the peak potentials for the anodic and cathodic sweep vs. scan rate on a logarithmic scale. For a simple, uncoupled electron transfer, the peak potentials should separate symmetrically and give a trumpet like shape [174] as shown in Figure 4.4

This so-called trumpet plot represents a funnel in which the horizontal axis relates to the ET process in different time domains, typically from several seconds down to microseconds. The average value of the anodic and cathodic peaks equals the reduction potential or standard potential E^0 of the redox couple, while their changes in shape and separation as the scan rate is increased yields information on the ET kinetic, i.e. the standard electron-transfer rate constant k^0.

Figure 4.4 displays an ideal trumpet plot, which shows that the oxidative and reductive peaks separate symmetrically as the scan rate increases and the reversibility of the reaction declines. A kinetic limitation of the electron transfer process at the redox centers causes a deviation of scan rate independent behaviour of the peak position at high scan rates,

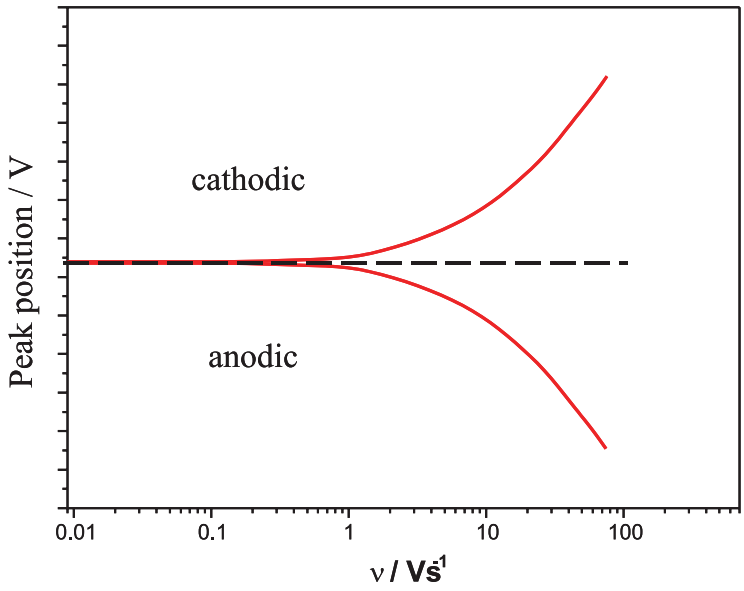

Figure 4.4: Scheme of a 'trumpet plot' for a one-electron reaction (equ. 4.9). The peak potential of the cathodic and anodic sweeps are plotted vs. the scan rate ν in a logarithmic scale. The average value (dotted line) equals to the formal reduction potential E^0.

represented by a straight line, which can be used to determine k^0.

Coupling with enzymatic reactions distorts the plots in different regions and the resulting shapes can be modelled in terms of kinetic schemes of varying complexity. Extended theoretical evaluations of this procedure can be found in the literature [154, 34, 174, 163].

For linear and cylic voltammetry of a surface confined redox couple in which the potential is a continuous function of time, the rate of change of the mole fraction of oxidized species Γ_O is given by

$$\frac{d\Gamma_O}{dt} = -k_f(t)\Gamma_O + k_b(t)(1-\Gamma_O) \tag{4.14}$$

with the assumption that the surface concentration of the confined species is constant for the duration of the experiment. The solution of the differential equation 4.14 is [34, 178] for the cathodic sweep:

$$\Gamma_O(t) = exp\left[-\int_0^t k_b(z) + k_f(z)dz\right]\left(\Gamma_{O,i} + \int_0^t k_b(z)\cdot exp\left[\int_0^z k_b(z) + k_f(z)dz\right]dz\right) \tag{4.15}$$

and for the anodic sweep:

$$\Gamma_O(t) = 1 - exp\left[-\int_0^t k_b(z) + k_f(z)dz\right](1-\Gamma_{O,i}) + \int_0^t k_b(z)\cdot exp\left[\int_0^z k_b(z) + k_f(z)dz\right]dz \tag{4.16}$$

where $\Gamma_{O,i}$ is the mole fraction of oxidized adsorbate at the beginning of the sweep (t = 0) and z is defined by

$$z = \frac{F}{RT}(E - E^0) \tag{4.17}$$

For the following procedure we introduce the dimensionless current [37, 34, 179, 180]

$$\Psi = \frac{RT}{nF\nu} \cdot \frac{d\Gamma_O}{dt} \tag{4.18}$$

where ν is the above mentioned scan rate.

Since we are only considering the effect of the electron transfer rate on the cyclic voltammograms, where the driving force is continuously increased, we can consider for both, cathodic and anodic sweep the irreversible case, that $k_f \gg k_b$ or $k_b \gg k_f$, respectively. Thus equation 4.15 and 4.16 simplify and when substituting into equation 4.18 results in the following relation for the cathodic and anodic sweep:

$$\Psi = \frac{RT}{nF\nu} \cdot k_f(t)\Gamma_{O,i} exp\left[-\int_0^t k_f(z)dz\right] \tag{4.19}$$

$$\Psi = \frac{RT}{nF\nu} \cdot k_b(t)(1 - \Gamma_{O,i}) exp\left[\int_0^t k_b(z)dz\right] \tag{4.20}$$

The peak potential can be found by taking the derivative of equation 4.19 or 4.20 and solving for $d\Psi_{c,a}/dt = 0$. If we consider again the irreversible case, the voltammetric peak occurs when

$$[k_{f,b}(t)]^2 = \frac{dk_{f,b}(t)}{dt} \tag{4.21}$$

Now we can substitute the Butler-Volmer expression for $k_f(t)$ and $k_b(t)$ from equ. 4.10 and 4.11 into eqs 4.19 and 4.20 yielding the dimensionless current and the peak potential derived by Laviron [34]

$$\Psi = \frac{1}{n\nu} \cdot k^0 e^{-\alpha\frac{F}{RT}(E-E^0)} \cdot \Gamma_{O,i} exp\left[-\int_0^t k^0 e^{-\alpha\frac{F}{RT}(E-E^0)} dE\right] \tag{4.22}$$

$$\Psi = \frac{1}{n\nu} \cdot k^0 e^{-\alpha\frac{F}{RT}(E-E^0)} \cdot (1 - \Gamma_{O,i}) exp\left[\int_0^t k_b e^{(1-\alpha)\frac{F}{RT}(E-E^0)} dE\right] \tag{4.23}$$

The peak potential ($E_{p,c/a}$), with the assumption of an irreversible ET process, due to the increasing driving force E, can be calculated with equation 4.21 to

$$E_{P,c} = E^0 - \left(\frac{RT}{\alpha nF}\right) ln\left[\alpha\frac{F}{RT}\frac{n\nu}{k^0}\right] \tag{4.24}$$

$$E_{P,a} = E^0 - \left(\frac{RT}{(1-\alpha)nF}\right) ln\left[(1-\alpha)\frac{F}{RT}\frac{n\nu}{k^0}\right] \tag{4.25}$$

For most reactions, in particular for reversible systems, α has a value of 0,5 [37, 154, 34, 178].

It is obvious from equations 4.24 and 4.25 that for very small scan rates, i.e. $\nu \rightarrow 0$, both cathodic and anodic peak tend to an equal peak position or an ideal reversible system. In a real system there are always various deviations from this simple form that reveal the intricacies of the coupling reactions [154, 155].

An alternative method to the analytical approximation is to perform a finite difference simulation of the cyclic voltammogram response [178]. In a finite differences simulation the swept potential range is divided in a finite number of potential steps. k_f and k_b have fixed values at each potential step, so the potential sweep can be simulated by solving equation 4.38 assuming k_f and k_b are independent of time. Under those conditions the increment change in Γ_O for a potential step from E_1 to E_2 of length Δt is

$$\Delta\Gamma_O = \left[\frac{k_b}{(k_b + k_f)} - \Gamma_{O,i}\right]\left(1 - e^{-(k_b+k_f)\Delta t}\right) \tag{4.26}$$

where $\Gamma_{O,i}$ is again the initial mole fraction of oxidized adsorbate, but at the beginning of each potential step E_1. k_f and k_b are the rate constants calculated at the final potential E_2. The value of Γ_O at the end of the potential step becomes the initial value in the next step and so on. The dimensionless current can then be calculated by substitution of $d\Gamma_O/dt$ into equation 4.18 with the scan rate $\nu = (E_2 - E_1)/\Delta t$.

The peak positions of oxidative and reductive branch, obtained by CV spectra at different scan rates, can then be used to calculate numerically the intrinsic electrochemical rate constants k_0 by different available algorithms [154, 178].

4.1.4 Differential Pulse Voltammetry

The analytical sensitivity of 'classical' voltammetry is usually sufficient for analyte concentrations down to about $5 \cdot 10^{-5} mol \cdot l^{-1}$. At very low substrate concentrations, however, the currents caused by side-effets, such as double-layer charging or other non-Faradaic sources, overlap the actual redox signal and causes the sensitivity to be unacceptably low. Pulse methods were first developed in the 1950s [37, 150] to improve the sensitivity of polarographic measurements made by pharmaceutical companies. At present the most prominent pulse method in the analytical field is 'differential pulse voltammetry' (DPV).

The application of a potential to the electrode causes its surface to take up a characteristic charge and this has electrostatic consequences, oppositely charged ions (and also dipoles) in solution being attracted to the surface; an 'electrical double layer' is formed. The arrangement of charged ions close to the surface, in turn, changes the potential field and this must also be taken into account in the description of the kinetics of electron transfer. Hence, the purpose of this chapter is first to discuss the structure of the interfacial region

and to define the dynamic change in the surface potential field over the few molecular dimensions of the electrode surface which will influence electron transfer. The second part will then focus on the differential pulse method, that enables this obstacle to be overcome.

Any change in potential of an electrode will lead to a change in the charge on the metal side of the interface and some reorganisation of the ions and dipols in the double layer on the solution side. The change in the charge in a certain time period on the surface of the metal is detected as an additive current to the Faradaic current, i.e. the actual current, which is due to electrons crossing the electrode/solution interface and bringing about a chemical change. If the potential is made more negative, electrons will flow into the surface in order to make the surface charge more negative. Since experimentally a current is observed although this current does not lead to chemical change at the surface it is called a non-Faradaic current. The result would be that for each electrode/electrolyte combination, there must be one potential where the surface has neither positive nor negative charge and this is known as the potential of zero charge, E_{pzc}. The charge on the electrode surface is always balanced by attracting ions of opposite charge from the bulk solution to the immediate vicinity of the surface, so that an electric double layer is formed.

The electrical double layer formed on the surface behaves as a dielectric layer as a capacitance and thus the charging current/charge compensating current can be approximated by an electrical circuit with a resistor R_s, being the solution resistance and a capacitor C_d, being the double layer at the electrode interface. The general equation for the charge, q, on a capacitor as a function of the applied voltage is

$$Q = C_d \cdot E_C \tag{4.27}$$

Due to the mesh rule the sum of the voltages across the resistor and the capacitor, E_R and E_C, respectively, must equal the applied voltage, hence

$$E = E_R + E_C = i_{RS} + \frac{q}{C_d} \tag{4.28}$$

With i = dq/dt and rearranging of equation 4.28 yields the differential equation

$$\frac{dq}{dt} = -\frac{q}{R_s \cdot C_d} + \frac{E}{R_s} \tag{4.29}$$

assuming that the capacitor is initially uncharged ($q = 0$ at $t = 0$) the solution of the differential equation becomes

$$q = E \cdot C_d \cdot \left[1 - e^{\frac{-t}{R_s \cdot C_d}}\right] \tag{4.30}$$

And by differentiation according to the time, we obtain

$$i = \frac{E}{R_s} \cdot e^{-\frac{t}{R_s \cdot C_d}} \tag{4.31}$$

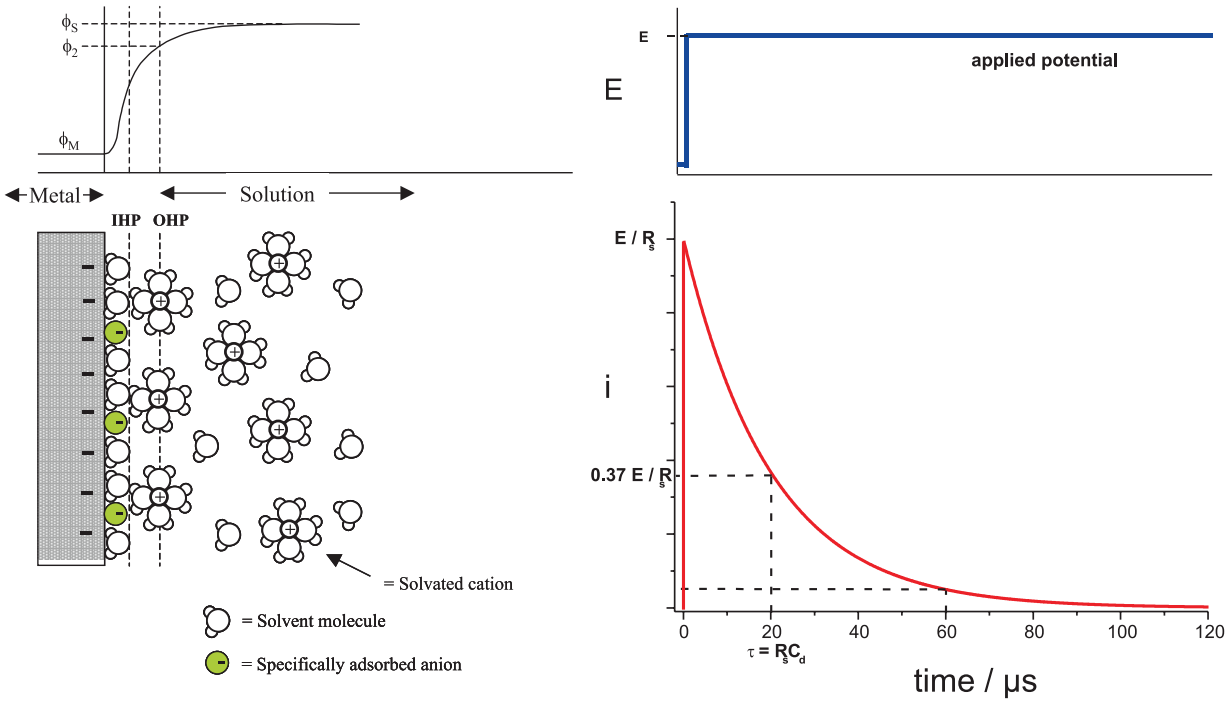

Figure 4.5: Model of the double layer region under conditions where anions are specifically adsorbed with a characteristic potential decay across the inner (IHP) and outer (OHP) plane. After applying a potential step (E) a charging current, caused by the capacitive double layer region, is flowing. For more details see text.

For a potential step, there is an exponentially decaying current having a time constant, $\tau = R_s \cdot C_d$ (see Fig. 4.5). The current for charging the double-layer capacitance drops to 37 % of its initial value at $t = \tau$ and to 5 % of its initial value at $t = 3\tau$. For example if $R_s = 1$ and $C_d = 20\ \mu F$, then $\tau = 20\ \mu s$ and double-layer charging is completed to 95 % in 60 μs.

Hence, since we are interested in the Faradaic processes, the influence of the charging current on data must be minimised. Once the double layer has reorganised to the structure appropriate to the new potential, the charging current will decay to zero. Therefore, the charging current is only a problem in short timescale experiments. A typical value of capacitance is 0.2 Fm^{-2} so that, at scan rates of 0.1 and 10 Vs^{-1}, the charging current will be approximately 2 μAcm^{-2} and 2 $mAcm^{-2}$, respectively [149].

The way that a Faradaic current trails off with time can be quantitative described by the *Cottrell* equation (4.32), assuming that diffusion is the sole form of mass transport:

$$i_{lim} = nc_{analyte}FA\sqrt{\frac{D}{t}} \tag{4.32}$$

where n is the number of electrons transferred in the reaction, $(O + ne^- \rightleftharpoons R)$, F is the

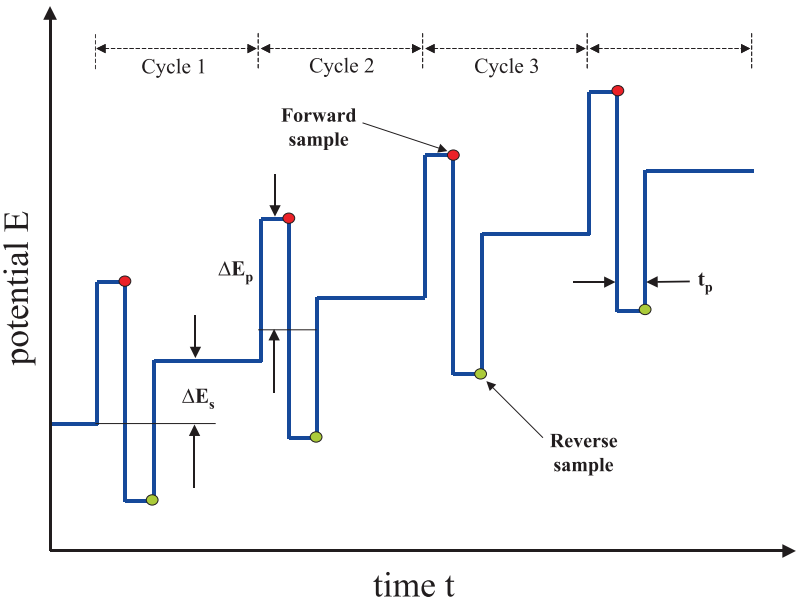

Figure 4.6: Waveform and measurement scheme for differential pulse voltammetry. Shown in blue is the actual potential waveform applied to the working electrode. The light intervening lines indicate the underlying staircase onto which the square is superimposed. In each cycle, a forward current sample is taken at the time indicated by the red dot, and a reverse current sample is taken at the time marked by the green dot. A difference current Δi is calculated from the difference of the forward and backward current $(i_f - i_b)$. The pulse is characterized by a pulse height ΔE_p, and the pulse width t_p. The shift of the baseline is given by ΔE_s.

Faraday constant, t is the time elapsing after the potential was stepped, D is the diffusion coefficient and A the surface area.

Differential pulse voltammetry [37, 149, 150, 181] is one of today´s most popular electroanalytical tools. By this method it is possible to selectively detect reversible capacitive processes that are related to redox reactions at the working electrode. The capacitive or charging current, which causes the main complication and contribution to the background current of cyclic voltammetry, is largely diminished by applying a differential procedure, thus providing an internal background correction. This increases the signal to noise ratio and therefore also the sensitivity can be improved to a magnitude of $10^{-8}\ mol \cdot l^{-1}$ [37, 149, 150]. This sensitivity is clearly superior to other voltammetrie methods.

The potential-time waveforms applied in differential pulse voltammetry is shown in Fig. 4.6. A linear potential ramp of dE/dt is applied to the working electrode, however, a succession of pulses is also applied to the working electrode. The difference beween the baseline potential and the peak in ΔE is a constant that is typically about 50 mV. The current associated with the forward part of the pulse is called I_f, while the current associated with the reverse part is I_r. In differential pulse voltammetry the pulses are superimposed

on a ramped baseline (Fig. 4.6), the peaks obtained during differential pulse voltammetry are not square since the plateau of the peak increases at the constant rate of dE/dt that the baseline follows.

In DPV the current is monitored twice. The first sample is taken just before the rise in potential when the pulse starts, while the second is taken at the end of the current pulse just before it decreases back to the baseline. The difference between these two currents is ΔI_{pulse}. The differential pulse voltammogram is then a plot of current difference ($I_{diff} = I_f - I_r$) against the potential prior to the pulse, so that the difference method here is a means of measuring the difference of current, i.e. the rate of change of current passage.

The difference between the Faradaic components of the two current samples is usually negligible so, in practice, the current difference ΔI_{pulse} is only significant when redox activity occurs. In summary, ΔI_{pulse} is zero unless there is reduction of analyte at the working electrode. The magnitude of ΔI_{pulse} increases more rapidly when the potential approaches $E_{1/2}$, than at other potentials, so that a differential pulse voltammogram contains a peak at $E_{1/2}$.

At potential well positive or negative of the redox potential, both forward and reverse currents are zero, so the difference current is also zero. As potentials pulse has no effect, the forward and reverse currents are equal, and the difference current is also zero. The largest difference between the forward and reverse currents and hence the largest current response is at the redox potential.

The potential of the peak can help identify the redox couple in solution, in a similar manner to normal polarography. The height of the current peak I_p is proportional to analyte concentration and E according to *Osteryoung-Parry* equation as follows:

$$I_p = \frac{n^2 F^2 A}{4RT} \cdot \frac{D}{t^{1/2}} \cdot c_{analyte} \tag{4.33}$$

with ΔE being pulse amplitude, $c_{analyte}$ the concentration of the analyte and t the time between the pulses.

The rooted term in brackets is seen to be very similar to the one seen in the *Cottrell* equation (equ. 4.32), implying that diffusion of analyte to the electrode is an important determinant of the magnitude of ΔI_p.

Larger values of ΔE are preferred since increasing the magnitude of the current peak will also increase the accuracy of the technique, although we need to be aware that such larger values will also decrease the ability of the technique to analyse more than one analyte at a time. We note, however, that it is easier to determine the magnitude of a peak than of a wave. Particularly if the wave is superimposed on a sloping baseline.

The charging current decays exponentially, whereas the Faradaic current (for a diffusion-controlled current) decays as a function of $t^{-1/2}$, that is the rate of decay of the charging current is considerably faster than the decay of the Faradaic current. The charging current is negligible at a time of about 5 $R_u C_{dl}$ after the potential step ($R_u C_{dl}$ is the *time constant* for the electrochemical cell and ranges from μs to ms). Therefore, after this time, the measured current consists solely of the Faradaic current. Thus measuring the current at the end of a potential pulse allows discrimination between the Faradaic and charging currents. The extraction of the Faradaic current allows therefore to analyze electrode reactions more precisely.
The sensitivity of DPV is adjusted by changing the pulse width and pulse period, since the current response to each pulse is comparable to an chronoamperometry experiment. The longer the pulse with the longer the current has to decay and since the current is sampled toward the end of the pulse width the sample current will be smaller, which can be used to improve the sensitivity.

A main advantage of this technique is that irreversible processes, such as oxygen reduction, that can cause complication in classical voltammetry, are not displayed. The magnitude of both I_f and I_r will contribute equally and hence they will cancel (almost) out or result in very asymmetric peaks. In contrast, reversible reactions show very symmetrical peaks. Thus reversible reactions can be clearly separated by this technique.

Pulse voltammetric techniques, such as DPV, have developed into widely used analytical method, with numerous applications in all kinds of practical areas such as pharmaceutical, clinical and einvironmental chemistry [182, 183, 184]. They can provide both qualitative and quantitative information about electrochemical mechanisms [185] as well as providing a basis for electroanalytical measurements [186]. Due to the fact that the major component of the difference current is the Faradaic current, which flows due to an oxidation or reduction at the electrode, DPV is able to study the redox properties of extremely small amounts of chemicals and makes it therefore particularly suitable to monolayers of redox active species on an electrode surface.

4.1.5 Electrochemical Impedance Spectroscopy

Electrochemical impedance spectroscopy (EIS) is a versatile technique to study the electrical properties of conducting or dielectric materials and their interfaces with electronically conducting electrodes [148]. Previously described voltammetry techniques, such as cyclic voltammetry or differential pulse voltammetry are designed to study electrode reactions through large perturbations to the system. By imposing potential sweeps the redox system is driven far from equilibrium, thus the response is a transient signal. In contrast, impedance spectroscopy follows another approach: the system is perturbed with an alternating potential of small magnitude at the steady state and the response of the system

is recorded. An analysis of this response provides information about the system, such as resistivity, capacitances, diffusion coefficient, double layer capacitance or electron transfer kinetic constants.
Electrochemical Impedance Spectroscopy (EIS) or ac impedance methods have seen tremendous increase in popularity in recent years. Impedance spectroscopy was traditionally applied to study corrosion processes, charge transfer processes, dynamics of ionic transport or surface charges at electrodes [148, 187, 188]. Hereby, EIS provides a very powerful and useful diagnostic tool due to its non-invasive characteristic, due to the small AC perturbation[3]. Currently EIS is used primarily to characterize the electrical properties of materials and interfaces with electrically conducting electrodes [148]. Recently EIS gained also more and more importance as an analytical as well as an biosensing tool for biological systems, such as lipid bilayer membranes. A variety of applications are available addressing the issue of active ion transport processes of proteins across lipid bilayer. [189, 190, 18]

EIS studies the system response to the imposition of a small amplitude AC signal. Therefore a small amplitude sinusoidal voltage

$$E(t) = E_0 \cdot sin(\omega \cdot t) \tag{4.34}$$

is superimposed on an applied potential or, more commonly, the equilibrium potential. For most electrode reactions the current response will also be sinusoidal with the same frequency but it will be different in amplitude and phase (from the applied voltage):

$$i(t) = i_0 \cdot sin(\omega \cdot t + \phi) \tag{4.35}$$

In these equations, E_0 is the maximum amplitude of the applied sinusoidal voltage, which is usually chosen to be less than 10 mV, ω is the frequency of the perturbation, i_0 is the maximum amplitude of the current response and ϕ is the phase angle between the current output and the potential perturbation. The shift in phase arises because the electrode reaction behaves equivalent to an electrical circuit which contains capacitances as well as resistances.
The impedance of the system, Z, is a complex resistance for alternating currents and is defined as:

$$Z(t) = \frac{E(t)}{i(t)} = \frac{E_0 \cdot sin(\omega \cdot t)}{i_0 \cdot sin(\omega \cdot t + \phi)} = |Z|(cos\phi + i \cdot sin\phi) = |Z| \cdot e^{i\phi} = Z' + iZ'' \tag{4.36}$$

with

$$|Z| = \frac{E_0}{i_0} = \sqrt{((Z')^2 + (Z'')^2)} \tag{4.37}$$

[3]The voltage is changed in a cyclic manner and induces an alternatic current (AC)

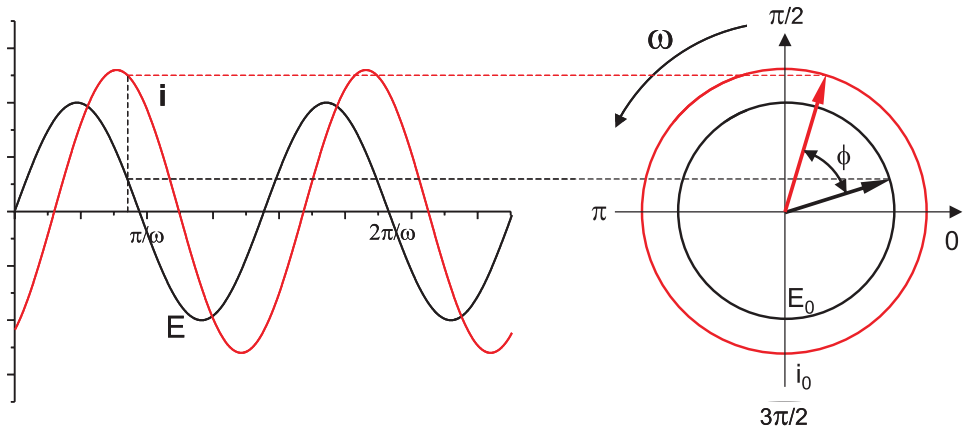

Figure 4.7: Principle of modulated excitation in impedance spectroscopy. Section of the appliedvoltage signal $U(t)$ and measured current response $I(t)$ in a frequency (ω) domain impedance measurement. U_0 and I_0 are the amplitudes of the respective signals and ϕ is the phase shift between the signals.

The phase angle is given by:

$$tan\phi = \frac{Z'}{Z''} \tag{4.38}$$

Regarding equation 4.11, the impedance is a complex quantity. Usually the frequency domain is used for the presentation and analysis for the impedance utilizing a harmonic analysis [148]. Therefore, the impedance is measured at various frequencies, ω, of the applied AC signal (typically 50kHz - 10 mHz). The complex impedance in the frequency domain follows according to equation 4.36 to:

$$Z(\omega) = \frac{\hat{U}(\omega)}{\hat{i}(\omega)} \tag{4.39}$$

with the Fourier-transform $\hat{U}(\omega)$ of the applied ac-voltage $U(T)$ as well as the Fourier-transform $\hat{i}(\omega)$, of the current response $i(t)$. Equations 4.37 and 4.38 follow the same way. Two modern techniques for the determination of the real and the imaginary components of the impedance is based on a phase sensitive detection in combination with a Fourier transform analysis. A detailed description of the technical aspects can be found the literature [148, 37].

Sometimes it is advantageous to analyze ac circuits in terms of the admittance, Y, which is the inverse impedance, and therefore represents a kind of a complex conductance:

$$Y = \frac{1}{Z} \tag{4.40}$$

A variation of the impedance with the frequency is often of interest and can be displayed in different ways. A common presentation of the impedance data is usually the so-called Nyquist or Argand plot, where Z", the imaginary, against Z', the real component of the impedance, is plottet as a function of frequency. The so-called Bode Plot, where log $|Z|$ and ϕ are plotted against log ω is another common representation of impedance measurements. This plot allows direct access to the resistances included in a system, as discussed below. The last important diagram is a complex plane-plot, where the imaginary part of the frequency normalized admittance Y''/ω is plotted against its real component Y'/ω as a function of the frequency, ω. This plot allows the direct determination of the capacitances present in the system.

In order to quantify the electrical properties of the system under investigation, it is necessary to construct a theoretical model circuit consisting of electrical components, which exhibits the same impedance behaviour. For the analysis of these plots either exact mathematical models based on physical theories can be used in order to solve the differential equations that describe the systems [191, 148]. The first case, the direct analysis, affords a lot of mathematical effort will be discussed later in section 4.2. The most common way is the passive analysis, utilizing electrical equivalent circuits, which offer a more schematic representation to simulate the behavior of the electrode reaction.

With these so-called equivalent circuits the impedance data can be converted into physical understanding [148]. It should be mentioned that any model circuit must be understood as simplification of the real system, since many minor contributions can not be resolved and must be neglected. In addition, the circuits are not imperatively unique, especially if the amount of consisting elements becomes large. Theoretical and experimental impedance spectra are fitted using non-linear curve fitting algorithm [148].

Starting with the reality fo the physical system a model, consisting of e.g. resistances and capacitances, is developed in order to describe the electrochemical properties of the system. The parameters of the model can be analyzed in terms of rate equations, diffusion coefficients or electron transfer kinetic constants [148, 192]. The following discussion will focus on the typical parameters that are important for surface confined structures, such as resistances or capacitances and their possible combinations in electric circuits, which represents the physical properties of the system.

Even if the amount of elements is kept small, the equivalent circuits provide a large amount of information about the complex biomimetic membrane - protein system and processes at this system. Resistances and capacitances are denoted as *ideal elements*, since they assume ideal system properties. For real systems it is also necessary to introduce special, so-called *distributed* elements, such as the constant phase element, taking into account inhomogenities, for example the distribution of different spacer molecules occurring in the same layer [167], distribution of conductivities in polycrystalline materials [148], roughness of interfaces [193, 194] or porous materials [148, 37, 149]

Different configurations and their mathematical description are will be represented in the following context:

1) **Resistor (R)**:

$$E = IR \tag{4.41}$$

$$Z = \frac{E}{i} = Z' = R \tag{4.42}$$

$$\phi = 0 \tag{4.43}$$

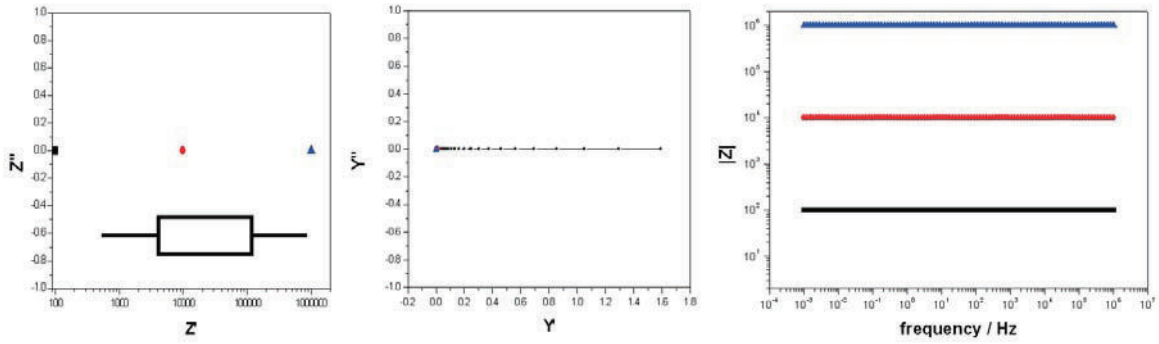

Figure 4.8: Complex plains and Bode plot of a single resistor, with 100 Ω (black), 1kΩ (red) and 1MΩ (blue).

2) **Capacitor (C)**:

$$E = E_C = E_0 \cdot sin(\omega t) = \frac{Q}{C} \tag{4.44}$$

with

$$Q = C \cdot U \tag{4.45}$$

$$i = \frac{Q}{dt} = C\frac{dE}{dt} = C \cdot E_0 \cdot cos(\omega t) \tag{4.46}$$

$$Z = \frac{E}{i} = iZ'' = -i\frac{1}{\omega C} \tag{4.47}$$

$$\phi = -\pi/2 \tag{4.48}$$

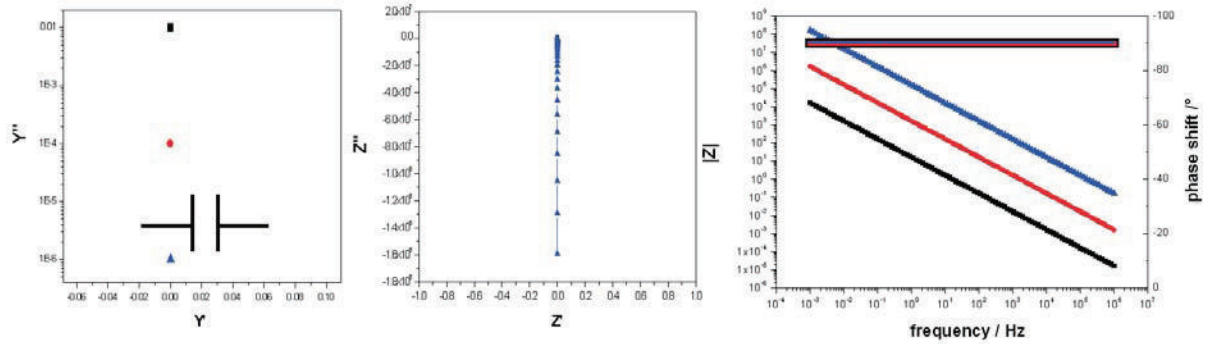

Figure 4.9: Complex plains and Bode plot of a single capacitor, with 10 mF (black), 100 μF (red) and 1μF (blue).

3) **Seriel circuit**:

$$E = E_R + E_C \tag{4.49}$$

$$Z = \frac{E}{i} = Z' + iZ'' = R - \frac{i}{C} \tag{4.50}$$

$$\phi = f(\omega) \tag{4.51}$$

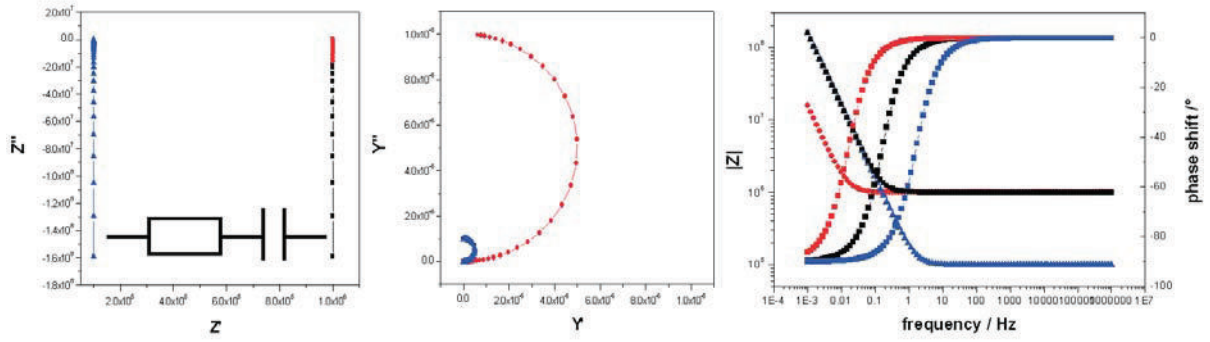

Figure 4.10: Complex plains and Bode plot of a resistor and a capacitor in series, with R = 1 MΩ and C = 1μF (black); R = 1 MΩ and C = 10μF (red) ; R = 0.1 MΩ and C = 1μF (blue).

4) **Parallel circuit**:

$$1/E = 1/ER + 1/EC \tag{4.52}$$

$$Y = Y' + iY'' = \frac{1}{+} i\omega C \tag{4.53}$$

$$Z = \frac{1}{Y} = \frac{R}{1 + i \cdot RC} = \frac{R}{1 + i\omega\tau} \tag{4.54}$$

$$\tau = RC \tag{4.55}$$

$$f = f(\omega) \tag{4.56}$$

$$\tag{4.57}$$

The time constant τ, which is also called the conductivity relaxation time of conductive materials [148]

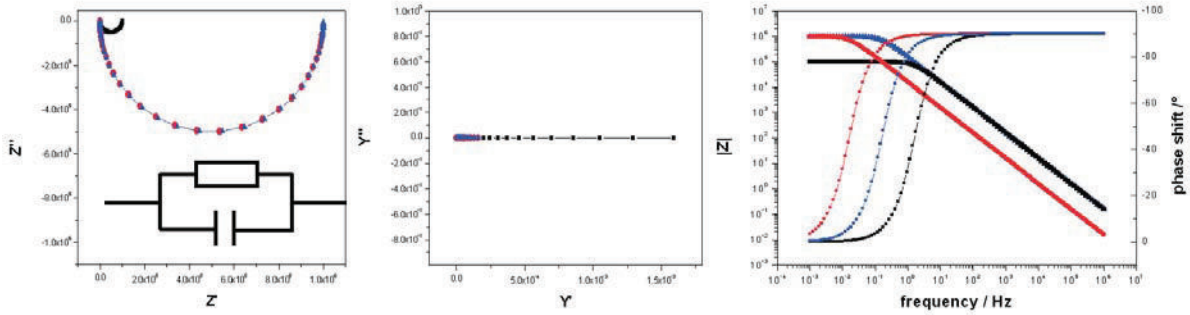

Figure 4.11: Complex plains and Bode plot of a parallel circuit of an resistor and a capacitor, with R = 0.1 MΩ and C = 1μF (black); R = 1 MΩ and C = 10μF (red) ; R = 1 MΩ and C = 1μF (blue).

Due to the relation $C = \epsilon\epsilon_0 \frac{A}{l}$ for the capacitance C, it is possible to determine the value of the dielectric constant. A reasonable value for dielectric constants of unpolar organic compounds is between 2 and 3 and the ϵ of water is about 80.

6)**Resistance in series to a RC circuit**:
The characteristic of R(RC) circuits is the typical 'role off' of the frequency normalized admittance plot at low frequencies (seen in Fig. 4.12). The intersection point in this complex plane-plot with the imaginary axis (Y''/ϵ) is an approximation for the capacitance C of the layer. The plateau-values for $|Z|$ in the Bode-plot respond to the resistances of the layer. The lower plateau corresponds to the solution resistance and the higher plateau with the resistance of the layer. The magnitude of the impedance |Z| becomes for high frequencies the value of the electrolyte resistance and for low frequencies the resistance of the observed system itself, such as a tBLM, and has in this region a slope equal zero.
For a pure capacitance the slope becomes -1. The phase angle is therefore in an ohmic controlled frequency 'region' 0° and decreases for a capacitive region to -90°. [148, 149, 195]

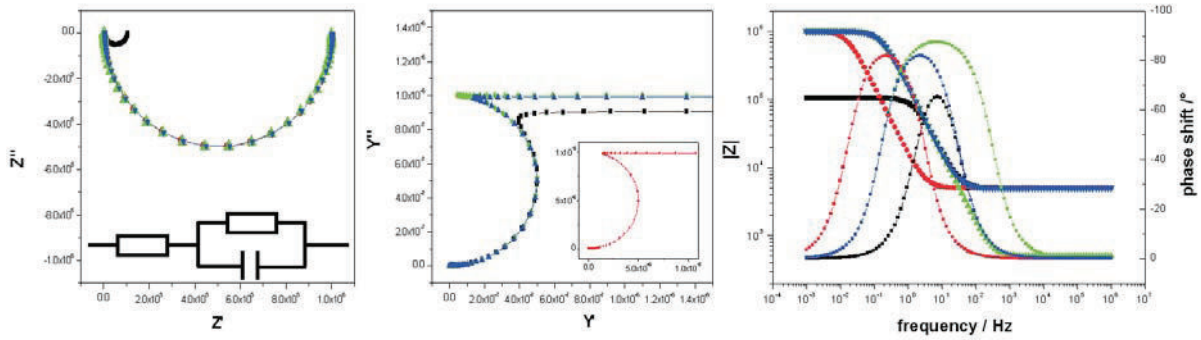

Figure 4.12: Complex plains and Bode plot of a resistor (R_1) in series with a parallel circuit of an resistor (R_2) and a capacitor (C_2), with $R_1 = 1$ kΩ, $R_2 = 0.1$ MΩ and $C_2 = 1$ μF (black); $R_1 = 1$ kΩ, $R_2 = 1$ MΩ and $C_2 = 10$ μF (red) ; $R_1 = 100$ Ω, $R_2 = 1$ MΩ and $C_2 = 1$ μF (green); $R_1 = 1$ kΩ, $R_2 = 1$ MΩ and $C_2 = 1$ μF (blue)

The frequency region between the two plateaus shows an capacitively controlled pathway for the current, reflected in an decrease of the phase angle down to -90°.
In the case that the time constants τ of a serial composition of RC-elements are sufficiently separated, typically an order of magnitude difference, different slopes are present in the Bode-plot, each representing a single time constant.
In the complex plot Z'' vs. Z', the intersection points with the real part axis is equal to the solution resistance R_S and the sum $R_S + R$ of the layer resitance. The frequency ω at the vertex point is equals the inverse of the time constants τ of the system:

$$\omega = \frac{1}{\tau} = \frac{1}{RC} \tag{4.58}$$

5) **Constant Phase Element (CPE)**:
The Constant Phase Element (CPE) takes into account non-linearities in real systems, hence, often used for the description of inhomogenities in a layer resulting in a distribution of capacitances in a system. In a real system these inhomogenities are a sum of different microscopic pathways in a macroscopic system. Thus, there is a need of an element that describes this distribution of different parameters.
In general, the CPE element expresses the electric impedance in terms of an empirical formula, which is based on a simple power law:

$$Z = K(i\omega)^{\alpha} = K(cos(\frac{\alpha \cdot \pi}{2}) + isin(\frac{\alpha \cdot \pi}{2}) \tag{4.59}$$

The CPE is determined by the two parameters K and α. For an ideal element, the frequency exponent is $\alpha = 1$ and $K = 1/C$ for an ideal capacitance and $\alpha = 0$ and $K = R$ for a resistance. The deviation of the exponent α from the ideal values is attributed to inhomogenities of the analyzed layers, like defects or roughness. Typical values of inhomogeneous layer or capacitances on rough surfaces are in the range of 0.9 and 1. With

$\alpha = 0.5$ the CPE becomes a so-called Warburg constant, which is used to describe diffusion controlled redox processes at an electrode, which results in a significant slope of 45° in the complex plain. Using the CPEs, the fit accuracy of the equivalent circuit models

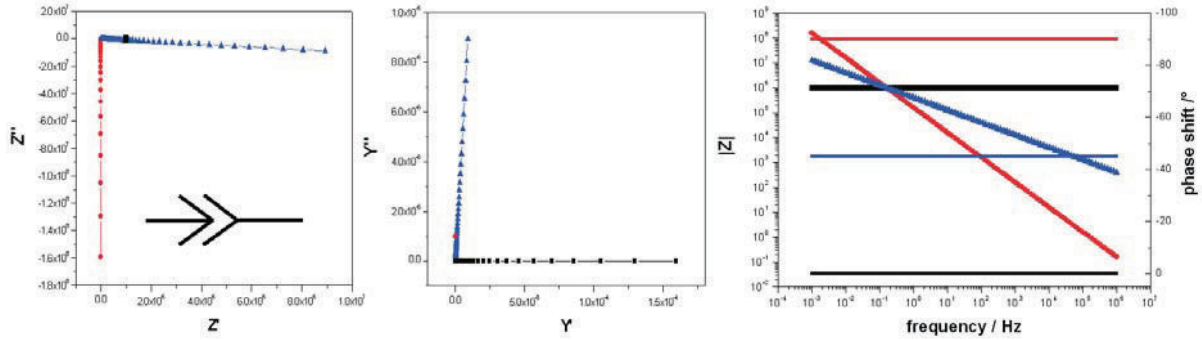

Figure 4.13: Complex plains and Bode plot of a single constant phase element, with $K = 1 \cdot 10^{-6}$ and $\alpha = 0$ (black), $\alpha = 1$ (red) and $\alpha = 0.5$ (blue).

to the experimental data can be improved drastically for most of the experiments. Since the CPE is just an empirical element, only qualitative information can be gained using this approach. A parallel circuit of a resistance with an CPE is resulting in a damped or flattened semi-circle in the complex plain.

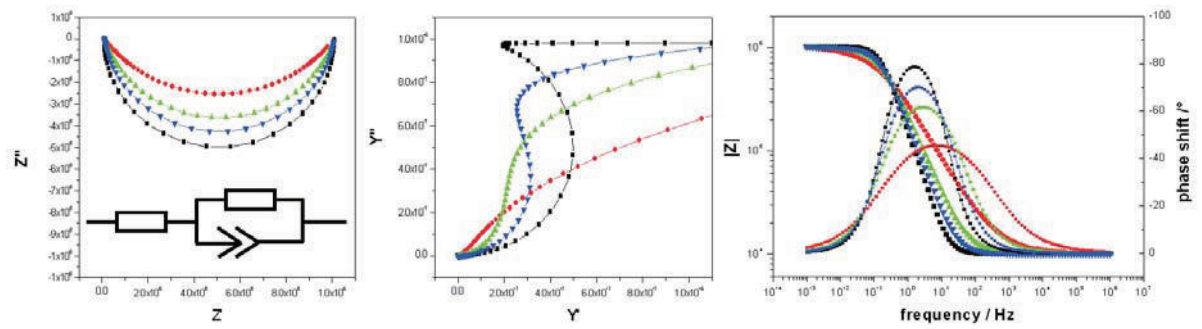

Figure 4.14: Complex plains and Bode plot of a resistor (R_1) in series with a parallel circuit of an resistor (R_2) and a constant phase element, with $R_1 = 10$ kΩ, $R_2 = 1$ MΩ, $K = 1 \cdot 10^{-6}$ (black) and $\alpha = 1$ (black), $\alpha = 0.9$ (blue), $\alpha = 0.8$ (green) and $\alpha = 0.6$(red).

A further resistance, e.g. representing the solution resistance, is added to this equivalent circuit, provides a simplified model for real tethered membrane systems. The exponent α is a measure for the (in-)homogeneity of the membrane. Especially in analyzing the impedance response of tethered lipid membranes, the CPE becomes an important tool. A sBLM or a tBLM with a certain sub-layer structure consists of many distributed dielectric elements, such as the electrode interface, the polar headgroups and a (mixed) spacer region,

which give rise to a high inhomogenity of the system. However, various reports in the literature report the utilization of CPE containing equivalent circuit in order to describe distributed time constants to account these sub-layer structures of supported BLMs [196].

4.2 SPICE

Modeling and simulation are indispensable when dealing with complex electron and ion transfer processes. Most biological systems are fairly complex. This holds in particular for the case of proteins embedded in a membrane environment. Here, active ion and electron transport processes through the enzymes are often influenced or controlled by charge transfer or charging processes at the membrane itself. Thus, a sufficient model is usually also a quite complex affair, taking into account all these different interfering processes. It is therefore insufficient to analyze these phenomena with simple CNLS (*complex non-linear least square fitting*) or passive element fitting. This method is an over-simplification representing all processes with simple circuits of serial and parallel resistors and capacitors (compare chapter 4.1.5) and can not take into account parameters such as concentrations, volumes, potential differences across different portions of a dielectric layer, e.g. a tethered lipid bilayer, or rate equations of enzymatic processes.

The limitation of conventional passive equivalent circuit can be overcome by utilizing numerical computer simulations, which allows simulation of electronic networks and in particular bioelectrochemical processes, involving membranes [197, 198]. SPICE (*Simulation Program with Integrated Circuit Emphasis*) is a general-purpose circuit simulation program designed to simulate the behaviour of electrical networks under different conditions and to perform nonlinear DC, transient, and AC analyses [197]. SPICE was originally developed at the Electronics Research Laboratory of the University of California, Berkley in the mid-70s and is widely used by engineers to simulate the performance of analogue electronic systems. SPICE solves sets of non-linear differential equations in the frequency domain, steady state and time domain and is able to simulate the behaviour of complex electronic circuits, such as those present in biolelectronic systems. Thereby, different algorithms[4], are utilized to solve the complex differential equations, that take the place of simple components such as resistors or capacitors and provide a more flexible source of components. SPICE includes programmable voltage and current sources which make it also possible to represent rate equations of bioelectrochemical processes, such as the permeation of ions or active protein-mediated ion transport through a membrane, in terms of electrical elements [197, 198].

Mathematical modelling of dynamic processes in bioelectrochemistry with numerical[5] simulations is a rather novel aspect in the field. However, it enables coupled processes to be

[4]For example like the Newton-Raphson algorithm or a trapezoid or Gear interrogation algorithm for transient analysis

[5]Analytical solution of these equations are tedious or impracticable except in very simple cases.

solved and independently analyzed, i.e. mass transfer, potential generation or current flow. It is even possible to simulate complex systems, such as redox-driven proton pumps and thus to learn more about the actual mechanism of these processes (see later in chapter 5), based on simulation of the experimentally measured current response. Furthermore, SPICE can program multiple types of experiments such as EIS, CV, AC voltammetry with one and the same single network model [197].

The first stage of modelling consists in designing a suitable model. The aim of mathematical modelling is to simulate the behaviour of a given system. The requirement for the model is that a fully mathematical description of the system is available, in particular the dependence of the flows on the parameters of the system. In this case modelling enables to understand and interpret data collected in experiments on the basis of the mechanisms and processes occuring in the system.

These parameters can include number of moles, number of charges, concentrations as well as electrical or chemical potentials. The flows may be due to diffusion, convection or the transport of electrical charges as well as to changes of chemical potentials.

In the equivalent electrical network all parameters of the system are represented as electrical potentials and all flows as electrical currents, where the electrical units are related to the units of the parameters and the flows of the model. In this network representation all parameters of the system are associated with nodes, so that the potential at these nodes, with respect to ground, indicate the values of the pertinent parameters.

In analog computing, a differential equation must be represented in term of the fundamental operations, such as integration, addition, multiplication or even more complex functions. This can be provided by different elements of SPICE that can be implemented into the model. A network usually consists of storage devices for a certain quantity, which can be represented by a capacitor, e.g. representing the spacer volume of a tethered bilayer lipid membrane [197, 198]. If a parameter in a system is constant or has a predetermined behaviour in time, e.g. a clamped concentration or an electrical potential difference that is swept during the experiment, its node in the electrical network is connected to a SPICE element called an independent voltage source. In the same way a flow in a system which is constant or has a predetermined behaviour, e.g. a controlled addition of a reactant to a compartment, can be introduced into the electrical network by an independent current source. The dependence of a flow on the parameters of the system can be modelled by inserting a so-called controlled current source into the network. Thus, any dependence of the parameters that can be expressed in terms of a polynomical function can be simulated. The important feature of a controlled source is that it provides the flexibility to include any kind of physically relevant parameters that control the flow, as the one mentioned above, into the circuit and to take into account all complications occurring in an biological system.

Figure 4.15 summarizes the most important elements required for bioelectrochemical sys-

tems. The relations given underneath the different symbols indicate the behaviour of each element with respect to its effect on the quantities in the electrical network. Passive elements, such as resistors and capacitors, introduce a dependence of the current i flowing through it according to the potential difference U between the nodes to which it is connected. These elements are in contrast to active elements, such as voltage sources or current sources. They determine either the potential difference between the nodes to which they are connected to or the current flow through the element with no respect to other parameters, i.e. current through a voltage source or potential difference across a current source. Furthermore, independent voltage sources, can generate any voltage waveforms, such as pulses, sinusoidal or self determined excitation signals, and by calculating these voltage current versus time or versus frequency it is possible to conduct transient analysis or AC analysis, respectively.

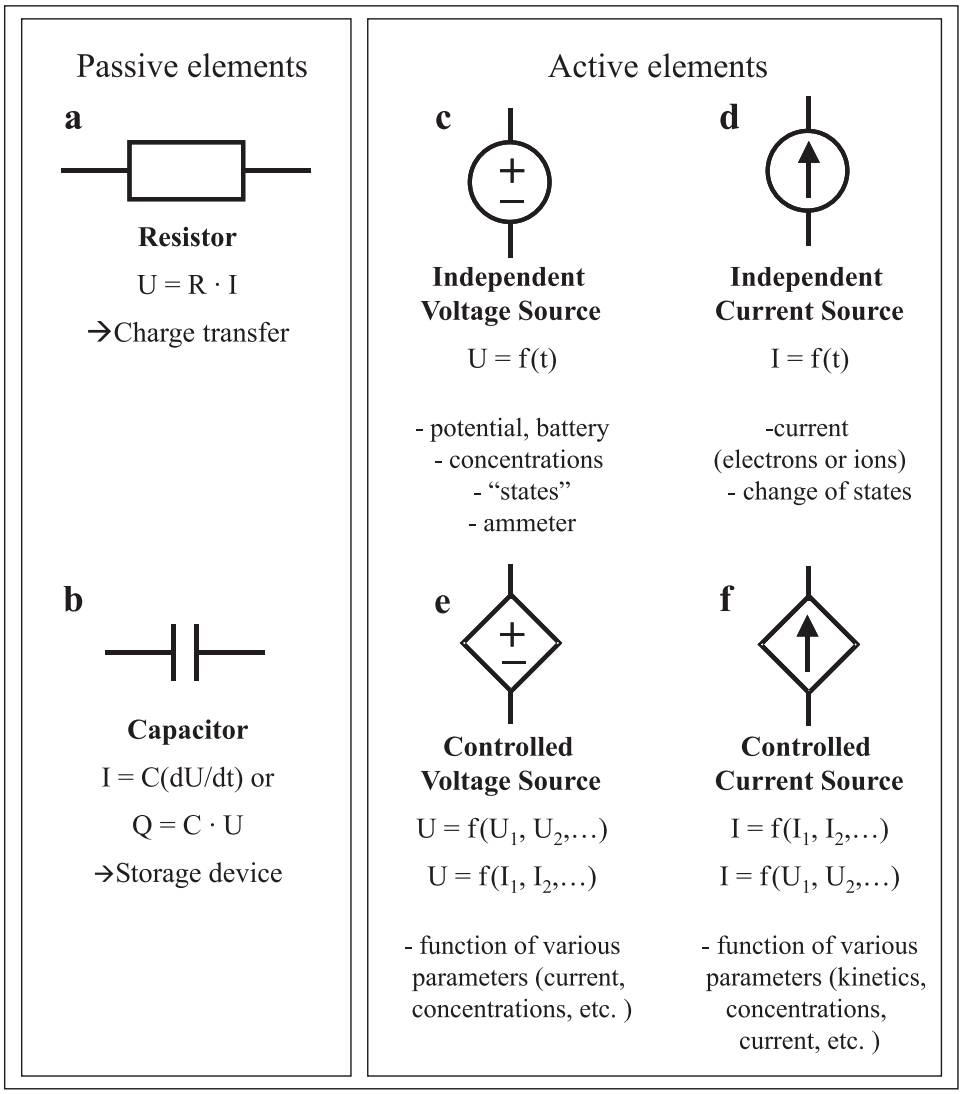

Figure 4.15: Components of Network modeling. The quantities appearing in the constitutive relations are electrical potential differences U, the currents I, resistances R, capacitances C, charges Q and time t. Whereas and f(t) as a function of time, f (U_1, U_2 ,...) and f (I_1, I_2 ,...) a function of different potential differences (U_i) or different currents (I_i).

4.3 Surface Analytical Vibration Spectroscopy

Various techniques for the elucidation of reaction mechanisms and the determination of kinetic parameters that have been described in the previous section relying on current measurements as a function of the applied potential. One of the useful features of these electrochemical techniques is that the current is a direct measure of the reaction rate, and therefore the rate parameters related to ET process are readily to be determined. The principle disadvantage of this approach is that such purely electrical measurements lack molecular specificity, i.e. the current only represents the aggregate rate of all processes occurring and no direct information about the identity of reaction products of intermediates is available. In particular it would be useful to be able to identify reaction intermediates and to monitor the time dependent redox linked structural changes of the species of interest.

Vibration spectroscopy providing molecular specificity is thus ready to be combined with electrochemical techniques. Vibrational modes reveal information about redox, coordination and ligation states of metal complexes, as present in most redox active membrane proteins, such as heme proteins.

As discussed in the introduction, the investigation of direct ET processes requires a surface confinement of the system of interest. Thus, we have to deal with a monolayer of proteins attached to the surface. The main drawback of vibrational spectroscopy, such as Raman and infrared spectroscopy, is the smaller cross section of these processes as compared to other spectroscopic techniques, such as fluorescence. Thus the sensitivity is very low and normally a high concentration of analyte is required. To be able to reach a sensitivity sufficiently high to study monolayers of protein, several enhancement effects, such as surface and resonant enhancement, have to be utilized to increase the signal.

Applying so-called surface-enhanced resonance Raman spectroscopy (SERRS) or surface enhanced infrared reflection absorption spectroscopy (SEIRAS) it is possible to directly obtain structural information that are difficult or only indirectly obtainable by fluorescent techniques, where SERRS and SEIRAS can reach sensitivities approaching those of fluorescence measurements. A further advantage of resonant enhancement Raman spectroscopy is the possibility to study selectively active site structures that consist of a chromophore, such as hemes, thus allowing to study individual redox centers in multi-centered enzymes [199, 200, 201, 166, 167]. This already illustrates the unique and powerful possibilities inherent in a combination of electrochemical techniques with surface enhanced vibration spectroscopy.

This section describes the important concepts, necessary for the understanding of the surface enhancement effects of noble metals. First the origin of surface plasmons on flat surfaces, based on the fundamental Maxwell theory is discussed, which is important to understand the surface enhancement phenomena of rough metal surfaces or nanoparticles discussed further below. Furthermore, this section will describe the fundamental principles

of Raman and infrared vibration spectroscopy and their application to rough surfaces, utilizing the surface enhancement effects to study monolayers, as well as the resonance enhanced Raman effect and their application to heme proteins. The state of knowledge on the physical understanding of the enhancement effects of roughend metal surfaces will be discussed as well as its application in surface analytical Raman and infrared spectroscopy. For a detailed summary of this topic the reader is refered to ref [202].

4.3.1 Theoretical Background of Surface Plasmons

This section will discuss the behaviour of harmonic electromagnetic waves in isotropic media as an example of the general treatment of wave propagation in matter and the way in which electromagnetic waves behave when they approach the boundaries between media. In particular the material properties and the geometry of the media influence the propagation of the light through different materials. The theoretical description is based on the Maxwell equations, which form the basis of classical electrodynamics [203]. These basic optical phenomena are of importance to understand the occurrence of surface plasmons (SP), which can be described as charge density oscillations of the free electron of a metal propagating along the interfaces shared with a dielectric. The electrons respond collectively and in resonance to an excitation, e.g. by a light wave, providing a characteristic electromagnetic field pattern associated with the charge oscillations at a metal surface. This field is an evanescent field, i.e. it extends exponentially in dielectric media. Due to the resonant response of the oscillating electrons the field features a strong enhancement close to the surface.

First, the fundamental processes at interfaces, i.e. refraction, reflection and transmission, that are also present in the Raman and infrared experiments discussed later, will be addressed in this chapter. Then a theoretical treatment of surface plamons within the framework of Maxwell's theory and the Drude model of metals is outlined. The basic theoretical understanding of surface plasmons is the basis for surface plasmon resonance spectroscopy.
Furthermore the occurence of localized surface plasmons on roughened surfaces is discussed, which are the basis of the electromagnetic surface enhancement effects at roughened surfaces. This enhancement is a fundamental requirement to achieve sufficient sensitivity of Raman and infrared spectroscopy on an ultrathin system, such as protein monolayers.

4.3.1.1 Plane Waves at Isotropic Materials

The electromagnetic radiation of an homogenous and isotropic media, where all directions are equivalent, can be described by the Maxwell's equations [203]:

$$\begin{aligned} \nabla \cdot \mathbf{D} &= 0 \qquad & \nabla \times \mathbf{E} &= -\frac{\partial \mathbf{B}}{\partial t} \\ \nabla \cdot \mathbf{B} &= 0 \qquad & \nabla \times \mathbf{H} &= -\frac{\partial \mathbf{D}}{\partial t} \end{aligned} \tag{4.60}$$

with **E** being the electric field, **B** the magnetic induction, **H** the magnetic field and **D** the electrical displacement. The relations between **D** and **E** on one side and **B** and **H** are given by:

$$\mathbf{D} = \underline{\epsilon} \cdot \mathbf{E} \tag{4.61}$$

$$\mathbf{B} = \underline{\mu} \cdot \mathbf{H} \tag{4.62}$$

with $\underline{\epsilon}$ being the dielectric constant and $\underline{\mu}$ being the magnetic permeability, that are generally complex tensors. Considering an isotropic material, these tensors are reduced to scalars $\epsilon\epsilon_0$ and $\mu\mu_0$, with ϵ_0 being the electric permittivity of vacuum and μ_0, being the permeability of free space. Thus, the Maxwell equations can be solved by planar waves as a function of time t at point **r**:

$$\mathbf{E}(\mathbf{r}, t) = \mathbf{E}_0 \cdot exp[i(\mathbf{k} \cdot \mathbf{r} - \omega t)] \tag{4.63}$$

which are characterized by their angular frequency ω, the electric field amplitude $\mathbf{E}_0$ and their wavevector **k**. Since $\mathbf{E}_0$ is always orthogonal to the direction of propagation, which is along **k**, for each pair of (**k**,ω) two mutually orthogonal electric field amplitudes may exist, corresponding to two possible polarisations. Besides the electric field, also the magnetic field contains the full information about the plane wave. They are related to each other by the following relations:

$$\mathbf{H}(\mathbf{r}, t) = \frac{1}{\omega\mu\mu_0} \cdot \mathbf{k} \times \mathbf{E}(\mathbf{r}, t) \tag{4.64}$$

$$\mathbf{E}(\mathbf{r}, t) = \frac{1}{\omega\mu\mu_0} \cdot \mathbf{k} \times \mathbf{H}(\mathbf{r}, t) \tag{4.65}$$

whereas the wavevector **k** and the angular frequency ω depend on each other and can be determined by the dispersion relation:

$$\frac{\omega^2}{|\mathbf{k}|^2} = \frac{1}{\mu\mu_0\omega} = \frac{c^2}{n^2} \tag{4.66}$$

The refractive index n is defined by the ratio of the velocity of light c in vacuum and in matter. Assuming a nonmagnetic material ($\mu = 1$) the dispersion equation can be further simplified to

$$|\mathbf{k}| = \omega \cdot \sqrt{\epsilon\epsilon_0\mu\mu_0} = k_0\sqrt{\epsilon} = k_0 \cdot n \tag{4.67}$$

which provides a more convenient way for the following considerations.

A complex dielectric function, $\epsilon(\omega) = \epsilon'(\omega) + i\epsilon''(\omega)$, is required to describe the macroscopic response of a material to an external electromagnetic field. In dielectric or insulating materials, electrons are bound tightly to the nuclei, so that only substantial electric fields are able to mobilize them. They usually show a small $\epsilon'(\omega)$ and a negligible $\epsilon''(\omega)$ in the

visible region. On the other hand, metals possess quasi-free electrons that are easily to be mobilized by an external electrical field. The electrical properties of metals are described by the Drude model [204, 205]. This model is based on a theory of an electron gas, where the conduction electrons are assumed to be freely movable, readily to be accelerated by an externally applied electrical field.
The dielectric constant of a metal, as a function of the angular frequency, can be derived as

$$\epsilon(\omega) = 1 - \left(\frac{\omega_P^2}{\omega^2 + i\frac{\omega}{\tau}} \right) \tag{4.68}$$

whereas the τ describes the collision time, within they undergo a scattering process with each other, with the plasma frequency ω_p, given by

$$\omega_P^2 = \frac{n_e e^2}{\epsilon_0 m_e} \tag{4.69}$$

with n_e the electron density, e the electron charge and m_e the effective electron mass. Alternatively, optical properties of materials can be characterized by the complex refractive index $n(\omega) + i\kappa(\omega)$ with the real part n being the refractive index and the imaginary part κ being the absorption coefficient. Both description are equivalent and can be easily converted into each other via the following equations

$$(n + i\kappa)^2 = \epsilon' + i\epsilon'' \tag{4.70}$$

$$\epsilon' = n^2 - \kappa^2 \tag{4.71}$$

$$\epsilon'' = 2n\kappa \tag{4.72}$$

4.3.1.2 Fresnel Equations and Evanescent Waves

When a plane electromagnetic wave with a wavevector $\mathbf{k}_i$ and frequency ω impinges an interface between two dielectrics, homogenous media of refractive indices n_1 and n_2 the incident wave can either be reflected, transmitted or elastically scattered (Fig. 4.16). We will focus in the following paragraphs on the reflection and transmission, due to their significance for the spectroscopic methods, such as surface plasmon spectroscopy, ATR-FTIR and external reflection Raman spectroscopy, discussed further below.

Characteristic for all these processes is the conservation of the wavevector $\mathbf{k}_{||}$ parallel to the interface. However, the modulus and direction of the wavevector itself are changed. In the case of a plane electromagnetic wave, the angle of reflection is equal to the angle of incidence. The angle for transmission can be determined via the Snell's law:

$$n_1 \cdot sin\theta_i = n_2 \cdot sin\theta_t \tag{4.73}$$

with θ_i and θ_t being the angles of incidence and of transmission, which are measured with respect to the surface normal. In a multilayer system the electromagnetic field can be

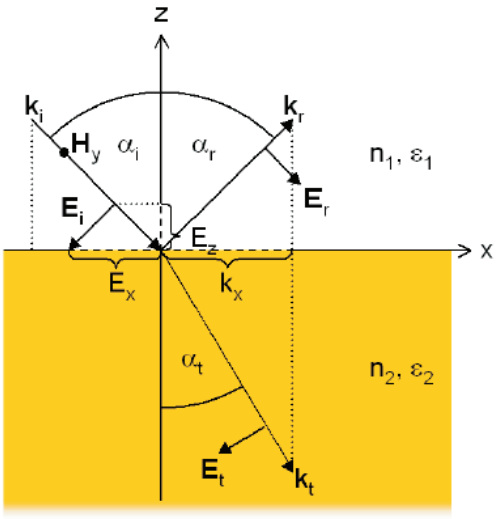

Figure 4.16: Schematic picture of an reflected and transmitted transverse magnetic polarized plane wave at an interface between two different dielectric media. The plane of incidence is spanned between the wavevector of the incident light beam and the surface normal. The in-plane components of the wavevectors are equal for all contributions.

decomposed, due to the conservation of $\mathbf{k}_{||}$, in each layer into an upward and a downward propagating plane wave. These two components of the electrical field completely describe the whole system.
In the case that light is passing an optical thinner medium 1 and reaching an optical thicker medium 2, $n_1 < n_2$, a unique situation occurs. Assuming an angle of incident θ_1 where θ_2 reaches a value of 90°, no light is transmitted into medium 2 and the full intensity is reflected. This is configuration is called total internal reflection, that starts at the so-called critical angle, θ_c.

$$\theta_c = arcsin\left(\frac{n2}{n1}\right) \tag{4.74}$$

At that point the reflectivity reaches a value of $R = 1$, i.e. the transmitted light is always equal to 0 for $\theta_i > \theta_c$. However at such high angles the component of the field normal to the surface is not longer oscillatory but decays in an exponential way, thus being the regime of evanescent waves.
Two different orthogonal polarisation vectors, which form the basis required to fully describe a plane wave with ($\mathbf{k}$,ω) can be defined. On the one hand, this is the transverse electric (TE) or *s*-polarisation, having its electric field component perpendicular to the plane of incidence, and on the other hand the transverse magnetic (TM) or *p*-polarisation, which has an magnetic field component perpendicular to the plane of incidence. These polarisations do not change their state of polarisation upon reflection or transmission. In general, all polarisations can be regarded as a linear superposition of both orthogonal polarisations.

In an optical experiment when light with a known wavelength, polarisation and intensity of the incident beam, approaches an interface of two different media the analysis of the reflected or transmitted beam intensity gives insight into the properties of the material. This process was first mathematically described by Fresnel. He based his theory on continuity conditions for the tangential components of **E** and **H** at the interface. Since both polarization behave differently they have to be distinguished. The Fresnel formulas are expressed as the ratios of the electric field amplitude of the reflected (r) or transmitted (t) wave and the incident wave amplitude, dependent on the certain polarisation

$$\begin{aligned} r_s^r &= \frac{E_r}{E_i} = \frac{n_2 cos\theta_i - n_1 cos\theta_t}{n_2 cos\theta_i + n_1 cos\theta_t} \qquad r_s^t = \frac{E_r}{E_i} = \frac{2n_1 cos\theta_i}{n_2 cos\theta_i + n_1 cos\theta_t} \\ r_s^r &= \frac{E_r}{E_i} = \frac{n_2 cos\theta_t - n_1 cos\theta_i}{n_2 cos\theta_t + n_1 cos\theta_i} \qquad r_s^t = \frac{E_r}{E_i} = \frac{2n_1 cos\theta_i}{n_2 cos\theta_t + n_1 cos\theta_i} \end{aligned} \tag{4.75}$$

Under experimental conditions, however, only intensities are detectable, i.e. the reflectivity R and the transmission T, the ratio of the respective intensities, respectively. Reflectivity and transmission are given by [206]

$$R = \frac{I_r}{I_i} = \frac{|\mathbf{E}_r|^2}{|\mathbf{E}_i|^2} = (r^r)^2 \qquad T = \frac{I_t}{I_i} = \frac{|\mathbf{E}_t|^2}{|\mathbf{E}_i|^2} = (r^t)^2 \tag{4.76}$$

4.3.1.3 Physical Properties of Surface Plasmons

Surface plasmons (SPs) are coherent oscillations of free electrons at an interface between a conductor and a dielectric, leading to electromagnetic fields confined to the interface [206]. Because of the strong coupling between surface electromagnetic modes involving photons and surface electric- as well as magnetic dipole excitations, the more accurate term of such an entity is a surface plasmon polariton [207]. SPs are wave-like electromagnetic modes that propagate along an interface between a metallic and a dielectric half-space/media and whose amplitudes decrease exponentially normal to the surface, which is also called an evanescent field. These surface waves have transverse magnetic (TM) polarization, and are evanescent in both the dielectric and the metal.

The different modes of surface plasmons can be derived as a solution to Maxwell's equation appearing as surface waves. Only p-polarized electrical fields can induce surface charges due to its field components along the z-axis and therefore generate SPs. Thus, in the following we will focus on p-polarised electrical fields.

The interface between two media of different frequency-dependent complex dielectric functions

$$\epsilon_1 = \epsilon_1' + i\epsilon_1'' \tag{4.77}$$

$$\epsilon_2 = \epsilon_2' + i\epsilon_2'' \tag{4.78}$$

is examined. The complex dielectric constant ϵ and the complex refractive index $(n + i\kappa)$ were shown to be related by equations (4.70)-(4.72). The imaginary part κ as the absorption coefficient is responsible for the attenuation of an electromagnetic wave. When assuming a non-magnetic material the magnetic permeabilities, μ_1 and μ_2 equal to 1. Thus there only exist surface polaritons for transverse magnetic polarised incident plane waves, with a general solution to the problem given by:

$$\begin{aligned} \mathbf{E}_1 &= \mathbf{E}_{01} \cdot exp[i(k_{x1}x + k_{z1}z - \omega t)] \\ \mathbf{E}_2 &= \mathbf{E}_{02} \cdot exp[i(k_{x2}x + k_{z2}z - \omega t)] \\ \mathbf{H}_1 &= \mathbf{H}_{01} \cdot exp[i(k_{x1}x + k_{z1}z - \omega t)] \\ \mathbf{H}_2 &= \mathbf{H}_{02} \cdot exp[i(k_{x2}x + k_{z2}z - \omega t)] \end{aligned} \tag{4.79}$$

k_{x1} and k_{x2} are the wavevectors in x-directions and k_{z1}, k_{z2} the ones along the z-axis. With the notation 1 and 2 for the two media involved for z $>$ 0 and z $<$ 0, respectively. Due to the continuity conditions of the tangential components of **E** and **H** at the surface, i.e. $E_{x1} = E_{x2}$ and $H_{y1} = H_{y2}$, it follows

$$k_{z1}H_{Hy1} = \frac{\omega}{c} \cdot \epsilon_1 E_{x1} \tag{4.80}$$

$$k_{z2}H_{Hy2} = \frac{\omega}{c} \cdot \epsilon_2 E_{x2} \tag{4.81}$$

After inserting equation (4.79) into Maxwell's equations (4.60) gives

$$k_{x1} = k_{x2} = k_x \tag{4.82}$$

leading to the only nontrivial solution, if

$$\frac{k_{z1}}{k_{z2}} = -\frac{\epsilon_1}{\epsilon_2} \tag{4.83}$$

The conclusion of this equation is that surface electromagnetic modes can only be excited at interfaces of media that have dielectric constants of opposite signs. The excitation by an appropriate electrical field, that follows the conditions, discussed above, results in a collective plasma oscillation of a nearly free electron gas in a metal around the charged metal ions, called plasmon surface polaritons or surface plasmons. In contrast to dielectrics, where the electrons are bound tightly to the nuclei the electrons in metals are quasi-free and may be moved easily by an external force. The classical Drude model [208, 204], which provides the theory for the free-electron situation in metals, derives a highly negative, complex dielectric constant:

$$\epsilon(\omega) = 1 - \frac{\omega_p^2}{\omega^2} \tag{4.84}$$

Hereby ω_p is the so-called plasma, which is usually in the UV range for metals. This equation is only valid up to a maximum frequency ω_{max}, which is given by

$$\omega_{max} = \frac{\omega_p}{\sqrt{1 + \epsilon_d}} \tag{4.85}$$

From equations (4.60) the wavevectors in the direction of the z-axis can be calculated

$$k_{zd} = \sqrt{\epsilon_d(\frac{\omega}{c})^2 - k_x^2} \qquad and \qquad k_{zm} = \sqrt{\epsilon_m(\frac{\omega}{c})^2 - k_x^2} \tag{4.86}$$

Finally, with equation (4.83) this leads to the plasmonic dispersion relation at a metal-dielectric interface:

$$k_x = k_x' + ik_x'' = \frac{\omega}{c}\sqrt{\frac{\epsilon_m \cdot \epsilon_d}{\epsilon_m + \epsilon_d}} \tag{4.87}$$

The complex nature of the wavevectors in x- and z-direction leads to an evanescent wave in z and the field may now become propagating rather than remaining evanescent along the x- axis leading to an attenuated wave. Methods based on this configuration are called attenuated total reflection (ATR). The finite propagation length L_x can be defined as

$$L_x = \frac{1}{k_x''} \tag{4.88}$$

For a gold-air interface [6] and an excitation wavelength of $\lambda = 632.8$ nm the propagation length is approximately 10 μm.

4.3.1.4 Surface Plasmon Resonance (SPR)

A further aspect of the dispersion relation of surface plasmons (equ. 2.20) is summarised in the following equation:

$$k_{x,SP} = \frac{\omega}{c}\sqrt{\frac{\epsilon_m \cdot \epsilon_d}{\epsilon_m + \epsilon_d}} \geq \frac{\omega}{c}\sqrt{\epsilon_d} = k_{x,(max),ph} \tag{4.89}$$

Due to the fact that the z-component of the wavevector of surface plasmons is purely imaginary, the surface plasmon is a nonradiative evanescent wave with a maximum field amplitude at the interface, decaying exponentially into the dielectric and the metal. This exponential decay of the evanescent electromagnetic field in the dielectric media is characterized by the penetration length,

$$l = \frac{\lambda}{\sqrt{2\pi((n \cdot sin\theta)^2 - 1)}} \tag{4.90}$$

which is a function of the angle of incidence and approximately half of the wavelength λ.

Another consequence of equation 4.89 is that an incident light beam with the maximum wavevector $k_{x(max),ph}$ at the interface, e.g. with grazing incidence conditions (equ. 4.74), cannot excite a surface plasmon with the wavevector $k_{x,SP}$ since the $k_{x,SP}$ of the wavevector

[6] $\epsilon_m = -12 + i \cdot 1.3$

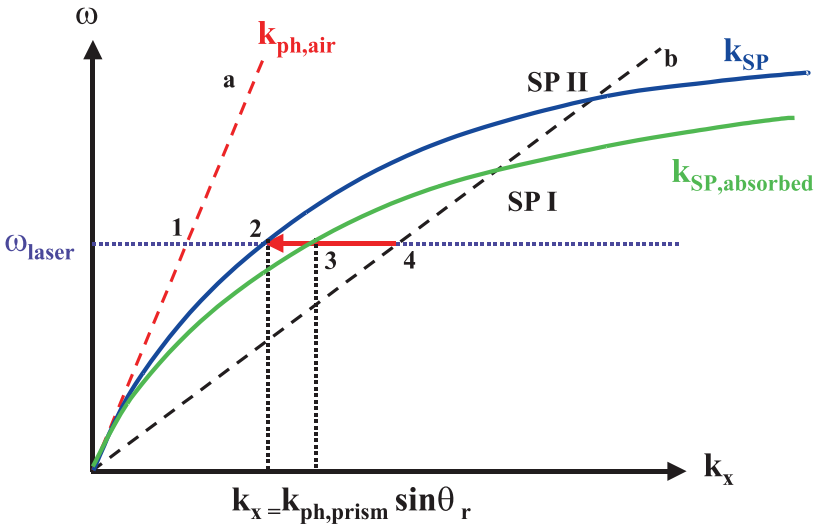

Figure 4.17: Plasmonic Dispersion relation of a free photons in a dielectric (curve a) and in a coupling prism (curve b). The photonic (red dashed line) and plasmonic dispersion curves (green solid curve) do not intersect apart from the origin (1). Introducing a higher refractive index dielectric lowers the slope of the free light line (black dashed line). By tuning the angle of incidence, the length of the photonic k_x can be reduced (see arrow) until it matches the plasmonic in-plane wavevector component and surface plasmon excitation becomes possible (2). Changing the dielectric environment, for example by adsorbing a material with a higher dielectric constant, will effect the plasmonic dispersion curve (blue solid curve) and thus result in a different resonance angle (3).

will always exceed the wavevector of the light. Figure 4.17 illustrates the relation between the photonic and plasmonic dispersion relation. The photonic dispersion relation (Fig. 4.17 dashed line) approaches asymptotically the dispersion curve of the surface plasmons without any intersection point of both curves, with neither the same energy $\hbar\omega$ or the same plane moment $\hbar k_x$, however, required for excitation. This illustrates the finding of equation 4.89 that the x-component of $k_{x,ph}$ is always smaller than the one for surface plasmons. For an interaction between photons and SPs, it is a fundamental requirement that the process obeys to the physical principles of both momentum as well as energy conservation. Among the methods developed to increase the momentum of the light in order to couple to surface plasmons there are nonlinear coupling [207] or coupling by means of a rough surface [209, 210]. By far the most predominant coupling techniques, however, are the prism coupling and the grating coupling [206]. The following theoretical description will focus on the prism coupling, since this method was utilized in the context of this thesis.

Figure 4.17 shows the change in the dispersion relation after introducing a prism with an refractive index n, higher than the one of the dielectric (Fig. 4.17. The slope of the photonic dispersion curve is tilted according to equation (4.67) by a factor equal to the refractive index $n = \sqrt{\epsilon(\omega)}$. Thus, at a given laser wavelength λ_{Laser} or ω_{Laser}, coupling

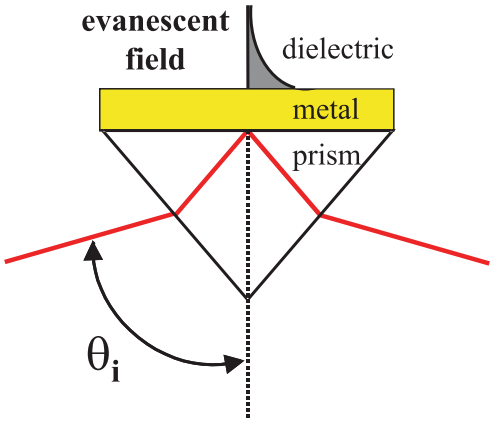

Figure 4.18: Prism coupling in the Kretschmann configuration.

to surface plasmons can be obtained. The intersection point of ω_{Laser} with the surface plasmon dispersion curve k_{SP} gives the maximum in-plane contribution of the light wavevector. However, since at point (1) the momentum of the light beam is too large, it has to be tuned according to the SP dispersions curve by varying the angle of incidence, θ_i. A rotation by θ_i causes a change of the wavevector according to $k_{x,Ph} = k_0 \cdot sin\theta_i$. As mentioned above, the excitation of surface plasmons occurs only in the case when the energy and the momentum of photons and plasmons match each other. This applies for the case when θ_i is sufficiently high, so that then intersection of the laser line coincides with the plasmonic dispersion curve.

The most prominent configurations of exciting surface plasmons utilizing a high refractive index prism to couple light to surface plasmons, is the so-called Kretschmann configuration [211, 206] (Fig. 4.18). A laser beam is directed onto the base of a high refractive index prism and the reflected intensity is measured. In this excitation scheme the light couples through a thin metal layer, which is in direct contact to a prism (Fig. 4.18). At the momentum matching condition a surface plasmon is then excited at the interface between the metal and the dielectric. Quantitatively, the finite thickness of the metal layer has to be taken into account, which allows in particular that a fraction of the surface plasmon light is coupled out through the metal and the prism. However, this thin additional metal layer can be considered as a minor disturbance to the surface plasmon electromagnetic wave [211, 212]. To obtain an optimal and most efficient coupling of the incident light, an optimum for the metal thickness has to be found and strictly controlled.

In the case of a too thin metal film the interaction between the metal film and the incident light is not sufficient so that too much intensity will pass through the metal and propagate freely as a transmitted wave or it will be simply reflected. If the metal layer is too thick

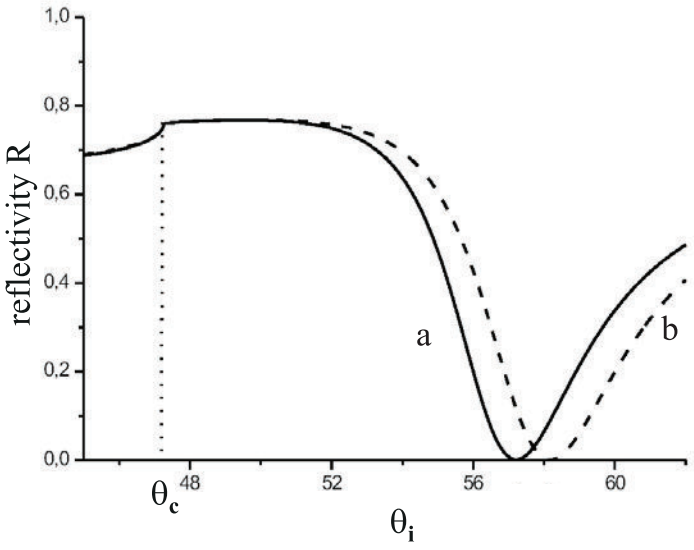

Figure 4.19: Reflectivity as a function of the angle of incidence ϕ_i (a) with a bare gold surface and (b) with an adsorbate on the surface, which is shifting the minimum of the SPR curve to higher angles.

the tunnel barrier would be too large, so that it will not reach the interface on the opposite side. For a gold film the optimum thickness for a laser wavelength of $\lambda = 632.8$ nm [7] lies between 45 μm and 50 μm, which can be easily controlled by evaporation. For the appropriate metal film thickness the surface plasmon resonance (SPR) can be optimally excited and the characteristic dip in the reflectivity scan appears if the power of the electromagnetic wave is nearly fully channelled into the surface wave.

Fig. 4.19 shows a typical measured SPR curve, where the reflectivity R ($R := \frac{I_i}{I_r}$) is plotted against the angle of incidence θ_i for the laser light. As discussed above, it is possible by changing the angle of incidence ($k_x - k_0 \cdot sin\theta_i$) to tune the system into resonance. At low angles, the reflected intensity increases as described by the Fresnel formulas (equ.4.73). Then, from a certain angle onwards, i.e. the angle of total reflection θ_c, the reflectivity reaches a plateau. The reflectivity before θ_c is quite high, since the evaporated metal film acts as a mirror reflecting most of the incident light. However, the maximum reflected intensity never reaches unity, as predicted by Snell´s law (equ. 4.73), since the photon energy is partly dissipated in the metal layer. The position of the critical angle only depends on the substrate and the neighbouring prism and water phase, but is not influenced by any of the absorbed layers.
If the projection of $\mathbf{k}_i$ to the interface matches $\mathbf{k}_{x,SP}$ resonance occurs and a surface plasmon is excited. This condition is displayed in figure 4.17. Once an angle θ_0' for the resonance condition is reached, where the wave vector of the incident photon of the laser matches the dispersion relation for surface plasmons, a dip in the reflected intensity is observed. The

[7] the excitation wavelength of a HeNe laser

minimum is given by

$$\theta_0' = arcsin\left(\sqrt{\frac{\epsilon_m \cdot \epsilon_d}{(\epsilon_m + \epsilon_d)\cdot \epsilon_m}}\right) \tag{4.91}$$

with ϵ_p, being the dielectric constant of the prism. Due to absorption and scattering processes in a real metal the oscillation created by the incident electric field is damped. If this damping process would not occur, the surface plasmon resonance would be infinitely sharp and would have an infinite propagation length. The damping in metals is caused by its imaginary part of the dielectric constant. Thus the dispersion relation for SPs has to be modified to

$$k_x = k_x' + ik_x'' = \frac{\omega}{c}\sqrt{\frac{(\epsilon_m' + i\cdot\epsilon_m'')\cdot\epsilon_d}{(\epsilon_m' + i\cdot\epsilon_m'') + \epsilon_d}} \approx \frac{\omega}{c}\sqrt{\epsilon_d(1 - \frac{\epsilon_d}{2\epsilon_m'})} + i\cdot\frac{1}{2}\frac{\omega}{c}\frac{\epsilon_m''(\epsilon_d)^{3/2}}{(\epsilon_m)^2} \tag{4.92}$$

The shift of the SP is inversely proportional to ϵ_m' whereas the width of the surface plasmon resonance, is linear proportional to ϵ_m'' and is inversely proportional to $((\epsilon_m')^2)$. This is also the reason for much sharper resonance in the case of silver instead of gold, due to a smaller imaginary part as well as a more negative real part(ϵ_{gold}=-12+i·1.2, ϵ_{silver}=-17+i·0.7).
The advantage of surface plasmon spectroscopy (SPS) lies in its sensitivity to surface processes due to its evanescent field. This means, that changes of the dielectric constant (ϵ_d) of the substrate, e.g. by adding an additional thin layer ($d \ll 2\pi/k_{zd}$) on the surface, changes the plasmonic dispersion curve and changes the surface plasmon response (equation 4.87 and 4.92). This change in overall refractive index integrated over the evanescent field results in a slight shift of the surface plasmon dispersion curve as can be seen in figure 4.19 for an additional layer with higher refractive index than the reference dielectric. At the same energy $\hbar\omega$ of incident light the dispersion curve of the surface plasmon intersects with the light line at higher wavevectors (Fig. 4.17). In terms of the reflectivity as a function of the angle of incidence the minimum is therefore shifted to higher angles. The minimum shift in the SPR curve does not depend on the absolute value of n but rather on the contrast, i.e. the refractive index difference between the layer and the surrounding medium.

When adding a layer to the existing system two parameters are changed, the refractive index n and the thickness d of the film. The surface plasmon resonance only provides a set of parameters (n, d), derived from such reflectivity curves. These two coupled parameters can only be separated if for example one of them is already known by independent measurements. Then the unknown parameter can be obtained from fits to the curves. If both parameters are unknown, at least two different measurements that are correlated to the addition are required. For example resonance curves can be taken at different laser wavelengths [213] or the surface plasmon curves can be measured with different solvents with different refractive indices [214].

4.3.1.5 Localized Plasmons on Rough Surfaces

Rough surfaces and nanoparticles of noble-metals can interact strongly with visible light due to the resonant excitation of surface plasmon modes. These modes are characterized by spectrally selective absorption and scattering, and give rise to an enhancement of the local field with respect to the exciting light field [215, 216]. A variety of applications are based on these effects, such as surface-enhanced Raman scattering [217, 218, 219, 216].

The simplest model to study enhancement effects of rough surfaces is to study the electromagnetic interaction of two or more nanoparticles in close proximity to one another. Such configurations give rise to tunable spectral shifts of the plasmon bands and to exceptionally strong field enhancements [220, 221]. There is a growing interest in this field as improved nanofabrication methods become available allowing for an advanced control of nanoparticle shape and arrangement. However, the application of nanoparticles in bioelectrochemical experiments remains difficult, in particular regarding good electrical contact to the electrode avoiding transition resistances and decomposition of the particles by illumination. For extended surface confined architectures, such as self-assembled monolayers or tethered bilayer systems, roughened surfaces are favoured, thus providing a continuous electrode surface ready for electrochemical measurements.

In the foregone discussion a planar surface was considered to derive the surface plasmon dispersion relations. Instead of enlarging the value of k_x with a prism, a sub-wavelength regular modulation of the surface structure may also provide the missing momentum to satisfy the law of momentum conservation:

$$k_{x,ph} + G_p = k_{x,SP} \tag{4.93}$$

where G_p is the reciprocal of the grating constant Λ, which is a function of the periodicity of the grating [206],

$$G_p = \frac{2\pi}{\Lambda} \tag{4.94}$$

so that also surface plasmon modes may be excited and radiate. A number of different values for G_p may be provided by a rough surface, since in a first approximation, all the randomly distributed structures, as hills, bumps and crevices, may be described as a superposition of gratings. However, for a substantially rough surface, the plasmon resonances can not be properly described by equation (4.87), which is valid only for flat surfaces or for the limit of superimposed small perturbations. Thus surface roughness or curvature is required for the excitation of surface plasmons by light.

More suitable concepts are then introduced to better describe the electronic behaviour and the corresponding electromagnetic field distribution in the proximity of subwavelength structures. Various models [202, 222] have been proposed using spheres, ellipsoids, cylindral rods or even arrays of particles or fractal structures to model the surface roughness.

As mentioned above, the surface plasmons are electromagnetic waves propagating along a flat surface. Any structure in their way acts as an obstacle of scattering center that converts the delocalized mode into a localized surface plasmon (LSP), as present in the case of a spherical particle, where the electromagnetic wave is confined into subwavelength structures [206]. The local field strength, amplitude and the resonant condition associated with the charge oscillations are all governed by the size and geometry of each structure as well as by their spatial arrangements.

4.3.2 Theoretical Treatment of Molecular Vibrations

In the classical treatment of the vibrational motion of molecules, the atoms are assumed to be connected with bonds that act like mechanical springs undergoing harmonic oscillations around the equilibrium position. Energy of incident photons can cause different types of vibrations, such as symmetric or asymmetric stretching, bending or so-called rocking vibrations of a bond between two atoms in a molecule. The frequency ω of the oscillation between two atoms is given by:

$$\omega = \sqrt{\frac{k}{\mu}} \tag{4.95}$$

where k represents the force constant and μ the reduced mass of the molecule. For two atoms having the masses m_1 and m_2, the reduced mass is defined as:

$$\mu = \frac{m_1 \cdot m_2}{m_1 \ + m_2} \tag{4.96}$$

Resulting in lower frequencies for heavier atoms as compared to lighter atoms. Vibrational frequencies involving carbon, oxygen or nitrogen atoms are therefore lower than these involving hydrogen atoms. On the other hand, the force or spring constant k is related to the type of bonding, thus stiffer bonds like double or triple bonds tend to have higher frequencies than a single bond. Since the force that acts on the two atoms is the elastic force and it is given by the negative derivative of the potential energy V, the following expression for the harmonic potential is obtained:

$$V = \frac{k \cdot q^2}{2} \tag{4.97}$$

where $q = x_2 - x_1$ represents the displacement of the two atoms from the equilibrium internuclear distance. Equation 4.95 indicates that by changing the reduced mass, the frequency of the vibration can be shifted.

A better description of the molecular vibrations can be obtained by treating the systems quantum mechanically. For this, the *Schrödinger* equation for the system of interest needs to be solved:

$$i\hbar\frac{\partial}{\partial t}\Psi(\mathbf{r},\mathbf{R},t) = \hat{H}\Psi(\mathbf{r},\mathbf{R},t) \tag{4.98}$$

Equation 4.98 is referred to as the *time-dependent Schrödinger* equation, where $\Psi(r, \mathbf{R}, t)$ represents the molecular wavefunction, which depends on the electronic coordinates $\mathbf{r}$, the nuclear coordinates $\mathbf{R}$ and time t. $\hat{H}$ represents the Hamilton operator of the system and can be written as the sum of the total kinetic energy of the electrons $\hat{T}_e$, total kinetic energy of the nuclei $\hat{T}_n$ and the potential energy consisting of the electron-electron $\hat{V}_{ee}$, electron-nuclei $\hat{V}_{ne}$ and nuclei-nuclei $\hat{V}_{nn}$ Coulomb interactions:

$$\hat{H} = \hat{T}_e + \hat{T}_n + \hat{V}_{ee} + \hat{V}_{ne} + \hat{V}_{nn} \tag{4.99}$$

Because in equation (3.5) of the Hamiltonian, the time does not appear explicitly, a separation of variables according to space and time can be performed. Hence, the molecular wavefunction of the system takes the form

$$\hat{H}\Psi(\mathbf{r},\mathbf{R}, t) = \Psi(\mathbf{r},\mathbf{R}) \cdot \varphi(t) \tag{4.100}$$

By substituting equation (3.6) in equation 4.98, two differential equations are obtained, one time-independent and one time-dependent. The time-independent Schrödinger equation for the spatial wavefunction has the form:

$$\hat{H}\Psi(\mathbf{r},\mathbf{R}) = E\Psi(\mathbf{r},\mathbf{R}) \tag{4.101}$$

For the time-dependent differential equation, the following solution is obtained:

$$\varphi(t) = exp\left(\frac{-iEt}{\hbar}\right), \qquad \hbar = \frac{h}{2\pi}, \qquad E = \hbar\omega = \frac{hc}{\lambda} \tag{4.102}$$

where E represents the eigenvalue of the Hamiltonian and h the Planck constant. The solutions of the time-independent Schrödinger equation are difficult to obtain, especially for large systems. Usually it is possible to introduce the $Born-Oppenheimer$ approximation, which considers that the motion of the heavy nuclei is much slower than that of the light electrons. As a consequence, the nuclei can be considered fixed and the wave function can be separated into an electronic and a nuclear part:

$$\Psi(\mathbf{r},\mathbf{R}) = \Psi_{el}(\mathbf{r},\mathbf{R}) \cdot \Psi_n(\mathbf{R}) \tag{4.103}$$

where $\Psi(\mathbf{r},\mathbf{R})$ represents the electronic wave function for a given configuration of the nuclei and $\Psi_n(\mathbf{R})$ represents the nuclear wavefunction. The Hamiltonian from equation 4.99 can be separated into an electronic $\hat{H}_{el}$ and a nuclear $\hat{H}_n$ part:

$$\hat{H}_{el} = \hat{T}_e + \hat{V}_{ee} + \hat{V}_{ne} \tag{4.104}$$

$$\hat{H}_n = \hat{T}_n + \hat{V}_{nn} \tag{4.105}$$

By introducing the separated wavefunction 4.103 into the time-independent Schrödinger equation, and considering the kinetic energy of the nuclei $\hat{T}_n$ equal to zero and the Coulomb interaction between the nuclei $\hat{V}_{nn}$ constant, the electronic equation is obtained:

$$\hat{H}_{el}\Psi_{el}(\mathbf{r},\mathbf{R}) = E_{el}(\mathbf{R})\psi(\mathbf{r},\mathbf{R}) \tag{4.106}$$

Equation (4.106) describes the electronic motion and can be resolved parametrically with respect to the nuclear set of coordinates R. The solutions give the electronic energies as a function of the nuclear displacement. If the electronic problem is solved, it is subsequently possible to approach the nuclear problem. Solutions to the nuclear Schrödinger equation,

$$(\hat{H}_n + E_{el}(\mathbf{R}))\Psi_n(\mathbf{R}) = E\Psi_n(\mathbf{R}) \tag{4.107}$$

describe the vibration, rotation and translation of a molecule. E is the *Born−Oppenheimer* approximation to the total energy and includes the electronic, vibrational, rotational and translational energy.

Returning to the harmonic oscillator treated classically at the beginning of the chapter, now a quantum mechanical explanation can be given. The potential energy V can be expressed in a general form as a power series expansion about the equilibrium position. In the case of the harmonic oscillator, only the quadratic term is considered and the potential energy can be expressed as in equation (4.97). By introducing V in the time-independent Schrödinger equation (4.101) and solving the equation, the energy values E allowed for the harmonic oscillator are obtained:

$$E = \hbar\omega\left(v + \frac{1}{2}\right), \qquad v = 0, 1, 2, ... \tag{4.108}$$

where ω represents the angular frequency. For $v = 0$ the zero point energy E_0 is obtained. Equation (4.108) indicates that for the harmonic potential the vibrational levels are equally separated from each other $\Delta E = E_{v+1} - E_v = h\nu = \hbar\omega$ The description of the vibrational motion for a two atomic system is rather simple, however polyatomic molecules present a large number of possible vibrations. For a molecule with N nuclei there are $3N$ degrees of freedom from which $3N-6$ for nonlinear molecules, respectively $3N-5$ for linear systems are left to describe the vibrational motions of a molecular systems. Accordingly, there are $3N-6$ ($3N-5$) normal coordinates to describe the vibrational motion. The other 6 (5) coordinates describe the rotational and translational motions of the molecule.

According to equation (4.97) the harmonic oscillator is characterized by a parabolic potential curve. This is generally true only for small displacements from the equilibrium distance. The potential energy and the restoring force increase infinitely when increasing the distance from the equilibrium. However, in real systems, at high internuclear distances, the attractive force is zero (the molecule dissociates) and the potential energy has a constant value which represents the dissociation energy. For larger amplitude vibrational motions, anharmonicities play an important role. The deviation from the potential curve described by equation (3.3) to the curve of a real molecule is due to *mechanical anharmonicity*. The simulation of a potential energy surface including the anharmonicities is difficult.

An approximate solution for two atomic system which describes well also the dissociation was given by P. M. Morse. [223, 205] He proposed a general formula for the potential

energy as:

$$V = D - e\left[1 - e^{-a(R-R_e)}\right]^2 \tag{4.109}$$

In equation (3.15), D_e represents the dissociation energy, R, the internuclear distance, R_e is the equilibrium bond length and the parameter a determines the width of the potential well

$$a = \sqrt{\frac{\mu}{2D_e}\omega_e} \tag{4.110}$$

with $\omega = 2\pi\nu_e$ denotes the harmonic vibrational frequency. The Morse potential accounts for the anharmonicity, which is defined through the parameter χ_e, refered to as the anharmonicity constant. The value of χ_e can be determined by the following equation:

$$\chi_e = \frac{\hbar\omega_e}{4D_e} \tag{4.111}$$

The values of the frequency ω_e for certain vibrational levels can be determined by considering the anharmonicity constant of the potential. Their values can be determined by evaluating the following equation:

$$\omega_v = \omega_e[1 - \chi_e(v + \frac{1}{2})] \tag{4.112}$$

A similar formula to (3.18) can be obtained for the energy levels:

$$E_v = \hbar\omega_e(v + \frac{1}{2})[1 - \chi_e(v + \frac{1}{2})] \tag{4.113}$$

A schematic representation of a Morse potential curve for a two atomic molecule is shown in Figure 4.20. Due to the anharmonicity constant the distance between the energy levels becomes smaller with increasing the energy.

4.3.2.1 Electronic and Vibrational Transitions

In the previous section it was shown that molecules consist of discrete energy levels. When interacting with light, molecules can only absorb photons of frequencies ($E_{ph} = h\nu = hc/\lambda$) corresponding to energies that exactly match the gaps between the electronic ground state and a higher electronic, a so-called excited state. Through the absorption of a photon the molecule can be promoted to an excited state. Different types of spectroscopy employ photons in different frequency ranges and therefore investigate different molecular transitions. Photons with frequencies in the infrared portion of the electromagnetic spectrum have the required energy to modulate molecular vibrational states. Photons from the ultraviolet and visible portion of the electromagnetic spectrum are energetic enough to promote ground state electrons to higher molecular orbitals. In the framework of this dissertation

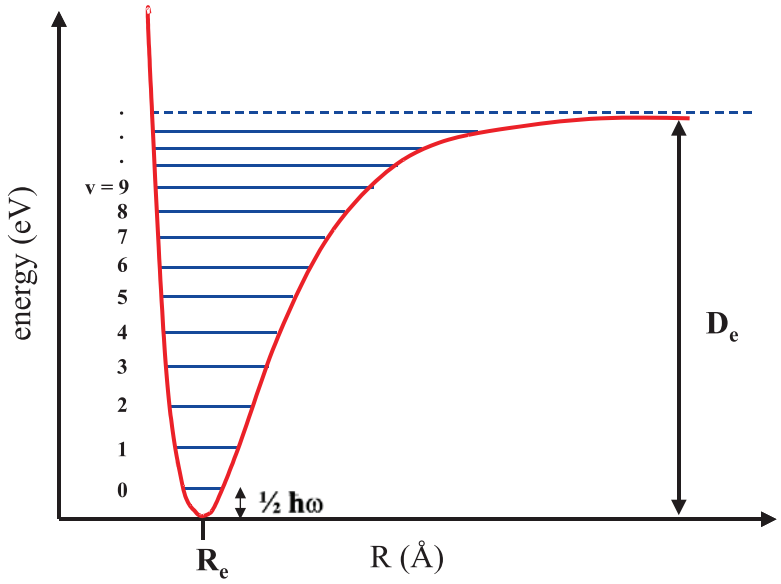

Figure 4.20: Schematic representation fo the Morse potential curve for a two atomic molecule. The potential energy is plotted as a function of the bond distance R. R_e and D_e are the equilibrium bond length and the dissociation energy, respectively. The numbers on the left side denote the vibrational levels v = 0,1,2,3 ...

spectroscopic techniques that probe vibrational transitions were employed. The distinction between these two types of moleculear transitions is shown from diatomic molecules in Figure 4.21.

The complete set of frequencies that can be absorbed by the molecule and cause transitions in the electronic or vibrational modes upon irradiation forms a characteristic spectrum for each molecule. During an electronic transition the absorbed photon promotes electrons from one molecular orbital to another of higher energy. One example is the transition of a π electron into a antibonding π^* orbital of C=C bonds. The longer the conjugated π-system of a chromophore, the lower is the required excitation energy, such as the porphyrin system of heme groups. This effect is called *bathochromic* effect. Cytochrome c oxidase contains two such chromophores, both hemes_a. The structure of heme_a is shown in Figure 4.22. Hemes are porphyrin rings, with multiple conjugated bonds and absorb photons in the 400-700 nm range, which is utilized in the resonance Raman spectroscopy. The structure of heme a is shown in figure 4.22.
In vibration spectroscopic technique, the incident photon causes a transition between the vibrational states (Fig. 4.21). Raman and infrared spectroscopy are two types of spectroscopy capable of monitoring vibrational transitions in molecules, i.e. when a molecule is excited from one vibrational level to a higher vibrational level. Each uses a different strategy for effecting the vibrational transition. Infrared spectroscopy employs a direct transition between the vibrational states, similar to the electronic transitions discussed above, whereas Raman spectroscopy employs a two photon scattering process to modu-

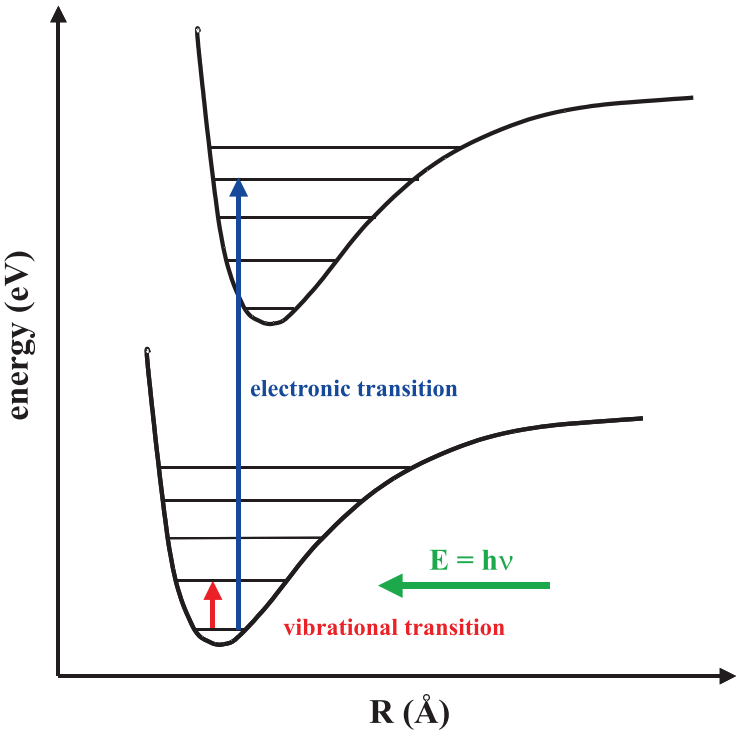

Figure 4.21: Electronic and vibrational energy transitions for a diatomic molecule. At room temperature, a population of molecules resides in the ground electronic and vibrational states. According to the energy of the incoming photon either an electronic transition or a vibrational transition is initiated. Irradiation with infrared light usually causes vibrational transition in the electronic ground state (red arrow), whereas irradiation with visible of ultra-violet light causes an electronic transition (blue arrow).

late the vibrational levels. In infrared spectroscopy, polychromatic incident radiation in the IR range is partially absorbed by the sample to effect vibrational excitation. The remaining radiation passes through the sample unabsorbed. The intensity difference between the incident and absorbed radiation is detected and correlated to specific frequencies as a spectrum. The processes occuring in Raman spectroscopy are discussed in the next section.

Transitions between vibrational levels, like in IR spectroscopy, can be achieved through interactions of electromagnetic radiation on a molecular system. If the influence of the electromagnetic radiation is small, it can be treated as a perturbation. In the dipole approximation the perturbation is defined as $\hat{H} = -\hat{\mu} \cdot \mathbf{E}$ and appears as an additional term to the Hamilton operator $\hat{H}$

$$\hat{H} = \hat{H}_0 + \hat{H}' \tag{4.114}$$

where $\hat{H}_0$ represents the unperturbed Hamiltonian. In this approximation, the molecule-field interaction is reduced to that of the dipole moment $\hat{\mu}$ of the molecule with the time-dependent electric field of the laser E. Within the electric dipole approximation, a molecule

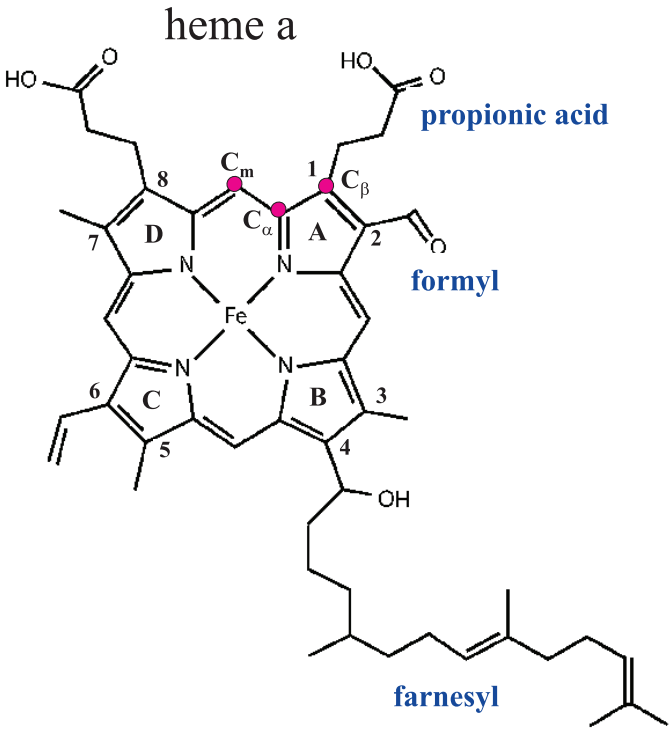

Figure 4.22: Structure of heme a.

is allowed to absorb radiation at the transition $i \rightarrow j$ only if the transition non-diagonal matrix element of its dipole moment operator is different from zero:

$$\langle j \,|\hat{\mu}|\, i\rangle \neq 0 \tag{4.115}$$

After an taylor expansion with respect to Q, around the Q_0, the selection rule (for IR absorption) follows to:

$$\left(\frac{\partial \mu_(Q)}{\partial Q}\right)_{Q_0} \neq 0 \tag{4.116}$$

Thus, the electrical dipol moment has to change during the absorption process

Considering small vibrations, the vibrational dipole moment of a molecule can be written as an expansion by the normal coordinates q_i. In a first approximation, this change can be considered linear:

$$\mu = \mu_0 + \sum_{i=1}^{3N-6} \left(\frac{\partial \mu}{\partial q_i}\right) q_i + ... \tag{4.117}$$

μ_0 represents the permanent dipole moment of the studied system associated with the equilibrium configuration[8]. If the second term in equation (4.117) is non-vanishing, the vibration is referred to as infrared active. In the opposite case, the vibration will be infrared inactive.
By using the equations (4.117) and (4.116), it can be shown that the selection rule for infrared transitions in the case of the harmonic oscillator is $\Delta v = \pm 1$. The line intensity for vibrational bands is predominantly proportional to the square of the vibrational dipole moment $((\frac{\partial \mu}{\partial q_i})^2)$. The anharmonicity gives rise to a change of the selection rule to $\Delta v = \pm 1, \pm 2, \pm 3....$ Usually, the anharmonicity is small and the intensity of the overtones is low. In polyatomic molecules the form of the potential is more complicated. The power series expansion of the potential energy will contain also higher terms than the quadratic considered for the harmonic case.

4.3.3 Raman Spectroscopy

In 1922, the Indian physicist Sir Chandrasekhara Venkata Raman published his work on the 'Molecular diffraction of light' [224]. Only eight years later (1930), he was awarded the Nobel prize in physics for his discovery of inelastic scattering of photons, what is called today in his honor as the Raman effect. Almost simultanuously, Raman and Mandelstam [225, 226] discovered experimentally in 1927 that when light is reemitted by a molecule after optical excitation, one can observe discrete spectral 'lines', whose frequencies are uniquely shifted relative to the excitation frequency. These shifted spectral lines occur due to the inelastic scattering of the incoming photons. The frequency shifts correspond to the frequencies of the molecular resonances. Frequency shifted lines can occur at the lower and higher energy side of the excitation depending on whether the incoming photons interact with a molecule in the vibrational ground state or an excited vibrational state.

In nonresonant Raman scattering, excitation and scattered photons are not in resonance with any real molecular transition. The interaction with the molecule is not due to an absorption and emission process. Raman spectroscopy differs from other optical spectroscopies, since it gains information by analyzing the inelastic scattered radiation collected from a sample. An intense monochromatic light, provided by a laser, of frequencies higher than those required for vibrational changes is scattered off the molecules in the sample. Most photons are elastically scattered, i.e. they have the same energy as the incident photons (Rayleigh scattering), but some of the collisions between sample molecules and photons are inelastic, meaning there is an exchange of energy between photons and sample molecules. After such collisions, scattered photons have frequencies that are shifted from the initial laser frequency due to this exchange (Stokes and anti-Stokes scattering). The magnitudes of the shifts exactly match the gaps between the vibrational energy levels of the molecule inducing a rotational or vibrational (de-)excitation of the molecule. The

[8]The appearance in the equation of the Taylor expansion of the dipole moment (4.117) of higher terms in qi represents another aspect of the anharmonicity. This is referred to as the electrical anharmonicity.

frequency shift between the excitation light and the scattered light is determined by the energy of the molecular vibrations, which in turn depends on the kinds of atoms and their bond strengths and arrangements in a specific molecule. Therefore, the spectrum of the scattered light provides a structural 'fingerprint' of a molecule.

Advances in laser technology, as a nearly perfect source of excitation light, had an significant influence on the development of this method. New laser systems enabled the measurement of very small frequency shifts in the light scattered from an analyte. Together with the ability to study and to characterize a compound based on intrinsic molecular vibrations, this made Raman spectroscopy a powerful technique that has become one of the most important tools in analytical chemistry and physics with many practical applications.

4.3.3.1 The Raman Effect

When a beam of monochromatic light impinges on a sample or molecule, almost all of the photons of light emerging from the sample are unchanged in either wavelength or energy. This type of light interaction is known as either elastic scattering or more commonly Rayleigh scattering, named after Lord Rayleigh. Rayleigh first described this scattering process when explaining why the sky is seen as the color blue then light from the sun strikes molecules in the earth's atmosphere.

While the vast majority of light bombarding a molecule will interact in an elastic fashion, a very small amount, about 1 in 10^{-7} molecules, will scatter photons at different wavelengths and energies from the incoming photons [223]. The differences in wavelength and energy are due to inelastic scattering processes. This type of scattering is indicative of a molecular vibrational mode being excited. When this type of event occurs, the scattered photons will be lower in energy, and thus longer in wavelength than the incoming radiation. Light can also scatter off of a vibrationally excited molecule, in which case the scattered photons will be higher in energy than the incoming light. Analysis of these changes in wavelength from the incident wavelength yield molecular information about the sample being analyzed. This inelastic scattering of light is what is known today as the Raman Effect. A Jablonski diagram illustrating both Rayleigh scattering and the Raman Effect is shown in 4.23.

After interacting with a molecule, the scattered photons can either be of higher or lower energy than the incident photons, as previously mentioned. This difference in frequency($\Delta\nu$), between what is known as the Raman line and the Rayleigh line will correspond to fundamental vibrational frequencies that are intrinsic to the scattering molecule. It is important to note that molecular vibrations can be of several different types including stretching, bending, torsion, and deformation. It is the correspondence between molecular vibrational frequency and the shift in incident light frequency that allows Raman spectroscopy the ability to gain specific molecular level insight of a sample.

Raman lines are divided into two regimes depending on whether the scattered photons are

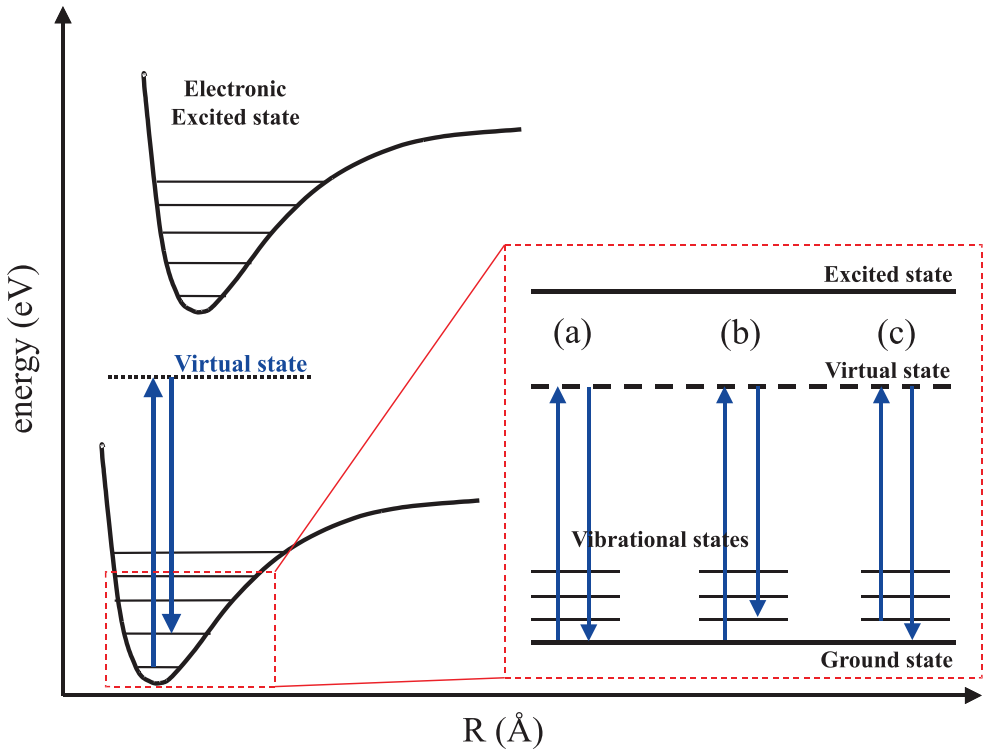

Figure 4.23: Scheme for the Raman scattering effect. (a) Rayleigh scattering and Raman scattering: (b) Stokes and (c) anti-Stokes Raman scattering (see text).

higher or lower in energy compared to the incident photons of light. When the energy of the scattered photon is less than the energy of the incident photons ($v - \Delta v$) what is known as a Stokes transition occurs. A Stokes transition gives rise to a Stokes line in the Raman spectrum. When the energy of the scattered photons is more than the energy of the incident photons ($v + \Delta v$) an anti-Stokes transition occurs. This gives rise to what is known as an anti-Stokes line in the Raman spectrum. Both the Stokes and anti-Stokes lines are symmetric about the Rayleigh line because they both correspond to the same vibrational quanta of energy (Δv) that is either gained or lost by the incident photons of light (Figure 4.23).

The Stokes lines are much more intense than the anti-Stokes lines at room temperature owing to the fact that anti-Stokes transitions can only occur from an excited vibrational state which is less probable to occur than a transition originating from the molecular ground state [223]. [9]

[9]The designation of which set of Raman lines would be named Stokes and anti-Stokes originated from Stokes' Law which states that the frequency of fluorescent light is always less than or at most equal to the frequency of the exciting light.
The lines in the Raman spectrum that 'obeyed' Stokes law were named Stokes lines and ones that 'disobeyed' Stokes' law were named anti-Stokes lines even though there are many differences between

For spectroscopic techniques such as infrared spectroscopy, as seen in the last section it is necessary for the molecule being analyzed to have a permanent electric dipole. This is not the case for Raman spectroscopy, rather it is the polarizability ($\underline{\alpha}$) of the molecule which is important. In the 'classical view' of the Raman effect, we consider light as an electromagnetic wave which generates a polarization. The oscillating electric field causes electrons in the molecule to oscillate. This leads to an induced electric dipole moment, μ_{ind}, where

$$\mu_{ind} = \underline{\alpha} \cdot \mathbf{E} \tag{4.118}$$

This induced dipole moment then emits a photon, leading to either Raman or Rayleigh scattering. The generation of this dipole moment by the incoming electric field is modulated by the molecular vibrations, since the polarizibility α is a function of the vibrational coordinate Q.
The electric field vector ($\mathbf{E}$) is given by

$$\mathbf{E} = \mathbf{E}_0 cos(2\pi\nu_0 t) \tag{4.119}$$

then equation (4.118) can be rewritten as

$$\mu_{ind} = \underline{\alpha} \cdot \mathbf{E}_0 cos(2\pi\nu_0 t) \tag{4.120}$$

If the molecule is excited to vibration, the atoms and electron cloud will be distorted during the oscillation, such that the polarization will change periodically.
A Taylor expansion can be performed on the polarizability tensor $\underline{\alpha}$,

$$\underline{\alpha} = \underline{\alpha}_0 + \left(\frac{\partial \underline{\alpha}}{\partial Q_k}\right)_0 Q_k + ... \tag{4.121}$$

which approximates the total polarizability along a given normal coordinate Q_k. Remembering that we have assumed a sinusoidal wave for the electric field vector then Q_k becomes

$$Q_k = A_k cos(2\pi\nu t) \tag{4.122}$$

When equation (4.122) is substituted back into equation (4.121), the polarizability tensor becomes

$$\underline{\alpha} = \underline{\alpha}_0 + \left(\frac{\partial \underline{\alpha}}{\partial Q_k}\right)_0 A_k cos(2\pi\nu t) + ... \tag{4.123}$$

Equation (4.123) can then be substituted into equation (4.120) to yield a fully expanded expression of the polarizability equation which is rewritten as

$$\mu_{ind} = \underline{\alpha}_0 \cdot \mathbf{E}_0 cos(2\pi\nu_0 t) + A_k \cdot \mathbf{E}_0 (\frac{\partial \underline{\alpha}}{\partial Q_k})_0 \cdot cos(2\pi\nu_0 t) \cdot cos(2\pi\nu t) \tag{4.124}$$

the Raman Effect and fluorescence [223].

If the identity for the product of two cosines, $cos(\alpha) \cdot cos(\beta) = \frac{1}{2}cos(\alpha - \beta) + \frac{1}{2}cos(\alpha + \beta)$ is used, then equation (4.124) becomes

$$\mu_{ind} = \underline{\alpha}_0 \cdot \mathbf{E}_0 cos(2\pi\nu_0 t) + \frac{1}{2}(\frac{\partial \underline{\alpha}}{\partial Q_k})_0 A_k \mathbf{E}_0 \cdot [\underbrace{cos(2\pi\nu_0 - \nu t)}_{Stokes} + \underbrace{cos(2\pi\nu_0 + \nu t)}_{Anti-Stokes}] \quad (4.125)$$

The first term of equation (4.125) corresponds to the unshifted scattered light or Rayleigh scattered light. The second term gives rise to two new frequencies those at $\nu_0 - \nu$ and $\nu_0 + \nu$. These new frequencies are the Stokes ($\nu_0 - \nu$) and the anti-Stokes ($\nu_0 + \nu$) frequencies. From equation 4.125 the selection rule for Raman spectroscopy derives to

$$\left(\frac{\partial \underline{\alpha}}{\partial Q_k}\right)_0 \neq 0 \quad (4.126)$$

This selection rule implies that for a Raman transition to occur, the polarizability tensor has to change during vibration. [223] Thus not all transitions will be 'Raman active', i.e. only vibrational transitions that fullfill this selection rule will appear in the Raman spectrum, but they can still be 'IR active' by a change of the dipole moment during excitation.

As opposed to IR spectroscopy, where a transition can only be observed when that particular vibration causes a net change in the dipole moment of the molecule, in Raman spectroscopy only such transitions can be observed, where the polarizability (α) of the molecule changes. This is the fundamental difference of how IR and Raman spectroscopy access the vibrational transitions. In Raman spectroscopy, the incoming photon causes a momentary distortion of the electron distribution around a bond in a molecule, followed by reemission of the radiation as the bond returns to its normal state. This causes temporary polarization of the bond and an induced dipole that disappears upon relaxation.

In 'normal' non-resonant Raman spectroscopy the electron is excited into a so-called 'virtual' electronic state (Fig. 4.24), which is not an inherent state of the molecule only existing for the short time of the photon-molecule interaction. If this state matches an inherent state of the molecule, with a much longer life time, the Raman signal is tremendously enhanced. This phenomena is called resonance Raman spectroscopy and will be discussed in the next section.

In second order time dependent perturbation theory of Raman scattering [223, 227], the intensity of a Raman signal (measured as number of scattered photons) is given by

$$I_s(\omega_S) = \frac{\pi^2}{\epsilon_0^2} \cdot \left(\sum_{\rho,\sigma} |[(\alpha_{\rho,\sigma})_{fi}][(\alpha_{\sigma,\rho})^*_{fi}]|\right) \cdot \omega_S^4 \cdot I_0 \quad (4.127)$$

whereas the Stokes intensity is proportional to the intensity of the incident laser beam (I_0) and increases with the fourth power of the respective scattered frequency (ω_S).

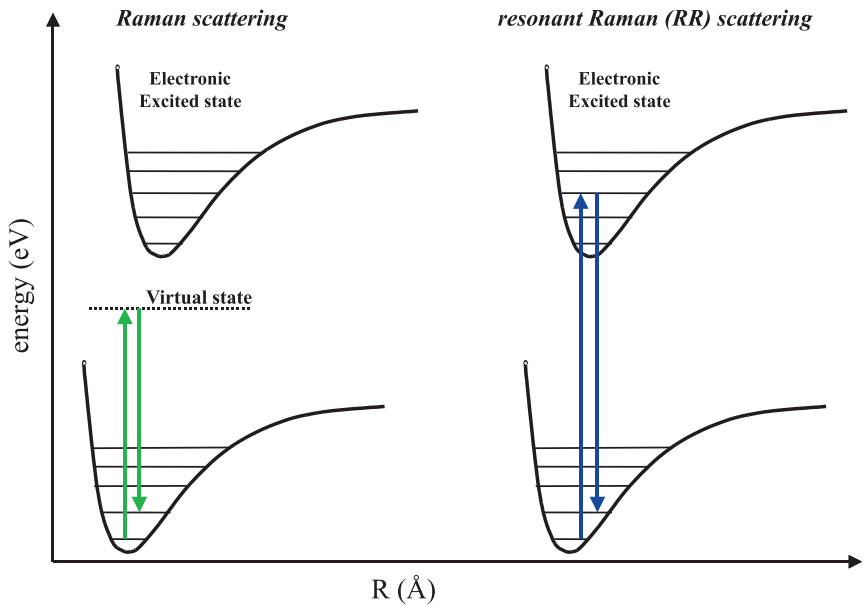

Figure 4.24: Comparision between non-resonant Raman scattering and resonant Raman scattering.

4.3.3.2 Resonance Raman Spectroscopy

The Resonance Raman (*RR*) effect was first mentioned roughly 20 years after the discovery of the Raman effect and first published by P.P. Shorygin 1947 [228].

In resonance Raman spectroscopy, the energy of the incoming laser energy is adjusted to coincide with an electronic transition of the molecule (Fig. 4.24). So, rather then exciting the molecule to a virtual energy state, it is excited to one of its excited electronic transition. When the frequency of the laser beam is in resonance with an electronic transition, the vibration modes associated with that particular transition exhibit a greatly increased Raman scattering intensity as compared to non-resonant Raman signals. Usually enhancement factors between 10^4 up to 10^6 can be obtained [229, 230, 231], which can also be explained by an increased cross section of 10^{-29} cm^2/molecule as compared to normal Raman scattering with 10^{-31} cm^2/molecule [222].

A main advantage of resonant Raman scattering is the possibility to selectively probe individual groups of a molecule. For instance resonance conditions with a $\pi - \pi^*$ transition enhances selectively the modes of the π bonds involved with the transition, while the other modes remain unaffected. This aspect of Raman spectroscopy becomes especially useful for large biomolecules with chromophores embedded in their structure. In such chromophores, the charge-transfer transitions of the metal complex generally enhance metal-ligand stretching modes, as well as some of the modes associated with the ligands alone. Hence, in a biomolecule such as heme containing proteins, tuning the laser to be in resonance with the

charge-transfer electronic transition of the iron center, results in a spectrum reflecting only the stretching and bending modes associated with the porhyrin-iron group. Consequently, in a molecule with thousands of vibrational modes, RR spectroscopy allows us to look at relatively few vibrational modes at a time. This reduces the complexity of the spectrum and allows for selective probing of structural changes in active sites independent from the protein environment. If a protein has more than one chromophore, it is possible to study them individually if their CT bands differ in energy.

Since RR spectra are fundamentally coupled to electronic transitions, between the ground state and the excited state of the molecule, Raman band intensities are controlled by the same Franck-Condon overlap integrals, as those that determine intensities of absorption band. Furthermore, RR scattering is described in the energy-frame, in terms of the Kramers-Heisenberg dispersion formula [232], obtained by second-order perturbation theory [233]. For the exact theoretical treatment the reader is refered to comprehensive textbooks or reviews [223, 233].

The result of the perturbation theoretical treatment is an intensity of a vibrational mode for a resonant Raman transition from the initial state $|i\rangle$ to an virtual state $|r\rangle$ back to a final state $|f\rangle$, given by [232, 233, 223] as

$$I_{fi} = \frac{\pi^2}{\epsilon_0^4}(\nu_0 \pm \nu_{fi})^4 I_0 \sum_{\rho,\sigma} |[(\alpha_{\rho,\sigma})_{fi}][(\alpha_{\sigma,\rho})^*_{fi}]| \tag{4.128}$$

with I_0 being the intensity of the incident laser light, ν_0 and ν_{fi} are the wave numbers of the exciting laser line and of the Raman transition $|f\rangle \leftarrow |i\rangle$, ϵ_0 is the permittivity of free space and $[(\alpha_{\rho,\sigma})_{fi}]$ is the $\rho\sigma$th element of the transition polarizability with ρ and σ as the normal coordinates of the molecule. The transition polarizability tensor, determined by the Kramers-Heisenberg dispersion relation is given by two time ordered terms [232, 234, 235]:

$$(\alpha_{\rho\sigma})_{fi} = \frac{1}{hc}\sum_r \left(\frac{\langle f|\,\mu_\rho\,|r\rangle\,\langle r|\,\mu_\sigma\,|i\rangle}{\omega_{ri} - \omega_0 - i\Gamma} + \frac{\langle f|\,\mu_\sigma\,|r\rangle\,\langle r|\,\mu_\rho\,|i\rangle}{\omega_{ri} + \omega_0 - i\Gamma} \right) \tag{4.129}$$

with μ_σ and μ_ρ as the transition dipole moment. $|i\rangle$,$|r\rangle$ and $|f\rangle$ are initial vibrational state of the electronic ground state, intermediate vibrational (with a damping rate $\Gamma = \hbar\omega_{rf}/\tau_r$ of state r depending on the lifetime τ_r of this state) and the final vibrational state of the electronic ground state of the molecule with the energies E_i, E_R and E_f ; $\hbar\omega_{ri} = E_r - E_i$ and $\hbar\omega_{rf} = E_r - E_f$. Equation 4.129 shows already the origin of the enhancement in the resonant case where the laser photon energy matches approximately the energy difference between the ground state and vibronic states $\omega_0 = \omega_{ri}$. In this case the two denominators reach their maximum value and therefore only vibrational modes that belong to an electronic transition matching the energy of the laser photons contribute to the Raman spectra, due to their strong enhancement.

In order to understand which Raman bands may undergo enhancement in RR scattering it is necessary to probe the dependency of $(\alpha_{\rho,\sigma})_{fi}$ on the properties of excited states.
In section 4.3.2 it was shown that under the assumption of the $Born - Oppenheimer$ approximation the electronic and the vibrational components can be separated

$$|i\rangle = |gm\rangle = |g\rangle\,|m\rangle \tag{4.130}$$

$$|f\rangle = |gn\rangle = |g\rangle\,|n\rangle \tag{4.131}$$

$$|r\rangle = |ev\rangle = |e\rangle\,|v\rangle \tag{4.132}$$

assuming that the system is initially in the electronic ground state $|g\rangle$. $|e\rangle$ represents the excited electronic state and $|m\rangle$, $|n\rangle$ and $|v\rangle$ represent vibrational states of the scattering species.
Thus the transition polarizability in equation 4.129 can be rewritten in the form

$$(\alpha_{\rho\sigma})_{fi} = \frac{1}{hc}\sum_{ev}\left(\frac{\langle n|\,[\mu_\rho]_{ge}\,|v\rangle\,\langle v|\,[\mu_\sigma]_{eg}\,|m\rangle}{v_{ri} - v_0 - i\Gamma} + \frac{\langle n|\,[\mu_\sigma]_{ge}\,|v\rangle\,\langle v|\,[\mu_\rho]_{eg}\,|m\rangle}{v_{ri} + v_0 - i\Gamma}\right) \tag{4.133}$$

with $[\mu_\rho]_{ge}$ as the pure electronic transition dipol moment $\langle g|\,[\mu_\rho]_{ge}\,|e\rangle$ associated with the transition $|g\rangle \leftarrow |e\rangle$.
The electronic transition dipolmoment can converg into a Taylor-expansion developed according to the normal coordinates of the nuclei (Q) around the equilibrium position:

$$[\mu_\rho]_{ge} = [\mu_\rho]^0_{ge} + \sum_k [\mu_\rho]'_{ge} Q_k + ... \tag{4.134}$$

$$\tag{4.135}$$

According to the describtion of the Herzberg-Teller perturbation [236] of vibronic coupling in a resonant Raman transition, the derivative of the transition dipol moment arises because the Hamiltonian H with respect to the normal coordinate Q_k can mix the state $|e\rangle$ with other (exited) states $|s\rangle$

$$[\mu_\rho]_{ge} = [\mu_\rho]^0_{ge} + \sum_s \sum_k [\mu_\rho]^0_{ge}{}' \frac{h^k_{es}}{\Delta v_{es}} Q_k + ... \tag{4.136}$$

$$h^k_{es} = \left\langle e \left| \frac{\partial H}{\partial Q_k} \right| s \right\rangle_{Q_{k=0}} \tag{4.137}$$

The term $\frac{h^k_{es}}{\Delta v_{es}}$ is a measure of the strength of vibronic coupling of the excited states $|e\rangle$ and $|s\rangle$, that is assumed to be weak, via the normal coordinate Q_k. For a more detailed theoretical treatment RR scattering via the Herzberg-Teller perturbation the reader is refered to the literature [223, 233]

By substitution of this Taylor expansion into equation (4.133) the transition polarizability tensor splits into a sum of different terms:

$$(\alpha_{\rho\sigma})_{gn,gm} = A + B + C + D \tag{4.138}$$

$$\tag{4.139}$$

$$A = \frac{1}{hc}[\mu_\sigma]^0_{ge}[\mu_\rho]^0_{eg} \sum_v \frac{\langle n_g|v_e\rangle \langle v_e|m_g\rangle}{v_{ev,gm} - v_0 + i\Gamma_{ev}} \tag{4.140}$$

$$\begin{aligned} B = &\frac{1}{h^2c^2} \sum_{s\neq e} [\mu_\sigma]^0_{gs}[\mu_\rho]^0_{eg} \frac{h^k_{se}}{\Delta v_{se}} \sum_v \frac{\langle n_g|Q_k|v_e\rangle \langle v_e|m_g\rangle}{v_{ev,gm} - v_0 + i\Gamma_{ev}} \\ &+\frac{1}{h^2c^2} \sum_{s\neq e} [\mu_\sigma]^0_{ge}[\mu_\rho]^0_{sg} \frac{h^k_{es}}{\Delta v_{es}} \sum_v \frac{\langle n_g|v_e\rangle \langle v_e|Q_k|m_g\rangle}{v_{eg,gm} - v_0 + i\Gamma_{ev}} \end{aligned} \tag{4.141}$$

$$\begin{aligned} C = &\frac{1}{h^2c^2} \sum_{s\neq g} [\mu_\sigma]^0_{se}[\mu_\rho]^0_{eg} \frac{h^k_{gs}}{\Delta v_{gs}} \sum_v \frac{\langle n_g|Q_k|v_e\rangle \langle v_e|m_g\rangle}{v_{ev,gm} - v_0 + i\Gamma_{ev}} \\ &+\frac{1}{h^2c^2} \sum_{s\neq e} [\mu_\sigma]^0_{ge}[\mu_\rho]^0_{sg} \frac{h^k_{sg}}{\Delta v_{es}} \sum_v \frac{\langle n_g|v_e\rangle \langle v_e|Q_k|m_g\rangle}{v_{eg,gm} - v_0 + i\Gamma_{ev}} \end{aligned} \tag{4.142}$$

$$D = \frac{1}{h^3c^3} \sum_{s,s'\neq e} [\mu_\rho]^0_{gs}[\mu_\sigma]^0_{s'g} \frac{h^k_{es}h^{k'}_{es'}}{\Delta v_{es}\Delta v_{es'}} \sum_v \frac{\langle n_g|Q_k|v_e\rangle \langle v_e|Q_{k'}|m_g\rangle}{v_{ev,gm} - v_0 + i\Gamma_{ev}} \tag{4.143}$$

This formalism was introduced by A.C. Albrecht [237] and thus these terms are also called Albrecht terms. The first term of the resulting sum, the A term, is mainly determined by the transition dipolmoment $[\mu]_{ir}$ and $[\mu]_{ir}$ and the product of the Franck-Condon factors, $\langle n_g|v_e\rangle \langle v_e|m_g\rangle$. Thus this term is normally the dominating term for RR scattering within strong absorption bands, i.e. strong electronic transitions, such as charge transfer (CT) or $\pi \rightarrow \pi^*$ transitions.

The second term, the B-term, is related to the vibronic coupling of the resonant state $|r\rangle$ with a second excited electronic state $|s\rangle$, a so-called *Herzberg-Teller* coupling. Compared to the A-term, the magnitude of the B-term of this term strongly depends on the vibronic coupling integral h^k_{es}, the energy difference between the coupled excited states $hc(v_s - v_e)$ and the vibrational transition integral $\langle n_g|Q_k|v_e\rangle$. Due to the presence of the factor $h^k_{se}/(v_s - v_e)$, the B-term is usually much smaller than the A-term and is only dominant for weaker transitions, where the A-term vanishes, such as the Q-band of heme proteins (see section 4.3.3.4), or in the case of a strong electronic transition, however with an excitation wavelength of bigger energy than the energy difference to the first excited state.

The difference of the C and the B-term is that in the C-term the ground state $|g\rangle$, rather than the resonant excited state, is vibronically coupled to another excited state $|r\rangle$. The C-term and D-term are usually very small due to the large energy separation between the ground and excited state and therefore the contribution can thus be neglected in normal RR scattering experiments. The D-term is usually even smaller and gives rise to first overtones ($k = k'$) and binary combination tones ($k \neq k'$) vibration modes.

The advantage of RR spectroscopy over traditional Raman spectroscopy is the strong enhancement of the Raman signal by a factor of up to 10^6 [223, 227], which allows RR spectra to be generated with very low sample concentrations. On the other hand the main drawback of this resonant condition is the increased uptake of energy of the incoming laser light, which can lead to photochemical degradation and decomposition of the molecule. Therefore, there is usually an upper limit of the incident laser power of a few mW, depending on the investigated species. Although RR scattering utilizes the transition between ground and excited states and *vice versa*, it is still a different and much weaker process compared with fluorescence. The cross section of the one-photon fluorescence process is determined by the product of the absorption cross section and fluorescence quantum yield, which can therefore reach cross sections up to 10^{-16} cm^2/molecule [222]. However, the advantage of RR spectroscopy tuned to transitions between inherent states of the molecule that it provides high sensitivity, chemical specificity, direct structural access and the possibility of selective analysis of individual chromophores inside e.g. a protein, without the necessity of insertion of fluorescent labels. Thus, RR spectroscopy is a powerful alternative to fluorescent measurements.

4.3.3.3 Surface-enhanced Raman Scattering

The main drawback of Raman spectroscopy is the extremely low cross section of the Raman event compared with the much higher probability of other optical processes such as fluorescence. Thus, powerful exciting sources, very sensitive detectors and a large number of scattering molecules are needed in order to record a Raman spectrum.

The requirement of high excitation intensities is a major problem for biological samples, causing photodamage and photoreduction of the rigid biomolecules. Furthermore, the last constraint would make Raman spectroscopy rather unsuitable for surface studies, where usually one has to deal with a small amount of material, down to monolayer level, or even less.

In contrast to this exception, Fleischmann observed in 1974 huge Raman intensities for certain adsorbates, on rough silver electrodes [238]. He performed experiments on pyridine on metallic surfaces to study redox-linked structural changes by combining electrochemistry and Raman spectroscopy. In order to increase the Raman signal of the atomic monolayer, the pyridine was deposited onto a roughened silver electrode. The idea was to increase the surface area of the electrode and therefore the amount of adsorbate on the sample. The experimental result supported this suggestion by an enormously increased intensity of the Raman signal. However, only three years later, Jeanmaire and van Duyne [239], as well as Albrecht and Creighton [240], recognized independently that the extraordinary large intensities observed was too big to be simply accounted for an increase of the number of scatterers on the surface, but rather due to a tremendous enhancement of the Raman cross section for the adsorbed molecules. A suitable choice of the metal (copper, silver and gold being the most used) and a roughening of the surface turned out to be the key factors for

the enhancement. Since then, this effect is known as the surface enhanced Raman scattering (SERS) and has been widely studied. [241, 242, 243, 244, 245].

They proposed an enhancement of the scattered intensity in the adsorbed state. Already at that time a surface plasmon enhancement mechanism of the scattered intensity was proposed [240, 246]. Since then, this effect was called surface enhanced Raman scattering (SERS) and captured the attention of chemists, physicists and engineers from around the world. It is not hard to see the motivation for such interest. The effect was large, completely unexpected, difficult to understand and of enormous practical utility if it could be understood and exploited. The investigation of the SERS still continues and the understanding of the phenomenon has increased considerably. Nowadays, it is accepted that the SERS effect is caused by greatly enhanced electromagnetic fields generated by surface plasmon resonances (SPR) in certain hot spots of the rough substrate. At this point, it is important to note that such strong and localized electromagnetic fields do not only find applications in the SERS. For example, they can also be employed in optical tweezers and to modify radiative rates in a variety of processes such as molecular fluorescence. Fluorescence spectroscopy is a typical technique for ultra-sensitive detection, which however, does not provide structural information. There is a rising need for a technique that is able to study surface related processes accompanied with structural changes, in small concentrations.

SERS has the potential to combine the structural information provided by Raman scattering with the sensitivity typically seen in fluorescence. Since its decovery in the 70s, surface-enhanced Raman scattering ($SERS$) has emerged as a powerful technique for studying species adsorbed on metal films, colloidal dispersions and roughened working electrodes. SERS occurs when molecules are adsorbed on certain metal surfaces, where Raman intensity enhancements of $\sim 10^5 - 10^6$ [216, 247, 218] may be observed. The enhancement is primarily due to plasmon excitation at the metal surface, thus the effect is limited to Cu, Ag and Au and a few other metals for which surface plasmons are excited by visible radiation.

The combination of surface- and resonance-enhancement ($SERRS$) can occur when adsorbates have intense electronic absorption bands in the same spectral region as the metal surface plasmon resonance, yielding an overall enhancement as large as $10^{10} - 10^{12}$ [216, 222, 247].

The high sensitivity of SERRS is unparalleled and exceeds by far that of any other technique which is capable of providing structural information and molecular specificity. A further advantage is that very often the intense luminescence background which sometimes results from laser excitation under resonance conditions is almost completely quenched in SERRS. This is because interaction with the metal surface provides an efficient pathway for rapid non-radiative decay.

In order to study the principles of the surface enhancement effect usually single metallic particles as SERS substrates are chosen to study the Raman spectra of single molecules adsorbed on them [248]. Metallic nanoparticles are choosen, since nowadays it is possible to produce an enormous variety of structures in the sub-micrometer scale. In particular, metallic structures with nanometer size and different shapes can be manufactured and their surface plasmon resonances can be tailored [216, 218, 249, 250]. This allows to provide a homogeneous condition for the investigation of the influence of different topological parameters, such as different surface curvatures, geometries and particle-particle distances, on the surface enhancement. These fundamental studies are impossible on rough surfaces, required for spectroelectrochemical experiments, since they provide a superposition of all kinds of shapes.

Silver is by far the most commonly used substrate, although gold and copper have also been fairly widely used, with only occasional reports of the use of other metals. The roughening technique is basically the same for all metals, i.e. repeated cycling, or pulsing, into a potential region where the metal is oxidised, preferably to form an insoluble surface film, followed by a period at a potential where the oxidation product is reduced back to the metal.

Today, it is commonly accepted that it arises mainly due to two different mechanisms operating at the same time. In the literature these are usually named the electromagnetic enhancement and the chemical enhancement. The so-called electromagnetic effect involves the excitation of surface plasmons of roughened substrate metal surfaces, which then couple to an adsorbate, thereby increasing its scattering cross-section. Thus the Raman scattering takes place in the enhanced local optical field of the roughened surface structure [222, 249, 250, 251].

The chemical enhancement effect appears, when the molecule is in direct contact with the metal surface, thus increasing the Raman cross section as compared to a free molecule and thus also called 'first-layer' effect. This is often described by the presence of metal adatom and adatom clusters at the electrode surface [251, 252]. These adatoms, stabilised by adsorbed anions, are formed during the reductive part of the roughening cycle and may act to enhance the coupling of the excited surface plasmon to the adsorbate. The different contributions of both effects is not yet fully understood and still under debate. Together, they may provide enhancement factors between 10^6 and 10^8. Yet the exact distinction between the two is still a matter of debate.

A full discussion of the surface-enhancement is beyond the scope of this chapter, but full details of current theories for SERS are discussed elsewhere [202, 249, 250, 247, 222, 253]. This chapter, however, briefly describes the state of knowledge of the surface-enhancement, required to understand the effect on roughened surfaces in the context of surface-enhances Raman spectroscopy (*SERS*). The following discussion describes as well the enhancement phenomenon present in surface-enhanced infrared reflection absorption spectroscopy

(*SEIRAS*), which is due to the longer wavelength mainly based on gold surfaces[10].

Electromagnetic Field Enhancement In Raman scattering, the total Stokes Raman signal $P(\nu_s)$ is proportional to the Raman cross section σ^R_{free}, the excitation laser intensity $I(\nu_L)$ and the number of molecules in the probed volume N.

$$P(\nu_s) = N \cdot I(\nu_L) \cdot \sigma^R_{free} \tag{4.144}$$

To estimating the SERS Stokes power the contributions of the surface-enhancement are expressed by field enhancement factors $A(\nu_L)$ for the laser and $A(\nu_S)$ for the Raman scattered field.

$$P^{SERS}(\nu_s) = N' \cdot I(\nu_L) \cdot |A(\nu_L)|^2 \cdot |A(\nu_S)|^2 \cdot \sigma^R_{ads} \tag{4.145}$$

Additionally the Raman cross section σ^R_{ads} of the adsorbed molecule increases as compared to the cross section in a 'normal' Raman experiment (σ^R_{free}). N' is the number of adsorbed molecules involved in the SERS process. This number can be smaller than the number of molecules in the probed volume, since normally not the whole surface is SERS active. There are preliminary proofs that only certain co-called 'hot spots' provide a sufficient surface-enhancement [217].

In Raman as well as in SERS experiments, the scattered power is proportional to the frequency of the scattered light to the fourth power. However, the strong frequency dependence of the field enhancement factors $A(\nu_L)$ and $A(\nu_S)$ and the resonances in σ^R_{ads} dominate and determine the overall frequency dependence of the SERS signal.

The simplest model for the description of the electromagnetic surface enhancement of metallic nanostructures of rough surfaces is a small sphere with the complex relative permittivity $\epsilon(\nu)$ in a surrounding medium, as shown in Fig. 4.25. A molecule in the vicinity of the sphere, with the distance d, is exposed to a field E_M, which is the superposition of the incoming field E_0 and the field of a dipole E_{SP}, induced in the metal sphere. Therefore, the effective optical field seen by the molecule is enhanced compared to the applied laser field. We can further assume that the diameter of the sphere (2r) is small compared to the wavelength of light[11], which reduces the problem to an electrostatic one.

The field of the induced dipole is be described by equation 4.146:

$$\begin{aligned} E_M &= E_0 + E_{SP} \\ E_{SP} &= r^3 \frac{\epsilon - \epsilon_0}{\epsilon + 2\epsilon_0} E_0 \frac{1}{(r+d)^3} \end{aligned} \tag{4.146}$$

[10] For the infrared regime, gold is more suited to excite surface plasmons
[11] This is the so-called Rayleigh limit

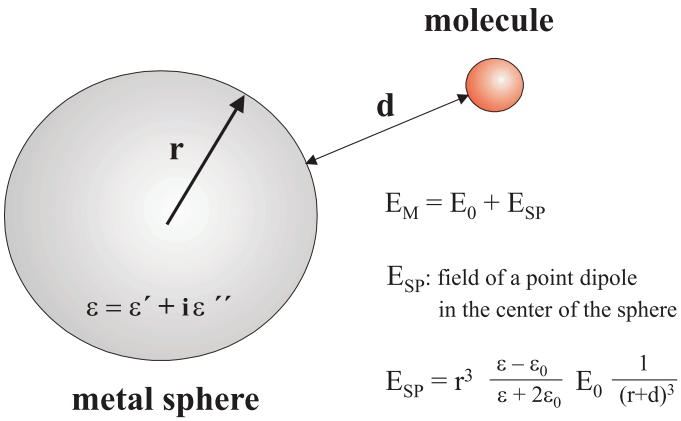

Figure 4.25: Scheme of the concept of electromagnetic SERS enhancement. (For explanation see text.)

with E_{SP} being a field of a dipole in the center of the sphere.

This field is particularly strong when the real part of $\epsilon(\nu)$ is equal to -2ϵ_0. This condition corresponds to the resonant frequency of the surface plasmons in the metallic sphere (compare section 4.3.1.3). Additionally, for a strong electromagnetic enhancement, the imaginary part of the relative permittivity needs to be small. In an analogous fashion to the laser field, the scattered Stokes or anti-Stokes field will be enhanced if it is in resonance with the surface plasmons of the metal sphere. Taking into account both field enhancing effects, the electromagnetic enhancement $G_{em}(\nu_s)$ for the Stokes power can be written as

$$\begin{aligned} A(\nu) &= \frac{E_M(\nu)}{E_0(\nu)} \\ G_{em}(\nu_S) &= |A(\nu_L)|^2 \cdot |A(\nu_S)|^2 \\ G_{em}(\nu_S) &\sim \left|\frac{\epsilon(\nu_L) - \epsilon_0}{\epsilon(\nu_L) + 2\epsilon_0}\right|^2 \cdot \left|\frac{\epsilon(\nu_S) - \epsilon_0}{\epsilon(\nu_S) + 2\epsilon_0}\right|^2 \cdot \left(\frac{1}{r+d}\right)^{12} \cdot E_0^4 \end{aligned} \tag{4.147}$$

These formulas, based on a very simple model, describe the most important properties and peculiarities of the electromagnetic SERS enhancement. It shows that the enhancement scales as the fourth power of the local field of the metallic nanostructure and that it is particularly strong when excitation and scattered fields are in resonance with the plasmon resonance. Electromagnetic SERS enhancement does not require direct contact between molecules and metal and the formula also describes the distance dependence of the electromagnetic enhancement, which is given by the decay of the field of a dipole over the distance ($1/d^3$) to the fourth power.

In general, the plasmon resonance frequency and also the size of the electromagnetic field enhancement factor depend on the size, shape, and the material of the metallic nanoparticle

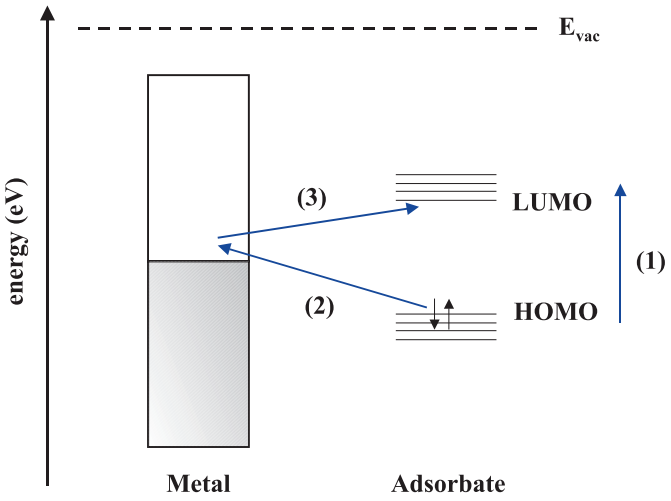

Figure 4.26: Typical energy level diagram for a molecule adsorbed on a metal surface. Possible charge transfer excitations are shown (see text).

and their environment [253, 217, 222]. Maximum values for electromagnetic enhancement for isolated single colloid silver and gold spheroids are of the order of 10^6 to 10^7 [222]. Theory predicts strong enhancement of electromagnetic fields for sharp features and large curvature regions, which may exist on silver or gold nanostructures as well as on roughened surfaces [222, 216, 217].

'Chemical' enhancement Beside the electromagnetic field enhancement effect, another phenomena arises to the enhancement of Raman signals in the case of a molecules directly adsorbed to the metal surface. Although the EM enhancement is only observed in the case of roughend surfaces the chemical enhancement effect is also present on flat surfaces.

The chemical or electronic SERS effect includes enhancement mechanisms, which are related to the specific interaction, i.e. electronic coupling between molecule and metal, resulting in an increased Raman cross section σ^R_{ads} of the adsorbed molecule compared to the cross section in a normal Raman experiment σ^R_{free}. Since these electronic interaction require close contact between the molecule and the metal, the effects are restricted to molecules in the first layer on the metal.

For species chemisorbed at metal surfaces there is a partial overlap of the molecular and metal orbitals. This can lead to the creation of a new set of energy states that are available for the Raman process. A simple mechanism, the 'charge transfer process' [222, 253, 254], has been proposed and experimentally confirmed.

Figure 4.26. Shows a typical energy level diagram for a 'system molecule metal', where the energies of the highest occupied molecular ortibal (HOMO) and the lowest unoccupied molecular orbital (LUMO) are approximately symmetric relative to the Fermi level

of the metal. The molecular energy levels of an absorbed molecule are usually shifted as compared to the free species, due the interaction of the molecular orbitals with the band structure of the metal.
The first layer SERS effect is usually ascribed to the dynamical charge transfer between metal and adsorbate, following a model by B. Persson [253]. Otto suggestes a chemical SERS enhancement based on dynamic charge transfer process between conductive band of the metal and HOMO and LUMO of the molecule [254, 253]. This can be described by the following steps:

In the first step the incident radiation $\hbar\omega_i$ excites an electron within the metal conduction band to an empty state in the half filled band, which is also called a hot electron state. This charge will be transferred form the metal to the LUMO of the molecule. E_{CT} is the electronic state given by the mixing of a molecule non-bonding state and an appropriate metal state. Thus it is obvious that E_{CT} can only exist, when the molecule is adsorbed at the surface.

The next step would be the transfer of the hot electron from the LUMO back to the metal. Upon excitation the LUMO changes the normal coordinates of some internal molecular vibrations. If the molecule is left in a different vibrational state, the e^-h^+ pair and, thus, the photon leaving the system has a (slightly) different energy.

The final step is the radiative annihilation of the e^-h^+ pair. The electron returns back to its initial state and a Stokes photon is created. The whole process can therefore be considered as a scattering process, involving an excited electron-hole pair (e^-h^+).[12] .

The excistence of 'atomic scale roughness', ceating so-called SERS-active sites or 'hot spots', seems to play an important role by providing pathways for the exchange of electrons between metal and molecule [254, 222, 217, 255].

In some experiments, the addition of salt seems to increase to chemical enhancement effect since ions may provide so-called 'acitve sites' [254]. For a deeper insight into chemical SERS enhancement mechanisms it is refered to reviews covering this topic [253, 254, 222]. The magnitude of chemical enhancement has been estimated to reach factors of 10 to 100 at most [256], and it is obvious that this effect alone cannot account for the experimentally observed SERS enhancement approaching 10^{14}. On the other hand, experimental observations such as SERS enhancement measured from flat metal surfaces as well as the dependence of the enhancement factor on the electrode potential, and on shifts in the Fermi level, are indications that a 'chemical' enhancement must also be operative [254, 253]. Compared to Raman spectra in solution, the bands can be shifted by few wavenumbers, due to the

[12] If the two discussed enhancing effects, EM and chemical, act cooperatively, the scattering of photons, as depicted by the CT mechanism, has to be replaced by the inelastic scattering of the LSP via CT process.

interaction between the metal and the molecule. However, the SERS spectrum remains still a specific spectrum for every molecule.

If the metal acts as an electrode in an electrochemical environment, the position of the Fermi level E_F may be shifted and will be changed by the applied voltage U. The optimal excitation energy for the overall resonance process it this defined gy the following :

$$\hbar\omega_i = E_{CT} - [E_F(0) + eU]. \tag{4.148}$$

Due to the interaction of the metal bands with the LUMO of the absorbed molecule, it is obvious that the chemical enhancement is changed, if the Fermi level is shifted. Equation (4.148) could be confirmed by experimental observations, such as potential dependent Raman intensities for different excitation laser frequencies [222].

The chemical enhancement is less understood than the electromagnetic enhancement, but brings some interesting considerations to a thorough discussion of SERS. As discussed above, the molecule adsorbed onto the surface, necessarily interacts with the surface. The metal-adsorbate proximity may allow pathways of electronic coupling from which novel charge-transfer intermediates emerge that have higher Raman scattering cross-sections than the analyte when it is not adsorbed onto the surface [257]. This is very much like a Resonance Raman effect. Another explanation is that the molecular orbitals of the adsorbate broaden into the conducting electrons of the metal, altering the analyte's chemistry [258] in contrast to the EME that is chemically non-selective. It is interesting to note that the chemical enhancement effect may be an alteration in the scattering cross-section. The chemical nature of the analyte changing due to its interaction with the metal, whereas the electomagentic effect (EME) was a change in the intensity of those analyte molecules that did scatter, not a change in scattering cross-section. To study the chemical enhancement effect is difficult, because most studied surfaces are roughened and the EME and CE effects can't be separated.

4.3.3.4 Raman Spectroscopy on Heme Proteins

Heme proteins account for many key reactions in respiration, photosynthesis and metabolism. The heme consists of a highly conjugated tetrapyrrol ring system, the porphyrins, enabling a high mobility of electrons. Depending on the intercalated metal ion (e.g. Fe, Mg or Co) the heme structure provides the protein with either an effective chromophore or a reversible electron transfer center that has generally a highly specific binding site for oxygen to carry out electron transport or catalytic reduction/oxidation reactions of the protein.

In the last decades the investigation of metalloporphyrins and heme proteins by Raman spectroscopy has developed into a major field of research since the pioneering work, over a decade ago, of Spiro and Gouterman [259, 260]. Nowadays the scattering processes at heme proteins with a multitude of vibrational modes, are quite well understood.

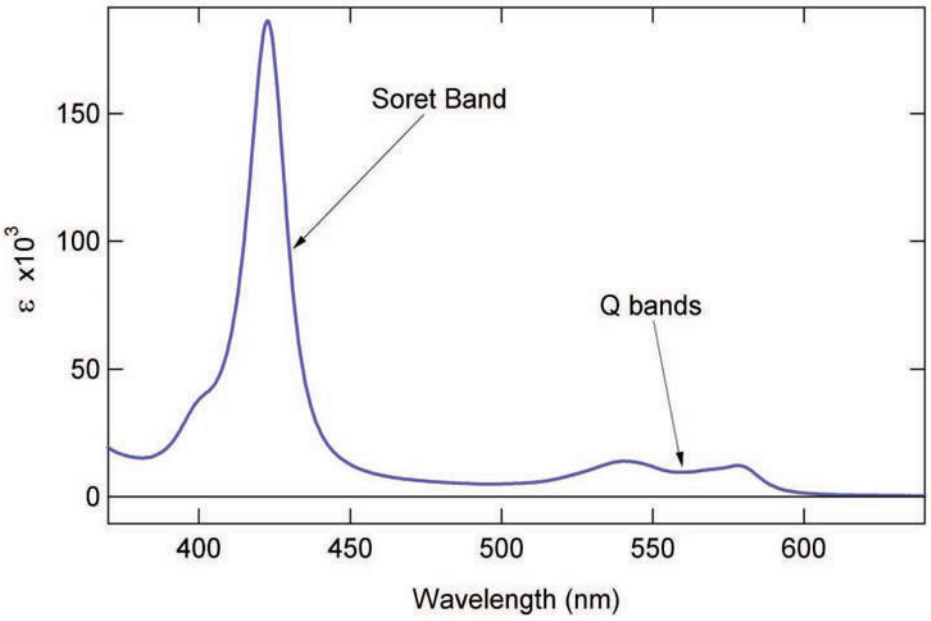

Figure 4.27: Typical absorption spectra of the prosthetic heme group, showing an intense Soret absorption band and weaker Q band structure [3].

[261, 262, 263, 264] Raman as well as IR spectroscopy provide a unique possibility to study electronic transitions, changes in the ligation and redox state or the environment of the prosthetic heme group [265, 266, 267]. A variety of different techniques have been employed to analyze the structure of the active sites in these enzymes, with resonance Raman and IR spectroscopy among them [199, 268, 269, 270, 271, 272, 273, 274, 275, 276, 277].

The heme protein that is mainly focused on in this thesis is cytochrome c oxidase, which contains two heme chromophores, heme a and a_3. As in many other cytochromes, the metal ion present in the heme center is iron, which interconverts between Fe^{2+} (reduced) and Fe^{3+} (oxidized) states. Cytochromes are thus capable of performing oxidation and reduction. The individual steps of the enzymatic process, i.e. electron transfer, proton transfer and oxygen binding, are intimately connected with changes of coordination pattern and the spin configuration of the heme iron and can be conclusively followed by vibrational spectroscopy. [273, 274] Since vibrational information yields insight into the structure and conformation of the heme and its interactions with the protein environment, it is possible to detect redox-linked changes induced by injections of electrons or after binding of a substrate.

The absorption spectra of hemes consist of two characteristic bands, which can be explained in terms of a model derived in 1959 by Gouterman [260]. This so-called four-orbital-model describes the electronic structure of a porphyrin with an idealized D_{4h}-symmetry. The

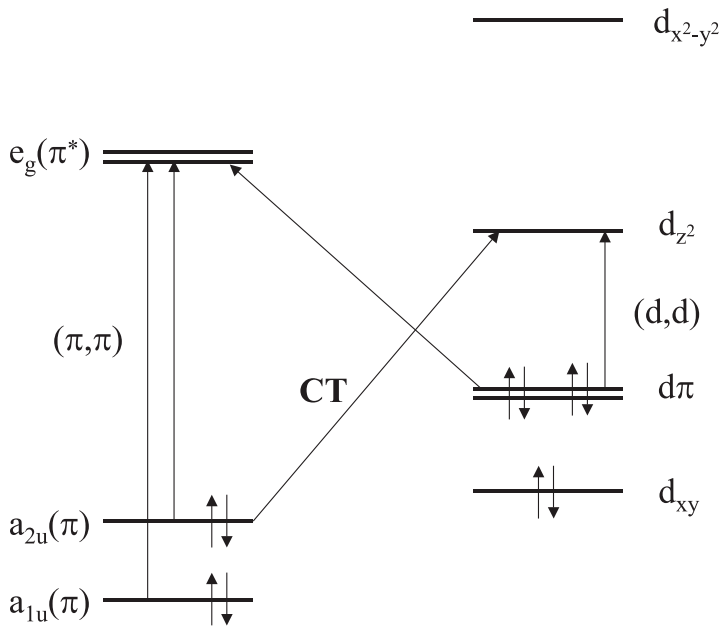

Figure 4.28: Orbital scheme of a metallo-porphyrin.

HOMO [13], i.e. the ground state, consists of two orbitals with a a_{1u} and a_{2u} symmetry (Fig. 4.28). Both orbitals are energetically very close. The LUMO [14], i.e. the excited state, consists of two degenerated π^*- orbitals of an e_g symmetry. Due to the similar energy differences of the transitions $a_{1u} \rightarrow e_g$ and $a_{2u} \rightarrow e_g$, both electronic transitions cannot be distinguished and thus observed at the same time. Taking into account an interaction of the transition of energetically close states, a linear combination of both electronic transistions has to be formed, resulting in two transitions with E_u symmetry [278, 237]. These two transitions can be observed in two characteristic band structures in the absorption spectra. The first is the so-called Soret[15] arising as a maximum at around 410 nm ($\epsilon \approx 10^5 M{-}1cm^{-1}$) [230]. The second group band are the so-called Q-bands[16], which are much weaker bands around 520 and 550 nm [223] ($\epsilon \approx 10^5 M{-}1cm^{-1}$) (see Fig 4.27) [230]. The Soret and the Q band can interact with each other due to vibronic coupling (*interstate mixing*) and thus forming side bands around the Q band, which can be distinguished at low temperature [279].

Heme *a* differs in two ways from the standard heme *c*. found in haemoglobin and cytochrome c: a formyl replaces a methyl group at position 8 in the porphyrin ring and a farnesyl chain replaces the vinyl group at position 2, as shown in Figure 4.22. These alterations significantly change the absorbance spectrum by a red-shifting of the Soret and

[13] highest occupied molecular orbital
[14] lowest unoccupied molecular orbital
[15] also known as or γ B-band
[16] also called α- band

Q bands compared to heme *c* [280]. The ligation of the heme groups within a protein environment further alters the absorbance spectrum. Moreover, the position and amplitude of these absorbance bands vary with the oxidation state of the heme iron. For oxidized ferriform of the heme in CcO, the Soret and Q bands are near 440 nm and 600 nn, respectively, and for reduced ferro-form of the hemes in CcO the bands are more intense, narrower and occur near 430 nm and 605 nm. [281, 38]

As in electronic transitions, which are transitions in the π system of the porphyrin ring, the frequencies and intensities of the heme vibrations are altered by ligation in the environment of the protein, as well as the redox state of the intercalated iron and the conformation and specific protonation state of the environment of the hemes [282] Through out several decades of experimental work, it has been possible to assign the complex vibration modes of heme vibrations of CcO in the oxidized and reduced state by either comparing spectra of model compounds with that of CcO [282] or with normal mode analysis [283]. The prominent bands of heme *a* in the CcO spectra derive from the formyl group. C=O formyl stretches of hemes *a* and a_3 occur at 1645 and 1670 cm^{-1}, respectively in the oxidized form, shifting to 1623 and 1662 cm^{-1} in the fully reduced form [284].
The vibrational modes are highly sensitive to the oxidation state, the iron spin and iron ligation state [273, 274, 277] making it an ideal method to study *in situ* reaction intermediates and conformational changes of the heme pocket. [270, 285, 273, 274, 275, 276, 277, 286] Compared to the other techniques that are often used, which are UV-Vis spectroscopy and circular dichroism, vibrational spectroscopy (such as Raman) has a specific advantage in that it provides more detailed information about the processes in the catalytic active heme environment and permits direct investigations of unstained samples. Therefore a number of studies have used Raman scattering in resonance with the Q-band [287, 288] and Soret absorption band [274] that are sensitive to the nature of the proximal ligand and to study structural rearrangement in the heme binding pocket and in the heme environment [274, 289, 290].

In RR scattering processes, as described in section 4.3.3.2, the Soret band transition, that have a high transition dipole moment ($[\mu_\sigma]^0_{ge}$), is dominated by the *A*-term (equ. 4.140). Hereby, only total symmetrical modes are enhanced, since only in this case the Franck-Condon integrals ($\langle n_g|v_e\rangle$ and $\langle v_e|m_g\rangle$) are different to zero.

The Q bands as weaker electronic transitions and that gain energy by vibrational coupling to the stronger Soret-Band transition, are dominated by the *B*-Term (equ. 4.141). In the case of Q band transitions, the overlap integrals can be, due to there dependence on the normal coordinates, also for modes with non-total symmetry different from zero. Effective resonance enhancement through the B-term do thus only apply for this modes that contribute according to their symmetry to the coupling of the electronic states. More details can be found in reference [291] und [260].

In the framework of this thesis only resonant transition due to the Soret band are utilized.

As mentioned above, RR spectroscopy in the Soret band region can only excite total symmetric bands. Examples of total symmetric modes in the RR spectra of CcO are vibrations of the symmetry group A_{1g}, such as ν_2, ν_3 and ν_4 or bands of the symmetry group B_{1g}, such as ν_{10}. These modes form the major bands in the marker band region of CcO between 1300 cm^{-1} and 1700 cm^{-1} and their position and intensity is characteristic for the ligation- and redox-state of the iron center. Although these bands derive from normal modes of the entire porphyrin ring, they are dominated by some coordinates. For example the ν_4 band is primary determined by the $C_\alpha - N$- stretching mode, whereas the ν_3 and ν_{10} modes are dominated by the $C_\alpha - C_m$ stretching mode (Fig. 4.22) [292].

The influence of the redox state to this modes can be the best demonstrate in the case of the ν_4 band. In the oxidized form this mode appears as 1370 cm^{-1}. After reduction of the iron center the back-coupling to the π^*-orbital becomes stronger, which mainly weakens the $C_\alpha - N$ - bond. Thus the ν_4 band is shifted by 10 cm^{-1} to lower wavenumbers (1358 cm^{-1}). Changes in the π -structure of the porphyrin ring system can result in significant shifts of the vibrational modes. In particular in the case of the ν_3 band, which appears for the 6 coordinated low-spin state of the reduced heme protein at 1490 cm^{-1} is shifted by approx. 20 cm^{-1} to higher wavenumbers as compared to the five coordinated high-spin state of the oxidized form (1470 cm^{-1}).

5 Results and Discussion

This chapter summarizes the results described in the papers published or submitted within the scope of my dissertation and which are attached in the Appendix. Results obtained in addition or other preliminary results are also described. Details of the experimental conditions are given in the attached manuscripts.

5.1 The Protein-Tethered Bilayer Lipid: A Novel Mimic of the Biological Membrane

As an approach to study transmembrane proteins and their catalytic function, a novel concept of a solid-supported tethered bilayer lipid membrane is introduced. In this biomimetic architecture the membrane protein of interest is the essential building block. The necessary surface modification is based on the concept of the well-established metal ion affinity chromatography [293]. Ion chelating nitrilotriacetic acid groups bearing a terminal amino group (ANTA) are coupled *in situ* to an self-assembled N-hydroxy succinimide (NHS) ester functionalized surface, which is attached *via* an thiol group to an gold or silver electrode (Fig. 5.1). The resulting NTA surface is activated by complexation alternatively with a divalent Cu^{2+} or Ni^{2+} ion [1], enabling it to reversible immobilize recombinant proteins with an genetically introduced His-tag *via* the coordination of the nitrogens of two of the imidazol side chains of the 6x His-tag (see Fig. 5.1). CcO absorbs to the Ni-NTA-cross-linker in an oriented fashion such that the cytochrome c binding site is freely accessible to the solution, since the His-tag is engineered into the C-terminus of subunit I (SU I).

The generation of a protein-tethered bilayer lipid membrane (ptBLM) on top of the NTA surface is illustrated schematically in Fig. 5.2. The His-tagged membrane protein is first attached to the surface in its detergent solubilized form. In the second step, the detergent molecules are substituted by lipid molecules thus forming a lipid bilayer that is tethered to the support by the protein itself. The coupling His-tag provides not only sufficient intramolecular flexibility to allow for activity in the reconstituted protein it also renders the proposed method universally applicable to all His-tagged membrane proteins.
Both, *in situ* affinity coupling of proteins [294, 295, 296] and *in situ* dialysis [297] were described before. However, the idea to combine the two to form a membrane protein- tethered lipid bilayer is new. The combined concept ensures both the oriented immobilization and the restoration intoa physicologically natural matrix that enhances the stability of the membrane proteins and preserves its functionality.

[1] The use of Ni^{2+} is prefered due to its broader electrochemical window as compared to Cu^{2+}.

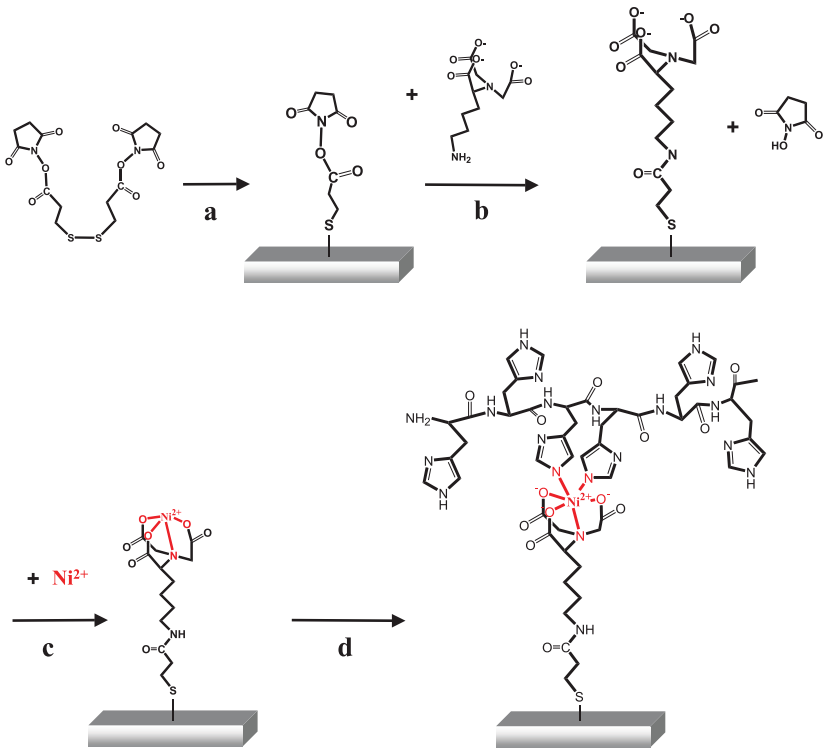

Figure 5.1: Surface modification. (a) Formation of a NHS-activated monolayer by self-assembly of DTSP on a bare Au surface. (b) Coupling of ANTA with the TSP monolayer. (c) Chelating of Ni^{2+} (or Cu^{2+}) by the NTA modified surface. (d) Adsorption of the protein on the Ni-NTA modified Au surface *via* the His-tag. Two nitrogen atoms of the imidazole rings from two of the histidines of the His stretch are coordinating the Ni^{2+} ion.

This section will present the sequence of chemical modification steps that are required to build a functionalized gold surface, ready to immobilize proteins, as well as the *in situ* dialysis to form the required membrane environment around the tethered membrane proteins. Finally, the catalytic activity of the surface-bound and reconstituted protein is probed by adding cytochrome c (cyt c), its natural electron donor. First examples of the experimental power of the new system are demonstrated by the use of surface analytical methods such as surface plasmon resonance (SPR), by quartz crystal microbalance (QCM) measurements and by surface-enhanced infrared reflection-absorption spectroscopy (SEIRAS). The great advantage of these systems is to *in situ* probe all of the modification steps of the gold surface.

As a model system we used recombinant CcO from proteobacterium *Rhodobacter sphaeroides*, which has a His-tag engineered into the C-terminus of subunit I. This specific site-mutation on CcO was chosen, since it orients the CcO to have the cytochrome c (cyt c) binding site freely accessible to the aqueous bulk phase during the immobilization procedure, as described further below. In particular, *electrochemical impedance spectroscopy* (EIS) is used, to measure active proton transport catalyzed by dioxygen reduction [40].

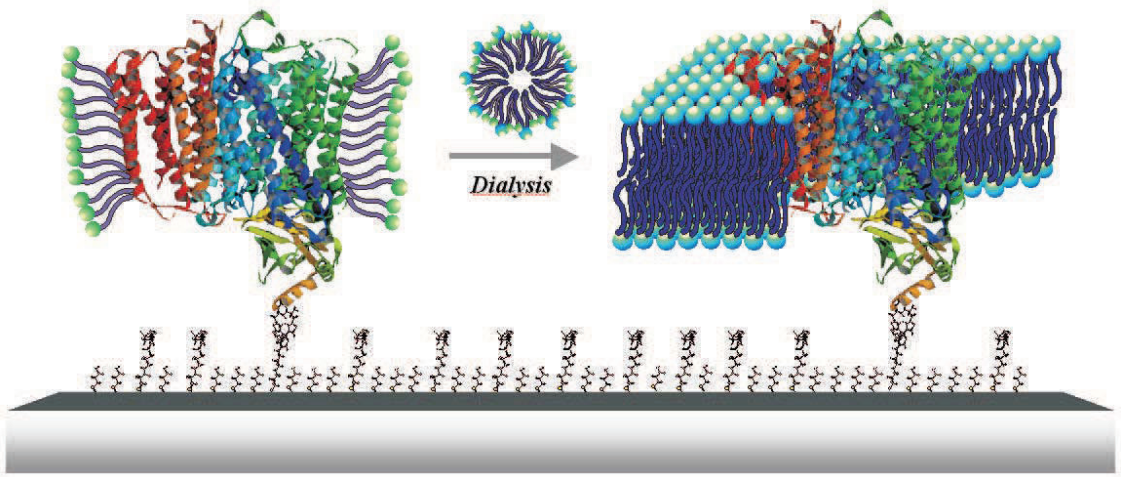

Figure 5.2: Schematic representation of the reconstitution of surface-tethered cytochrome c oxidase into a lipid bilayer. The surface-adsorbed cytochrome c oxidase *via* the affinity of the His-tag to the Ni-NTA surface (see Figure 5.1) is surrounded by the detergent dodecylmaltoside (left). After reaching maximum surface coverage, the protein is exposed to detergent-destabilized lipid vesicles (DphyPC) and either dialysis is started or microporous Bio-Beads are added. The retreat of the detergent molecules *via* both procedures drives the lipids to form a layer around the membrane protein (right).

5.1.1 Functionalization of the Electrode Surface

The first step in the construction of an functionalized layer, which is able to tether membrane proteins, is to employ the hetero-bifunctional cross-linker dithio-bis-(succinimidyl-propionate) (DTSP), which forms a covalent thio-adduct with the gold surface. The surface-bound succinimidylester moiety of TSP is then employed to react with the primary amine of $N_{\alpha'}, N_{\alpha''}$-bis(carboxymethyl)-L-lysine or amino-nitrilotriacetic acid (ANTA) (cf. Fig. 5.1B). This reaction yields an NTA surface dedicated to finally ligate a Cu^{2+} or Ni^{2+} ion. After formation of the TSP monolayer on gold, the sample is rinsed with DMSO and dried under a stream of nitrogen. The TSP monolayer is covered by an aqueous solution of 0.5 M K_2CO_3 buffer (pH 9.8), and a reference IR spectrum is taken. Then, an aqueous solution of ANTA is applied, and a series of IR spectra is recorded during the coupling process (Figure 5.3). The negative bands in the difference spectra indicate the vibrations of the reactant at the surface (TSP), while positive bands represent the product species (NTA). A negative feature is observed at 1721 cm^{-1}. Since this bands has been assigned to the succinimidylester vibrations of TSP, this provides direct evidence for the reaction of the succinimidylester. Concomitant with the appearance of the negative band of DTSP, two intense bands appear at 1658 and 1570 cm^{-1}. These bands originally exist in neither the bulk spectra of ANTA nor DTSP (data not shown). The bands are assigned to the amide I (C=O stretching vibration) and the amide II mode (C=N stretch coupled to the

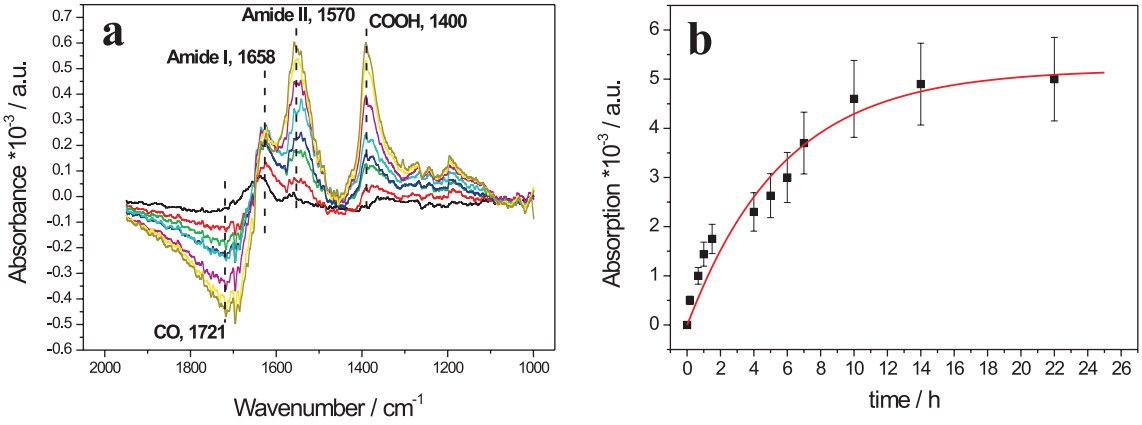

Figure 5.3: (a) Surface-enhanced IR difference absorption (SEIDA) spectra of the coupling process of ANTA with the surface-bound TSP monolayer recorded. The reference spectrum is taken from the TSP modified Au surface. The negative bands correspond to the vibrations of the molecules which are consumed at the surface (reactant), while the positive bands arise from those formed at the surface (product). (b) Peak height of the amide I band as a function of time during coupling.

N-H bending vibration) of the carboxamide (-CONH-) linkage [298] respectively. The appearance of these bands provides unequivocal evidence for the presence of the cross-link between ANTA and TSP.

The band at around 1400 cm^{-1} region is assigned to the corresponding symmetric stretching mode of the three carboxylate groups of NTA. The DFT calculations revealed that the COO- stretching vibrations appear in the range of 1424-1380 cm^{-1} for each of the three carboxylates [299]. However, the detailed assignment of the symmetric carboxylate vibrations is hampered by the strong coupling to the C-H in-plane bending and the C-N stretching modes of the molecule.

It should be noted that the occurrence of the carboxylate bands is suppressed by the addition of a 1:4 mixture of amino-ethanol and ANTA (data not shown). This result suggests that aminoethanol reacts with TSP and, thus, prevents the coupling reaction with ANTA. Hence, this experiment supports our conclusion, which assigns the bands around 1400 cm^{-1} to the symmetric carboxylate vibrations of the NTA layer.

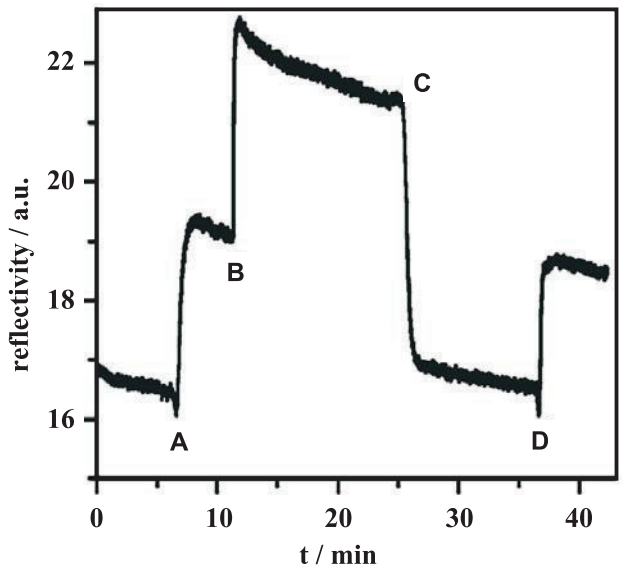

Figure 5.4: Reversible binding of CcO monitored by SPR. Infusion of solubilized CcO into the measuring cell at points A and D, respectively, leads to a thickness increase due to binding of CcO. At point B the cell is rinsed with buffer containing 200 mM imidazole. The strong increase is due to change of refractive index. At point C the cell is flooded again with pure DDM/PBS changing the refractive index back to the initial value. The resulting reflectivity shows that almost complete desorption is achieved. When a new portion of solubilized CcO is infused at point D the increase in reflectivity indicates binding to be fully reversible.

5.1.2 SPR Monitoring of the CcO Binding Process

The thickness of the individual dielectric layers on the gold film is determined by surface plasmon resonance spectroscopy (SPS). Reflectivity scans versus the angle of incident light are recorded (not shown). The simulation of these scans in terms of the four-layer model yields the thickness of the different layers listed in Table 5.1. SPS recordings, however, indicate the optical thickness of the dielectric layer as well as the refractive index of the bathing solution. Hence the reflectivity as a function of time at a fixed angle of incidence shown in Figs. 5.4 and 5.5 contains information not only about the thickness of the layers but also about changes in the refractive index of the buffer solution.

The thickness of the DTSP-SAM as well as the thickness change due to the coupling of ANTA are both too small to be accurately determined by SPR (see Table 5.1) considering that the coupling reaction consists of the substitution of the NHS residue with the ANTA molecule. The estimated length of the entire construct is $\sim$1 nm. However, the formation of these layers can be clearly detected by surface-enhanced infrared absorption spectroscopy (SEIRAS). Changing pure PBS buffer against DDM containing buffer results in a shift of the angle of total reflection as well as an increase in reflectivity. This was simulated by a change in the bulk refractive index and additionally by a layer thickness increase of 0.9

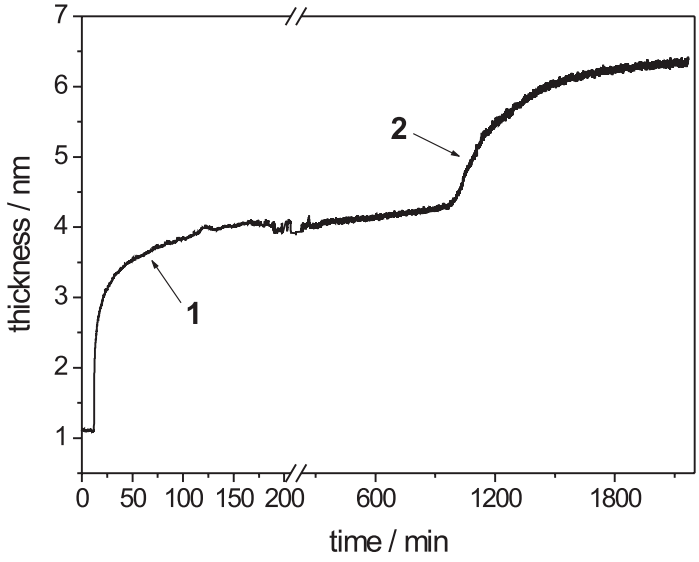

Figure 5.5: Binding of CcO and reconstitution monitored by SPR. The increase in reflectivity in part (1) shows the binding of CcO to the modified surface. (2) shows the reconstitution of the lipid membrane *dialysis*. Note the different timescales. The inset shows the reflectivity scans as a function of the angle of incidence before, after CcO binding and reconstitution (from left to right).

nm. The thickness increase indicates an accumulation of detergent molecules at the surface also found by QCM measurements described below. A further increase of reflectivity is observed if CcO binds to the surface as shown in the kinetic trace of the SPR signal (Fig. 5.4).

Extensive washing with buffer results in a minor loss of material. Addition of the imidazole-containing buffer (Fig. 5.4, point B) results in a further increase in reflectivity that is attributed to a mere change of the refractive index of the bulk solution. The reflectivity returns to almost the same level as the one before protein adsorption if the imidazole buffer is replaced by the original PBS/DDM buffer (Fig. 5.4, point C). This indicates an almost complete desorption of CcO is from the surface as imidazole molecules compete with the His-tag for the binding sites at the Cu^{2+} /NTA complex. Nonetheless a second addition of another aliquot of CcO (Fig. 5.4, point D) leads to similar increase in reflectivity as the first one, showing that the adsorption of CcO is reversible and mediated by the interaction of the His-tag with the Cu^{2+}-NTA complex. Table 5.1 lists the thickness increment at each functionalization step. Functional incorporation of CcO requires the enzyme to remain in its native conformation. The metal affinity surface causes two distinct effects both of which should promote the formation of ptBLMs: binding of the protein by the His-tag moiety prearranges the protein to form a uniform array of molecules with the His-tag in

Adsorption step	Δd_{SPR}/nm	Δd_{QCM}/nm ^{2}
DTSP-ANTA	0.3 ± 0.2	N/D
Cu^{2+}/Ni^{2+}	0.3 ± 0.2	N/D
DDM	0.9 ± 0.2	2.6 ± 0.3
CcO	2.1 ± 0.3	5.5 ± 0.3

Table 5.1: Thickness increments linked to the different preparation stages: SPR versus QCM

close proximity to the surface. Thus the orientation of the protein with respect to the membrane normal is dependent on the location of the histidine stretch within the protein. Consequentially, it should be possible to selectively define a vectorial ptBLM by alternation of the His-tag position. Another effect is the promotion of high surface concentrations of the protein. Although not necessarily required for highly insulating ptBLMs, this is a key advantage of ptBLMs with respect to 'classical' tBLMs. Accumulation of the protein at the surface can be controlled by the surface concentration of the binding molecules. The lipid molecules then fill in the gaps during the last step of the reconstitution.

The generation of a ptBLM is completed by replacing detergent molecules of the bound protein by lipids, thus forming small patches of lipid bilayers between the protein molecules, which eventually would seal the whole assembly to a closed membrane. As shown in Fig. 5.5, the increase in reflectivity in slope (1) indicates protein binding because a change in the refractive index is not involved (composition of the solution is unchanged). After reaching a plateau in the SPR binding curve, the enzyme/detergent solution is replaced by a lipid containing buffer solution and the dialysis is started (slope (2)). Alternatively, the reconstitution can be done with polystyrene beads (Bio-Beads) which remove detergent molecules by adsorbtion in inner cavities.

Simultaneously with the increase in reflectivity during dialysis, the electrical capacitance of the layer decreases and the resistance increases (see also Fig. 5.6), as described below. The combined findings are explained in terms of the successful incorporation of lipid molecules. However, the absolute thickness increment due to incorporation of lipid as estimated by SPS is not given in Table 5.1, because the exact degree of substitution of detergent molecules by lipid molecules is hard to assess.

5.1.3 QCM Measurements

The resonant frequency of the quartz crystal depends on the total oscillating mass. When a thin film is adsorbed to the crystal the frequency decreases. If the film is rigid the decrease in frequency is proportional to the mass of the film. The mass of the adhering layer is calculated by using the Sauerbrey relation [300]:

$$\Delta f = -\Delta m/nC \tag{5.1}$$

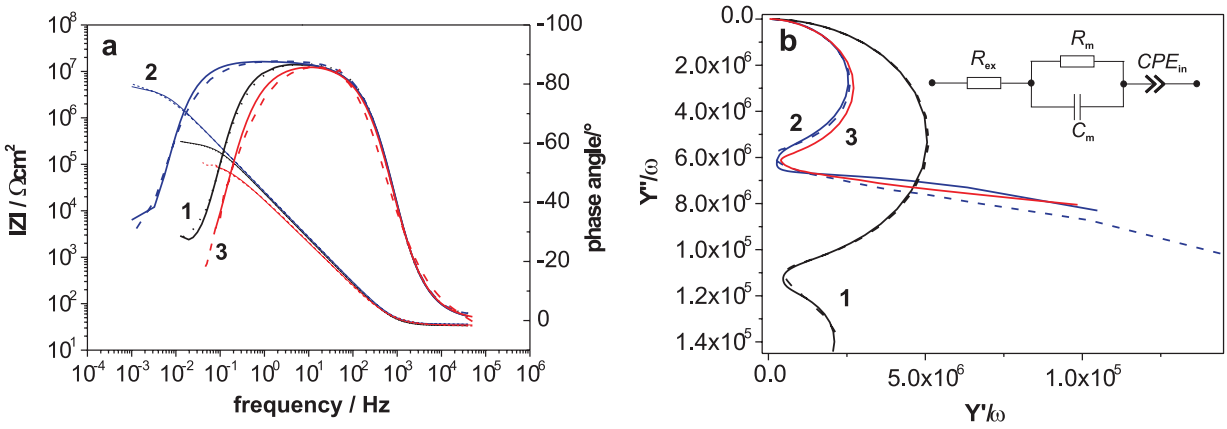

Figure 5.6: Impedance spectra measured at different stages of the experiment. (a) Bode plot and (b) complex plain of immobilized CcO (black curve), after reconstitution for 36 h (blue curve) and after activation with cyt c (red curve). The respective equivalent circuit is shown as inset in (b): R_s solution resistance; R_m resistance and C_m capacitance of the lipid membrane; CPE_{in} constant phase element of the inner tether region. A CPE instead of a capacitor was used to cover the inhomogenities of the tether region as shown further down in section 5.5.

where C is the mass sensistivity constant ($C = 17.7ng \cdot cm^{-2} \cdot Hz^{-1}$ at 5 MHz) and n is the overtone number ($n = 1, 3, 5, \ldots$).

A 'soft' (viscolelastic) film (e.g., lipids, proteins, or coupled water) will not fully couple to the oscillation of the crystal leading to a damping of the oscillation. In this case the Sauerbrey relation is not valid anymore. The dissipation of the oscillation energy contains information about the viscoelastic properties of the film. Incubation of the NTA surface with Cu^{2+} ions results in a slight decrease in frequency shift, whereas the dissipation remains constant (see Fig. 7). According to the Sauerbrey model this frequency shift corresponds to a mass adsorption of 42 ng/cm^2, or in other terms to an area of 16.5 $Å^2$ for each bound Cu^{2+} ion (disregarding any contribution from surface roughness). This value fits well to the cross-sectional area of a modeled DTSP-ANTA molecule ($\sim 17Å^2$). Because the NTA/Cu^{2+} complex has a high formation constant [301], all NTA residues are complexed by Cu^{2+}. Therefore, DTSP should form a closely packed layer on the gold film that reacts quantitatively with ANTA. Adsorption of DDM and CcO at the surface results in a decreasing resonance frequency as well as in an increasing dissipation. Hence the adsorbed mass was determined by fitting according to a Voigt-based viscoelastic model [302, 300].

Considerable differences between thickness values determined by SPR and the QCM measurements are observed (Table 5.1). QCM is not only sensitive to the directly adsorbed mass, but also to entrapped and closely coupled molecules, e.g., water. Although this surface coupled water does not contribute to an increase in optical thickness and hence is invisible in SPR, it adds a notable amount of viscoelastic mass, which is detected by the

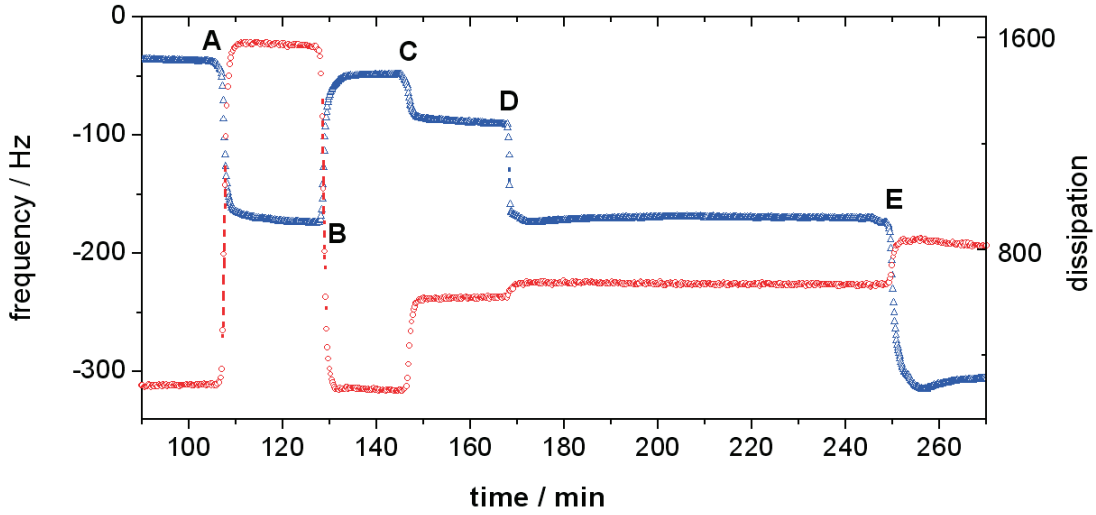

Figure 5.7: Frequency shift (blue curve) and dissipation (red curve) at different stages of the binding experiment, measured by QCM. The DTSP-NTA SAM was prepared ex situ. At point A the cell was flushed with 40 mM CuSO4 buffer that is changed to pure water at point B. Points C and D indicate perfusion with PBS and PBS/DDM buffer solution, respectively. CcO was added at point E.

QCM. The reconstitution could not be measured by the QCM because of the design of the flow cell that did not allow for an *in situ* dialysis.

5.1.4 Adsorption of Detergent-Solubilized CcO to the Ni-NTA Layer probed bei SEIRAS

After activation of the gold surface, CcO is bound through the affinity of the genetically introduced His-tag for the Cu/Ni-NTA layer (Figure 1C). To monitor the adsorption of CcO by SEIRAS, a reference spectrum is taken in the presence of buffer solution (including 0.1% dodecyl-maltoside as detergent). Then, detergent-solubilized CcO was added to yield a final concentration of 2 μM, and the IR measurements were started.

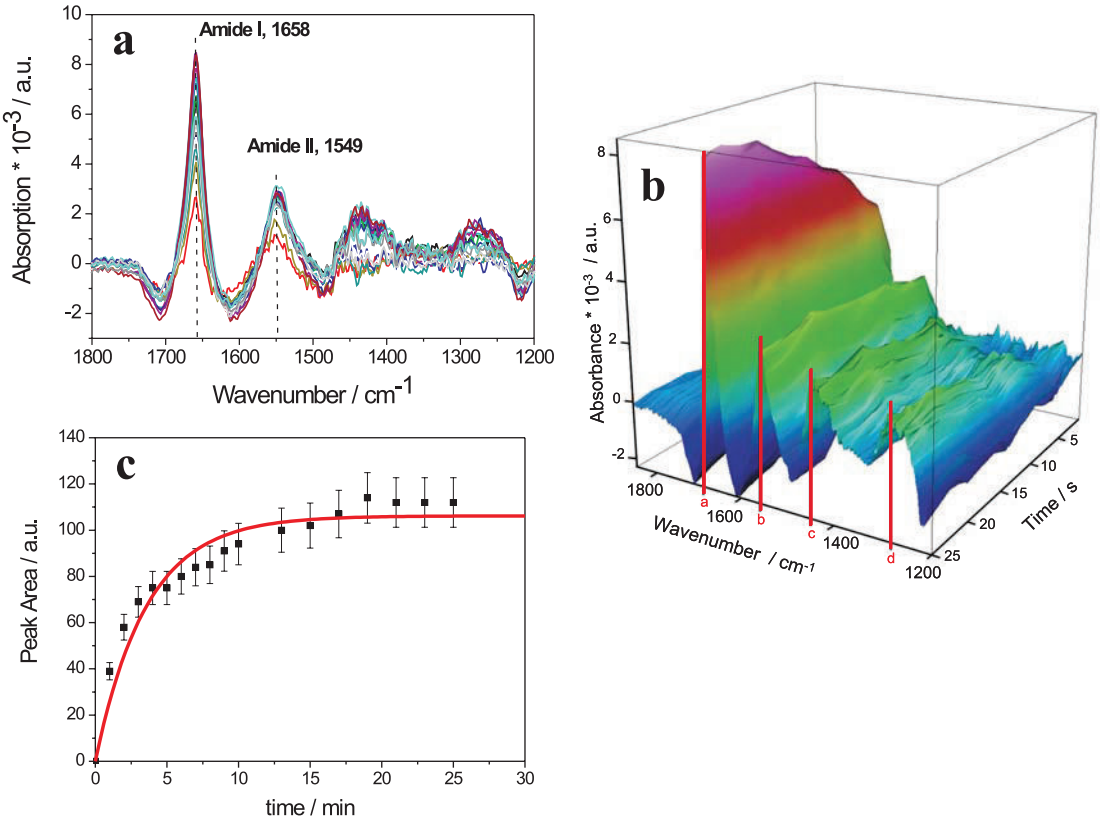

Figure 5.8: (A) SEIRA spectra of cytochrome c oxidase adsorbed to the Ni-NTA modified Au surface *via* the affinity for the genetically introduced His-tag. The rising bands indicate the binding of the protein to the surface and are discussed in the text. (B) Adsorption kinetics of CcO on the Ni-NTA SAM/Au surface. The peak height of the amide II band at 1550 cm^{-1} is plotted versus adsorption time. The filled circles represent the first adsorption of CcO, while the triangles represent the adsorption process of CcO after removing the previous CcO layer by imidazole. The reference spectrum is taken from the CcO covered surface.

As shown in Figure 5.8a, bands appear at 1658, 1549, 1436, and 1290 cm^{-1}. The former two bands are readily assigned to the amide I and the amide II modes of the protein

backbone vibrations of CcO, respectively [270]. The peak position of the amide I band is characteristic for a predominantly R-helical protein such as CcO. The increase of the band intensities in the course of incubation reflects the accumulation of CcO onto the Cu/Ni-NTA surface. The contribution of CcO from the bulk phase is negligible since its signal is hardly detectable at this concentration (2 μM). Moreover, the observed IR bands (fig. 5.8a) arise exclusively from surface-bound CcO molecules because the effective distance of the SEIRAS enhancement is less than 10 nm [303].

The assignment of the bands at 1436 and 1290 cm^{-1} is unclear. These bands do not arise from CcO since they appear at the same position irrespective of the nature of the protein used (data not shown). Neither of the detergent dodecylmaltoside exhibits such vibrational bands. Therefore, we suggest that they originate from the Ni-NTA layer, which may experience a conformational change due to the adsorption of CcO. Consequently, the band at 1436 cm^{-1} can be assigned to the symmetric stretching vibration of the carboxylate group of NTA which complexes the Cu^{2+} and $Ni2+$ ion. As soon as the His-tag of CcO ligates the Ni^{2+} ion, the interaction with the carboxylates of NTA may be disturbed and the corresponding vibrational bands may be shifted. The kinetics of adsorption of His-tagged CcO to the Ni-NTA surface is depicted in Figure 5.8c, where the intensity of the amide II band is plotted versus the adsorption time. The continuous line represents an exponential fit to the data, which yields a time constant of $\tau = 216$ s for the adsorption kinetics. The intensity becomes saturated at about 25 min or 1500 s.

5.1.5 Reconstitution of Surface-Tethered CcO into a Lipid Layer

The binding procedure of CcO to the Cu/Ni-NTA modified Au surface involves the use of detergent to solubilize the membrane protein. For embedding the protein into a membrane-like environment, the detergent solution was replaced by a lipid containing detergent/buffer solution and Bio-Beads were added, as a substitute for *in situ* dialysis.
A reference spectrum of the CcO covered surface was measured and then Bio-Beads were added to the solution. Sample spectra were recorded after 48 hours of reconstitution. The incorporation of DPhyPC is clearly indicated by the appearance of vibrational bands at 2955, 2932 and at 1726 cm^{-1} (Figure 5.9). The former bands can be readily assigned to the C-H stretching modes of the two alkyl chains of DPhyPC (symmetrical and asymmetrical CH_3 and CH_2 modes), while the latter band is due to the C=O stretching mode of its ester headgroup [304]. The positive differential absorbance in the C-H stretching region indicates that the number of C-H groups increases when the lipid DPhyPC replaces the detergent DM. This plausible suggestion is well supported by the appearance of the C=O stretching vibration, which is present in DPhyPC but absent in DDM. The bands as 1648 and 1506 cm^{-1} can be assigned to the Amide I and II bands of the immobilized CcO. The decrease of these bands indicates an ordering of the protein during reconstitution.

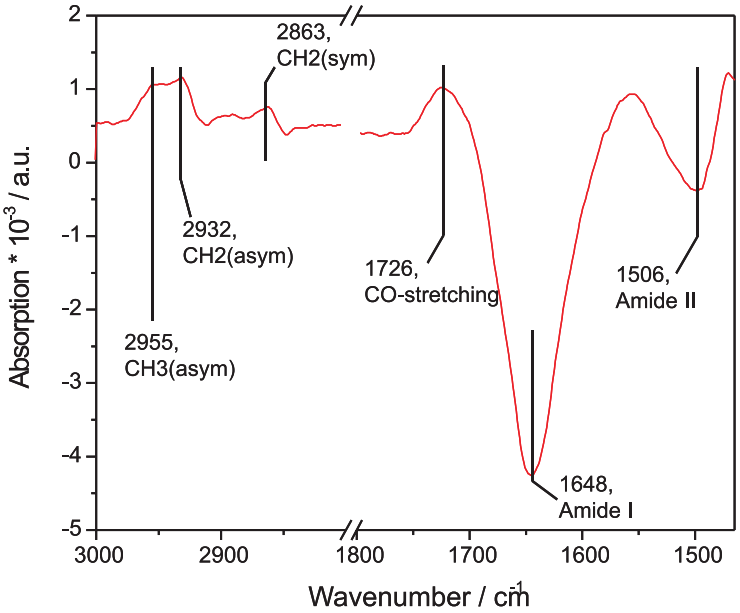

Figure 5.9: Surface-enhanced IR difference absorption (SEIDA) spectrum of the reconstituted membrane, 48h after starting dialysis. The increasing methyl bands and the CO-stretching modes show the formation of the membrane, the decreasing Amide I and II bands indicate an ordering of the protein.

5.1.6 EIS Measurements

EIS spectra were recorded after every preparation step described above. Capacitance and resistance values obtained by fitting the data to the equivalent circuit shown in the insert of Fig. 5.6 are given in Table 5.2.
As deduced from fig. 5.6, the capacitance of the dielectric layer decreases from 13.1 ± 3.9 $\mu F cm^{-2}$ for the CcO/detergent/water layer to 7.3 $\pm 0.5 \mu F cm^{-2}$ for the ptBLM, while the resistance increases from 300 $\pm 80 k\Omega cm^2$ to 12.2 $\pm 7 M\Omega cm^2$, see also Table 5.2. Considering the dielectric constant of lipids (2.2) is smaller than that of water (80) and proteins (typically 30) [305], the decrease of the capacitance indicates that detergent and water molecules residing between the proteins are replaced by the lipid bilayer patches. Thereafter, the capacitance is still dominated by the protein indicating a high degree of surface coverage. The capacitance of a protein layer with $\epsilon = 30$ and a thickness of 5 nm can be estimated to be 6 $\mu F cm^{-2}$ in reasonable agreement with 7.3 $\pm 0.5 \mu F cm^{-2}$ found experimentally. On the other hand, the mobility of ions between the CcO complexes is substantially reduced if lipid bilayer patches are present, since the resistance obtained for the ptBLM is in fact comparable to that of a pure BLM or tBLM.

To test whether or not the reconstituted CcO can be activated under these conditions, reduced cyt c was added to the oxygenated solution to obtain a final concentration of 40 mM. The impedance spectrum showed a drastic decrease in resistance (see the example

	Resistance / $M\Omega \cdot cm^2$	Capacitance / $\mu F cm^{-2}$
DTSP-ANTA-CcO complex	0.3 ± 0.08	13.1 ± 3.9
Reconstitution	12.2 ± 7	7.3 ± 0.5
After cyt c activation	0.23 ± 0.02	7.9 ± 0.6
After washing	4.3 ± 5	7.8 ± 0.5
After activation in the presence of KCN	7.6 ± 6	7.6 ± 0.6

Table 5.2: Resistance and capacitance values from EIS data fitted to the equivalent circuit given in Fig. 5.6 for different preparation steps

shown in fig. 5.6 from 12.2 $\pm 7 M\Omega cm^2$ to $230 \pm 20 k\Omega cm^2$ indicating that the protein actively transports protons during the catalytic redox cycle. After washing off the cyt c with buffer solution, the resistance returns almost to the initial value illustrating that the activation is fully reversible. Infusion of reduced cyt c together with 0.6 mM KCN, on the other hand, did not lead to a decrease in resistance, showing that in this case the CcO is specifically inhibited.

5.1.7 Conclusion

Protein-tethered bilayer lipid membranes have been shown to be a feasible concept to reconstitute complex membrane proteins in a tethered lipid bilayer system. Because affinity metal chromatography is a routinely applied protein purification system, ptBLMs can be seen as a universally applicable system for immobilization and surface-focused reconstitution of His-tagged membrane proteins. The Cu^{2+} or Ni^{2+}-NTA modified surface is ready to bind recombinant cytochrome c oxidase (CcO) *via* the coordination of the nitrogen atoms of two imidazol side chains of the 6x His-tag. CcO absorbs to the Cu/Ni-NTA-cross-linker in an oriented fashion. Purification of the proteins could even be avoided, if the preparation of ptBLMs would be performed using the crude cell lysate. This allows for the application of integrated proteomics (for review see Catimel et al., [306]) to membrane proteins.
Control of the orientation is achieved by adsorption of CcO through the His-tag. The orientation of the membrane protein is determined on the position of the affinity tag.

Two types of recombinant CcO, which carry the His-tag on different subunits, have been utilized in further investigations, as described in the next sections. As a model of the 500 kDalton large CcO complex located in the inner mitochondrial membrane of higher organisms [307], the smaller version (125 kDalton) in the cell membrane of bacteria, e.g. *Rhodobacter sphaeroides* [308] or *Paracoccus denitrificans* [309] was used. All of these

variants are identical with respect to their electron and proton translocation pathways [3, 310, 311, 312, 313]. His-tags were attached to the C-terminus of SU II of *R. sphaeroides* and to C-terminus of SU I of *P. denitrificans*. The enzyme can thus be immobilized in different orientations, either with the cytochrome c binding side[3] or, in the inverted orientation, with the O_2 reduction side, respectively, directed towards the electrode.

We were able to follow each modification step of the functionalized electrode to form the ptBLM architecture, by employing SPR, QCM, EIS and SEIRAS. EIS spectra before and after the addition of reduced cyt c show unequivocally that the enzyme is in the active state and that the activation is fully reversible. This opens new possibilities to investigate enzyme-catalyzed ion transport as a function of a defined transmembrane potential. As far as ion transport is concerned but also for structural studies, a critical issue for all membrane systems tethered to surfaces is the submembrane space. The advantage of the ptBLM is that the cytosolic part of the protein itself defines the submembrane space. In the case of the CcO this seems to be sufficiently large to allow for ion transport to occur across the lipid bilayer as demonstrated by EIS. Nonetheless, it is also possible to design longer affinity spacer molecules to expand the submembraneous space thus changing the electrochemical properties of the system. This is facilitated by the simplicity of the developed surface chemistry that is based exclusively on commercially available chemicals.

The surface attachement could also be shown for other bacterial transmembrane proteins, such as for the ATPase, the Reaction center and the Light Harvesting Complex (LHC II). The binding and reconsitution of these proteins leads to similar binding behaviours and electrical properties of the formed ptBLM as compared to the CcO described before. Some of the results of these measurements will be shown in the further context.

In summary, the ptBLM seems to open promising new ways to investigate membrane proteins in a biomimetic lipid environment. The ptBLM provides a platform that allows the direct application of a combination of electrochemical and surface analytical vibrational spectroscopy as required for kinetic as well as mechanistic studies of redox-active membrane proteins. This will be shown in the next sections.

5.2 Setup for Surface-Enhanced Resonance Raman Spectroscopy

A new setup had to be established in order to perform potential dependent surface analytical Raman spectroscopy in combination with electrochemical methods to measure and/or trigger electron transfer processes to the protein. The necessary sensitivity of the Raman

[3]The periplasmatic extension of subunit II embeds the docking site for cytochrome and therefore the natural electron entry side [3].

signal was achieved by two different enhancement effects, a resonance enhancement of the heme chromophors embedded in the protein and an electromagnetic surface enhancement by the roughened silver surface.

5.2.1 Optical Beampath

Figure 5.10 shows schematically the beam path and the different components of the home-built Raman setup utilized to perform SERRS measurements.

A monochromatic light source of a Kr^+ laser (*Innova 90K, Coherent*) was used, providing an excitation wavelength of $\lambda_{exc} = 413$nm ($I_{Laser} = 30$ mW). To maintain certain flexibility for the measurement of other proteins or analytes a flexible mirror system was designed in a way that the the beam path can directly be combined with an alternative light source, i.e. an Argon laser (*Innova 400-10, Coherent*) and a HeNe laser (*Q4001-K7654, Siemens*), providing different excitation wavelength. The laser source was run in the intensity control modus, to provide a stable excitation intensity.

At the beginning of the beam path a home-built electronically controlled shutter was positioned to provide an external control of the illumination time of the sample. Additionally a $\lambda/4$ plate (*Laser2000*) or a fresnel rhombus (*OWIS GmbH*) was placed in the beam path to obtain circular polarized light to prevent polarization dependent effects on the Raman signal. The laser beam was first directed through a (pre-)monochromator (*LaserspecIII, Spectrolab Research Laboratory, Newbury England*) in order to remove the background radiation consisting of plasma lines produced by the laser medium. These plasma lines are in the near UV region, thus interfering with the excitation wavelength at 413nm. The laser beam is then collimated with achromatic lenses[4]. with an 100 mm focal length (*UV, f = 100mm, λ_{opt}=257 nm*), optimized for an transmission in the (near) UV regime, focusing the laser beam onto a quartz crystal of an acoustic optical modulator (AOM) (*A.A. MT200/A0,5400nm01/24091, A.A. opto-éléctronique, St. Remy, France*), which is coated with TeO_2 and optimized for the wavelength regime between 400-442nm providing a transmission of $> 95\%$. To prevent the damage of the quartz crystal the laser intensity of the focused laser beam was kept smaller than 30mW. The AOM is operated by a radio frequency (RF) wave generator (*Mod.200.B26 N-01, RF_{out} = 2W/+24V, A.A. opto-éléctronique, St. Remy, France*). This wave generator applies a RF signal to a piezoelectric transducer, attached to the crystal, which generates an acoustic wave. This acts like a 'phase grating', travelling through the crystal at the acoustic velocity of the material and with an acoustic wavelength dependent on the frequency of the RF signal. The incident laser beam is diffracted by this grating, generally giving a number of diffracted beams (Fig. 5.11). The zero order is the beam directly transmitted through the cell. The first order is the diffracted beam generated when the laser beam interacts with the acoustic

[4]It was shown, that the use of an long-distance lens for focusing the laser beam onto the quartz crystal leads to the same result in the optical performance of the AOM than an telescope construction which leads to an reduced laser beam diameter.

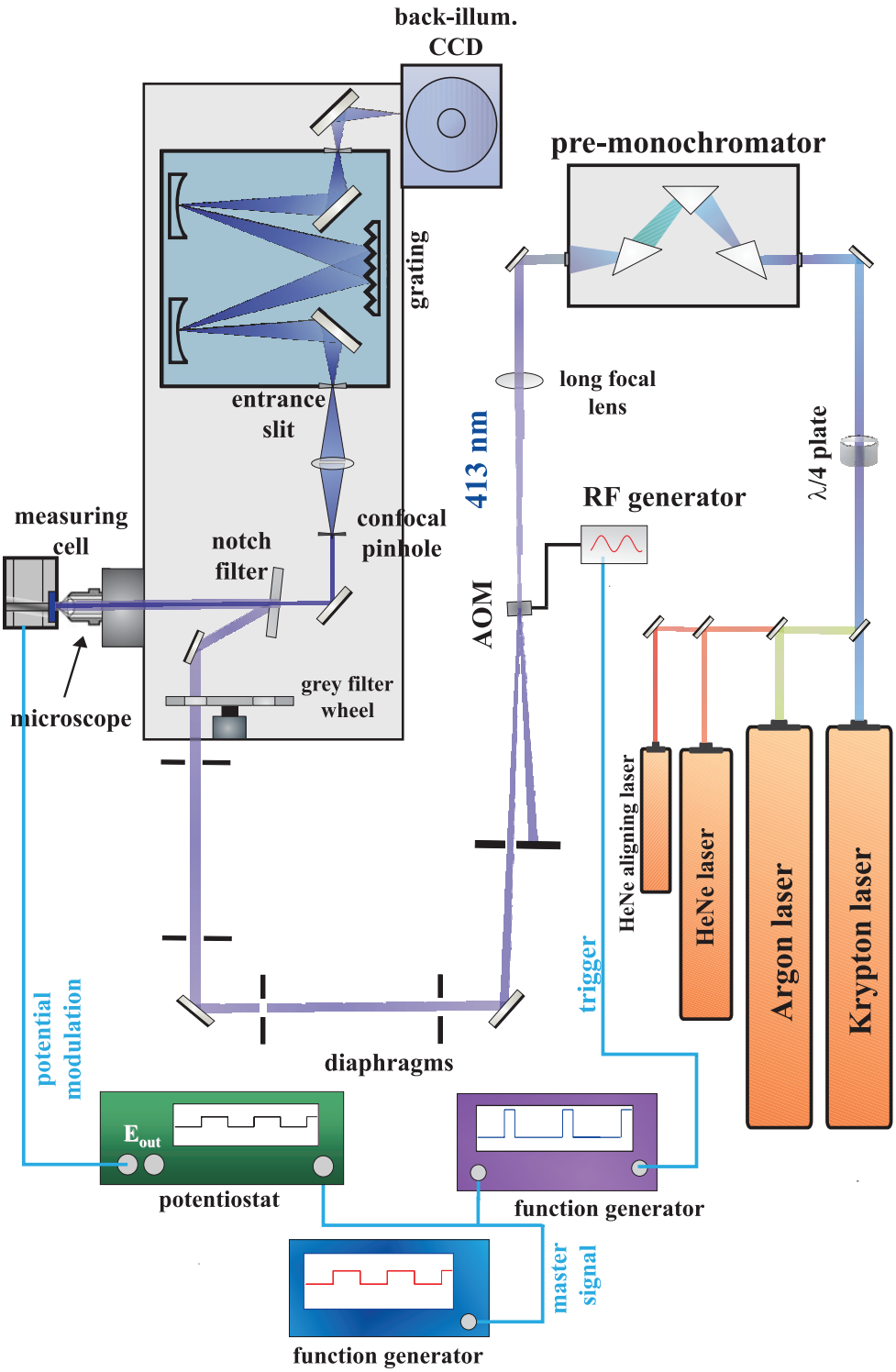

Figure 5.10: Schema of the home-build SERRS setup for time-resolved measurements.

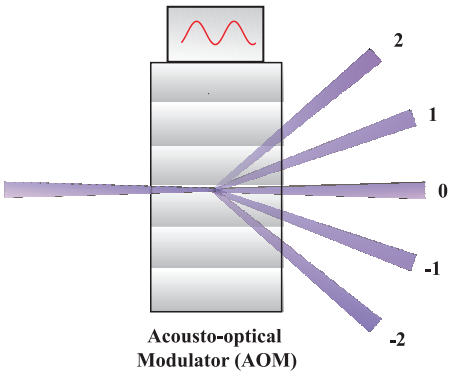

Figure 5.11: Principle of an acousto-optical modulator (AOM).

wave. The intensity of the diffracted light depends on the angle of incidence and can be optimized when approaching the Bragg angle (θ_B), giving efficient diffraction into the first diffracted order.

$$\theta_B = \frac{\lambda F}{2\nu} \tag{5.2}$$

With $\lambda = \lambda_0/n$ being the wavelength inside the crystal, ν the acoustic velocity and F the RF frequency. The AOM was therefore mounted on a stage (*Spindler & Hoyer*), free to move in xyz- direction as well as to change angular positions, θ and ϕ, in order to efficiently couple the focus of the laser beam onto the quartz crystal to achieve an optimum of intensity of the 1^{st} order diffraction. To obtain a sufficient spatial distance to effectively separate the different diffraction order a diaphragm was placed in ca. 15 cm distance, allowing only the 1^{st} order diffraction to follow the further beam path. Moreover, the AOM can be triggered by a TTL signal, provided by a pulse/function generator (*80 MHz, Agilent, 8021*), to perform time resolved measurements, as described further down.

The laser beam is further directed through a mirror [5] system into a microscope (*Olympus BX41*) combined with a confocal Raman microscope (*LabRam, HR800, HORIBA Jobin Yvon*). The laser beam was then focused to the sample surface *via* a water immersion objective (*Olympus LUMPLFL, 100 XW, WD=1.5, BFOBJ*) with an magnification of 100x, a numerical aperture (NA) of 1.00, a working distance of 1.5 mm and optimized transmission for near UV light, onto the surface of the sample. The backscattered light is collected by the same objective, and guided through a holographic notch filter (*413 nm*) to eliminate Rayleigh scattering and to cut off stray light. The Raman scattering light was then focused onto a confocal pinhole to provide spatial resolution and on the entrance slit for a polychromator (*Jobin Yvon*) controlling the spectral resolution. Both pinhole and slit are variable and can be adopted to the certain experiment. The spectral analysis can be done with a 1800 grooves/mm grating for high resolution spectra or alternatively with

[5] All mirrors in the beam path are coated silver mirrors provided by *Laser2000* with an optimized reflection of $> 98\%$ in the wavelength region between 400-700 nm

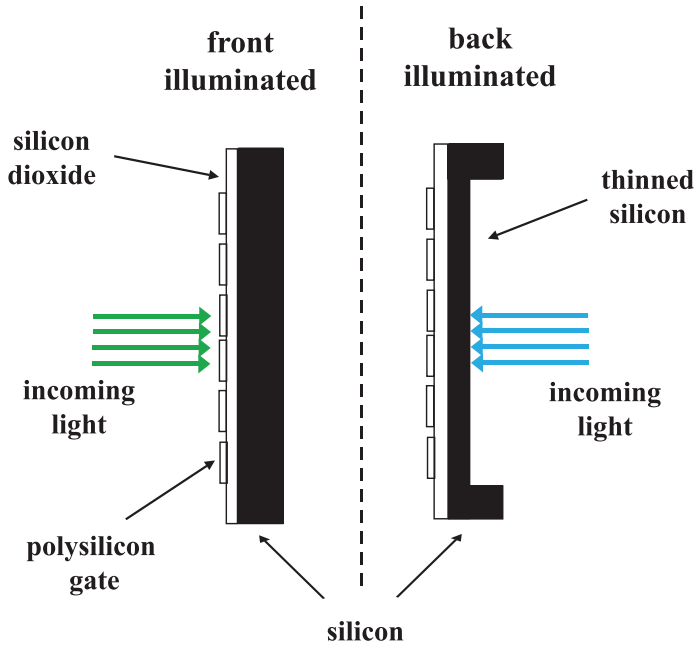

Figure 5.12: Comparison: (a) front illuminated and (b) backilluminated CCD

a 600 grooves/mm grating in order to obtain coarse spectra. The light is then detected by a high performance liquid-N2 cooled back-illuminated CCD (*charge coupled device*) detector (*Symphony, Jobin Yvon,*) optimized for (near) UV light optimized. Back-illuminated CCD means that the CCD chip is illuminated from the back side (Fig. 5.12). In a normal (front-illuminated) CCD detector the detection beam has to pass a silicon dioxide insulating layer as well as the electrically conductive gate structures in order to reach the silicon area where photons conversion actually takes place. This causes a significant absorbance in the UV range and therefore a decrease in the apparent quantum efficiency. To prevent this decrease, the silicon layer of back-illuminated CCD detectors is thinned/etched to typically 10-15 μm and the incoming light is focused on the back of the CCD register where there is no gate structure. The cooling to low temperatures dramatically diminishes the dark count (less then 3 e^-/pixel/hr), thereby allowing a long period of data acquisition when necessary, as in the case of time resolved measurements.

Furthermore, the CCD detector has an area of 2048 × 512 pixel, so that by a focal length of the spectrograph of 800 mm and a combination with the 1800 g/mm grating, spectral resolutions of 0.32 cm^{-1} can be achieved[6].

[6]for the laser wavelength of 413 nm

5.2.1.1 Alignment and Measuring Conditions

Since (near) UV light is hard to see by the human eye, the optical beam path (Fig. 5.10) is pre-aligned with a HeNe laser (*Q4001-K7656, Siemens*), which is coupled with a combination of two mirrors into the same beam path as the Kr^+ laser. The HeNe laser provides a low-intensity wavelength in the visible regime (λ = 633 nm; I = 1-2 mW), capable for the alignment of the system. The pre-monochromator has to be changed accordingly to the 633 nm.

The spectrograph has an internally implemented HeNe laser (633 nm), which aligned in the direction of the incoming laser pathway and which allows to align the illuminating beam with the main optical axis of the microscope and the objective. The mirrors that direct the laser beam into the spectrograph have to be adjusted so that the laser beam passes through the center of the microscope objective and impinges perpendicular on the sample surface. The spectrometer, which is controlled by a software called LabSpec (*Jobin Yvon*), has to be calibrated first by adjusting the zero order position of the grating. This can be done by introducing white light by a Neon lamp and centering the zero order reflection at the center of the CCD chip. Illumination with white light can also be used in combination with a color camera (*CSB-465(C)-CCIR, Jobin Yvon, PC*), allowing the sample to be visualized, permitting a rough estimation of the surface quality. The Raman spectrum is then calibrated by focusing the 413 nm laser line on a silicon sample and the spectrograph was adjusted to the known Raman band at 520.7 cm^{-1} of the Si spectrum.

The parameters to record Raman spectra of protein monolayer are usually set to the following values:

- Entrance slit of the spectrograph = 150 μm
- Confocal hole = 1000 μm
- Grating = 1800 l/mm
- Center position of the grating = 1500 cm^{-1}

5.2.2 Combination of Electrochemistry and SERRS - The Measuring Cell

To perform potential dependent SERRS on protein monolayer in an aqueous oxygen-free environment, a novel custom-made measuring cell was designed. Figure 5.13 shows a scheme of the spectroelectrochemical cell.

The cell based on an upside-down rotating disc electrode construction, with a roughened silver surface (diameter 10 mm) inserted into a Teflon mantle. In order to prevent photoreduction ([269]) or photo-degradation of the heme proteins, the electrode has to be rotated at least with 15 Hz or 900 rpm, respectively, while the laser intensity on the sample surface was kept below 100 μW, by the insertion of different grey filters at the entrance to the

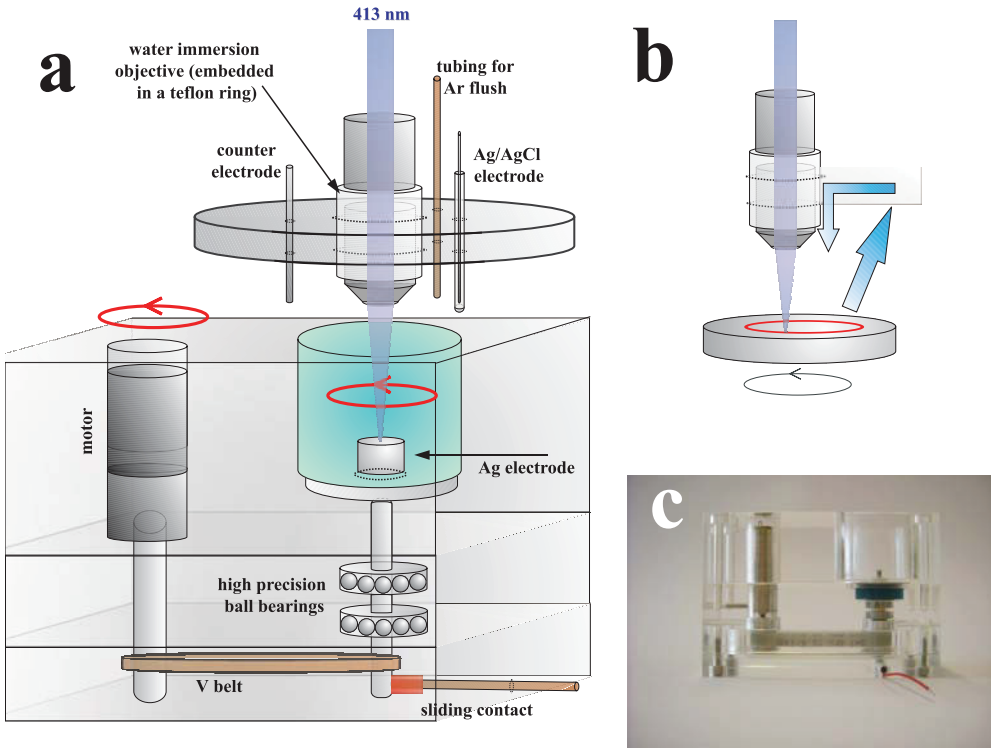

Figure 5.13: (a) Custom made SERRS cell, consisting of three different compartments and allowing for the combination of electrochemical techniques and Raman spectroscopy on a protein monolayer.(b) Principle of the 'wave-breaker', which directs the whirled up water back to the sample surface (blue arrows), preventing the surface to run dry. (c) Photograph of the cell without Teflon trough.

microscope. The measuring cell comprises three compartments:

1. An upper compartment, which contains the actual measuring cell,

2. a middle part, which contains a motor (*Faulhaber*), required to rotate the measuring cell and on the other side high (micrometer) precision ball bearings (*Miniatur Kugellager, Germany*) stabilizing the driving shaft to keep the sample surface perpendicular to the focus , and finally

3. a lower part, which connects the driving shaft of the measuring cell with the motor by a V-belt.

Electric contact of the silver working electrode of the spectroelectrochemical cell was provided by a sliding contact, which is connected to an Potentiostat (*Autolab, PGSTAT302, Eco Chemie, B.V., Utrecht, Netherlands*) applying potentials by a three-electrode configuration. The rotation speed can be controlled by an external control unit. It should be mentioned that in order to permit a high flexibility of the setup, the cell can be completely

disassembled, where every single compartment is exchangeable.

The cell can be combined with the microscope of the Raman setup (decribed above), by a special sample holder. The xz stage of the Microscope was modified with a new sample holder for the measuring cell which permits to freely move the mounted measuring cell in z and in x direction in micrometer precision. This allows for moving the measuring cell with respect to the fixed objective in order to direct the laser beam to different positions on the sample surface and to focus the laser beam onto the surface.

In order to enable measurements under anaerobic conditions, the cell is sealed to ambient air by a lid provided with inlets for the counter electrode, reference $(Ag|AgCl, KCl_{sat})$ electrode, an inlet for a KelF-tube[7] for deoxygenation as well as for the teflon covered microscope objective. The inner Teflon trough[8] was fixed to the RDE rotating in-line with the electrode. The cell was flushed through the tube with Argon, purged from oxygen by washing through the oxygen trap (see section 5.6.1) containing buffer solution. The Argon strem sets the measuring cell under a slight overpressure, which prevents the diffusion of oxygen into the measuring chamber.

In order to prevent the surface from running dry by the movement of the buffer towards the outer cell walls due to the centrifugal force, a 'wave-breaker' was fixed to the microscope objective. This 'wave-breaker' is 'L' shaped with a small angle so that the surface is tilted a bit downwards. While providing a0 fixed barrier for the whirled up water layer, the water is guided back to the surface. This concept is displayed in Figure 5.13b.

5.2.3 Sample Preparation

SERR active silver surfaces were prepared according to reference [314], by a sequence of electrochemical reduction and oxidation steps in a 0.1 M KCl [9] solution. Figure 5.14 shows the current trace of the roughening steps. Moreover, different surface preparations, with different time periods of the reduction and oxidation step, are shown, resulting in different SERRS signals. The peak maxima of the ν_4 mode at 1370 cm^{-1} (compare section 4.3.3.4) of cytochrome c absorbed to thio-propionic acid under the same conditions. The topographic picture of the surface whith an optimum of SERR activity is shown. The parameters for the preparation are given in the figure caption. (Fig. 5.14c).

[7] KelF is impermeable to

[8] The whole measuring chamber as well as the cover of the objective was made of Teflon to be able to clean with Piranha solution, providing sufficient cleanliness for surface analytical electrochemical measurements

[9] It has been shown, that the SERR activity of the prepared silver surfaces is very sensitive to the concentration of KCl in the solution during the roughening process.

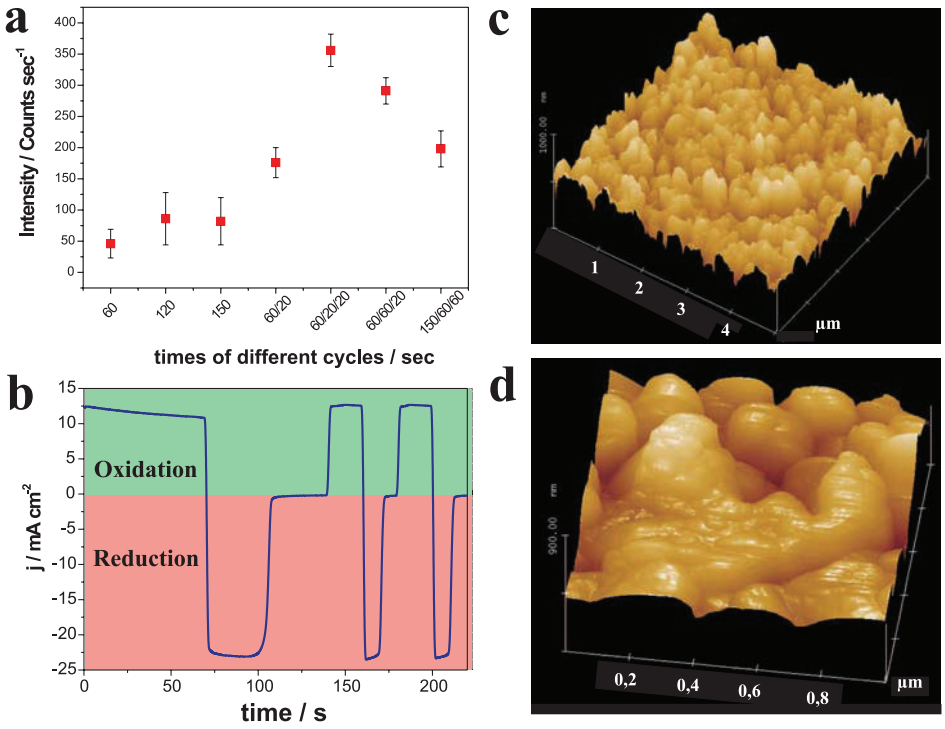

Figure 5.14: (a) Surface-enhanced Raman intensity of the peak maxima of the ν_4 mode at 1370 cm^{-1} of cyt c absorbed to thio-propionic acid for different sequence of electrochemical reduction and oxidation steps ($\lambda_{exc} = 0.7mW$ on the sample surface). The number indicates the time span of one oxidation-reduction cycle. (b) The current profile for a roughening procedure and (c) the morphology of the surface ($5 \times 5\mu m$) and (d) ($1 \times 1\mu m$) under optimal enhancement conditions (60/20/20). The height profile provides a surface roughness (RMS) of 80.2 nm.

5.2.4 Principle of Time Resolved SERRS Measurements

The in section 5.2.1 described setup is readily applicable to perform time resolved measurements. Figure 5.15 shows the principle for time resolved measurements.
The potentials generated by the potentiostat can be triggered by a pulse/function generator (20 MHz, Tabor Electronics, 8021) providing the master signal. To permit a fast external triggering the driver software of the Autolab potentiostat had to be reprogrammed. [10]
The potential is instantaneously changed from an initial potential (E_i), where the proteins are fully oxidized, to a final potential (E_f), where they are fully reduced, in a rectangular function. The measuring interval is determined by the pulse width Δt, which can be different for the forward ΔT_{E_i} and the backward pulse ΔT_{E_f} and is determined by the master signal of the pulse/function generator. This potential jump and therefore the induced electrochemical reaction perturbs the potential-dependent equilibrium of the absorbed species and causes a change in the concentration of the certain species (C). In this context this

[10]The Macro is attached in the appendix.

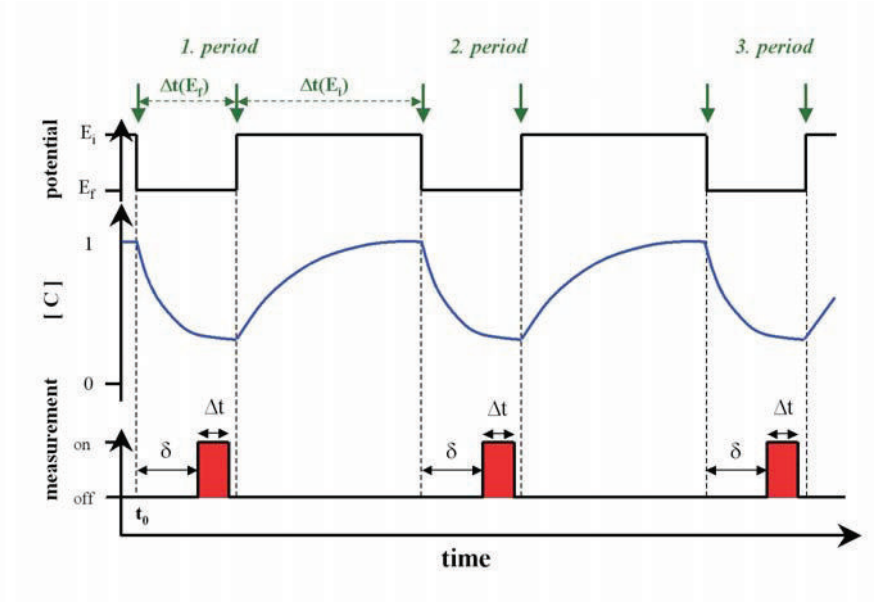

Figure 5.15: Principle of the time-resolved SERRS experiment.

would be either the fully oxidized or the fully reduced enzyme. The redox-linked structural changes or the change of the concentration of the surface confined species can be monitored at different delay times δt, which is defined by the second pulse/function generator, which is triggered by the master signal giving the starting point of the measurement. Since the beam path is aligned according to the 1^{st} order diffraction of the AOM, the external TTL[11] signal, provided by the second function/potential generator, causes a controlled direction of the light through the diaphragm. Thus the sample is illuminated for a preset time interval Δt, defining the time resolution. Assuming a reversible process, the potential is reset after the measuring event to the initial value E_i to re-establish the initial equilibrium concentration. Thus the sequence of potential jumps can be repeated under exactly the same conditions in a periodic fashion. The time $\Delta T_{E_i}/E_i$ has to be sufficiently long, to allow a complete relaxation to the initial equilibrium. The sequence of potential jumps is repeated z times so that the effective accumulation time for measuring the spectra, $z \cdot (\Delta T_{E_i} + \Delta T_{E_f})$, is sufficient long to provide an acceptable signal-to-noise ratio. During the entire experiment the CCD detector is active, implying that the dark noise is accumulated during the time $z \times \Delta T_{E_f}$ [12], whereas the SERR signals are detected during $z \times \Delta T_{E_f}$. All of the time settings can be controlled by an oscilloscope (*LeCroy, 935AM, 50MHz*).

The maximal time resolution is determined by the electrical response of the different equipments involved in the time resolved measurement. The rise time of the AOM is < 160 ns,

[11] Transistor-to-transistor logic. This is a defined potential region for trigger signals going from 0V (=off) to 1V (=on).

[12] A gating of the CCD camera is only be possible in the ms time regime, thus impracticable for fast time resolved measurements.

of the Autolab 350 ns (in the fast external trigger mode) and of the both pulse/function generators < 200 ns. The main contribution , however, is caused by the cables which due to capacitive effects cause , even for the shortest versions (30 cm), a rise time of about 500-600 ns.

5.2.5 Conclusion

A SERRS setup was established providing sufficient sensitivity to investigate the structural properties of monolayers of heme proteins immobilized on silver, with a high spectral resolution and a high sensitivity to near UV light. The use of an excitation wavelength of $\lambda_{exc} = 413$ nm allows to combine a resonance enhancement of the heme chromophores in enzymes and the electromagnetic surface enhancement provided by the roughened silver surface.

The custom-made spectroelectrochemical cell allows the combination of Raman spectroscopy with Electrochemical techniques, which permits to measure either redox-linked changes in potentiostatic experiments or by a potential modulation in a time resolved fashion. This and the choice of another excitation wavelength, provided by the different laser sources, makes the setup flexible and general applicable for different types of experiment as well as a variety of surface attached species.

5.3 Preservation of the Active Site Structure and Redox Processes of the Immobilised CcO

Redox activity of cytochrome c oxidase toward cytochrome c as well as concomitant proton transport has been shown, however, these studies do not allow conclusions about the full structural integrity of the enzyme that acts as a redox-driven proton pump. This can only conclusively be demonstrated by vibrational spectroscopy.

In this section, we have utilised the novel approach of the protein-tethered bilayer membrane [315], in which the lipid bilayer membrane is tethered to an roughened Ag electrode *via* CcO from Rhodobacter sphaeroides [316]. This system offers the possibility to analyse the immobilised enzyme by surface enhanced resonance Raman (SERR) spectroscopy which selectively probes the protein cofactors and thus can provide insight into the interfacial protein redox processes on a molecular level [201, 317]. Therefore, a surface-enhanced resonance Raman setup was established, as described before.

In this construct, the His-tag has been introduced to the C-terminus of subunit (SU) II at the periplasmic surface of CcO [318], i.e. at the binding domain for the natural reaction partner cyt c. Thus the natural electron entry side is directed towards the silver electrode, which could rise to an direct electron injection into the enzyme. Thus a direct method to modify the redox state would be possible.

The exposed hydrophilic protein domain serves as a spacer between the membrane and the electrode and thus generates a submembrane space, which is electrically insulated against the bulk solution as demonstrated by impedance measurements [315]. Although the His-tag is attached to the rather flexible helix H of subunit II [318] the surrounding phospholipid bilayer is likely to force the membrane-spanning helices of CcO in an approximately perpendicular orientation with respect to the electrode.

5.3.1 Surface-Enhanced Resonance Raman Spectroscopy on CcO Immobilized on a Silver Surface

Figure 5.17 shows the SERR spectra of surface confined cytochrome c oxidase with different bias potentials in comparison with resonance Raman (RR) spectra of the oxidized and reduced solubilized form.
These spectra display the so-called marker band region [199, 313]. This spectral region includes modes that are sensitive indicators for the oxidation, spin and ligation state of the hemes [199]. They allow to distinguish between the six-coordinated low-spin (6cLS) heme a and the high spin (HS) heme a_3 as well as determining the redox activity of the enzyme. In the RR spectrum of fully oxidised CcO in solution, characteristic heme a marker bands are at 1585 (ν_2), 1635 (ν_{10}), 1500 (ν_3), and 1647 cm^{-1} (formyl stretching) whereas the

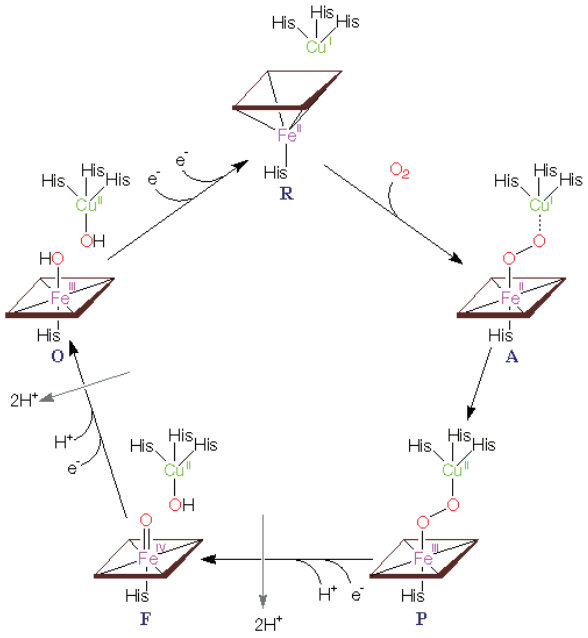

Figure 5.16: Expected conformational changes of the heme a_e structure at the binuclear (catalytic center) of CcO [319, 320]. The enzyme in the resting state (fully oxidised; compound O) is reduced by cyt c yielding a_3^{II}-Cu_B^I form R (fully reduced). Dioxygen (O_2) reacts with R to form the short-lived ferrous oxy intermediate (compound A). A is converted into the bridging peroxide (compound P). One-electron reduction results in a ferryl intermediate (compound F). F undergoes further one-electron reduction to form oxidised compound O. The two latter successive electron transfers are coupled to proton translocation across the membrane. Interestingly, the haem a_3 is pentacoordinate in the crystal structure of 'fully oxidised' CcO [48] and no bridging ligand between haem a_3 and Cu_B has been found. However, a further determination of the structure of intermediates in detail is necessary to understand the mechanism of action of CcO.

1370 cm^{-1} band originates from the ν_4 modes of both heme a and heme a_3 (Fig. 5.17A). The doublet at 1477 and 1490 cm^{-1} results from the mode ν_3 of a ferric HS heme that is hexa- (6cHS) and pentacoordinated (5cHS), respectively. This finding indicates that for a fraction of the heme a_3-Cu_B catalytic site the bridging ligand is dissociated from heme a_3 [199]. The 5cHS and 6cHS configuration can only be distinguished by the frequency of the ν_3 mode whereas for the ν_3 and the formyl stretching mode the bands of both coordination states coincide and give rise to the relatively strong bands at 1570 and 1671 cm^{-1}, respectively.

SERR spectra of the CcO-tethered lipid bilayers on the Ag electrode display surprisingly intense signals of the hemes a and a_3 despite a separation of these groups from the metal surface of more than 50 $\AA$ (Fig. 5.18). At +0.2 V vs. NHE or at open circuit, the band frequencies reveal a good agreement with those of the RR spectrum of oxidised CcO (Fig. 5.17A,B). However, the shoulder at 1358 cm^{-1} on the low-frequency side of the prominent

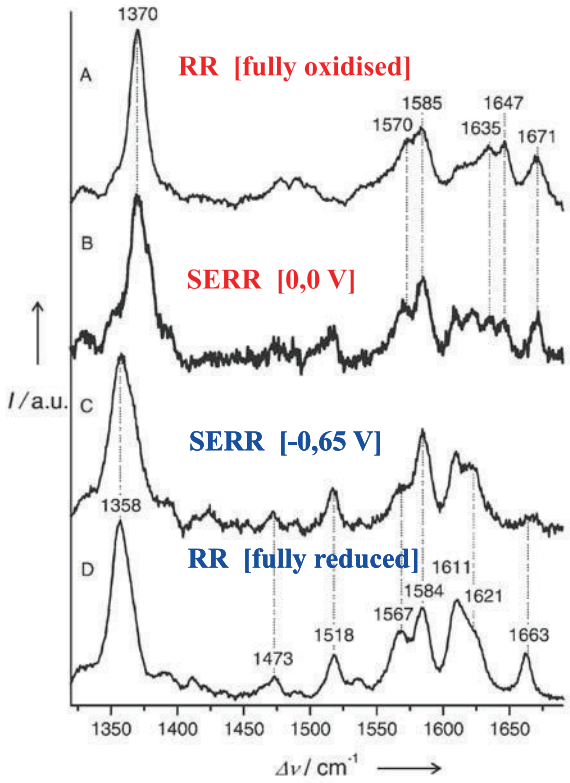

Figure 5.17: SERR spectra (λ_{exc} = 413 nm) of CcO in a ptBLM on a roughened Ag electrode, measured at (B) open circuit and (C) -0.65 V, compared with the RR spectra of CcO in solution, (A) in the fully oxidised and (D) dithionite-reduced form.

1370 cm^{-1} band as well as the concomitant appearance of the characteristic 1517 and 1611 cm^{-1} bands indicates a small contribution from reduced heme a (*vide infra*), which may (partly) result from photoreduction by the exciting laser beam. Whereas under these conditions the immobilised enzyme is largely in the oxidised state, the SERR spectrum measured at -0.45 V (Fig. 5.17C) displays the vibrational band pattern of the reduced enzymes as revealed by comparison with the RR spectrum of fully reduced CcO in solution (Fig. 5.17D). Also for the reduced state, we note a very good agreement between the band frequencies in the RR and SERR spectra. While the ν_4 modes of both hemes coincide at 1358 cm^{-1}, the modes ν_2 (ν_{38}) of hemes *a* and a_3 are well separated at 1584 and 1567 cm^{-1}, respectively. Correspondingly, the weak bands at 1473 and 1492 cm^{-1} are readily assigned to the ν_3 modes of hemes *a* and a_3, respectively. A unique property of heme a is the large frequency downshift of the formyl stretching from 1647 to 1611 cm^{-1} which reflects a substantial redox-linked change of the hydrogen bond interactions of this substituent with *Gln*471 and *Arg*52 [316, 313]. Only a small downshift is observed for the stretching of the heme a_3 formyl group that remains in a largely hydrophobic environment.

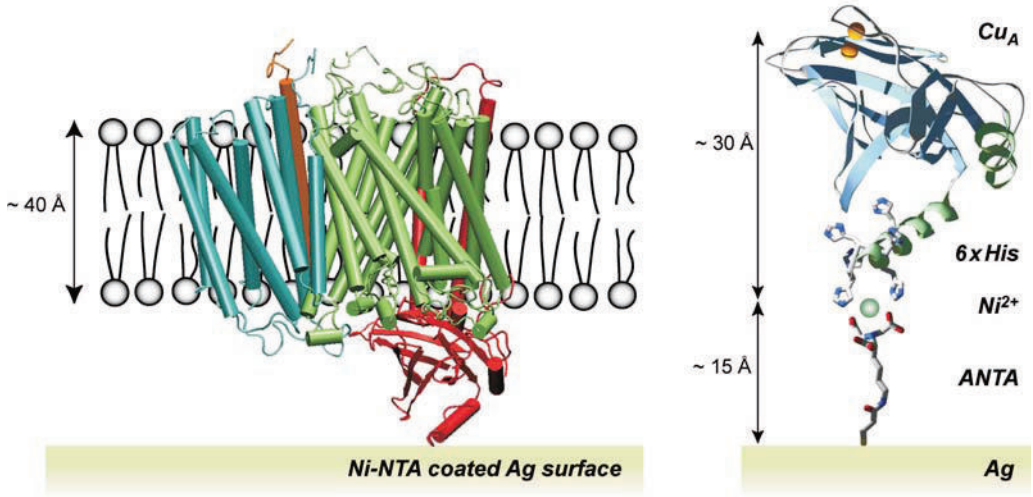

Figure 5.18: Schematic representation of the CcO-tethered lipid bilayer. The left panel depicts the structure of CcO from R. sphaeroides embedded in the lipid bilayer on the Ag surface. The subunits SU I comprising heme a, heme a3 and CuB, SU II attached to the surface, SU III, and SU IV are displayed in green, red, cyan and ocher, respectively. The right panel shows the peripheral domain of SU II with the binuclear Cu_A center (yellow spheres) and the C-terminal his-tag.

5.3.2 Comparitive Study of SERR and RR

Comparison of the RR and SERR spectra unambiguously shows that in both the ferric and the ferrous state the structures of the hemes a and a_3 as well as the specific interactions with the protein environment remain unchanged upon immobilisation. This is also true for the distribution between the 5cHS and 6cHS configuration in the ferric form of heme a_3, which has been shown to respond most sensitively to changes of the quaternary structure of the enzyme [199]. This finding can be taken as an indication that the entire enzyme structure is largely preserved in the immobilised state. The only noticeable differences between the RR and SERR spectra refer to relative intensities of the formyl stretchings that are weaker in the SERR spectra presumably due to the lower surface enhancement for the largely localised substituent modes as compared to the porphyrin modes. The immobilised CcO can be reduced and re-oxidised by varying the electrode potential. No time-dependent changes are observed in the SERR spectra measured immediately after changing the potential. Thus, electron transfer reactions are fast compared to the time scale of the SERR experiments ($<$ 1 min). Taking into account the considerable electron transfer distance to the primary acceptor CuA ($>$ 40 $\AA$; Fig. 5.18), we conclude that immobilisation of CcO *via* His-tags allows an efficient electron exchange with the electrode. The redox potentials for CuA, heme a, and heme a_3 are estimated to be +0.294, +0.334, and +0.294 V, respectively [321]. However, complete reduction of the immobilised enzyme is not possible at electrode potentials positive to -0.45 V. Only to a minor extent, this large overpotential may result from the interfacial potential drops [317]. Instead, it is very

likely that traces of oxygen already in solution, which were unavoidable in the present experimental setup, cause the consumption of electrons at the catalytic heme a_3-Cu_B site. Under these steady state conditions, the oxidation states of the hemes are essentially controlled by the oxygen concentration in solution. This interpretation implies that the immobilised CcO is (largely) catalytically active. In fact, CcO that was immobilised to the electrode *via* a His-tag on the cytoplasmic side reveals enzymatic activity towards ferrous cyt c and is capable of transporting protons across the bilayer [315].

5.3.3 Conclusion

In summary, we conclude that protein-tethered immobilisation of lipid bilayers allows the binding of CcO in a biomimetic environment and defined orientations while it is electronically coupled to the electrode. First, experimental results already show the possibility of a direct electron transfer from the metal electrode to the enzyme, while oriented with its natural electron entry side towards the electrode. This will be then further discussed in a combination study of electrochemistry and vibrational spectroscopy, such as surface-enhanced resonance Raman spectroscopy, in the following sections. A comparative study between CcO immobilized on the surface and of the solubilized species shows that the structure of the heme sites is preserved. This finding, together with the fact that the surface confined CcO in this biomimetic membrane architecture can be activated with its natural electron donor cyt c (see section 4.1.5), demonstrates conclusively that the enzyme remains active on the surface and the catalytic activity appears to be retained. This forms the basis for all of the following kinetic and mechanistic investigations on the immobilized CcO.

5.4 Electronic Wiring of Cytochrome c Oxidase

In the previous section it was shown, that the biomimetic ptBLM architecture electrically couples the protein to the electrode, providing direct electrochemical access to the ET pathway of the protein [270] while simultaneously providing an aqueous layer between the protein and the electrode. Bioelectronic coupling is further controlled by the strict orientation, whether or not the protein is immobilized with the electron entry side, i.e. the CuA center of the CcO, directed towards the electrode.

Electrochemically induced ET to multi-centered redox proteins has been the subject of research in recent years, but due to the lack of a biomimetic membrane system, mostly for soluble [35] or membrane-extrinsic proteins [36]. The benefit of direct ET is the accessibility of the internal redox centers avoiding the diffusion limitation of mediators. The intriguing question to be answered in this study is whether or not the primary ET step to the initial electron acceptor is sufficiently fast to cope with successive reactions. Fast ET is a prerequisite for the kinetic analysis through all the redox centers. Furthermore, the extent in which electrochemistry in combination with spectroscopic methods such as

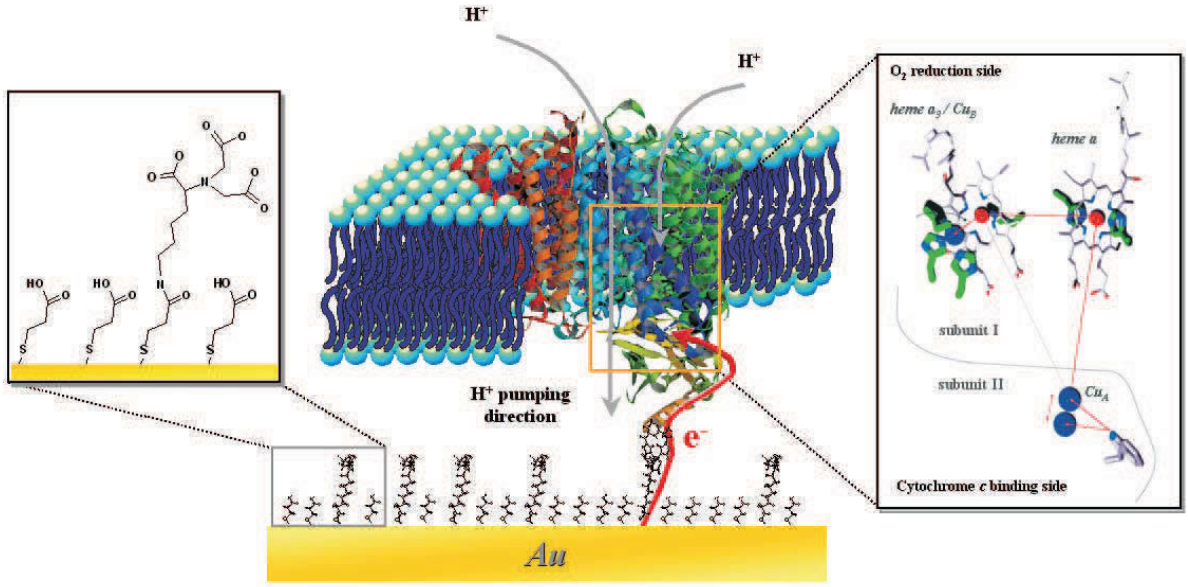

Figure 5.19: Schematic representation of cytochrome c oxidase (CcO) embedded into a protein-tethered bilayer lipid membrane. The protein is attached to the template stripped gold film on the surface by the his-tag attached to SU II, allowing for direct electron transfer to take place. The lipid bilayer is assembled around the protein. The box on the right shows the stepwise electron transfer inside the CcO [323] and the box on the left shows the details of the surface modification.

surface-enhanced resonance Raman (SERRS) [270] and infrared reflection absorption spectroscopy [322] provide additional mechanistic or structural information about the redox processes, particularly regarding the orientational specificity of the ET, has to be clarified. A further advantage inherent in the geometry of the system is the aqueous phase between the electrode and the lipid membrane provided by the tether molecules. The experimental benefit of this is the sensitivity of the small interstitial reservoir ($\sim$0,5 $nLcm^{-2}$) to changes in proton concentration as a result of enzyme activity. Thus our methodology presents a new approach to separately examine proton and electron transfer reactions in membrane proteins with significant consequences for the elucidation of the mechanism of proton pumping.

5.4.1 Direct Electron Transfer

CcO from *R. sphaeroides* engineered with a His-tag on subunit II (SU II) [308], was tethered to the surface of a gold electrode and reconstituted *in situ* into a ptBLM, as described in section 5.1. Under these conditions with the entry point of electrons, i.e. Cu_A, oriented towards the electrode surface.

Cyclic voltammetry (CV) at low scan rates (below 1 Vs^{-1}) and at *strictly anaerobic con-*

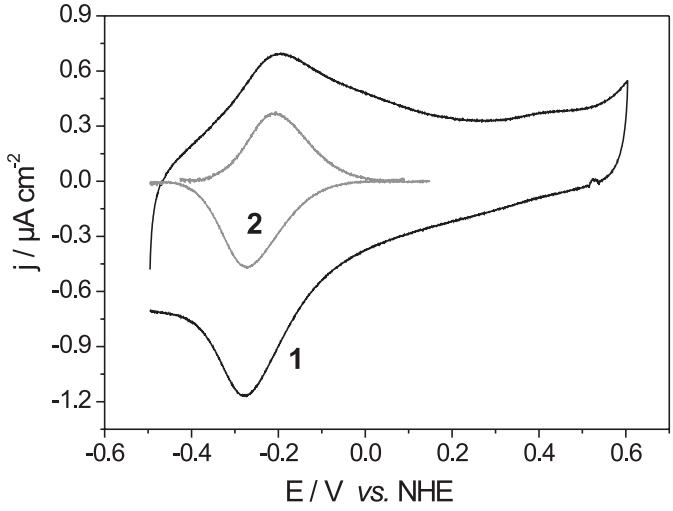

Figure 5.20: Cyclic voltammogram of CcO with the his-tag attached to SU II under strictly anaerobic conditions, scan rate 0.01 Vs^{-1}, without (1) and with baseline correction (2).

ditions, shows a single reduction peak at -274 ± 7 mV and a corresponding oxidation peak at -209 ± 6 mV (Fig. 5.20). Reference experiments with non redox active membrane proteins incorporated a ptBLM, such as bacterial ATPase, under identical conditions did not show any redox peak (not shown), which supports the finding that the observed redox peak originates from the immobilized CcO.
As the scan rate is increased to $\sim 1\ Vs^{-1}$, the peak positions remain largely unchanged and the baseline-corrected current density increases linearly (Fig. 5.21), which is consistent with surface confined ET [37]. The peak separation of 65 mV unchanging with the scan rate is consistent with a (quasi-)reversible ET [13] The quality of the membrane is of paramount importance for subsequent spectro-electrochemical measurements. A poor quality of a ptBLM affects not only the kinetics of the direct ET, but also the long-term stability. Some samples of CcO within a ptBLM of good quality lasted for more than a week in a functionally competent state. If the membrane is of insufficient quality, the direct ET is considerably slowed down as shown by broad and shallow peaks in the CVs of CcO, indicating a distribution of rate constants. In addition, the lifetime of samples is substantially reduced. [37]. Assuming symmetrical behaviour of the redox system, we have estimated the apparent standard potential, E^0_{app}, to be -242 ± 7 mV. This E^0_{app} is shifted $\sim$ -450 mV from the standard potential of +230 mV determined for the Cu_A center in isolated CcO [324].

[13] To efficiently perform this kind of experiment, it is obligatory to make sure that the biomimetic membrane had been formed around the protein. This can be seen from electrochemical impedance measurements.

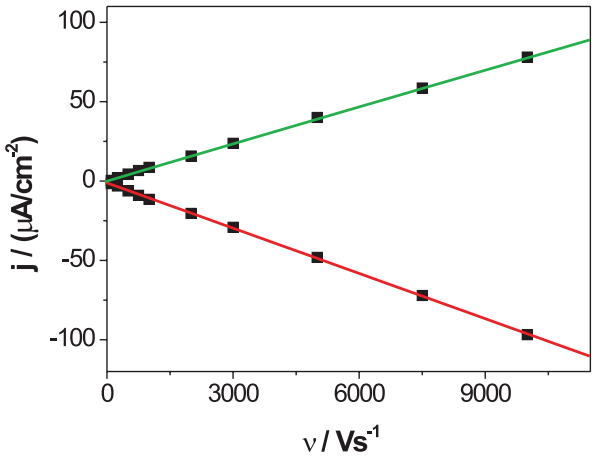

Figure 5.21: Baseline-corrected current density plotted as a function of scan rate, reductive branch (red), oxidative branch (green). The current density is increasing linear with respect to the scan rate, typical for surface confined redox species.

The large potential shift observed for the tethered CcO can be rationalized through a detailed examination of the surface confinement geometry. A kinetic effect of the peak shift must be excluded due to observed reversible appearance of the data. The first possible source of the shift can be found in the surface of the enzyme itself. The surface of CcO is highly negatively charged, particularly at the cytochrome c binding site [200]. As a consequence, the CcO-tether interface carries a permanent charge density, which can cause a negative shift in E^0_{app}. Rivas et al. described such a shift for an immobilized enzyme system based on the tetraheme enzyme, cytochrome c_3 [285]. A further negative shift of the peaks in the voltammograms of CcO is expected if ET occurs *via* the Ni complex as an intermediate step, due to the low standard potentials of chelated Ni^{2+}/Ni^{+} couples [325]. The redox process to the Ni complex is considered to be transient, due to the absence of redox peaks observed when the Ni-NTA is chelated with imidazole instead of the His-tag (data not shown). This is in agreement with results presented by Blankespoore et al. [326] and is further supported by preliminary simulations which will be shown later in section 5.9.3.

Further evidence for the direct ET as well as for the structural integrity of CcO was derived from Soret band excited SERRS. Spectra of CcO recorded at *strictly anaerobic* conditions, at constant potentials are shown in Fig. 5.22a. Difference spectra (Fig. 5.23) taken in potential region between -100 and -400 mV show three distinct region, 1350- 1370 cm^{-1}, 1500- 1520 cm^{-1} and 1600- 1620 cm^{-1}, which show significant changes during the transition from the oxidized to the reduced form. The characteristic bands at 1358 cm^{-1} and 1370 cm^{-1} originate from the ν_4 modes of both hemes in the reduced (-350 mV) and oxi-

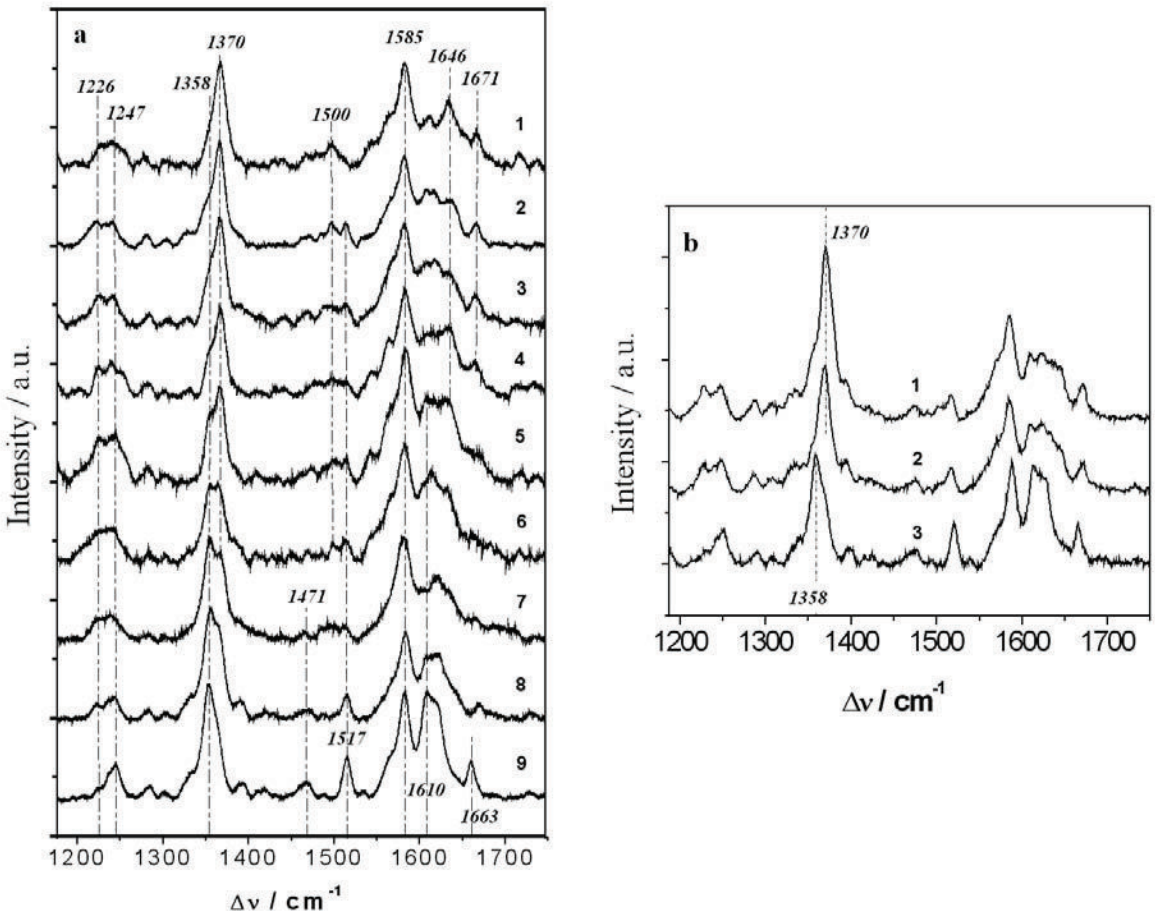

Figure 5.22: SERR spectra of CcO at different potentials applied across the biomimetic protein-membrane architecture immersed in buffer solution. (a) with the his-tag on SU II at -150 mV (1), -175 mV (2), -200 mV (3), -225 mV (4), -250 mV (5), -275 mV (6), -300 mV (7), -325 mV (8) and -350 mV (9). (b) with the his-tag on SU I, spectrum taken at +200 mV (1), -1100 mV (2) and after chemical reduction with dithionite (3).

dized state (-150 mV), respectively [270, 327] (Fig. 5.24). Furthermore, the type-*a* hemes of CcO include a conjugated vinyl and formyl substituent, which give rise to resonance Raman-active stretching modes between 1610 and 1680 cm^{-1}. Characteristic redox linked changes of the weakly-bound formyl substituent of heme a_3 giving rise to a small change from 1663 to 1671 cm^{-1} in the oxidised and the reduced state (Fig. 5.25c and d), since the formyl group remains in a hydrophobic environment. A further characteristic marker band for the reduced heme a is the intense and well seperated band at 1517 cm^{-1} (ν_{11}) not present in the oxidized state (Fig. 5.25b). Redox induced changes of the C=O side group of heme a_3 can be observed by a larger frequency downshift from 1646 to 1610 cm^{-1} which reflects a substantial redox-linked change of the stronger hydrogen bond interactions of this substituent with $Gln471$ and $Arg52$ [270, 327]. Both porphyrin modes (ν_4 and ν_{11}) and the formyl stretching modes allow monitoring the oxidation states of the individual hemes of the immobilised CcO. The bands at 1477 and 1490 cm^{-1} result from the mode ν_3 of a ferric high-spin (HS) heme a_3 that is hexa- (6cHS) and pentacoordinated (5cHS), respectively or at 1500 (ν_3) and 1585 cm^{-1} (ν_2) a ferric hexacoordinated low-spin (6cLS) [270, 327, 199]. This finding shows a potential-dependent structural rearrangement in the environment of the catalytic center and of the bridging ligand, which is partially dissociated from the heme a_3. In summary, it is evident that a gradual transition of the redox state as well as the coordination and spin state of both heme centers occurs in the potential range between -150 mV and -350 mV, in agreement with the CV data (see Fig. 5.20).

Under the present experimental conditions, the Cu centers are not visible because of a selective resonance enhancement of the heme structure. However, it has been previously shown that electrons arriving at Cu_A are transferred to the other redox centers [328, 329]. It thus follows from the Raman spectra that the electrochemical reduction peak is in fact due to direct ET to Cu_A and further on to the heme centers.

As a control, CcO from *P. denitrificans* with a His-tag engineered to the C-terminus of subunit I (SU I) [309] was immobilized in the same biomimetic system. The electron entry side, Cu_A is oriented towards the outside of the membrane opposite to that described above. This inverted orientation shows identical Raman spectra identical to those of CcO with the His-tag on SU II, thus indicating the same structural integrity of the protein. No indication of reduction can be seen in the potential range between +200 mV and -1100 mV (Fig. 5.22b), i.e. CcO remains in the oxidized state. Accordingly no electron transfer peaks can be observed with CV. This is not due to a functional impairment of the redox centers since they can be reduced chemically by adding dithionite (Fig. 5.22b), and CcO can still be activated by reduced cytochrome c [315]. This control experiment proves conclusively that ET between the electrode and CcO does not occur nonspecifically to any of the redox centers, but is possible only *via* Cu_A. Thus, exquisite control of the orientation of the enzyme allows direct, verifiable ET reactions to and within CcO to be elucidated.

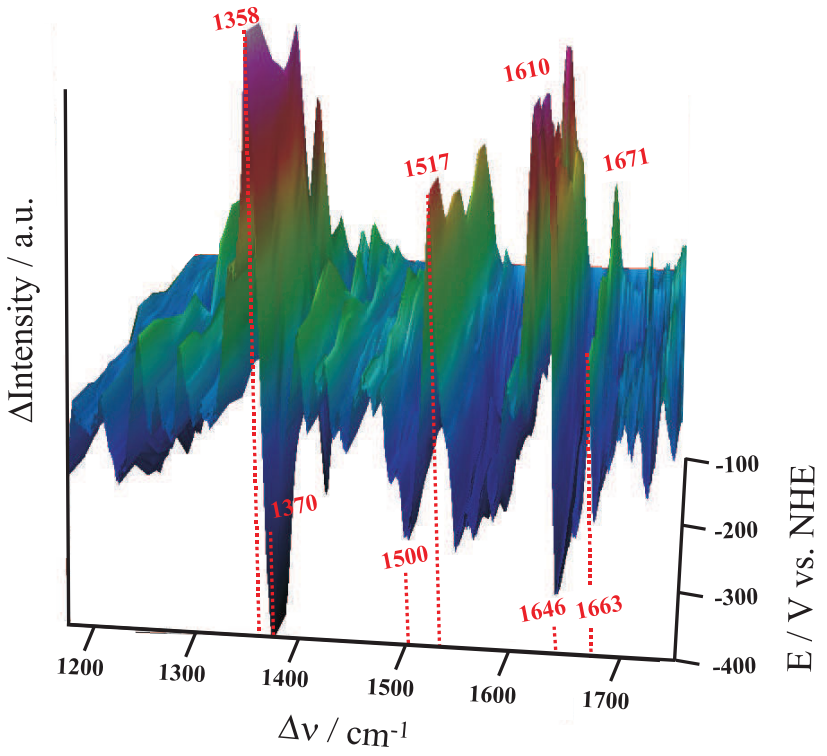

Figure 5.23: Difference spectra (with CcO in the oxidized form as the reference) showing the transition of the SERR spectra of CcO from the oxidized (-100 mV) to the reduced state (-400 mV). The 3D representation shows clearly three regions, 1350- 1370 cm^{-1}, 1500- 1520 cm^{-1} and 1600- 1620 cm^{-1}, with significant changes.

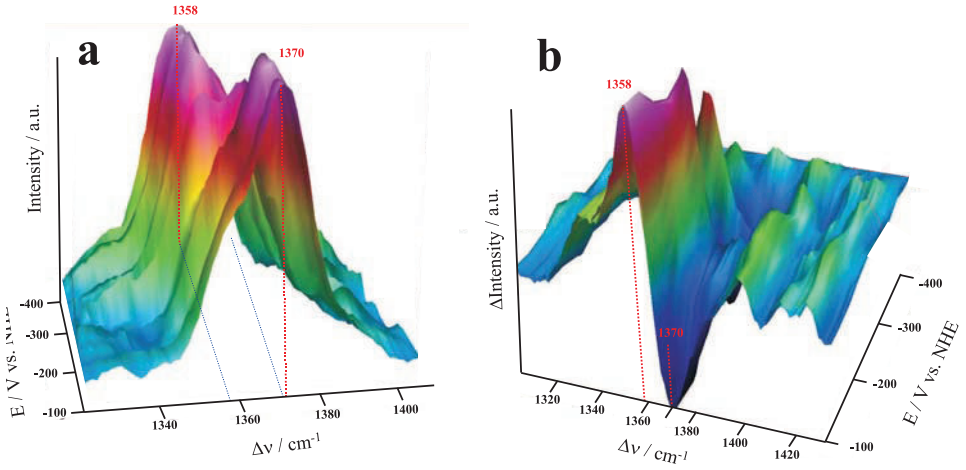

Figure 5.24: (a) Transition of the redox-sensitive ν_4 modes of both hemes [1358 cm^{-1} (reduced) and 1370 cm^{-1} (oxidized)]. (b) Difference spectra of the same spectral region.

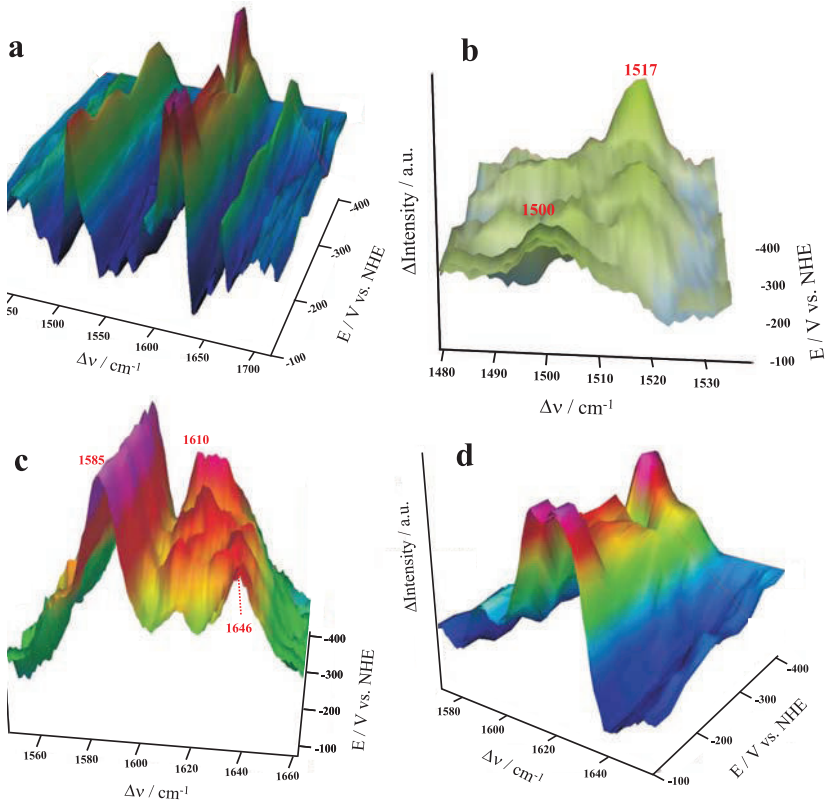

Figure 5.25: (a) Difference spectra of the high frequency region 1450 - 1700 cm^{-1}. (b) Expansion of the region between 1480 and 1530 , showing the transition of the ν_{11} (1517 cm^{-1}) mode of reduced heme *a* (not present in the oxidized form) and the ν_3 mode (1500 cm^{-1}) of the reduced heme a_3. (c) Absolute and (d) difference spectra of the heme and fromyl stretching region between 1580 and 1650 cm^{-1}.

5.4.2 Conclusion

The reversible electron transfer to the surface confined cytochrome c oxidase could be demonstrated in the case of orienting it with its natural electron entry site (Cu_A) towards the electrode. ET is assumed to occur along the tether, including the chelated metal center, of the functionalized surface and the highly conjugated His-tag. Electrochemical and SERRS experiments could conclusively show that a direct electron transfer occurs specifically to the Cu_A site, embedded in the periplasmatic extension of subunit II, and continues further to the following redox centers, present as the heme centers. The specific ET could be confirmed by the use of the inverted orientation, which remains uneffected upon the applied potential, but shows activity due to cytochrome c activation and cyanide inhibition (see section 5.1.6). The ET into the enzyme is accompanied by specific structural changes, which could be monitored by surface-enhanced resonance Raman spectroscopy.
The large shift of the redox potential could be explained in terms of an ET *via* the Ni-center of the chelating surface architecture as well as the high negative charge density of

the interfacial membrane region. This potential shift could be further explained by SPICE simulation, which will be discussed further below (5.9).

5.5 Functionality of Membrane Proteins Immobilized on Surfaces as a Function of Packing Density

A central issue of studying proteins confined to surfaces is the preservation of their activity. This is particularly critical for membrane proteins since they require a lipid environment but are still subject to denaturation in the immediate vicinity of surfaces. Among the benefits of the protein tethering strategy, in addition to defining the orientation of the protein with respect to the surface, is the possibility to systematically vary the surface concentration of the protein. One can, therefore, test the possibility that inter-protein interactions might affect the activity of the enzymes. The distance between single proteins could be an important parameter considering that electrostatic and other interaction forces between molecules could influence charge transfer and other kind of processes involved in protein function. The ptBLM system is well designed for this purpose. The surface concentration of proteins can be easily varied by varying the concentration of the chelator (NTA) molecules. Indications of the significance the surface concentration as a critical parameter were obtained in previous investigations of the CcO. In particular, electron transfer initiated by direct electrochemical electron injection into the protein, which can be used as a measure of the protein activity was shown to be affected by different packing densities. Two opposite orientations of the protein were investigated, either with the cytochrome c binding site directed towards the electrode surface or pointing away from it [315], simply by engineering the His-tag on the C-terminus of subunit II or subunit I, respectively. The aim of the present section is a more detailed investigation of the influence of the surface density of CcO on its activity.

A systematic study of the influence of the packing density of proteins on their activity is performed with cytochrome c oxidase (CcO) from *R. sphaeroides* incorporated into a protein-tethered bilayer lipid membrane. This membrane protein is used as an example for the investigation of the effect of the packing density on the activity of the protein.

5.5.1 Varying the Composition of the CcO Monolayer

Figure 5.26 displays a schematic drawing of the protein-tethered bilayer lipid membrane architecture attached to a mixed TSP/TP monolayer. To modify the concentration of CcO on the surface, the surface concentration of chelating NTA molecules was varied. This was done on the level of the first monolayer consisting of a thiol terminated active ester (DTSP) used for the functionalization with ANTA molecules. The structure of the molecules is given in Fig. 5.27. DTSP was mixed with DTP in different ratios. DTP is the starting material for the synthesis of DTSP and has a similar structure. However, DTP

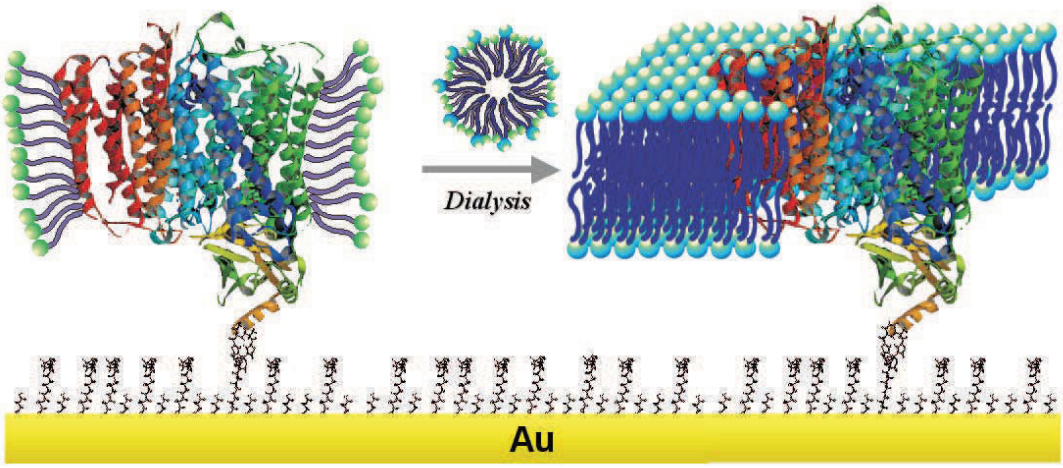

Figure 5.26: Schematics of the reconstitution of the protein (cytochrome c oxidase with the his-tag attached to SU II) bound via the Ni-complex to the NTA modified gold surface into a protein-tethered bilayer lipid membrane (ptBLM)

is terminated by a COOH group which is unable to couple to ANTA. The di-thio-groups split up into two Au-S bonds upon self assembly. DTSP becomes thio-(N)-succinimidyl propionate, (TSP), and DTP is converted to thio- propionic acid (TP). ANTA reacts with TSP resulting in an NTA terminated surface mixed with COOH terminated TP molecules. After chelation with Ni, the NTA group is ready to form a stable complex with the poly-histidine tail of the CcO in order to anchor the enzyme to the surface. The binding and reconstitution of the CcO are illustrated in (Fig. 5.26).

XPS measurements (Fig. 5.28) revealed that the composition of the mixed NTA-TP/TP monolayer on the surface corresponds to the mixing ratio of DTSP/DTP in solution (Fig. 5.28).

Coupling of ANTA to a monolayer with a mixing ratio of 0.6 of DTSP/DTP, was monitored by SEIRAS as a function of time (see Fig. 5.3, section 5.1), illustrates that the dilution with DTP leads to a smaller amount of bound ANTA molecules.
Fig. 5.29 shows the peak height of the amide I band during the coupling of ANTA to TSP as a function of time (open and closed symbols are for the diluted (TSP/TP) and undiluted (TSP alone) layers, respectively). In any case, ANTA coupling as monitored by SEIRAS, takes up to 24 hours. The time constant of the mixed layer is slightly smaller than that of the undiluted layer (time constants $\tau = 4.4$ vs. 5.7 hrs). Binding of CcO to the diluted NTA layer thus formed (mixing ratio 0.6 in this case) was also monitored by SEIRAS (Fig. 5.8). The bands at 1658 and 1549 cm^{-1} assigned previously [330] to the amide I, II modes of the protein backbone vibrations of the CcO increase with time. The

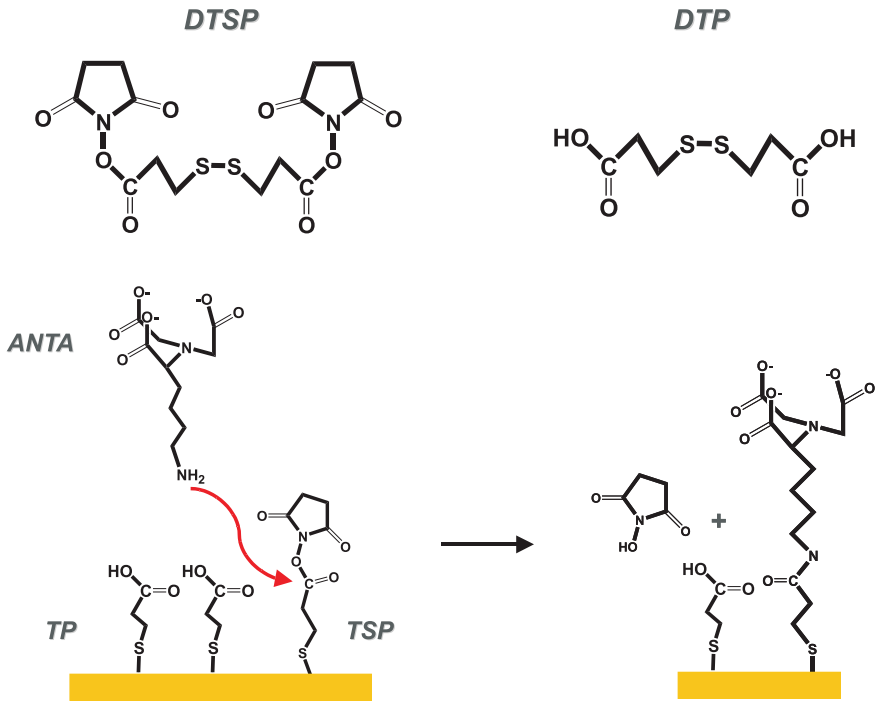

Figure 5.27: Upper part: the molecules used for the mixed monolayer: dithiobis (N-succinimidyl propionate) (DTSP), dithiobis (propionic acid) (DTP), the dithio-groups split up into two Au-S bonds upon self assembly, DTP becomes thio (N-succinimidyl propionate), (TSP), DTP becomes thio (propionic acid) (TP) lower part: coupling of N-(5-Amino-1-carboxypentyl) iminodiacetic acid (ANTA) to form the NTA modified (mixed) monolayer of TSP mixed with TP.

peak position of the amide I band at 1658 cm^{-1} is characteristic for the predominantly α-helical conformation of the CcO. Bands at 1436 and 1290 cm^{-1} also appear which have been assigned to conformational changes of the Ni-NTA. The peak areas of the amide I and II bands increase with time (τ = 3.6 min) (Fig. 5.8) with binding kinetics similar to the undiluted layer [331].

5.5.2 Electrochemical Properties of the ptBLM as a Function of the Mixing Ratio

NTA-TP/TP monolayers with different mixing ratios to which CcO was bound and reconstituted were characterized by a combination of SPR and EIS, as described in section 5.1. Changes of SPR spectra as a function of the mixing ratio depend strongly on experimental parameters such as the conditions used for the replacement of the initial buffer with the CcO-containing buffer used for the binding. The same applies to the conditions for the *in situ* reconstitution. Characteristic changes due to the formation of the layer-by-layer structure, as a function of the DTSP/DTP mixing ratio, were obtained by EIS spectra. Examples of a single set of spectra, before and after binding and reconstitution, are shown

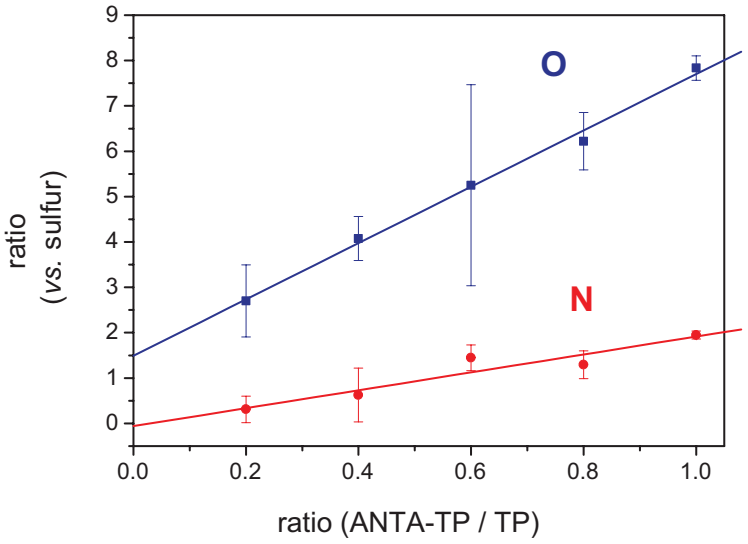

Figure 5.28: XPS analysis of the surface concentration of the NTA modified (mixed) monolayer of TSP mixed with TP. Mixing ratios in solution are plotted versus the ratio of the elements oxygen and nitrogen vs. sulphur. A linear function with respect to the mixing ration was observe, in good agreement with the theoretical values: ANTA-TP and TP containig 7 oxygens and 2 nitrogens and 2 oxygens and 0 nitrogens per one sulphur, respectively.

in Fig. 5.30. These data are fitted to the equivalent circuits given in Fig. 5.30c and 5.30d to yield the resistance and capacitance of the protein and the protein-lipid layer respectively, as a function of mixing ratio.

A statistical presentation of the collected data is displayed in Figs. 5.31 and 5.32. For a low mixing ratio (0.2), the capacitance of the protein layer is 68 $\pm 6 \mu F cm^{-2}$, and decreases with increasing mixing ratio, with the largest drop between 0.4 and 0.6, finally reaching 9 $\pm 1 \mu F cm^{-2}$ with a layer made from pure DTSP (Fig. 5.31). When the bilayer is reconstituted around the protein, the capacitance decreases for all mixing ratios except for the 100% DTSP, where an increase of the capacitance is only observed in some cases. (The error bars represent standard deviations of 7-10 sets of measurements). The resistance of the protein layers is already quite high at all mixing ratios (Fig. 5.32). This is an indication of a random orientation of the enzymes before reconstitution. They may be more or less tilted with respect to the surface, thereby coming in close contact with each other to form a sealing layer to the bathing solution. This conclusion is based on the observation that the resistance of the protein layer decreases while conducting a series of potential sweeps, which could be due to reorientation and separation of the highly charged proteins. After reconstitution, the resistance increases in all cases, with the most significant change for the 0.6 mixing ratio. To better understand these changes, it has to be considered that

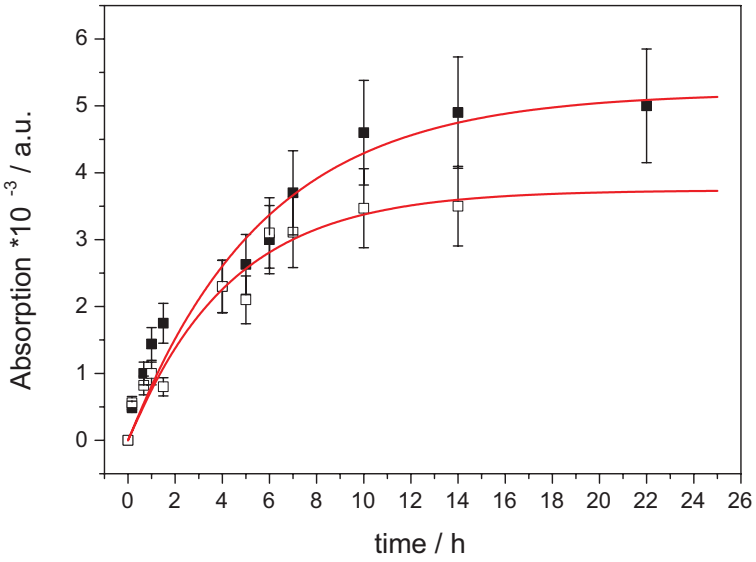

Figure 5.29: Peak height of the amide I band as a function of time during coupling of ANTA to the mixed TSP/TP monolayer (open and closed symbols are for the diluted (mixing ratio = 0.6) and undiluted layer (mixing ratio = 1), respectively).

the capacitance of a dielectric layer is determined by thickness and dielectric constant of the material. The capacitance of a pure protein monolayer is estimated to be 6 $\mu F cm^{-2}$, taking into account the dielectric constant of protein molecules (typically $\epsilon = 30$) and the thickness of 5 nm. Higher values of 13.1 $\pm$ 3.9 to 68 $\mu F cm^{-2}$ as observed for different mixing ratios are likely due to the large amount of water molecules separating the protein molecules. The dielectric constant of the lipid is much smaller, $\epsilon = 2.2$, than that of either water ($\epsilon = 80$) or protein (typically $\epsilon = 30$). This explains the decreases of the capacitance upon reconstitution when water and detergent molecules are replaced by lipid bilayer patches. The lowest values reached are 7.3 $\pm$ 0.5 $\mu F cm^{-2}$ for the 60% mixing ratio. The lowest values obtained after reconstitution (6.8 $\mu F cm^{-2}$) are close to the calculated capacitance of a pure protein layer, indicating a high surface coverage with enzymes. This is in agreement with the estimate of more than 90% coverage of CcO molecules as deduced from the charge transferred by CV measurements due to the direct electron transfer to the CcO.

5.5.3 AFM Characterization of the CcO Monolayers

Surface layers were exclusively prepared on template stripped gold (TSG) surfaces, due to their low roughness over large surface areas (RMS $<$ 0.2 nm). The roughness hardly changes when mixed NTA layers were prepared on this surface (Fig. 5.33a).

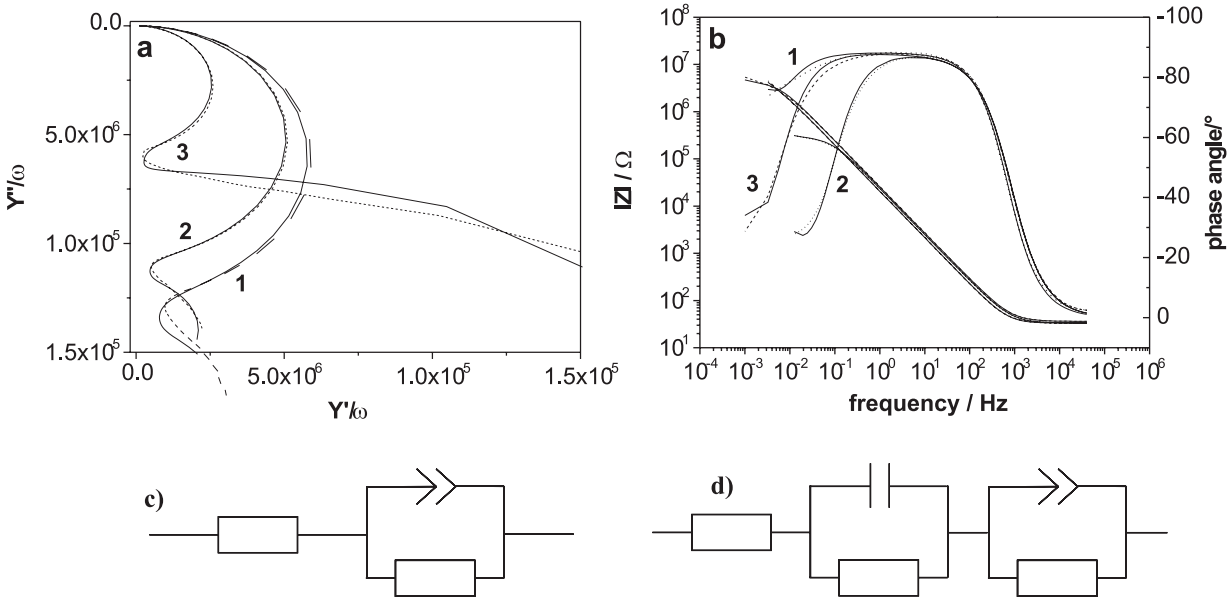

Figure 5.30: Impedance spectra, frequency normalized admittance (a) and Bode plots (b), of the Ni-ANTA modified surface before (1) after binding of CcO before (2) and after reconstitution of the protein (3). Dotted lines represent experimental data, solid lines show the curves fitted to the equivalent circuit (d) except for the Ni-ANTA modified surface which was fitted to the circuit (c).

AFM images of CcO monolayers at mixing ratios varying from 0.001, 0.1, 0.6 to 1 were then recorded (Fig. 5.33b-e). Clear differences were obtained between the pure NTA layer and the protein layers, even for the very low mixing ratios 0.001 and 0.1. For the 0.001 ratio, structures with lateral dimensions in the range of 50-80 nm and a height of up to 15 nm are seen. For the 0.1 ratio such structures are even larger, 50-180 nm in the lateral dimension and up to 25 nm high. This is not compatible with dimensions of single enzymes obtained from the X-ray crystallography (4.5 nm × 7.0 nm for the in-plane dimension and 9 nm for the height of CcO from *R. sphaeroides* [330]). These structures indicate the formation of aggregates, possibly due either to non-specific protein binding (not NTA-dependent) or to agglomeration of NTA-tethered proteins due to the flexibility of the immobilized enzymes without the stabilizing environment of a membrane. In the case of the 0.6 mixing ratio, the structures are smaller with 10-20 nm laterally and $\sim$ 10 nm in height. This is consistent with a monolayer of proteins with the dimensions according to X-ray crystallography. In this case, the arrangement of the enzymes could be stabilized by the high surface coverage. For the NTA layer formed on a 100% TSP layer, the structures are still smaller, mostly 10 nm in the lateral dimension and $<$ 10 nm in height. This is consistent with the assumption of a very tightly packed monolayer of CcO molecules.

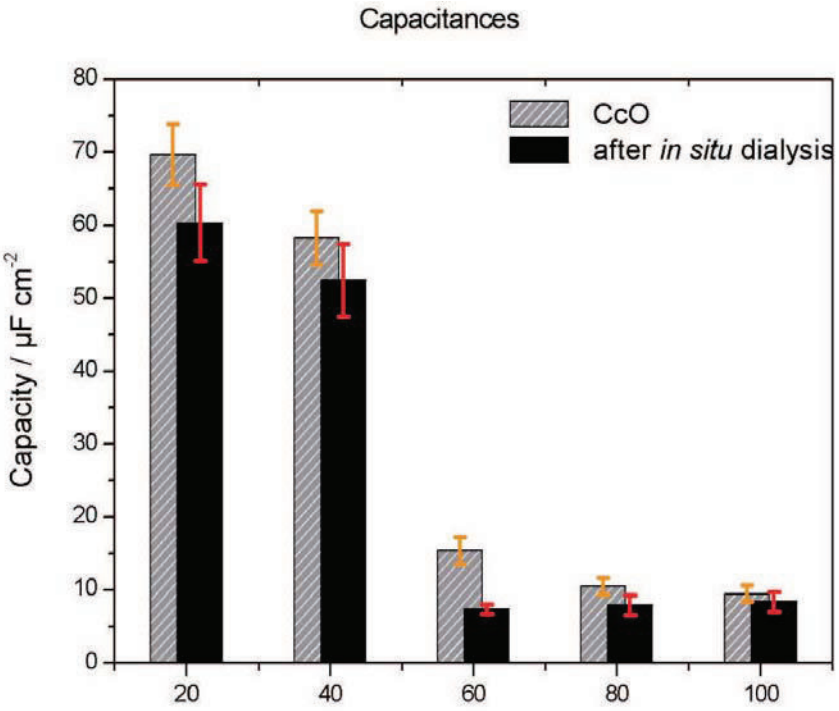

Figure 5.31: Capacitances of the membrane obtained from EIS, before (shaded bars) and after (full bars) *in situ* dialysis as a function of the mixing ratio DTSP vs. DTP. The capacitance generally decreases during dialysis. The biggest change is at a ratio of 60 %, at the same time reaching reasonably low values.

5.5.4 Direct Electron Transfer (ET) probed by CV

It was shown previously that the activity of a redox-active membrane protein can be probed by direct heterogeneous electron injection from a gold electrode into the redox sites of the protein [270]. Direct electron transfer (ET) can be effectively probed by cyclic voltammetry (CV) in combination with spectroscopic methods such as surface-enhanced resonance Raman spectroscopy (SERRS). This combination of measurements conclusively demonstrated that electron injection into the primary redox site of CcO gives rise to consecutive ET through all four redox centers within the protein. The direct ET was also shown, under aerobic conditions, to initiate the catalytic turnover of the enzyme as well as proton translocation across the membrane. The peak shaped signals obtained by CV reflect the kinetics of the ET. For example, the theoretical peak width of a reversible one electron transfer to an absorbed species has a value of 90 mV [37]. The area of the peak reflects the overall charge transferred during the ET process. Assuming 4 electrons transferred per molecule under anaerobic conditions, the number of active molecules per area can be obtained. CcO incorporated in ptBLMs based on 100% DTSP monolayers give rise to direct ET. However, in many cases with lower surface coverage one observes broad and shallow peaks or no peaks at all in the CV. This could indicate a large distribution of ET rate coefficients or alternatively, a strong interaction between the densely packed enzymes,

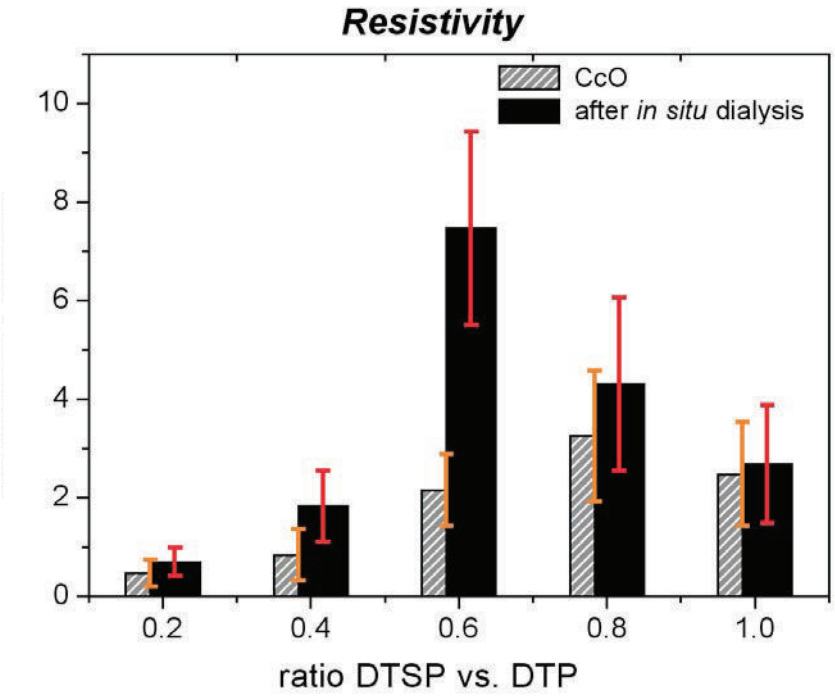

Figure 5.32: Resistivities of the membrane obtained from EIS, before (shaded bars) and after (full bars) *in situ* dialysis as a function of the mixing ratio DTSP vs. DTP. Resistivities generally increase during dialysis. The optimum is at 0.6.

inhibiting electron and other charge transfer pathways.

The dependence of the direct ET, as a measure of enzyme activity, on the packing density, determined by the mixing ratio, is illustrated in Fig. 5.34. The cathodic peaks (baseline corrected and scan rate normalized) are displayed as a function of different mixing ratios. An example of an untreated CV is given in Inset (b) of Fig. 5.34. For the 0.2 and 1.0 DTSP layers, the peaks are hardly visible, becoming narrower and higher for the 0.4 and 0.8 layers, and reaching an optimum at 0.6. Integration of the peak current yields the charge and, hence, the surface coverage of the redox active CcO molecules. The result is plotted vs. the mixing ratio of DTSP/DTP in Inset (c) of Fig. 15. An optimum of activity was obtained at a mixing ratio of 0.6. This optimum of the mixing ratio therefore represents the standard value for all further mechanistic and kinetic investigations of the immobilized enzymes.

5.5.5 Conclusion

It could be shown, that relatively small dilution factor of the chelator molecules have significant effects on the formation of the biomimetic architecture and the activity of the proteins. Large dilution factors (0.001 and 0.1) seem to result in non-specific adsorption

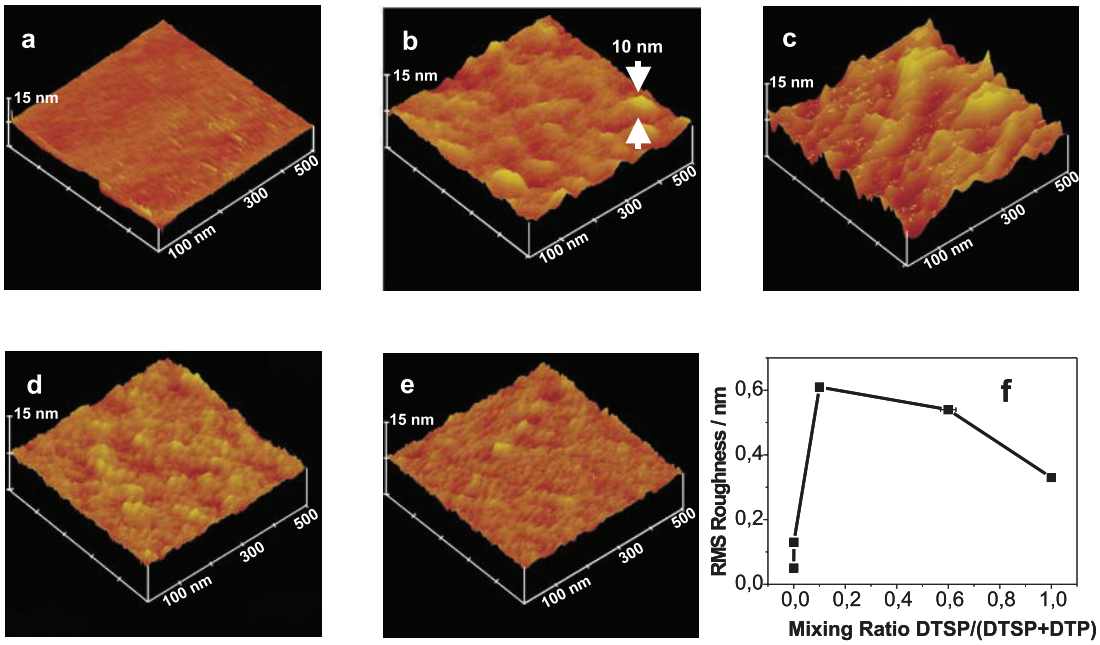

Figure 5.33: AFM images (recorded in tapping mode) of the pure NTA layer (a) and of CcO bound to mixed NTA layers, mixing ratio DTSP/DTP 0.001 (b), 0.1 (c), 0.6 (d) and 1.0 (e). Surface roughness (RMS) as a function of the mixing ratio DTSP vs. DTP (f). The roughness reaches a maximum at 0.1 and decreases again for higher values because of a more densily packed protein monolayer.

of the protein to aggregates, as seen in the AFM. This is consistent with the observation that at these dilution factors, an electrically sealed bilayer is not formed (Fig. 5.32b). A sufficient amount of chelator molecules (NTA-TSP) must be present to avoid unspecific adsorption and to provide a strict orientation of the enzymes. Even the 0.2 dilution layer does not form a closed layer of protein molecules. This is deduced from the capacitance values obtained by EIS, which indicate a high amount of water after reconstitution even at mixing ratios of up to 0.4. The mixing ratio of 0.6 is the clear optimum for the formation of a lipid bilayer, as far as the electrical properties of the ptBLM is concerned. According to AFM, with 100% DTPS to maximize enzyme coverage, the enzymes are very tightly packed, such that the interaction between single molecules must be very strong. Lipid molecules can hardly be incorporated in between the protein molecules, which results in more intense inter-molecular forces between enzymes. In the moderately diluted cases, e.g. at a mixing ratio of 0.6, the packing density of the protein is less than when using 100% DTSP is used. Small gaps still appear to be present, as deduced by the impedance and capacitance data. A higher dilution would be desirable, however, the lipid layer does not appear to uniformly span the gaps between proteins so as to form a well sealed ptBLM. The coverage with protein molecules at the 0.6 mixing ratio is obviously an optimum for the surface coverage, neither of which permits the formation of an electrically sealed protein/lipid bilayer. The undiluted layer seems to accommodate a few lipids only, as deduced

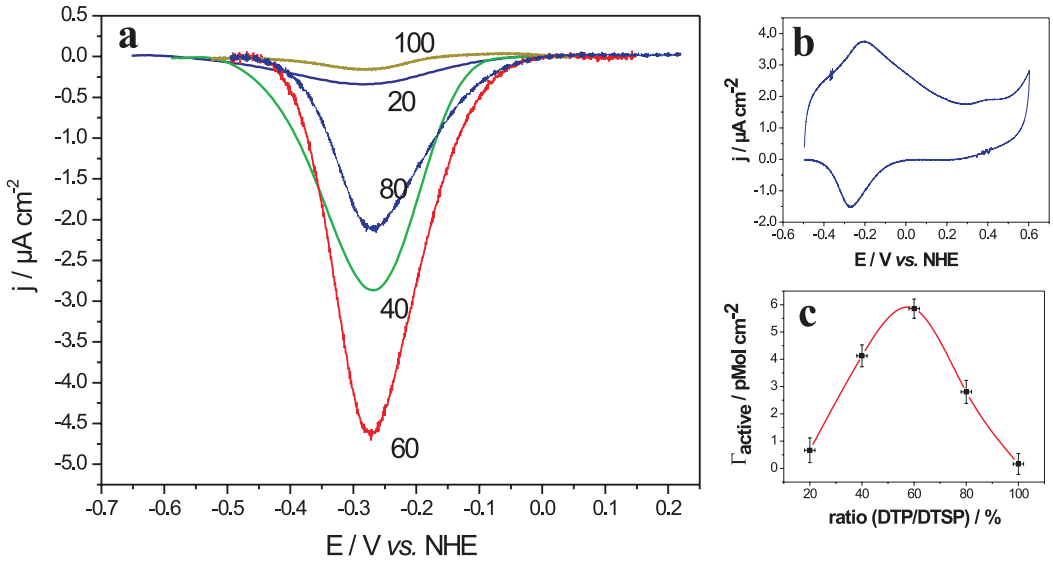

Figure 5.34: Baseline corrected and scan rate normalized reductive peaks from cyclic voltammograms of the direct electron transfer to CcO at different mixing ratios (a) (an example of the full CV is shown in the inset (b), recorded under strictly anaerobic conditions), the surface coverage by active CcO molecules calculated from the integrated area of the current peaks is plotted vs. the mixing ratio (c).

from the small decrease in the capacitance as compared to the diluted layers. The development of the resistance is in accordance with this interpretation. The undiluted layer, furthermore, does not show full enzyme activity even though a closed layer seems to be formed according to the AFM image. The preservation of CcO activity seems to require the insertion of lipids to form a bilayer.

Protein flexibility within the reconstituted layer is also required for the enzyme activity. When the surface density of CcO is too high, electrostatic or other interactions between the single proteins within a layer result in inhibition of enzyme function. Charge transfer processes inside the protein could well be affected by these interactions, resulting in deleterious effects on the activity of the enzymes.

5.6 Electrochemical Investigation into the Kinetics and Mechanism of Cytochrome c Oxidase

The optimal conditions thus obtained for full enzymatic activity are now utilized to conduct kinetic studies of the direct electron transfer as well as mechanistic studies of the proton

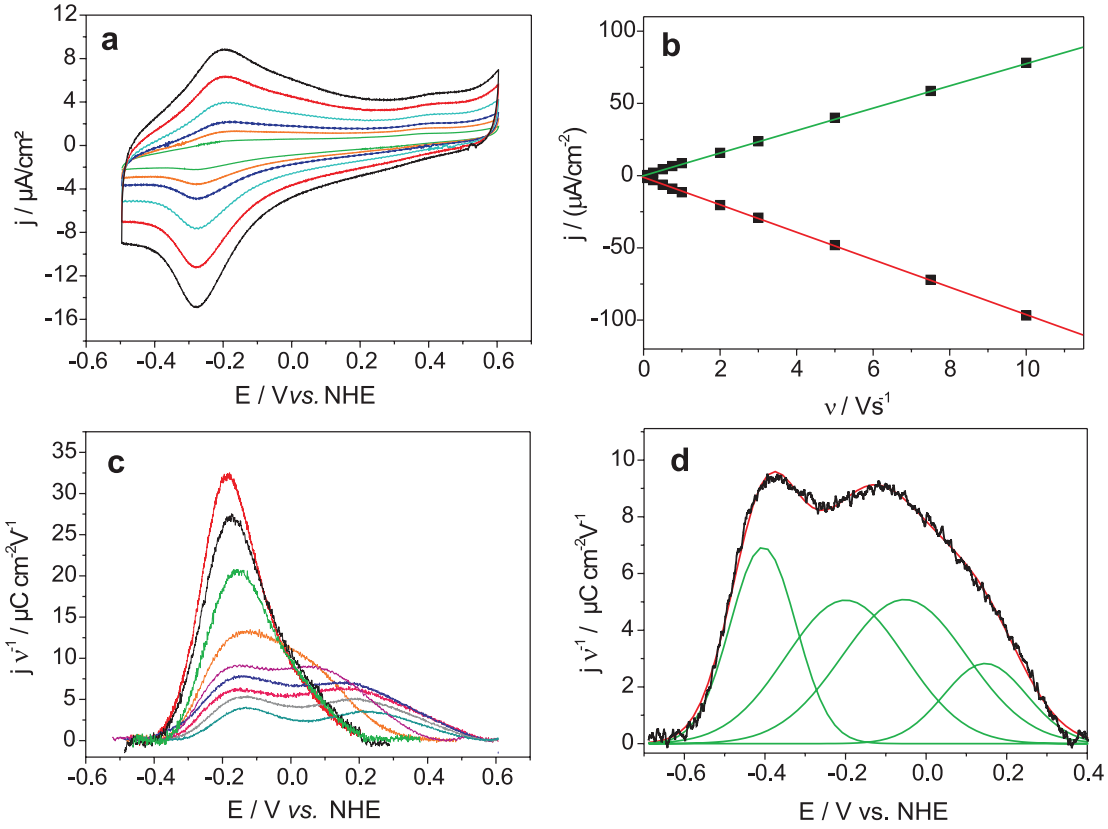

Figure 5.35: Cyclic voltammogramms of CcO with the his-tag attached to SU II at strictly anaerobic conditions. (a). Scan rates (ν) between 0.1 and 1 Vs^{-1}, 0.01 Vs^{-1} (green), 0.02 Vs^{-1} (orange), 0.03 Vs^{-1} (dark blue), 0.05 Vs^{-1} (light blue), 0.075 Vs^{-1} (red), and 0.1 Vs^{-1} (black). Inset: Baseline-corrected current density plotted as a function of scan rate, reductive branch (red), oxidative branch (green) (b) Oxidative branches (baseline-corrected) of CVs at scan rates between 1 and 600 Vs^{-1} (current densities normalized by the scan rate, ν/Vs^{-1}) 1 Vs^{-1} (red), 3 Vs^{-1} (black), 7.5 Vs^{-1} (green), 20 Vs^{-1} (orange), 40 Vs^{-1} (pink), 300 Vs^{-1} (blue), 400 Vs^{-1} (violet), 500 Vs^{-1} (grey), 600 Vs^{-1} (light blue), inset: example of a deconvolution into four Gaussian components

transfer on cytochrome c oxidase. A deeper understanding on the kinetics of the ET to the Cu_A and the heme centers, which can be used as a direct and effective triggering of the redox state, is a prerequisite to conduct vibrational spectroscopy in the time resolved regime. These epxeriments will be shown in the next section.

5.6.1 Kinetics of Electron Transfer

While slow scan rate cyclic voltammetry is sufficient to obtain basic ET mechanistic information, scan rates $\gg 1\ Vs^{-1}$ must be utilized to extract kinetic information (Fig. 5.35b). The baseline-corrected current in the CV of a surface-confined redox couple can be represented by a Gaussian curve whose peak position and width are determined by the standard

potential of the couple, the rate constant of ET (k_s) and the scan rate [37]. At low scan rates the peak position is approximately constant and close to the standard potential. As the scan rate is increased to several Vs^{-1}, kinetic constraints cause the peaks to separate, with reductive and oxidative peaks shifting to more negative and more positive potentials, respectively.

The four redox center CcO enzyme exhibits a more complicated behavior. At anaerobic conditions the redox currents display single slightly asymmetric peaks to a scan rate of $\sim 1\ Vs^{-1}$ (cf. Fig. 5.35a) indicating the contributions from multiple redox centers. At scan rates above $1\ Vs^{-1}$ the baseline-corrected peaks become more asymmetric, a second maximum with clear shoulders gradually appears as the scan rate increases above $20\ Vs^{-1}$ (Fig. 5.35b). These curves require four Gaussian components to adequately describe the system. The four Gaussian kernels correspond to the four redox centers Cu_A, heme a, heme a_3 and Cu_B in the enzyme (see the inset of Fig. 5.35b). Measurements were done in a phosphate buffer solution containing in addition the oxygen trap for anaerobic conditions (see Fig. 5.36).

The oxygen trap works as an coupled catalytic reduction of oxygen and oxidation of glucose:

$$Glucose + O_2 + H_2O \xrightarrow{glucoseoxidase} Gluconate + H_2O_2 \tag{5.3}$$

$$2H_2O_2 \xrightarrow{catalase} 2H_2O + O_2 \tag{5.4}$$

In this case solutions were additionally purged with Ar for one or two hours prior to the measurements to assure a completely deoxygenated solution.
CVs were treated first by a baseline correction procedure comprising a polynomial function, to subtract the capacitive component of the current. An example was shown in Fig. 5.20. Baseline correction was then followed by a deconvolution into Gaussian components by fitting to four Gaussian curves, as shown in the inset of Fig. 5.35b.

Baseline corrected reduction and oxidation peaks of the CV recorded under anaerobic conditions were evaluated in terms of the surface coverage of CcO molecules per area, $\Gamma = Q/(nF)$, where Q is the charge density given by the peak area, n is the number of electrons transferred per mole of protein and F is the Faraday constant. The evaluation yields 8.4 and 5.9 $pMolcm^{-2}$, for the reduction and oxidation peak, respectively. The value of 5.9 $pMolcm^{-2}$ is in reasonable agreement with 6 $pMolcm^{-2}$ calculated for a densely packed monolayer from the crystal structure of CcO assuming an ellipsoidal disk of 4.5 nm $\times$ 7.0 nm for the in-plane dimension of CcO from *R. sphaeroides* [332]. This result indicates a more than 90% coverage of CcO in agreement with EIS data.

Information about the kinetics of ET can be obtained when plotting the peak potentials vs. scan rate on a logarithmic scale, which yields the so-called 'trumpet' plot (Fig. 5.37) [34]. This plot was analyzed with the simplifying assumption of an individual one-step ET to each redox center, and by means of the algorithm described by Jeuken et al. [154].

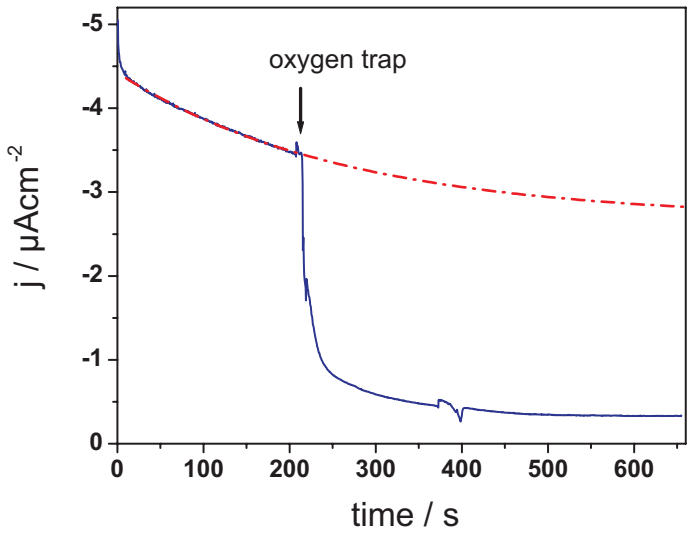

Figure 5.36: Effect of oxygen trap consisting of glucose as well as the enzymes glucose oxidase and catalase. The current trace shows the reduction of oxygen to water under under a bias potential of -550 mV vs. NHE on a DTSP-ANTA modified gold surface. It takes more than the 10 minutes until a constant current is achieved. However a complete oxygen-free solution can not be achieved which is obvious du to continuous redox process. After adding the oxygen trap, the current decreses inbetween seconds to zero due to the catalytic oxygen consumption

The values for the rate constant k_s and the apparent standard potential E^0_{app} shown in Table 5.3 were obtained. Since ET between redox centers in CcO occurs sequentially, the values of k_s for redox centers 2, 3 and 4 are approximations of lumped rate constants [333] for the overall ET from the electrode to heme a, heme a_3, and Cu_B through the ET chain and hence cannot be compared directly with rate constants for ET between these centers. Nevertheless, they indicate a fast ET between the centers most likely comparable to that of CcO *in situ*. However, the value for redox center 1 is related to the true electrochemical ET from the electrode to Cu_A. Previous attempts at coupling proteins to surfaces have yielded k_s between 100 s^{-1} to 1600 s^{-1} [35, 36, 334, 335]. The $Ni^{1+/2+}$ surface tethering architecture yields $k_s > 4000$ s^{-1}, which is comparable to the rates reported for intramolecular ET between cytochrome c to CuA in *R. sphaeroides* [336]. Hence, it can be excluded that ET to the subsequent redox centers is restricted or rate-limited by the electrochemical ET to Cu_A. This assertion suggests that the measurements in the ptBLM yield results of biological relevance.

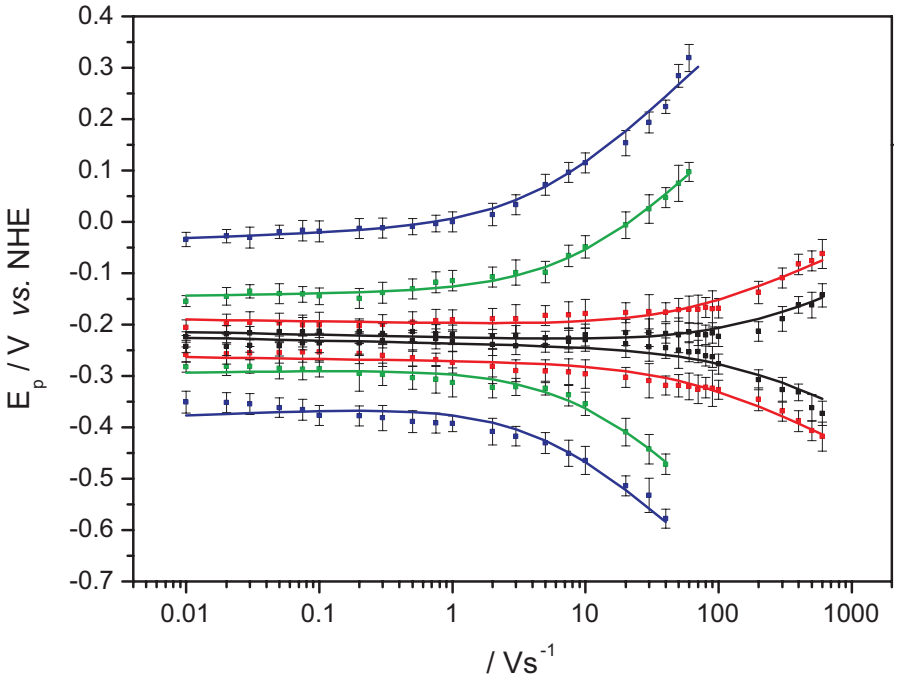

Figure 5.37: Figure 4. Peak potentials as a function of scan rate (trumpet plots) of the four redox centers. Peak potential are obtained by deconvolution of CVs into Gaussian components of oxidation and reduction branches of CcO with the his-tag attached to SU II under anaerobic conditions (cf. Fig. 2b), redox center 1 ($\equiv Cu_A$) (black), 2 (red), 3 (green), 4 (blue). The error bars represent ranges resulting from the deconvolution procedure.

Redox center	E_{app}/mV	k_s/s^{-1}
1 (black $\equiv Cu_A$)	-231 ± 8	4130 ± 390
2 (red)	-234 ± 7	1650 ± 170
3 (green)	-211 ± 6	68 ± 8
4 (blue)	-183 ± 7	11 ± 2

Table 5.3: Apparent standard potentials E_{app} and rate constants k_s obtained from CV of CcO under anaerobic conditions (Fig. 5.37). The errors represent ranges resulting from experimental errors, the deconvolution procedure and the fit routine applied to the trumpet plot for four data sets of the same enzyme preparation.

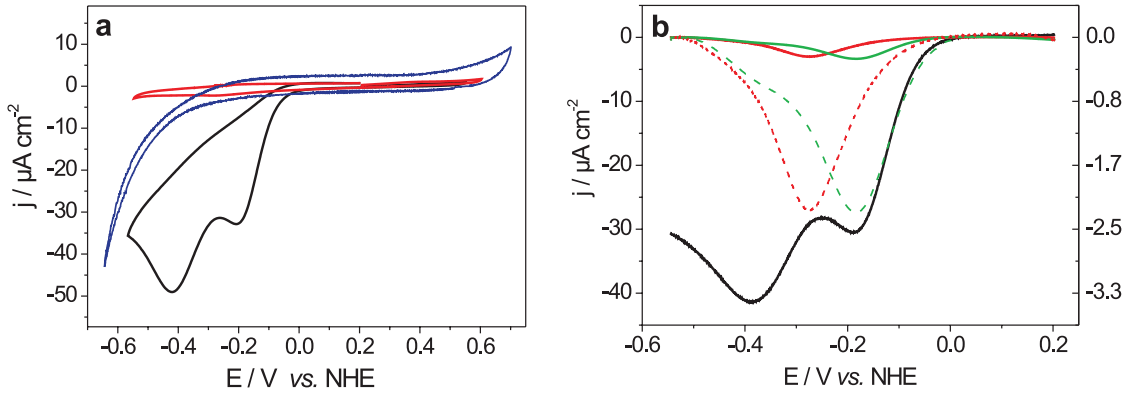

Figure 5.38: Voltammogramms of CcO with the his-tag attached to SU II under aerobic and anaerobic conditions. (a) Cyclic voltammograms at a scan rate of 0.01 V^{s-1} anaerobic (red), aerobic (black) and CcO with the his-tag on SU I (blue). (b) Differential pulse voltammograms, anaerobic (red), aerobic (black) and aerobic in the presence of 40 M cyanide (green). The dashed curves are enlarged for clarity, corresponding to the y-axis on the right hand side.

5.6.2 Proton Transport coupled to Electron Transfer

Under *aerobic conditions* the CV on CcO with the His-tag on SU II shows two peaks in the reductive sweep (Fig. 5.38a, black curve). The first peak at -202 ± 5mV, due to CcO reduction, shows a significant increase in the current density as compared to that under anaerobic conditions due to the catalytic turnover of the redox enzyme. Electrons transferred from the electrode to the redox centers of CcO are irreversibly transferred to oxygen, which leads to continuous electron transport [35, 36, 334]. The current density of 35 $\mu A cm^{-2}$ is comparable to that obtained with highly active soluble redox enzymes adsorbed to an electrode [35, 36], but is considerably larger than that measured previously for membrane proteins in a tBLM with mediators ($\leq 0.6 \mu A cm^{-2}$) [337]. The second peak at -422 ± 6 mV (Fig. 5.38a black curve) can be attributed to the reduction of protons in the submembrane space to form H_2 at the electrode. In the orientation with the His-tag attached to SU II, protons are pumped by the enzyme from the bulk solution into the interstitial space between the electrode and the ptBLM, and due to its small volume, this interstitial space is thereby highly acidified.

The range of pH values accessible by this measurement was tested by a control experiment of the pure DTSP/NTA-modified surface in phosphate buffer solution titrated with hydrochloric acid to different pH values. The result of the control experiment is shown in Fig. 5.39. A cathodic peak is formed at around -430 mV (vs. NHE), starting at a pH value of about pH 3 becoming more and more prominent at decreasing pH values. Using the plot of the current density as a function of pH (see inset of Fig. 5.39) as a calibration curve,

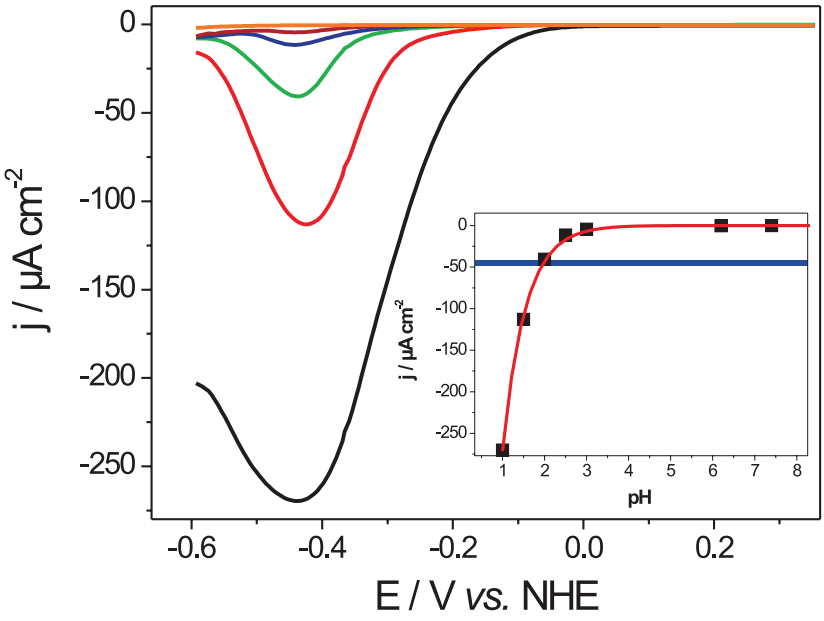

Figure 5.39: Differential pulse voltammogramms of a ANTA modified surface as a function of different pH values: pH 1 (black), pH 1.5 (red), pH 2 (green), pH 2.5 (blue), pH 3 (brown) and pH 6.2 (orange). The inset shows the current density as a function of pH, and blue horizontal line indicates the value of the second reduction peak in Fig. 5 of the main article.

the pH value indicated by the second peak in Fig. 5.38 can be estimated to be around pH 2.

The absence of this H^+ reduction peak in the inverted orientation, His-tag on SU I, (Fig. 5.38a, blue curve) provides further confirmation that the electron transfer chain drives the transmembrane proton transport. Moreover, a similar proton reduction peak has already been observed for H^+/ATP-synthase reconstituted into a tBLM [338]. Differential pulse voltammetry (DPV) was used to examine the reductive peaks without the capacitive background artifacts inherent in cyclic voltammetry. Differential pulse voltammograms of CcO with the His-tag on SU II show again the amplified current density of the reductive peak due to the catalytic turnover and the subsequent proton peak at aerobic conditions. At anaerobic conditions no proton peak can be recorded even with the much higher sensitivity provided by DPV (Fig. 5.38b, red curve). It can be estimated that a proton peak of at least 0.8 μAcm^{-2} should occur if only one proton per four electrons were transported which would be easily detectable with DPV. It becomes evident that no protons are transported across the membrane as the redox centers are reduced. Moreover, if cyanide is added at aerobic conditions the proton peak almost disappears and the reductive peak is decreased to the level typical for anaerobic conditions (Fig. 5.38b, green curve). Cyanide is a specific

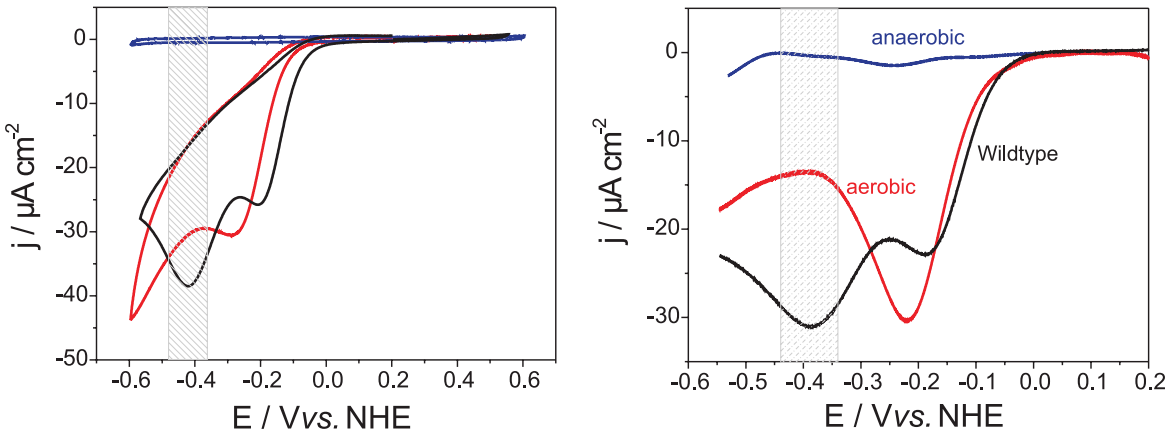

Figure 5.40: (a) Cyclic voltammetry and (b) differential pulse voltammetry of a N139D Mutant of cytochrome c oxidase [339]. Experiments under anaerobic (red) an aerobic (blue) conditions show a catalytic current of the ET process, whereas the H^+ reduction peak is completely suppressed. The region of H^+ reduction is marked by a grey column. A comparison with the wild type CcO (black) shows an affection of the redox potential due to the site mutation.

inhibitor of CcO and effectively blocks electron transport by occupying the binding site for oxygen. This sensitivity to cyanide is another indication that CcO in the ptBLM is functionally intact.

Further promising results regarding the proton translocation mechanism were obtained with experiments on mutants, such as N139D[14] (Fig. 5.40) [339]. Site mutation in the *D*-pathway, which is expected to be responsible for the proton translocation, showed a complete suppression of the H^+ reduction peak in CV and DPV experiments (Fig. 5.40a and b). The electron transfer, however, remains unaffected and still shows a catalytic current under the aerobic conditions (red curves), as compared to anaerobic conditions (blue curves). A comparison with the wild type (black curve) shows, that the mutation effects the redox potential of the redox centers. This conclusively shows the uncoupling of the electron and the proton transfer mechanism by a single site mutation, while leaving the ET activity unaffected.

5.6.3 Conclusion

We can show that the ptBLM is competent to overcome some of the most serious drawbacks of previous biomimetic membrane systems for CcO and other membrane proteins, such as the lack of orientational control and direct addressability. Bioelectronic coupling is shown to be specifically dependent on the orientation of the CcO immobilized in the tBLM. Direct ET between electrode and enzyme only occurs when the CcO is immobilized with

[14]The notation N139D indicates an exchange of the amino acid asparagine (asp)-132 by an Aspartic acid (asn) in the *D*-proton pathway of CcO

the electron entry side directed towards the electrode. This is clearly demonstrated by electrochemical and potential controlled SERRS experiments. The rate constant of the direct ET is shown to be exceptionally high as compared to those of proteins previously investigated. Three factors are held responsible for the fast direct ET:

- tethering or wiring *via* the His-tag provides a very efficient pathway for electrons [340]
- the CcO molecules are strictly oriented with the electron entry side directed towards the electrode, and
- the protein orientation is supported and stabilized by the lipid bilayer

These contributions taken together increase the rate constant of direct ET almost to the same order of magnitude as ET from cytochrome c, the natural electron donor of CcO. Thus electronic wiring opens the possibility to analyze the kinetics of consecutive ET steps up to the catalytic center [35], undisturbed by artificial compounds such as soluble mediators or uncouplers often employed in classical assays. Complementary information on redox and ligation, spin and coordination state of the heme a/a_3 structure is obtained from SERR spectra as a function of potential, demonstrating the power of the combination of electrochemistry with vibrational spectroscopy.

Proton transfer can be distinguished from ET by the appearance of an additional reduction peak in the CV. Proton transfer across the membrane toward the electrode surface appears to take place but only in the presence of oxygen. There is an ongoing debate about proton pumping [310, 328, 311, 94, 341] expected to occur in the reductive half of the enzyme cycle [323]. It follows from our findings, however, that protons are not released during reduction, i.e. proton pumping does not occur without oxygen present, whereas the uptake of protons in the 'reductive half', e.g. the so-called charge compensating proton [342] is compatible with our experiments.

The approach presented here using the widely applicable His-tag technology for immobilization followed by the reconstitution into a lipid bilayer makes the ptBLM a generic approach applicable to a large number of membrane proteins, redox proteins in particular. Other membrane proteins could also benefit from this strategy, considering that electric fields are often a controlling parameter, for example in the case of ion transport through channel proteins. Considering the pharmacological relevance of this class of proteins, the ptBLM could be useful for screening or biosensing purposes. This option is particularly attractive with respect to the combined application of electrochemical and a large number of surface analytical, e.g. spectroscopic methods. All of these possibilities taken together make the ptBLM a promising novel platform for the investigation of membrane proteins.

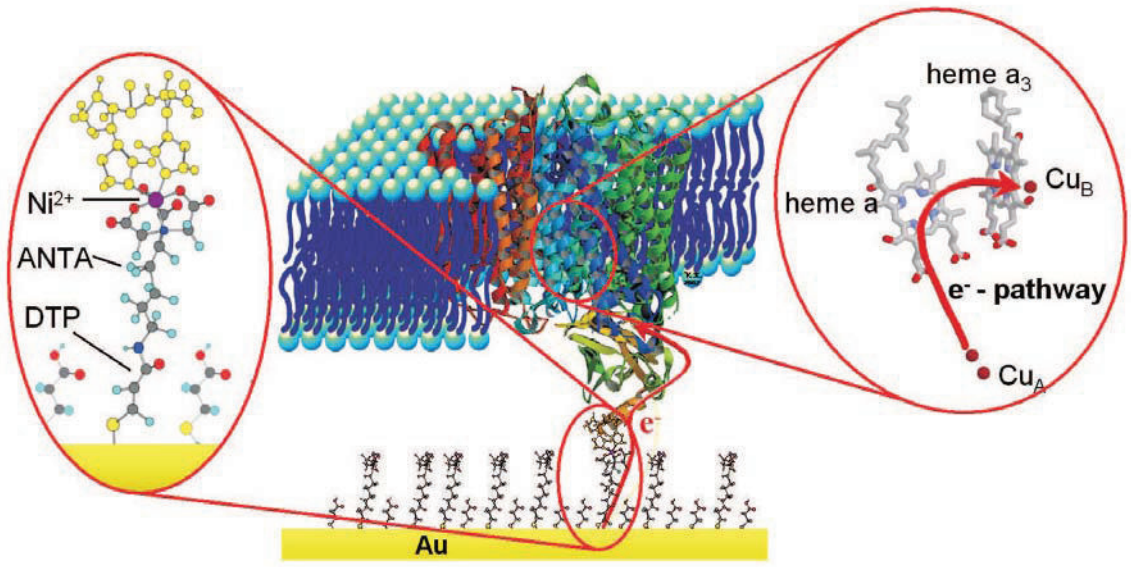

Figure 5.41: CcO immobilized with the cytochrome c binding site directed towards the gold electrode.This permits a direct ET to the active sites, which can be used as a trigger to perform time resolved IR measurements. Left panel: the anchor group. Right panel: the four redox centers of the protein

5.7 Time Resolved Surface-Enhanced Infrared Reflection-Absorption Investigations

Utilizing direct electron transfer as an trigger time resolved surface-enhanced infrared reflection absorption spectroscopy (SEIRAS) measurements were performed. The metal sites themselves are not accessible by IR spectroscopy, however, vibrational modes of amino acids in the environment of the Cu and heme centers can be excited, which were assigned previously to different redox states [343]. ET reactions inside the protein can thus be followed as a function of time.

5.7.1 Principle of Time resolved SEIRAS triggered by electrochemical potentials

Potentials are applied in a square wave function to the ptBLM on the gold film periodically changing the redox state from the fully oxidized to the fully reduced state (compare 5.2). The sudden potential changes at the end of the pulse are used to trigger the FT-IR spectrometer to record a succession of spectra that indicate the kinetics of the redox transition in an exponential function (fig. 5.42). These functions are analyzed in terms of a single exponential if the reaction can be considered monomolecular. More complicated reactions require multi-exponentials to fit the data. The frequency of the electrochemical excitation

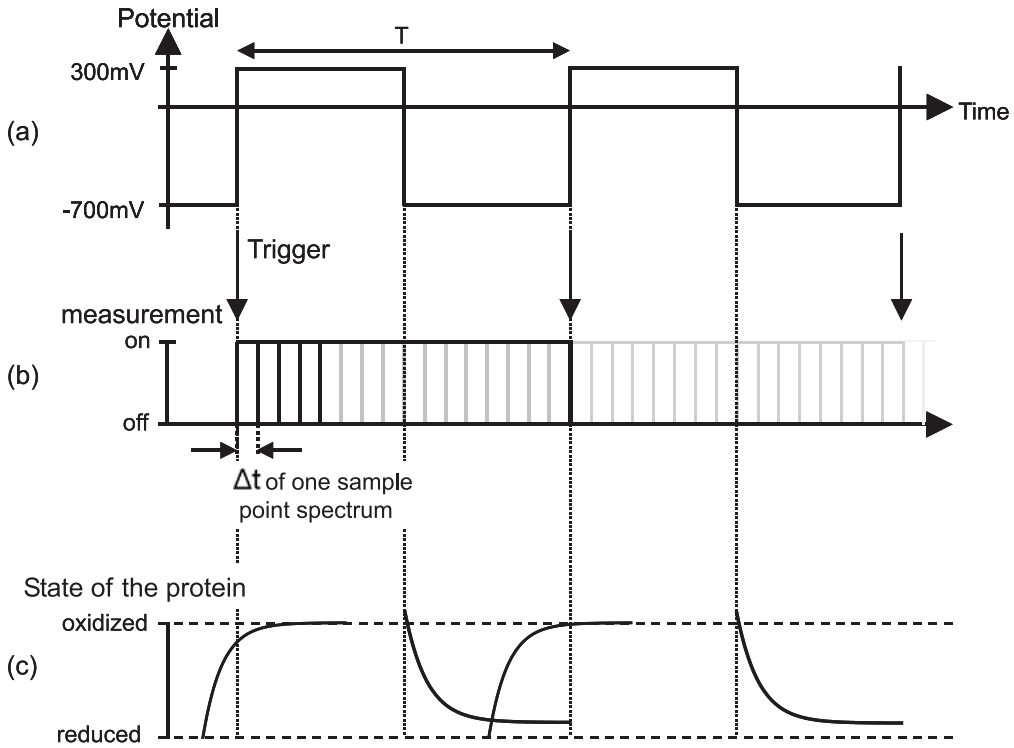

Figure 5.42: Principle for time resolved measurements: (a) Potentials applied to the ptBLM on the gold film (b) IR Measurement, triggered by the positive edge of the exciting potential (c) Corresponding state of the protein during the excitation cycle

depends on the kinetic parameters of the redox transition to be observed. Slow transitions (in the range of 10 to 100 μs) are followed in the rapid scan mode, whereas the step scan mode is used for rapid transitions down to 1 μs.

5.7.2 The Setup for tr-SEIRAS

The home-build spectro-electrochemical cell and the SEIRAS set-up designed for time resolved SEIRAS measurements are depicted in fig. 5.43 and 5.44.
A fluid cell with a lid, made from Teflon is mounted on top of half-cylinder-shaped silicon prism required for a single reflection in the Attenuated Total reflection Spectroscopy (ATR) mode. The flat surface of the prism is covered with a thin gold film by a chemical deposition technique, providing a nano-particular surface to the gold film with a RMS roughness of 5 nm [344]. Figure 5.45 shows AFM images of the chemically deposited film as compared to traditionally evaporated gold.

The IR beam of the FTIR spectrometer (*VERTEX 70 FTIR spectrometer, Bruker, Karlsruhe*) is coupled into the prism at an incident angle of 60°. The reflected beam is recorded

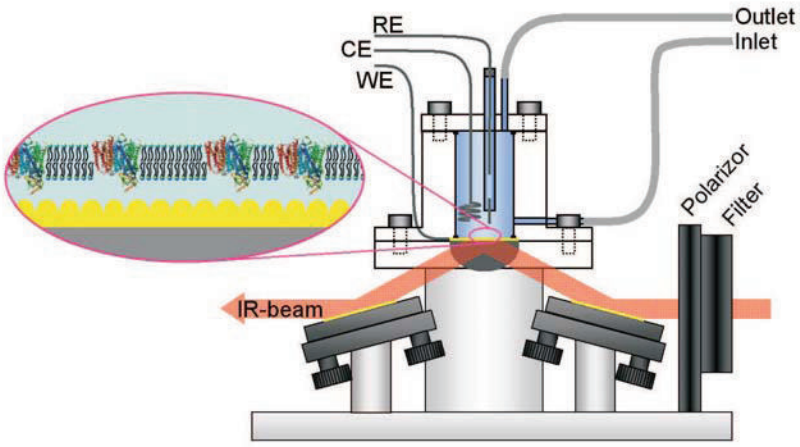

Figure 5.43: The spectro-electrochemical setup. Details are explained in the text.

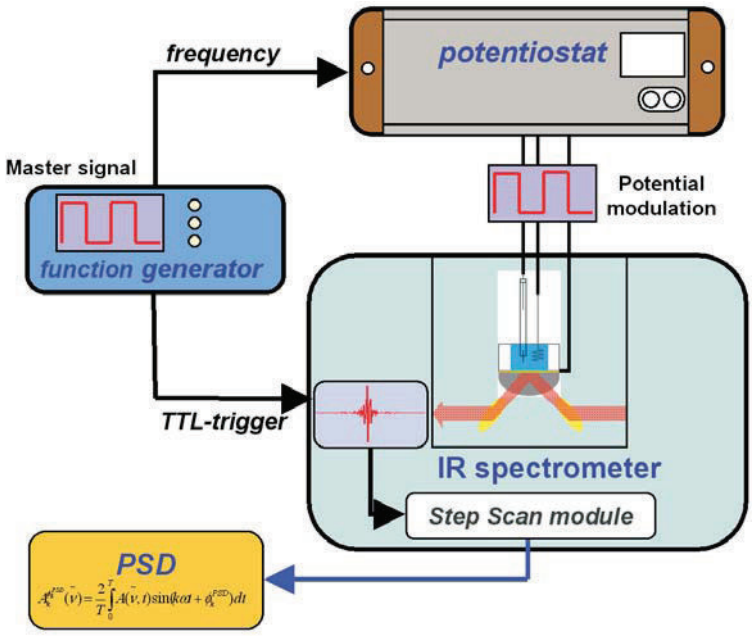

Figure 5.44: The SEIRAS setup. A function generator provides the signal form which is then applied to the ptBLM by the potentiostat. The IR spectrometer is triggered by the same signal of the function generator. The IR signal is processed in the internal step scan module of the spectrometer. The phase sensitive detection (PSD) is then applied externally.

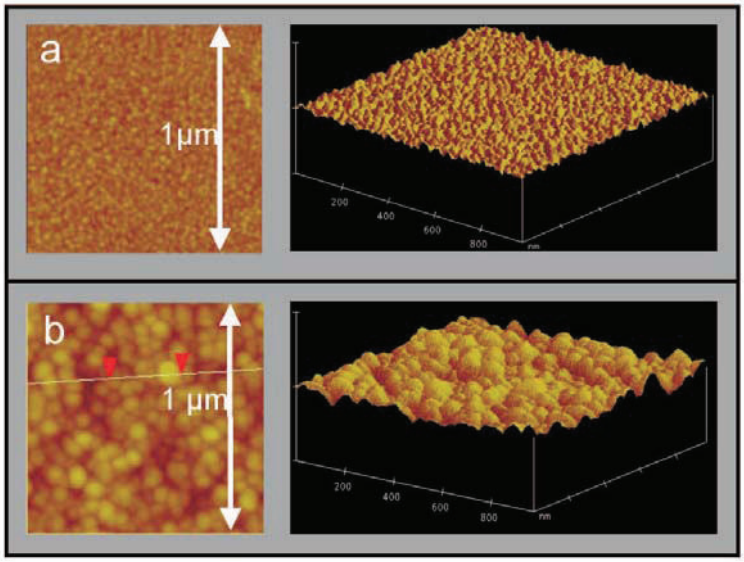

Figure 5.45: AFM images of an evaporated gold film with a roughness of about 1nm (a) and of the chemically deposited gold film with a roughness of about 5 nm (b). The nano-particular structure of the gold surface is obvious.

with a photovoltaic MCT (mercury cadmium telluride) detector. Spectra were recorded with 4 cm^{-1} spectral resolution. Spectra were analyzed by the software package OPUS 6 (*Bruker, Karlsruhe*). The FTIR spectrometer is equipped with an air cooled Globar infrared source.

For static measurements the mirror velocity was 60 kHz, the phase resolution was 32 cm^{-1}, 100 scans were taken for one spectrum. For each spectrum 100 interferograms are averaged using a Blackmann-Harris 3-Term [345, 346] as the apodisation function.

In the Rapid Scan (RS) mode the mirror velocity was 160kHz, the highest time resolution in this mode was Δt = 120 ms, meaning the measurement time for one sample point spectrum (sps) is equal to 120ms. Taking 64 sps over one redox cycle, measurements with an excitation frequency of 0,13Hz were carried out.

In the Step Scan (SS) mode measurements with a time resolution up to 25 μs were carried out. With an excitation frequency of 1kHz, this corresponds to 40 sps.Also spectra with an excitation frequency of 0,5 kHz and 2 kHz were taken in the SS mode.

Phase sensitive detection (PSD) was applied to the time resolved spectra, in order to increase the signal to noise (S/N) ratio. Electron transfer induced structural changes at the active sites with different time constants can also be distinguished with the PSD method due to certain phase shifts of the respective IR mode as compared to the external modula-

tion signal. PSD works by demodulating the IR signal, which is modulated by the applied periodically changing potential. The basic idea of PSD is to suppress all signals which do not change with a frequency close to the exciting frequency. This results in a discrimination of background signals which do not change with a constant frequency, for example non-protein related peaks, peaks that do not depend on the potential modulation etc.

The method of PSD is described in ref. [347], [345] and [346]. However, a short overview about the principle will be discussed:
The periodic response of the system to the exciting modulated signal leads to a periodic response of the time dependent absorbance $A(\tilde{\nu},t)$. At a given wavenumber, this time dependent absorbance is convoluted by a sinusoidal function $sin(k\omega t + \phi_k^{PSD})$ followed by a normalized integration over the modulation period:

$$A_k^{\varphi_k^{PSD}}(\tilde{\nu}) = \frac{2}{T}\int_0^T A(\tilde{\nu},t)sin(k\omega t + \phi_k^{PSD}) \tag{5.5}$$

with ϕ_k^{PSD} being the phase angle. Applying equ. 5.5 to all wavenumbers $\tilde{\nu}$ of the spectrum leads to a vector PSD where the absorbance spectra $A(\tilde{\nu},t)$ and $A_k^{\varphi_k^{PSD}}(\tilde{\nu})$ are treated like vectors (vector PSD). $A(\tilde{\nu},t)$ is the time-resolved absorbance spectrum and $A_k^{PSD}(\tilde{\nu})$ is referred to as phase-resolved modulation spectrum or phase-resolved absorbance spectrum associated with the frequency $k \cdot \omega$. Whereas, k = 1 corresponds to the fundamental, i.e. to the excitation frequency ω and a certain phase ϕ_k^{PSD}. For ϕ_k^{PSD} =0°and ϕ_k^{PSD} =90°, $A_k^{PSD}(\tilde{\nu})$ is equivalent to the in-phase and out-of-phase components (equation 5.6 and 5.7).

$$A_k^{90^\circ}(\tilde{\nu}) = A_k(\tilde{\nu})sin[\varphi_k(\tilde{\nu})] = \frac{2}{T}\int_0^T A(\tilde{\nu},t)cos(k\cdot\omega t)dt \quad (k=1,2,...) \tag{5.6}$$

$$A_k^{0^\circ}(\tilde{\nu}) = A_k(\tilde{\nu})cos[\varphi_k(\tilde{\nu})] = \frac{2}{T}\int_0^T A(\tilde{\nu},t)sin(k\cdot\omega t)dt \quad (k=1,2,...) \tag{5.7}$$

In equation 5.6 and 5.7, $A_k(\tilde{\nu})$ is the modulation amplitude of the absorbance and $\varphi_k(\tilde{\nu})$ the corresponding phase lag. $A_k(\tilde{\nu})$ can be calculated from $A_k^{90^\circ}(\tilde{\nu})$ and $A_k^{0^\circ}(\tilde{\nu})$ using equation 5.10:

$$A_k(\tilde{\nu}) = \sqrt{A_k^{0^\circ}(\tilde{\nu}) + A_k^{90^\circ}(\tilde{\nu})} \tag{5.8}$$

$$sin(\varphi_k) = \frac{A_k^{90^\circ}(\tilde{\nu})}{A_k(\tilde{\nu})} \tag{5.9}$$

$$cos(\varphi_k) = \frac{A_k^{0^\circ}(\tilde{\nu})}{A_k(\tilde{\nu})} \tag{5.10}$$

The purpose of the PSD is the evaluation of the phase-resolved absorbance spectra $A_k^{\varphi_k^{PSD}}(\tilde{\nu})$, if the response of the system is in-phase with the exciting frequency, the process to be investigated has the same time constant. If there is a phase shift, the time constant is slower.

5.7.3 Time resolved Measurements

Time resolved (tr-)SEIRAS measurements were performed in the absence of oxygen, triggered by a periodic change of potentials between +300 and -700 mV. Under these conditions, the enzyme cycles between fully oxidized and fully reduced state. With a sinusoidal excitation of very low frequency, 0.13 Hz, in the RS mode, changes in the spectra in the frequency region 1000 to 1750 cm^{-1} were observed, indicating changes in the redox state particularly of Cu_A, but also of heme a_3 and heme a (fig. 5.46). In the frequency range 3045-3150 cm^{-1}, a change is observed at 3050 cm^{-1} which can be assigned to the redox transition of Cu_B (inset of fig. 5.46) [343]. With the slow changes of the potential, each spectrum displayed in fig. 5.46 can be considered to represent a quasi-stationary state at a certain potential. These potentials derived from the sine wave function, are given in the figure caption of fig. 5.46. Due to the periodic excitation, each difference spectrum represents the average of the same stationary state attained during repeated multiple turnovers of the enzyme. The fully oxidized state is used as the reference spectrum such that changes in the spectra are due to reduction of the enzyme. The most prominent change is seen in the band at 1647 cm^{-1} which was assigned (1651 cm^{-1}) to the amide I band (α-helix, ν(C=O) vibration of reduced Cu_A). A second band at 1602 cm^{-1} is also attributed to the formation of reduced Cu_A (amide I band, β-sheet, ν(C=O)) with the oxidized state indicated by a band at 1592 cm^{-1} [343]. From this result, the periodic reduction and reoxidation of all four redox sites is concluded to occur, initiated by the direct electrochemical electron transfer to Cu_A. This is in full agreement with recently performed combined electrochemical and SERRS measurements.

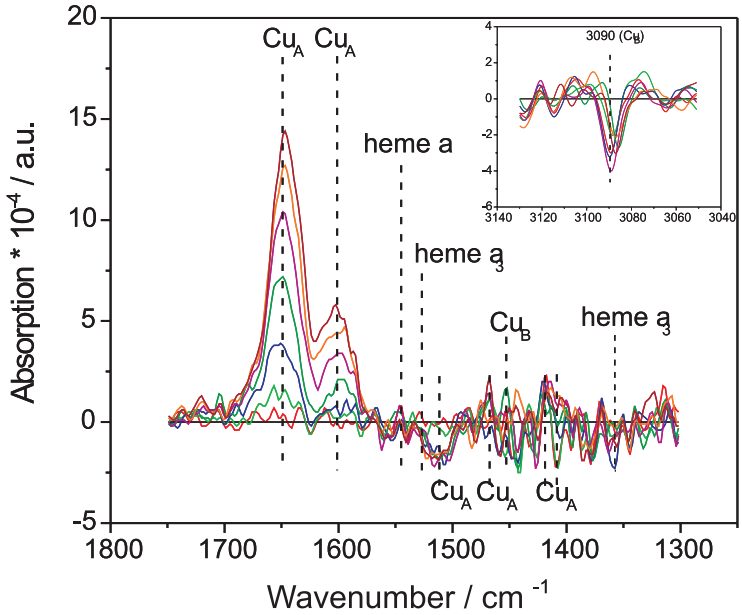

Figure 5.46: SEIDA spectra at different potentials starting at +287 mV vs. NHE(with the fully oxidized form as the reference)

In the above mentioned investigation, Cu_A and heme a were shown to be reduced with rate coefficients of $k_s = 4130 \pm 390\ s^{-1}$ and $k_s = 1650 \pm 170\ s^{-1}$, respectively. tr-SEIRAS measurements were therefore conducted in the step scan mode with a square wave excitation of a frequency of 500 Hz. Phase sensitive detection was used to improve the spectral resolution and the S/N ratio. As a result, time resolved changes of Cu_A and heme a were observed (fig. 5.47). The set of data taken at a frequency of 500 Hz was analyzed in terms of the peak height and could be fitted to a single exponential (Fig.11), yielding a rate coefficient of 1980 s^{-1}. This compares reasonably well with the rate coefficient of 4130 s^{-1} found by fast scan cyclic voltammetry.

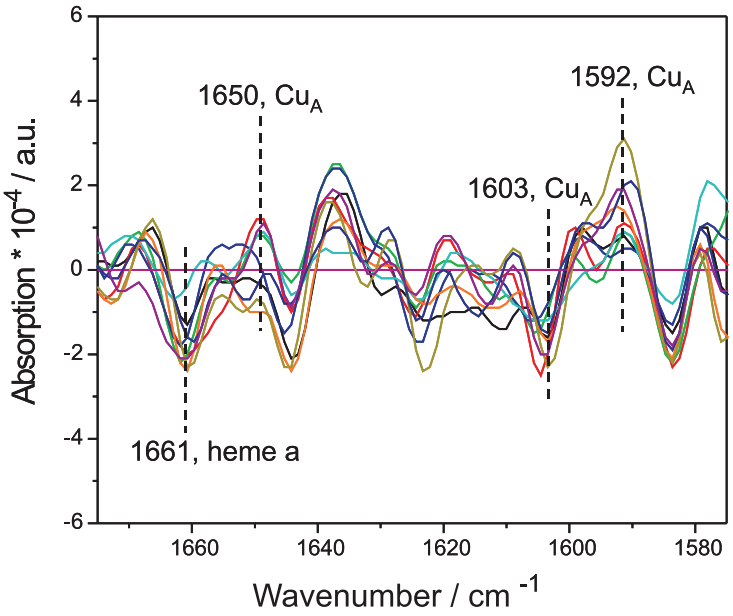

Figure 5.47: tr-SEIRAS spectra of the CcO with an excitation frequency of 500 Hz. [100μs (black), 300 μs (orange),500μs (dark yellow), 700μs (navy), 900μs (purple), 1100μs (red), 1300μs (light green), 1500μs (blue), 1700μs (light blue), 1900μs (pink)(= reference).]

For an experiment with a modulation frequency of 1 kHz a critical reference experiment was performed under identical conditions, however, using the CcO in the inverted orientation with the cyt c binding site pointing into the bathing solution. No changes in the spectra could be recorded, strongly supporting the assertion, made earlier, that direct ET does not occur non-specifically to any of the redox centers. Instead, direct ET occurs specifically to Cu_A the binding site of which must be close to the surface. This is shown clearly in the reference spectrum (fig. 5.49).

5.7.4 Conclusion

Tr-SEIRAS has been successfully applied to the CcO in the ptBLM. Time resolution down to the μs time scale has been achieved, due to the electrochemical triggering of the ET

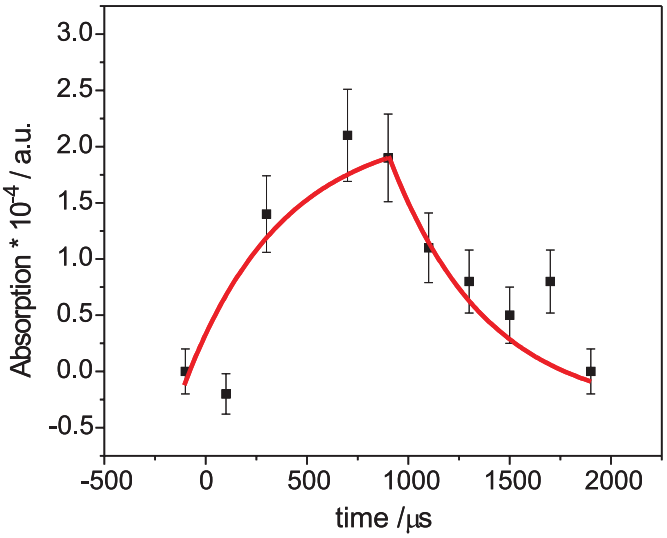

Figure 5.48: Peak hight of the Cu_A-peak at 1592 cm^{-1} plotted in dependence of time. A monoexponential curve was fitted, the corresponding time constant is t =1980 s^{-1}.

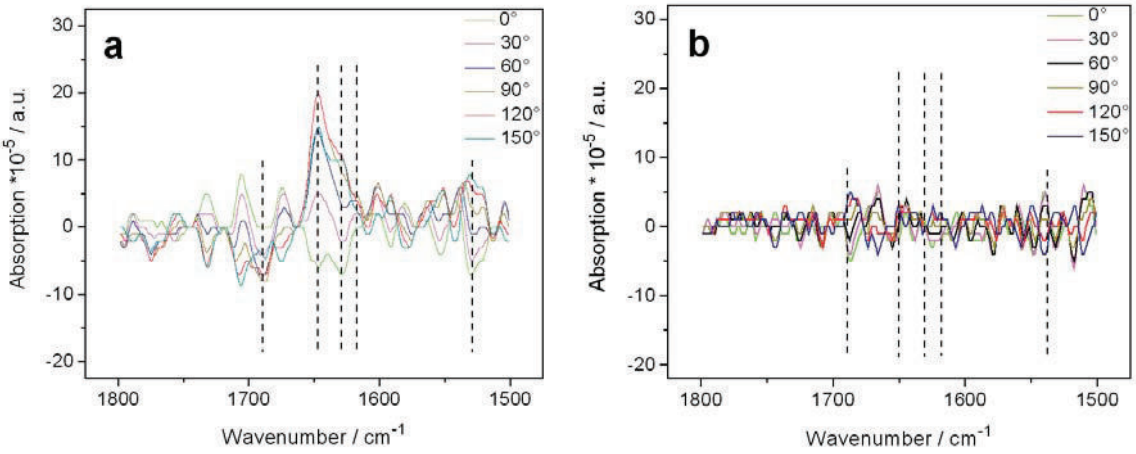

Figure 5.49: PSD spectra of a 1kHz modulation experiment of CcO (a) with its natural electron entry side directed toward the electrode and (b) directed away from the electrode into the bathing solution. No redox-processes could be observed in the case of the inverted orientation.

chain. This time resolution should be sufficient to perform a more detailed kinetic analysis of the enymatic cycle of the CcO. Preliminary experiments show a ET rate constant to Cu_A of 1980 s^{-1}, which is in fully agreement with ET rates determined by electrochemical methods. The minor deviation can be attributed to the roughend gold film, which does not provide a complete homogeneous orientation of the immobilized protein.

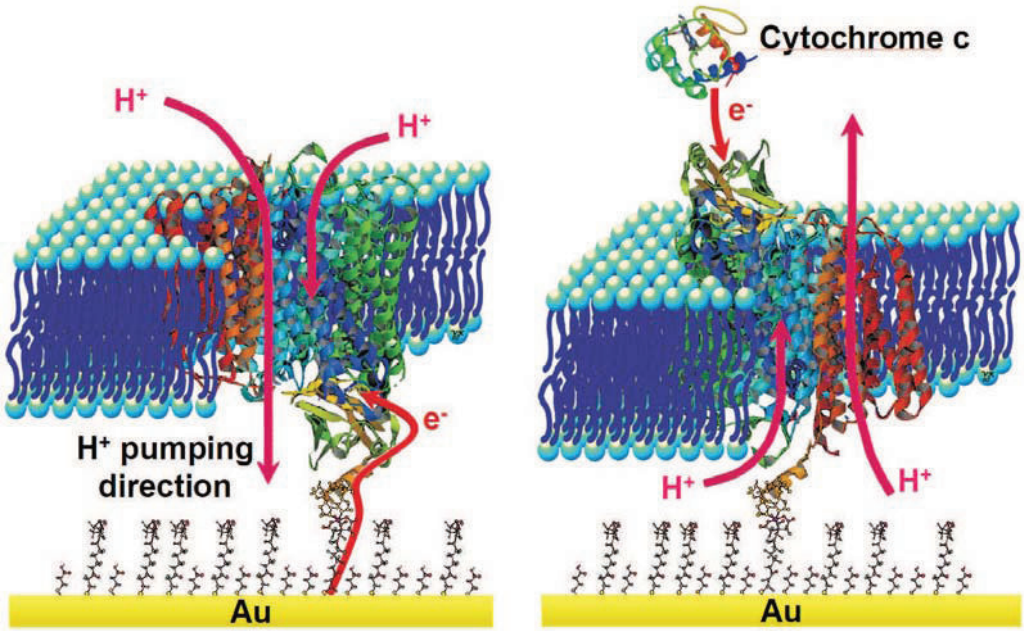

Figure 5.50: Schematic representation of cytochrome c oxidase (CcO) embedded into a protein-tethered bilayer lipid membrane. The protein is attached to the template stripped gold film on the surface by an his-tag attached to either SU II (a) or SU I (b). The lipid bilayer is assembled around the protein. CcO is activated either by direct electron transfer from the electrode (a), or by electron transfer from cytochrome c (b).

5.8 In-situ Monitoring of the Catalytic Turnover of Cytochrome c Oxidase

In the previous sections it could be shown, that the CcO from *R. sphaeroides*, embedded in such a system, with the His-tag attached to SU II (Fig. 5.50a), can be effectively activated by direct electron transfer (ET). This was demonstrated by electrochemical in combination with Surface-Enhanced Resonance Raman Spectroscopy (SERRS) investigations. When, on the other hand, the CcO from *P. denitrificans* is immobilized with the His-tag attached to SU I, the cytochrome *c* (cyt *c*) binding site is directed away from the electrode to the outer side of the tBLM architecture (Fig. 5.50b). The protein can then be activated by cytochrome *c* to actively transport protons across the lipid bilayer structure. These processes will be investigated in greater detail in this section.

5.8.1 Activation of the CcO with Reduced Cytochrome c Monitored by Impedance Spectroscopy

CcO from *P. denitrificans* was reconstituted in the ptBLM, thus pointing with the cytochrome c binding site towards the bathing solution. Thus the enzyme can be activated by cyt *c* in the reduced form. Impedance spectra were recorded as a function of the con-

centration of reduced cyt *c*, ready to transfer an electron to CcO, in an oxygen-saturated buffer solution at a bias potential of 200 mV vs. NHE, according to 0 mV vs. Ag|AgCl, sat.KCl (Fig. 5.51a). Spectra fitted to the equivalent circuit, given in Fig. 5.30d, yield the resistance of the membrane decreasing as a function of cyt *c* added in an exponential decay (Fig. 5.51b). As a consequence of the turnover of the enzyme, protons are actively transported from the submembrane space into the bathing solution. The translocation of protons is expected to give rise to a flux of ions across the membrane thus decreasing the resistance as a function of the concentration of cyt *c* added. This explanation of an cyt *c* mediated enzymatic ion transport is supported by the fact that the decrease of resistance can be reversed by cyanide, which inhibits the activity of CcO (see section 4.1.5). The occurrence of proton transport could be directly detected at the CcO in the inverted orientation (sketched in Fig. 5.50), showing the cathodic reduction of the translocated protons at the electrode surface. Moreover, the decrease of the resistance is critically dependent on the quality of the reconstituted lipid membrane (see also further below).
As a consequence of this turnover, CcO in the present orientation, should generate a potential difference across the membrane, of +50 mV across the membrane with respect to the outer side, in accordance with measurements of the membrane potential of CcO reconstituted in liposomes [348]. Potential dependent measurements with different cyt *c* concentrations were performed to probe the effect of potentials applied to the ptBLM structure on proton transfer.

Applying an additional bias potential should change the self generated potential difference and hence, should affect proton transport. Impedance spectra were recorded as a function of bias potentials applied at different concentrations of cyt *c*. As a control, the resistivity of the CcO-ptBLM in the absence of cyt *c* as a function of the applied potential was measured. (Fig. 5.52b, blue curve). They reflect passive ion permeation as a function of the applied potential. Differences are displayed for the CcO with and without cyt *c* within a range of potentials between 50 and 400 mV. Resistances in the presence of cyt *c* show a complex behaviour of two maxima in the region of 160-200 mV and 300-350 mV and a minimum at around 250 mV, which cannot be explained in terms of proton transport alone. Proton translocation could be accompanied by electron transfer to cyt *c* possibly catalysed by the enzyme. This question will be clarified in the following.

5.8.2 Cyclic Voltammetry in the presence of Oxidized Cytochrome c

Cyclic voltammetry was performed in the presence of CcO reconstituted into a tBLM as described above with cyt *c* added in the oxidized form. Voltammograms were recorded, in the absence and presence of oxygen. (Fig. 5.53, red and blue curve). A reduction peak was obtained at 389 mV at a scan rate of 50 mVs^{-1} followed by a re-oxidation peak at 468 mV. The apparent standard potential, E^0_{app}, deduced from the potential difference between reductive and oxidative peak was +428 mV vs. NHE. This is about 200 mV more positive than the standard potential of cyt *c* obtained on mercaptopropanol modified or carboxylated surfaces, reported to be 225-230 mV [349]. The value of 428 mV corresponds,

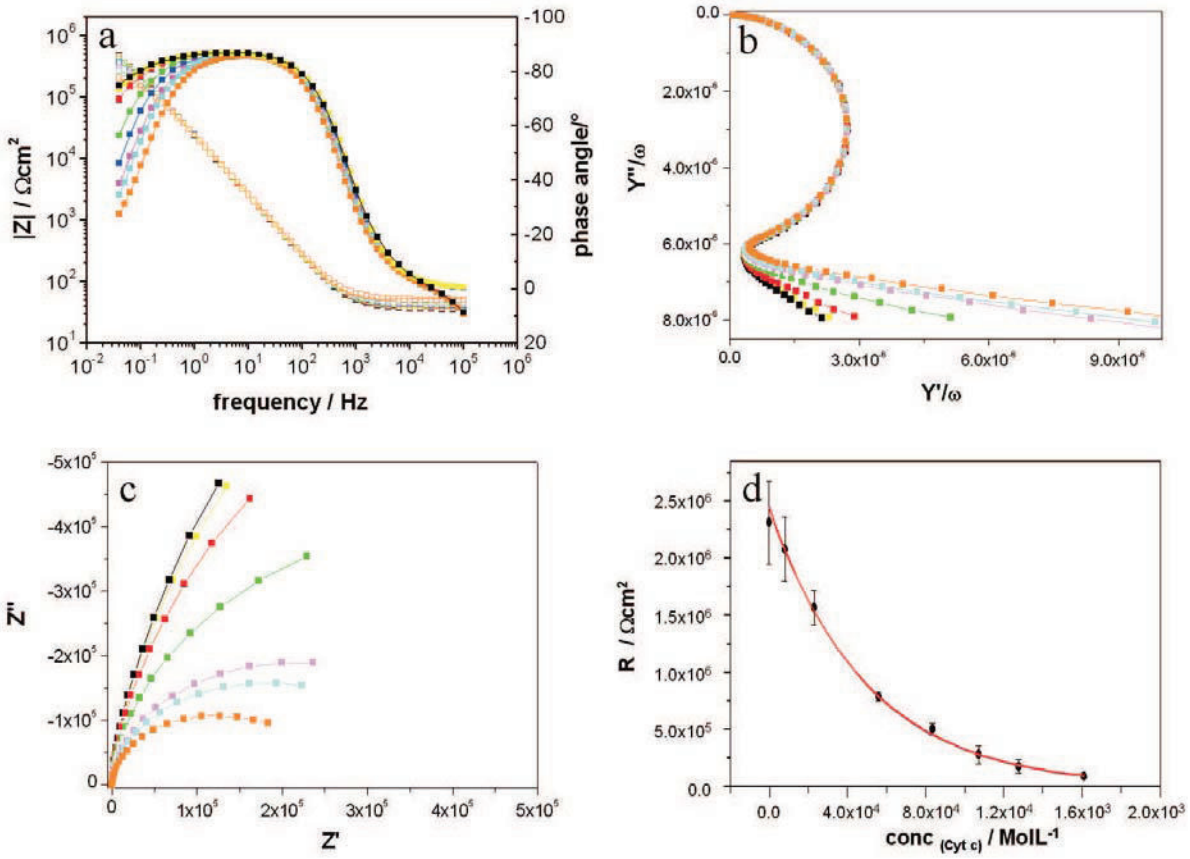

Figure 5.51: (a) Impedance spectra of CcO embedded in a ptBLM recorded at a bias potential of + 200 mV vs. NHE, as a function of the concentration of reduced cyt c, black (0 M), red (2.3 · 10-4 M), green (5.6· 10-4 M), blue (8.4 · 10-4 M), magenta (1.07 · 10-3 M), cyan (1.28 · 10-3 M), orange: 1.6 · 10-3 M). Spectra were fitted to the equivalent circuit shown in Fig. 5.30d. (d) Resistances thus obtained were plotted vs. the concentration of cyt c. The decrease is considered in terms of proton transfer due to the activation with reduced cyt c.

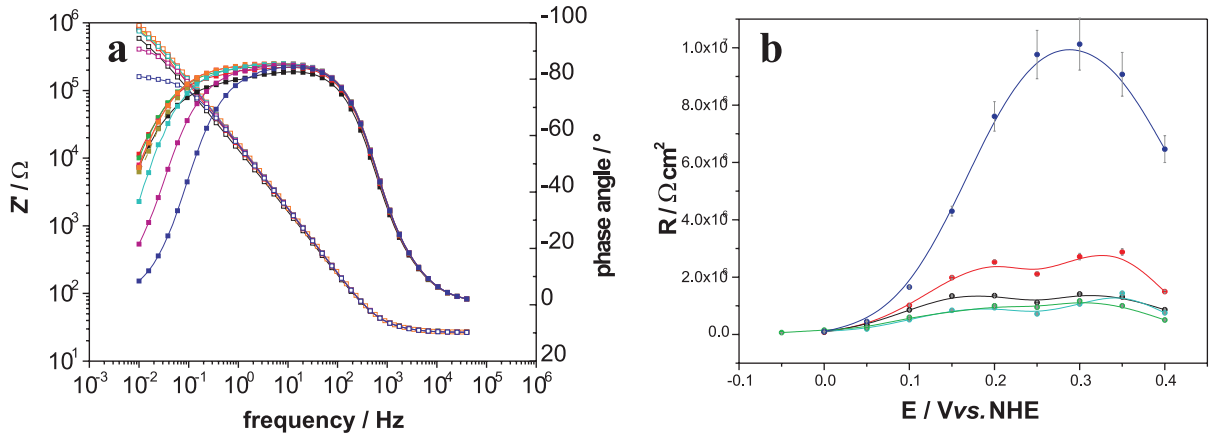

Figure 5.52: A series of impedance spectra of CcO embedded in a ptBLM recorded at different bias potentials vs. NHE, at a fixed concentration of 1.8 $\cdot 10^{-4}$ M cyt c, +400mV (black), +350mV (red), +300mV (green), +250mV (yellow), +200mV (pink), +150mV (orange), +100mV (cyan), +50mV (magenta), 0mV (violet). (a) Such spectra were recorded for various concentrations of cyt c. (b) Resistivities for the different concentrations plotted vs. potentials, 0 M (blue), 1.07 $\cdot 10^{-4}$ M (red), 1.82 $\cdot 10^{-4}$ M (black), 5.07 $\cdot 10^{-4}$ M (green).

however, to 430 mV found by Hawkridge and coworkers for cyt *c* bound to CcO incorporated into a supported lipid bilayer membrane [350, 351].
In this case, the cyt *c* binding site of CcO is pointing to the distal side of the membrane, the same as in our case. We conclude from this, that cyt *c* absorbed to the cyt *c* binding site of the CcO (Fig. 5.50), is reduced and oxidized at CcO immobilized on the electrode in the biomimetic membrane architecture. This ET process through the enzyme could be a reasonable explanation for the shift in the redox potential. A control experiment of cyt *c* on a DTP modified surface gives the value of the standard potential (E^0 = +230 mV, not shown), also obtained by potentiometry [324]. This was corroborated by SERR spectra of cyt *c* on a roughened silver electrode, modified with DTP, taken at different potentials (Fig. 5.54). Cytochrome c is shown to be oxidized between +90 mV and +240 mV in accordance with the standard potential of 230 mV.

Fig. 5.53 also displays the increase of the peak current under aerobic as compared to anaerobic conditions. This effect is referred to as catalytic current, which is an indication of the repeated cathodic reduction of cyt c_{ox} while it is reoxidized by oxygen catalyzed by the enzyme. Under anaerobic conditions, the peak current density is (-0.8 μAcm^{-2}) whereas in the presence of O_2, the current density at the peak is (-4.9 μAcm^{-2}) at a scan rate of 50 mVs^{-1} and a concentration of cyt *c* of 1mM. The catalytic current is high compared to 0.7 $nAcm^{-2}$, and 0.6 μAcm^{-2} according to references [337, 349], measurable but only at very slow scan rates (1-2 mVs^{-1}). At higher scan rates, catalytic currents were not observed because the turnover of the enzyme was considered to be too slow to follow the potential scan. By contrast, in our case, the increased current in the presence of oxygen, could be measured in a large range of scan rates up to 1 Vs^{-1}. Fig. 5.54 displays

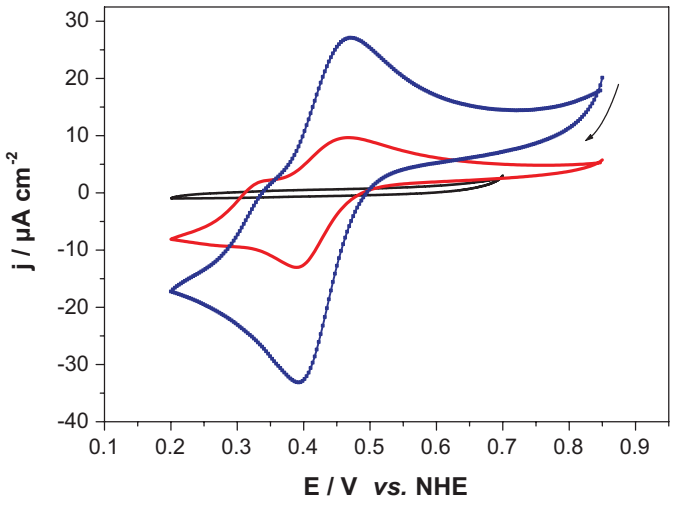

Figure 5.53: Cyclic voltammogram of oxidized cytochrome c (1 mM in the bathing solution) on CcO immobilized in a ptBLM under aerobic (blue) and anaerobic conditions (red), scan rate 50 mV/s

cathodic and anodic current densities recorded by cyclic voltammetry, taken at aerobic conditions, of cyt c in the oxidized and reduced form in the absence and presence of CcO. The currents are linearly dependent of the square root of the scan rate, consistent with a diffusion controlled process [37]. The catalytic effect is indicated by an increased slope of the current density measured with cyt c present in the bathing solution in the oxidized form (Fig. 5.54, green curve). This effect is accounted for by the electrochemical reduction of cyt c_{ox} to cyt c_{red}, which delivers its electron to CcO, thereby regenerating the oxidized form, so that it has to be electrochemically reduced repeatedly. This explains the increased slope obtained for cyt c_{ox} in the presence as compared to the absence of CcO (Fig. 5.54, black curve). Although, these electrochemical processes are clearly diffusion controlled, binding and adsorption of cyt c to the immobilized CcO layer is also indicated in the CVs at low scan rates (Fig. 5.53). The pre-peaks seen in Fig. 5.54 are characteristic for the absorption of the reduced form of a redox couple, in this case cyt c_{red} [37]. Other aspects of these processes will be discussed in the following paragraph.

5.8.3 Cyclic Voltammetry in the presence of Reduced Cytochrome c

Reduced rather than oxidized cytochrome c was considered above to induce proton translocation. Hence, anodic currents due to the oxidation of reduced cyt c promised to be more interesting from the physiological point of view. CVs of reduced cyt c on a CcO containing ptBLM under *aerobic* and *anaerobic* conditions also show an increase of the current

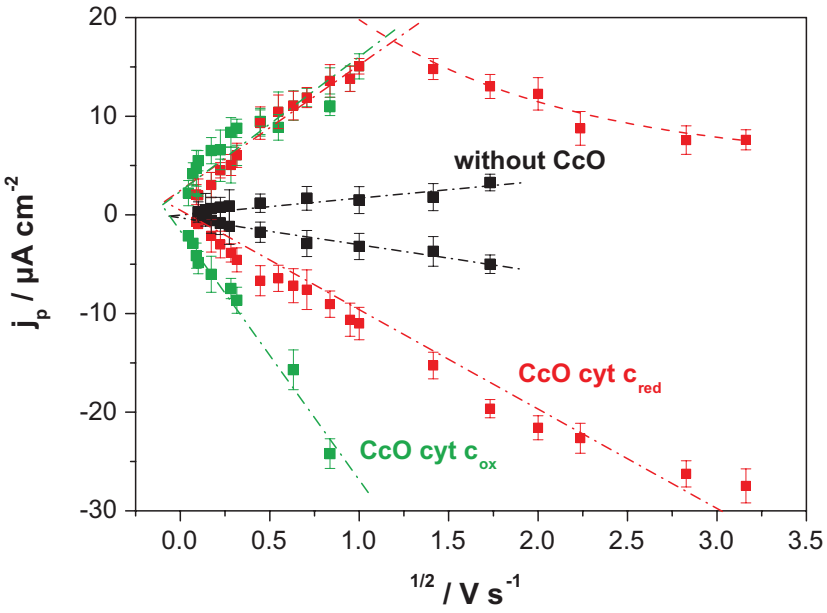

Figure 5.54: Current densities of the peaks of cytochrome c reduction/oxidation as a function of the square root of the scan rate. Cyt c was applied in the reduced (red) and oxidized state (green and black) in the presence (red, green) and absence (black) of CcO

density (Fig. 10). Such an increase was also found by Hawkridge and coworkers [350, 351], at exactly the same potential of 430 mV, mentioned above, however, with lower current densities in the range of 20-100 $nAcm^{-2}$. In this reference CcO was reconstituted into a hybrid alkanethiol-phospholipid bilayer and activated it by adding reduced cyt *c*. They considered the anodic currents in terms of an electrochemical oxidation of oxyferryl or ferredoxyl species of the enzyme on the level of heme a_3/Cu_B. This would be in accordance with the assumption, mentioned above, that electrons are accepted by the electrode *via* heme a_3, whose standard potential is reported to be +430 mV. Anodic oxidation of the lower oxidation states, such as oxyferryl or ferredoxyl, on the other hand, would mean that oxygen is regenerated, that had before been reduced by the enzyme. In other words, the anodic current also, can be considered as a true catalytic current, driven by the enzyme. Catalytic turnover rates of the enzyme can be calculated [351] from the electron transfer rate as obtained from the current density divided by the number of molecules per area. From the quasi-stationary current of 4.5 μAcm^{-2} deduced from Fig. 10 under aerobic conditions, and the number of CcO molecules per cm^2 obtained by direct ET to the CcO in the inverted orientation (6 $nMolcm^{-2}$) the turnover was estimated to be ca. 750 ± 30 s^{-1}. This value is of the same order of magnitude as that of a fully active enzyme in the solubilized form or reconstituted in liposomes. Samples used for the present investigation

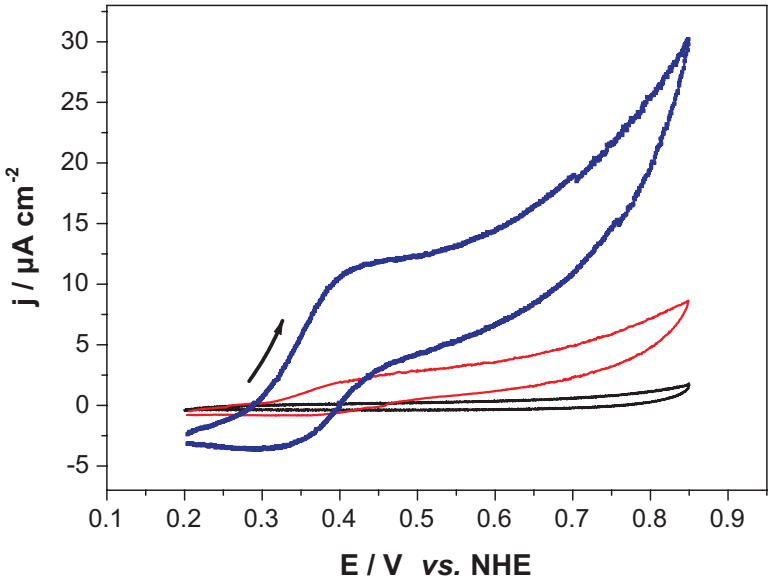

Figure 5.55: Cyclic voltammogram of reduced cytochrome c (1 mM in the bathing solution) on CcO immobilized in a ptBLM under aerobic (blue) and anaerobic conditions (red), scan rate 50 mVs^{-1}

were analyzed by a standard biochemical assay to show turnover rates of 1070 ± 40 s^{-1} (see Fig. 5.56). It is concluded from this result, that the ptBLM architecture is designed to fully preserve the activity of the CcO, both with respect to the activity of the single enzymes.
Anodic currents were also measured by Dutton and co-workers [349] with CcO solubilized in detergent electrostatically attached to reduced cyt *c* bound to a 3-mercapto-1-propanol modified gold film. The standard potential of cyt *c* in this case was (+ 230 mV) in accordance with our measurement at the DTP modified surface. Anodic currents were (ca. 85 $nAcm^{-2}$), lower than in our case (4.5 μAcm^{-2}) (Fig. 5.55) and again measurable only at low scan rates (1 mVs^{-1}). By contrast, the catalytic effect of the anodic current of the CcO in the present investigation, was measurable up to scan rates of 1 Vs^{-1}. The catalytic effect can be deduced from the increased slope of the anodic current as a function of the scan rate of cyt c_{red} in the presence as compared to the absence of CcO (Fig. 5.54, green and red curve). It should be noted that both branches of the current density are plotted, showing that cyt *c* absorbed to the enzyme in either the oxidized or reduced form can exchange electrons almost reversibly with the electrode. The anodic branches of both forms of cyt *c* have the same slope and are linear to the square root of the scan rate, whereas the current densities of the cathodic branch of cyt c_{red} are definitely smaller than that of cyt c_{ox}. This is due to the fact that cyt c_{red} has to formed in the faradaic process before

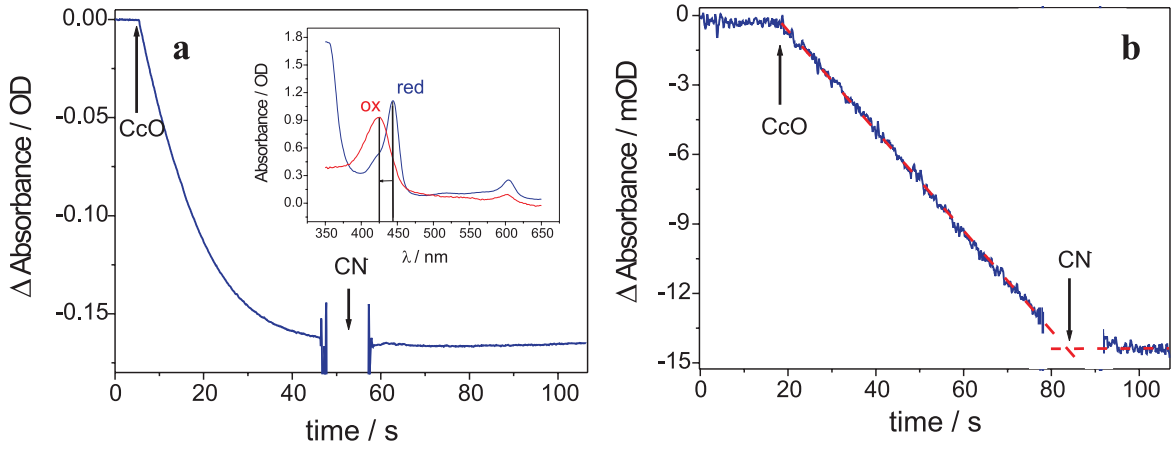

Figure 5.56: Probing of enzymatic activity of the solubilized CcO. A concentrated cyt c solution is first reduced by dithionite and then CcO is added to the solution. (a) The time coarse of the cyt c oxidation by CcO is measured at a fixed wavelength $\lambda = 450$ nm. The absorption spectra of reduced (blue) and oxidized (red) cytochrome c is shown in the inset. The decrease of the absorption peak at 450 nm is related to the turnover of cyt c by CcO. By adding of a diluted KCL [352] the inhibition of CcO can be probed, resulting in a horizontal line, since cyt c reduction is inhibited. (b) When the added CcO concentration is sufficiently low, the slope becomes linear and the turnover can be calculated according to: $turnover = \frac{\Delta E/t \cdot Volume}{\Delta \epsilon_{cytc}}$ with E being the extinction, $\epsilon_{cytc} = 19,4 mM^{-1} cm^{-1}$ and $c_{CcO} = 20 pM$. The resulting turnover rate of the solubilized CcO follows therefore to $1070 \pm 40 s^{-1}$.

catalytic turnover can take place at the expense of oxygen consumption.

In the case of reduced cyt c_{red} present in the bulk solution, only the amount of cyt c_{ox} formed by the turnover of the enzyme gives rise to a cathodic current which is naturally smaller than the current with cyt c_{ox} in the bulk phase.

Another important phenomenon is that the anodic branch is linear only up to $\sim 1\ Vs^{-1}$ (Fig. 5.54). After that the current decreases in an exponential decay. This effect is considered in terms of the turnover of the enzyme, which is, at a certain scan rate, no longer able to follow the changing potential. Less and less cyt c_{red} molecules are regenerated such that the current decreases gradually.
This assumption is supported by an analysis of the peak potentials as a function of the scan rate plotted in a logarithmic scale (Fig. 5.57). The so-called 'trumpet' plot is designed to extract quantitative information on the kinetics of ET, by analyzing the deviation from the standard potential of oxidative and reductive peak potentials with increasing scan rates [34]. This deviation starts at about the same scan rate $\sim 1\ Vs^{-1}$ where the slope of the anodic current densities of cyt c_{red}, (Fig. 5.54) start to deviate from the linear dependency. The trumpet plot was analyzed by means of the algorithm described by Jeuken et al. [154] with the simplifying assumption that cyt c is reduced while it is adsorbed to the CcO.

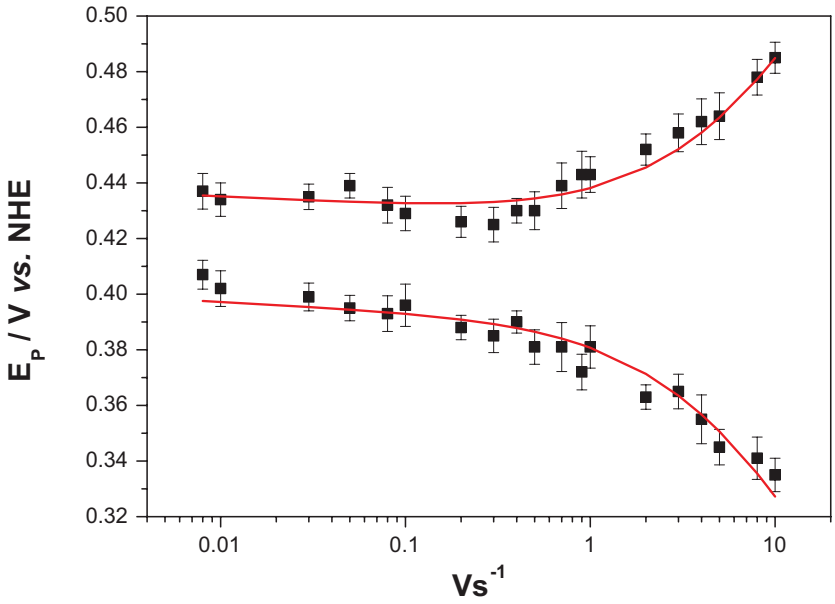

Figure 5.57: Peak potentials as a function of scan rate (trumpet plots) of cyt c (oxidized) attached to CcO with the his-tag attached to SU I under aerobic conditions, concentration in the bathing solution 1 mM at a temperature of 20°C. An intrinsic rate constant of $k_0 = 73.13\ s^{-1}$ and a standard potential of $E_0 = 0.409$ V could be determined.

Values for the heterogenous rate constant $k_0 = 73\ s^{-1}$ and the apparent standard potential $E^0_{up} = 409$ mV were obtained. This value is very well comparable with the electron transfer rate of a cyt c/CcO complex of 20 s^{-1} reported by Dutton and coworkers [349], with cyt c being in the reduced form.

5.8.4 Conclusion

Having clarified some of the questions with regard to faradaic currents, attempts can now be made to explain the complex potential dependence of the impedance spectra, (Fig. 5.52b), at least qualitatively. Several processes have to be considered to contribute to changes of the resistance in the potential window 0 mV to +400 mV:

- passive ion permeation driven by potential and concentration differences across the membrane,
- active proton transport driven by the enzymatic redox processes and
- faradaic currents due to reduction and oxidation of cyt c.

The maximum of passive ion transport (with no cyt *c* present) at around +300 mV can be explained in terms of permeabilities of cations and anions which balance at this potential. The maximum of the traces at 350 mV with cytochrome c present can be explained in terms of the apparent standard potential of the cyt c_{ox} / cyt c_{red} pair, where faradaic processes are at equilibrium and hence do not contribute. The minimum at +250 mV can be explained in terms of faradaic currents due to cyt *c* reduction superimposed on active proton translocation. The increase of the resistance to the maximum at around +200 mV can be due to the potential difference across the membrane, positive inside, which counteracts active proton translocation.

For a closer inspection of the faradaic processes, occurring at CcO residing in the ptBLM with cyt *c* adsorbed to the cyt *c* binding site pointing up (Fig. 5.50b), one has to consider that direct ET between cyt *c* and the electrode is highly unlikely. The high enzyme surface coverage and the sealing membrane prohibits the approach of cyt *c* to the electrode surface leading to an direct exchange of electrons. On the other hand, the tunnel barrier across the membrane would be at least 10 nm, taking into account the height of the CcO (9 nm) [353] added to the thickness of the chelating layer. Direct ET between the enzyme and the electrode, on the other hand, without cyt *c* present, would have a higher probability. The tunnel barrier between heme a_3/Cu_B and the highly conductive electron wire, consisting of the Ni-chelating tether and the highly conjugated His-tag, is approx. 2 nm. This direct ET, however, definitely does not take place, as its has been conclusively demonstrated by reference experiments without cyt *c* (Fig. 5.53 and 5.55) supported strongly by SERRS measurements. According to the experiments presented here, electron exchange with the electrode does take place, but only when cyt *c* is adsorbed to the CcO. Only then, ET seems to occur, most probably *via* the heme a_3/Cu_B catalytic center being the redox center nearest to the electrode. One explanation for this finding could be that ET could be initiated by a kind of a gating of the electron pathway due to the binding of cyt *c* to cytochrome c oxidase. The mechanism of this process is not yet understood. Further vibrational spectroscopic measurements, sensitive to small dynamic structural changes, in combination with electrochemical measurements could provide more insight into this process.

Nevertheless, the appearent rate of ET to the electrode appears to be of the same order of magnitude as in the arrangement described in ref. [349], where cyt *c* is located between the electrode and the enzyme nand thus in direct contact with the electrode. The CcO, on the other hand, seems to preserve its activity while it is incorporated in the ptBLM. As a result, catalytic currents are high compared to those measured for CcO in other biomimetic systems. These currents seem to reflect the turnover rate of the enzyme measured by independent methods.

In summary, the activity of the CcO can be monitored effectively. Different processes such as electron and ion transfer, can be discriminated. This demonstrates the possibilities of the ptBLM as a general platform for further investigations with other proteins or for protein-proteins interaction studies.

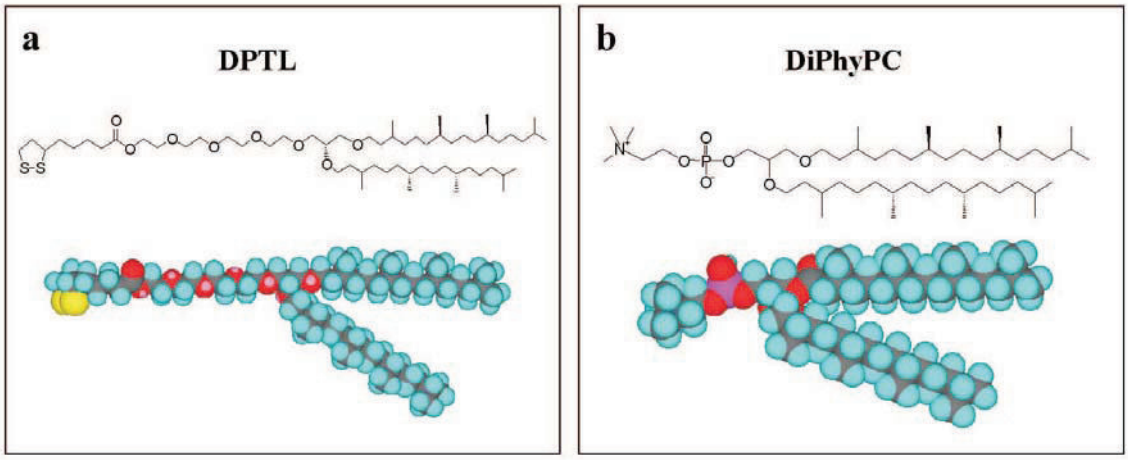

Figure 5.58: Chemical structure and van der Walls representation of (a) the tethered Lipid molecule DPTL and (b) the lipid DiPhyPC which forms the upper leaflet of the tBLM.

5.9 Simulation of Electron Transfer and Ion Transport across Tethered Bilayer Systems

In order to develop a full understanding of the mechanism of a proton pump such as the cytochrome c oxidase, the result of electrochemical and spectroscopic measurements have to be analyzed quantitatively. For this purpose a set of differential equations has to be solved taking into account the different steps of an enzyme cycle. This procedure can be conveniently facilitated by the computer program SPICE, designed to solve a set of differential equations numerically. To treat the entire enzyme cycle of the CcO would be too complex to begin with. Therefore, it has to be started with the fundamental process present at a biomimetic membrane systems, such as tethered lipid bilayer system (tBLMs).

5.9.0.1 EIS of a tBLM System

Electochemical impedance spectroscopy (EIS) is a very useful electrochemical technique for examining mechanistic information in a tBLM system. By separating ion transport phenomena into the frequency domain, ion transport processes can be examined with transport components that have distinctly different time scales. Utilizing a wide range of frequencies allows for the non-specific background current to be separated from the ion transport mediated by the protein.
Figure 5.59 shows EIS traces for tBLMs at several different bias potentials. The impedance was measured from +0.3 V to -0.4 V. As the potential is stepped negatively, the high frequency impedance, determined essentially by the membrane capacitance, is unchanged ($\sim$ 0.6 $\mu F cm^{-2}$). At low frequencies, however, the impedance varies systematically. Often tBLM surfaces with incorporated spacer groups (e.g. OEG tethers) show a second time

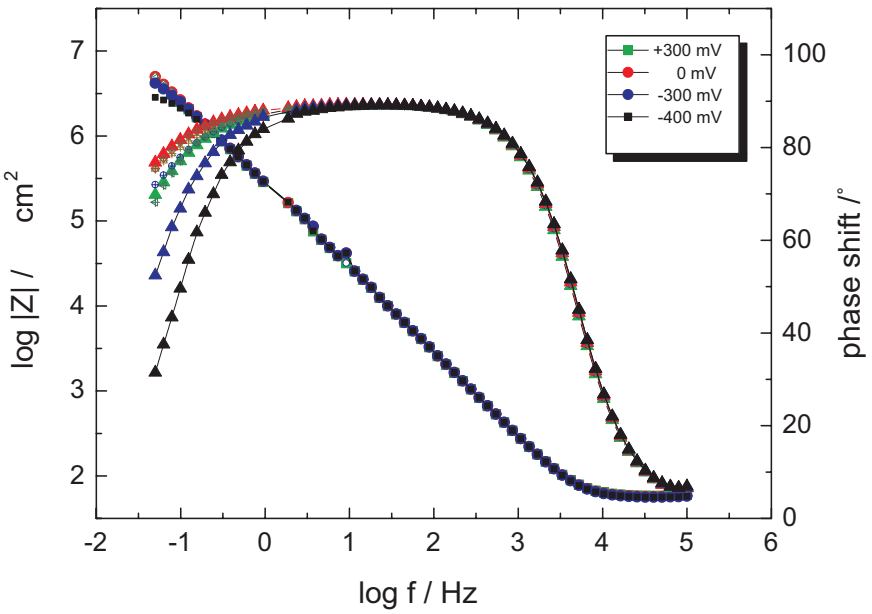

Figure 5.59: EIS of a tBLM at different bias potentials. The magnitude of the impedance Z (circles) and the phase shift (triangles) are plotted as a function of frequency (Bode plot). DiPhyPC bilayer in 0.1 M KCl solution at bias potentials of +300 mV (green), 0 mV (red), -300 mV (blue), and -400 mV (black).

constant resulting from the separation of the τ_{RC} for the spacer and τ_{RC} for the membrane, but this particular surface has an effective membrane resistance too high to see the impedance behavior of the tether [192, 354]. At the extreme potentials, -0.3 V and -0.4 V, O_2 reduction begins to contribute to the low frequency portion of the spectra. However, the faradaic effects for O_2 reduction were ignored for the purposes of the simulations.
To extract further information from these data, they were analyzed with an equivalent circuit consisting of a solution resistance R_{ex} in the reservoir, in series with the membrane, which is modeled by a parallel resistance R_{mem} and capacitance C_{mem}, and a capacitance C_{sr} representing the spacer region (Fig. 5.59 inset). C_{mem} appears to be nearly constant at $\sim 0.7\ \mu F cm^{-2}$ over the entire potential window. R_{mem} shows high background impedance of the membrane in the order of $M\Omega cm^2$. Moreover the resistance peaks at ~ 0 V, decreasing both at positive and negative potentials. Qualitatively, this behavior can be considered in terms of anions which should be attracted to the electrode surface at positive potentials and cations to be attracted at negative potentials. It is important to note that the position of the maximum is highly sensitive to the individual sample preparation and can vary by as much as 200 mV for any given surface.

5.9.0.2 Simulation Procedure

Ion transport through biological [355] and electrochemical [356, 357] interfaces has a significant history of theoretical development, which is directly applicable to tBLM systems. The method used herein for calculating the bioelectrochemical response of ion transport non-specifically through the membrane utilizes the software package SPICE (MacSPICE or WinSPICE). The advantage of SPICE over simply integrating the equations arising from the various processes involved is the modular construction of the model that allows rapid alterations to the modeled parameters as well as the ability to simulate many different types of experiment (e.g. EIS or transient behavior) [197]. A further advantage in the system is real-time access to the multitude variables that arise in a model, such as the ion flux, ion concentrations, and electrical potential profiles, such as the potential drop across the membrane, relative to the potential drop across the tether.

5.9.0.3 Development of the Model Circuit

Models that describe passive ion permeation through phospholipid bilayers have been developed on the basis of the solubility-diffusion theory which, however, proved unsatisfactory particularly for small ions such as Na^+ [358]. Alternative models were introduced in terms of hydrated transient defects produced by thermal fluctuations of the lipid molecules. This model seems to apply for halide ions when the lipid layer is thin enough [358, 359]. However, a model of general applicability has so far not been agreed upon. Moreover, permeability coefficients, determined experimentally, vary considerably [358]. For the time being, we do not focus on particular mechanisms. Instead, the permeation of K^+ and Cl^- ions is considered in terms of a very general approach, using the integrated Nernst-Planck equation which relates the flux j_i of the ith ion (i.e. the flow per unit membrane area) to the permeability coefficient P_i, the ion concentrations $c_{i,1}$ and $c_{i,2}$ on the two sides of the membrane, and the membrane potential $\Delta\varphi_m$, defined as the difference in electrical potential on both sides of the membrane (for details of the derivation see ref. [197])

$$j_i = P_i \frac{z_i F \Delta\varphi_m}{RT} \frac{c_{i,1} \cdot exp[z_i F \Delta\varphi_m / RT] - c_{i,2}}{exp[z_i F \Delta\varphi_m / RT] - 1} \tag{5.11}$$

$$\Delta\varphi_m = \varphi_1 - \varphi_2 \tag{5.12}$$

Here z_i is the charge number of the ion, while R, T, and F have their usual meaning. The electrical current density associated with the ion flux is then given by:

$$i_i = z_i F j_i \tag{5.13}$$

Strictly speaking, activities should be used in equation 5.11, however, for the present purpose it is legitimate to approximate them by concentrations.

In terms of simulations with SPICE it is convenient to comprise the elements modeling the permeation of an ion through the membrane in a so-called subcircuit [197] as shown in Fig. 5.60. Parameters supplied to the subcircuit as nodes are the concentrations $c_{i,1}$ and $c_{i,2}$ of the ion on both sides of the membrane (c_1 and c_2 in Fig. 5.60) and the respective potentials φ_1 and φ_2 (phi_1 and phi_2), as well as the permeability coefficient P_i (P), the charge number z_i (z), and the temperature (T). The non-linear dependent voltage sources at nodes 1, 2, and 3 serve to program eq. 5.11, and the result obtained as voltage at node 3 is used to generate the ion flux j_i and the current density i_i through the controlled current sources between node pairs c_1, c_2 and phi_1, phi_2, respectively. The source code of the subcircuit is given in the Appendix.

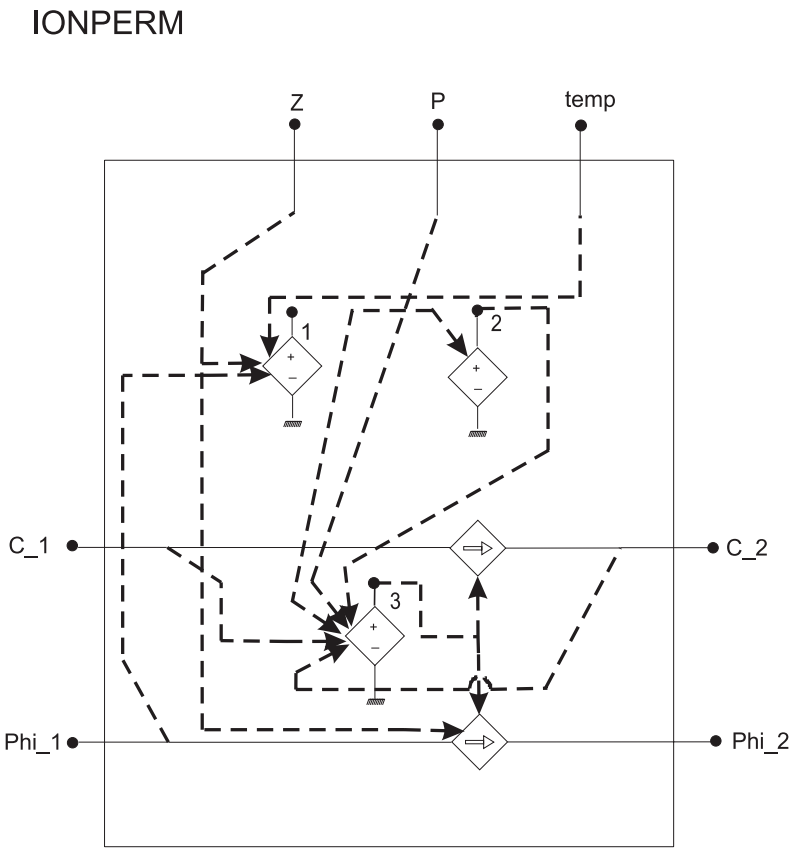

Figure 5.60: Subcircuit ionperm used to simulate ion permeation with SPICE. Broken arrows indicate parameters which control programmable voltage and current sources. For further explanation see text.

Two such subcircuits, one for each ion, are then inserted into the circuit used to simulate the behavior of the tBLM (Fig. 5.61). The constant voltage sources at nodes K_ex and Cl_ex define the constant concentrations $c_{K,ex}$x and $c_{Cl,ex}$ for K^+ and Cl^- in the reservoir,

respectively, while the capacitors at nodes K_in and Cl_in represent the volume of the sub-membrane space, and the voltages at these nodes then indicate the concentrations $c_{K,in}$ and $c_{Cl,in}$ of the respective ion in this space. The constant voltage sources at nodes P_K, P_Cl and z_K, z_Cl define respectively the permeability coefficient and the charge number for K^+ and Cl^-, while that at node temp defines the temperature. The electrical properties of the tBLM are modeled with the membrane capacitance C_mem, the capacitance of the spacer region C_sr, and the solution resistance R_ex in the reservoir. The voltages at nodes phi_in and phi_ex then represent the electrical potentials φ_{in} and φ_{ex} at the membrane surfaces facing the sub-membrane space and the reservoir, respectively. The voltage source v_bias provides the bias potential between the electrode and the reservoir, and in addition the sinusoidal AC voltage if needed. The voltage at node phi_el represents the electrical potential φ_{el} at the electrode/spacer region interface, and the ammeter vi_el between nodes bias and phi_el reports the current density i_{el} flowing through the electrode. Note that all potentials are with respect to a reference point in the reservoir, and that possible surface potentials are neglected.

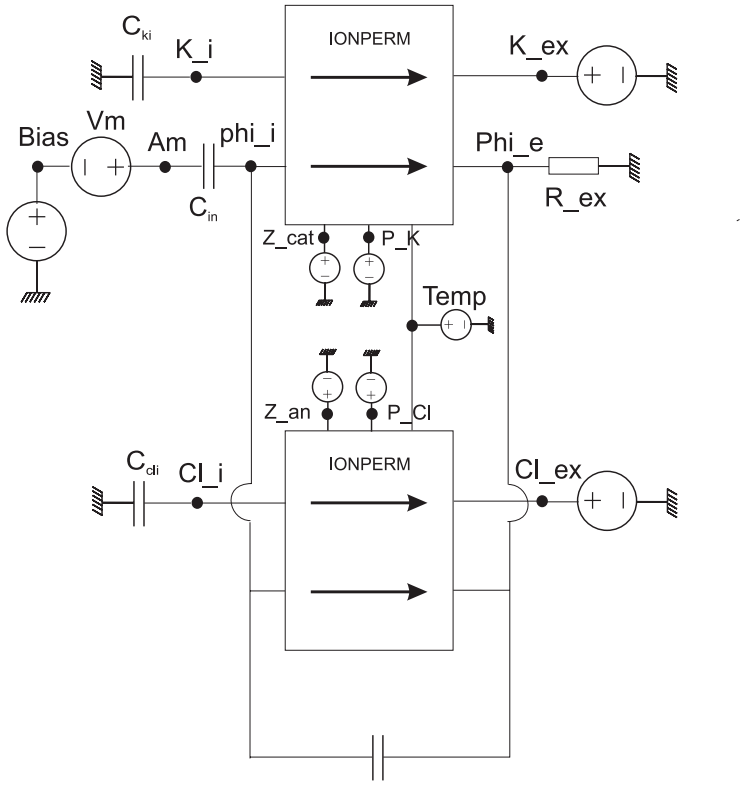

Figure 5.61: Circuit used for EIS simulations with SPICE. The element named ionperm represents the subcircuit shown in Fig. 5.60. For further explanation see text.

5.9.0.4 Assignment of Parameter Values

To perform simulations, values have to be assigned to the parameters of the elements in the circuit shown in Fig. 5.61. For the electrical elements C_{mem} = 0.67 $\mu F cm^{-2}$, C_{sr} = 5 $\mu F cm^{-2}$, and R_{ex} = 50 Ωcm^2 are used. Parameters pertaining to ion permeation are $C_{K,ex} = C_{Cl,ex}$ = 0.1 M, and 0.22 nL for the volume of the sub-membrane space, which can be estimated from the length of the spacer. Moreover, z_K = 1, z_{Cl} = -1, and the temperature is 25°C. The assignment of values to the permeability coefficients P_K and P_{Cl} for K^+ and Cl^- is less straightforward. However, relations between these coefficients and the membrane resistance can be established. According to eq. 5.11 the flux of the ith ion at equal concentrations on both sides of the membrane, $c_{i,ex} = c_{i,in} = c_i$, is

$$j_i = P_i z_i c_i F \Delta\varphi_m/(RT) \tag{5.14}$$

Hence the current density due to permeation of K^+ and Cl^- across the membrane at $c_K = c_{Cl} = c_{KCl}$ amounts to (cf. Eq. 5.13)

$$i = F(z_K j_K + z_{Cl} j_{Cl} = \Delta\varphi_m[F^2 c_{KCl}(z_K^2 P_K + z_{Cl}^2 P_{Cl})/(RT)] = \Delta\varphi_m/R_{mem} \tag{5.15}$$

and can be related to the resistance of the membrane R_{mem} determined under the particular conditions, as shown in eq. 5.15. A total permeability coefficient can then be defined as

$$P_{tot} = z_K^2 P_K + z_{Cl}^2 P_{Cl} = RT/(F^2 c_{KCl} R_{mem}) \tag{5.16}$$

and related to R_{mem}. With the ratio of coefficients $p = P_K/P_{Cl}$ we finally obtain

$$P_K = \frac{P_{tot} p}{(z_K^2 p + z_{Cl}^2)} \tag{5.17}$$

and

$$P_{Cl} = \frac{P_{tot}}{(z_K^2 p + z_{Cl}^2)} \tag{5.18}$$

P_K values reported in the literature vary between 10^{-9} cm/s and 10^{-13} cm/s [358]. On the other hand, $P_{Cl} = 7.5 \times 10^{-11}$ cm/s and $P_K = 5 \times 10^{-12}$ cm/s was reported for BLMs [3], hence $P_{tot} = 8 \times 10^{-11}$ cm/s and R_{mem} = 33 $M\Omega cm^2$ for c_{KCl} = 0.1 M (eq. 5.16) which is too large compared to the value of the membrane resistance obtained by EIS for the tBLM. In the course of the simulations it was found that $P_{tot} = 1.8 \times 10^{-10}$ cm/s ($R_{mem} \approx 14 M\Omega cm^2$) is a suitable value. P_K seems to be larger than P_{Cl} because the effect of negative bias potentials on impedance and phase shift at low frequencies is stronger than that of positive bias potentials (see Fig. 5.59), hence p = 10 was chosen.

5.9.0.5 Impedance Spectra from Simulations

Spectra were simulated in three steps essentially following the experimental protocol. First the tBLM was formed with no bias potential applied and 0.1 M KCl in the reservoir. In

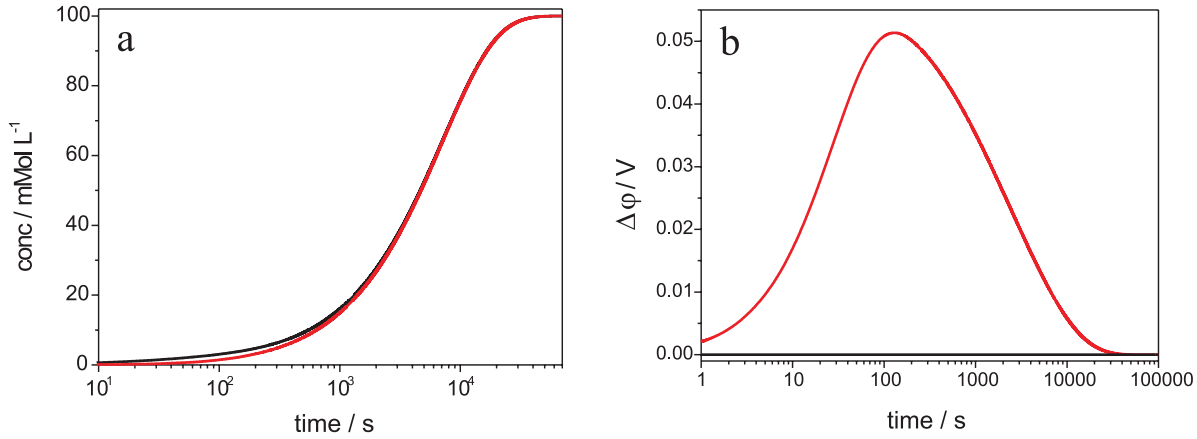

Figure 5.62: Simulation of ion equilibration during formation of the tBLM in 0.1 M KCl solution. (A) Ion concentrations $c_{K,in}$ (black) and $c_{Cl,in}$ (red) in the sub-membrane space, (B) potential differences $\Delta\varphi_m$ (red) and $\Delta\varphi_{sr}$ (black). Note the logarithmic time scale.

this step the ions partition into the sub-membrane space, which is simulated in a transient analysis with the voltage source *vbias* disconnected (see Fig. 5.61), using the initial conditions $c_{K,in} = c_{Cl,in} = \varphi_{in} = 0$. Since $P_K > P_{Cl}$ the flux of K^+ is initially faster than that of Cl^-, hence $c_{K,in}$ rises faster than $c_{Cl,in}$ (Fig. 5.62a), but also a current across the membrane ensues by which the membrane capacitance is charged and a membrane potential $\Delta\varphi_m = \varphi_{in} - \varphi_{ex}$ is built up (Fig. 5.62b). However, no potential difference $\Delta\varphi_{sr} = \varphi_{el} - \varphi in$ across the spacer region is formed because the electrode potential φ_{el} is floating. With increasing time $\Delta\varphi_m$ gradually collapses while $c_{K,in}$ and $c_{Cl,in}$ essentially coincide, and the equilibrium state is eventually attained where $c_{K,in} = c_{Cl,in} = 0.1$ M and $\Delta\varphi_m = 0$. Note that after about 12 hours $c_{K,in}$, $c_{Cl,in}$, and $\Delta\varphi_m$ have essentially reached their values at equilibrium.
In the second step different bias potentials were applied. Except for a zero bias potential, the ions then repartition and a new equilibrium state is attained. This is again simulated in a transient analysis, but with the voltage source vbias connected and using the initial conditions $c_{K,in} = c_{Cl,in} = 0.1$ M, and $\varphi_{in} = 0$. In a fast process with a relaxation time $\tau = R_{ex}(C_{mem}^{-1} + C_{sr}^{-1})^{-1} \approx 30\mu s$ (not shown in Fig. 5.63) C_{mem} and C_{sr} are charged, and the respective potential differences built up are as expected for two capacitors in series, i.e.

$$\Delta\varphi_m = \varphi elC_{sr}/(C_{mem} + C_{sr}) \tag{5.19}$$

$$\Delta\varphi_{sr} = \varphi elC_{mem}/(C_{mem} + C_{sr}) \tag{5.20}$$

The altered membrane potential initiates the considerably slower ion permeation, which discharges the membrane capacitance thus causing $|\Delta\varphi_m|$ to decrease. Concomitantly $|\Delta\varphi_{sr}|$ increases since φ_{el} is clamped to the bias potential, so that at equilibrium 97% of the applied potential drops across the spacer region (Fig. 5.63a). The time course of the ion concentrations in the sub-membrane space is biphasic. As expected, the final values of $c_{K,in}$ are larger and smaller while those for $c_{Cl,in}$ are smaller and larger than those at zero

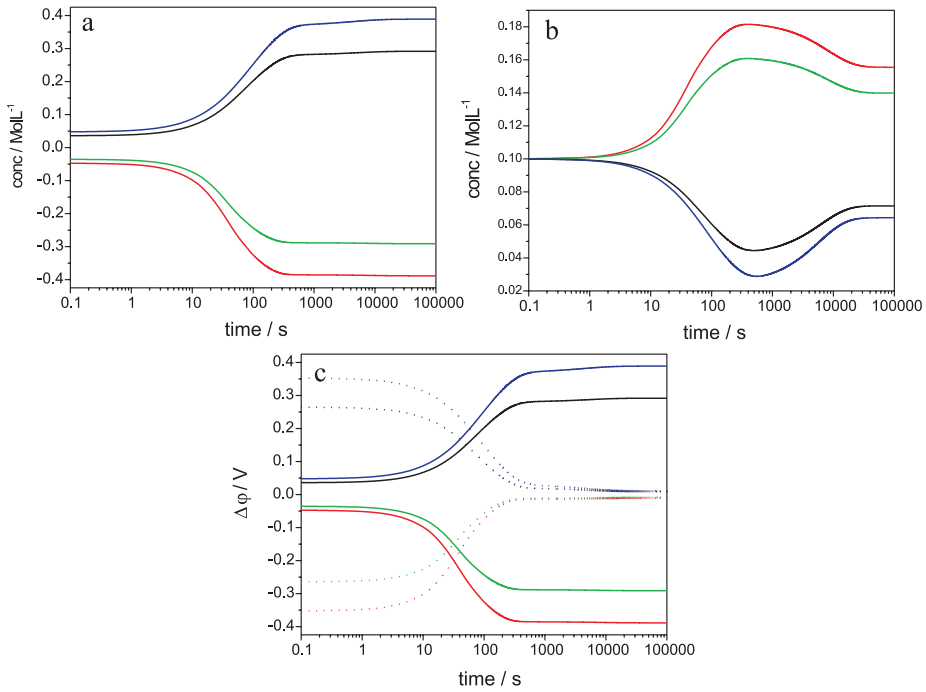

Figure 5.63: Simulation of the re-equilibration of ions when different bias potentials are applied to the pre-equilibrated tBLM. (A) Potential differences $\Delta\varphi_m$ (dotted lines) and $\Delta\varphi_{sr}$ (solid lines), ion concentrations $c_{K,in}$ (B) and $c_{Cl,in}$ (C) in the sub-membrane space for bias potentials of +400 mV (blue), +300 mV (black), -300 mV (green), and -400 mV (red). Note the logarithmic time scale.

bias potential for positive and negative bias potentials, respectively (Figs. 5.63a and b). Again, it takes about 12 h for the variables $c_{K,in}$, $c_{Cl,in}$, $\Delta\varphi_m$, and $\Delta\varphi_{sr}$ to reach values close to those at equilibrium.

As a control the simulations in both steps were repeated with different values for P_{tot} and p. This altered the time courses of the variables, but the constant values eventually reached for all variables were always those shown in Figs. 5.62 and 5.63, as it should be for true equilibrium states. Moreover, simulations in step 2 were performed with different values for C_{mem} and C_{sr}. Varying C_{mem} at a constant $C_{sr} = 5\mu F cm^{-2}$ has very little effect on the time courses of $c_{K,in}$ and $c_{Cl,in}$ yielding essentially the same result as shown in Figs. 5.63a and b. The potential differences formed in the fast initial phase differ (cf. eq. 5.19 and 5.20) but the constant values eventually reached are practically equal to those shown in Fig. 5.63a. On the other hand, varying C_{sr} at a constant $C_{mem} = 0.67\mu F cm^{-2}$ yields similar time courses for $c_{K,in}$ and $c_{Cl,in}$, but with equilibrium values which vary considerably depending on the particular value of C_{sr}. However, the potential differences, starting from the values according to eq. 5.20, reach values at equilibrium which are close to those shown in Fig. 5.63b, indicating a potential drop across the spacer region between 99 and 91% of the applied potential for C_{sr} between 2.5 and 20 $\mu F cm^{-2}$, respectively.

In the third step EIS was performed. It has been shown previously that the ac analysis implemented in SPICE is not suitable for simulating the spectra (15), hence every single frequency has to be simulated separately in a transient analysis, using the final values of $c_{K,in}$, $c_{Cl,in}$, and φ_{in} from the simulations in the second step as initial conditions. A sinusoidal AC voltage with an amplitude of 10 mV and the given frequency is added to the respective bias potential applied by the voltage source v_bias (Fig. 5.61). The AC voltage elicits oscillations of $c_{K,in}$, $c_{Cl,in}$, $\Delta\varphi_m$, and $\Delta\varphi_{sr}$, whose baselines, except for that of $\Delta\varphi_m$, initially change with time (Fig. 5.64a and b). When constant baselines are reached the current density i_{el} and the electrode potential φ_{el} (Fig. 5.64c) are used to calculate the impedance and the phase shift by means of a nonlinear fit program, and the spectra thus obtained for different bias potentials are shown in Fig. 5.65. In the case of zero bias potential both impedance and phase shift agree well with the experimental data (Fig. 5.59), except for a deviation in phase shift at frequencies larger than 20 kHz whose reason is not yet known. This also confirms that 1.8×10^{-10} cm/s is a proper value for P_{tot}. However, only a slight dependence of the phase shift on the applied bias potential at low frequencies is detectable and even in the wrong direction for positive potentials, while hardly any change in impedance occurs, both in contrast to the experimental data. Choosing p values larger than 10 has hardly any effect, while decreasing p diminishes the existing slight dependence of the phase shift on the bias potential. Hence it is concluded that the decrease in membrane resistance for positive and negative bias potentials and the corresponding differences in phase angle at low frequencies cannot be explained by the different ion concentrations in the sub-membrane space and different but constant permeabilities for K^+ and Cl^-.

The observed behavior of the tBLM is most likely due to a dependence of the permeability on the membrane potential. Such a dependence can arise if ion transport occurs through pores, which result from thermal fluctuations of the lipid molecules. Potential pulse experiments with UO_2^{2+}-modified BLMs have shown that the formation rate constant of pores $k_{p,f}$ is dependent on the membrane potential, i.e. $k_{p,f} \propto exp[(\Delta\varphi_m/K_s)^2]$, where K_s is a scaling factor [360]. The resealing of the pores is a first order process with a rate constant $k_{p,f}$ which appears to be independent of $\Delta\varphi_m$, hence the number of pores at steady state is proportional to $exp[(\Delta\varphi_m/K_s)^2]$. Since the total permeability of the membrane is proportional to the number of pores

$$P_{tot}(\Delta\varphi_m) = P_{tot}(0)[(\Delta\varphi_m/K_s)^2] \tag{5.21}$$

where $P_{tot}(0)$ denotes the total permeability coefficient at $\Delta\varphi_m = 0$ arising from the intrinsic steady state number of pores.

Simulations of EIS spectra were performed with P_{tot} in eq. 5.16 substituted from eq. 5.21, and with $P_{tot}(0) = 1.8 \times 10^{-10}$ cm/s and $p = 10$ as before. Since the actual values of $k_{p,f}$ and $k_{p,r}$ are not known and eq. 5.21 pertains to the steady state of pore formation only, a constant value for $\Delta\varphi_m$ is used as an approximation and set equal to the value reached at equilibrium in step 2. With K_s adjusted to 9.3 mV the result shown in Fig. 5.66 is obtained. The simulated spectra now satisfactorily represent the experimental data,

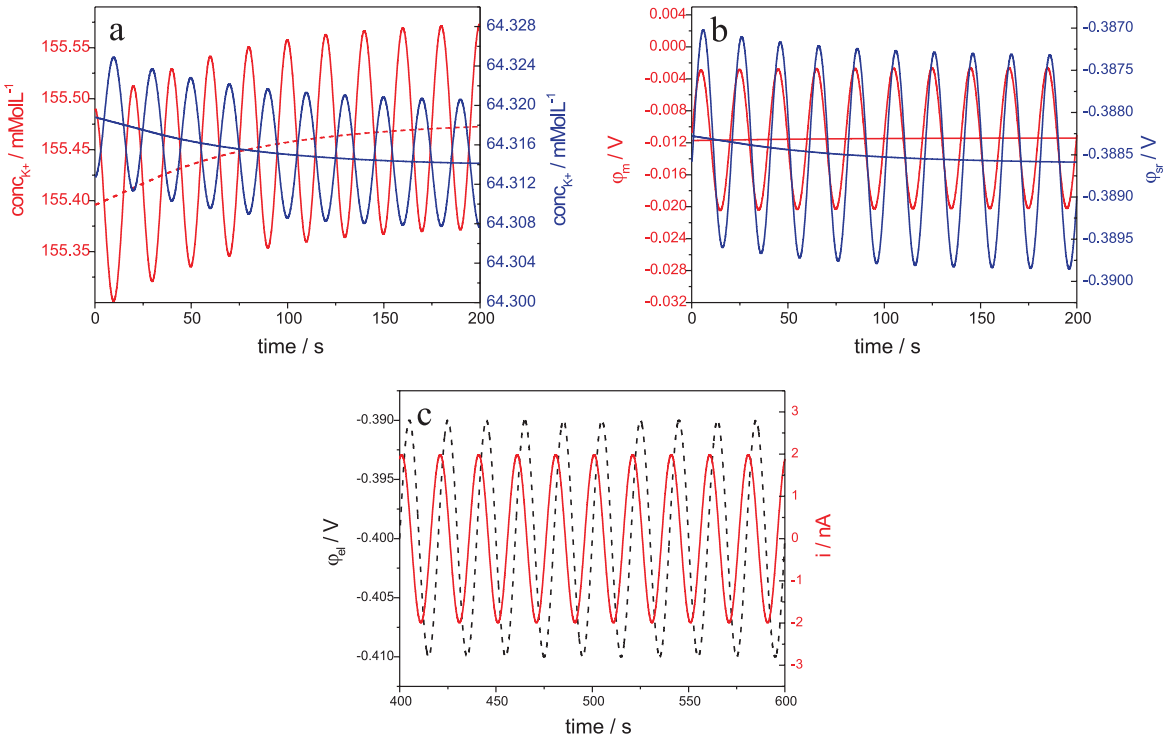

Figure 5.64: Example for the simulated response of ion concentrations (A) and potential differences (B) to a sinusoidal AC voltage. Initially the baselines (broken line) of the some oscillations vary. When constant baselines are reached the current density i_{el} and the electrode potential φ_{el} (C) are analyzed for impedance and phase shift. Bias potential -400mV, AC amplitude 10 mV and frequency 50 mHz

particularly when taken into account that O_2 reduction contributes to the low frequency portion of the experimental spectra at bias potentials of -0.3 V and -0.4 V.

5.9.0.6 Conclusion

The benefit of SPICE is the possibility to highlight single processes and parameters as a function of different variables. This helps to understand the system such as the tBLM under the influence of various conditions. It can be deduced from the simulations, for example, that the basic process of the equilibration of monovalent ions due to passive ion permation can take quite a long period of time of up to several hours assuming even moderate permeabilities. Passive ion permeation plays a role in all kinds of electrochemical experiments with tethered bilayer membranes.

Another significant result is the distribution of potential differences across the layer structure following the application of different bias potentials. Only in the first rapid phase of ion redisribution, the overall potential drops mainly across the lipid membrane as intuitively expected from the higher restistance of the lipid bilayer as compared to the aqeous-like

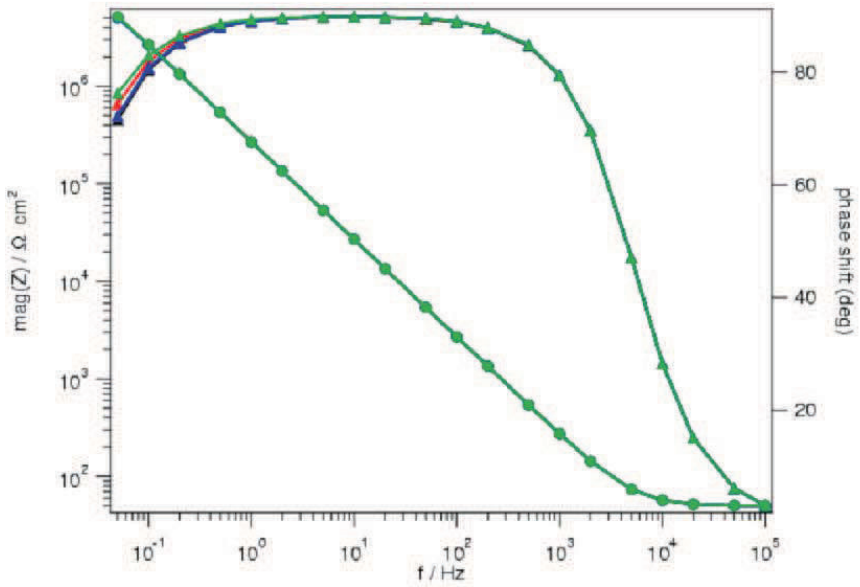

Figure 5.65: Bode plot of EIS spectra simulated for different bias potentials with constant ion permeabilities. Color code as in Fig. 1, i.e. +300 mV (green), 0 mV (red), -300 mV (blue), and -400 mV (black). $P_{tot} = 1.8 \times 10^{-10}$ cm/s and p = 10.

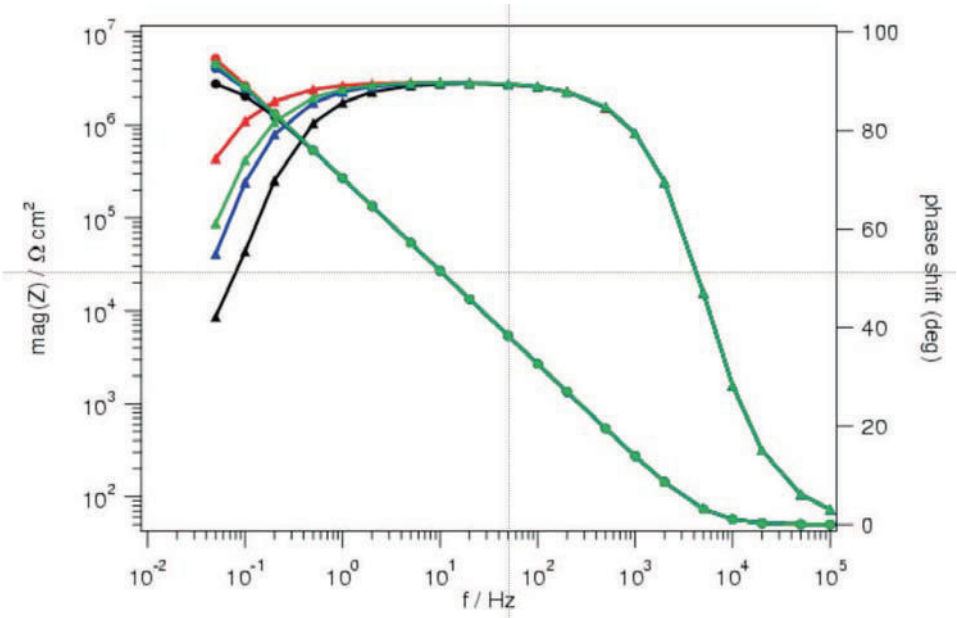

Figure 5.66: Bode plot of EIS spectra simulated for different bias potentials but with ion permeabilities which depend on membrane potential. Color code as in Fig. 5.59, i.e. +300 mV (green), 0 mV (red), -300 mV (blue), and -400 mV (black). Dependence of P_{tot} on $\Delta\varphi$, according to eq. 5.21 with $P_{tot}(0) = 1.8 \times 10^{-10}$ cm/s, $K_s = 9.3$ mV, and p = 10.

sub-membrane layer. However, in the course of the accumulation of ions in the vicinity of the electrode, the potential drops to the larger extent across the sub-membrane space, where the potential drop across the sub-membrane space is generated by the charge separation between the electrode and the adjacent layer of accumulated ions.

The parameter directly accessible from EIS spectra is the total permeability of ions across the bilayer of the tBLM. It was shown to be more than one order of magnitude higher ($2 \times 10^{-10} cm/s$) than the ones reported for freely suspended BLMs ($8 \times 10^{-11} cm/s$), however, well within the range of values reported for P_{K^+} for all kinds of bilayer membranes [358, 359]. A very convenient way to learn about the ratio of permeabilities of anions and cations, for example $p = P_K/P_{Cl}$, is to carry out EIS spectra as a function of bias potentials. The particular experiment displayed in Fig. 1 could best be modeled with $P_{total} = 1.8 \cdot 10^{-10}$ and a ratio $p = P_K/P_{Cl} = 10$, unusual as compared to BLMs.

This unusual high ratio needs to be reconsidered in terms of another interesting result, namely that a permeability independent from potential does not seem sufficient to describe the potential dependence of EIS spectra. This result is interesting from the mechanistic point of view because a potential dependence of the permeabilities would be in accordance with a pore model of ion permeation. This model predicts an increase of the number of pores with an increase in the membrane potential. The permeability would then no longer be independent of the potential in agreement with the simulations presented in this paper.

Utilizing ion permeability subcircuits within the tBLM network model will provide a more realistic baseline for the further examination of ion transport mechanics from proteinaceous ion channels, ion carriers and ion pumps that can be incorporated into tBLMs.

5.9.1 Protein-mediated Ion Transfer across Lipid Bilayer

5.9.1.1 Ion Transfer by Carriers

After having established a model for passive ion transfer across a lipid bilayer, the ion transport behavior of valinomycin, as the simples example of a membrane protein, was simulated.

Valinomycin is a cyclodepsipeptid which forms a complex with a single monovalent cation with a preference for K^+. The structure (Fig. 5.67) of the complex somewhat resembles a cage with the potassium in the center, stabilized by interactions with ester carbonyls (see Fig. 5.67). Valinomycin is a ion carrier, whereas the valinomycin-K^+ complex acts as a hydrophobic ion which can easily cross the bilayer.

Figure 5.68 shows the Bode plots of a K^+- titration experiment. To obtain different K^+ concentrations, aliquots of a KCl stock solution were stepwise added and impedance spec-

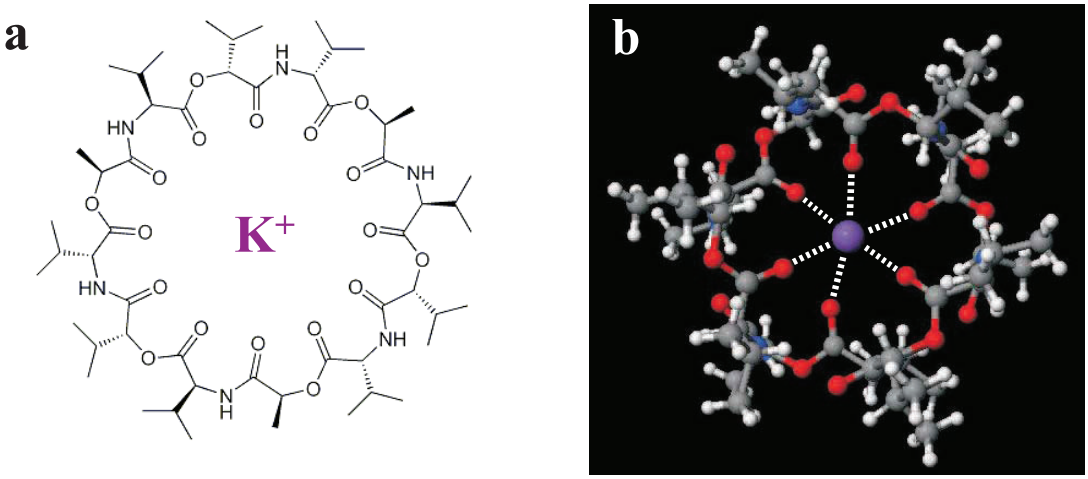

Figure 5.67: (a) Structure of the K^+-Valinomycin complex. (b) 3D structure of the complex [361].

tra are taken for each K^+ concentration. Experimental details are shown elsewhere [191]. From the results it is evident that the impedance decreases with increasing K^+ concentration.

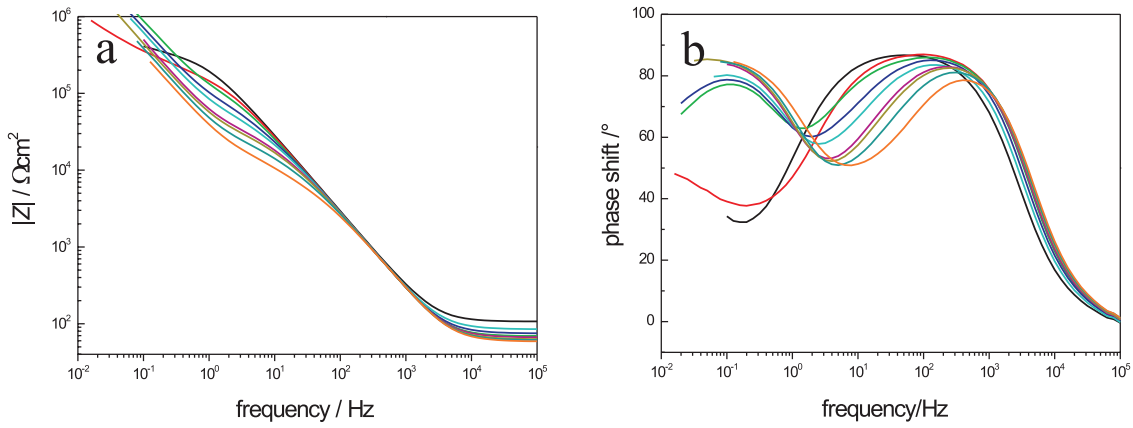

Figure 5.68: Bode plots of Valinomycin incorporated in a tBLM in a 0.1 M NaCl and a valinomycin concentration of $c_{val,0} = 4 \times 10^{-6}$ M. The KCl concentration was stepwise increased: 0 (black), 0.02 (red), 0.04 (green) 0.09 (blue), 0.19(light cyan), 0.39 (violet), 0.89 (dark yellow), 1.89 (cyan), 6.89 (orange) mMolL^{-1}.

In order to simulate these results a subcircuit for Valinomycin was designed, which is shown in figure 5.70. The valinomycin subunit utilizes the kinetic scheme for K^+ transport first proposed by Stark et al. [362]. In this model valinomycin exists in six different states (nodes

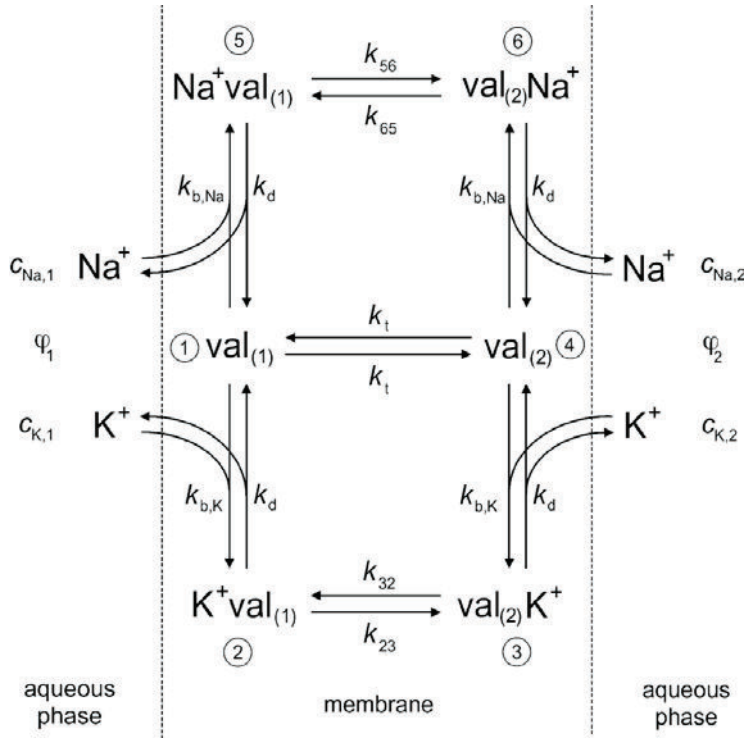

Figure 5.69: Schema for valinomycin-mediated K^+ transport according to Stark et al. [362]. $c_{K,1}$, $c_{K,2}$, $c_{Na,1}$ and $c_{Na,2}$ denote the K^+ and the Na^+ concentrations respectively. φ_1 and φ_2 are the two Galvani potantials in the two aqueous phases.

1-6). Nodes 1 and 4 represent uncomplexed valinomycin at the interior spacer-membrane interface and the membrane-solution interface, respectively. Nodes 2 and 3 represents the complimentary complexed states with K^+. Taking into account the small Na^+-transport activity, two more states 5 and 6, with represent the complexation and transition of Na^+, however with a much smaller binding constants than K^+. Valinomycin incorporated into the membrane can adopt two conformations for each ion, indicated by the subscripts 1 and 2, which are able to bind K^+ and Na^+ from and release it to the adjacent aqueous phases. k_{b,K^+} and k_{b,Na^+} are the binding rate constant for K^+ and Na^+, respectively, whereas k_{d,K^+} and k_{d,Na^+} are the dissociation rate constant of the complex formation. The rate constants k_{23} and k_{32} for the transition between the two conformation of the charged K^+/valinomycin complex is given by:

$$k_{23} = k_t \cdot exp(F(\phi_1 - \phi)/(2RT)) \tag{5.22}$$

$$k_{32} = k_t \cdot exp(-F(\phi_1 - \phi)/(2RT)) \tag{5.23}$$

with k_t being the transition rate constant and ϕ_1, ϕ_2 the potentials in the adjacent aqueous phases. The same formalism holds for the K^+/valinomycin complex:

$$k_{56} = k_t \cdot exp(F(\phi_1 - \phi)/(2RT)) \tag{5.24}$$

$$k_{65} = k_t \cdot exp(-F(\phi_1 - \phi)/(2RT)) \tag{5.25}$$

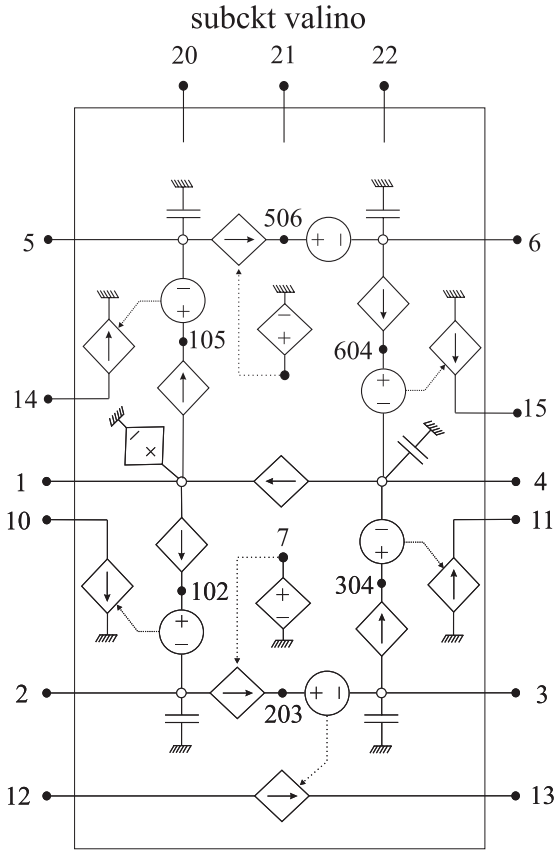

Figure 5.70: Valinomycin subcircuit. The mole number of valinomycin in the membrane and the temperature are supplied as voltages to nodes 20 and 21, respectively. The concentrations $c_{K,1}$, $c_{K,2}$, $c_{Na,1}$ and $c_{Na,2}$ for the K^+ and Na^+ concentrations are represented by voltages at nodes 10, 11 and 14, 15, respectively. The Galvani potentials φ_1 and φ_2 are represented by voltages at nodes 12 and 13.

The parameter values used in the simulation are those given in ref. [362, 191], $k_b = 3 \times 10^3 M^{-1}s^{-1}$; $k_d = 5 \times 10^4 M^{-1}s^{-1}$; $k_t = 2 \times 10^4 M^{-1}s^{-1}$. The K^+ concentration c_1 and c_2 in the two aqueous phases are applied as potentials to nodes 10 and 11, whereas the Na^+ concentration are applied as potentials to nodes 14 and 15. The current through the branches attached to these nodes represent the flows of K^+ and Na^+ into and out of the membrane, respectively. The potentials ϕ_1 and ϕ_2 are applied as potentials to nodes 12 and 13 as well as 16 and 17 for both ions. The charge between these nodes indicates the transfer of charge across the membrane due to the K^+ and Na^+ transport.

Using the modular strategy provided by SPICE, the subcircuit of valinomycin (fig. 5.71) was included into the ion permeability subcircuit that was introduced in the previous section. The simulated Bode plot can be seen in figure 5.71. The calculation represent reasonably well the experimental data, showing an decrease of resistance as a function of the added K^+. Furthermore the influence the Na^+ binding constants is shown to have an

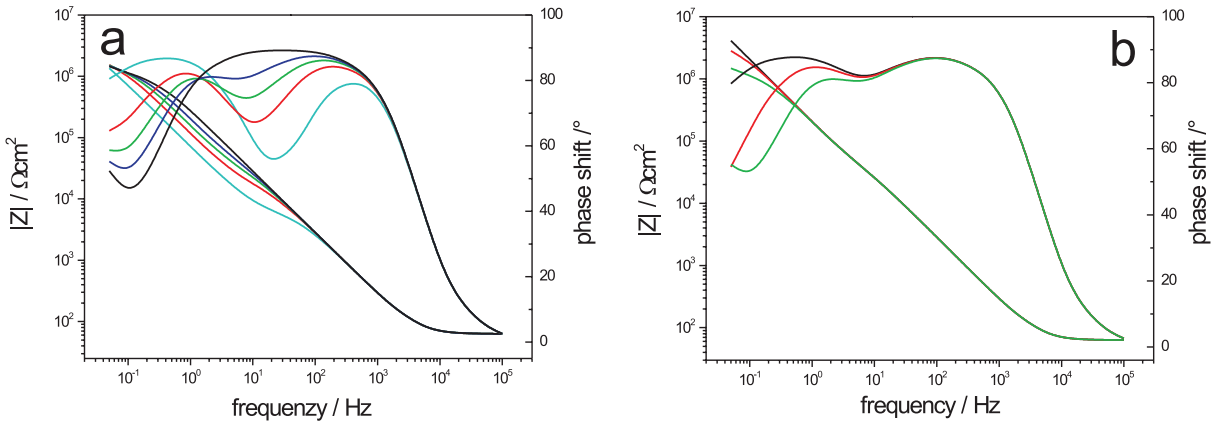

Figure 5.71: Simulated Bode plots of valinomycin incorporated in a tBLM at a potential of 0.2 V vs. NHE. The valinomycin concentration was set to $c_{val} = 4\mu M$ with a binding constant of $k_{b,K} = 500 s^{-1}M^{-1}$. (a) Variation of the KCl concentration ($k_{b,Na} = 0.2 s^{-1}M^{-1}$)): 0 (black), 0.39 (blue), 0.89 (green), 1.89 (red) and 6.89 mMolL^{-1} (light cyan). (b) Dependency of the Bode plot on the Na^+ binding constant of valinomycin ($c_{K^+} = 1.89$ mMolL^{-1}): 0 (black), 0.06 (red) and (0.2) $s^{-1}M^{-1}$.

influence on the Bode plot (fig. 5.71b).

5.9.2 Simulation of the Active Ion Transport Process of CcO

After the successful incorporation of a simple membrane protein, valinomycin, into the tethered bilayer circuit it should also be possible to implement even more complex enzymes, such as the cytochrome c oxidase, into the modular SPICE construct. The aim would be to simulate the ET and ion transfer processes, to obtain information about the protein/membrane system that are not directly accessible, such as the shift in redox potential.

5.9.2.1 Simulation of Ni-mediated ET

This model simulation is introduced for the single purpose of showing the influence of the Ni^+/Ni^{2+} pair to the ET process between the electrode and the Cu_A of the CcO.

The simulation is based on a model enzyme which contains three redox centers corresponding to Ni^+/Ni^{2+}, Cu_A, and heme a. A simplified model reduced to three redox centers is utilized with the single purpose to demonstrate the role of the Ni^{2+}/Ni^+ redox pair as a transient acceptor/donator to the redox potentials of the nearest next redox centers. The enzyme with different redox states of the centers are considered as different conformations numbered 1 through 8, as shown in Fig. 5.72. The rate of a transition due to ET between

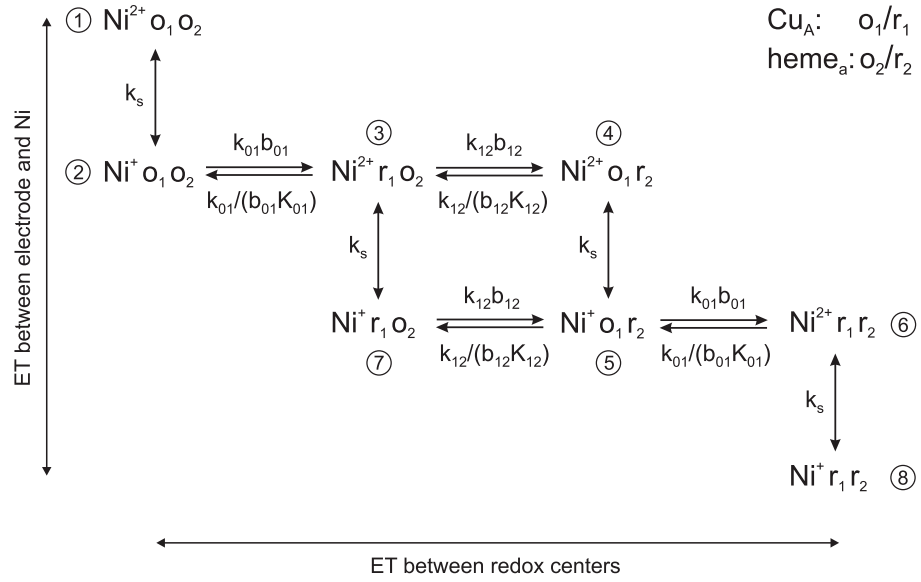

Figure 5.72: Conformations of the model enzyme used for simulating ET to the redox centers Cu_A and hemea *via* the Ni complex. Horizontal and vertical transitions indicate ET between redox centers and between the electrode and the Ni complex, respectively.

the electrode and the Ni-complex is governed by the Butler-Volmer equation (see chapter 4.1.1) with rate constant k_s. ET between the redox centers i and j is described by an intrinsic rate constant k_{ij}, a Boltzman factor b_{ij} comprising the electrical potential difference between the redox centers (cf. ref. [197]), and the equilibrium constant K_{ij} (see Fig. 5.72).

The model enzyme is placed in a ptBLM represented by a membrane capacitance, C_m, and a membrane resistance, R_m, a capacitance in the submembrane space, C_{in}, and a resistance of the external solution, R_{ex}. Simulations were performed by means of the network simulation program SPICE, and assuming the following values for the parameters: standard redox potentials E^0_{Ni} = -0.442 V [325], E^0_1 = 0.23 V (Cu_A), E^0_2 = 0.34 V (heme *a*); rate constants $k_s = 10^5 s^{-1}$, $k_{01} = 3 \cdot 10^5 s^{-1}$, $k_{12} = 10^4 s^{-1}$; ptBLM parameters $C_{in} = 73 \mu F/cm^2$, $C_m = 7.3 \mu F/cm^2$, $R_m = 12 M\Omega cm^2$, $R_{ex} = 60 \Omega cm^2$; and the number of enzymes per area $N_e = 10 pmol/cm^2$.
The simulated current density as a function of bias potential (Fig. 5.73), which represents the baseline-corrected CV of the model enzyme, displays a peak at -270 mV, in agreement with the experimental data. The corresponding probabilities of the conformations with different redox states as a function of bias potential are shown in Fig. 5.74. It is evident that the probabilities of the conformations with Ni in the reduced state do not exceed 6×10^{-8} (see Fig. 5.74)b), which indicates that the Ni complex is merely a transient electron acceptor.

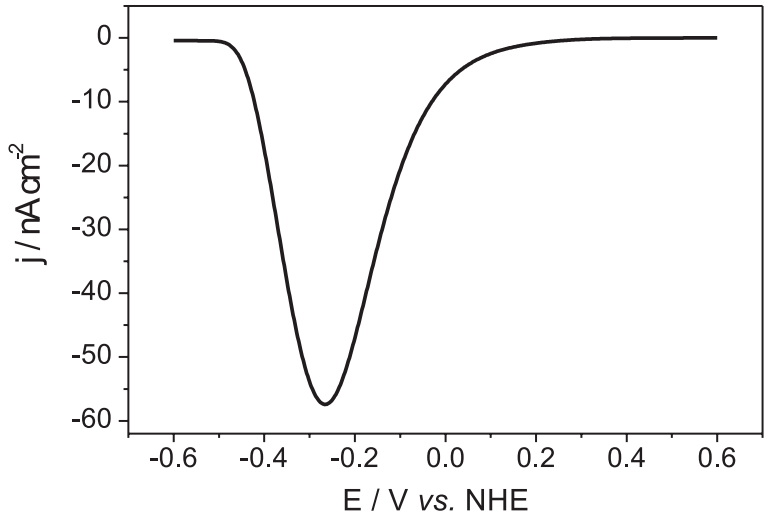

Figure 5.73: Simulated current density as a function of bias potential representing the baseline-corrected CV of the model enzyme, scan rate $\nu = 0.01$ Vs^{-1}.

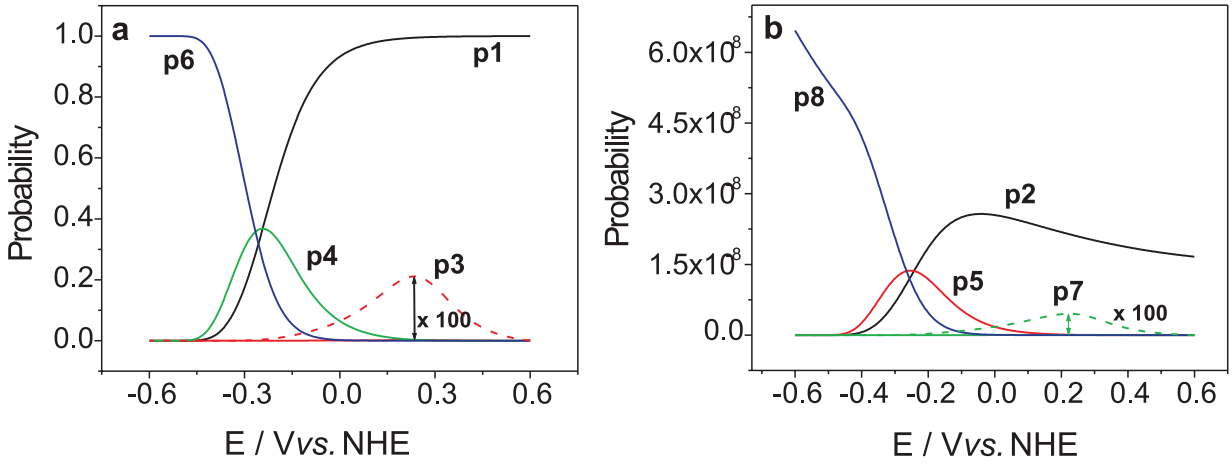

Figure 5.74: Probabilities of the conformations of the model enzyme (cf. Fig. 5.72) as a function of bias potential. (a) Conformations with Ni^{2+}: 1 (black), 3 (red, dashed line enlarged by a factor of 100), 4 (green), 6 (blue), and (b) conformations with Ni^{+}: 2 (black), 5 (red), 7 (green, dashed line enlarged by a factor of 100), 8 (blue).

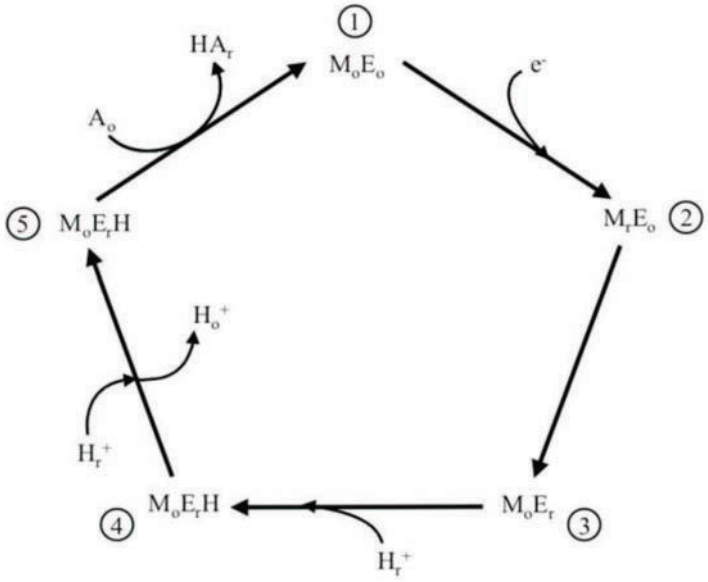

Figure 5.75: Simplified model for CcO consisting of 5 states. The model comprises a one-electron transfer, one proton uptake and one transfered proton.

5.9.3 Simulation of Proton Translocation by Cytochrome c Oxidase

Figure 5.75 shows a simplified 5 state model of cytochrome c oxidase (E), including the transition Ni center (M). Starting with an one-electron transfer step the fully oxidized state M_oE_o is transferred into the reduced transient state M_rE_o, with the Ni center being reduced. The electron is further transferred to the Enzyme forming the M_OE_r state, which is able to take up an charge compensating proton (M_OE_rH state). The next step is a proton translocation across the membrane. The last step is the reduction of oxygen[15] into water, regenerating the initial state of the simplified enzymatic cycle.

Figure 5.76 shows the respective subcircuit for the simulation of the proton transfer process by CcO. The subcircuit includes all experimental parameters, such as the surface concentration N_e (node 20), the redox potential of the enzyme E_O (node 22) and the Ni center E_{OM} (node 21), the temperature t (node 25) or the pH value of the bathing solution (node 24), as well as the intrinsic rate constant k_0 (node 23), determined by CV scan rate studies of time resolved vibrational spectroscopy.

A simulated voltammogram is shown in Fig. 5.77. In agreement with experimental data two peaks can be simulated in the presence of oxygen, an electron transfer as well as an proton transfer peak. Assuming a standard potential for the chelated Ni complex of E^0_{Ni} = -0.5 V and a standard potential for the Cu_A of $E^0_{Cu_A}$ = 0.2 V, the ET peak appears at

[15]The notation A derives from the fact that oxygen acts as the electron acceptor in this enzymatic step

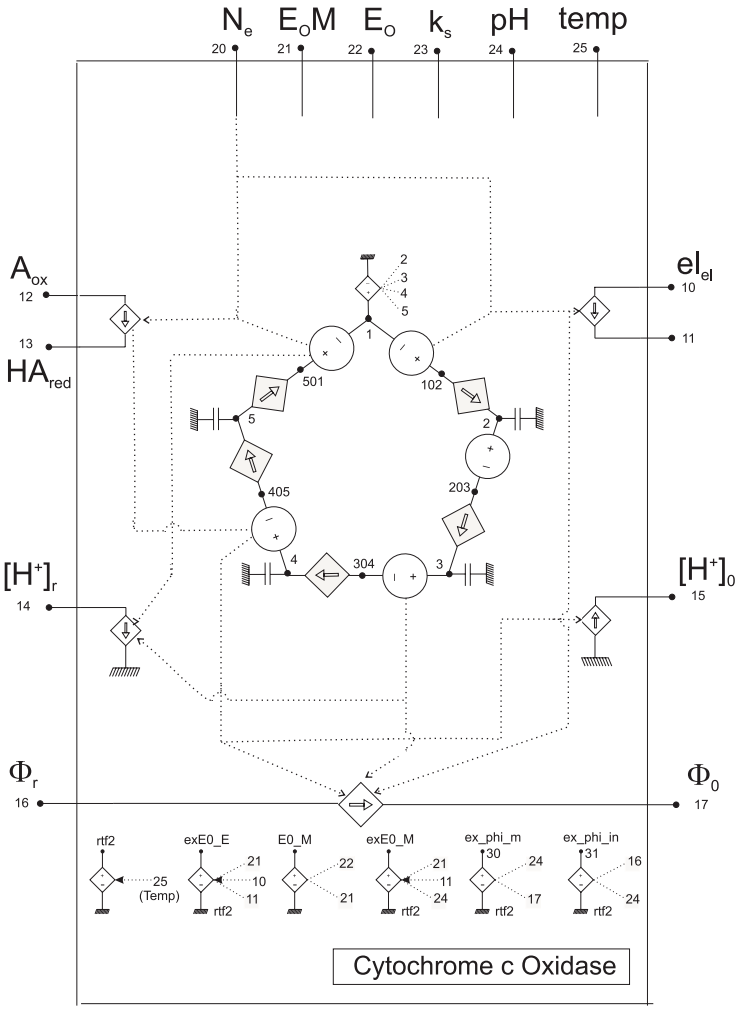

Figure 5.76: Subcircuit of the 5-state model for cytochrome c oxidase.

$E_{ET} = -0.25$ V and the proton transfer peak, coupled to reduction of H^+ to hydrogen, at $E_{H^+} = -0.75$ V. Although the ET peak is in high agreement with the measurements the proton peak is shifted to negative potentials. The reason for this downshift can be found in the simplified 5-state model, which accounts only for a one-electron transfer step coupled to a single proton uptake and a single proton translocation step.

Therefore a new and more detailed model for the enzymatic cycle was developed, utilizing the new mechanistic information about the proton translocation step (see section 3.4) as well as the kinetic rate constants of the ET transfer steps. This model is shown in figure 5.78 and includes four separated ET steps as well as four up taken and four transfered protons. The development of the respective source code is in preparation and simulations of this complex model are forthcoming.

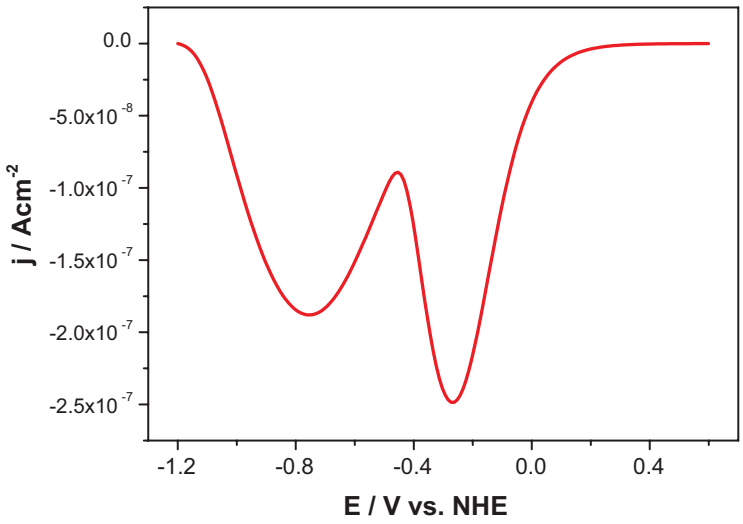

Figure 5.77: Simulated voltammogram, utilizing a 5-state model for CcO in the presence of oxygen.

5.9.3.1 Conclusion

Electron transfer as well as proton translocation could be convincingly simulated by SPICE simulations. The shift in the redox potential of CcO could be reproduced by a simplified model, demonstrating the influence of the transient Ni^{+}/Ni^{2+} state. By stepwise including kinetic as well as mechanistic information, provided by experiments, the CcO model can be further improved, to obtain more detailed predictions about the enzymatic cycle. This paves the way to further combine simulations with mechanistic and kinetic studies of immobilized membrane proteins, CcO in particular, in order to obtain a more detailed picture of their enzymatic activity.

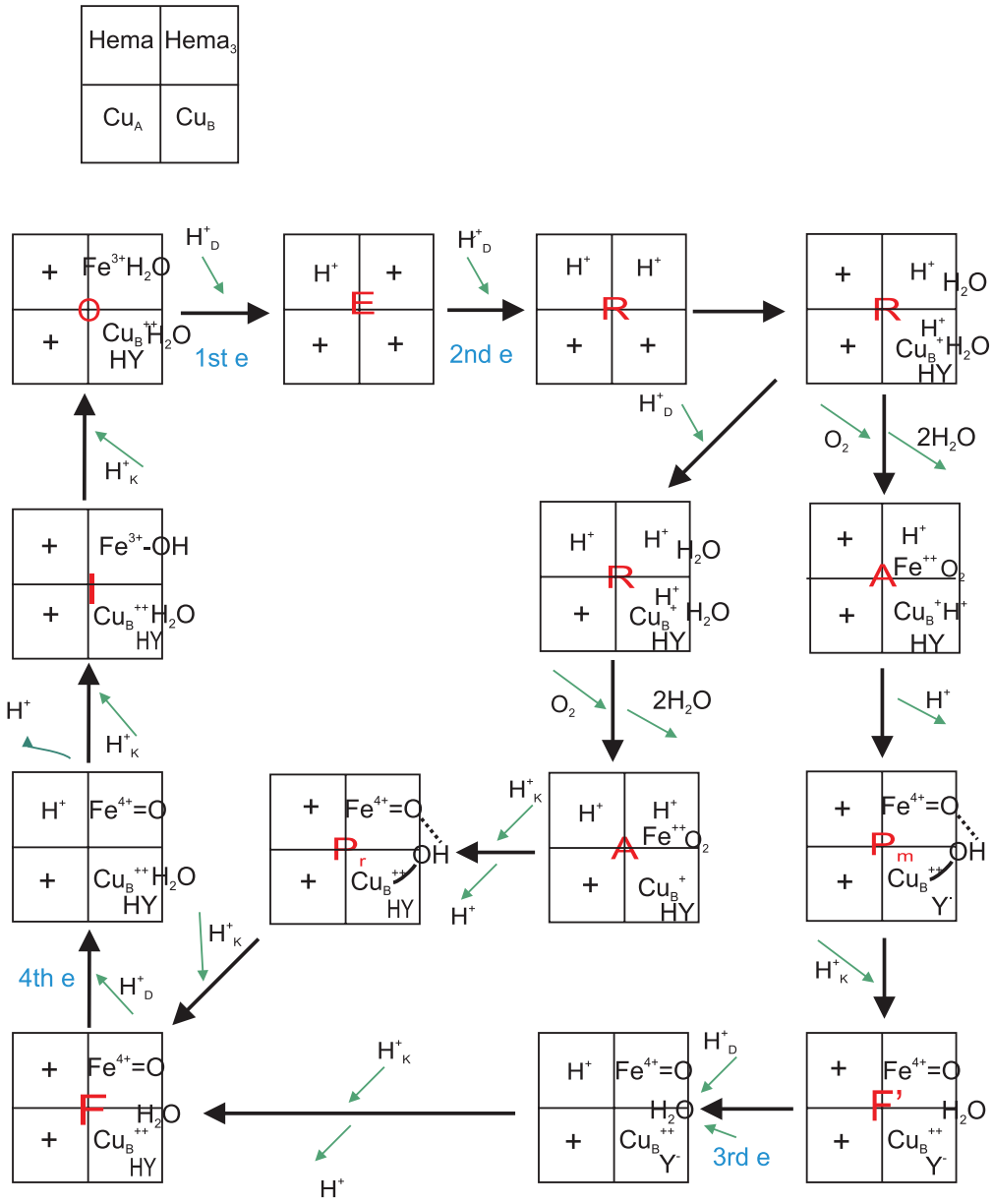

Figure 5.78: Detailed scheme of the enzymatic cycle of cytochrome c oxidase, including four ET steps, four protons taken up for the reduction of oxygen to water and four protons transferred. The models includes the fact that electron are only transferred across the membrane within the oxidative part of the enzymatic cycle. The squares, which are divided into four parts represents the CcO with its four redox centers (Cu_A, heme a, heme $a3$ and Cu_B). The respective state (compare chapter 3) of each step is indicated in red.

6 Conclusion

The novel concept of the protein-tethered bilayer lipid membrane has been shown to be a general approach for the investigation of immobilized membrane proteins under physiologically relevant conditions.

The most significant result of the present work is the bioelectronic coupling of cytochrome c oxidase (CcO) *via* the tethering structure consisting of a chelated metal ion (Ni^{2+}) and the π-system of Histidine. This electronic wire provides an effective electron pathway allowing for an ultra fast direct electron transfer (ET) ($k_0 > 4000s^{-1}$) to the redox sites of the protein, in the same order of magnitude as the ET rate between cyt c and Cu_A. Thus, electronic wiring permits experiments with biological relevance. The direct ET has been shown conclusively to be possible only when the CcO is immobilized in a ptBLM in a specific orientation with the natural electron entry site directed towards the electrode. As a consequence a kinetic analysis of the ET through all four redox sites was possible.

The fast ET to the proteins opened the possibility to use it as an electrochemical trigger for vibration spectroscopy. Setups for SERRS and SEIRAS measurements were designed to perform *in-situ* potential-dependent spectroscopy on the surface confined protein-monolayer. Surface enhanced resonance Raman spectroscopy (SERRS) provided information on the redox state, the ligation, spin and coordination state of the heme a/a_3 structure, whereas infrared reflection-absorption spectroscopy (SEIRAS) allowed to probe changes in the amino-acid environment of the active sites along the electron and proton pathways.

More importantly, the feasibility of direct electron transfer as a trigger for time resolved SEIRAS measurements was demonstrated. Time dependent changes of the redox state of all four redox centers could be detected. The rate constant of ET to Cu_A was in the same order of magnitude as the rate constant determined by electrochemistry.

The chelating surface architecture not only allows for electronic wiring. It also separates the protein as well as the lipid membrane from the surface providing a submembrane aqueous layer. This layer can serve as a reservoir for ions such as protons in the case of the CcO in the orientation mentioned above. Protons are pumped across the membrane when the protein works under turnover conditions, in the presence of oxygen. No proton pumping could be observed under anaerobic conditions. This finding was considered to have consequences for the mechanism of proton pumping.

The CcO immobilized in the inverted orientation was activated by cyt c, the natural sub-

strate of the CcO. Cyt c bound to the distal side of the protein/lipid layer appeared to communicate with the electrode through the entire layer structure. This was explained in terms of a gating mechanism with the formation an open heme pocket of the CcO. In the presence of oxygen, the enzyme showed a turnover rate comparable to the on in solution.

First attempts in analyzing ion transfer processes across tethered lipid bilayer systems, simulations were performed using the computer program SPICE. It is a software package, designed to analyze electronic circuits. SPICE can be used to analyze bioelectronic processes across membranes. The ultimate aim of such studies is the simulation of the enzyme cycle of CcO. However, to begin with, this is a much too complicated system. Therefore, more simple cases were treated first, e.g. passive ion permeation and potassium transport mediated by valinomycin. Crucial information were obtained also for cytochrome c oxidase, e.g. the potential drop across the inner submembrane layer rather than the lipid membrane. Furthermore a simplified model of the CcO was also simulated, showing the shift of the peak potential in the cyclic voltammetry experiments *vs.* the standard potential.

The principle goal of the present work to establish the protein-tethered bilayer lipid membrane as a novel platform to investigate complex membrane proteins was accomplished. The main advantage is the combined application of electrochemistry and spectroscopy, which has been convincingly demonstrated. With the advantages of site mutations, this new technology paves the way to future studies of a large variety of proteins under different conditions.

7 Future Directions

Utilizing the concept of the protein-tethered bilayer lipid membrane the kinetics of the direct ET to cytochrome c oxidase along the chain of redox centers could be determined under anaerobic conditions. However, in order to probe the complete enzymatic cycle, the enzyme has to be further investigated under aerobic conditions, preferably at a controlled oxygen concentration in the bulk solution. The the oxygen-bound states of the catalytic cycle could be investigated. Triggering the redox state of CcO *via* direct ET and probing the structural changes by Raman and infrared spectroscopies in a time resolved regime would give a detailed picture of the processes in the oxidative part of the catalytic cycle.

The kinetics of the binuclear center, which reduce oxygen to water, could be probed under steady-state conditions using a rotating disc electrode experiment. This would give rise to constant catalytic currents, giving quantitative information regarding the turnover rate. CcO could be investigated at various oxygen concentrations controlled either by a Clark electrode or by oxygen dependent dyes, as a parameter determining the kinetics of the catalytic reaction of the enzyme. Another important parameter is the pH value, which also has an influence on the kinetic of the single redox centers, in particularly of the hemes and the catalytic centers. Preliminary results has already been obtained and show a dependence on the standard potential of the redox centers as well as on the single ET rate constants. The proton translocation across the could be further visualized by 3D- laser scanning microscopy (LSM), probing the pH-dependent fluorescence change of dyes in the solution.

Another method to investigate the kinetic of the catalytic center on a single molecule basis would be the application of Scanning Electrochemical Microscopy (SECM). Preliminary experiments with the group of Prof. Wittstock (University of Oldenburg, Germany) have already shown the potential of these measurements. By approaching a conductive tip-electrode the mediated current flow to both reported orientations can be measured under various experimental conditions. Figure 7.1 shows different different experiments that can probe different aspects of enzymatic activity of CcO. The electron flow to the surface confined enzymes can be probed by the interaction and regeneration of an soluble electron mediator (Fig. 7.1a) that can shuffle electrons between the electrode an the tip. Protons can be specifically produced at the tip by reduction of hydrogen (Fig. 7.1b) permiting to probe the the active proton translocation process or to create oxygen by oxidizing water of OH^- at the tip to probe the kinetics of the catalytic oxygen reduction (Fig. 7.1c,d) [363, 364, 365, 366].

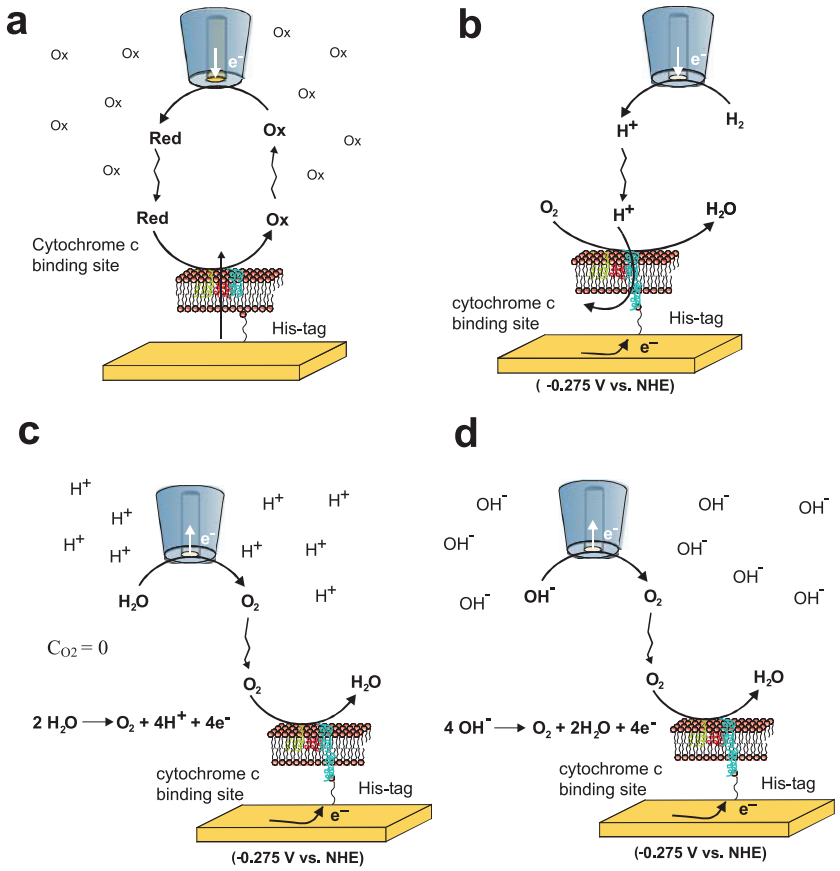

Figure 7.1: Proposed experiments with the Scanning electrochemical microscope (SECM) under various conditions. For details see text.

These approaches would open the field to the study of ET as well as catalytic turnover on a single molecule level. The advantage of a microscale tip-electrode is the steady state current, due to the inherent diffusion profile of the point-shaped surface.

The next step in order to study the proton pathway inside the protein would be the use of different mutants. The effect of mutations along the two proton pathways or in the vicinity of the active sites to the catalytic or kinetic properties of the enzyme can be directly probed in a analogous way to that described in this dissertation, by direct electrochemistry in combination with time resolved Raman and IR spectroscopies on the membrane protein.

Finally, the ptBLM concept is certainly not restricted to cytochrome c oxidase. This biomimetic architecture provides a general approach for the investigation of a wide variety of (redox-active) membrane proteins. As an example, the binding and reconstitution of a bacterial reaction center in a ptBLM (Fig. 7.2) as well as the direct electrochemical access to the inherent redox centers,are parts of a further investigation. Another possibility would be the immobilization of several membrane proteins (e.g. of the respiratory chain) into the

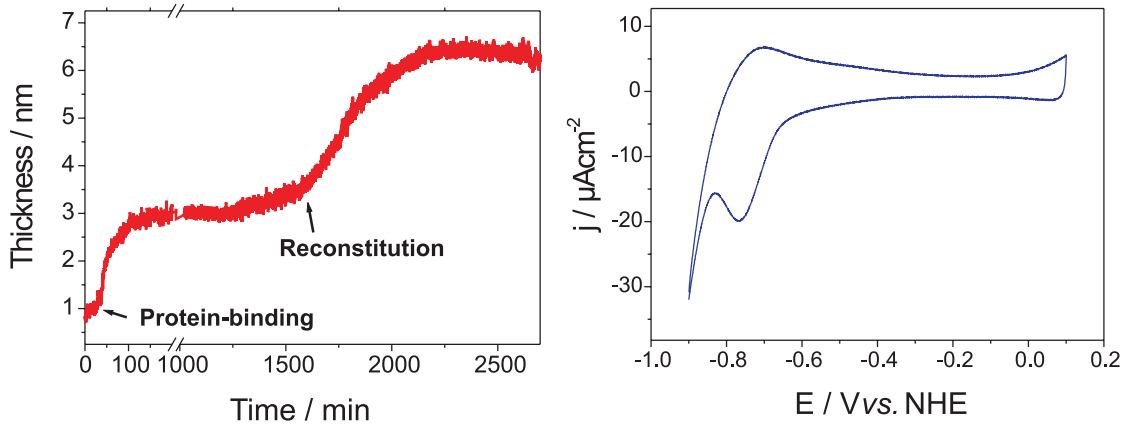

Figure 7.2: (a) Binding and reconsitution of the bacterial Reaction center into a ptBLM, probed by SPR. (b) Cyclic voltammetry, showing the direct electron transfer into the redox centers of the enzyme.

same ptBLM and to study their interaction.

Until now, sulfur chemistry has been employed in order to immobilize the ptBLM on gold or silver. By changing to silanes, the ptBLM architecture can be attached to on ultraflat silicon or on conductive semiconductors, such as indium-tin-oxide (ITO). This would be a great benefit for fluorescence measurements, where the fluorescence signal is (partially) quenched by an adjacent metal electrode. Single molecule fuorescence spectroscopy could provide insights into e.g. protein-protein interactions probed on the surface. Moreover, the insertion of small proportions of fluorescent enzymes, such as the light harvesting complex II, e.g. beside cytochrome c oxidase, could be used to measure *in-situ* the actively generated membrane potential by the change of the fluorescence or absorbance spectra due to the Stark-effect. Figure 7.3 shows first experimental results of the immobilization and reconstituition of the autofluorescent light harvesting complex. A further attemps would be to achieve an higher dilution in order to conduct single molecule experiments.

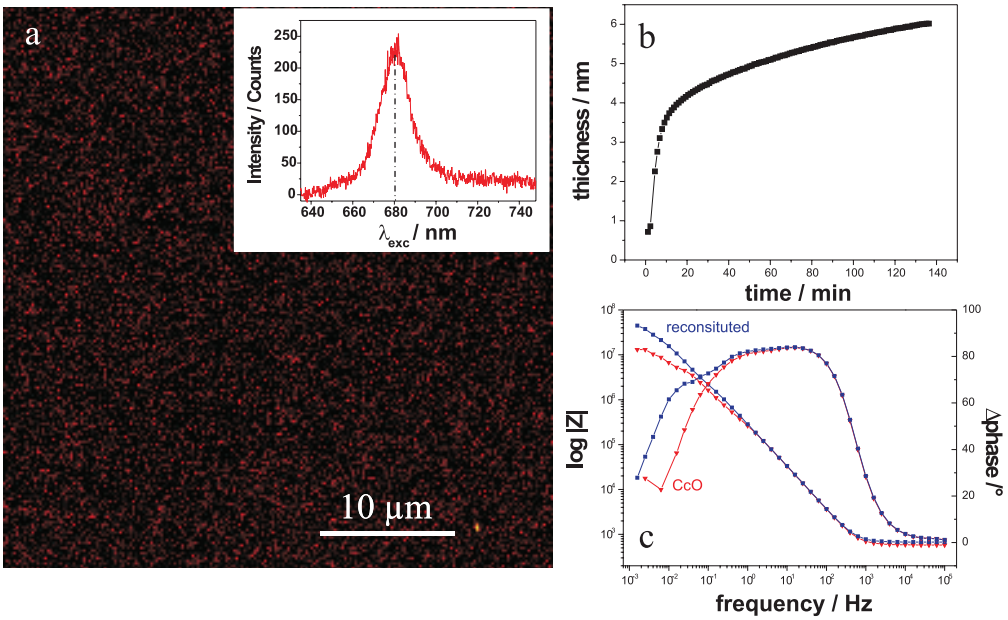

Figure 7.3: Immobilization of Light Harvesting Complex II (LHC II) on Silicon. a) Laser scanning microscopy picture of immobilized LHC II immobilized into a ptBLM on a Silicon wafer recorded with $\lambda_{exc} = 488$ nm. The inset shows the respective fluorescence spectra of the surface confined LHC II with an fluorescence maxima at $\lambda_{fluor} = 680$ nm. b) Binding curve probed by ellipsometry. c) EIS spectra of the LHC II layer before (red curve) and after (blue curve) reconstitution. (In cooperation with Asmoron Kibrom and Dr. Uli Jonas, MPIP Mainz)

9 Abbreviations

A	Area
AFM	Atomic force microscopy
AOM	Acusto-optical modulator
APD	Avalanche photodiode
ATR-FTIR	Attenuated total reflection Fourier-transform infrared spectroscopy
A.U.	Arbitrary units
B	Magnetic induction
BLM	Bilayer Lipid Membrane; Black Lipid Membrane
C	Capacitance [F]
CCD	Charge-coupled device
CN^-	Cyanide ion
CNLS	Complex non-linear least square fitting
CO	Carbon monooxide
CT	Charge transfer
CV	Cyclic voltammetry
d	Distance [m]
D	Electrical displacement
DPV	Differential pulse voltammetry
E	Potential [V]
E	Electrical field
E^0	Standard potential [V]
EIS	Electrochemical impedance spectroscopy
ET	Electron transfer
F	Faraday constants [$9.64846 \times 10^4 Cmol$]
FWHM	Full width at half maximum
H	Magnetic field
H_2O	Water
i	Current [A]
IR	Infrared
j	Current density [$A \cdot cm^{-1}$]
k	Boltzmann constants [$1.3806505 \times 10^{-23}\ J/K$]
k^0	Standard/intrinsic rate constant
kD	Kilo Dalton
LSP	Localized surface plasmon
m	Mass [g]

M	Molecular mass [g· mol^{-1}
n	Refractive index
N_A	Avogadro constants [$6.0221415 \times 10^{23} mol^{-1}$]
NA	Numerical apperture
NHE	Normal hydrogen electrode
ptBLM	Protein-tethered bilayer lipid membrane
OD	Optical density
pH	Potential hydrogenii / -log[H^+]
PMT	Photomultiplier tube
Q	Charge [C]
R	Reflectivity
	Resistance [Ω]
	Molar gas constants [8.31441 $Jmol^{-1}K^{-1}$
RDE	Rotating disc electrode
RR	Resonance Raman
RPM	Rotations per minute
SAM	Self-assembled monolayer
SECM	Scanning electrochemical microscope
SEIDAS	Surface-enhanced IR difference absorption spectroscopy
SEIRAS	Surface-enhanced infrared reflection absorption spectroscopy
SER(R)S	Surface-enhanced (resonance) Raman spectroscopy
SHE	Standard hydrogen electrode
SWV	Square wafe voltammetry
SP	Surface plasmon
SPR	Surface plasmon resonance
SPS	Surface plasmon spectroscopy
SPICE	Simulation Program with Integrated Circuit Emphasis
SU	Subunit
t	Time [s]
T	Temperature [°K] or [°C]
tBLM	Tethered bilayer lipid membrane
UV	Ultraviolett
XPS	X-ray photoelectron spectroscopy
Y	Admittance
Z	Impedance
ϵ	Dielectric constant
ϵ_0	Electric permittivity of vacuum [$8.854 \times 10^{-12} C^2 J^{-1} m^{-1}$
λ	Wavelength [nm]
$\Delta\nu$	Raman shift or Wavenumber [cm^{-1}]
Γ	Surface coverage [mol·m^{-2}]
Γ	Frequency [Hz]
μ_0	Permeability of free space

Proteins:

CcO	Cytochrome c oxidase
Cyt c	Cytochrome c
LHC II	Light harvesting complex II

Chemical compounds:

Ag	Silver (= *Agentum*)
$AgCl$	Silver chloride
Au	Gold (= *Aurum*)
ADP	Adenosine diphosphate
ATP	Adenosine triphosphate
$ANTA$	$N_{\alpha'}, N_{\alpha''}$-bis(carboxymethyl)-L-lysine or amino-nitrilotriacetic acid
Cl^-	Chloride ion
$DMSO$	Dimethylsulfoxide
$DPhyPC$	1,2-Diphytanoyl-sn-glycero-3-phosphocholine
DTP	dithio-bis-propionate
$DTSP$	Dithio-bis-(succinimidyl-propionate)
$EtOH$	Ethanol
H_2SO_4	Sulfuric acid
H_2O_2	Hydrogen peroxide
K^+	Potassiuim ion
KCl	Potassium chloride
K_3PO_4	Potassium phosphate
K_2HPO_4	Potassium hydrogen phosphate
$MeOH$	Methanol
Na^+	Sodium ion
$NaCl$	Sodium chloride
TSP	Thio-succinimidyl-propionic acid

References

[1] M. Gerstein and H. Hegyi. *FEMS Microbiol. Rev.*, 22:277–304, 1998.

[2] W.L. Smith., R.M. Garavito, and S. Ferguson-Miller. *J. Biol. Chem.*, 276:32393–32394, 2001.

[3] L. Stryer. *Biochemistry*, volume 4th Ed. Spektrum, New York, 1995.

[4] B. Ludwig, E. Bender, S. Arnold, M. Hattemann, I. Lee, and B. Kadenbach. *Chem Bio Chem*, 2:392–403, 2001.

[5] O. M. Richter and B. Ludwig. *Rev. Physiol. Biochem. Pharmacol.*, 147:47–74, 2003.

[6] P.L Yeagle and A.G. Lee. *Biochim. Biophys. Acta*, 1565:143, 2002.

[7] R.J. Bertz and G.R. Granneman. *Clin. Pharmacokinet.*, 32:210–258, 1997.

[8] W.E. Evans and M.V. Relling. *Science*, 286:487–491, 1999.

[9] M. Ingelman-Sundberg. *TRENDS in Pharmacological Sciences*, 25(4):193–200, 2004.

[10] J. Deisenhofer, O. Epp, K. Miki, R. Huber, and H. Michel. *Nature*, 318:618–624, 1985.

[11] H. Stahlberg, A. Engel, and A. Philippsen. *Biochem. Cell Biol.*, 80:563–568, 2002.

[12] J. Torres, T. J. Stevens, and M. Samso. *Trends Biochem. Sci.*, 28:137–144, 2003.

[13] J.U. Bowie. *Curr. Opin. Struct. Biol.*, 11:397–402, 2001.

[14] J. H. Hurley. *Chem. Biol.*, 10:2–3, 2003.

[15] S. H. White, A. S. Ladokhin, S. Jayasinghe, and K. Hristova. *J. Biol. Chem.*, 276:32395–32398, 2001.

[16] J. Vecer, P. Herman, and A. Holoubek. *Biochim. Biophys. Acta*, 1325:155–164, 1997.

[17] M. Winterhalter. *Curr. Opin. Colloid Interface Sci.*, 5:250–255, 2000.

[18] E. Sackmann. *Science*, 271:101–112, 1996.

[19] M. Stelzle, G. Weissmueller, and E. Sackmann. *J. Phys, Chem.*, 97:2974–2981, 1993.

[20] A. Janshoff and C. Steinem. *Anal Bioanal Chem*, 385:433–451, 2006.

[21] R. Guidelli, G. Aloisi, L. Becucci, A. Dolfi, M. R. Moncelli, and F. T. Buoninsegni. *J. Electroanal. Chem.*, 504:1–28, 2001.

[22] W. Knoll, C. W. Frank, C. Heibel, R. Naumann, A. Offenhausser, J. Ruhe, E. K. Schmidt, W. W. Shen, , and A. Sinner. *J. Biotechnol.*, 74:137–158, 2000.

[23] G. Krishna, J. Schulte, B. A. Cornell, R. J. Pace, and P. D. Osman. *Langmuir*, 19:2294–2305, 2003.

[24] R. Naumann, T. Baumgart, P. Graber, A. Jonczyk, A. Offenhausser, and W. Knoll. *Biosens. Bioelectron.*, 17:25–34, 2002.

[25] R. Naumann, S. M. Schiller, F. Giess, B. Grohe, K. B. Hartman, I. Koper I. Karcher, J. Lubben, K. Vasilev, , and W. Knoll. *Langmuir*, 19:5435–5443, 2003.

[26] R. Naumann, E. K. Schmidt, A. Jonczyk, K. Fendler, B. Kadenbach, T. Liebermann, A. Offenhausser, and W. Knoll. *Biosens. Bioelectron.*, 14:651–662, 1999.

[27] B. Raguse, V. Braachmaksvytis, B. A. Cornell, L. G. King, R. J. Pace P. D. J. Osman, and L. Wieczorek. *Langmuir*, 14:648–659, 1998.

[28] S. M. Schiller, R. Naumann, K. Lovejoy, H. Kunz, and W. Knoll. *Angew. Chem., Int. Ed.*, 42(2):208, 2003.

[29] E. K. Sinner and W. Knoll. *Curr. Opin. Chem. Biol.*, 5:705–711, 2001.

[30] G. Krishna, J. Schulte, B. A. Cornell, R. Pace, L. Wieczorek, and P. D. Osman. *Langmuir*, 17:4858–4866, 2001.

[31] C. Peggion, F. Formaggio, C. Toniolo, L. Becucci, M. R. Moncelli, and R. Guidelli. *Langmuir*, 17:6585–6592, 2001.

[32] O.-M.H. Richter and B. Ludwig. *Rev Physiol Biochem Pharmacol*, 147:47–74, 2003.

[33] L.J.C. Jeuken, J.P. McEvoy, and F.A. Armstrong. *J. Phys. Chem. B.*, 106:2304–2313, 2002.

[34] E. Laviron. *J. Electroanal. Chem.*, 101:19–28, 1979.

[35] Ch. et al. Laeger. *Biochemistry*, 42:8653–8662, 2003.

[36] J. Hirst, A. Sucheta, B.A.C. Ackrell, and F.A. Armstrong. *J. Am. Chem. Soc.*, 118:5031–5038, 1996.

[37] A.J. Bard and L.R. Faulkner. *Electrochemical Methods: Fundamentals and Applications*, volume Second edition. John Wiley and Sons, Inc. New York, 2001.

[38] O.-M.H. Richter and B. Ludwig. *Rev. Physiol. Biochem. Pharmacol.*, 147:47–74, 2003.

[39] D. Zaslavsky and R.B. Gennis. *Biochim. Biophys. Acta*, 1458:164, 2000.

[40] M. Wikstroem. *Biochimica et Biophysica Acta*, 1655:241, 2004.

[41] M. Saraste, L. Holm, L. Lemieux, M. Labben, and J. van der Oost. *Biochem Soc Transac*, 19:608–612, 1991.

[42] M. Mitchell. *Nature*, 191:144–148, 1961.

[43] B.L. Trumpower and R.B. Gennis. *Annu. Rev. Biochem.*, 63:675–716, 1994.

[44] D.A. Proshlyakov, M.A. Pressler, and G.T. Babcock. *Proc Natl Acad Sci USA*, 95:8020–8025, 1998.

[45] S . Ferguson-Miller and G. Babcock. *Chem. Rev.*, 96:2889–2907, 1996.

[46] S. Iwata, C. Ostermeier, B. Ludwig, and H. Michel. *Nature*, 376:660–669, 1995.

[47] T. Tsukihara, H. Aoyama, E. Yamashita, T. Tomizaki, H. Yamaguchi, K. Shinzawa-Itoh, R. Nakashima, R. Yaono, and S. Yoshikawa. *Science*, 269:1069–1074, 1995.

[48] T. Tsukihara, H. Aoyama, E. Yamashita, T. Tomashi, H. Yamaguchi, K. Shinzawa-Itoh, R. Nakashima, R. Yaono, and S. Yoshikawa. *Science*, 272:1136–1144, 1996.

[49] C. Ostermeier, A. Harrenga, U. Ermler, and H. Michel. *Proc Natl Acad Sci USA*, 95:10547–10553, 1997.

[50] K. Shinzawa-Itoh, R. Nakashima, R. Yaono, E. Yamashita, N. Inoue, M. Yao, M.J. Fei, C. Peters-Libeu, T. Mizushima, H. Yamaguchi, T. Tomizaki, and T. Tsukihara. *Science*, 280:1723–1729, 1998.

[51] A. Harrenga and H. Michel. *J Biol Chem*, 274:33296–33299, 1999.

[52] T. Soulimane, G. Buse, G.P. Bourenkov, H.D. Bartunik, R. Huber, and M.E. Than. *EMBO J*, 19:1766–1776, 2000.

[53] B. Ludwig and et al. *Nature*, 376:660–669, 1995.

[54] Garcia-Horsman, J.A., Puustinen, A., Gennis, R.B., Wikstroem, and M. *Biochemistry*, 34:4428–4433, 1995.

[55] J. Fetter, J. Qian, J. Shapleigh, J. Thomas, A. Garcia-Horsman, E. Schmidt, J. Hosler, G. Babcock, R. Gennis, and S. Ferguson-Miller. *Proc Natl Acad Sci USA*, 92:1604–1608, 1995.

[56] S. Hosler, J.P.and Ferguson-Miller, M.W. Calhoun, J.W. Thomas, J. Hill, L. Lemieux, J. Ma, C. Georgiou, Fetter. J., J. Shapleigh, M.M.J. Tecklenburg, G.T. Babcock, and R.B. Gennis. *J. Bioenerg. Biomembrane*, 25:121–136, 1993.

[57] J. Hosler. *JBC*, 267:24264, 1992.

[58] U. Pfitzner, A. Odenwald, A. Ostermann, L. Weingard, B. Ludwig, and O. Richter. *J. Bioenerg. Biomembranes*, 30:3089, 1998.

[59] M. Pereira, M. Santana, and M. Teixeira. *Biochim. Biophys. Acta*, 1505:185–208, 2001.

[60] D. Yang, Y. Oyaizu, H. Oyaizu, G. Olsen, and C. Woese. *Proc. Natl. Acad. Sci.*, 82:4443–7, 1985.

[61] T. Haltia, M. Finel, N. Harms, T. Nakari, M. Raitio, M. Wikstroem, and M. Saraste. *EMBO J*, 8:3571–3579, 1989.

[62] V. Frank and B. Kadenbach. *FEBS Lett*, 382:121–124, 1996.

[63] T. Kitagawa and T. Ogura. *Progress in inorganic chemistry*, volume 431-479. Wiley and New York, 1997.

[64] M. (ed.) Wikstroem. *Minireview Series. J Bioenerg Biomembr*, 30:1–146, 1998.

[65] H. Michel. *Proc Natl Acad Sci USA*, 95:12819–12824, 1998.

[66] B.E. Schultz and S.I. Chan. *Annu Rev Biophys Biomol Struct*, 30:23–65, 2001.

[67] Y.A. Ivashchuk-Kienbaum. *J. Membrane Biol.*, 151:1996, 247-259.

[68] M. Wikstroem. *Nature*, 266:271–273, 1977.

[69] G. Babcock. *Proc. Natl. Acad. Sci.*, 96:12971–3, 1999.

[70] D. Zaslavsky and R. Gennis. *Biochim. Biophys . Acta*, 1458:164–179, 2000.

[71] R. Fillingame. *Science*, 286:1687–88, 1999.

[72] J. Castresana and M. Saraste. *Trends Biochem. Sei.*, 20:443–8, 1995.

[73] D. Zaslavsky, I. Smirnova, S. Siletsky, A. Kaulen, F. Millett, and A. Konstantinov. *FEBS Lett.*, 359:27–30, 1995.

[74] G. Babcock and M. Wikstroem. *Nature*, 356:301–309, 1992.

[75] M. Svensson-Ek, G Abramson, G. Larsson, S. Tornroth, and S. Brzezinski, P.and Iwata. *J.Mal. Biol.*, 321:329–339, 2002.

[76] R. Capaldi. *Annu Rev Biochem*, 59:569–596, 1990.

[77] Y. Zhen, C.W. Hoganson, G.T. Babcock, and S. Ferguson-Miller. *J Biol Chem*, 274:38032–38041, 1999.

[78] K. Wang, Y. Zhen, R. Sadoski, S. Grinnell, L. Geren, S. Ferguson-Miller, B. Durham, and F. Millett. *J Biol Chem*, 274:38042–50, 1999.

[79] V. Drosou, F. Malatesta, M. Brunori, and B. Ludwig. *Eur J Biochem*, 269:2980–2988, 2002.

[80] H. Witt, F. Malatesta, F. Nicoletti, M. Brunori, and B. Ludwig. *J. Biol. Chem.*, 273:5132–5136, 1998.

[81] I. Szundi, J.A. Cappucino, N. Borovok, B. Kotlyar, and O. Einarsdottir. *Biochemistry*, 40:2186–2193, 2001.

[82] M. Wikstroem. *Biochim. Biophys. Acta*, 1458:188–198, 2000.

[83] H. Gray and J. Winkler. *Annu. Rev.Biochem.*, 65:537–61, 1996.

[84] J. Regan, B. Ramirez, J. R. Winkler, H. Gray, and B. Malmstroem. *J.Bioenerg . Biomembr.*, 30:35–9, 1998.

[85] C. Page, C. Moser, X. Chen, and P. Dutton. *Nature*, 402:47–52, 1999.

[86] M.I. Verkhovsky, A. Jasaitis, and M. Wikstroem. *Biochim. Biophys. Acta*, 1506:143–146, 2001.

[87] A.A. Konstantinov, D. Siletsky, S .and Mitchell, A. Kaulen, and R.B . Gennis. *Proc . Natl. Acad. Sci.*, 94:9085–90, 1997.

[88] P. Aedelroth and P. Brzezinski. *Biochim. Biophys. Acta*, 1367:107–17, 1998.

[89] B.G . Oliveberg, M. andMalmstroem. *Biochemistry*, 30:7053–7, 1991.

[90] M.I. Verkhovsky, J.E . Morgan, and M. Wikstroem. *Biochemistry*, 31:11860–3, 1992.

[91] O. Einarsdottir, K.E . Georgiadis, and A. Sucheta. *Biochemistry*, 34:496–508, 1995.

[92] M. Karpefors, P. Aedelroth, A. Aagaard, H. Sigurdson, E. M. Svensson, and P. Brzezinski. *Biochim. Biophys. Acta*, 1365:159–169, 1998.

[93] G. T. Babcock, R. Floris, T. Nilsson, M. Pressler, C. Varotsis, and E. Vollenbroek. *Inorg. Chim. Acta*, 243:345–53, 1996.

[94] H. Michel. *Biochemistry*, 38:15129–15140, 1999.

[95] Chance, C. Saronio, and Jr. J .S . Leigh. *J.Biol. Chem.*, 250:9226–37, 1975.

[96] D.A. Proshlyakov, T. Ogura, K. Shinzawa-Itoh, S. Yoshikawa, and T. Kitagawa. *Biochemistry*, 35:76–82, 1996.

[97] M. Fabian, W.W. Wong, R.B . Gennis, and G. Palmer. *Proc. Natl. Acad. Sci.*, 96:13114–7, 1999.

[98] H. Michel. *Biochemistry*, 38:15129–15140, 1999.

[99] M.I. Verkhovsky, A. Jasaitis, M.I . Verkhovskaya, J .E. Morgan, and M. Wikstroem. *Nature*, 400:480–483, 1999.

[100] H. Michel. *Nature*, 402:602–3, 1999.

[101] M. Wikstroem. *Biochemistry*, 39:3515–9, 2000.

[102] M. Ruitenberg, A. Kannt, E. Bamberg, K. Fendler, and H. Michel. *Nature*, 417:99–102, 2002.

[103] M. Wikstrom. *Nature*, 338:776–778, 1989.

[104] W.H. Vanneste. *Biochemistry*, 5:838–848, 1966.

[105] T. Kitagawa. *J. Inorg. Biochem.*, 82:9–18, 2000.

[106] M. Ruitenberg, A. Kannt, E. Bamberg, B. Ludwig, H. Michel, and K. Fendler. *Proc. Natl. Acad. Sci.*, 97:4632–6, 2000.

[107] P. Aedelroth, R. Gennis, and P. Brzezinski. *Biochemistry*, 37:2470–6, 1998.

[108] M.I . Verkhovsky, J .E. Morgan, and M. Wikstroem. *Biochemistry*, 34:7483–91, 1995.

[109] A.J. Moody. *Biochem. Soc. Trans.*, 19:617–22, 1991.

[110] M. Wikstroem, A. Jasaitis, C. Backgren, A. Puustinen, and M.I. Verkhovsk. *Biochim. Biophys. Acta*, 1459:514–20, 2000.

[111] P. Brzezinski and B. Malmstroem. *FEBS Lett.*, 187:111–4, 1985.

[112] P. Aedelroth, P. Brzezinski, and B.G. Malmstroem. *Biochemistry*, 34:2844–9, 1995.

[113] S .N . Witt and S .I . Chan. *J. Biol. Chem*, 262:1446–8, 1987.

[114] M. Braenden, H. Sigurdson, A. Namslauer, R. Gennis, P. Aedelroth, and P. Brzezinski. *Proc. Natl. Acad. Sei.*, 98:5013–8, 2001.

[115] H. Michel. *Proc. Natl. Acad. Sci.*, 95:12819–24, 1998.

[116] A. Konstantinov. *J. Bioenerg . Biomemb.*, 30:121–130, 1998.

[117] T. Ogura, S . Takahashi, S . Hirota, K. Shinzawa-Itoh, S. Yoshikawa, E. Appelman, and T. Kitagawa. *J. Am. Chem . Soc.*, 115:8527–36, 1993.

[118] D. Proshlyakov, M. Pressler, C. DeMaso, J. Leykam, D. De-Witt, and G. Babcock. *Science*, 290:1588–91, 2000.

[119] P. Nicholls and G.A. Chanady. *Biochim.Biophys. Acta*, 634:256–265, 1981.

[120] S . Juenemann, P. Heathcote, and P.R. Rich. *Biochim. Biophys . Acta*, 1456:56–66, 2000.

[121] C. Pecoraro, R.B. Gennis, T.V . Vygodina, and A.A. Konstantinov. *Biochemistry*, 40:9695–708, 2001.

[122] M. Oliveberg, P. Brzezinski, and B.G . Malmstroem. *Biochim. Biophys. Acta*, 977:322–8, 1989.

[123] T. Kitagawa and T. Ogura. *Prog. Inorg. Chem .*, 45:431–479, 1997.

[124] C. Ostermeier, A. Harrenga, U. Ermler, and H. Michel. *Proc.Natl. Acad. Sci.*, 94:10547–53, 1997.

[125] R. Gennis. *Biochim. Biophys.Acta*, 1365:241–248, 1998.

[126] T.K. Das, F.L. Tomson, R.B . Gennis, M. Gordon, and D. Rousseau. *Biophys. J.*, 80:2039–45, 2001.

[127] M. Wikstroem. *Biochim Biophys Acta*, 1458:188–198, 2000.

[128] M. Wikstroem and M.I. Verkhovsky. *Biochim Biophys Acta*, 1555:128–132, 2002.

[129] J.F. Nagle, M. Mille, and H.J. Morowitz. *J. Chem . Phys. and*, 72:3959–3971, 1980.

[130] N. Agmon. *Chem. Phys. Lett.*, 244:456–462, 1995.

[131] Zheng, X., Medvedev, D.M., Scanson, J., Stuchebrukhov, and A.A. *Biochimica et Biophysica Acta*, 1557:99–107, 2003.

[132] S. Janemann, B. Meunier, N. Fisher, and P.R. Rich. *Biochemistry*, 38:5248–5255, 1999.

[133] R.P. Rich. *Aust J Plant Physiol*, 22:479–486, 1995.

[134] J .P. Hosler, S . Ferguson-Miller, M.W. Calhoun, J.W. Thomas, L. Lemieux J. Hill, J. Ma, C. Georgiou, J. Fetter, J. Shapleigh, M.M.J. Tecklenburg, G.T. Babcock, and R.B. Gennis. *J. Bioenerg . Biomembr.*, 25:121–36, 1993.

[135] C.M. Gomes, C. Backgren, M. Teixeira, A. Puustinen, M.L. Verkhovskaya, M. Wikstroem, and M.I. Verkhovsky. *FEBS Lett.*, 497:159–164, 2001.

[136] J. Morgan, M. Verkhovsky, and M. Wikstroem. *J. Bioenerg . Biomembr.*, 26:599–608, 1994.

[137] J.W. Thomas, A. Puustinen, J.O. Alben, R.B. Gennis, and M. Wikstroem. *Biochemistry*, 32:10923–8, 1993.

[138] J.A. Garcia-Horsman, A. Puustinen, R.B. Gennis, and M. Wikstroem. *Biochemistry*, 34:4428–33, 1995.

[139] J.R. Fetter, J. Qian, J. Shapleigh, J.W. Thomas, A. Garcia-Horsman, E. Schmidt, J. Hosler, G.T. Babcock, R.B. Gennis, and S. Ferguson-Miller. *Proc. Natl. Acad. Sci. USA*, 92:1604–8, 1995.

[140] U. Pfitzner, K. Hoffmeier, A. Harrenga, A. Kannt, H. Michel, E. Bamberg, O.M. Richter, and B. Ludwig. *Biochemistry*, 39:6756–62, 2000.

[141] M. Bratton, M. Pressler, and J. Hosler. *Biochemistry*, 38:16236–16245, 1999.

[142] M.W. Mather and H. Rottenberg. *FEBS Lett*, 433:93–97, 1998.

[143] M. Wikstroem, A. Bogachev, M. Finel, J.E. Morgan, A. Puustinen, M. Raitio, M. Verkhovskaya, and M.I. Verkhovsky. *Biochim Biophys Acta*, 1187:106–111, 1994.

[144] S. Riistama, L. Laakonen, M. Wikstroem, M. Verkhovsky, and A. Puustinen. *Biochemistry*, 38:10670–10677, 1999.

[145] H. Michel. *Proc. Nat Acad. Sci USA*, 95:12819–12824, 1998.

[146] J .E. Morgan, M.I. Verkhovsky, and M. Wikstroem. *Biochemistry*, 35:12235–12240, 1996.

[147] M. Ruitenberg, A. Kannt, E. Bamberg, K. Fendler, and H. Michel. *Nature*, 417:99–102, 2002.

[148] J.R. Macdonald. *Impedance Spectroscopy.* John Wiley and Sons, New York, 1987.

[149] D. Pletcher. *A First Course in Electrode Processes.* The Electrochemical consultancy, 1991.

[150] Paul M. S. Monk. *Fundamentals of Electroanalytical Chemistry.* John Wiley and Sons LTD, Chichester, 2001.

[151] E. Faulkner, B. und Laviron. *J. Electroanal. Chem.*, 52:335–395, 1974.

[152] S. Srinivasan and E. Gileadi. *Electrochim. Acta*, 11:321, 1966.

[153] E. Laviron. *Electroanal. Chem. And Interfacial Electrochem.*, 52:355–393, 1974.

[154] J.P. McEvoy L.J.C. Jeuken and F.A. Armstrong. *J. Phys. Chem. B.*, 106:2304–2313, 2002.

[155] L.J.C. Jeuken. *Biochim. Biophys. Acta*, 1604:67–76, 2003.

[156] H. Kim, D. Xia, C.A. Yu, J.Z. Xia, A.M. Kachurin, L. Zhang, L. Yu, and J. Deisenhofer. *Proc. Natl. Acad. Sci. USA*, 95:8026–8033, 1998.

[157] Z.L. Zhang, L.S. Huang, V.M. Shulmeister, Y.I. Chi, K.K. Kim, L.W. Hung, A.R. Crofts, E.A. Berry, and S.H. Kim. *Nature*, 392:677–684, 1998.

[158] S. Iwata, J.W. Lee, K. Okada, J.K. Lee, M. Iwata, B. Rasmussen, T.A. Link, S. Ramaswamy, and B.K. Jap. *Science*, 281:64–71, 1998.

[159] R.A. Marcus and N. Sutin. *Biochim. Biophys. Acta*, 811:265–322, 1985.

[160] R.S. Farid, C.C. Moser, and P.L. Dutton. *Curr. Opin. Struck. Biol*, 3:225–233, 1993.

[161] G.W. Canters and M. van de Kamp. *Curr. Opin. Struc. Biol.*, 2:859–869, 1992.

[162] G.L. Closs and J.R. Miller. *Science*, 240:440–447, 1988.

[163] H. A. Heering F. A. Armstrong and J. Hirst. *Chem. Soc. Rev.*, 26:169, 1997.

[164] J.F. Rusling. *Acc. Chem. Res.*, 31:363–369, 1998.

[165] F.A. Armstrong. *J. Chem. Soc.*, Dalton Trans.:661–671, 2002.

[166] M.G. Friedrich, F. Giess, R. Naumann, W. Knoll, K. Ataka, J. Heberle, J. Hrabakova, D. Murgida, and P. Hildebrandt. *Chem. Commun.*, 21:2376–2377, 2004.

[167] M. Friedrich, J.W.F. Robertson, D. Walz, W. Knoll, and R.L.C. Naumann. *PNAS (submitted)*, 2007.

[168] E.F. Bowden J.L. Anderson and P.G. Pickup. *Anal. Chem.*, 68:R379–R444, 1996.

[169] Z. Q. Feng, S. Imabayashi, T. Kakiuchi, and K.J. Niki. *Chem. Soc. Faraday Trans.*, 93:1367–1370, 1997.

[170] L.J.C. Jeuken, P. van Vliet L. J. C, M. Verbeet, R. Camba, F.A. Armstrong J.P. McEvoy, and G.W. Canters. *J. Am. Chem. Soc.*, 122:12186–12194, 2000.

[171] A. El Kasmi, J. M. Wallace, E. F. Bowden, S. M. Binet, and R. J. Linderman. *J. Am. Chem. Soc.*, 120:225–226, 1998.

[172] A. E. F. Nassar, Z. Zhang, N. F. Hu, J. F. Rusling, and T. F. Kumosinski. *J. Phys. Chem. B*, 101:2224–2231, 1997.

[173] W. Cho M. Bayachou, R. Lin and P.J. Farmer. *J. Am. Chem. Soc.*, 120:9888–9893, 1998.

[174] J. Hirst and F.A. Armstrong. *Anal. Chem.*, 70:5062, 1998.

[175] E. Laviron. *Electroanal. Chem. And Interfacial Electrochem.*, 63:245, 1975.

[176] E. Laviron. *Bull.Soc.Chim.Fr.*, page 3717, 1967.

[177] S. Lecompte, H. Wackerbarth, T. Soulimane, G. Buse, and P. Hildebrandt. *J. Am. Chem. Soc.*, 120:7381, 1998.

[178] M.J. Honeychurch. *Langmuir*, 15:5158–5163, 1999.

[179] M.J. Honeychurch and G.A. Rechnitz. *Electroanaysis*, 10:285–293, 1998.

[180] M.J. Honeychurch and G.A. Rechnitz. *Electroanaysis*, 10:453–457, 1998.

[181] H.E. Keller and R.A. Osteryoung. *Anal. Chem.*, 43:342, 1997.

[182] G.J. Patriarche, Chateau-Gosselin, J.L. M, Vandenbalck, and P. Zuman. *Electroanalytical Chemistry*, volume 11. Marcel Dekker, New York, 1979.

[183] W.F. Smyth. *Electroanalysis in Hygiene, Environmental, Clinical and Pharmaceutical Chemistry, Analytical Chemistry Symposia Series*, volume 2. Elsevier, Amsterdam, 1980.

[184] S.A. Borman. *Anal. Chem.*, 54:698A, 1982.

[185] J. Tong, X.J. Dang., H.L. Li, and M. Yang. *Anal. Lett*, 30:585, 1997.

[186] A.J. Saterlay, J.S. Foord, and R.G. Compton. *Analyst*, 124:1791, 1999.

[187] A. Lasia. *Electrochemical Impedance Spectroscopy and its Application, Modern Aspects of Electrochemistry*, volume 32. Kuwer Academic/Plenum Publishers, New York, 1999.

[188] M. Sluyters-Rehbach. *Pure and Applied Chemistry*, 66(9):1831–1891, 1994.

[189] F. Giess, M.G. Friedrich, J. Heberle, R.L. Naumann, and W. Knoll. *Biophysical J.*, 87:3213–3220, 2004.

[190] R. Naumann, S. M. Schiller, F. Giess, B. Grohe, K. B. Hartman, I. Karcher, I. Koeper, J. Luebben, K. Vasilev, and W. Knoll. *Langmuir*, 19(13):5435–5443, 2003.

[191] R. Naumann, D. Walz, S.M. Schiller, and W. Knoll. *J. Electroanal. Chem.*, 550-551:241–252, 2003.

[192] L. Becucci, M. R. Moncelli, R. Naumann, and R. Guidelli. *J. Am. Chem. Soc.*, 127(38):13316–13323, 2005.

[193] R. De Levie. *Adv. Chem. Phys.*, 37:99–137, 1978.

[194] Lindholm-Sethson. *Langmuir*, 12:3305–3314, 1996.

[195] K.B. Oldham and Myland J.C. *Fundamentals of Electrochemical Science*. Academic Press, San Diego, 1994.

[196] G. Wiegand, T. Jaworek, G. Wegner, and E. Sackmann. *J. Colloid Interface Sci.*, 196:299–312, 1997.

[197] D.R.L. Scriven D. Walz, S.R. Caplan and D.C. Miculecky. *Bioelectrochemistry: Principles and Practice*, volume 1. Birkhaeuser Verlag, 1995.

[198] R. Naumann, D. Walz, S.M. Schiller, and W. Knoll. *Journal of Electroanalytical Chemistry*, 550-551:241–252, 2003.

[199] G. Heibel, P. Hildebrandt, B. Ludwig, P. Steinruecke, T. Soulimane, and G. Buse. *Biochemistry*, 32:10866–10877, 1993.

[200] S. Doepner, J. Hudecek, B. Ludwig, H. Witt, and P. Hildebrandt. *Biochim. Biophys. Acta*, 1480:57–64, 2000.

[201] D. H. Murgida and P. Hildebrandt. *J. Am. Chem. Soc.*, 123:4062, 2001.

[202] Faraday Discussions. *Surface enhanced Raman spectroscopy*, volume 132. RSC, London, 2005.

[203] J. D. Jackson. *Classical Electrodynamics*. Wiley, 1998.

[204] P. Drude. *Annalen der Physik*, 1:566, 1900.

[205] N. W. Ashcroft and N. D. Mermin. *Solid State Physics*. International Thomson Publishing, 1976.

[206] H. Raether. *Surface Plasmons on Smooth and Rough Surfaces and on Gratings*. Springer, 1988.

[207] E. Brustein, W. Chen, Y. Chen, and A. Hartstein. *Journal of Vacuum Science and Technology*, 11 (6):1004–1019, 1974.

[208] C. Kittel. *Introduction to solid state physics*. John Wiley and Sons, Inc. London, 1953.

[209] E. Kretschmann. *Optics Communications*, 6 (2):185–187, 1972.

[210] J. Sambles. *Contemporar Phy.*, 32 (3):173–183, 1991.

[211] E. Kretschmann. *Zeitschrift für Physik*, 216:398–410, 1968.

[212] H. Raether. *Physics of Thin Films*. Academic Press New York, 1977.

[213] K. Peterlinz and R. Georgiadis. *Opics Communications*, 130(4-6):260–266, 1996.

[214] W. Knoll, R. Hjummel, and P. Wißmann. *Handbook of Optical Properties*, pages 373–399, 1997.

[215] U. Kreibig and M. Vollmer. *Optical Properties of Metal Clusters*, volume 25. Springer, Berlin, Springer Series in Material Science, 1995.

[216] G. C. Schatz and R. P. van Duyne. *Handbook of Vibrational Spectroscopy*, volume 759-774. Wiley, New York, 2001.

[217] M. Moskovits. *Rev. Mod. Phys.*, 57:783–826, 1985.

[218] A. Haes and R.P. van Duyne. *J. Am. Chem. Soc.*, 124:10596, 2002.

[219] M. Quinten, A. Leitner, J. R. Krenn, and F. R. Aussenegg. *Opt.Lett.*, 23:1331, 1998.

[220] W. Rechberger, A. Leitner, A. Hohenau, J. R. Krenn, and F.R. Aussenegg. *Opt. Commun.*, 220:137, 2003.

[221] L. Gunnarson, T. Rindzevicius, J. Prikulis, B. Kasemo, M. Kaell, S. Zou, and G. C. Schatz. *J. Phys. Chem. B*, 109:1079, 2005.

[222] K. Kneipp, H. Kneipp, I. Itzkan, R.R. Dasari, and M.S. Feld. *J. Phys.: Condens. Matter*, 14:R597–R624, 2002.

[223] D.A. Long. *The Raman Effect. A Unified Treatment of the Theory of Raman Scattering by Molecules.* John Wiley and Sons, 2002.

[224] C. V. Raman. *Molecular Diffraction of Light.* Calcutta: Calcutta University Press, 1922.

[225] C.V. Raman and K.S. Krishnan. *Nature*, 121:619, 1928.

[226] G. Landsberg and L. Mandelstam. *Naturwissenschaften*, 16:557, 1928.

[227] I. Pockrand. *Surface Enhanced Raman Vibrational Studies at Solid/Gas Interfaces.* Springer-Verlag, New York, 1984.

[228] P.P. Shorygin. *Zh. Fiz. Khim.*, 21:1125, 1947.

[229] W. Kiefer. *Infrared and Raman Spectroscopy -Methods and Applications*, volume 21. VCH, Weinheim, 1995.

[230] R.J.H. Clark and T.J. Dines. *Angew. Chem., Int. Ed.*, 25:131–158, 1986.

[231] D Long W Kieder. *Non-Linear Raman Spectroscopy and its chemical applications.* Reidel, Dordrecht, 1982.

[232] Kramers and W. Heisenberg. *Z. Physik*, 31:681, 1925.

[233] R.J.H. Clark and T.J. Dines. *Angew. Chem. Int. Ed.*, 25:131–158, 1986.

[234] R.J.H. Clark and Steward B. *Structure and Bonding*, 36:1, 1979.

[235] A.C. Albrecht. *J. Chem. Phys.*, 34:1476, 1961.

[236] G. Herzberg and E. Teller. *Z. Phys. Chem.*, 21:410, 1933.

[237] A. Albrecht. *J. Chem. Phys.*, 34:1476, 1961.

[238] M. Fleischmann, P.J. Hendra, and A.J. McQuillan. *Chem. Phys. Lett.*, 26:163–166, 1974.

[239] D.L. Jeanmaire and R. van Duyne. *J. Electroanal. Chem.*, 84:1–20, 1977.

[240] M. Albrecht and J. Creighton. *J. Am. Chem. Soc.*, 99:5215–5217, 1977.

[241] K. Kneipp, Y. Wang, H. Kneipp, I. Itzkan, R. R. Dasari, and M.S. Feld. *Phys. Rev. Lett.*, 76:2444, 1996.

[242] K. Kneipp, Y. Wang, H. Kneipp, L.T. Perelman, I. Itzkan, R.R. Dasari, and M. S. Feld. *Phys. Rev. Lett.*, 78:1667, 1997.

[243] S. Nie and S.R. Emory. *Science*, 275:1102, 1997.

[244] K. Kneipp, H. Kneipp, G. Deinum, I. Itzkan, R.R. Dasari, and M.S. Feld. *Appl. Spectrosc.*, 52:175, 1998.

[245] K. Kneipp, H. Kneipp, V.B. Kartha, R. Manoharan, G. Deinum, I. Itzkan, R.R. Dasari, and M.S. Feld. *Phys. Rev. E*, 57:R6281, 1998.

[246] M. R. Philpott. *J. Chem. Phys.*, 62:1812–1817, 1975.

[247] A. Campion and P. Kambhampati. *Chem. Soc. Rev.*, 27:241–250, 1998.

[248] S. Nie and S. R. Emory. *Science*, 275:1102–1106, 1997.

[249] S.G. Schultz, M. Janik-Czachor, and R.P. Van Duyne. *Surface Science*, 104(2-3):419–434, 1981.

[250] T.R. Jensen, M.D. Malinsky, C.L. Haynes, and R.P. Van Duyne. *J. Phys. Chem. B*, 104:549, 2000.

[251] A. Otto, I. Mrozek, H. Grabhorn, and W. Akemann. *J. Phys.: Condens. Matter*, 4:1143–1212, 1992.

[252] A. Otto. *J. Ram. Spec.*, 22:743–752, 1991.

[253] A. Otto. *Surface-enhanced Raman scattering: classical and chemical origins Light Scattering in Solids IV. Electronic Scattering, Spin Effects, SERS and Morphic Effects.* Springer, 1984.

[254] A. Otto. *Phys. Status Solidi*, 188:1455, 2001.

[255] M. Moskovits. *J. Ram. Spec.*, 36:485–496, 2005.

[256] P. Kambhampati, C.M. Child, M.C. Foster, and A. Campion. *J. Chem. Phys*, 108:5013–5026, 1998.

[257] K. Kneipp, H. Kneipp, I. Itzkan, R.R. Dasar, and M.S. Feld. *Chem. Rev.*, 99:2957–29758, 1999.

[258] A. Champion and P. Kambhampati. *Chem. Soc. Rev.*, 27:241–250, 1998.

[259] T. G. Spiro and T.M. Loehr. *Adv. Infrared Raman Spectrosc.*, 1:98, 1975.

[260] M. Gouterman. *The Porphyrins*, volume 3. Academic Press, New York, 1978.

[261] N.-T. Yu R. H. Felton. *The Porphyrins*, volume 3. Academic Press, New York, 1978.

[262] P.M. Champion and A.C. Albrecht. *Annu. Rev. Phys. Chem.*, 33:353, 1982.

[263] T.G. Spiro and P. Stein. *Annu. Rev. Phys. Chem.*, 28:501, 1977.

[264] T.G. Spiro. *Phys. Bioinorg. Chem. Ser.*, 2:89, 1983.

[265] P. Hildebrandt, G. Anzenbacher, R. Lange, V. Kruger, and A. Stierl. *Biochemistry*, 33:12920–12929, 1994.

[266] P. Hildebrandt, R. Greinert, A. Stier, and H. Tahiguchi. *Eur J. Biochemi*, 186:291–302, 1989.

[267] M. Unno, D. Christian, N. Benson, S. Gerber, P. Sligar, and P. Champion. *J. Am. Chem. Soc.*, 119:6614–6620, 1997.

[268] J. Behr, H. Michel, W. Maentele, and P. Hellwig. *Biochemistry*, 39:1356–1363, 2000.

[269] H. Wackerbarth, U. Klar, W. Gunther, and P. Hildebrandt. *Appl. Spectrosc.*, 53:283–291, 1999.

[270] M. Friedrich, F. Giess, R. Naumann, W. Knoll, K. Ataka, J. Heberle, J. Hrabakova, D. Murgida, and P. Hildebrandt. *Chem. Commun.*, 21:2376–2377, 2004.

[271] R. M. Nyquist, D. Heitbrink, C. Bolwien, R. B. Gennis, and J. Heberle. *Proc. Natl. Acad. Sci. USA*, 100:8715–8720, 2003.

[272] K. Ataka and J Heberle. *J. Am. Chem. Soc.*, 125:4986–4987, 2003.

[273] R. Hildebrandt, G. Anzenbacher, R. Lange, V. Kruger, and A. Stierl. *Biochemistry*, 33:12920–12929, 1994.

[274] P. Hildebrandt, R. Greinert, A. Stier, and H. Tahiguchi. *Eur J. Biochemi.*, 186:291 –302, 1989.

[275] M. Unno, D. Christian, N. Benson, S. Gerber, P. Sligar, and P. Champion. *J. Am. Chem. Soc.*, 119:6614–6620, 1997.

[276] M. Unno, D. Christian, N. Benson, S. Gerber, P. Sligar, and P. Champion. *J. Am. Chem. Soc.*, 119:6614–6620, 1997.

[277] R. Champion, I. Gunsalus, and G. Wagner. *J. Am.Churn. Sos.*, 100:3743–3751, 1978.

[278] M. Gouterman. *J. Chem. Phys.*, 30:1139, 1959.

[279] J. Radziszewski, J. Waluk, and J. Michl. *J. Mol. Spectrosc.*, 140:373, 1990.

[280] T. Babcock. *Biological Applications of Raman Spectroscopy and John Wiley and Sons*, 3:chapter 7, 1988.

[281] R.B. Gennis, R.P. Casey, A. Azzi, and B. Ludwig. *Eur. J. Biochem.*, 125:189–195, 1982.

[282] G. T. Babcock. *Raman scattering by cytochrome oxidase and heme a model compounds.*, volume Biological applications of Raman spectroscopy, Vol 3, Chapter 7. John Wiley and Sons, New York, 1988.

[283] M. Abe, T. Kitagawa, and Y. Kyogoku. *J. Chem. Phys.*, 69:4526–34, 1978.

[284] H. Lee, T. K. Das, D. Rousseau, D. Mills, S. Ferguson-Miller, and R.B. Gennis. *Biochem.*, 39:2989–96, 2000.

[285] L. Rivas, C.M. Soares, A.M. Baptista, J. Simaan, R.E. Di Paolo, D.H. Murgida, and P. Hildebrandt. *Biophys. J.*, 88:4188–4199, 2005.

[286] T. Spiro. *Physical hioinorganic chemistry*, 11:ch. 3, 1982.

[287] I. Macdonald., W. Smith, and A. Munro. *Eur. Biophys. J.*, 28:437–445, 1999.

[288] I. Macdonald., W. Smith, and A. Munro. *FEBS Lett.*, 396:166–200, 1996.

[289] S. Hu, K. Smith, and J. Spiro. *Am. Chem. Soc.*, 118:12638–12646, 1996).

[290] P. Anzenbacher and J. Hudecek. *Journal of Inorganic Biochemistry*, 87:209–213, 2001.

[291] M. Perrin, M. Gouterman, and C. Perrin. *J. Chem. Phys.*, 50:4137, 1969.

[292] M. Abe and et al. *J. Chem. Phys.*, 69(10):4526–4534, 1978.

[293] E. Hochuli, H. Dobeli, and A. Schacher. *J. Chromatogr.*, 411:177–184, 1987.

[294] D. Kroger, M. Liley, W. Schiweck, A. Skerra, and H. Vogel. *Biosens. Bioelectron.*, 14:155–161, 1999.

[295] J. Madoz-Gurpide, J. M. Abad, J. Fernandez-Recio, M. Velez, L. Vazquez, C. Gomez-Moreno, and V. M. Fernandez. *J. Am. Chem. Soc.*, 122:9808–9817, 2000.

[296] P. Rigler, W. P. Ulrich, P. Hoffmann, M. Mayer, and H. Vogel. *ChemPhysChem*, 4:268–275, 2003.

[297] A. Devadoss and J. D. Burgess. *Langmuir*, 18:9617–9621, 2002.

[298] K. Wang, L. Geren, Y. Zhen, L. Ma, S. Ferguson-Miller, B. Durham, and F. Millett. *Biochemistry*, 41:2298–2304, 2002.

[299] K. Ataka, F. Giess, W. Knoll, R. Naumann, S. Haber-Pohlmeier, B. Richter, and J. Heberle. *J. Am. Chem. Soc.*, 126:16199–16206, 2004.

[300] G. Sauerbrey. *Z. Phys.*, 155:206–222, 1959.

[301] F. H. Arnold. *Metal Affinity Protein Separations.* Academic Press, San Diego, CA., 1992.

[302] M. V. Voinova, M. Rodahl, M. Jonson, and B. Kasemo. *Phys. Scr.*, 59:391–396, 1999.

[303] J. D. Burgess, M. C. Rhoten, and F. H. Hawkridge. *J. Am. Chem. Soc.*, 120:4488–4491, 1998.

[304] R. Vogel and F. Siebert. *Curr. Opin. Chem. Biol.*, 4:518–523, 2000.

[305] P.E. Smith, R.M. Brunne, A.E. Mark, and W.F. Van Gunsteren. *J. Phys. Chem.*, 97:2009–2014, 1993.

[306] B. Catimel, J. Rothacker, and E. Nice. *J. Biochem. Biophys. Methods.*, 49:289–312, 2001.

[307] T. et al. Tsukihara. *Science*, 269:1069–1074, 1995.

[308] Hosler J. P. et al. *JBC*, 267:24264–24273, 1992.

[309] U. Pfitzner, A. Odenwald, Th. Ostermann, L. Weingard, B. Ludwig., and O.-M.H. Richter. *J. Bioenerg. Biomembranes*, 30:3089–97, 1998.

[310] D. Zaslavsky and R.B. Gennis. *Biochim. Biophys. Acta*, 1458:164–179, 2000.

[311] R.B. Gennis. *1998Proc. Nat. Acad. Soc.*, 95:12747–12749.

[312] D.M Mitchell and Gennis R.B. *FEBS Lett.*, 368(1):148–150, 1995.

[313] H.M. Lee, T.K.Das, D. L. Rousseau, D. Mills, S. Ferguson-Miller, and R. B. Gennis. *Biochemistry*, 39:2989, 2000.

[314] H. Wackerbarth, U. Klar, W. Guenther, and P. Hildebrandt. *Applied Spectroscopy*, 53:283–291, 1999.

[315] F. Giess, M. Friedrich, J. Heberle, R. Naumann, and W. Knoll. *Biophys. J.*, 87:3213–3220, 2004.

[316] M. Svensson-Ek, J. Abramson, G. Larsson, S. Tornroth, P. Brzezinski, and S. Iwata. *J. Mol. Biol.*, 321:329, 2002.

[317] D. H. Murgida and P. Hildebrandt. *J. Phys. Chem. B*, 105:1578, 2001.

[318] C. Hiser, D. A. Mills, M. Schall, and S. Ferguson-Miller. *Biochemistry*, 40:1606, 2001.

[319] S. Ferguson-Miller and G.T. Babcock. *Chem. Rev.*, 96:2889–2907, 1996.

[320] http://metallo.scripps.edu/promise/COX.html.

[321] F. Malatesta, G. Antonini, P. Sarti, and M. Brunori. *Biophys. Chem.*, 54:1, 1995.

[322] K. et al. Ataka. *J. Am. Chem. Soc.*, 126:16199–16206, 2004.

[323] D. et al. Bloch. *Proc. Nat. Acad. Soc. USA*, 101:529–533, 2004.

[324] A. J. Moody, U. Brandt, and P.R. Rich. *FEBS Lett.*, 293:101–105, 1991.

[325] M.V. Smirnov and A.M. Potapov. *Electrochim. Acta*, 39:143–49, 1994.

[326] R. Blankespoor, B. Limoges, B. Schoellhorn, J-L. Syssa-Magalae, and D. Yazidi. *Langmuir*, 21:3362–3375, 2005.

[327] H.M. et al. Lee. *Biochemistry*, 39:2989–2996, 2000.

[328] M.I. Verkhovsky, J.E. Morgan, and M. Wikstroem. *Biochemistry*, 34:7483–7491, 1995.

[329] I. Szundi, J.A. Cappucino, N. Borovok, B. Kotlyar, and O. Einarsdottir. *Biochemistry*, 40:2186–2193, 2001.

[330] M. et al. Svensson-Ek. *J. Mol. Biol.*, 321:329–339, 2002.

[331] K. et al. Ataka. *J. Am. Chem. Soc.*, 126:16199–16206, 2004.

[332] M. et al. Svensson-Ek. *J. Mol. Biol.*, 321:329–339, 2002.

[333] Hill T.L. *Free Energy Transduction in Biology.* Academic Press, New York, 1977.

[334] L.J.C. Jeuken. *Biochim. Biophys. Acta*, 1604:67–76, 2003.

[335] J. et al Hirst. *J. Am. Chem. Soc.*, 120:7085–7094, 1998.

[336] K. et al Wang. *J. Biol. Chem.*, 274:38042–38050, 1999.

[337] L. J. C. et al. Jeuken. *J. Am. Chem. Soc.*, 128:1711–1716, 2006.

[338] R Naumann, Baumgart T, Graeber P, Jonczyk A, Offenhaeusser A, and Knoll W. *Biosens. Bioelectr.*, 17:25–34, 2002.

[339] A. S. Pawate, J. Morgan, A. Namslauer, D. Mills, P. Brzezinski, Sh. Ferguson-Miller, and R.B. Gennis. *Biochemistry*, 41:13417–13423, 2002.

[340] P. et al. Hellwig. *Biochemistry*, 41:9116–9125, 2002.

[341] M.I Verkhovsky, A Jasaitis, M.L Verkhovskaya, J.E Morgan, and M. Wikstroem. *Nature*, 400:480–483, 1999.

[342] M Ruitenberg, A Kannt, E Bamberg, K Fendler, and H. Michel. *Nature*, 417:99–102, 2002.

[343] E. A. Gorbikova, K. Vuorilehto, M. Wikstroem, and M. I. Verkhovsky. *Biochemistry*, 45:5641–5649, 2006.

[344] H. Miyake, S. Osawa, and M. Ye. *Electroch. Comm.*, 4:973–977, 2002.

[345] U. P. Fringeli, H. H. Guenthard, and D. Baurecht. *Infrared and Raman Spectroscopy of Biological Materials, Chapter 5*, volume 143-192. Marcel Dekker, New York, Basel, 2000.

[346] D. Baurecht and U. P. Fringeli. *Rev. Sci. Instrum.*, 72:3782, 2001.

[347] D. Baurecht and I. Porth. *Vibrational Spectroscopy*, 30:85–92, 2002.

[348] P.E. Smith, R.M. Brunne, A.E. Mark, and W.F. Van Gunsteren. *J. Phys. Chem.*, 97:2009–2014, 1993.

[349] A. S. Haas, D. L. Pilloud, K. S. Reddy, G. T. Babcock, C. C. Moser, J. K. Blasie, and P. L. Dutton. *J. Phys. Chem. B*, 105:11351–11362, 2001.

[350] J.K. Cullison, F.M. Hawkridge, N. Nakashima, and Sh. Yoshikawa. *Langmuir*, 10:877–882, 1994.

[351] J. D. Burgess, M. C. Rhoten, and F. H. Hawkridge. *J. Am. Chem. Soc.*, 120:4488–4491, 1998.

[352] personal communication by prof. b. ludwig.

[353] M. Svensson-Ek, J. Abramson, G. Larsson, S. Tornroth, P. Brzezinski, and S. Iwata. *J. Mol. Biol.*, 321(2):329–39, 2002.

[354] G. Krishna, J. Schulte, B. A. Cornell, R. Pace, L. Wieczorek, and P. D. Osman. *Langmuir*, 17(16):4858–4866, 2001.

[355] D. Walz and S. R. Caplan. *Nonequilibrium thermodynamics and kinetics. In Bioelectrochemistry: Principles and Practice*, volume 1-48. Birkhaeuser Verlag, Basel, 1995.

[356] R. P. Buck and C. Mundt. *J. Chem. Soc. Farad. Trans.*, 92(24):4987–4992, 1996.

[357] B. Conway. *Impedance Behavior of Electrochemical Supercapacitors and Porous Electrodes. In Impedance Spectroscopy: Emphasizing Solid Materials and Systems*, volume 2nd ed., 469-497. Wiley, Hoboken, NJ, 2005.

[358] S. Paula, A. G. Volkov, A. N. VanHoek, T. H. Haines, and D. W. Deamer. *Biophys. J.*, 70(1):339–348, 1996.

[359] S. Paula, A. G. Volkov, and D. W. Deamer. *Biophys. J.*, 74(1):319–327, 1998.

[360] Chizmadzhev, Y. A., J. Teissiae, and D. Walz. *Lipid bilayer electropermeabilization. In Bioelectrochemistry: Principles and Practice. Bioelectrochemistry of Membranes*, volume 6, pp. 173-203. Birkhaeuser Verlag, Basel, 2004.

[361] http://www.biochem.arizona.edu/classes/bioc462/462a/jmol/valinomycin/vali.htm.

[362] G. Stark, B. Ketterer, R. Benz, and P. Laeuger. *Biophys. J.*, 11:981, 1971.

[363] G. Fernandez and A. Bard. *Anal. Chem.*, 76:2281–2289, 2004.

[364] G. Fernandez, Mano, Heller, and A. Bard. *Angew. Chem., Int. Ed.*, 43:6355–6357, 2004.

[365] G. Fernandez and A. Bard. *Anal. Chem.*, 75:12801–12806, 2003.

[366] L. Liu and A. Bard. *J. Phys. Chem*, 116:12801–12806, 2002.

A Appendix

A.1 Design of the SERRS Cell

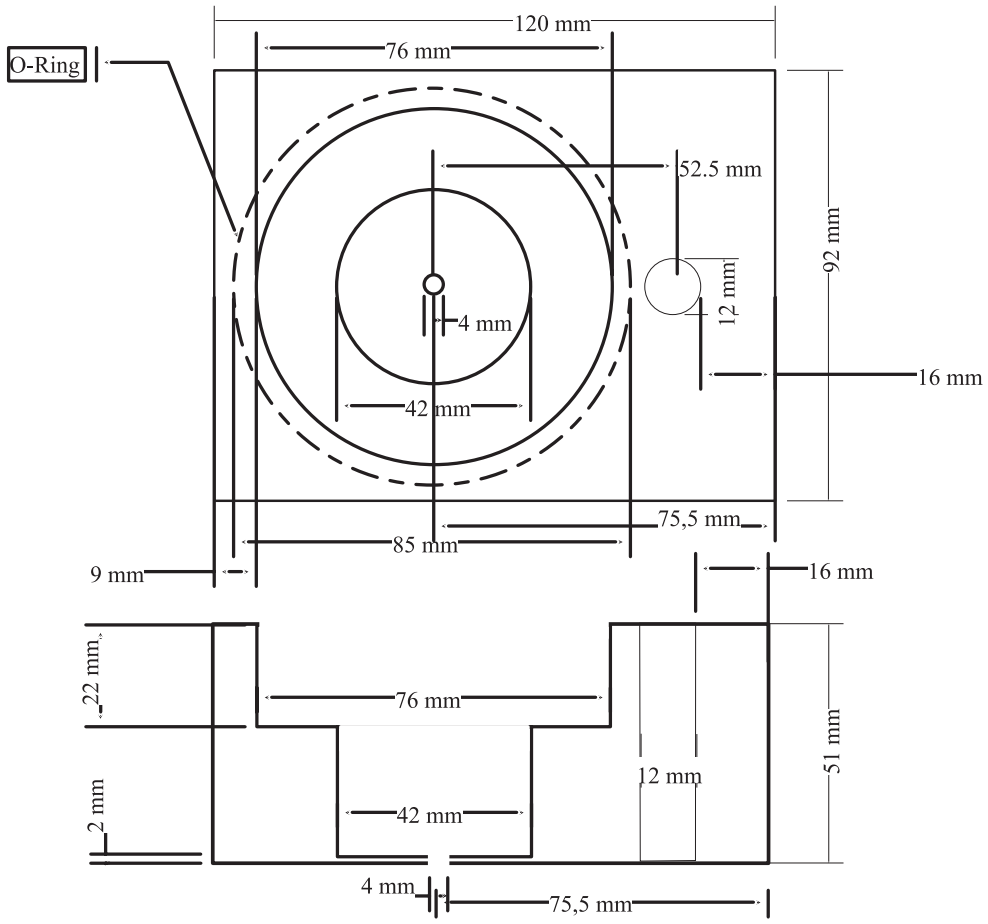

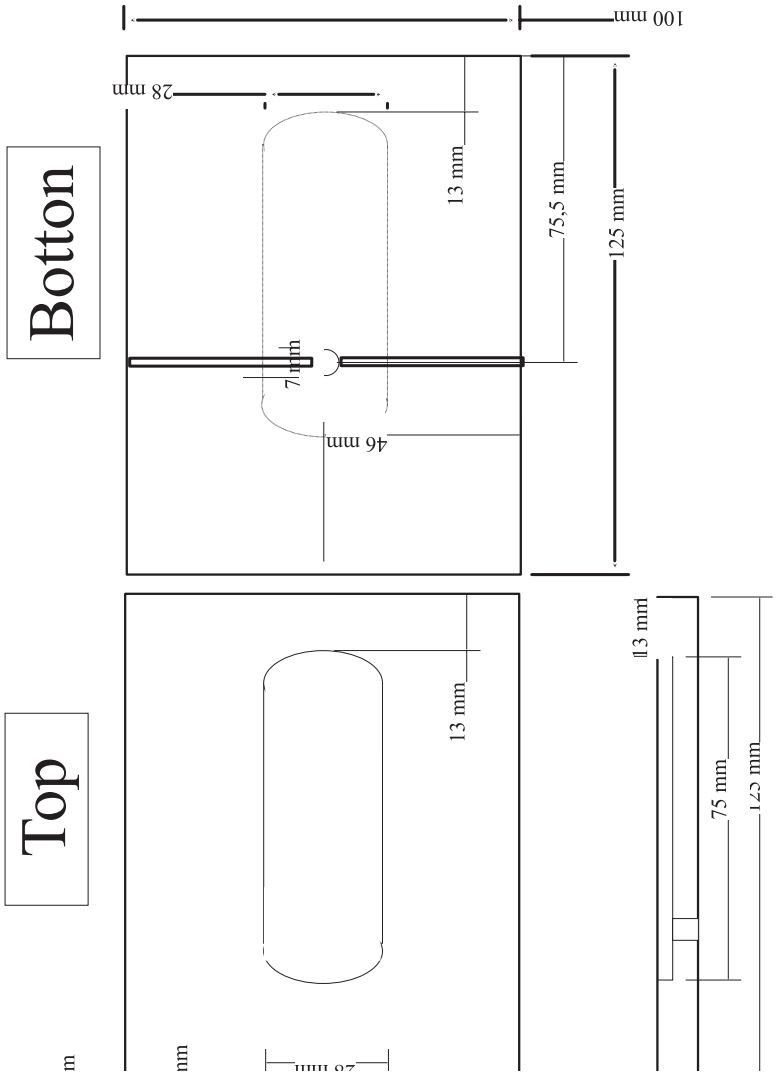
Botton
100 mm
28 mm
13 mm
75,5 mm
125 mm
7 mm
46 mm
Top
13 mm
75 mm
125 mm

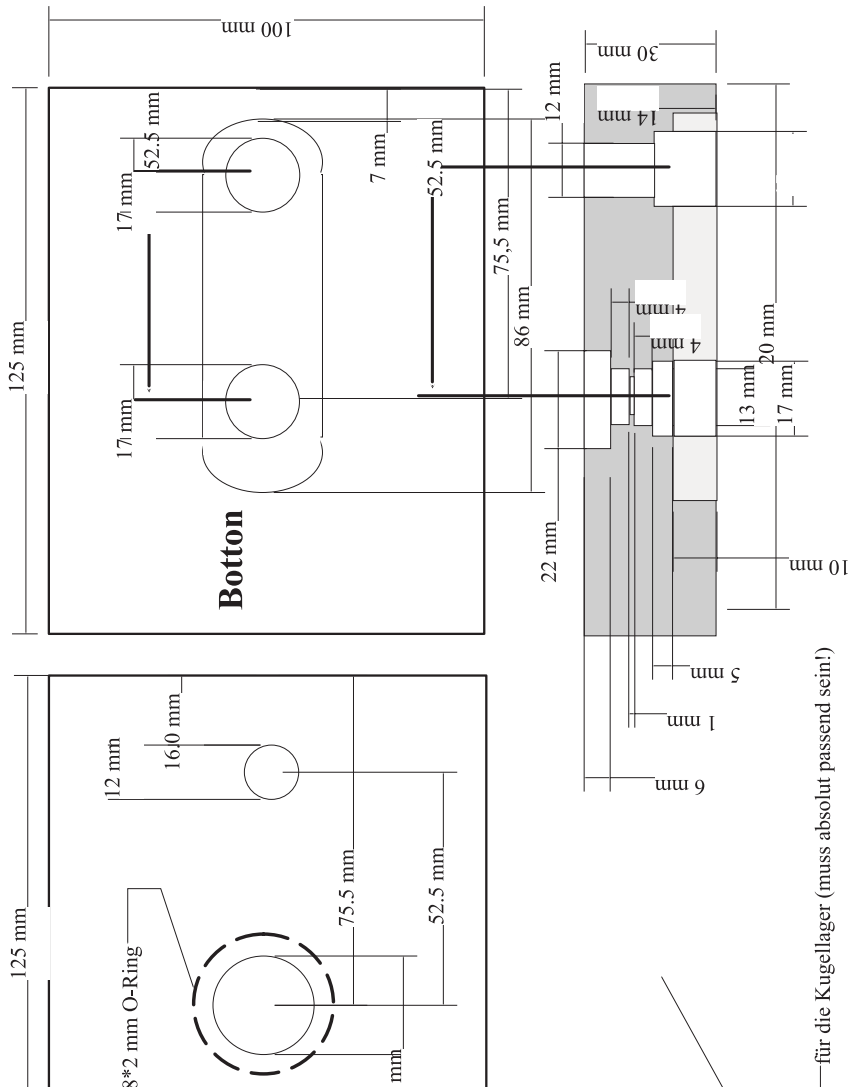
100 mm
125 mm
52.5 mm
17 mm
17 mm
7 mm
52.5 mm
75,5 mm
86 mm
12 mm
22 mm
Botton
30 mm
14 mm
4 mm
20 mm
13 mm
17 mm
10 mm
5 mm
1 mm
6 mm
125 mm
12 mm
16,0 mm
75.5 mm
52.5 mm
3*2 mm O-Ring
mm
für die Kugellager (muss absolut passend sein!)

Teflon Trough

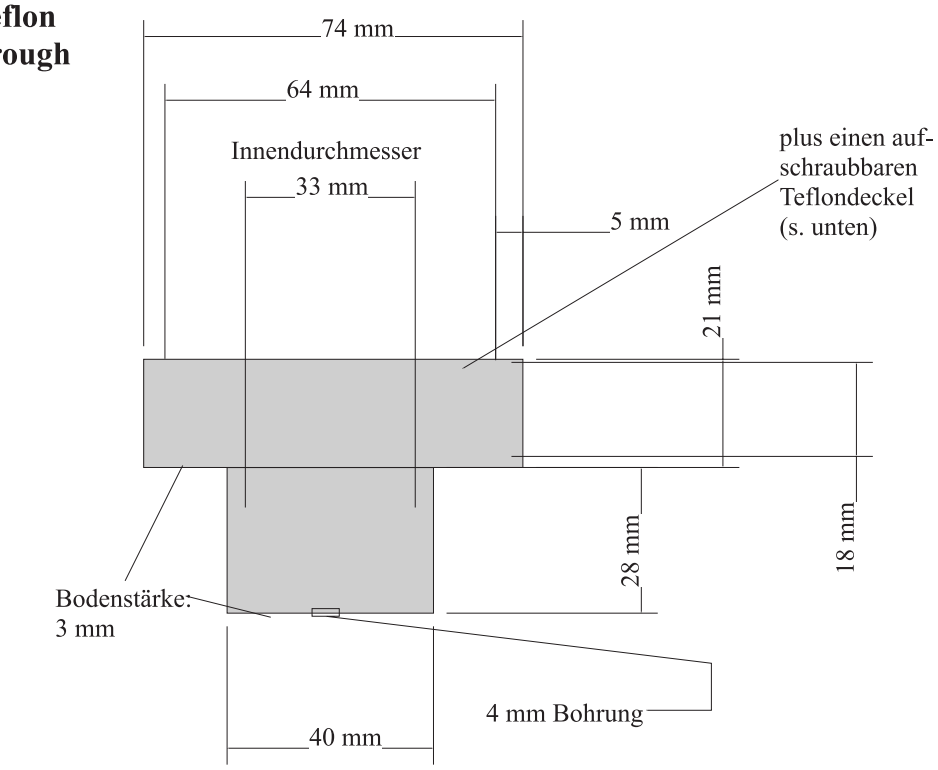

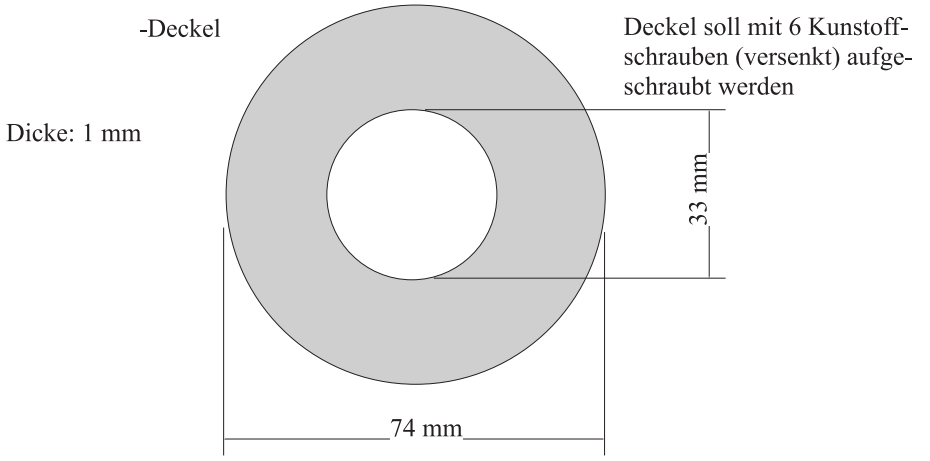

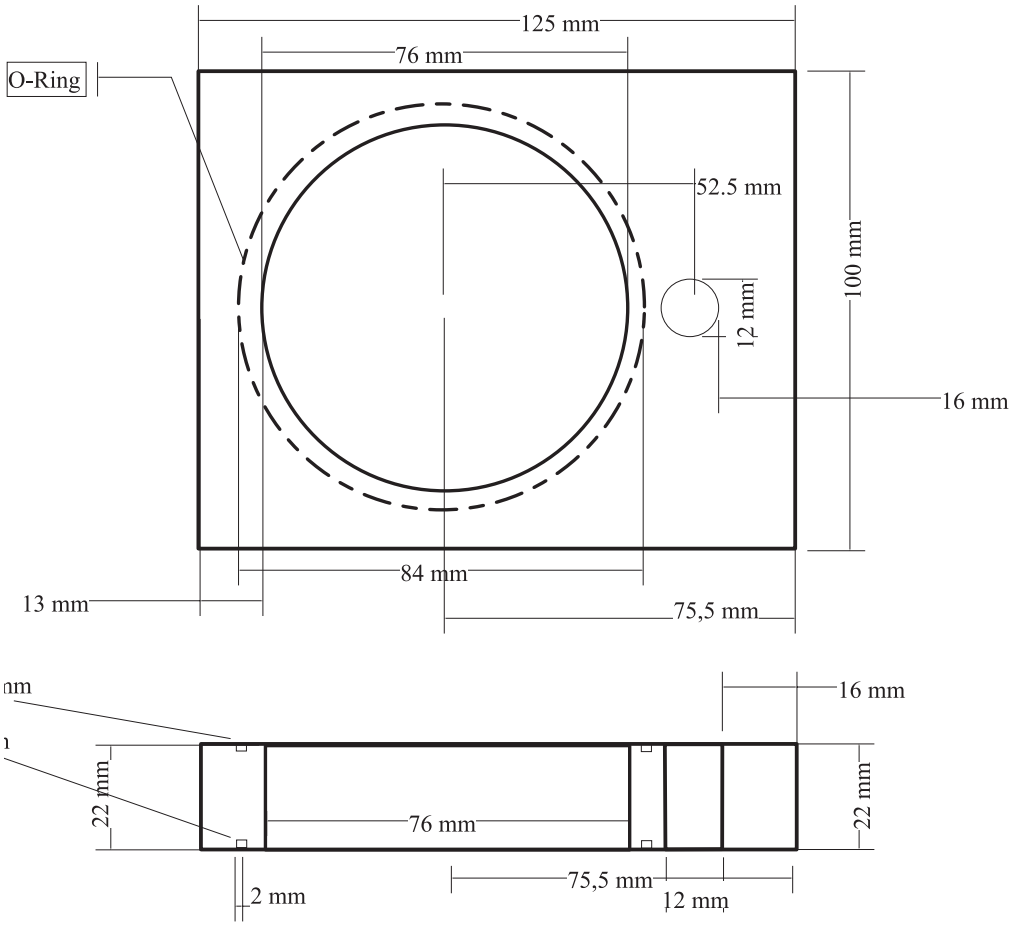
125 mm
76 mm
O-Ring
52.5 mm
100 mm
12 mm
16 mm
84 mm
13 mm
75,5 mm
16 mm
22 mm
22 mm
76 mm
2 mm
75,5 mm
12 mm

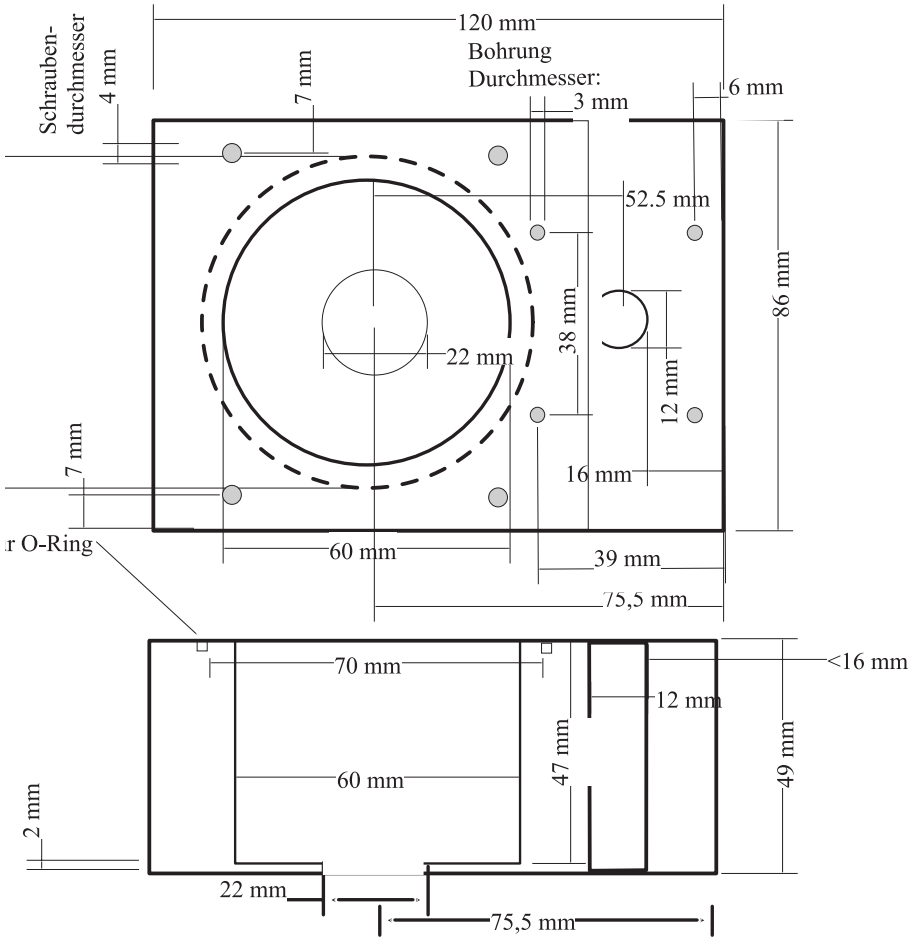
120 mm
Schrauben-
durchmesser
4 mm
7 mm
Bohrung
Durchmesser:
3 mm
6 mm
52.5 mm
86 mm
38 mm
22 mm
12 mm
7 mm
16 mm
r O-Ring
60 mm
39 mm
75,5 mm
70 mm
<16 mm
12 mm
47 mm
49 mm
60 mm
2 mm
22 mm
75,5 mm

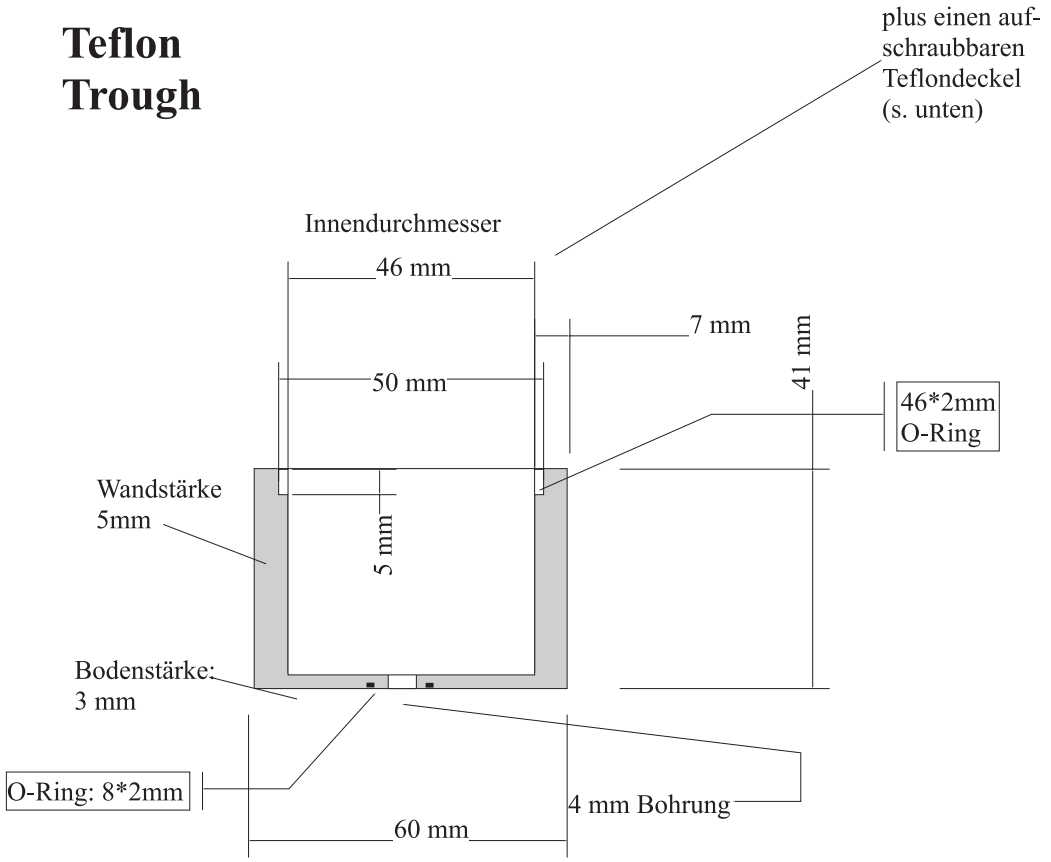
Teflon
Trough
plus einen auf-
schraubbaren
Teflondeckel
(s. unten)
Innendurchmesser
46 mm
7 mm
41 mm
50 mm
46*2mm
O-Ring
Wandstärke
5mm
5 mm
Bodenstärke:
3 mm
O-Ring: 8*2mm
4 mm Bohrung
60 mm

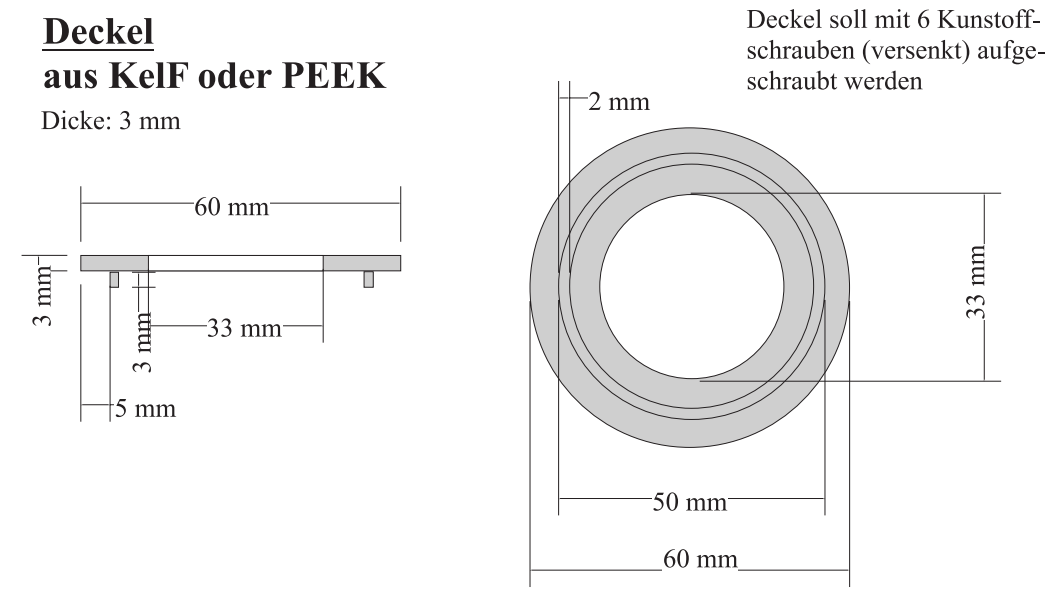
Deckel
aus KelF oder PEEK
Dicke: 3 mm
Deckel soll mit 6 Kunstoff-
schrauben (versenkt) aufge-
schraubt werden
60 mm
3 mm
3 mm
33 mm
5 mm
2 mm
33 mm
50 mm
60 mm

Cover

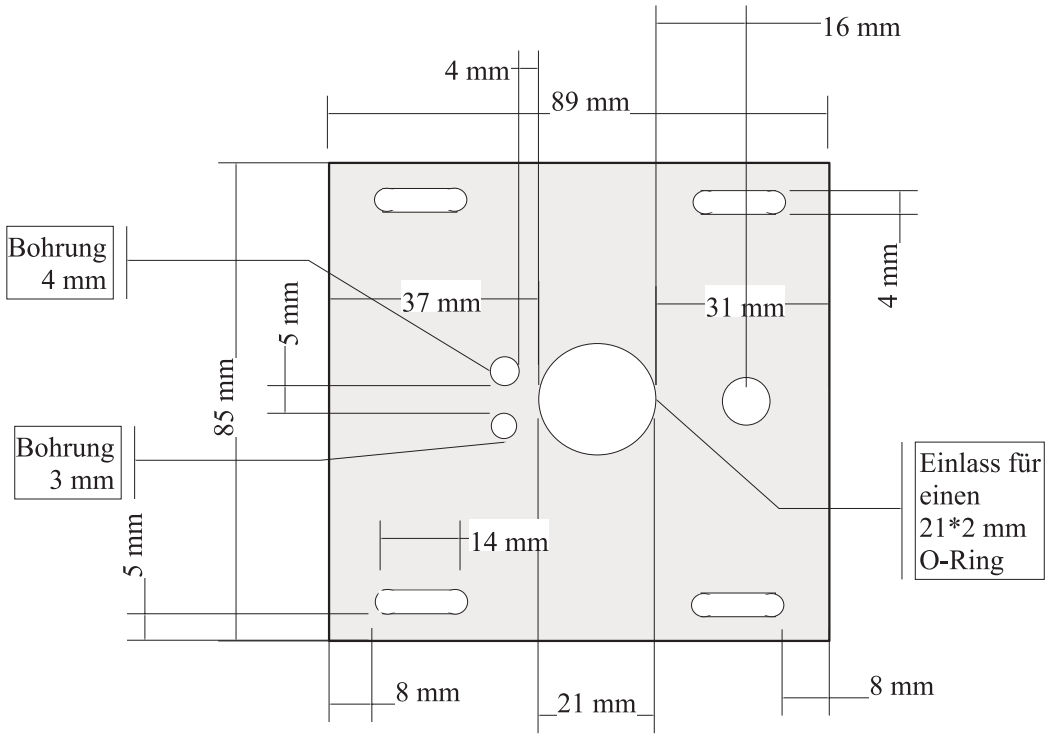

Dicke: 5 mm

Material: KelF oder PEEK

Variation

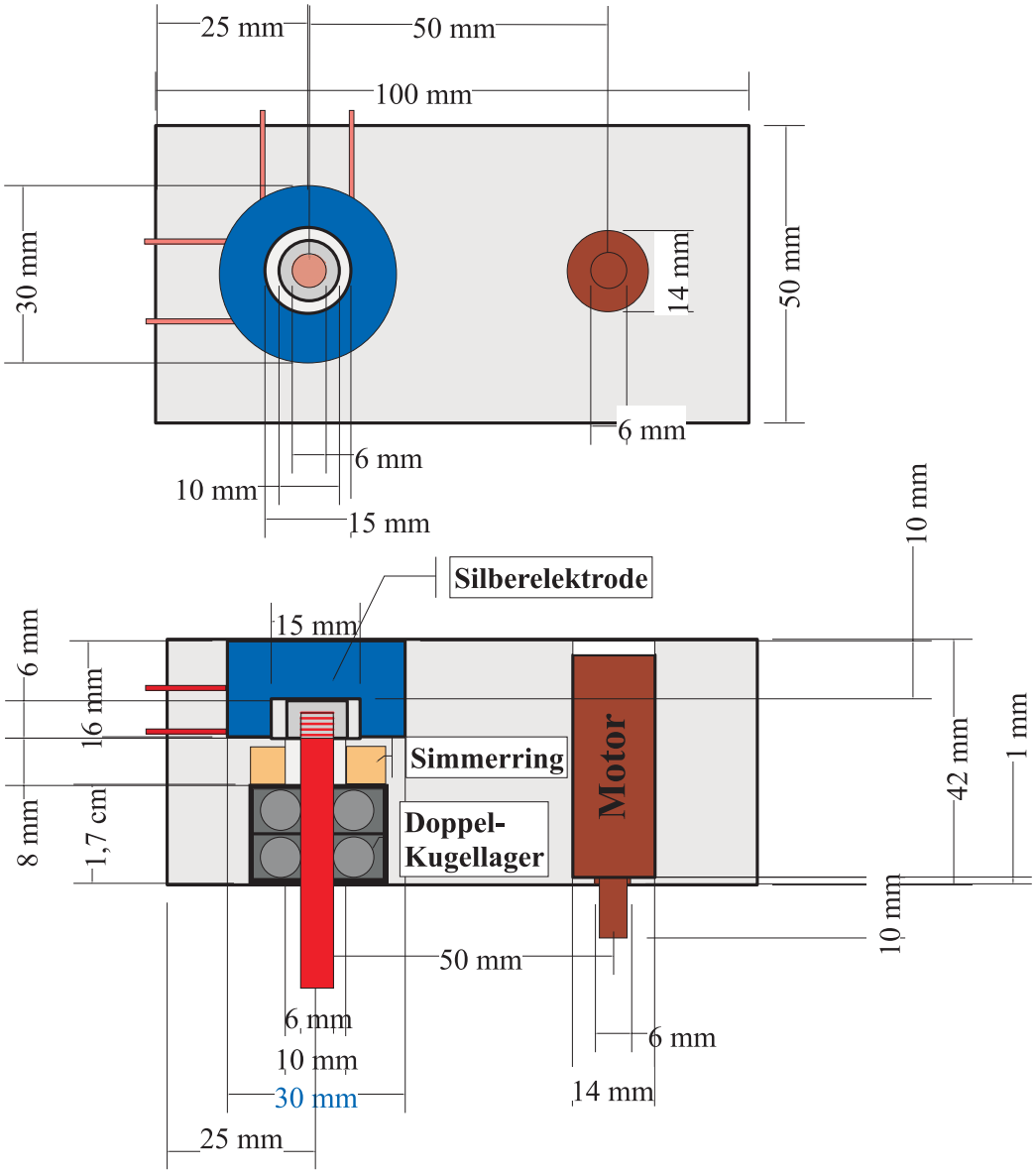
25 mm
50 mm
100 mm
30 mm
50 mm
14 mm
6 mm
6 mm
10 mm
15 mm
Silberelektrode
10 mm
15 mm
6 mm
16 mm
Simmerring
Motor
8 mm
1,7 cm
Doppel-
Kugellager
42 mm
1 mm
10 mm
50 mm
6 mm
10 mm
30 mm
25 mm
6 mm
14 mm

einfache Einbohrung
Bohrung für Nachstellschraube
50 mm
28 mm
8 mm
4 mm
4 mm
8 mm
8 mm
10 mm
10 mm
6 mm
100 mm
86 mm
6,5 mm
3 mm
6 mm
25 mm
25 mm
23 mm
19 mm
86 mm
6 mm
6,5 mm
25 mm
35 mm
9 mm
28 mm
19 mm
13 mm
3 mm
27 mm
35 mm
9 mm
3 mm
8,9 mm
6,5 mm
3 mm
6 mm
ur Elektrode
chraube

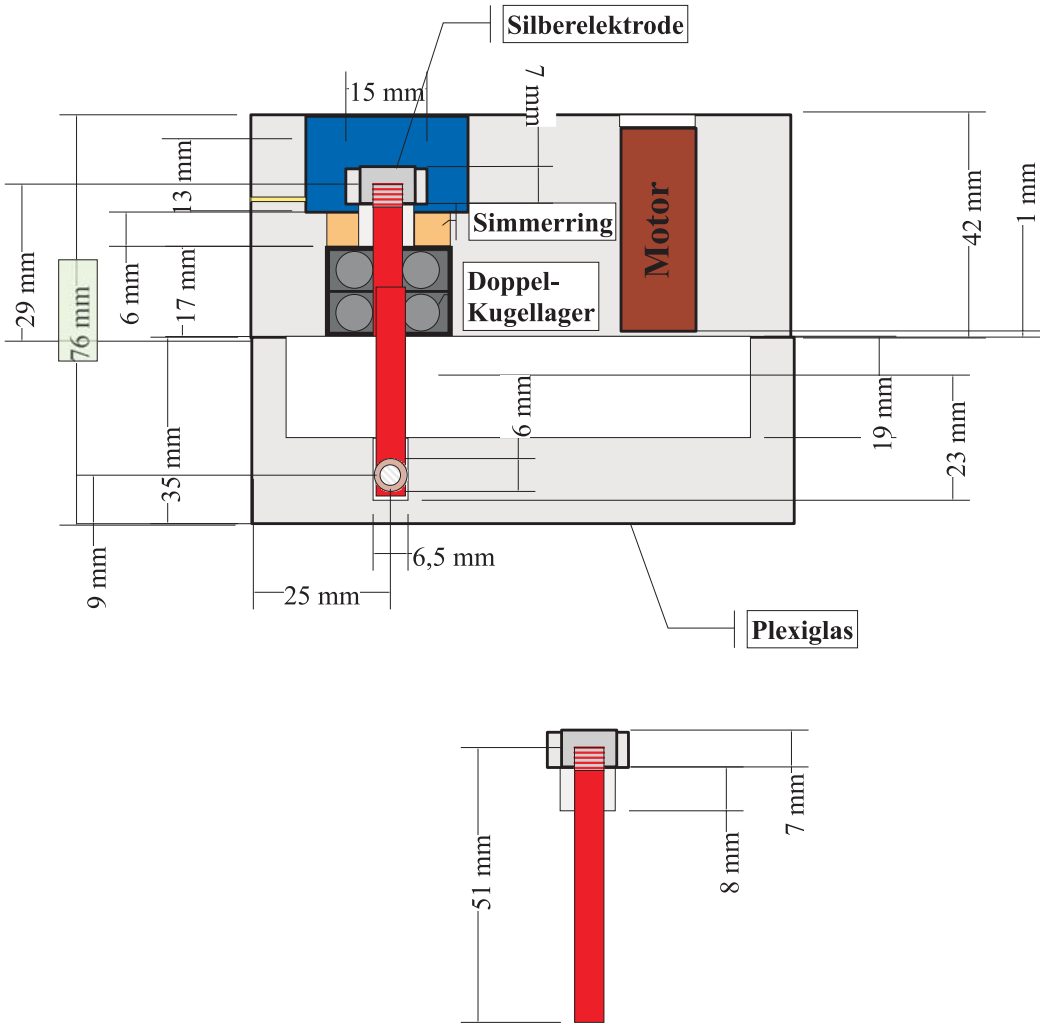
Silberelektrode
15 mm
7 mm
13 mm
Simmerring
Motor
42 mm
1 mm
29 mm
76 mm
6 mm
17 mm
Doppel-
Kugellager
6 mm
19 mm
23 mm
35 mm
9 mm
6,5 mm
25 mm
Plexiglas
51 mm
8 mm
7 mm

A.2 Macro for Ultra-fast External Triggering of an Autolab Potentiostat

SYSDEF40.INP

1 : 99,5,+PGSTAT20+PG30EXT+F_RA_2+SCANGEN+INT+FILTER+ADC750,1,
2 : ,,,,
3 : 1024,1,10000,30000,10000
4 : 0,0,0,0,0
5 : 0,0,0,1,2
6 : 1,1,3,1500,5000
7 : &H280,&H200,,,
8 : &H0,&H1,&HE,&HF,&H9
9 : &HA,&HB,3,&H8,&H5
10: &H6,&H7,&HC,&HD,&H8
11: &H6,&H1,,,
12: 1,2,3,,
13: 4,3,4,,
14: 9.9,4,3,0,0
15: 1,14,2,13,12
16: 11,9,16,15,1
17: 7,8,,,
18: &HE,&HF,&H3,,
19: 10,-10,65536,50,15000
20: 0,100,40,18,40
21: 10,-10,65536,,
22: &H6,&HF,&HA,&H20000&,
23: &H80,&H80,,,
24: 0,50,20,20,10000
25: 60,.0001,1,0,1
26: 1,1,1,1,13333333
27: 1,1,1,1,1
28: 0,0,5,1,1
29: 7,6,5,4,1
30: 0,1,4,0,
31: -1,4,.05,1,3
32: 2,2,10,2.5,2

33: 500,60,.1,9.9,2400
34: 5,6,1,3,6000
35: 5,6,1,2.5,3.6
36: 4000,0.002,0.001,.1,.001
37: 2000,.00005,.0005,4,12000
38: 3,9,1,5,5
39: Burette 1,Burette 2,Burette 3,Burette 4,
40: Burette 5,Burette 6,Burette 7,Burette 8,
41: 9000,50,22,0,8
42: 1E-9,55,20,25,
43: 2,0.005,40,1,
44: 30,110,0,,
45: ,,,,
46: ,,,.03,1E-9
47: 1.0E-10,1.0E-6,1.0E-9,1.0E-9,1E-9
48: .03,0.03,0.3,0.03,0.03
49: 12920000,64,2048,4,8
50: &H0,&HC,&H1,&H2,&HD
51: 1,2,.2,5,.1
52: 1500,100,2E+7,5,128
53: ,4.8,1,10,
54: 10,5,500,5,10
55: 1,0,1,0,0
56: ,,0,,
57: 10,1,,,
58: 1,2,3,4,
59: 1,,,,
60: 1000;0;7,51000;0;7,51000;3;7,51000;3;7,51000;3;7
61: 10000;3;7,1500;3;7,150;3;7,15;3;9,1;3;9
62: 1;3;9,1;3;9,500,,
63: 100,10000,,10,1000
64: 1,9,0,0,0
65: 0,9,4,10,12
66: 13,12,10,8,6

67: 13,14,11,9,7
68: 5,3,6,7,8
69: 5,,,,
70: 4,2,1,,
71: ,,,,
72: 1,0,,,
73: .1,.7,125000,.5,
74: 1,3,3,3,1
75: 1,,0,,
76: ,,,,
77: 1,11,11,11,1
78: ,10,1,15,
79: ,,,,
80: 1000;0;8,4E6;0;8,4E6;0;8,4E6;0;8,4E6;0;8
81: 10000;0;8,1500;0;8,150;0;8,15;0;8,1;0;8
82: ,,,,
83: 0,25,2,1,1e6
84: 5,6,,,
85: 10,128,50000,1,
86: 1.724,2.212,1.462,2.016,
87: 0,3,,,
88: ,,,,
89: ,,,,
90: 10000;0;8,4E6;0;8,4E6;0;8,4E6;0;8,4E6;0;8
91: 100000;0;8,50000;0;8,10000;0;8,1000;0;8,100;0;8
92: &H20,&H21,,,
93: ,0.01,,,
94: ,,,,
95: ,2,,,
96: 3,4,5,6,7
97: &H0,&HFF,1,1,
98: ,,,,
99: ,,,,*EOF

Paper 1

The Protein-Tethered Lipid Bilayer: A Novel Mimic of the Biological Membrane

Frank Giess,* Marcel G. Friedrich,* Joachim Heberle,† Renate L. Naumann,* and Wolfgang Knoll*
*Max Planck Institute for Polymer Research, Mainz, Germany; and †Research Centre Juelich, Juelich, Germany

ABSTRACT A new concept of solid-supported tethered bilayer lipid membrane (tBLM) for the functional incorporation of membrane proteins is introduced. The incorporated protein itself acts as the tethering molecule resulting in a versatile system in which the protein determines the characteristics of the submembraneous space. This architecture is achieved through a metal chelating surface, to which histidine-tagged (His-tagged) membrane proteins are able to bind in a reversible manner. The tethered bilayer lipid membrane is generated by substitution of protein-bound detergent molecules with lipids using in-situ dialysis or adsorption. The system is characterized by surface plasmon resonance, quartz crystal microbalance, and electrochemical impedance spectroscopy. His-tagged cytochrome *c* oxidase (C*c*O) is used as a model protein in this study. However, the new system should be applicable to all recombinant membrane proteins bearing a terminal His-tag. In particular, combination of surface immobilization and membrane reconstitution opens new prospects for the investigation of functional membrane proteins by various surface-sensitive techniques under a defined electric field.

INTRODUCTION

Membrane proteins play a major role in every living cell. With the advances in genome mapping it was revealed that ~20–30% of the genes of an organism encode for membrane proteins (Gerstein and Hegyi, 1998). These proteins are the key factors in the cell's metabolism, for example in cell-cell interaction, signal transduction, and transport of ions and nutrients. Due to this important function, they are a preferred target for pharmaceuticals (currently >60% of consumed drugs). Additionally, membrane proteins account for the two key reactions of biochemistry: respiration and photosynthesis (Ludwig et al., 2001; Richter and Ludwig, 2003).

Contrary to this fundamental role in biology, accessibility of membrane proteins by experimental techniques remains challenging. Structural as well as functional characterization of membrane proteins is difficult due to their amphiphilic properties that interfere with crystallization necessary for x-ray crystallography. Consequently, few examples of the atomic structure of membrane proteins are reported (see Stahlberg et al., 2002; Torres et al., 2003 for review). The limitation of NMR experiments to low-molecular-weight particles forces investigators to use organic solvents or detergent solutions rather than lipid bilayer systems. Obviously all of these structural methods are unable to reflect the importance of the membrane water interface for the structural and functional properties of membrane proteins (Hurley, 2003; White et al., 2001).

Various model systems of the biological membrane address this issue. Solubilized membrane proteins are purified and reconstituted; i.e., reintegrated in an (artificial) lipid bilayer, which mimicks their native environment in the plasma membrane. In the classical liposomal system the lipid bilayer encloses an inner cavity. Therefore, experimental difficulties arise when there is a need to control contents or solute concentrations of the inner compartment. The same holds for the application of a transmembrane potential that is limited to the generation of a diffusion potential by the usage of ion-specific ionophores (Vecer et al., 1997). These problems do not arise when using black lipid membranes (BLMs) that provide equal access to both sides of a membrane. However, BLMs lack mechanical and long-term stability (Winterhalter, 2000). For both of these systems it is impossible to apply surface-sensitive techniques such as AFM, SPR, QCM, or ATR-FTIR, and will probably never evolve to a routinely used and/or large-scale technology for biosensing or lab-on-a-chip applications.

To overcome these problems, solid-supported lipid membranes were developed in the recent decade, starting from bilayers floating freely on top of a quartz, indium tin oxide, or gold surface, to polymer-supported and tethered bilayer lipid membranes (tBLMs). The latter ones address the necessity of a submembraneous space serving both as an ionic reservoir as well as providing adequate space for incorporated membrane proteins (Guidelli et al., 2001; Knoll et al., 2000; Krishna et al., 2003; Naumann et al., 2002, 2003, 1999; Raguse et al., 1998; Schiller et al., 2003; Sinner and Knoll, 2001). The most demanding problem in tBLMs is to achieve electrical properties that are competitive with BLMs, i.e., show a capacitance of ~0.5 μF/cm^2 and resistances >1 MΩ cm^2 (Krishna et al., 2001; Naumann et al., 2003; Peggion et al., 2001; Schiller et al., 2003). Albeit many different systems were developed in the recent years, few show the functional incorporation of complex membrane proteins (Naumann et al., 2002, 1999; Schmidt et al., 1998; Sevin-Landais et al., 2000) .

Submitted May 21, 2004, and accepted for publication July 7, 2004.

Address reprint requests to Renate L. Naumann, E-mail: naumannr@mpip-mainz.mpg.de.

0006-3495/04/11/3213/08 $2.00

doi: 10.1529/biophysj.104.046169

All tBLMs reported to date are defined by bifunctional molecules, providing a lipophilic domain and a hydrophilic spacer. The lipophilic part inserts into one or both leaflets of the lipid membrane and can consist of phospholipids (Naumann et al., 2002, 1999; Peggion et al., 2001; Schmidt et al., 1998), cholesterols (Becucci et al., 2002; Lang et al., 1994), alkyl chains (Cornell et al., 1997; Glazier et al., 2000; Williams et al., 1997) or phytanyl groups (Cornell et al., 2001; Krishna et al., 2001; Naumann et al., 2003; Raguse et al., 1998; Schiller et al., 2003; Terrettaz et al., 2003; Vanderah et al., 1998; Woodhouse et al., 1998). The hydrophilic spacer attaches the tethering molecule to the support and determines the hydrophilic environment as well as the volume of the submembraneous space. Successful applications of polyethylene oxide (Naumann et al., 2003; Schiller et al., 2003; Terrettaz et al., 2003) and peptide spacer groups were reported for the generation of highly insulating tBLM systems (Peggion et al., 2001), necessary to investigate membrane proteins under a defined electric field.

However, the tethering molecules inevitably apply diffusional constraints to the lipid molecules of the tBLM in a way as to prevent the membrane protein to undergo conformational or diffusional changes necessary for its biological activity. Furthermore the tethering portion may not be compatible with bulky extramembraneous domains. Finally, the tethering part requires a certain amount of space that is not accessible to the protein, water, or ions.

To overcome these limitations, a tBLM was developed with the membrane protein of interest being the essential building block. The necessary surface modification is based on the concept of the well-established metal ion affinity chromatography (Hochuli et al., 1987). Ion chelating nitrilotriacetic acid groups bearing a terminal amino group (ANTA) are coupled in situ to an *N*-hydroxy succinimide (NHS) ester functionalized surface. The resulting NTA surface is activated by complexation of Cu^{2+} ions rendering it capable of reversible immobilization of His-tagged proteins (see Fig. 1).

The generation of a protein-tethered bilayer lipid membrane (ptBLM) on top of the NTA surface is illustrated schematically in Fig. 2. The His-tagged membrane protein is first attached to the surface in its detergent solubilized form. In the second step, the detergent molecules are substituted by lipid molecules thus forming a lipid bilayer that is tethered to the support by the protein itself. The coupling His-tag provides sufficient intramolecular flexibility to allow for activity in the reconstituted protein. Above all, it renders the proposed method universally applicable to all His-tagged membrane proteins.

Both, in situ affinity coupling of proteins (Kroger et al., 1999; Madoz-Gurpide et al., 2000; Rigler et al., 2003) and in-situ dialysis (Devadoss and Burgess, 2002; Singh and Keller, 1991) were described before. However, the idea to combine the two to form a membrane protein-tethered lipid bilayer is new. First examples of the experimental power of the new system are demonstrated by the use of surface analytical methods such as surface plasmon resonance (SPR) and by quartz crystal microbalance (QCM) measurements. In particular, electrochemical impedance spectroscopy (EIS) is used, with C*c*O from *Rhodobacter sphaeroides* as a model protein, to measure active proton transport catalyzed by dioxygen reduction (Wikstrom, 2004).

MATERIALS

If not otherwise stated all chemicals including equine heart cyt *c* were purchased from Sigma-Aldrich Chemie GmbH (Munich, Germany). 1,2-diphytanoyl-*sn*-glycero-3-phosphocholine (DiPhyPC) was obtained from Avanti Polar Lipids (Alabaster, AL). C*c*O from *R. sphaeroides* with the

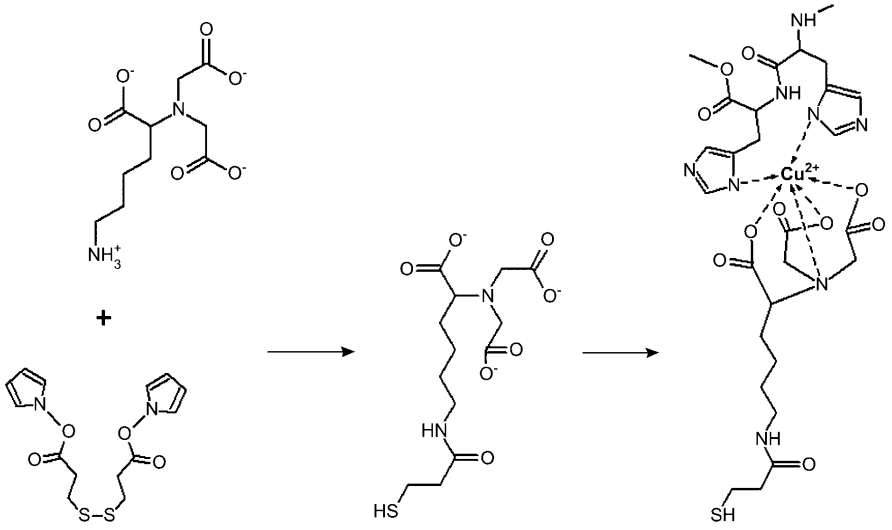

FIGURE 1 Coupling reaction leading to the chelating surface. An NHS-activated monolayer is prepared by self-assembly of DTSP (*left*) that is thereafter coupled with ANTA (*middle*). Complex formation is achieved by immersing the electrode in $CuSO_4$ solution, ready for complexation with the His-tagged C*c*O (*right*).

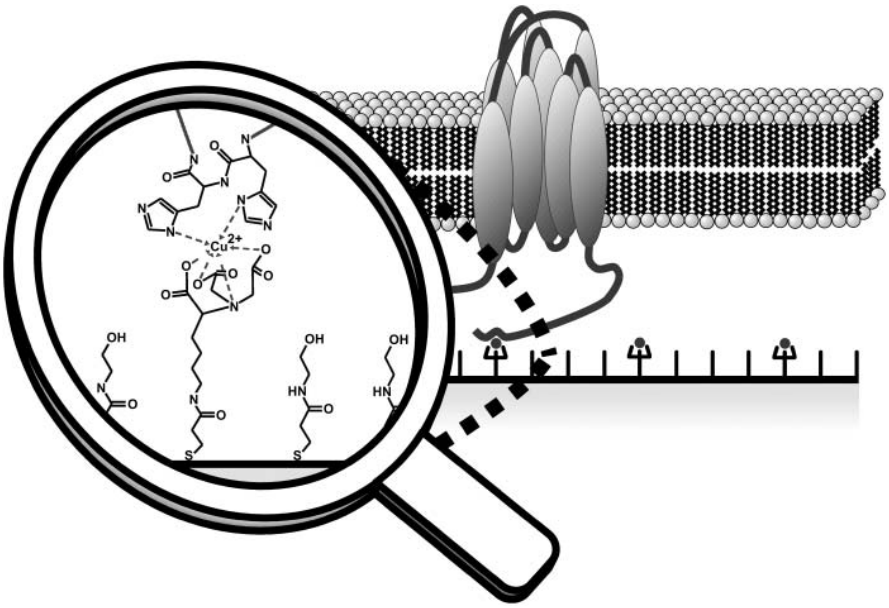

FIGURE 2 Conceptual representation of the protein-tethered lipid bilayer. The interaction between the terminal His-tag of the membrane protein and the NTA functionality is magnified at the left side. Note that the size of the His-tagged hydrophilic domain will determine the submembraneous space. The figure is not drawn to scale.

His-tag fused to the C-terminus of subunit I was expressed and purified according to Mitchell and Gennis (1995).

The protein was solubilized in PBS/DDM buffer (100 mM KCl, 50 mM phosphate, pH 8 0.1% dodecyl maltoside (DDM)). Buffer and detergent concentrations were kept constant during the binding experiments. To probe the reversibility of the binding, PBS/DDM buffer was substituted with a buffer of the same composition, albeit with additional 100 mM imidazole. For dialysis pure PBS buffer (without detergent) was used.

METHODS

Preparation of the template stripped gold (TSG) electrodes was done as described (Naumann et al., 2003): briefly, 50-nm-thick gold films were deposited by electrothermal evaporation (rate 0.01–0.05 nm/s, 2 10^{-6} mbar) on silicon wafers (roughness according to AFM was <1 nm). Gold films on silicon wafers were then glued with EPO-TEK 353ND-4, ($n = 1.5922$) to LaSFN9 high index match glass slides and cured for 60 min at 150°C. The silicon wafer was detached from the gold film just before use.

Quartz crystals (Q-Sense AB, Vaestra Froelunda, Sweden) were cleaned in an H_2O_2-NH_3-water solution (1:1:5, 70°C for 10 min) and rinsed with water and ethanol.

Functionalization of the gold films

Both glass slides and cleaned quartz crystals, to be prepared for SPR/EIS and QCM measurements, respectively, were immersed for 30 min in a solution of dithiobis (*N*-succinimidyl propionate) (DTSP; see Fig. 2) in dry DMSO (2 mg/ml). The slides were rinsed with dry DMSO, water, and ethanol and dried in a stream of nitrogen. The slides were then immersed for 2 h in a 0.15-M solution of *N*-(5-amino-1-carboxypentyl) iminodiacetic acid (ANTA) buffered to pH 9.8 by adding 0.5 M KCO_3. As a last step the glass slide was immersed for 30 min in 40 mM $CuSO_4$ in acetate buffer (50 mM, pH 5.5). After Cu^{2+} incubation the slides were rinsed with water and PBS buffer.

Reversible protein binding and lipid reconstitution by in-situ dialysis

The protein solution was infused into the SPR or the QCM cell, respectively, by pumping 500 μl aliquots of an 830-nM protein solution at a constant velocity of 250 μl/min, followed by immediate washing with PBS/DDM buffer. Subsequently, the solution was exchanged to the imidazole-containing PBS/DDM buffer and thereafter back to the imidazole-free PBS/DDM solution, completing one cycle of protein binding/desorption.

For the reconstitution, the bound protein was incubated with buffer containing solubilized DiPhyPC at a concentration 0.05 mg/ml in PBS/DDM. After 45 min the detergent was removed by pumping pure PBS buffer through the outer compartment of the dialysis cell. As an alternative to dialysis, the detergent was removed by adding biobeads to the PBS/DDM buffer (Bio-Rad Laboratories GmbH, Munich, Germany).

Surface plasmon resonance measurements

Surface plasmon resonance measurements were performed in a homebuilt SPR setup allowing for simultaneous EIS measurements as described before (Naumann et al., 1999). Surface plasmons were excited by a He/Ne laser ($\lambda = 632.8$ nm). SPR spectra were simulated using a four-layer model representing the prism glass, gold, DTSP-ANTA/protein, and lipid with refractive indices of $n = 1.7$, 3.1, 1.45, 1.5, respectively. The refractive index of the PBS buffer was assumed at $n = 1.33$. Measurements were carried out in a custom-made sandwiched dialysis cell, made from Plexiglas (see Fig. 3), separated by a dialysis membrane (molecular weight cutoff of 6000) generating an inner sample compartment ($\sim$150 μl) and an outer compartment. Dialysis was achieved by circulation of pure buffer through the outer compartment.

Electrochemical impedance spectroscopy measurements

Electrochemical impedance spectroscopy measurements were conducted using an EG&G potentiostat (model 273A, Princeton Applied Research Group, Oak Ridge, TN), controlled by a FRA analyzer (model 1260, Solartron Analytical, Farnborough, UK). Spectra were recorded over

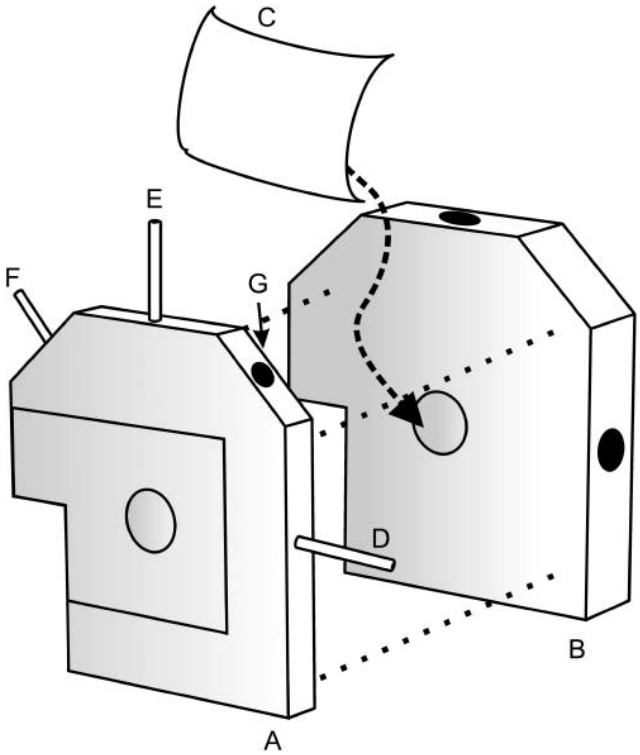

FIGURE 3 Basic cell design used for simultaneous measurements of SPR and EIS. A dialysis membrane (*C*) is placed between the two parts. The gold electrode is pressed to the front part (*A*) thus defining the sample compartment. For dialysis buffer solution is pumped continuously through the rear compartment (*B*). Proper sealing is achieved by O-rings. Sample inlet (*D*), sample outlet (*E*), connection to counter electrode (*F*), bore hole for reference electrode (*G*).

a frequency range of 3 mHz to 1 MHz with an excitation amplitude of 10 mV and a bias potential of 0 V against a $Ag/AgCl/KCl_{sat}$ reference electrode (with a platinum wire as counter electrode). Spectra were recorded firstly after immobilization of C*c*O, then after reconstitution and at last after activation. Data were subsequently analyzed by the complex nonlinear fitting algorithm supplied in ZVIEW (Version 2.6, Scribner Associates, Southern Pines, NC).

Cytochrome *c* (cyt *c*) from equine heart was used as the electron donor for C*c*O. The reduced form of cyt *c* was obtained by reaction with sodium dithionite. The excess reducing agent was removed by gel filtration through a Sephadex column. Activation was triggered by adding 20 μl of reduced cyt *c* solution (4 mg/ml), giving a final concentration of 40 mM.

Quartz crystal microbalance measurements

All quartz crystal microbalance (QCM) measurements were performed on a QSense D300 multifrequency QCM (Q-Sense AB, Vaestra Froelunda, Sweden) in a flow-through cell. Data from 5 MHz, 15 MHz, 25 MHz, and 35 MHz were collected. Reconstitution was achieved by gradually lowering the detergent concentration. The 5-MHz AC cut quartz crystals had an active surface area of $\sim$0.2 cm^2.

RESULTS AND DISCUSSION

SPR monitoring of the C*c*O binding process

The thickness of the individual dielectric layers on the gold film is determined by surface plasmon resonance spectroscopy (SPS). Reflectivity scans versus the angle of incident light are recorded (not shown). The simulation of these scans in terms of the four-layer model (see Methods) yields the thickness of the different layers listed in Table 1. SPS recordings, however, indicate the optical thickness of the dielectric layer as well as the refractive index of the bathing solution. Hence the reflectivity as a function of time at a fixed angle of incidence shown in Figs. 4 and 5 contains information not only about the thickness of the layers but also about changes in the refractive index of the buffer solution.

The thickness of the DTSP-SAM as well as the thickness change due to the coupling of ANTA are both too small to be accurately determined by SPR (see Table 1) considering that the coupling reaction consists of the substitution of the NHS residue with the ANTA molecule. The estimated length of the entire construct is $\sim$1 nm. However, the formation of these layers can be clearly detected by surface-enhanced infrared absorption spectroscopy (SEIRAS) (Ataka and Heberle, 2003) as will be shown in a forthcoming article. Changing pure PBS buffer against DDM containing buffer results in a shift of the angle of total reflection as well as an increase in reflectivity. This was simulated by a change in the bulk refractive index and additionally by a layer thickness increase of 0.9 nm. The thickness increase indicates an accumulation of detergent molecules at the surface also found by QCM measurements described below. A further increase of reflectivity is observed if C*c*O binds to the surface as shown in the kinetic trace of the SPR signal (Fig. 4, point *A*). Extensive washing with buffer results in a minor loss of material. Addition of the imidazole-containing buffer (Fig. 4, point *B*) results in a further increase in reflectivity that is attributed to a mere change of the refractive index of the bulk solution. The reflectivity returns to almost the same level as the one before protein adsorption if the imidazole buffer is replaced by the original PBS/DDM buffer (Fig. 4, point *C*). This indicates an almost complete desorption of C*c*O is from the surface as imidazole molecules compete with the His-tag for the binding sites at the Cu^{2+}/NTA complex. Nonetheless a second addition of another aliquot of C*c*O (Fig. 4, point *D*) leads to similar increase in reflectivity as the first one, showing that the adsorption of C*c*O is reversible and mediated by the interaction of the His-tag with the Cu^{2+}/NTA complex. Table 1 lists the thickness increment at each functionalization step.

Functional incorporation of C*c*O requires the enzyme to remain in its native conformation. The metal affinity surface

TABLE 1 Thickness increments linked to the different preparation stages: SPR versus QCM

Adsorption step	Δd_{SPR}/nm	Δd_{QCM}/nm*
DTSP-ANTA	0.3 ± 0.2	N/D
Cu^{2+}	0.3 ± 0.2	N/D
DDM	0.9 ± 0.2	2.6 ± 0.3
C*c*O	2.1 ± 0.3	5.5 ± 0.3

*Fitted according to the Voigt model.

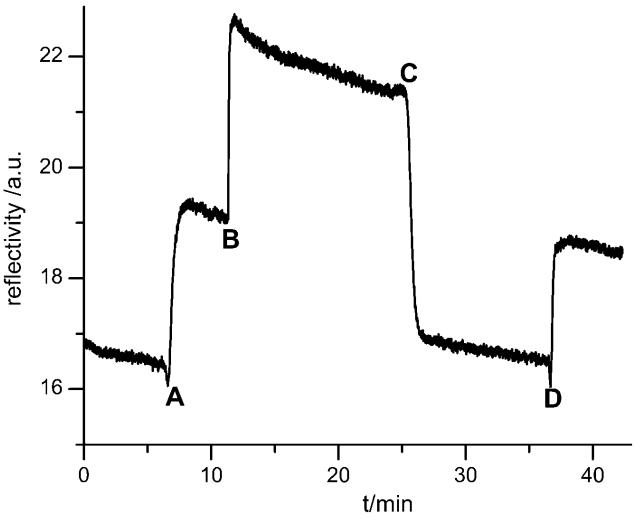

FIGURE 4 Reversible binding of C*c*O monitored by SPR. The cell is first filled with DDM/PBS. Into this solution, solubilized C*c*O is infused at points *A* and *D*, respectively, indicating the thickness increase due to binding of C*c*O. At point *B* the cell is rinsed with DDM/PBS containing 200 mM imidazole. The strong increase is due to change of refractive index. At point *C* the cell is flooded again with pure DDM/PBS changing the refractive index back to the initial value. The resulting reflectivity shows that almost complete desorption is achieved. When a new portion of solubilized C*c*O is infused at point *D* the increase in reflectivity indicates binding to be fully reversible.

causes two distinct effects both of which should promote the formation of ptBLMs: binding of the protein by the His-tag moiety prearranges the protein to form a uniform array of molecules with the His-tag in close proximity to the surface. Thus the orientation of the protein with respect to the membrane normal is dependent on the location of the histidine stretch within the protein. Consequentially, it should be possible to selectively define a vectorial ptBLM by alternation of the His-tag position. Another effect is the promotion of high surface concentrations of protein. Although not necessarily demanding for highly insulating ptBLMs, this is a key advantage of ptBLMs with respect to ''classical'' tBLM. Accumulation of the protein at the surface can be controlled by the surface concentration of the binding molecules. The lipid molecules then fill in the gaps during the last step of the reconstitution.

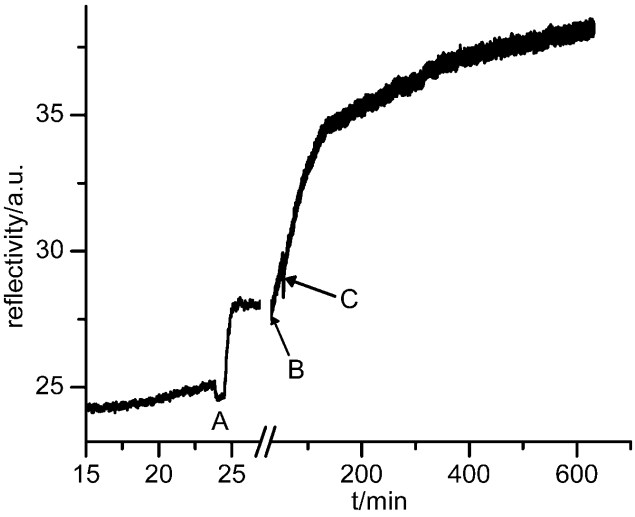

FIGURE 5 Binding of C*c*O and reconstitution monitored by SPR. At point *A*, C*c*O is infused in a DDM/PBS solution. The increase in reflectivity indicates adsorption. At point *B*, the cell is incubated with the lipid/DDM/PBS solution and dialysis sets in at point *C*. Note the different timescales.

Reconstitution of C*c*O in the bound state

The generation of a ptBLM is completed by replacing detergent molecules of the bound protein by lipids, thus forming small patches of lipid bilayers between the protein molecules, which eventually would seal the whole assembly to a closed membrane.

The design of our SPR dialysis cell allows monitoring the reconstitution process in real time. As shown in Fig. 5, the increase in reflectivity at point *A* indicates protein binding because a change in the refractive index is not involved (composition of the solution is unchanged). At point *B* the lipid/DDM/buffer is infused resulting in a change in refractive index, whereas point *C* indicates the onset of dialysis (note the different timescales). Simultaneously with the increase in reflectivity during dialysis, the electrical capacitance of the layer decreases and the resistance increases (see also Fig. 6), as described below. The combined findings are explained in terms of the successful incorporation of lipid molecules. However, the absolute thickness increment due to incorporation of lipid as estimated by SPS is not given in Table 1, because the exact degree of substitution of detergent molecules by lipid molecules is hard to assess.

QCM measurements

The resonant frequency of the quartz crystal depends on the total oscillating mass. When a thin film is adsorbed to the crystal the frequency decreases. If the film is rigid the decrease in frequency is proportional to the mass of the film. The mass of the adhering layer is calculated by using the Sauerbrey relation (Sauerbrey, 1959):

$$\Delta f = -\Delta m/nC,$$

where C is the mass sensitivity constant ($C = 17.7$ ng·cm^{-2}·Hz^{-1} at 5 MHz) and n is the overtone number ($n = 1, 3, \ldots$).

A ''soft'' (viscolelastic) film (e.g., lipids, proteins, or coupled water) will not fully couple to the oscillation of the crystal leading to a damping of the oscillation. In this case the Sauerbrey relation is not valid anymore. The dissipation of the oscillation energy contains information about the viscoelastic properties of the film.

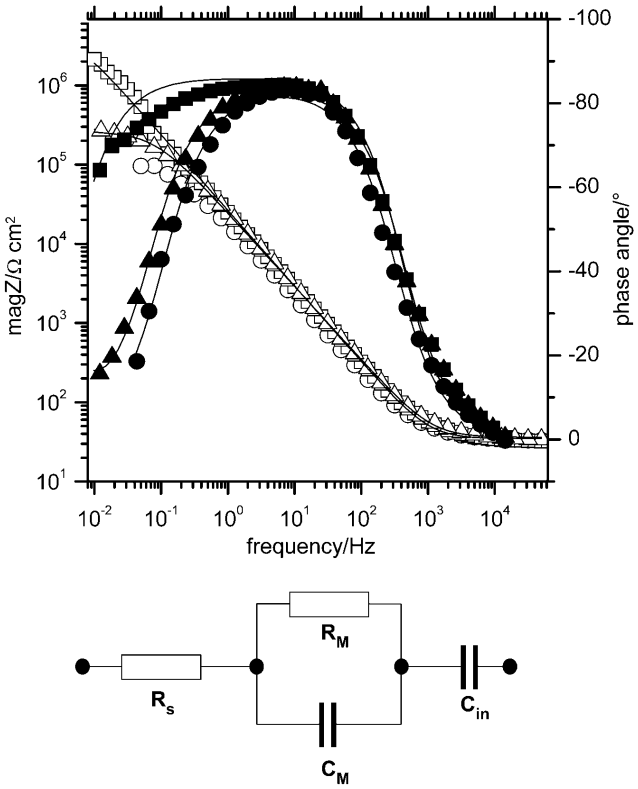

FIGURE 6 Impedance spectra measured at different stages of the experiment. Adsorbed C*c*O (Δ, ▲); after dialysis for 12 h (□, ■); after activation with cyt *c* (○, ●). Equivalent circuit used to fit the electrochemical data are: R_s solution resistance; R_m resistance of the lipid membrane; and C_m capacitance of the lipid membrane.

Incubation of the NTA surface with Cu^{2+} ions results in a slight decrease in frequency shift, whereas the dissipation remains constant (see Fig. 7). According to the Sauerbrey model this frequency shift corresponds to a mass adsorption of 42 ng/cm^2, or in other terms to an area of 16.5 Å^2 for each bound Cu^{2+} ion (disregarding any contribution from surface roughness). This value fits well to the cross-sectional area of a modeled DTSP-ANTA molecule (~17 Å^2). Because the NTA/Cu^{2+} complex has a high formation constant (Arnold, 1992), all NTA residues are complexed by Cu^{2+}. Therefore, DTSP should form a closely packed layer on the gold film that reacts quantitatively with ANTA.

Adsorption of DDM and C*c*O at the surface results in a decreasing resonance frequency as well as in an increasing dissipation. Hence the adsorbed mass was determined by fitting according to a Voigt-based viscoelastic model. Considerable differences between thickness values determined by SPR and the QCM measurements are observed (Table 1). QCM is not only sensitive to the directly adsorbed mass, but also to entrapped and closely coupled molecules, e.g., water. Although this surface coupled water does not contribute to an increase in optical thickness and hence is invisible in SPR, it adds a notable amount of viscoelastic

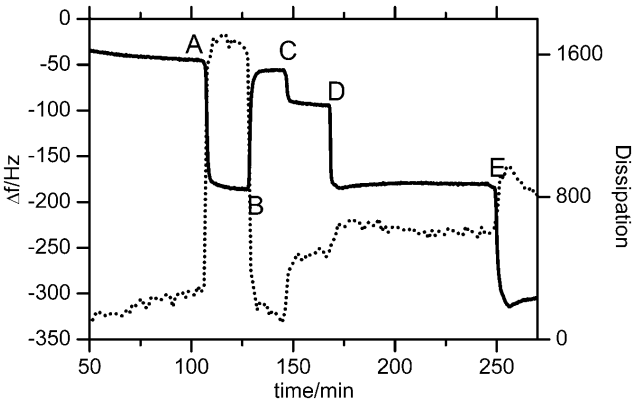

FIGURE 7 Frequency shift (*solid line*) and dissipation (*dotted line*) at different stages of the binding experiment, measured by QCM. The DTSP-NTA SAM was prepared ex situ. At point *A* the cell was flushed with 40 mM $CuSO_4$ buffer that is changed to pure water at point *B*. Points *C* and *D* indicate perfusion with PBS and PBS/DDM, respectively. C*c*O was added at point *E*.

mass, which is detected by the QCM. The reconstitution could not be measured by the QCM because of the design of the flow cell that did not allow for an in-situ dialysis.

EIS measurements

EIS spectra were recorded after every preparation step described above. Capacitance and resistance values obtained by fitting the data to the equivalent circuit shown in the insert of Fig. 6 are given in Table 2.

The resistance of the NTA-DTSP SAM decreases somewhat upon complexation of Cu^{2+} ions (not shown). A similar effect has been reported by Madoz-Gurpide et al. (2000) and was attributed to the shielding of the negative surface charges by complexed Cu^{2+} ions.

Incubation of the complexed monolayer with DDM containing buffer as well as the binding of C*c*O to the surface did not lead to significant changes in resistance and capacitance. Further incubation with lipid containing buffer and, in particular, the removal of detergent by dialysis, however, increased the resistance to values higher than 800 kΩ·cm^2 whereas the capacitance decreased considerably to

TABLE 2 Resistance and capacitance values from EIS data fitted to the equivalent circuit given in Fig. 6 for different preparation steps

	Resistance/kΩ·cm^2	Capacitance/μF/cm^2
DTSP-ANTA-Cu^{2+}-C*c*O complex	35 ± 10	10 ± 2
Reconstituted	800 ± 300	6 ± 1
After activation	100 ± 20	6 ± 1
After washing	750 ± 300	6 ± 1
After activation in the presence of KCN	750 ± 300	7 ± 1

$\sim$6 μF cm^{-2}. Examples of EIS spectra are shown in Fig. 6. This finding is consistent with the formation of a lipid bilayer, although the numerical values obtained are not those expected for a perfect bilayer lipid membrane, which should have capacitances approaching 0.5 μF cm^{-2} and resistances $>$1 MΩ cm^2. It has to be considered, however, that ptBLMs contain a large amount of protein with a dielectric constant higher than that of the lipid. From this the capacitance of the system is expected to be higher than that of the pure lipid bilayer. Assuming a dielectric constant of 30 for C*c*O (Smith et al., 1993) and 2 for DiPhyPC, the overall capacitance is estimated to be in the range of 2 μF cm^{-2} for a bilayer thickness of 5 nm and a protein content of 30%. To test whether or not the reconstituted C*c*O can be activated under these conditions, reduced cyt *c* was added to the oxygenated solution to obtain a final concentration of 40 mM. The impedance spectrum showed a drastic decrease in resistance (see the example shown in Fig. 6 from $>$1 MΩ cm^2) to 130 kΩ cm^2 indicating that the protein actively transports protons during the catalytic redox cycle. After washing off the cyt *c* with PBS, the resistance returned to the previous value illustrating that the activation is fully reversible. Infusion of reduced cyt *c* together with 0.6 mM KCN, on the other hand, did not lead to a decrease in resistance, showing that in this case the C*c*O is specifically inhibited. Electrical data are collected in Table 2 for comparison.

CONCLUSION

Protein-tethered bilayer lipid membranes have been shown to be a feasible concept to reconstitute complex membrane proteins in a tethered lipid bilayer system. Because affinity metal chromatography is a routinely applied protein purification system, ptBLMs can be seen as a universally applicable system for immobilization and surface-focused reconstitution of His-tagged membrane proteins. Purification of the proteins could even be avoided, if the preparation of ptBLMs would be performed using the crude cell lysate. This allows for the application of integrated proteomics (for review see Catimel et al., 2001) to membrane proteins.

EIS spectra before and after the addition of reduced cyt *c* show unequivocally that the enzyme is in the active state and that the activation is fully reversible. This opens new possibilities to investigate enzyme-catalyzed ion transport as a function of a defined transmembrane potential. The respective investigation in the case of the C*c*O is currently under way.

Preliminary studies have shown that activation can be followed by electrochemical and spectroscopic techniques simultaneously. Using roughened silver or gold films as the substrate for the ptBLM surface-enhancement techniques like SERRS (surface enhanced resonance Raman spectroscopy) (Wackerbarth et al., 1999) and SEIRAS (Heberle and Ataka, 2004) can be applied as will be shown in forthcoming articles. Surface analytical techniques can be exploited, like SPR and QCM as shown above, as well as AFM and STM. The immobilization procedure provides the advantage that the surface concentration of the protein can be optimized individually for every single technique.

As far as ion transport is concerned but also for structural studies, a critical issue for all membrane systems tethered to surfaces is the submembrane space. The advantage of the ptBLM is that the cytosolic part of the protein itself defines the submembrane space. In the case of the C*c*O this seems to be sufficiently large to allow for ion transport to occur across the lipid bilayer as demonstrated by EIS. Nonetheless, it is also possible to design longer affinity spacer molecules to expand the submembraneous space thus changing the electrochemical properties of the system. This is facilitated by the simplicity of the developed surface chemistry that is based exclusively on commercially available chemicals. Preliminary experiments using two coupling steps to engraft an oligoethylene glycol moiety between the Au anchor and the affinity tag showed already-promising results.

In summary, the ptBLM seems to open up promising new ways to investigate membrane proteins in a biomimetic lipid environment.

REFERENCES

Arnold, F. H. 1992. Metal Affinity Protein Separations. Academic Press, San Diego, CA.

Ataka, K., and J. Heberle. 2003. Electrochemically induced surface-enhanced infrared difference absorption (SEIDA) spectroscopy of a protein monolayer. *J. Am. Chem. Soc.* 125:4986–4987.

Becucci, L., R. Guidelli, Q. Y. Liu, R. J. Bushby, and S. D. Evans. 2002. A biomimetic membrane consisting of a polyethyleneoxythiol monolayer anchored to mercury with a phospholipid bilayer on top. *J. Phys. Chem. B.* 106:10410–10416.

Catimel, B., J. Rothacker, and E. Nice. 2001. The use of biosensors for microaffinity purification: an integrated approach to proteomics. *J. Biochem. Biophys. Methods.* 49:289–312 [Review].

Cornell, B. A., V. L. B. Braachmaksvytis, L. G. King, P. D. J. Osman, B. Raguse, L. Wieczorek, and R. J. Pace. 1997. A biosensor that uses ion-channel switches. *Nature.* 387:580–583.

Cornell, B. A., G. Krishna, P. D. Osman, R. D. Pace, and L. Wieczorek. 2001. Tethered-bilayer lipid membranes as a support for membrane-active peptides. *Biochem. Soc. Trans.* 29:613–617.

Devadoss, A., and J. D. Burgess. 2002. Detection of cholesterol through electron transfer to cholesterol oxidase in electrode-supported lipid bilayer membranes. *Langmuir.* 18:9617–9621.

Gerstein, M., and H. Hegyi. 1998. Comparing genomes in terms of protein structure: surveys of a finite parts list. *FEMS Microbiol. Rev.* 22:277–304.

Glazier, S. A., D. J. Vanderah, A. L. Plant, H. Bayley, G. Valincius, and J. J. Kasianowicz. 2000. Reconstitution of the pore-forming toxin alpha-hemolysin in phospholipid/18-octadecyl-1-thiahexa(ethylene oxide) and phospholipid/n-octadecanethiol supported bilayer membranes. *Langmuir.* 16:10428–10435.

Guidelli, R., G. Aloisi, L. Becucci, A. Dolfi, M. R. Moncelli, and F. T. Buoninsegni. 2001. New directions and challenges in electrochemistry: bioelectrochemistry at metal/water interfaces. *J. Electroanal. Chem.* 504:1–28 [Review].

Heberle, J., and K. Ataka. 2004. SEIDAS: oberflächenverstärkte differenzspektroskopie zur funktionellen untersuchung von proteinmonolagen. *Biospektrum.* 10:42–44. [in German].

Hochuli, E., H. Dobeli, and A. Schacher. 1987. New metal chelate adsorbent selective for proteins and peptides containing neighbouring histidine residues. *J. Chromatogr.* 411:177–184.

Hurley, J. H. 2003. Membrane proteins: adapting to life at the interface. *Chem. Biol.* 10:2–3.

Knoll, W., C. W. Frank, C. Heibel, R. Naumann, A. Offenhausser, J. Ruhe, E. K. Schmidt, W. W. Shen, and A. Sinner. 2000. Functional tethered lipid bilayers. *J. Biotechnol.* 74:137–158.

Krishna, G., J. Schulte, B. A. Cornell, R. J. Pace, and P. D. Osman. 2003. Tethered bilayer membranes containing ionic reservoirs: selectivity and conductance. *Langmuir.* 19:2294–2305.

Krishna, G., J. Schulte, B. A. Cornell, R. Pace, L. Wieczorek, and P. D. Osman. 2001. Tethered bilayer membranes containing ionic reservoirs: the interfacial capacitance. *Langmuir.* 17:4858–4866.

Kroger, D., M. Liley, W. Schiweck, A. Skerra, and H. Vogel. 1999. Immobilization of histidine-tagged proteins on gold surfaces using chelator thioalkanes. *Biosens. Bioelectron.* 14:155–161.

Lang, H., C. Duschl, and H. Vogel. 1994. A new class of thiolipids for the attachment of lipid bilayers on gold surfaces. *Langmuir.* 10:197–210.

Ludwig, B., E. Bender, S. Arnold, M. Huttemann, I. Lee, and B. Kadenbach. 2001. Cytochrome c oxidase and the regulation of oxidative phosphorylation. *Chembiochem.* 2:392–403.

Madoz-Gurpide, J., J. M. Abad, J. Fernandez-Recio, M. Velez, L. Vazquez, C. Gomez-Moreno, and V. M. Fernandez. 2000. Modulation of electroenzymatic NADPH oxidation through oriented immobilization of ferredoxin: NADP(+) reductase onto modified gold electrodes. *J. Am. Chem. Soc.* 122:9808–9817.

Mitchell, D. M., and R. B. Gennis. 1995. Rapid purification of wildtype and mutant cytochrome c oxidase from Rhodobacter sphaeroides by Ni2+-Nta affinity chromatography. *FEBS Lett.* 368:148–150.

Naumann, R., T. Baumgart, P. Graber, A. Jonczyk, A. Offenhausser, and W. Knoll. 2002. Proton transport through a peptide-tethered bilayer lipid membrane by the H^+-ATP synthase from chloroplasts measured by impedance spectroscopy. *Biosens. Bioelectron.* 17:25–34.

Naumann, R., S. M. Schiller, F. Giess, B. Grohe, K. B. Hartman, I. Karcher, I. Koper, J. Lubben, K. Vasilev, and W. Knoll. 2003. Tethered lipid bilayers on ultraflat gold surfaces. *Langmuir.* 19:5435–5443.

Naumann, R., E. K. Schmidt, A. Jonczyk, K. Fendler, B. Kadenbach, T. Liebermann, A. Offenhausser, and W. Knoll. 1999. The peptide-tethered lipid membrane as a biomimetic system to incorporate cytochrome c oxidase in a functionally active form. *Biosens. Bioelectron.* 14:651–662.

Peggion, C., F. Formaggio, C. Toniolo, L. Becucci, M. R. Moncelli, and R. Guidelli. 2001. A peptide-tethered lipid bilayer on mercury as a biomimetic system. *Langmuir.* 17:6585–6592.

Raguse, B., V. Braachmaksvytis, B. A. Cornell, L. G. King, P. D. J. Osman, R. J. Pace, and L. Wieczorek. 1998. Tethered lipid bilayer membranes: formation and ionic reservoir characterization. *Langmuir.* 14:648–659.

Richter, O. M., and B. Ludwig. 2003. Cytochrome c oxidase: structure, function, and physiology of a redox-driven molecular machine. *Rev. Physiol. Biochem. Pharmacol.* 147:47–74.

Rigler, P., W. P. Ulrich, P. Hoffmann, M. Mayer, and H. Vogel. 2003. Reversible immobilization of peptides: surface modification and in situ detection by attenuated total reflection FTIR spectroscopy. *Chemphyschem.* 4:268–275.

Sauerbrey, G. 1959. Verwendung von Schwingquarzen zur Wägung dünner Schichten und zur Mikrowägung. *Z. Phys.* 155:206–222. (In German).

Schiller, S. M., R. Naumann, K. Lovejoy, H. Kunz, and W. Knoll. 2003. Archaea analogue thiolipids for tethered bilayer lipid membranes on ultrasmooth gold surfaces. *Angewandte Chemie-International Edition.* 42:208–210.

Schmidt, E. K., T. Liebermann, M. Kreiter, A. Jonczyk, R. Naumann, A. Offenhausser, E. Neumann, A. Kukol, A. Maelicke, and W. Knoll. 1998. Incorporation of the acetylcholine receptor dimer from Torpedo californica in a peptide supported lipid membrane investigated by surface plasmon and fluorescence spectroscopy. *Biosens. Bioelectron.* 13:585–591.

Sevin-Landais, A., P. Rigler, S. Tzartos, F. Hucho, R. Hovius, and H. Vogel. 2000. Functional immobilisation of the nicotinic acetylcholine receptor in tethered lipid membranes. *Biophys. Chem.* 85:141–152.

Singh, S., and D. Keller. 1991. Atomic force microscopy of supported planar membrane bilayers. *Biophys. J.* 60:1401–1410.

Sinner, E. K., and W. Knoll. 2001. Functional tethered membranes. *Curr. Opin. Chem. Biol.* 5:705–711.

Smith, P. E., R. M. Brunne, A. E. Mark, and W. F. Van Gunsteren. 1993. Dielectric properties of trypsin inhibitor and lysozyme calculated from molecular dynamics simulations. *J. Phys. Chem.* 97:2009–2014.

Stahlberg, H., A. Engel, and A. Philippsen. 2002. Assessing the structure of membrane proteins: combining different methods gives the full picture. *Biochem. Cell Biol.* 80:563–568.

Terrettaz, S., M. Mayer, and H. Vogel. 2003. Highly electrically insulating tethered lipid bilayers for probing the function of ion channel proteins. *Langmuir.* 19:5567–5569.

Torres, J., T. J. Stevens, and M. Samso. 2003. Membrane proteins: the ''Wild West'' of structural biology. *Trends Biochem. Sci.* 28:137–144.

Vanderah, D. J., C. W. Meuse, V. Silin, and A. L. Plant. 1998. Synthesis and characterization of self-assembled monolayers of alkylated 1-thiahexa(ethylene oxide) compounds on gold. *Langmuir.* 14:6916–6923.

Vecer, J., P. Herman, and A. Holoubek. 1997. Diffusion membrane potential in liposomes: setting by ion gradients, absolute calibration and monitoring of fast changes by spectral shifts of Dis-C-3(3) fluorescence maximum. *Biochim. Biophys. Acta.* 1325:155–164.

Wackerbarth, H., U. Klar, W. Gunther, and P. Hildebrandt. 1999. Novel time-resolved surface-enhanced (resonance) Raman spectroscopic technique for studying the dynamics of interfacial processes: application to the electron transfer reaction of cytochrome c at a silver electrode. *Appl. Spectrosc.* 53:283–291.

White, S. H., A. S. Ladokhin, S. Jayasinghe, and K. Hristova. 2001. How membranes shape protein structure. *J. Biol. Chem.* 276:32395–32398.

Wikstrom, M. 2004. Cytochrome c oxidase: 25 years of the elusive proton pump. *Biochim. Biophys. Acta.* 1655:241–247.

Williams, L. M., S. D. Evans, T. M. Flynn, A. Marsh, P. F. Knowles, R. J. Bushby, and N. Boden. 1997. Kinetics of the unrolling of small unilamellar phospholipid vesicles onto self-assembled monolayers. *Langmuir.* 13:751–757.

Winterhalter, M. 2000. Black lipid membranes. *Curr. Opin. Colloid Interface Sci.* 5:250–255 [Review].

Woodhouse, G. E., L. G. King, L. Wieczorek, and B. A. Cornell. 1998. Kinetics of the competitive response of receptors immobilised to ion-channels which have been incorporated into a tethered bilayer. *Faraday Discuss.* 111:247–258.

Paper 2

COMMUNICATION

ChemComm
www.rsc.org/chemcomm

Active site structure and redox processes of cytochrome *c* oxidase immobilised in a novel biomimetic lipid membrane on an electrode

Marcel G. Friedrich,[a] Frank Gieß,[a] Renate Naumann,[a] Wolfgang Knoll,[a] Kenichi Ataka,[b] Joachim Heberle,[b] Jana Hrabakova,[c] Daniel H. Murgida[c] and Peter Hildebrandt*[c]

[a] *Max-Planck-Institut für Polymerforschung, Ackermannweg 10, D-55128 Mainz, Germany*

[b] *Forschungszentrum Jülich, IBI-2: Biolog. Strukturforschung, D-52425 Jülich, Germany*

[c] *Technische Universität Berlin, Institut für Chemie, Sekr. PC14, Straße des 17. Juni 135, D-10623 Berlin, Germany. E-mail: hildebrandt@chem.tu-berlin.de; Fax: +49-30-31421122; Tel: +49-30-31421419*

Received (in Cambridge, UK) 20th July 2004, Accepted 1st September 2004
First published as an Advance Article on the web 28th September 2004

Membrane-bound cytochrome *c* oxidase was attached to an electrode *via* a His-tag linker and studied by surface enhanced resonance Raman spectroscopy, demonstrating intact redox site structures and electron transfer between the electrode and the immobilized enzyme.

Nanostructured and mesoscopically scaled electronic devices including biomolecules as molecular building blocks represent one of the main topics in contemporary nano-biotechnology.[1] As a prerequisite for these devices, biomolecules such as enzymes must be immobilised under preservation of their native structures and functions. In this respect, immobilisation of membrane proteins still represents a challenge since it requires the embedment of the protein into a biomimetic system of lipid (analogues) on a solid support. To this end, various types of solid supported lipid membranes have been developed, including bilayers floating freely on quartz, indium tin oxide or gold surfaces, to polymer-, polyelectrolyte-supported and tethered bilayer lipid membranes.[2] Cytochrome *c* oxidase (CcO), a structurally, functionally, and spectroscopically well characterised membrane protein,[3–7] is one of the few complex enzymes that has been incorporated in supported lipid membranes.[8,9] Although redox activity toward cytochrome *c* (Cyt-c) as well as concomitant proton transport has been shown, these studies do not allow conclusions about the full structural integrity of the enzyme that acts as a redox-driven proton pump.

In this work, we have utilised a novel approach,[10] in which a lipid bilayer membrane is tethered to an Ag electrode *via* the integral protein, the aa_3-type CcO from *Rhodobacter sphaeroides*.[4] This system offers the possibility to analyse the immobilised enzyme by surface enhanced resonance Raman (SERR) spectroscopy which selectively probes the protein cofactors and thus can provide insight into the interfacial protein redox processes on a molecular level.[11,12]

Histidine(His)-tagged CcO, attached to a metal ion chelating coating of the metal surface, serves as a building block for a protein-tethered lipid bilayer membrane (Fig. 1). In this construct, the His-tag has been introduced to the C-terminus of subunit (SU) II at the periplasmic surface of CcO,[14] *i.e.* at the binding domain for the natural reaction partner Cyt-c.

For binding His-tagged CcO, the electrochemically roughened Ag surface was immersed in a solution of dithiobis-(*N*-succinimidyl propionate) in dry DMSO (2 mg ml^{-1}) for about 60 min. After rinsing with dry DMSO and ethanol, the dried modified surface was placed into an aqueous solution (pH 9.8, 0.5 M K_2CO_3) of 0.15 M N_α,N_α-bis(carboxymethyl)-L-lysine (ANTA) for 3 h. Finally, the coordination sites for the His ligands were created by treatment with 40 mM $NiCl_2$ (50 mM acetate buffer, pH 5.5) for 30–60 min. After rinsing with buffer solution (100 mM KCl, 50 mM potassium phosphate, pH 8), the protein was immobilized by immersing the modified Ag surface for about 2 h into the buffer solution containing 0.5 μM CcO and 0.1% dodecyl maltoside (DDM). For reconstitution of the lipid enviroment, the bound protein was incubated with buffer/DDM solution containing additionally 0.05 mg ml^{-1} 1,2-diphytanoyl-*sn*-glycero-3-phosphocholine (DPGPC). Then the detergent was removed by addition of biobeads (Bio-Rad) to the solution.

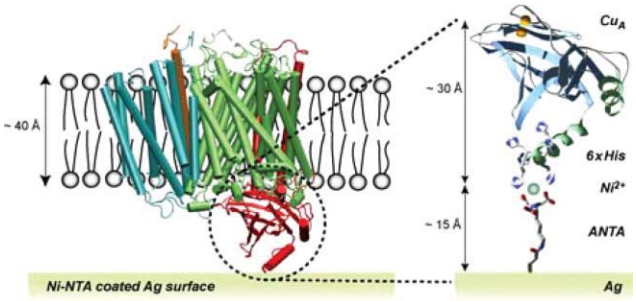

Fig. 1 Schematic representation of the CcO-tethered lipid bilayer. The left panel depicts the structure of CcO from *R. sphaeroides*[4] (sketch created by VMD[13]) embedded in the lipid bilayer on the Ag surface. The subunits SU I comprising heme a, heme a3 and CuB, SU II attached to the surface, SU III, and SU IV are displayed in green, red, cyan and ocher, respectively. The right panel shows the peripheral domain of SU II with the binuclear CuA center (yellow spheres) and the C-terminal his-tag that has been modelled into C-terminus with the program Swiss PDB viewer.

In this way, a protein-tethered lipid bilayer is created on the metal surface (Fig. 1). The exposed hydrophilic protein domain serves as a spacer between the membrane and the electrode and thus generates a submembrane space, which is electrically insulated against the bulk solution as demonstrated by impedance measurements.[10] Although the His-tag is attached to the rather flexible helix H of subunit II,[14] the surrounding phospholipid bilayer is likely to force the membrane-spanning helices of CcO in an approximately perpendicular orientation with respect to the electrode.

SERR and RR spectra display the so-called marker band region,[5,6] which allows distinguishing between the six-coordinated low-spin (6cLS) heme *a* and the high spin (HS) heme a_3 as well as determining the redox activity of the enzyme. In the RR spectrum of fully oxidised CcO in solution, characteristic heme *a* marker bands are at 1585 (ν_2), 1635 (ν_{10}), 1500 (ν_3), and 1647 cm^{-1} (formyl stretching) whereas the 1370 cm^{-1} band originates from the ν_4 modes of both heme *a* and heme a_3 (Fig. 2A). The doublet at 1477 and 1490 cm^{-1} results from the mode ν_3 of a ferric HS heme that is hexa- (6cHS) and pentacoordinated (5cHS), respectively. This finding indicates that for a fraction of the heme a_3–Cu_B catalytic site the bridging ligand is dissociated from heme a_3.[5] The 5cHS and 6cHS configuration can only be distinguished by the frequency of the ν_3 mode whereas for the ν_2 and the formyl stretching mode the bands of both coordination states coincide and give rise to the relatively strong bands at 1570 and 1671 cm^{-1}, respectively.

SERR spectra of the CcO-tethered lipid bilayers on the Ag electrode display surprisingly intense signals of the hemes *a* and a_3

DOI: 10.1039/b410998h

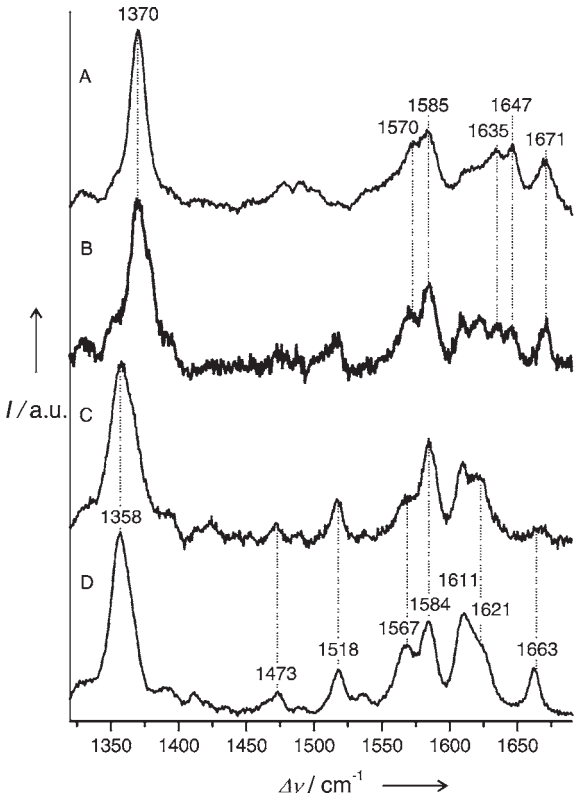

Fig. 2 SERR spectra of CcO tethered to a Ni-NTA functionalised Ag electrode and reconstituted with DPGPC, measured at (B) open circuit and (C) −0.65 V, compared with the RR spectra of CcO in solution, (A) in the fully oxidised and (D) dithionite-reduced form. Solutions contained 100 mM KCl and 50 mM potassium phosphate (pH 8) and, in RR experiments, 25 μM CcO and 0.1% DDM. All spectra were measured with 413 nm excitation. Further details of the spectroscopic experiments will be published elsewhere.

despite a separation of these groups from the metal surface of more than 50 Å (Fig. 1). At 0.0 V (*versus* Ag/AgCl) or at open circuit, the band frequencies reveal a good agreement with those of the RR spectrum of oxidised CcO (Fig. 2A,B). However, the shoulder at 1358 cm^{-1} on the low-frequency side of the prominent 1370 cm^{-1} band as well as the concomitant appearance of the characteristic 1517 and 1611 cm^{-1} bands indicates a small contribution from reduced heme *a* (*vide infra*), which may (partly) result from photoreduction by the exciting laser beam. Whereas under these conditions the immobilised enzyme is largely in the oxidised state, the SERR spectrum measured at −0.65 V (Fig. 2C) displays the vibrational band pattern of the reduced enzymes as revealed by comparison with the RR spectrum of fully reduced CcO in solution (Fig. 2D). Also for the reduced state, we note a very good agreement between the band frequencies in the RR and SERR spectra. A unique property of heme *a* is the large frequency downshift of the formyl stretching from 1647 to 1611 cm^{-1} which reflects a substantial redox-linked change of the hydrogen bond interactions of this substituent with Gln471 and Arg52.[4,6] Only a small downshift is observed for the stretching of the heme a_3 formyl group that remains in a largely hydrophobic environment.

Comparison of the RR and SERR spectra unambiguously shows that in both the ferric and the ferrous state the structures of the hemes *a* and a_3 as well as the specific interactions with the protein environment remain unchanged upon immobilisation. This is also true for the distribution between the 5cHS and 6cHS configuration in the ferric form of heme a_3, which has been shown to respond most sensitively to changes of the quaternary structure of the enzyme.[5] This finding can be taken as an indication that the entire enzyme structure is largely preserved in the immobilised state. The only noticeable differences between the RR and SERR spectra refer to relative intensities of the formyl stretchings that are weaker in the SERR spectra presumably due to the lower surface enhancement for the largely localised substituent modes as compared to the porphyrin modes.

The immobilised CcO can be reduced and re-oxidised by varying the electrode potential. No time-dependent changes are observed in the SERR spectra measured immediately after changing the potential. Thus, electron transfer reactions are fast compared to the time scale of the SERR experiments (< 1 min). Taking into account the considerable electron transfer distance to the primary acceptor Cu_A (> 40 Å; Fig. 1), we conclude that immobilisation of CcO *via* His-tags allows an efficient electron exchange with the electrode.

The redox potentials for Cu_A, heme *a*, and heme a_3 are estimated to be +0.09, +0.14, and +0.09 V, respectively.[15] However, complete reduction of the immobilised enzyme is not possible at electrode potentials positive to −0.65 V. Only to a minor extent, this large overpotential may result from the interfacial potential drops.[12] Instead, it is very likely that traces of oxygen already in solution, which were unavoidable in the present experimental set-up, cause the consumption of electrons at the catalytic heme a_3–Cu_B site. Under these steady state conditions, the oxidation states of the hemes are essentially controlled by the oxygen concentration in solution. This interpretation implies that the immobilised CcO is (largely) catalytically active. In fact, CcO that was immobilised to the electrode *via* a His-tag on the cytoplasmic side reveals enzymatic activity towards ferrous Cyt-c and is capable of transporting protons across the bilayer.[10]

In summary, we conclude that protein-tethered immobilisation of lipid bilayers allows the binding of CcO in a biomimetic environment and defined orientations while it is electronically coupled to the electrode. The structure of the heme sites is preserved and the catalytic activity appears to be retained. The present concept is not restricted to CcO but may be applicable to membrane proteins in general and thus opens new possibilities for studying and utilising immobilised proteins in fundamental and applied science.

We thank P. Brzesinski (Stockholm) for providing the *Rh. sphaeroides* strain with his-tagged CcO and B. Richter (Jülich) for expression and purification of the enzyme. The work was supported by the Deutsche Forschungsgemeinschaft (Sfb498, P.H, D.H.M) and the Volkswagen-Stiftung (J.H., W.K.).

Notes and references

1 I. Willner and E. Katz, *Angew. Chem. Int. Ed.*, 2000, **39**, 1180.
2 E. Sackmann, *Science*, 1996, **271**, 43; W. Knoll, K. Morigaki, R. Naumann, B. Saccà, St. Schiller and E.-K. Sinner, in *Ultrathin Electrochemical Chemo- and Biosensors, Technology and Performance*, ed. V. M. Mirsky, Springer, 2004.
3 H. Michel, J. Behr, A. Harrenga and A. Kannt, *Annu. Rev. Biophys. Biomol. Struct.*, 1998, **27**, 329.
4 M. Svensson-Ek, J. Abramson, G. Larsson, S. Tornroth, P. Brzezinski and S. Iwata, *J. Mol. Biol.*, 2002, **321**, 329.
5 G. Heibel, P. Hildebrandt, B. Ludwig, P. Steinrücke, T. Soulimane and G. Buse, *Biochemistry*, 1993, **32**, 10866.
6 H. M. Lee, T. K. Das, D. L. Rousseau, D. Mills, S. Ferguson-Miller and R. B. Gennis, *Biochemistry*, 2000, **39**, 2989.
7 R. M. Nyquist, D. Heitbrink, C. Bolwien, R. B. Gennis and J. Heberle, *Proc. Natl. Acad. Sci. U.S.A*, 2003, **100**, 8715.
8 J. D. Burgess, M. C. Rhoten and F. M. Hawkridge, *Langmuir*, 1998, **14**, 2467.
9 R. Naumann, R. K. Schmidt, A. Jonczyk, K. Fendler, B. Kadenbach, T. Liebermann, A. Offenhäuser and W. Knoll, *Biosens. Bioelectron.*, 1999, **14**, 651.
10 F. Giess, M. G. Friedrich, J. Heberle, R. Naumann and W. Knoll, *Biophys. J.* accepted.
11 D. H. Murgida and P. Hildebrandt, *J. Am. Chem. Soc.*, 2001, **123**, 4062.
12 D. H. Murgida and P. Hildebrandt, *J. Phys. Chem. B*, 2001, **105**, 1578.
13 W. Humphrey, A. Dalke and K. Schulten, *J. Mol. Graph.*, 1996, **14**, 33.
14 C. Hiser, D. A. Mills, M. Schall and S. Ferguson-Miller, *Biochemistry*, 2001, **40**, 1606.
15 F. Malatesta, G. Antonini, P. Sarti and M. Brunori, *Biophys. Chem.*, 1995, **54**, 1.

Paper 3

Electronic Wiring of a Multi-Redox Site Membrane Protein in a Biomimetic Surface Architecture

CONDENSED RUNNING TITLE: **ELECTRONIC WIRING OF MEMBRANE PROTEINS**

Marcel G. Friedrich,* Joseph W. F. Robertson, *† Dieter Walz,‡ Wolfgang Knoll, * and Renate L. C. Naumann *

* *Max Planck Institute for Polymer Research, Ackermannweg 10, 55128 Mainz, Germany*; † *Present address: Semiconductor Electronics Division, Electronics and Electrical Engineering Laboratory, National Institute of Standards and Technology, Gaithersburg, MD, 20899, USA*; ‡ *Biozentrum, University of Basel, Switzerland, present address Lerchenstr. 21, 4095 Basel*;

ABSTRACT

Bioelectronic coupling of multi-redox-site membrane proteins was accomplished with cytochrome c oxidase (CcO) as an example. A biomimetic membrane system was employed for the oriented immobilization of the CcO on a metal electrode. When the protein is immobilized with the cytochrome c binding side directed towards the electrode and reconstituted in-situ into a lipid bilayer, it is addressable by direct electron transfer to the redox centers. Electron transfer to the enzyme via the spacer, referred to as electronic wiring, shows an exceptionally high rate constant. This allows to perform a kinetic analysis of all four consecutive electron transfer steps within the enzyme. Electron transfer followed by rapid scan cyclic voltammetry in combination with surface-enhanced resonance Raman spectroscopy provides mechanistic and structural information about the heme centers. Probing the enzyme under turnover conditions revealed mechanistic insights into proton translocation coupled to electron transfer. This bioelectronic approach opens a new field of activity to investigate complex processes in a wide variety of membrane proteins.

Received for publication "Staff will complete" and in final form "Staff will complete"

Address reprint requests and inquiries to

Max Planck Institute for Polymer Research, Ackermannweg 10, 55128 Mainz, Germany;

KEYWORDS

Cytochrome c Oxidase, Direct Electron Transfer, Surface-enhanced Resonance Raman Spectroscopy, Protein-tethered Bilayer Lipid Membrane, tethered Bilayer Lipid Membrane, Protein Film Voltammetry

INTRODUCTION

Membrane proteins represent a crucial class of biological agents. They are the key factors in many vital functions of the cell, including respiration. Typically the proteins of the respiratory chain are multi-redox site membrane proteins. They use the energy released by electron transfer (ET) between the redox centers to actively transport protons across the lipid membrane. This process is also referred to as proton pumping. Cytochrome c oxidase (CcO) is the most prominent example of such a proton pump, illustrated schematically in (Fig.1). ET is shown to proceed stepwise along four redox centers, Cu_A, heme a, heme a_3 and Cu_B and to be coupled to proton transfer (Fig.1, inset) (1). Although X-ray crystallography[2] and genetic engineering (3,4) have revealed a great deal of detail regarding amino acids involved in the proton pumping process, the precise mechanism is not completely elucidated (5,6).

For mechanistic studies, CcO must be functionally-reconstituted in a lipid membrane. A majority of the previous investigations made use of proteoliposomes, with reconstituted enzymes (3,4). In these preparations the proteins are arranged in random orientations not allowing the application of defined electric fields, an essential parameter to control the charge transfer processes. Likewise, proteoliposomes do not allow for bioelectronic coupling, i.e. the direct electron transfer between the protein and an electrode. Control of the oxidation state of redox centers in potentiometric titrations (3) or spectroscopic investigations (4) was accomplished indirectly by the use of soluble redox mediators that shuttle electrons to and away from redox centers.

Attempts have been made to pinpoint membrane proteins on surfaces. CcO for example has previously been incorporated into solid supported bilayer lipid membranes (sBLMs) (7,8). With sBLMs the application of defined electric fields was possible (8) and direct ET to the protein was achieved, albeit slow and without alluding to catalytic activity (7). These systems are limited by the absence of a hydrophilic layer adjacent to the electrode which separates the membrane from the surface thus providing a reservoir for ions. Aqueous submembrane layers have been provided through tethered bilayer lipid membranes (tBLMs) (9,10). tBLMs, however, do neither solve the problem of the random orientation nor do they offer the possibility of biolectronic coupling. ET into the CcO was achieved, but only indirectly via cytochrome c, the natural substrate of the CcO.

To overcome all of these limitations, we developed a biomimetic membrane system, which tethers proteins to electrode surfaces through a histidine (his)-tag engineered onto the enzyme in a strict orientation (Fig. 1). A lipid bilayer is then reconstituted *in-situ* around the bound proteins, forming a protein-tethered bilayer lipid membrane (ptBLM) (11,12). First attempts to address the protein by direct electronic coupling seemed promising indicating the direct electrochemical access to the ET pathway of the protein using electrochemically controlled Surface-Enhanced Resonance Raman Spectroscopy (SERRS) (13). Electrochemically induced ET to multi-centered redox proteins has been the subject of research in recent years, providing a vast amount of kinetic information, but due to the lack of a biomimetic membrane system, mostly for soluble (14) or membrane-extrinsic proteins (15). The benefit of direct ET is the accessibility of the internal redox centers avoiding the diffusion limitation of mediators.

A further advantage inherent in the geometry of the ptBLM is the hydrophilic layer between the electrode and the lipid membrane provided by the tether molecules. The experimental benefit is the sensitivity of the small interstitial reservoir (~0,2 nL cm^{-2}) to changes in proton concentration as a result of enzyme activity. Thus this methodology presents a new approach to separately examine proton and electron transfer reactions in membrane proteins with significant consequences for the elucidation of the mechanism of proton pumping.

As a model of the 500 kDa large CcO complex located in the inner mitochondrial membrane of higher organisms (2), this study employs the smaller versions (125 kDa) from the cell membrane of bacteria, i.e. *Rhodobacter sphaeroides* (16) and *Paracoccus denitrificans* (17). X-ray crystallography suggests these versions are identical with respect to their electron and proton pathways (2,16,17). His-tags were attached to the C-terminus of SU II of *R. sphaeroides* and to C-terminus of SU I of *P. denitrificans*. The enzyme can thus be immobilized in different orientations, either with the cytochrome c binding side (Fig.1) or, with the O_2 reduction side, directed towards the electrode.

MATERIALS AND METHODS

If not otherwise stated, materials and methods were used as previously described (11). CcO from *Rhodobacter sphaeroides* with a His-tag engineered to the C-terminus of subunit II was expressed and purified according to Mitchell and Gennis (18). Template stripped gold (TSG) (19) electrodes, used for surface plasmon resonance (SPR) and electrochemistry measurements, were immersed for 120 min in a solution of dithiobis (N-succinimidyl propionate) (DTSP) and dithiobis (propionic acid) (DTP) in a 60:40 ratio, in dry DMSO (2mg/ml). After rinsing with DMSO and ethanol, the slides were functionalized for 48 h in a 0.15 M solution of *N*-(5-amino-1-carboxypentyl) iminodiacetic acid (ANTA) buffered to pH 9.8 by adding 0.5 M KCO_3. Finally, the glass slides were immersed for 30 min in 40 mM $NiSO_4$ in acetate buffer (50 mM, pH 5.5) followed by thorough rinsing with the acetate buffer to remove the excess $NiSO_4$. Immobilisation of the protein was performed as previously described (11). Dialysis was

done by adding biobeads (Bio-Rad Laboratories GmbH, Munich, Germany) to the lipid-detergent-containing phosphate / dodecyl β-D- maltoside (DDM) buffer, DiPhyPC 0.05 mg/ml in phosphate/DDM buffer (K_2HPO_4 0.1 M, KCl 0.05 M, pH=8, 0.1%DDM).

Electrochemistry:

Electrochemical measurements were performed using an Autolab instrument (PGSTAT302) equipped with an FRA2-module for impedance measurements, an ECD-module amplifier for low-currents, an ADC750 module for rapid scan measurements and a SCAN-GEN module for analog potential scanning. Cyclic voltammetry experiments were conducted with IR drop compensation, particularly at high scan rates. Measurements under anaerobic conditions were performed in a buffer solution containing K_2HPO_4 0.1M, KCl 0.05M, pH=8 and the oxygen trap consisting of glucose (0.3%w/w), glucose oxidase (75µg/ml) and catalase (12.5µg/ml) (20). This solution was flushed with Ar purged from oxygen by bubbling through the oxygen trap containing buffer solution for one or two hours prior to the measurements to assure a completely deoxygenated solution. All electrochemical measurements were taken in a three electrode configuration with TSG as the working electrode, a Ag|AgCl,KCl_{sat} reference, and a platinum wire as the counter electrode. All electrode potentials are quoted versus NHE.

Surface Enhanced Resonance Raman Spectroscopy:

Surface Enhanced Resonance Raman Spectroscopy (SERRS) was performed in a custom-made spectroelectrochemical cell also connected to an Autolab instrument using an upside-down RDE (rotating disc electrode) with a roughened silver surface (diameter 10 mm) inserted into a Teflon mantle. An inner Teflon trough was fixed to the RDE rotating in-line with the electrode. The cell was sealed to ambient air by a lid provided with inlets for the counter, reference (Ag|AgCl,KClsat) electrodes, an inlet for deoxygenation as well as for the microscope objective. The cell was flushed with Ar, purged from oxygen by washing through the oxygen trap containing buffer solution (see above). Surface enhanced resonance Raman (SERR) spectra were collected using a confocal Raman microscope (LabRam, HR800, HORIBA Jobin Yvon) equipped with a liquid nitrogen cooled back-illuminated CCD camera. The laser beam from a Kr^+ laser (excitation wavelength 413 nm) was focussed on the surface of the above mentioned Ag-disc electrode by means of a water immersion objective. In order to prevent photoreduction of the enzyme, the electrode was rotated with 15 Hz or 900 rpm and the laser intensity at the sample surface was kept smaller than 100 µW. SERR spectra of several independent measurements and different samples were averaged in order to improve the signal to noise ratio.

RESULTS

Direct Electron Transfer

CcO from R. sphaeroides engineered with a his-tag on subunit II (SU II) (16), was tethered to the surface of a gold electrode and reconstituted in-situ into a ptBLM. Under these conditions, the cytochrome c binding side, and hence also the first electron acceptor, Cu_A, is oriented towards the electrode surface. The cyclic voltammogram (CV), taken in a strictly anaerobic bathing solution, shows a single reduction peak at –274 ± 7 mV and a corresponding oxidation peak at –209 ± 6 mV (Fig. 2a) at low scan rates (< 1 V s^{-1}). As the scan rate is increased to ~1 V s^{-1}, the peak positions remain largely unchanged and the baseline-corrected current density increases linearly (inset Fig. 2a), which is consistent with surface confined ET (21). The constant peak separation at scan rates (< 1 Vs^{-1}), compatible with a fast ET (22), is observed only with the lipid membrane formed around the protein. Membrane formation was checked by surface plasmon resonance and electrochemical impedance measurements (see Supplementary Figs. 1 and 2 online). Finally, we have estimated the apparent standard potential, $E^0_{app,}$ assuming symmetrical behavior of the redox system, to be -242 ± 7 mV. This E^0_{app} is shifted ~ -450 mV from the standard potential of 230 mV determined for the CuA center in isolated CcO (23). Potential shifts as large as 700 to 800 mV were observed for ET to Au nanoclusters decorated with thiolated peptides based on α-aminoisobytyric acid (Aib) (25). The shifts were shown to depend on the length and the concentration of the surface bound peptides. This effect was explained in terms of the molecular dipole moments of the Aib peptides, which cause the redox potentials to shift considerably without affecting the rate constant of electron transfer. That means the peaks in the voltammogram change position but not the shape and not the position relative to each other (e.g. peak separation between forward and backward reaction). This agrees with the findings, observed with CcO immobilized in a ptBLM. The peak separation hardly changes so that a kinetic limitation of the direct ET must be excluded. However, a large dipole moment can be deduced from the charge distribution on the CcO molecules. X-ray crystallography data show a large number of negative charges accumulating on the cytochrome c binding side facing the electrode and likewise a large number of positive charges on the side pointing into the bathing solution (16). The negative shift of the peak potential is an indication of the accumulation of negative charges on the side of the electrode. The opposite

effect is observed if the CcO is immobilized in the inverse orientation. A positive shift of the redox potential by 200 mV was found for cytochrome c bound to the CcO in the ptBLM (27). This relatively smaller effect can be explained by a smaller number of positive charges present on the distal side of the CcO.

The reversible behaviour of the ET, on the other hand, can be explained by the ET pathway to the enzyme via the Ni complex, taking into account the low standard potentials of chelated Ni^{2+}/Ni^{+} couples (26). Simulations were carried out utilizing concepts developed by Walz et al. (29) designed for analyzing bioelectrochemical processes across membranes. In the simulations of the heterogeneous ET to the enzyme, the Ni complex is treated as a transient electron acceptor. Details can be found in the supplementary information (see supplementary Fig. 5-7 online), showing that the probabilities of the conformations with Ni in the reduced state do not exceed 6×10^{-8} (see supplementary Fig. 7b online), in accordance with the absence of redox peaks when the Ni-NTA is chelated with imidazole instead of the his-tag (28).

Strong evidence that ET observed by CV does take place directly into the enzyme was derived from Soret band excited SERRS taken as a function of potential, under strictly *anaerobic* conditions (Fig. 3a). The characteristic marker band region (1300-1750 cm^{-1}) is very sensitive to the integrity of the enzyme, and provides information on the redox state, the ligation, spin and coordination state of the heme a/a_3 structure. The bands at 1358 cm^{-1} and 1370 cm^{-1} originate from the ν_4 modes of both hemes in the reduced (-350 mV) and oxidized state (-150 mV), respectively (13,30). Furthermore, the type-a hemes of CcO include conjugated vinyl and formyl substituents, which give rise to resonance Raman-active stretching modes between 1610 and 1680 cm^{-1}. Characteristic redox linked changes of the weakly bound formyl substituent of heme a_3 cause a small change from 1663 cm^{-1} in the oxidized state to 1671 cm^{-1} in the reduced state, because the formyl group remains in a hydrophobic environment. A further characteristic marker for the reduced heme a is the intense and well-separated band at 1517 cm^{-1} (ν_{11}) not present in the oxidized state. Redox induced changes of the C=O side group of heme a_3 can be observed by a larger frequency downshift from 1646 to 1610 cm^{-1}, which reflects a substantial redox-linked change of the stronger hydrogen bond interactions of this substituent with Gln471 and Arg52 (13,30). Both porphyrin modes (ν_4 and ν_{11}) and the formyl stretching modes allow monitoring of the oxidation states of the individual hemes of the immobilized CcO. The bands at 1500 (ν_3) and 1585 cm^{-1} (ν_2) result from a ferric hexacoordinated low-spin (6cLS) heme (13,30,31). These findings corroborate the results of earlier studies, showing the SERR spectra on the surface to be identical to Resonance Raman (RR) spectra in solution. Furthermore, they demonstrate a gradual transition of the redox state as well as the coordination and spin state of both heme centers in the potential range between -150 mV and -350 mV, in agreement with the CV data (Fig. 2).

Since the SERRS experiment is particularly designed for a selective resonance enhancement of the heme structure, the Cu centers are not visible. Evidence that ET to the hemes indeed occurs via Cu_A as described in previous studies 32,33) was derived from potential-controlled Surface Enhanced IR Reflection Absorption Spectroscopy performed on CcO immobilized in the same orientation in a ptBLM. These measurements make use of amide I bands of the protein environment assigned to specific redox states of Cu_A (3). Results will be presented in a forthcoming publication. Taken together with the Raman spectra, these results indicate that the electrochemical reduction peak is in fact due to direct ET to Cu_A and further on to the heme centers. This is further corroborated by the charge calculated from the integrated area of the reductive and oxidative peaks (see supplementary Fig. 3). These results are consistent with a densely packed protein monolayer, assuming an ellipsoidal disk of 4.5 nm × 7.0 nm for the in-plane dimension of the protein deduced from the crystal structure of CcO from *R. sphaeroides* (34), but only if 4 electrons transferred per molecule are considered.

As a control, CcO from *P. denitrificans* with a his-tag engineered to the C-terminus of subunit I (SU I) (20) was immobilized in the same biomimetic system. The cytochrome c binding side, and hence Cu_A, is oriented towards the outside of the membrane opposite to that described above. This inverted orientation shows Raman spectra identical to those of CcO with the his-tag on SU II, thus indicating the same structural integrity of the protein. No indication of reduction can be seen in the potential range between +200 mV and –1100 mV (Fig. 3b), suggesting that the enzyme remains in the oxidized state. Accordingly, no electron transfer peaks can be observed with CV (Fig. 5a, blue curve). Nevertheless, this is not due to a functional impairment of the redox centers since they can be reduced chemically by adding dithionite (Fig. 3b), and CcO may be activated by reduced cytochrome c (11). This experiment proves conclusively that ET between the electrode and CcO does not occur non-specifically to any of the redox centers, but is possible only via Cu_A, with the cytochrome c binding side oriented towards the electrode. Thus, exquisite control of the orientation of the enzyme allows direct, verifiable ET reactions to and within CcO to be elucidated.

Kinetics of Electron Transfer

While slow scan rate CV is sufficient to obtain basic ET mechanistic information, scan rates larger than 1V s^{-1} must

be utilized to extract kinetic information (Fig. 2b). The baseline-corrected current in the CV of a surface-confined redox couple can be represented by a Gaussian curve whose peak position and width are determined by the standard potential of the couple, the number of electrons, the rate constant of ET (k_0) and the scan rate (21). At low scan rates the peak position is approximately constant and close to the standard potential. As the scan rate is increased to several Vs^{-1}, kinetic constraints cause the peaks to separate, with reductive and oxidative peaks shifting to more negative and more positive potentials, respectively.

The four redox center CcO enzyme exhibits a more complicated behavior. Under anaerobic conditions the redox currents display single slightly asymmetric peaks up to a scan rate of ~1 Vs^{-1} (cf. Fig. 2a) indicating the contributions from multiple redox centers. At scan rates above 1 Vs^{-1} the baseline-corrected peaks become more asymmetric, a second maximum gradually appears as the scan rate exceeds 20 Vs^{-1} (Fig. 2b). Complex voltammograms of multi-redox-site proteins were previously deconvoluted into a number of Gaussian components with the area of each peak corresponding to the number of electrons transferred in each step (35). Accordingly, the curves shown in Fig. 2b were found to require four Gaussian components to adequately describe the system. However, due to the strong overlap, the peak areas are not evenly distributed, particularly regarding the last component. This is assumed to be caused by the strong coupling of the ET occurring sequentially through the four redox centers Cu_A, heme a, heme a_3 and Cu_B in the enzyme (Fig. 2b, inset), not observed in other enzymes (35).

Established procedures (35) were used to obtain kinetic rate constants by plotting the peak potentials versus scan rate in a logarithmic scale, to yield a “trumpet” plot (Fig. 4) (36). This plot was analyzed by means of the algorithm described by Jeuken et al. with the simplifying assumption of an individual one-step ET to each redox center (35,37). Values for the rate constant k_0 and the apparent standard potential E^0_{app} thus obtained are shown in Table 1. Because ET between redox centers in CcO occurs sequentially, the values of k_0 for redox centers 2, 3 and 4 are approximations of lumped rate constants (38) to heme a, heme a_3, and Cu_B through the ET chain. However, k_0 for redox center 1 is attributed to ET to Cu_A. Hence, it is clear that ET to the subsequent redox centers is not restricted or rate-limited by the electrochemical ET to Cu_A. Therefore, the measurements in the ptBLM yield results of biological relevance.

Proton Transport coupled to Electron Transfer

To investigate the enzyme undergoing catalytic turnover, *aerobic* conditions were used. The CV of CcO with the cytochrome c binding side oriented towards the electrode showed two cathodic peaks (Fig. 5a, black curve). The first peak at -202 ± 5mV, attributed to reduction of the four redox centers of CcO, showed a significant amplification of the current density compared to the peak under *anaerobic* conditions (Fig. 5a, red curve). This is a clear indication of the catalytic turnover of the enzyme. Electrons transferred from the electrode to the redox centers of CcO are irreversibly transferred to oxygen, leading to a continuous electron transfer (30,32). The current density (35 $\mu A\,cm^{-2}$) of this peak is considerably larger than the one measured previously with the help of soluble substrates of membrane proteins immobilized in a tBLM ($\leq$0.6 $\mu A\,cm^{-2}$) (10), indicating a comparatively high activity of the CcO embedded in the ptBLM.

As a consequence of catalytic turnover of the CcO in the orientation with the his-tag attached to SU II, protons are pumped from the bulk solution into the interstitial space between the electrode and the ptBLM. Due to its small volume, this interstitial space is thereby highly acidified (as low as pH 2, see supplementary Fig. 4). These protons are electrochemically reduced to H_2 giving rise to the second peak at -422 ± 6 mV (Fig. 5a, black curve), as confirmed by experiments using the modified surface without the enzyme and lipid membrane being present (see supplementary Fig. 4). Moreover, a similar proton reduction peak has already been observed for H^+/ATP-synthase reconstituted into a tBLM (39). The absence of direct ET and the H^+ reduction peak in the inverted orientation (Fig. 5a, blue curve) further confirms the orientation-dependence of direct electron transfer as well as transmembrane proton transport. The sloping baseline in the negative potential range of the control experiment (Fig. 5a, blue curve) is explained in terms of the irreversible reduction of oxygen at the modified electrode. This holds also for the baseline in the CV of CcO subject to direct ET under aerobic (Fig. 5a, black curve) as compared to anaerobic conditions (Fig. 5a, red curve).

Improved sensitivity can be achieved by using differential pulse voltammetry (DPV). Under *aerobic* conditions the amplified current density of the reductive peak (-190 mV) and the resultant proton reduction peak (-390 mV) can be observed (Fig. 5b, black curve). More importantly, under *anaerobic* conditions no proton peak was recorded while a single peak is observed due to the reduction of the enzyme (Fig. 5b, red curve). If only one proton was transferred across the membrane as all four redox centres are reduced, a proton reduction current of ~0.8 $\mu A\,cm^{-2}$ can be expected, which would be easily detectable by DPV. The same applies when the enzyme is reduced in the presence of the inhibitor cyanide under *aerobic* conditions; (Fig. 5b, green curve) in this case no proton reduction peak is observed.

DISCUSSION

Bioelectronic coupling of a multi-redox-site membrane protein in a functionally active form was verified using CcO as an example. This is clearly demonstrated by electrochemical and potential-controlled SERRS experiments. Direct ET to the enzyme is very specifically controlled by the orientation of the CcO immobilized on the surface. Electrons are transferred but only when the CcO is immobilized with the cytochrome c binding side directed towards the electrode, suggesting that the primary electron acceptor is Cu_A as in other biochemical assays. Electron transfer appears to be facilitated by the $Ni^{1+/2+}$ complex, as deduced from the heterogeneous rate coefficient $k_0 > 4000\ s^{-1}$, which is fast as compared to other (soluble) proteins. Previous attempts at coupling proteins to surfaces have yielded k_0 values between 100 s^{-1} to 1600 s^{-1} (40,41). Electron injection into the CcO by other methods, (see for example Ref. 42) is faster, for example by pulse radiolysis or photochemical excitation (43). In these methods, however, a substrate has to be bound first to the enzyme in a slow diffusion-controlled process before electron injection can be initiated. As a consequence, fast electron injection occurs only once, and a continuous or repetitive process is not possible. By contrast, electrochemical ET is not limited by diffusion. It can be repeatedly performed many times in both the reductive and oxidative direction or alternatively it can be used to elicit a stationary state of ET. This makes electrochemical ET the method of choice for time-resolved measurements particularly for processes occurring in cycles, e.g. enzymatic cycles. The full enzyme cycle apparently occurs in CcO immobilized in the ptBLM as is evident from CV scans obtained under aerobic conditions.

ET is often rate-limited by protonation reactions; for example, proton uptake of the so-called charge compensating proton of reduced heme a/a_3 occurs in the time scale of 200 μs (45) which would yield a first order rate constant of 5000 s^{-1}. Protonation of the hemes is very likely to occur on electrochemical reduction of the CcO which would account for an overall $k_0 > 4000\ s^{-1}$. Rates of transitions between other states in the enzyme cycle, e.g. transitions between the states labelled P and F, or F and O are considerably slower (in the ms time scale) (46). It is thus concluded that the bioelectronic approach is designed to perform kinetic measurements of biological relevance.

Regarding mechanistic details, first insights into the performance of the electrochemical method have been gained by comparative measurements under aerobic and anaerobic conditions. Proton transfer into the interstitial space underneath the membrane only occurs in the presence of oxygen. This observation supports the proposed mechanism of proton pumping, in conjunction with the transition from state O to E, which requires a preceding full turnover (or an activated state O_H) (46,47). Other proposals contradict this idea, claiming that the transfer of two electrons from state O to E is followed by a proton pumping step even with no preceding turnover of the catalytic cycle (45,49). The latter hypothesis seems questionable in the light of our findings which suggest that protons are not released to the submembrane space upon a mere reduction of the hemes, i.e. proton pumping does not occur without oxygen present (46,47,49). It should be mentioned, however, that the uptake of protons in the O to E transition, [the so-called charge compensating protons (45)] is compatible with our experiments.

The result presented in this work demonstrate that the ptBLM is a promising new platform for kinetic and mechanistic studies of a large number of membrane proteins, in particular redox proteins. Studies of other membrane proteins would certainly also benefit from this strategy, considering that electric fields are often a controlling parameter, for example for ion transport through channel proteins. These options are particularly attractive with respect to the combined application of electrochemical and multiple surface analytical methods, including vibrational spectroscopy.

ABBREVIATION

Cytochrome c oxidase (CcO), electron transfer (ET), tethered bilayer lipid membranes (tBLMs), protein-tethered bilayer lipid membranes (ptBLMs) Surface-Enhanced Resonance Raman Spectroscopy (SERRS), normal hydrogen electrode (NHE)

ACKNOWLEDGEMENT

We are grateful to Shelagh Ferguson-Miller, Michigan State University, for providing us with CcO from *R. sphaeroides* engineered with the his-tag on SU II and to Bernd Ludwig, university of Frankfurt Germany, for providing us with CcO from *P. denitrificans* engineered with the his-tag on SU I.

REFERENCES

1. Richter, O.-M.H., and B.Ludwig. 2003. Cytochrome c oxidase – structure, function and physiology of a redox-driven molecular machine. *Rev Physiol Biochem Pharmacol* 147: 47-74.
2. Tsukihara, T. et al. 1995. Structures of metal sites of oxidized bovine heart cytochrome c oxidase at 2.8 Å. *Science*, 269: 1069-1074.
3. Gorbikova, E.A., K. Vuorilehto, M. Wikström, and M.I. Verkhovsky. 2006. Redox Titration of All Electron Carriers of Cytochrome c Oxidase by Fourier Transform Infrared Spectroscopy. *Biochemistry*, 45: 5641-5649.
4. Hellwig, P. et al. 2002. Vibrational Modes of Tyrosines in Cytochrome c Oxidase from Paracoccus denitrificans: FTIR and Electrochemical Studies on Tyr-D_4-labeled and on Tyr280His and Tyr35Phe Mutant Enzymes. *Biochemistry*, 41: 9116-9125.
5. Zaslavsky, D., and R.B. Gennis. 2000. Proton Pumping by cyctochrome c oxidase: Progress, problems and postulates. *Biochim. Biophys. Acta* 1458: 164-179.
6. Wikström, M. 2004. Cytochrome c oxidase: 25 years of the elusive proton pump. *Biochimica et Biophysica Acta*, 1655:241-247.
7. Salamon Z., J. Hazzard, and G. Tollin. 1993. *Proc Natl Acad Sci USA* 90:6420-23.
8. Cullison, J.K., F.M. Hawkridge, N. Nakashima, and Sh. Yoshikawa. 1994. A study of Cytochrome c Oxidase in Lipid Bilayer Membranes on Electrode Surfaces. *Langmuir* 10:877-882.
9. Naumann, R., E.K. Schmidt, A. Jonczyk, K. Fendler, B. Kadenbach, T. Liebermann, A. Offenhäusser, and W. Knoll, 1999. The peptide-tethered lipid membrane as a biomimetic system to incorporate cytochrome c oxidase in a functionally active form. *Biosens. Bioelectr.* 14:651-662.
10. Jeuken, L.J.C. et al., 2006. Redox Enzymes in Tethered Membranes. *JACS* 128:1711-1716.
11. Giess, F., M.G. Friedrich, J. Heberle, R.L. Naumann, and W. Knoll. 2004. The protein-tethered lipid bilayer: A novel mimic of the biological membrane. *Biophys. J.* 87:3213-3220.
12. Ataka, K. et al., 2004. Oriented attachment and membrane reconstitution of his-tagged cytochrome c oxidase to a gold electrode: In-situ monitoring by surface enhanced infrared absorption spectroscopy. *JACS* 126:16199-16206.
13. Friedrich, M.G., et al. 2004. Active Site Structure and redox processes of cytochrome c oxidase immobilised in a novel biomimetic lipid membrane. *Chem. Comm.* 2376-2377.
14. Léger, Ch. et al. 2003. Enzyme electrokinetics: Using protein film voltammetry to investigate redox enzymes and their mechanisms. *Biochemistry* 42:8653-8662.
15. Hirst, J., A. Sucheta, B.A.C. Ackrell, and F.A. Armstrong. Electrocatalytic voltammetry of succinate dehydrogenase: direct quantification of the catalytic properties of a complex electron-transport enzyme. *J. Am. Chem. Soc.* 118:5031-5038 (1996).
16. Hosler J. P. et al. 1992. Cytochrome aa_3 of *Rhodobacter sphaeroids* as a Model for Mitochondrial Cytochrome c Oxidase. *JBC* 267: 24264-24273.
17. Pfitzner U., A. Odenwal, Th. Ostermann, L. Weingard, B. Ludwig, O.-M.H. Richter. 1998. Cytochrome c oxidase (Heme aa_3) from *Paracoccus denitrificans*: Analysis of Mutations in Putative Proton Channels of Subunit I. *J. Bioenerg. Biomembranes* 30:3089-97.
18. Mitchell, D.M., and R.B. Gennis. 1995. Rapid purification of wildtype and mutant cytochrome c oxidase from *Rhodobacter Sphaeroides* by Ni^{2+}-NTA affinity chromatography. *FEBS Letters* 368(1):148-150.
19. Naumann, R., et al. 2003. Tethered lipid bilayers on ultra flat gold surfaces. *Langmuir,* 19:5435-5443.
20. Vanderkooi J. M., G. Maniar, T.J. Green, and D. Wilson. 1987. An optical method for measurement of dioxygen concentration based upon quenching of phosphorecence *The Journal of biological chemistry*, 262(12) :5476-82.
21. Bard, A.J. and L.L. Faulkner. 2001. *Electrochemical Methods: Fundamentals ands Applications.* second edition John Wiley & Sons, New York.
22. Jeuken, L.J.C.; J.P. McEvoy, and F.A. Armstrong. 2002. *Journal of Physical Chemistry B* 106(9):2304-2313.
23. Moody, A. J., U. Brandt, P.R. and Rich. 1991. Single electron transfer of slow and fast cytochrome-c oxidase. *FEBS Lett.* 293:101-105.
24. Döpner, S., J. Hudecek, B. Ludwig, H. Witt, and P. Hildebrandt. 2000. Structural changes in cytochrome c oxidase binding. A resonance Raman study. *Biochim. Biophys. Acta* 1480:*57-64*.
25. Holm, A. H., M. Ceccato, R.L. Donkers, L. Fabris, G. Pace, and F. Maran. 2006. Effect of peptide ligand Dipole Moments on the Redox Potentials of Au_{38} and Au_{140} Nanoparticles, *Langmuir* 22: 10584-10589.
26. Budnikova, Yu., G. Petruksina, and M. Kargin. 1996. Metallocomplexnij catalys v organicheskom electrosynthese. Complexy nikelja(II) c PPh3, 2,2'-bipyridylom, 1,10-phenanthrolinom, ych redox-cvoistva i catalys reactii vostanovlenija digalogenorganocheskych cojedineniji. *Journal Obtschej Chimii*, 66:610-614.
27. Friedrich, M. G., M.A. Plum, V. U. Kirste, W. Knoll, B. Ludwig, and R.L.C. Naumann. 2007. In-situ Monitoring of the Catalytic Activity of Cytochrome c Oxidase in a Biomimetic Architecture *submitted* to *JACS*
28. Blankespoor, R., B. Limoges, B. Schöllhorn, J.-L. Syssa-Magalé, and D. Yazidi. 2005. Dense Monolayer of Metal-Chelating Ligands Covalently Attached to Carbon Electrodes Electrochemically and Their Useful Application in Affinity Binding of Histidine-Tagged Proteins. *Langmuir* 21:3362-3375.
29. Walz, D., S.R. Caplan, D.R.L. Scriven, D.C. Miculecky in: S.R. Caplan, I.R. Miller, and G. Milazzo (Eds.). 1995. *Bioelectrochemistry: Principles and Practice.* vol. 1, Birkhäuser Verlag, Basel, Ch. 2.
30. Heibel, G.E., P. Hildebrandt, B. Ludwig, P. Steinrücke, T. Soulimane, and G. Buse. 1993. Comparitive Resonance Raman Study of Cytochrome c Oxidase from Beef Heart and *Paracoccus denitrificans. Biochemistry*, 32:10866-10877.
31. Lee, H.M., et al. 2000. Mutations in the putative H-channel in the cytochrome c oxidase from *Rhodobacter sphaeroides* show that this channel is not important for proton conduction but reveal modulation of the properties of the heme a. *Biochemistry*, 39:2989-2996.
32. Verkhovsky, M.I., J.E. Morgan, and M. Wikström. 1995. Control of electron delivery to the oxygen reduction site of cyctochrome c oxidase, a role for protons. *Biochemistry* 34:7483-7491.
33. Szundi, I., J.A. Cappucino, N. Borovok, B. Kotlyar, and O. Einarsdottir. 2001. Photo-induced electron transfer in the cytochrome c oxidase oxidase complex using thioredopyrenetrisulfonate-labeled cytochrome c. Optical multichannel detection. *Biochemistry* 40:2186-2193.
34. Svensson-Ek, M. et al. 2002. The X-ray Crystal Structures of Wild-type and EQ(I-286) Mutant Cytochrome c Oxidases from Rhodobacter sphaeroides, *J. Mol. Biol.,* 321:329-339.
35. Armstrong, F.A. 2002. Insights from protein film voltammetry into mechanisms of complex biological electron-transfer reactions. *J. Chem Soc. Dalton Trans*. 661-671.
36. Laviron, E. 1979. General expression of the linear potential sweep voltammogram in the case of diffusionless electrochemical systems. *J. Electroanal. Chem.* 101:19-28.
37. Jeuken, L.J.C., J.P. McEvoy, and F.A. Armstrong. 2002. Insights into Gated Electron-Transfer Kinetics at the Electrode-Protein Interface: A Square wave Study of the Blue Copper Protein Azurin. *J. Phys. Chem. B.* 106:2304-2313.

38. Hill T.L. 1977. *Free Energy Transduction in Biology.* Academic Press, New York.
39. Naumann, R., T. Baumgart, P. Gräber, A. Jonczyk, A. Offenhäusser, and W. Knoll. 2002. Proton transport through a peptide-tethered bilayer lipid membrane by the H^+-ATP synthase from chloroplasts measured by impedance spectroscopy. *Biosens. Bioelectr.* 17:25-34.
40. Jeuken, L.J.C. Conformational reorganization in interfacial protein electron transfer. 2003. *Biochim. Biophys. Acta*, 1604:67-76.
41. Hirst, J. et al. 1998. Kinetics and mechanism of redox-coupled, long-range proton transfer in an iron-sulfur protein. Investigation by fast-scan protein-film voltammetry. *JACS* 120:7085-7094.
42. Winkler, J.R., B.G. Malmström, and H.B. Gray. 1995. Rapid electron injection into multisite metalloproteins: intramolecular electron transfer in cytochrome oxidase, *Biophys. Chem.* 54:199-205.
43. Kobayashi, K., H. Une, and K. Hayashi. 1989. Electron Transfer Processes in Cytochrome Oxidase after Pulse Readiolysis, *J. Biol. Chem.* 264:7976-7980.
44. Nilsson T. 1992. Photoinduced electron transfer from tris(2,2'-bipyridyl)ruthenium to cytochrome c oxidase, *Proc. Natl. Acad. Sci. USA,* 89:6497-501.
45. Michel, H. 1999. Cytochrome c oxidase: Catalytic cycle and Mechanisms of Proton Pumping- A Discussion. *Biochemistry* 38, 15129-15140.
46. Verkhovsky, M.I., A. Jasaitis, M.L. Verkhovskaya, J.E. Morgan, , and M. Wikström. 1999. Proton translocation by cytochrome c oxidase. *Nature* 400:480-483.
47. Verkhovsky, M.I., Belevich, I., Bloch, D.A., and Wikström, M. 2006. Elementary steps of proton translocation in the catalytic cyle of cytochrome c oxidase *Biochim. Biophys. Acta, Bioenergetics* 1757:401-407.
48. Ruitenberg, M., Kannt, A., Bamberg, E., Fendler, K., and Michel, H. 2002. Reduction of cytochrome c oxidase by a second electron leads to proton translocation. *Nature* 417:99-102.
49. Faxen, K., G. Gilderson, P. Adelroth, and P. Brzezinski. 2005. A mechanistic principle for proton pumping by cytochrome c oxidase, *Nature,* 437(7056) :286-9.

TABLES

Table 1: Apparent standard potentials E^0_{app} and rate constants k_0 obtained from CV of CcO under anaerobic conditions.

Redox center	E^0_{app} /mV	k_0/s^{-1}
1 (black) ≙ Cu_A	–231 ± 8	4130± 390
2 (red)	–234 ± 7	1650 ± 170
3 (green)	–211 ± 6	68 ± 8
4 (blue)	–183 ± 7	11 ± 2

The errors represent ranges resulting from experimental errors, the deconvolution procedure and the fit routine applied to the trumpet plot for four data sets of the same enzyme preparation.

FIGURE LEGENDS

Figure 1:

Schematic representation of cytochrome c oxidase (CcO) embedded into a protein-tethered bilayer lipid membrane. The protein is attached to the surface of a template stripped gold film by the his-tag attached to SU II, allowing for direct electron transfer. The lipid bilayer is assembled around the protein. The box on the right shows the stepwise electron transfer inside the CcO (Michel, 1999) and the box on the left shows the details of the surface modification (Bloch et al., 2004).

Figure 2:

Cyclic voltammogramms of CcO with the his-tag attached to SU II under strictly anaerobic conditions. (a) Scan rates (a) between 0.1 and 1 Vs^{-1}, 0.01 V s^{-1} (green), 0.02 V s^{-1} (orange), 0.03 V s^{-1} (dark blue), 0.05 V s^{-1} (light blue), 0.075 V s^{-1} (red), and 0.1 V s^{-1} (black). Inset: Baseline-corrected current density plotted as a function of scan rate, reductive branch (red), oxidative branch (green), (b) Oxidative branches (baseline-corrected) of CVs at scan rates between 1 and 600 Vs^{-1} (current densities normalized by the scan rate, ≅ 1 Vs^{-1}) 1 V s^{-1} (red), 3 V s^{-1} (black), 7.5 V s^{-1} (green), 20 V s^{-1} (orange), 40 V s^{-1} (pink), 300 V s^{-1} (blue), 400 V s^{-1} (violet), 500 V s^{-1} (gray), 600 V s^{-1} (light blue), inset: example of a deconvolution into four Gaussian components

Figure 3:

SERR spectra of CcO at different potentials applied across the biomimetic protein-membrane architecture immersed in buffer solution (a) with the his-tag on SU II at –150 mV (1), -175 mV (2), -200 mV (3), -225 mV (4), -250 mV (5), -275 mV (6), -300 mV (7), -325 mV (8) and –350 mV (9), (b) with the his-tag on SU I, spectrum taken at +200 mV (1), -1100 mV (2) and after chemical reduction with dithionite (3).

Figure 4:

Peak potentials as a function of scan rate (trumpet plots) of the four redox centers. Peak potentials are obtained by deconvolution of CVs into Gaussian components of oxidation and reduction branches of CcO with the his-tag attached to SU II under anaerobic conditions (cf. Fig. 2b), redox center 1 (Cu_A) (black), 2 (red), 3 (green), 4 (blue). The error bars represent ranges resulting from the deconvolution procedure.

Figure 5:

Voltammogramms of CcO with the his-tag attached to SU II under aerobic and anaerobic conditions. (a) Cyclic voltammograms at a scan rate of 0.01 Vs^{-1} anaerobic (red), aerobic (black) and CcO with the his-tag on SU I (blue). (b) Differential pulse voltammograms, anaerobic (red), aerobic (black) and aerobic in the presence of 40 μM cyanide (green). The dashed curves are enlarged for clarity, corresponding to the y-axis on the right hand side.

FIGURES

1

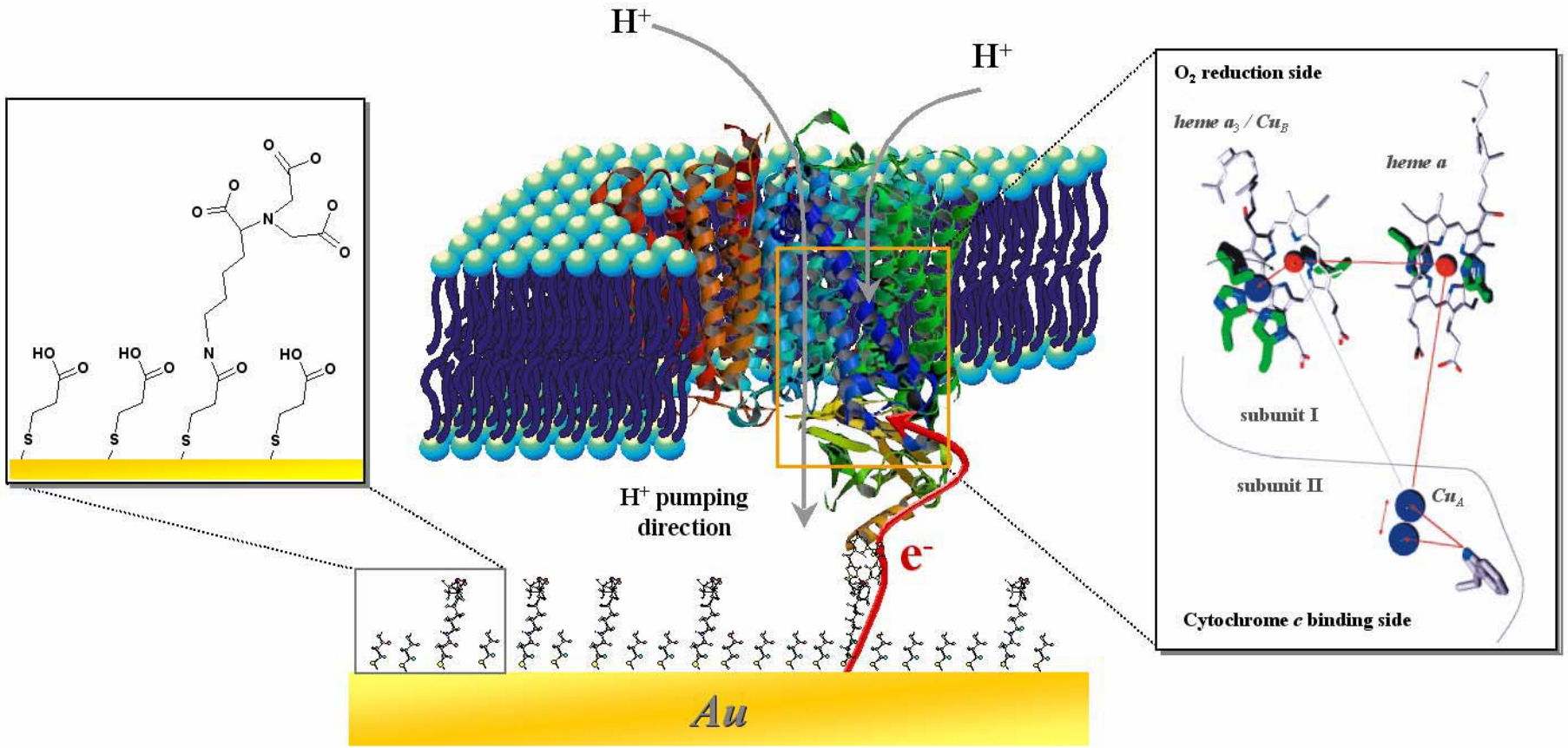
H+
H+
O2 reduction side
heme a3 / CuB
heme a
subunit I
subunit II
CuA
Cytochrome c binding side
H+ pumping direction
e-
Au

2

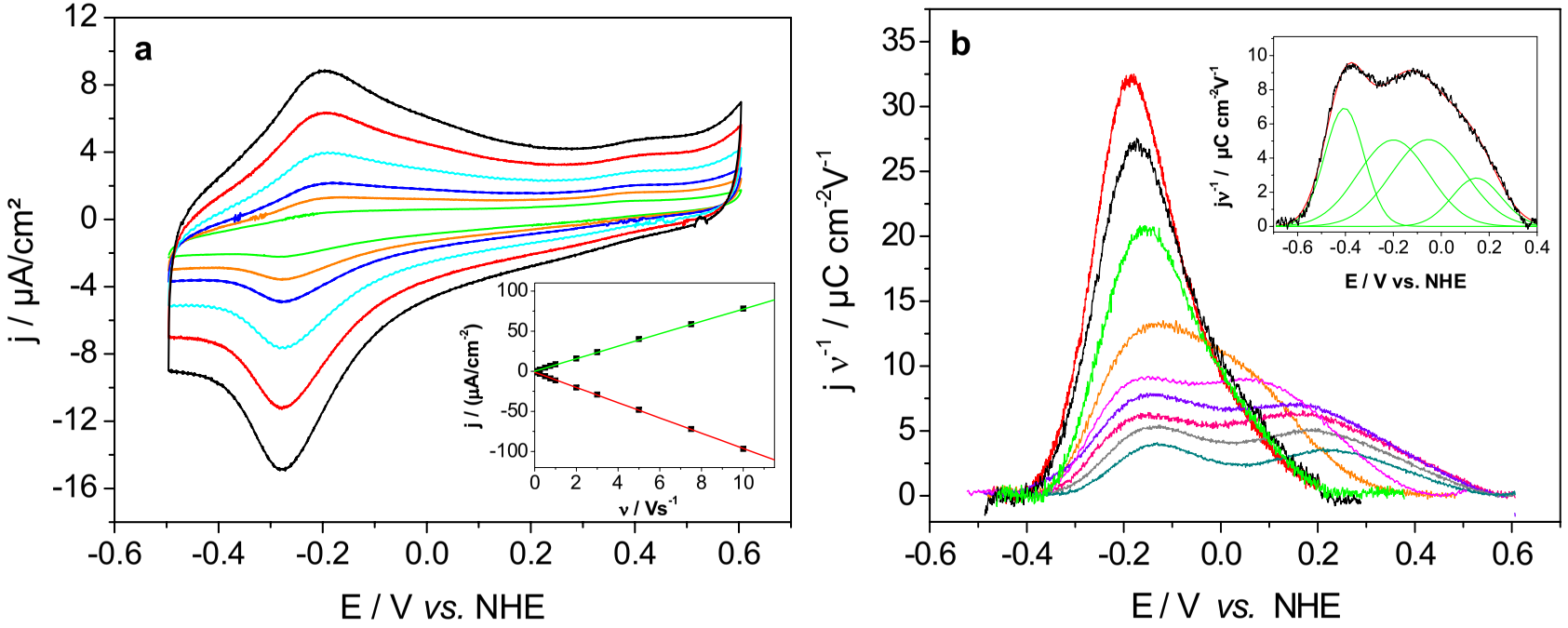
a
j / μA/cm²
E / V vs. NHE
j / (μA/cm⁻²)
ν / Vs⁻¹
b
j ν⁻¹ / μC cm⁻²V⁻¹
E / V vs. NHE
jν⁻¹ / μC cm⁻²V⁻¹
E / V vs. NHE

3

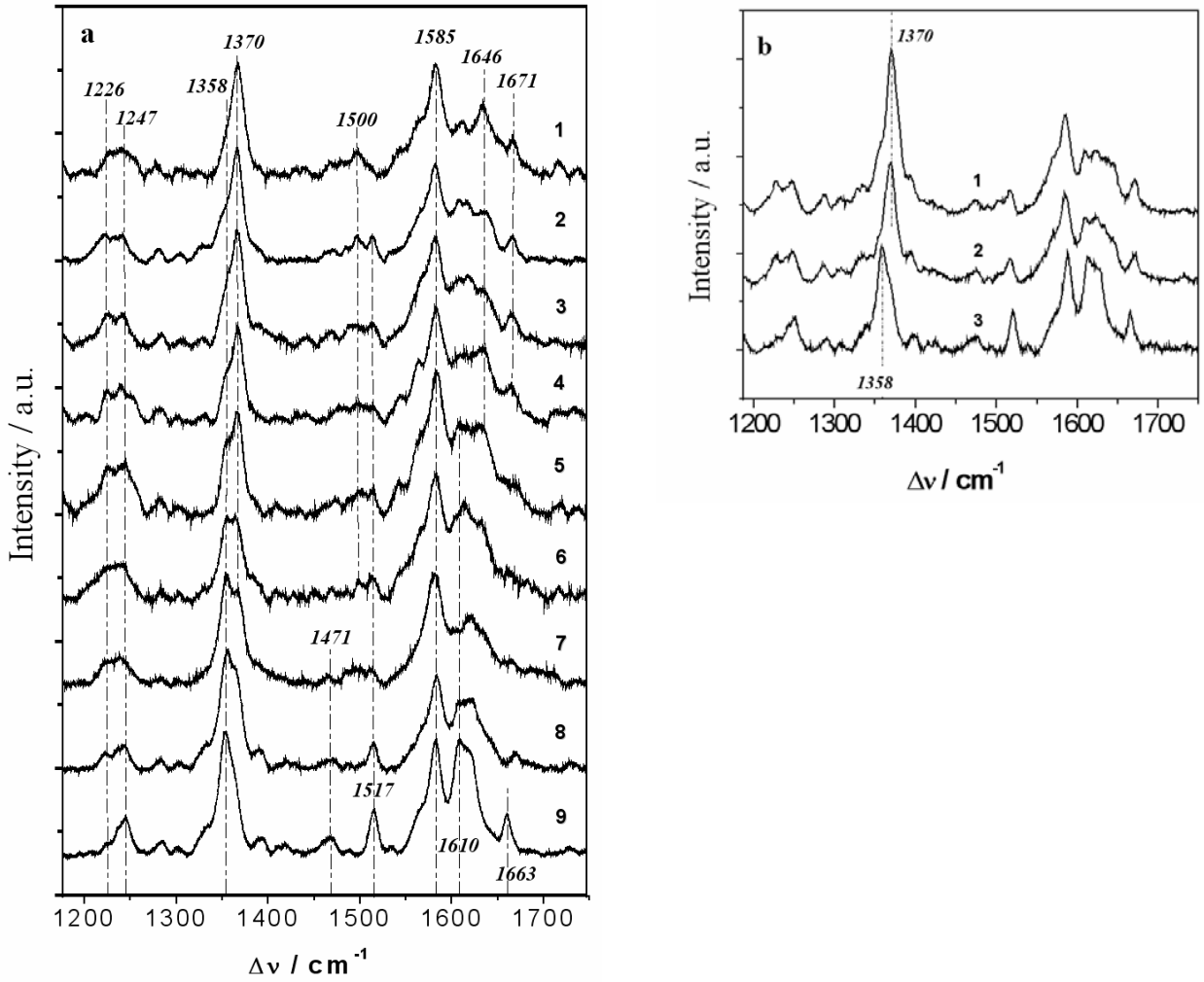
a
1370
1585
1646
1671
1226
1358
1247
1500
1
2
3
4
5
6
1471
7
8
1517
9
1610
1663
Intensity / a.u.
1200
1300
1400
1500
1600
1700
Δν / cm-1
b
1370
1
2
3
1358
Intensity / a.u.
1200
1300
1400
1500
1600
1700
Δν / cm-1

4

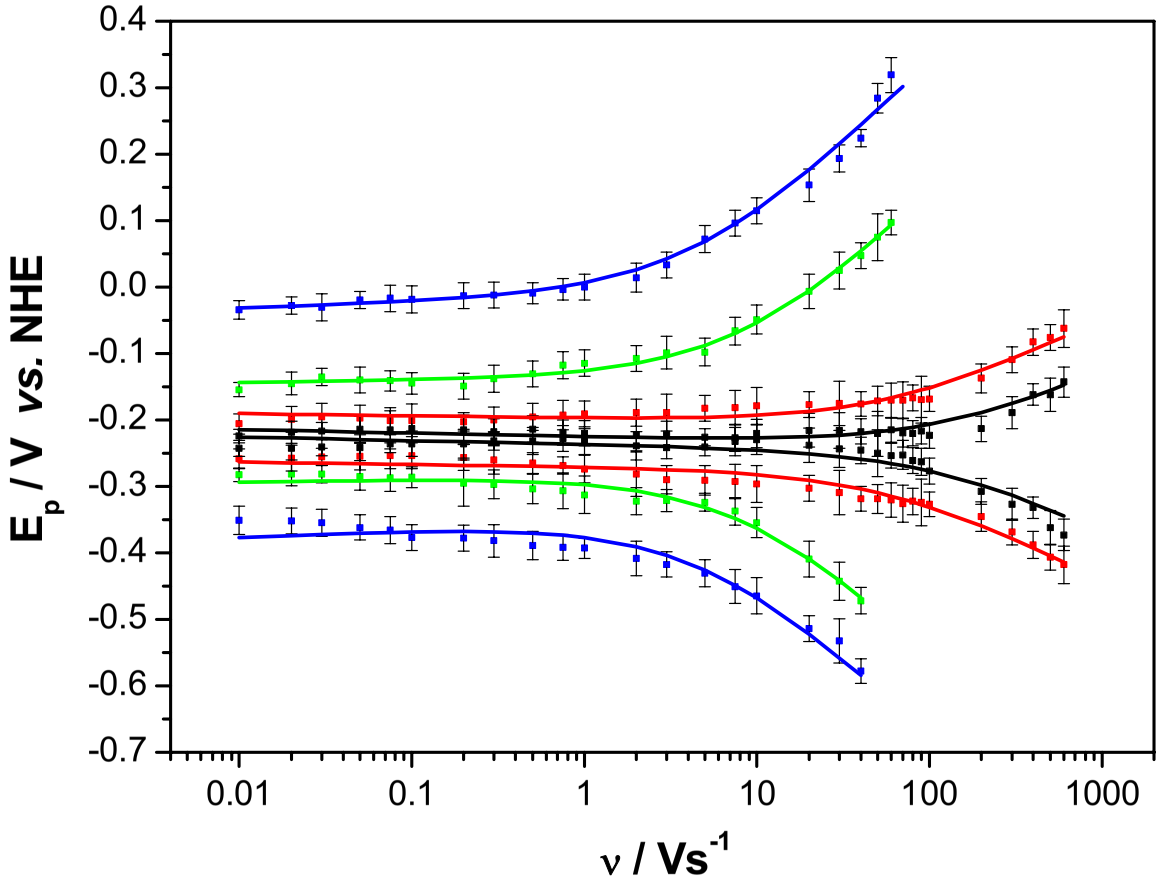
0.4
0.3
0.2
0.1
0.0
-0.1
-0.2
-0.3
-0.4
-0.5
-0.6
-0.7
0.01
0.1
1
10
100
1000
E_p / V vs. NHE
ν / Vs^-1

5

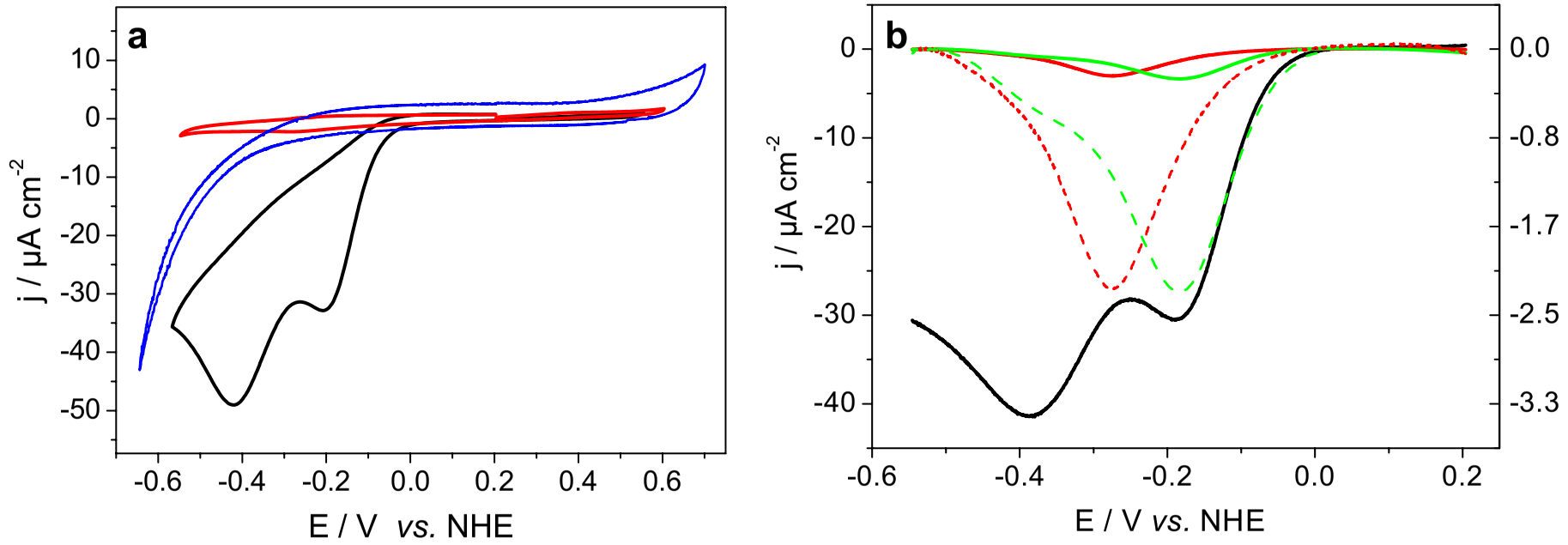
a
10
0
-10
-20
-30
-40
-50
j / μA cm-2
-0.6
-0.4
-0.2
0.0
0.2
0.4
0.6
E / V vs. NHE
b
0
-10
-20
-30
-40
j / μA cm-2
0.0
-0.8
-1.7
-2.5
-3.3
-0.6
-0.4
-0.2
0.0
0.2
E / V vs. NHE

Supporting Information

Samples were prepared according to procedures described in the main article. Layer by layer formation was checked by Surface Plasmon Resonance (SPR) and Electrochemical impedance spectroscopy (EIS).

SURFACE PLASMON RESONANCE (SPR):

SPR was performed in a setup using the Kretschmann-configuration using a measuring cell designed for use of SPR in a combination with electrochemistry. The glass slide (LaSFN9 glass from Hellma Optik, Jena, refractive index n=1.85 at 633 nm) was optically matched to the base of a 90° glass prism (LaSFN9). Monochromatic light from a He/Ne Laser, (Uniphase, San Jose, CA, λ = 632.8 nm) was directed through the prism and collected by a custom made photodiode detector. Reflectivity scans as a function of the angle of incidence (Fig. 1, inset) are used to determine the thickness before (-□-) and after (-○-) protein binding and reconstitution (-∇-) of the layers by a fitting routine using the Fresnel equations as described previously (Solid lines are the fitted curves) (11). Reflectivity at a fixed angle of incidence transferred into a thickness (Supplementary Fig. 1) yields the time course of protein binding and reconstitution. CcO binding is finished within 30 min [*1*] while the reconstitution of the CcO into a lipid bilayer takes more than 10 hours [*2*].

ELECTROCHEMICAL IMPEDANCE SPECTROSCOPY (EIS):

EIS was conducted using an Autolab instrument (PGSTAT302) equipped with an FRA2-module for impedance measurements. Evaluation of the data was done with the frequency response analyzer software provided by Eco Chemie, B.V. (Utrecht, The Netherlands). The spectra were recorded in a frequency range of 50 kHz - 3 mHz with an excitation amplitude of 10 mV and a bias potential of 0 V against an $Ag|AgCl,KCl_{sat}$ reference electrode and a platinum wire as counter electrode. Spectra were recorded before and after CcO binding and reconstitution into the ptBLM (Supplementary Fig. 2). Data were subsequently analyzed by the complex nonlinear fitting algorithm supplied in the data processing software ZVIEW (Version 2.6, Scribner Associates, Inc.) applied to the equivalent circuits depicted in (Supplementary Fig. 2c and d). The CPEs in series with the resistance (Supplementary Fig. 2c) or in the RC circuit (Supplementary Fig. 2d) account for the heterogeneity of the mixed DTP/DTSP-NTA layer.

As deduced from (Supplementary Fig. 2), the capacitance of the dielectric layer decreases from 13.1 ± 3.9 $\mu F\,cm^{-2}$ for the CcO/detergent/water layer to 7.3 ± 0.5 $\mu F\,cm^{-2}$ for the ptBLM (Supplementary Fig. 2a), while the resistance increases from 300 ± 80 $k\Omega\,cm^2$ to 12 ± 7 $M\Omega\,cm^2$ (Supplementary Fig. 2b), see also Supplementary Table 1. Considering the dielectric constant of lipids [2.2] is smaller than that of water [80] and proteins (typically 30) (A) the decrease of the capacitance indicates that detergent and water molecules residing between the proteins are replaced by the lipid bilayer patches. Thereafter, the capacitance is still dominated by the protein indicating a high degree of surface coverage. The capacitance of a protein layer with ε = 30 and a thickness of 5 nm can be estimated to be 6 $\mu F cm^{-2}$ in reasonable agreement with 7.3 ± 0.5 $\mu F\,cm^{-2}$ found experimentally. On the other hand, the mobility of ions between the CcO complexes is substantially reduced if lipid bilayer patches are present, since the resistance obtained for the ptBLM is in fact comparable to that of a pure BLM or tBLM. The quality of the ptBLM thus assessed is of paramount importance for subsequent spectro-electrochemical measurements.

A poor quality of a ptBLM affects not only the kinetics of the direct ET, but also the long-term stability. Some samples of CcO within a ptBLM of good quality lasted for more than a week in a functionally competent state.

EVALUATION OF CYCLIC VOLTAMMETRY DATA (CV):

CVs were treated first by a baseline correction procedure comprising a polynomial function included in the GPES software of the Autolab, to subtract the capacitive component of the current. An example is shown in (Supplementary Fig. 3). Baseline correction was then followed by the deconvolution into Gaussian components by fitting to four Gaussian curves using the software Origin (version 6.0), as shown in the inset of (Fig. 2b) of the main article.

Baseline corrected reduction and oxidation peaks of the CV recorded under anaerobic conditions, (see e.g. Supplementary Fig. 3 or Fig. 2a of the main article), were evaluated in terms of the surface coverage of CcO molecules per area, $\Gamma = Q/(nF)$, where Q is the charge density given by the peak area, n is the number of electrons transferred per mole of protein and F is the Faraday constant. The evaluation yields 8.4 and 5.9 pMol cm^{-2}, for the reduction and oxidation peak, respectively. The value of 5.9 pMol cm^{-2} is in reasonable agreement with 6 pMol cm^{-2} calculated for a densely packed monolayer from the crystal structure of CcO assuming an ellipsoidal disk of 4.5 nm × 7.0 nm for the in-plane dimension of CcO from *R. sphaeroides* (33) as mentioned in the main article. The higher value for the reductive peak is possibly due to uptake of the charge-compensating protons (47).

PROTON TRANSLOCATION UNDER AEROBIC CONDITIONS:

Catalytic turnover of the enzyme as well as coupled proton translocation was claimed in the main article to be indicated by CV and DPV measurements of the CcO performed under aerobic conditions (Fig. 2). The first peak (at around –202 mV) indicates the repeatedly occurring ET due to multiple turnover of the enzyme. The second peak was explained in terms of protons transported into the interstitial space between the protein/membrane structure and the electrode, followed by the reduction of the protons to H_2 at the DTSP/NTA modified electrode surface. Due to the small volume of this space, the pH value in the interstitial volume should shift to very low values indicated by the second peak in the voltammogram. The range of pH values accessible by this measurement was tested by a control experiment of the pure DTSP/NTA-modified surface in phosphate buffer solution titrated with hydrochloric acid to different pH values. The result of the control experiment is shown in (Supplementary Fig. 4). A cathodic peak is formed at around -430 mV (vs. NHE), starting at a pH value of about pH = 3 becoming more and more prominent at decreasing pH values. Using the plot of the current density as a function of pH (Supplementary Fig.4, inset) as a calibration curve, the pH value indicated by the second peak in Fig. 2c of the main article can be estimated to be around pH = 2.

SIMULATION OF NI-MEDIATED ET:

The simulation is based on a model enzyme which contains three redox centers corresponding to Ni^{2+}/Ni^{+}, Cu_A, and $heme_a$. This simplified model reduced to three redox centers is utilized with the single purpose to demonstrate the role of the Ni^{2+}/Ni^{+} redox pair as a transient acceptor/donator to the nearest next redox centers. According to the algorithm for simulating bioelectrochemical processes (29), the enzyme with different redox states of the centers are considered as different conformations numbered 1 through 8 (Supplementary Fig. 5). The rate of a transition due to ET between the electrode and the Ni-complex is governed by the Butler-Volmer equation with rate constant k_s. ET between the redox centers i and j is described by an intrinsic rate constant k_{ij}, a Boltzman factor b_{ij} comprising the electrical potential difference between the redox centers (29), and the equilibrium constant K_{ij} (see Supplementary Fig. 5).

The model enzyme is placed in a ptBLM represented by a membrane capacitance, C_m, and a membrane resistance, R_m, a capacitance in the submembrane space, C_{in}, and a resistance of the external solution, R_{ex}. Simulations were performed by means of the network simulation program SPICE (29), and assuming the following values for the parameters: standard redox potentials $E_{Ni}^{o} = -0.442$ V, $E_1^{o} = 0.23$ V (Cu_A), $E_2^{o} = 0.34$ V ($heme_a$); rate constants $k_s = 10^5\ s^{-1}$, $k_{01} = 3 \cdot 10^5\ s^{-1}$, $k_{12} = 10^4\ s^{-1}$; ptBLM parameters $C_{in} = 73\ \mu F/cm^2$, $C_m = 7.3\ \mu F/cm^2$, $R_m = 12\ M\Omega\ cm^2$, $R_{ex} = 60\ \Omega\ cm^2$ (see also Table 1); and the number of enzymes per area $N_e = 10$ pmol/cm^2.

The simulated current density as a function of bias potential (Supplementary Fig. 6), which represents the baseline-corrected CV of the model enzyme, displays a peak at –270 mV, in agreement with our measurements. The corresponding probabilities of the conformations with different redox states as a function of bias potential are shown in (Supplementary Fig. 7). It is evident that the probabilities of the conformations with Ni in the reduced state do not exceed 6×10^{-8} (see Supplementary Fig. 7b), which indicates that the Ni complex is merely a transient electron acceptor, in agreement with the absence of redox peaks observed when the Ni-NTA is chelated with imidazole instead of the his-tag (data not shown). Similar results were presented by Blankespoore et al. (28)

SUPPLEMENTARY TABLE

Fit parameters of the impedance spectra

	C_m / $\mu F\ cm^{-2}$	R_m / $M\Omega\ cm^2$	CPE^*_{spacer} / $(\mu F\ cm^{-2})^{\alpha}$	α
Ni-ANTA			16 ± 2	0.9 ± 0.05
CcO	15.1 ± 1.9	0.3 ± 0.08	73 ± 10	0.95 ± 0.03
CcO reconstituted	7.3 ± 0.5	12 ± 7	73 ± 5	0.85 ± 0.05

R_m and C_m are the resistance and capacitance of the protein-membrane layer CPE^*_{spacer} is the fit parameter for the CPE for the spacer region obtained from the ZVIEW fit routine, and α represents the distribution parameter of time constants. For α = 1, the CPE becomes a pure capacitor, Standard deviations were obtained from n > 10 measurements

FIGURE CAPTIONS

Figure 1

Kinetic trace of an SPR spectrum recorded during CcO binding (1) and reconstitution (2) at a constant angle of incidence (55°)

and transferred into a optical thickness by using the Fresnel equation. The inset shows the reflectivity scans as a function of the angle of incidence before (-□-) and after (-○-) CcO binding and reconstitution (-Δ-), solid lines are the fitted curves.

Figure 2

Impedance spectra, frequency normalized admittance (a) and Bode plots (b), of the Ni-ANTA modified surface before (1) after binding of CcO before (2) and after reconstitution of the protein (3). Dotted lines represent experimental data, solid lines show the curves fitted to the equivalent circuit (d) except for the Ni-ANTA modified surface which was fitted to the circuit (c).

Figure 3

Cyclic voltammogram of CcO with the his-tag attached to SU II under strictly anaerobic conditions, scan rate 0.01 Vs^{-1}, without (1) and with baseline correction (2).

Figure 4

Differential pulse voltammogramms of a ANTA modified surface as a function of different pH values: pH 1 (black), pH 1.5 (red), pH 2 (green), pH 2.5 (blue), pH 3 (brown) and pH 6.2 (orange). The inset shows the current density as a function of pH, and the blue horizontal line indicates the current of the second reduction peak in Fig. 5 of the main article.

Figure 5

Conformations of the model enzyme used for simulating ET to the redox centers Cu_A and $heme_a$ via the Ni complex. Horizontal and vertical transitions indicate ET between redox centers and between the electrode and the Ni complex, respectively.

Figure 6

Simulated current density as a function of bias potential representing the baseline-corrected CV of the model enzyme, scan rate $\nu = 0.01 Vs^{-1}$.

Figure 7

Probabilities of the conformations of the model enzyme (Fig. 6) as a function of bias potential. (a) Conformations with Ni^{2+}: 1 (black), 3 (red, dashed line enlarged by a factor of 100), 4 (green), 6 (blue), and (b) conformations with Ni^{+}: 2 (black), 5 (red), 7 (green, dashed line enlarged by a factor of 100), 8 (blue).

FIGURES

1

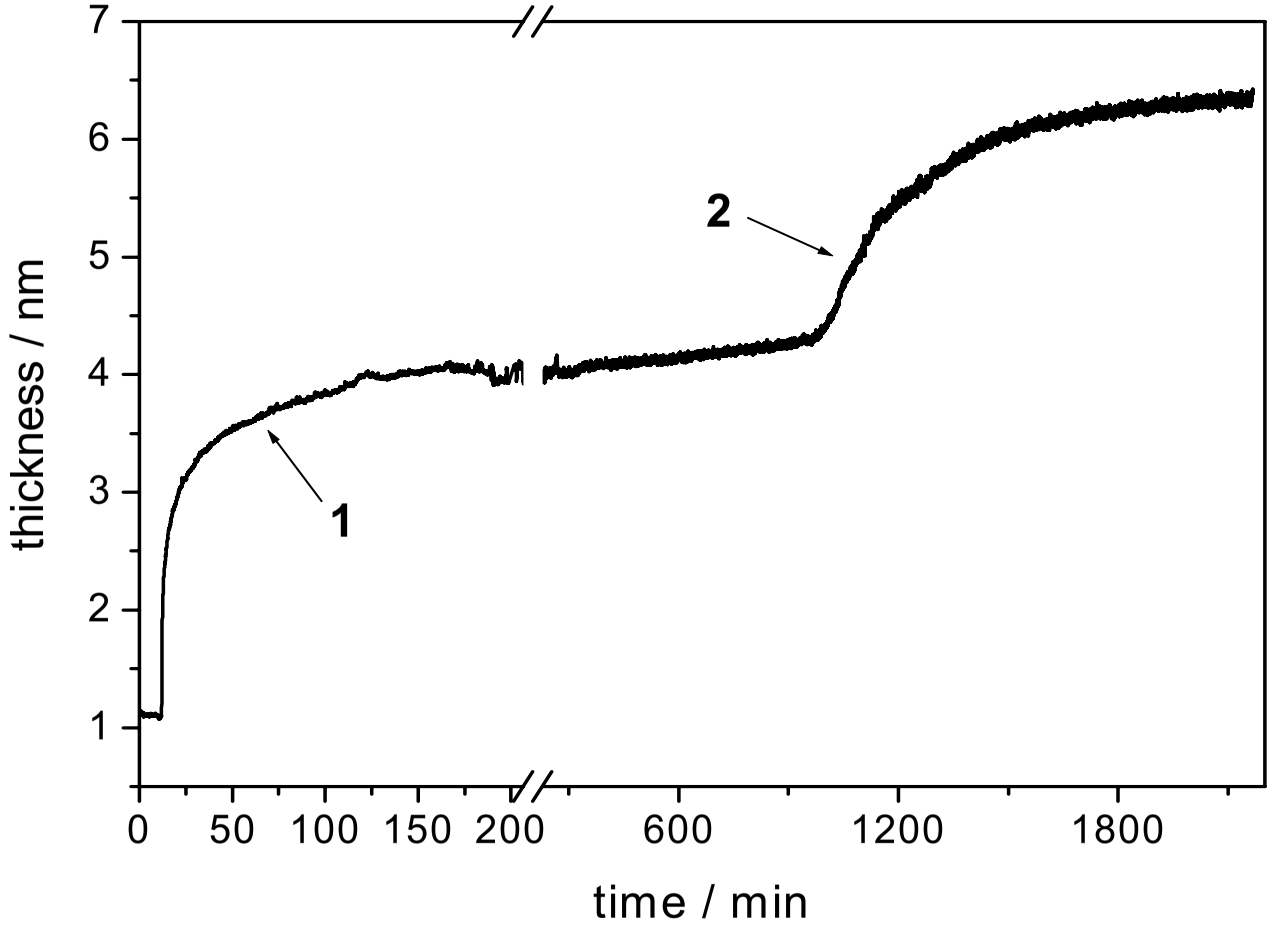
thickness / nm
time / min
1
2
0
50
100
150
200
600
1200
1800
1
2
3
4
5
6
7

2

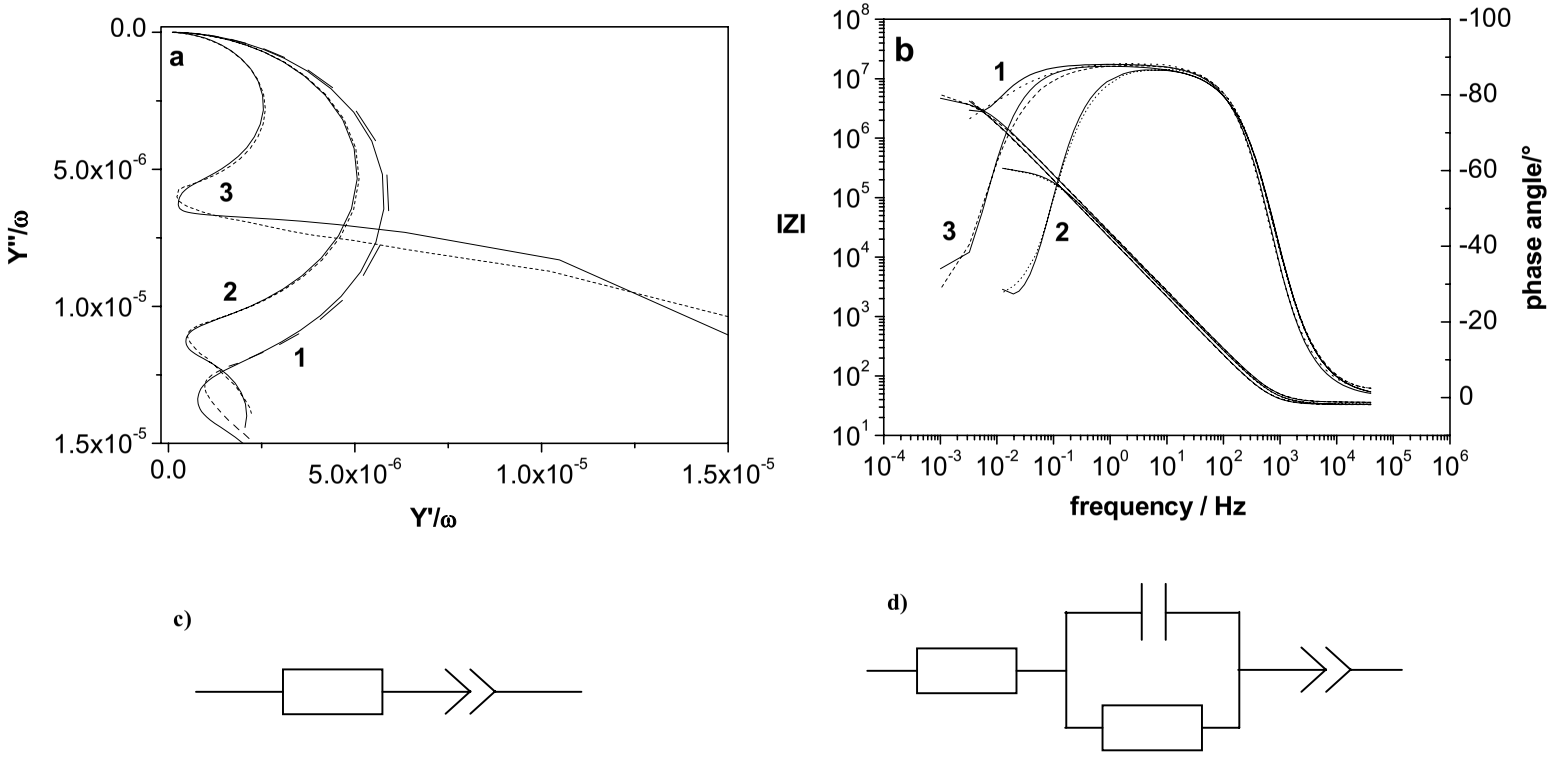
a
b
c)
d)
Y''/ω
Y'/ω
IZI
phase angle/°
frequency / Hz
1
2
3
0.0
5.0x10-6
1.0x10-5
1.5x10-5

3

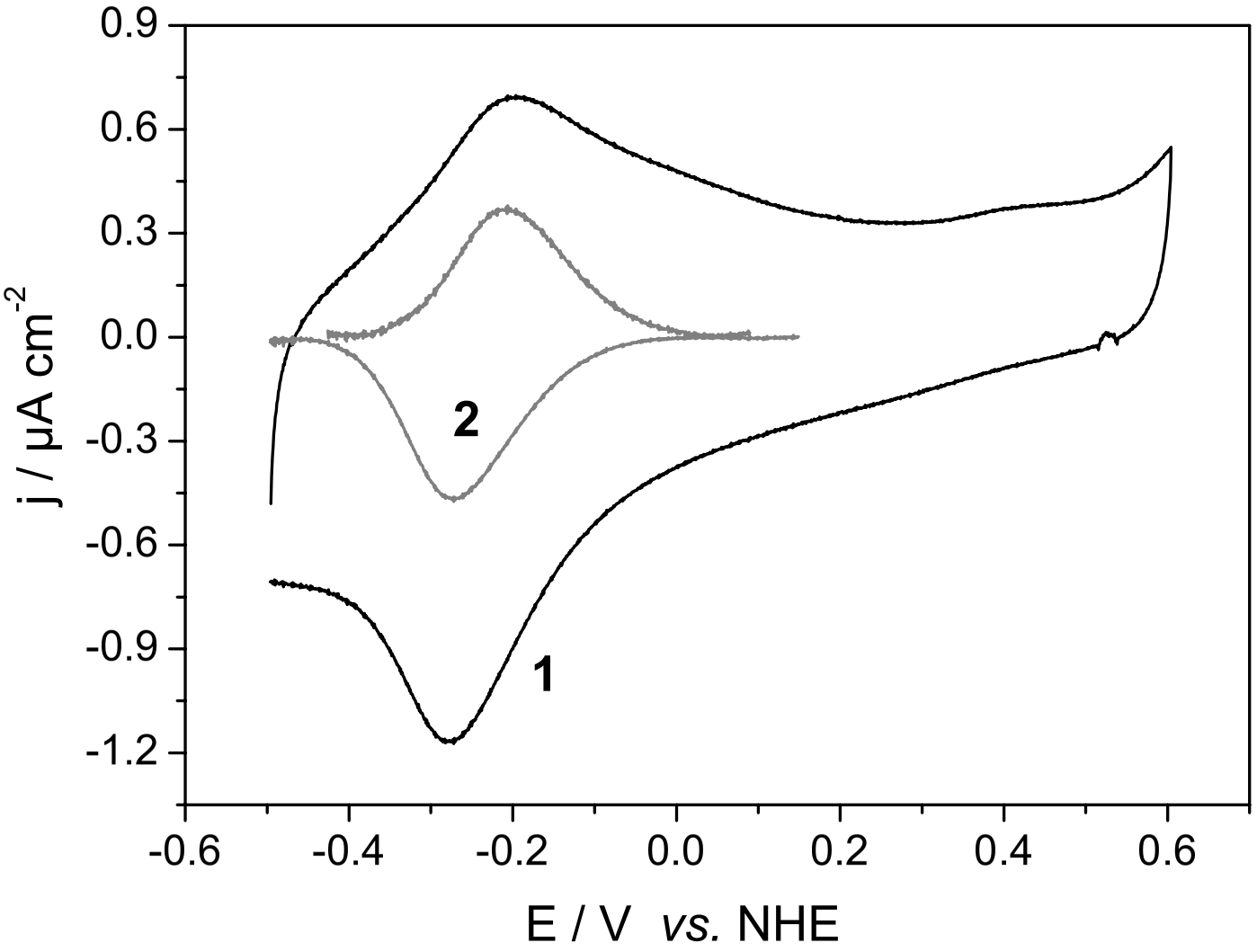

4

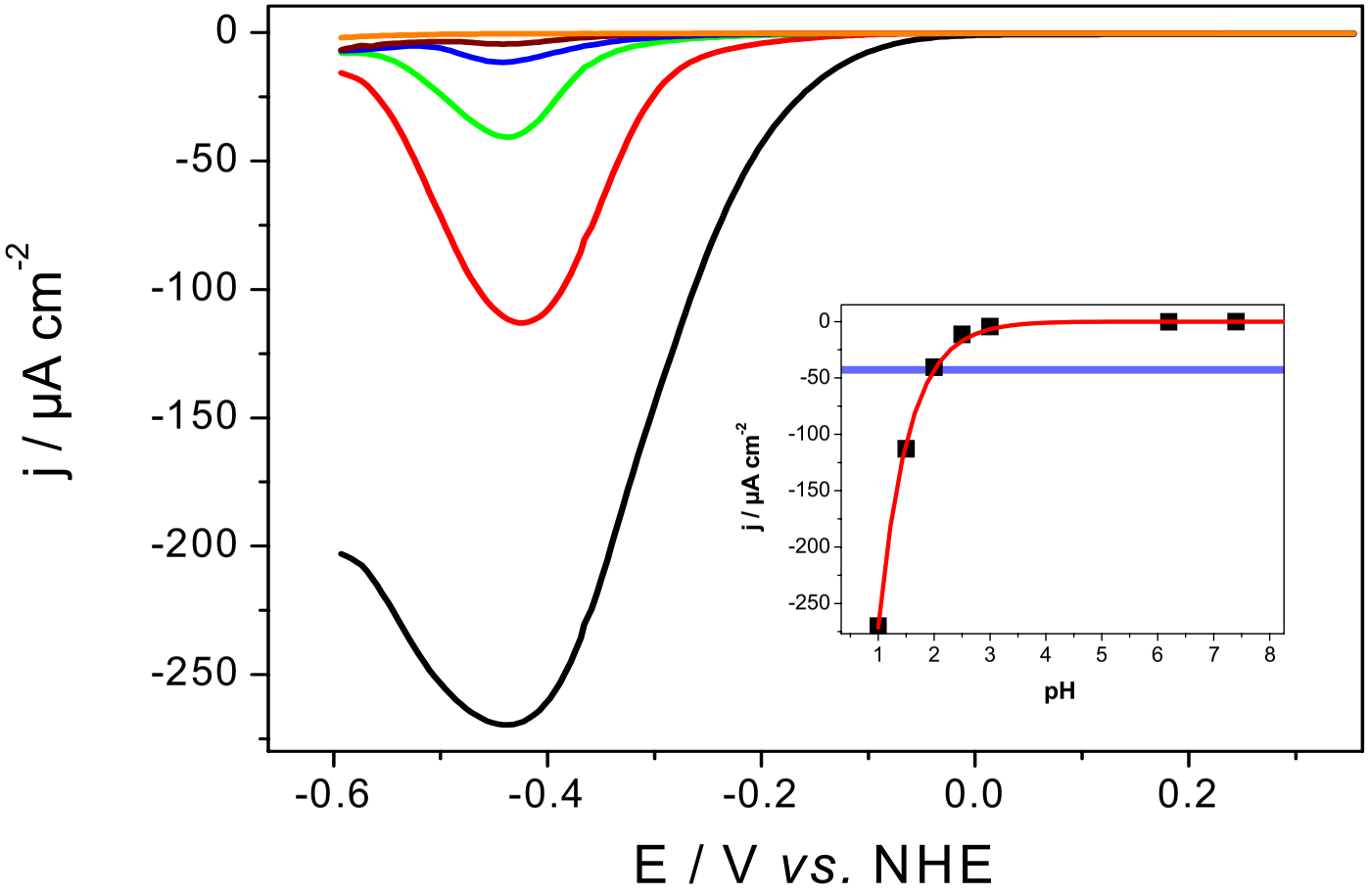
0
-50
-100
-150
-200
-250
j / μA cm-2
-0.6
-0.4
-0.2
0.0
0.2
E / V vs. NHE
0
-50
-100
-150
-200
-250
j / μA cm-2
1
2
3
4
5
6
7
8
pH

5

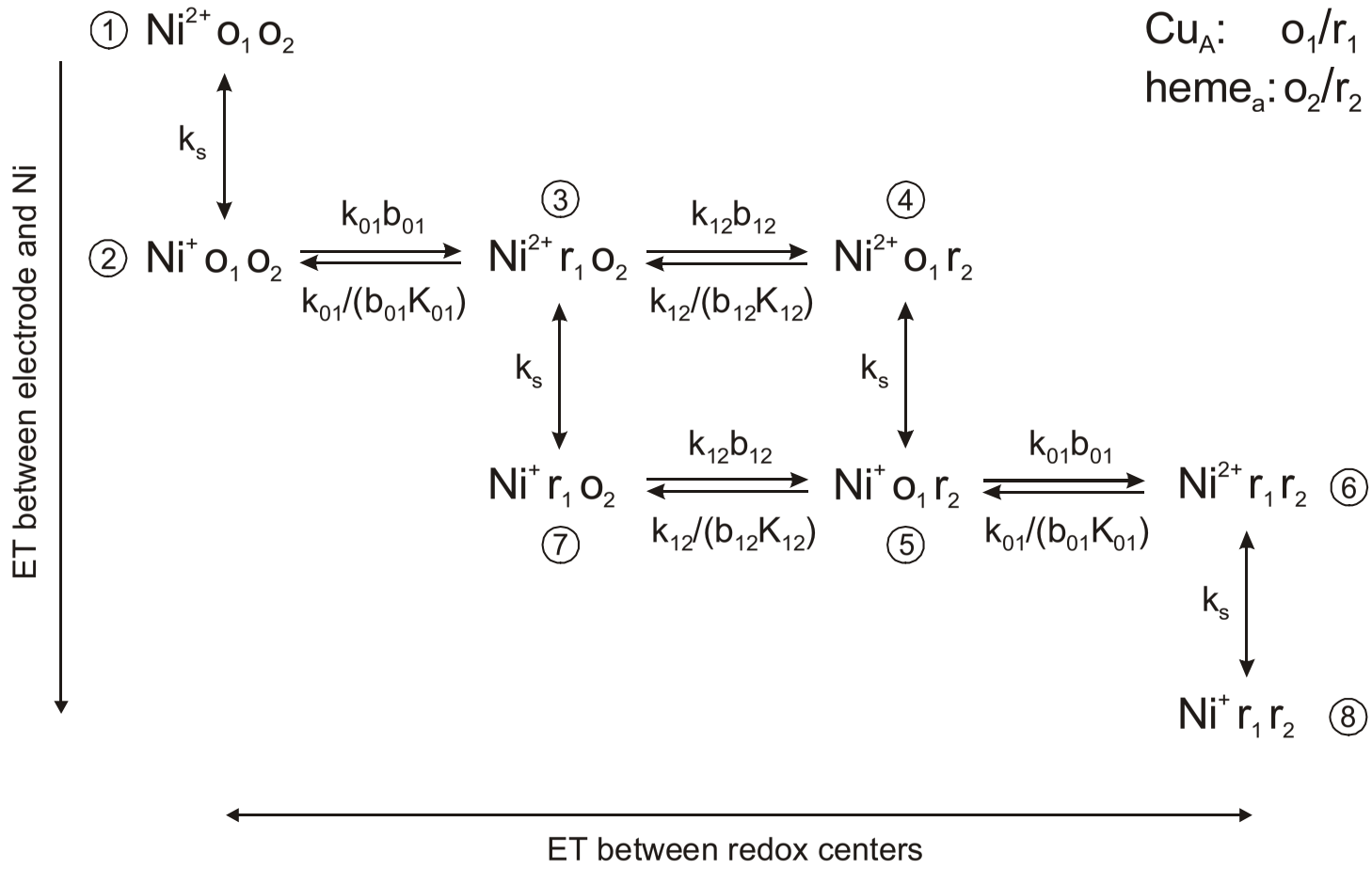
① Ni^{2+} o_1 o_2
Cu_A: o_1/r_1
$heme_a$: o_2/r_2
k_s
② Ni^{+} o_1 o_2
$k_{01}b_{01}$
$k_{01}/(b_{01}K_{01})$
③ Ni^{2+} r_1 o_2
$k_{12}b_{12}$
$k_{12}/(b_{12}K_{12})$
④ Ni^{2+} o_1 r_2
k_s
k_s
Ni^{+} r_1 o_2 ⑦
$k_{12}b_{12}$
$k_{12}/(b_{12}K_{12})$
Ni^{+} o_1 r_2 ⑤
$k_{01}b_{01}$
$k_{01}/(b_{01}K_{01})$
Ni^{2+} r_1 r_2 ⑥
k_s
Ni^{+} r_1 r_2 ⑧
ET between electrode and Ni
ET between redox centers

6

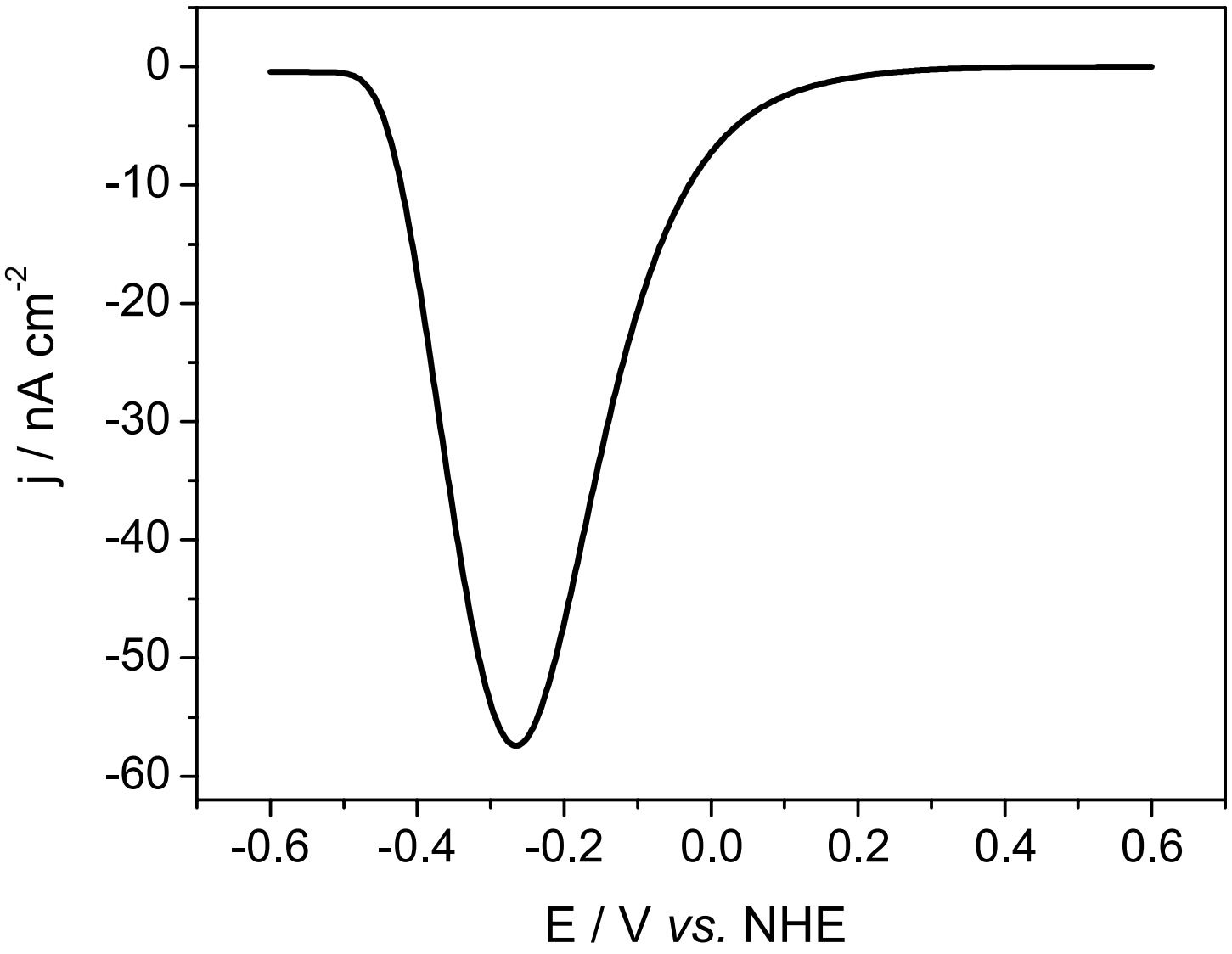

7

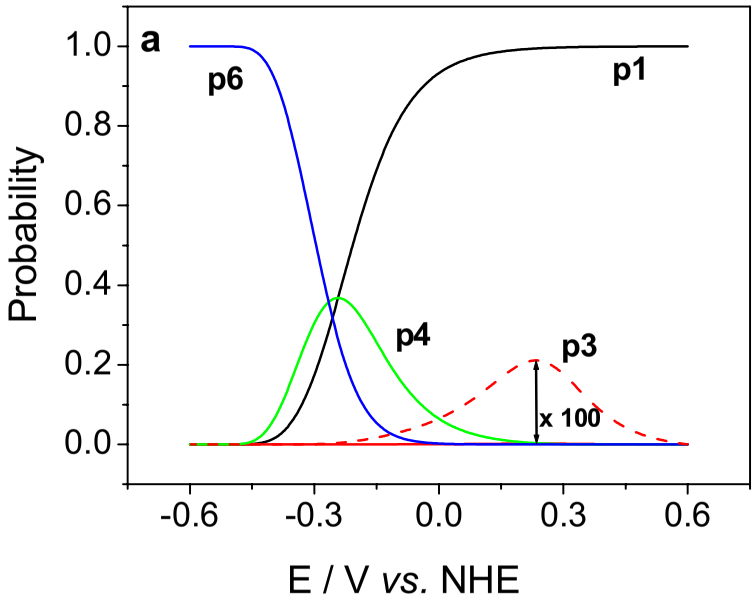
a
p6
p1
p4
p3
x 100
Probability
1.0
0.8
0.6
0.4
0.2
0.0
-0.6
-0.3
0.0
0.3
0.6
E / V vs. NHE

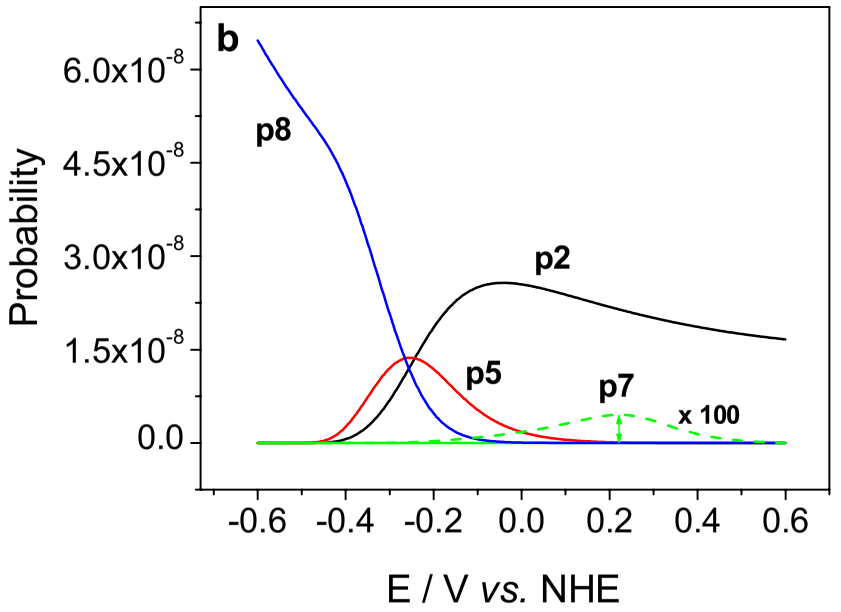
b
p8
p2
p5
p7
x 100
Probability
6.0x10-8
4.5x10-8
3.0x10-8
1.5x10-8
0.0
-0.6
-0.4
-0.2
0.0
0.2
0.4
0.6
E / V vs. NHE

Paper 4

In-situ Monitoring of the Catalytic Activity of Cytochrome c Oxidase in a Biomimetic Architecture

Marcel G. Friedrich, [1,#] Markus A. Plum, [1] Vinzenz U. Kirste, [1] Wolfgang Knoll, [1] Bernd Ludwig[2] and Renate L. C. Naumann[1]*

[1]Max Planck Institute for Polymer Research, Ackermannweg 10, 55128 Mainz, Germany

[2]Goethe University in Frankfurt, Institute of Biochemistry, Max-von-Laue-Str. 9,

60438 Frankfurt am Main, Germany

Condensed running title: Catalytic Activity of Cytochrome Oxidase

Keywords: Cytochrome c oxidase, cytochrome c, electron transfer, electrochemistry, surface-enhanced resonance Raman spectroscopy (SERRS).

Abbreviations: Cytochrome c oxidase (CcO), cytochrome c (cyt c), tethered bilayer lipid membranes (tBLMs), black lipid membranes (BLMs), protein-tethered bilayer lipid membrane (ptBLM), subunit (SU), histidine(his)-tag, electron transfer (ET), Surface-Enhanced Resonance Raman Spectroscopy (SERRS), Di-thio-bis(N-succinimidyl propionate) (DTSP), di-thio-bis(propionic acid) (DTP), *N*-(5-Amino-1-carboxypentyl) iminodiacetic acid (ANTA), dodecyl-β-D-maltoside (DDM), Nitrilotriacetic acid (NTA), rotating disc electrode (RDE), Surface Plasmon Resonance Spectroscopy (SPR), electrochemical impedance spectroscopy (EIS)

current address: Harvard University, Dep. of Chemistry and Chemical Biology, 12 Oxford Street, Cambridge, MA-02138, USA

* correspondence author, E-mail: naumannr@mpip-mainz.mpg.de

Abstract

Cytochrome c oxidase (CcO) from *P. denitrificans* was immobilized in a strict orientation, via an his-tag attached to subunit I, on a gold film and reconstituted *in-situ* into a protein-tethered bilayer lipid membrane (ptBLM). In this orientation, the cytochrome c (cyt c) binding site is directed away from the electrode pointing to the outer side of the ptBLM architecture. The CcO can thus be activated by cyt c under aerobic conditions. Catalytic activity was monitored by impedance spectroscopy, with contributions from passive ion permeation, active proton translocation and faradaic currents due to electrochemical oxidation/reduction of cyt c. The latter processes were investigated in detail using cyclic voltammetry of the CcO with cyt c added to the bulk solution under aerobic and anaerobic conditions. The communication of cyt c bound to the CcO with the electrode is considered in terms of a hopping mechanism through the redox sites of the enzyme. Electrochemical redox processes are thus discussed in terms of a gating mechanism in line with a conformational transition in the heme environment initiated by cyt c binding to the CcO. Catalytic activity could be monitored by an increased current density due to repeated electrochemical oxidation/reduction of the CcO/cyt c complex in the presence of oxygen.

Introduction

Much effort has been directed towards the design of model systems of the bilayer lipid membrane, such as tethered (tBLMs) (1,2) and pore-spanning bilayer lipid membranes (nano-BLMs) (3), aiming at investigating membrane proteins in a functionally active state. The motivation for these studies was to obtain a deeper understanding of ion transport mechanisms across lipid membranes by membrane proteins. Channel peptides, such as mellittin and gramicidin and ion carriers such as valinomycin were successfully incorporated (4-8). They were shown to transport ions with similar ion transfer rates as in classical bilayer or black lipid membranes (BLMs) (6). Larger and more complex enzymes such as the cytochrome c oxidase (CcO) were incorporated as well, catalytic currents were measured by cyclic voltammetry, however, only at low scan rates (9-13). Similar results were obtained for CcO immobilized in a complex with cytochrome c (14). In an attempt to preserve, in the best possible way, the catalytic activity of such proteins immobilized on surfaces, we developed a biomimetic membrane system in which the proteins are immobilized using the histidine(his)-tag technology on a planar electrode. A lipid bilayer is then reconstituted by in-situ dialysis around the bound proteins to form the protein-tethered bilayer lipid membrane (ptBLM) (15) (Fig. 1). The most obvious advantage of this system is the strict control over the orientation of the protein. Recently it could be shown, that the CcO from *R. sphaeroides,* embedded in such a system, with the his-tag attached to subunit (SU) II, can be effectively activated by direct electron transfer (ET). This was demonstrated by electrochemical methods in combination with Surface-Enhanced Resonance Raman Spectroscopy (SERRS) (16,17). When, on the other hand, the CcO from *P. denitrificans* is immobilized with the his-tag attached to SU I, the cytochrome c binding site is directed away from the electrode to the outer side of the tBLM architecture (Fig. 1), the protein can be activated by cytochrome c to actively transport protons across the lipid bilayer structure (15). These processes will be investigated in greater detail in the present paper.

Materials and Methods

Di-thio-bis(N-succinimidyl propionate) (DTSP), di-thio-bis(propionic acid) (DTP), *N*-(5-Amino-1-carboxypentyl) iminodiacetic acid (ANTA), dodecyl-β-D-maltoside (DDM), cytochrome c from bovine heart, glucose oxidase and catalase were purchased from Sigma, biobeads from Bio-Rad Laboratories GmbH, Munich, Germany were washed with ethanol and deionized water from a MilliQ water purification system (80MΩ cm), 1,2-Diphytanoyl-sn-glycero-3-phosphocholine (DPhyPC) was provided by Avanti Polar Lipids. All other chemicals were of analytical grade.

The stock solution of reduced cytochrome c was prepared by adding 10 mg of sodium dithionite to an aqueous solution of 40 mg cytochrome c in 1 ml water, whereafter the reductive was removed by gel filtration utilizing a Sephadex column (G-25 M, GE Healthcare Bio-Science AB, Uppsala).

CcO from *P. denitrificans* with a His-tag at the C-terminus of subunit I, was prepared according to ref. (18)

Preparation of the samples. Template stripped gold (TSG) electrodes (19) were used for SPR and electrochemistry measurements, immersed for 120 min in a solution of DTSP and DTP in a 60:40 ratio, in dry DMSO (2mg/ml). After rinsing, the slides were functionalized for 48 h in a 0.15 M solution of ANTA buffered to pH 9.8 by adding 0.5 M KCO_3. Finally, the glass slides were immersed for 30 min in 40 mM $NiSO_4$ in acetate buffer 50 mM, pH 5.5. The excess Ni was removed by thorough rinsing with the same acetate buffer without Ni. Immobilisation of the protein was performed in a solution of 100 nM CcO in detergent-containing phosphate/DDM buffer (K_2HPO_4 0.1 M, KCl 0.05 M, pH=8, 0.1% DDM) to the Ni-chelated NTA surface (15). Biobeads were added to the lipid-detergent-containing phosphate/DDM buffer, (DiPhyPC 0.05 mg/ml, K_2HPO_4 0.1 M, KCl 0.05 M, pH=8, 0.1% DDM) in order to remove the detergent and to form a lipid bilayer.

Electrochemical measurements were performed using an Autolab instrument (PGSTAT302) equipped with a FRA2-module for impedance measurements, an ECD-module amplifier for low-currents, an ADC750 module for rapid scan measurements, and a SCAN-GEN module for analog potential scanning as well as the frequency response analyzer (FRA) software provided by Eco Chemie, B.V. (Utrecht, The Netherlands). Cyclic voltammetry experiments were conducted with IR drop compensation, particularly at high scan rates. Measurements under anaerobic conditions were done in a buffer solution containing K_2HPO_4 0.1 M, KCl 0.05 M, pH=8 and the oxygen trap glucose (0.3%w/w), glucose oxidase (75µg/ml) and catalase (12.5µg/ml) (20). This solution was flushed with Ar purged from oxygen by washing through the oxygen trap containing buffer solution for one or two hours prior to the measurements to assure a completely deoxygenated solution. Impedance spectra were recorded in a frequency range of 50 kHz - 3 mHz with an excitation amplitude of 10 mV. Data were subsequently analyzed by the complex nonlinear fitting algorithm supplied in the data processing software ZVIEW (Version 2.6, Scribner Associates, Inc.). All electrochemical measurements were taken in a three electrode configuration with TSG as the working electrode, a $Ag/AgCl,KCl_{sat}$ reference, and a platinum wire as the counter electrode. All electrode potentials are quoted vs. NHE taken at pH=8, with no difference found for pH=7.

Surface Plasmon Resonance Spectroscopy (SPR) was performed in a setup using the Kretschmann configuration with a measuring cell designed for use of SPR in combination with electrochemistry. The glass slide (LaSFN9 from Hellma Optik, Jena, refractive index n=1.85 at λ = 633 nm) was optically matched to the base of a 90° glass prism (LaSFN9). Monochromatic light from a He Ne Laser (Uniphase, San Jose, CA, λ = 632.8 nm) was directed through the prism and collected by a custom made photodiode detector. Recording the change of reflectivity at a fixed angle in the linear regime of the SPR curve (Fig. 2), yields the time course of protein binding and reconstitution.

Surface Enhanced Resonance Raman Spectroscopy (SERRS) was performed in a custom-made spectroelectrochemical cell also connected to an Autolab instrument using an upside-down RDE (rotating disc electrode) made of a roughened silver rod (diameter 10 mm) inserted into a Teflon mantle. (17) An inner Teflon trough was fixed to the RDE rotating in-line with the electrode. The cell was sealed by a lid provided with inlets for the counter, reference ($Ag/AgCl,KCl_{sat}$) electrodes, as well as for the microscope objective. Surface Enhanced Resonance Raman (SERR) spectra were collected using a confocal Raman microscope (LabRam, HR800, HORIBA Jobin Yvon) equipped with a liquid nitrogen cooled back-illuminated CCD camera. The laser beam from a Kr^+ laser (excitation wavelength λ=413 nm) was focused on the surface of the above mentioned Ag-disc electrode by means of a water immersion objective. In order to prevent photoreduction of the enzyme, the electrode was rotated with 15 Hz or 900 RPM and the laser intensity at the sample surface was kept smaller than 0.1mW.

Results and Discussion

The formation of the protein-tethered bilayer lipid membrane (ptBLM)

The formation of the ptBLM was performed in two steps as described earlier (15). In the first step the his-tagged CcO from *P. denitrificans* with a his-tag on SU I was bound to the NTA/Ni-modified gold surface. In the second step detergent solubilized lipid molecules added to the bulk solution were subjected to in-situ dialysis to assemble the lipid membrane around the CcO molecules (Fig. 1). The two-step procedure was followed by a combination of SPR and electrochemical impedance spectroscopy (EIS). SPR allows to measure the optical thickness as a function of time (Fig. 2). From this recording, the time course of CcO binding was shown to be complete after 40 min, whereas in-situ dialysis taking more than 20 hours was usually done overnight. Approximate layer thicknesses (Table 1) were obtained by fitting the parameters of the angle scans shown in the inset of Fig. 2. Protein binding yields an increase in layer thickness of 8.7 nm which corresponds to the height of the protein (9 nm) obtained from X-ray crystallography data indicating a relatively high surface coverage with the CcO. Impedance spectra were evaluated by fitting the parameter values of equivalent circuits to the measured impedance data obtained before and after CcO binding and formation of the ptBLM (Fig. 3 a and b, respectively). The equivalent circuit of Ni-NTA layer (Fig. 3c) was assumed to be a RC circuit representing the resistance R_{sp} and constant phase element CPE_{sp} of the spacer region in series with the resistance of the bulk solution R_{ex}. The equivalent circuit of the protein layer as well the composite protein-lipid membrane layer (Fig. 3d) was assumed to consist of one RC element represented by R_m and C_m (m stands for membrane) for the protein layer mixed with detergent or the protein/lipid layer and a second RC element for the spacer layer (R_{sp} and CPE_{sp}) in series with R_{ex}. Constant phase elements (CPE) are introduced instead of pure capacitors due to the heterogeneity of the spacer layer. The parameter values obtained from the fitting procedure are collected in table 1, showing that the capacitance of the membrane decreases from 12.1 ± 2.8 $\mu F\,cm^{-2}$ for the CcO/detergent/water layer to 7.1 ± 0.5 $\mu F\,cm^{-2}$ for the ptBLM (Fig. 3b), while the resistance increases from 500 ± 80 $k\Omega\,cm^2$ to 13 ± 6 $M\Omega\,cm^2$ (Fig. 3b). The high resistance is well in accordance with the sealing resistance of a bilayer lipid membrane (BLM), whereas the capacitance is an order of magnitude higher than that of a BLM. The capacitance of a dielectric layer is determined by thickness and dielectric constant of the material. The dielectric constant of the lipid is much smaller, ε = 2.2, than that of water (ε = 80) and protein molecules (typically ε = 30) (21). Therefore, a decrease of the capacitance is expected if the detergent and water molecules between the CcO molecules are replaced by lipid bilayer patches. The capacitance (C) of a pure protein monolayer is estimated to be 6 $\mu F cm^{-2}$ using $C = \frac{\varepsilon\varepsilon_0 A}{d}$ with A as the area (1 cm^2), d the thickness (5 nm), ε the dielectric constant of the dielectric layer and ε_0 the permittivity of free space. The higher value of 12.1 ± 2.8 $\mu F\,cm^{-2}$ accounts for roughly 20 % of water (assuming a thickness of 5 and 2 nm for

the CcO and water layer, respectively) to be replaced by lipid molecules, when the capacitance decreases to 7.1 ± 0.5 $\mu F\,cm^{-2}$. The still high capacitance value is in agreement with the high surface coverage (more than 90%) found for CcO in the inverted orientation (17) with only few lipid molecules inserted in between. This explanation is also in accordance with the relative thickness increase obtained by SPR for the protein and lipid layer (Table 1). Impedance data of both orientations are virtually the same, indicating a similar high surface coverage with CcO molecules (> 90%).

Activation of the CcO with reduced cytochrome c monitored by impedance spectroscopy

CcO reconstituted in the ptBLM with the cytochrome c binding site directed towards the outside of the membrane can activated by reduced cyt c. This was shown before by the decrease of the membrane resistance R_m if cyt c was added to the bulk solution (15). The decrease was explained in terms of proton translocation across the membrane. This assumption was supported by the fact that the decrease of the resistance could be inhibited in the presence of cyanide. The occurrence of proton transport could be directly detected at the CcO in the inverted orientation, showing the cathodic reduction of the translocated protons at the electrode surface (17). For a closer inspection of these effects in the present investigation, impedance spectra were recorded as a function of the concentration of reduced cyt c in an oxygen-saturated buffer solution at a bias potential of 0 mV vs. Ag | AgCl, sat.KCl according to 200 mV vs. NHE (Fig. 4a). Spectra fitted to the equivalent circuit, given in Fig. 3d, yield the resistance of the membrane decreasing as a function of cyt c added in an exponential decay as expected if a current flows due to proton translocation (Fig. 4b). However, the curve does not seem to saturate as expected for an enzymatic process, even at cyt c concentrations as high as 1.6 mM. This finding suggests that proton translocation alone cannot be taken accountable for the decreasing resistance found by the impedance spectra.

For a closer inspection, impedance spectra were recorded at several fixed concentrations each one at different bias potentials applied across the metal electrode ptBLM structure (Fig. 5a). The resistivities obtained from the fitting were then plotted vs. the bias potential for every concentration of cyt c (Fig. 5b). Resistances in the presence of cyt c show a complex behavior of two maxima in the region of 160-200 mV and 300-350 mV and a minimum at around 250 mV. As a control the resistivity of the CcO-ptBLM in the absence of cyt c as a function of the applied potential was measured. (Fig. 5b, trace -▼-). This measurement reflects passive ion permeation as a function of the applied potential going through a maximum of the resistance as observed earlier for pure tBLMs with no protein incorporated (22). As for the resistivities in the presence of cyt c, CcO in the present orientation has to be considered, as a consequence of turnover, to generate a potential difference across the membrane, of +50 mV with respect to the outer side, in accordance with measurements of the membrane potential of CcO reconstituted in liposomes (23). The application of an additional bias potential is expected to change the self generated potential difference and hence, should affect proton transport. Potentials positive from 50 mV would inhibit proton translocation in agreement with increasing resistivities in the range from 50 to 200 mV. The minimum 250 mV, however, cannot be accounted for by the same process. From this it is concluded that proton translocation could be accompanied by electron exchange of cyt c with the electrode possibly catalyzed by the enzyme. The superposition of both processes could give rise to the complex behavior of the resistance observed in Fig. 5. A charge-transfer resistance would have to be inserted into the in the equivalent circuit is series with the resistance due to proton translocation to account for the electron exchange with the electrode. Two resistances in series, however, cannot be discriminated by the fitting procedure so that no further information can be obtained from EIS. Electron exchange with the electrode can better be investigated by cyclic voltammetry. This will be described in the following paragraph.

Cyclic voltammetry in the presence of reduced cytochrome

Cyclic voltammetry was performed in the presence of CcO reconstituted into a tBLM with cyt c added in the reduced form. Voltammograms were recorded, in the absence and presence of oxygen. (Fig. 6, solid and dash-dotted line). Anodic (oxidation) waves were obtained at potentials positive from 400 mV followed by smaller cathodic (reduction) waves at potential negative from 400 mV. The waves were baseline corrected and analyzed regarding peak position and current. Peak potentials are bracketed around 400 mV vs. NHE very similar to voltammetric signals found by Hawkridge and coworkers for CcO reconstituted into a hybrid alkanethiol-phospholipid bilayer in the same orientation as in our case and also activated it by adding reduced cyt c (9,10). These authors discussed the anodic waves in terms of the enzyme undergoing catalytic turnover considering electrochemical oxidation of oxyferryl or ferredoxyl species of the enzyme on the level of heme a_3 / Cu_B. This was concluded from the redox potentials of these species which are around 350 mV close to 430 mV found for the anodic wave in their work (24). In any case, CVs of reduced cyt c on a CcO containing ptBLM under *aerobic* and *anaerobic* conditions show a clear increase of the current density of both cathodic and anodic currents (Fig. 6, solid and dashed line). Such an amplification is characteristic for a catalytic current controlled by the turnover of the enzyme.
To explain this amplification, reduced cyt c is considered to be oxidized by the enzymatic reaction

$$4\ \text{Cyt}\ c_{red} + O_2 + 8\ H^+ \rightleftharpoons 4\ \text{cyt}\ c_{ox} + 2\ H_2O + 4\ H^+_{pumped} \qquad (1)$$

Parallel to this enzymatic reaction, cyt c exchanges electrons with the electrode, in the cathodic direction (Fig. 7), i.e. at potentials negative from 400 mV, cyt c_{ox} is re-reduced in the electrochemical reaction giving rise to a cathodic current according to

$$\text{Cyt}_{ox} + e^- \rightleftharpoons \text{cyt}\ c_{red} \qquad (2)$$

Since Cyt c_{red} is repeatedly oxidized by the enzyme (eq (1)), cyt c_{red} has to be regenerated electrochemically (eq. 2) over and over again so that the cathodic current is amplified compared to the one with no oxygen or with no enzyme present on the surface.
As to the anodic current (Fig. 8), the Hawkridge group considers the oxidation of oxyferryl or ferredoxyl species of the enzyme on the level of heme a_3 / Cu_B according to

$$Fe(IV)=O^{2-} \rightleftharpoons Fe(III) + O_2 + e^- \qquad (3)$$

It is well known from independent studies that electron transfer between redox centers is accelerated after oxygen is taken up by the enzyme in the reduced (R) state, to form the ferredoxyl and peroxy (P/F) species (25) (Fig. 8). When these are reoxidized, oxygen is regenerated (eq (3)). Oxygen can be repeatedly reduced by the enzyme eq(1) thus amplifying the anodic current. The difference of the reaction mechanisms of eq (1) and (3) explains the asymmetry between the two current branches, seen in Fig. 6.
Considering the oxidation of the heme species oxyferryl or ferredoxyl at the electrode, this would also mean that cyt c_{red} is reoxidized to cyt c_{ox} through the enzyme**,** a conclusion drawn by Hawkridge and coworkers, in agreement with the apparent redox potentials bewtween 400 mV and 430 mV and also in agreement with the orientation of the CcO with the cyt c binding site directed to the outside of the membrane. In this configuration the heme a_3 / Cu_B catalytic center would be closest to the electrode. The sigmoidic shape of the current could then be explained by the irreversibility of the electrochemical oxidation of peroxy species.
The mechanism of electrochemical reduction and oxidization of cyt c would best be described as a hopping mechanism according to the terminology introduced by Armstrong (26), with electrons proceeding along the chain of redox sites inside the protein, in contrast to the non-hopping mechanism

where the substrate, e.g. cyt c exchanges electrons directly with the electrode. The hopping mechanism seems to operate both ways in the reductive (cathodic, eq (2)) and oxidative (anodic, eq(3)) direction. Electron exchange with the electrode, however, only occurs with cyt c bound to the enzyme whereas CcO alone, in the present orientation, does not exchange electrons with the electrode as shown in the reference measurement Fig. 6, dotted line. This finding was supported by SERRS measurements as described in a previous publication (17).

Catalytic currents were also measured by Dutton and co-workers with CcO in the reverse orientation, electrostatically attached to cyt c_{red} bound to a 3-mercapto-1-propanol modified gold film such that cyt c is closest to the electrode and CcO is bound to it with the cyt c binding site pointing to the electrode (14). Cyt c can thus exchange electrons directly with the electrode in the non-hopping mode (26), in agreement with the standard potential of cyt c (+ 230 mV). Amplified anodic currents were found in the presence of oxygen, measurable but only at low scan rates (2 mV s^{-1}). By contrast, the catalytic effect of anodic and cathodic currents of the CcO in the present investigation, was measurable up to scan rates of 1 V s^{-1}. This was shown by plotting the current densities recorded by cyclic voltammetry, taken under aerobic conditions, of cyt c in the reduced form in the absence (-•-) and presence of CcO (-■-) vs. the scan rate (Fig. 9). The currents are linearly dependent of the square root of the scan rate, consistent with a diffusion controlled process (27). Another important phenomenon is that the anodic branch is linear but only up to ~1V s^{-1}(Fig. 9). After that the current decreases in an exponential decay. This effect is considered in terms of the turnover of the enzyme (eq.(1)) which at some point is no longer able to follow the scan rate.

Cyclic voltammetry in the presence of oxidized cytochrome c

It had been stated above that the hopping mechanism of cyt c electron exchange with the electrode through the enzyme seems to operate both ways in the reductive (cathodic, Fig. 7) and oxidative (anodic, Fig. 8) direction. If this is true, cyt c_{ox} also can be expected to show interesting effects in the voltammograms of CcO in the ptBLM configuration.

Cyclic voltammetry was performed in the presence of CcO reconstituted into a tBLM as described above this time with cyt c in the oxidized form added to the bulk solution. Voltammograms were recorded, in the absence and presence of oxygen. (Fig. 10, solid and dash-dotted line). A reduction peak was obtained at 389 mV at a scan rate of 50 mV s^{-1} followed by a reoxidation peak at 468 mV. The apparent standard potential, E^0_{app}, deduced from the potential difference between reductive and oxidative peak was +428 mV vs. NHE. This corresponds to the peak potentials found with cyt c_{red} (Fig. 6) and also to 430 mV found by Hawkridge and coworkers mentioned above (9,10).

Peak heights are increased in the presence of oxygen both in the cathodic (negative from 428 mV) and anodic direction (positive from 428 mV) indicating the catalytic activity of the enzyme. For an explanation one has to consider that the sequence of events is now opposite to the one described above for cyt c_{red} present in the bulk solution, i.e. reaction eq (2) precedes reaction eq (1). For example, during the cathodic branch (Fig. 7), cyt c_{ox} will be electrochemically reduced through the enzyme according to eq (2) generating cyt c_{red} which is reoxidized by the enzymatic reaction eq (1) in the presence of oxygen to form cyt c_{ox} which can thus be reduced repeatedly. This explains the catalytic effect. In the anodic branch (Fig. 8), on the other hand, cyt c_{red} is reoxidized to cyt c_{ox} which had been generated in the cathodic branch competing with the formation of the ferredoxyl and peroxy (P/F) species. This interpretation accounts for the almost symmetrical shape of cathodic and anodic peaks. The electrochemical reoxidation seems to be faster or at the same order of magnitude than the formation of the oxyferryl or ferredoxyl species observed when cyt_{red} is present in the bulk solution. The steps in the CcO enzymatic cycle involving these species are known to occur in the ms time scale, much slower than the preceding electron transfer steps between heme centers taking place in the µs time scale which are

even accelerated in the presence of oxygen (25). Single steps of the enzyme attached to the surface may be slower. For the kinetics of the electrochemical redox process see further below. Peak currents plotted again vs. the square root of the scan rate (Fig. 9, -▲-) of cyt c_{ox} in the presence (-▲-) as compared to the absence of CcO (Fig. 9, -•-). show a linear dependency indicating a diffusion controlled process. Cathodic currents are larger when cyt_{ox} is present in the bulk compared to cyt c_{red}. This is an indication of the repeated electrochemical reduction of cyt c_{ox} to obtain cyt c_{red} (eq (2)) preceding the enzymatic reoxidation (eq (1)) mentioned above.

Another important finding of Fig. 10 is the prepeak at about 320 mV which disappears at high scan rates (not shown). Such prepeaks are characteristic for redox species adsorbed to the electrode, in our case to the CcO immobilized on the surface (27). It can be concluded from this that cyt c is adsorbed to the CcO while it exchanges electrons with the electrode, although the amount adsorbed to the cyt c binding site is controlled by diffusion. Assuming cyt c adsorbed to the CcO during reduction/oxidation the kinetics of electron exchange can be evaluated using a so-called trumpet plot in which peak potentials are plotted vs. the scan rate in a logarithmic scale (28). The trumpet plot was analyzed by means of the algorithm described by Jeuken et al. (29) assuming a two-electron hopping process (26). Values for the heterogenous rate constants $k_0^1 = 256.64\ s^{-1}$ and $k_0^2 = 43.26\ s^{-1}$ and the apparent standard potential E^0_{app} = 402 mV were obtained.

As a control experiment, a cyclic voltammogram of the CcO immobilized in a ptBLM was recorded in the absence of neither oxidized nor reduced cyt c (Fig. 10, dashed line). No direct electron transfer to the electrode was detected as illustrated by the absence of redox peaks in this case. It can be concluded from this that the hopping mechanism of electron transfer operates only with cyt c adsorbed to the enzyme. Only then the electrode seems to exchange electrons via the heme a_3/Cu_B catalytic center either in the O/R or the P/F state (25). This is used as an explanation for the shift in the redox potential of cyt c.

As a further control experiment, a cyclic voltammogram of cyt c_{red} on a DTP modified surface gives the value of the standard potential (E^0 = +230 mV, not shown), also obtained by potentiometry (24). This was corroborated by SERR spectra of cyt c on a roughened silver electrode, modified with DTP, taken at different potentials (Fig. 11). Cytochrome c is shown to be oxidized between +90 mV and +240 mV in accordance with the standard potential of 230 mV. Unfortunately, SERRS measurements of cyt c reduction and oxidation adsorbed to CcO are not possible because of the thiolated layers that would be desorbed from the silver electrode at such positive potentials.

Conclusion

The principal conclusion from these measurements is that cyt c exchanges electrons with the electrode via a hopping mechanism through the redox sites of the enzyme while it is adsorbed to the far side of the CcO. Adsorption is controlled by diffusion. Catalytic activity can be monitored by repeated electrochemical oxidation/reduction in the presence of oxygen in a wide range of scan rates.
The hopping mechanism is in line with the consideration that direct ET between cyt c and the electrode is highly unlikely. The high surface coverage with the enzyme and the sealing properties of the bilayer lipid membrane prohibit the cyt c to approach the electrode surface leading to a direct exchange of electrons. Tunneling across the membrane is also unlikely considering the tunnel barrier of least 10 nm, taking into account the height of the CcO (9 nm) (30) added to the thickness of the chelating layer. Direct ET between the enzyme and the electrode, on the other hand, without cyt c present, would have a higher probability. The tunnel barrier between heme a_3 /Cu_B and the highly conductive electron wire, consisting of the Ni-chelating tether and the highly conjugated His-tag, is approx. 2 nm. This direct ET, however, definitely does not take place, as it has been conclusively demonstrated by reference experiments without cyt c (Fig. 6 and 8) supported strongly by SERRS measurements (17). According to

the experiments presented here, electron exchange with the electrode does take place, but only when cyt c is adsorbed to the CcO. Only then, ET seems to occur, most probably via the heme a_3 /Cu_B catalytic center being the redox center nearest to the electrode. This assumption is supported by changes in resonance Raman spectra of the CcO measured following the binding of cyt c (31). These changes were considered to induce a conformational transition of CcO in the environment of both heme a and heme a_3. Electrostatic interactions of cyt c with its binding site and a long range communication to the catalytic site of the CcO are held responsible for this effect. It would account for a kind of ligand gating to heme a_3 due to the binding of cyt c to cytochrome c oxidase. This is in agreement with the assumption brought forward by Hawkridge et al. (9,10) that the electrode communicates with the heme a_3 center during the catalytic reaction of cyt c with oxygen. It would also explain the apparent shift of the redox potential of cyt c bound to CcO which is nearer to the redox potential of heme a_3 /Cu_B than to cyt c directly adsorbed to the electrode. Not withstanding these complexities, the apparent rate of ET to the electrode appears to be of the same order of magnitude as in the arrangement described in ref. 14, where cyt c is in direct contact with the electrode.

From the voltammetry measurements it is also clear that proton transfer across the membrane is superimposed by electron transfer at almost all potentials considered in this paper. The only exception seems to be the maximum of the resistances measured for all cyt c concentrations at 350 mV which can be explained in terms of the apparent standard potential of the cyt c_{ox} / $cytc_{red}$ pair, where electron exchange processes are at equilibrium and hence do not contribute. Proton translocation is therefore considered to dominate the conductivity at this potential where the enzyme is exclusively activated by reduced cyt c present in the bulk solution. The minimum at +250 mV can be explained in terms of faradaic currents due to cyt c reduction superimposed on active proton translocation. The increase of the resistance to the maximum at around +200 mV can be due to the potential difference across the membrane, positive inside, which counteracts active proton translocation. EIS is, however, not designed to resolve these processes quantitatively.

Further vibrational spectroscopic measurements, sensitive to small dynamic structural changes, in combination with electrochemical measurements could provide more insight into these processes.

In summary, the activity of the CcO immobilized on a metal film can be monitored effectively. This demonstrates the possibilities of the ptBLM as a general platform for further investigations also with other proteins or for protein-protein interaction studies.

Acknowledgements

We thank Christian Groß for protein purification. B.L. acknowledges support by DFG (SFB 472) and CEF (Cluster of Excellence Frankfurt "Macromolecular Complexes").

References

1. Guidelli, R., G. Aloisi, L. Becucci, A. Dolfi, M. R. Moncelli, and F. T. Buoninsegni. 2001. New directions and challenges in electrochemistry - Bioelectrochemistry at metal/water interfaces. Journal of Electroanalytical Chemistry 504:1-28.

2. Knoll, W., K. Morigaki, R. Naumann, B. Sacca, S. Schiller, and E. K. Sinner. 2004. Functional Tethered Bilayer Lipid Membranes. In Ultrathin Electrochemical Chemo- and Biosensors, Technology and Performance. Mirsky V. M., editor. Springer-Verlag, Berlin. 239-254.

3. Römer, W., Steinem, C. 2004, Impedance Analysis and Single-Channel Recordings on Nano-Black Lipid Membranes Based on Porous Alumina, Biophys. J., 86, 955-965

4. Cornell, B. A., V. L. B. Braach-Maksvytis, L. G. King, P. D. J. Osman, B. Raguse, L. Wieczorek, and R. J. Pace. 1997. A biosensor that uses ion-channel switches. Nature 387:580-583.

5. Schiller, S. M., R. Naumann, K. Lovejoy, H. Kunz, and W. Knoll. 2003. Archaea analogue thiolipids for tethered bilayer lipid membranes on ultrasmooth gold surfaces. Angewandte Chemie-International Edition 42:208.

6. Naumann, R., D. Walz, S. M. Schiller, and W. Knoll. 2003. Kinetics of valinomycin-mediated K+ ion transport through tethered bilayer lipid membranes. Journal of Electroanalytical Chemistry 550:241-252.

7. Becucci, L., R. Guidelli, C. Peggion, C. Toniolo, and M. R. Moncelli. 2005. Incorporation of channel-forming peptides in a Hg-supported lipid bilayer. Journal of Electroanalytical Chemistry 576:121-128.

8. He, L. H., J. W. F. Robertson, J. Li, I. Karcher, S. M. Schiller, W. Knoll, and R. Naumann. 2005. Tethered bilayer lipid membranes based on monolayers of thiolipids mixed with a complementary dilution molecule. 1. Incorporation of channel peptides. Langmuir 21(25):11666-11672.

9 Cullison, J.K., Hawkridge, F.M., Nakashima, N., Yoshikawa, Sh., 1994, A study of Cytochrome c Oxidase in Lipid Bilayer Membranes on Electrode Surfaces. Langmuir 10: 877-882

10. Burgess, J. D., Rhoten, M. C.; Hawkridge, F. H., 1998, Cytochrome *c* Oxidase Immobilized in Stable Supported Lipid Bilayer Membranes, Langmuir, 14:2467 -2475

11. Naumann, R., Schmidt, E.K., Jonczyk, A., Fendler, K., Kadenbach, B., Liebermann, T., Offenhäusser, A., Knoll, W., 1999, The peptide-tethered lipid membrane as a biomimetic system to incorporate cytochrome c oxidase in a functionally active form. Biosens. Bioelectr. 14: 651-662

12. Jeuken, L.C. et al., 2005, Direct Electrochemical Interaction between a Modified Gold Electrode and a Bacterial Membrane Extract. Langmuir 21:1481-1488

13. Jeuken, L. J. C. et al. R.J., 2006, Redox Enzymes in Tethered Membranes. J.Am.Chem.Soc. 128, 1711-1716

14. Haas, A. S., Pilloud, D. L.; Reddy, K. S., Babcock, G. T.; Moser, C. C., Blasie, J. K., Dutton, P. L., 2001, Cytochrome c and cytochrome c oxidase: Monolayer assemblies and catalysis, J. Phys. Chem. B, 105:11351-11362.

15. Giess, F., Friedrich, M.G., Heberle, J., Naumann, R.L., Knoll, W., 2004, The protein-tethered lipid bilayer: A novel mimic of the biological membrane. Biophys. J. 87:3213-3220

16. Friedrich, M.G., et al., 2004, Active Site Structure and redox processes of cytochrome c oxidase immobilised in a novel biomimetic lipid membrane. Chem. Comm. 2376-2377

17. Friedrich, M.G ., Robertson, J W R, Walz, D, Knoll, W, Naumann, R L C, Electronic wiring of cytochrome c oxidase in a biomimetic surface architecture, submitted to Biophys. J.

18. Lucioli, S., Hoffmeier, K., Carrozozzo, R., Tessa, A., Ludwig, B. and Santorelli, F.M., 2006,

Introduction a novel human mtDNA mutation into the Paracoccus denitrificans COX I gene explains functional deficits in a patient. Neurogenetics, 7: 51-57

19. Naumann, R., et al., 2003, Tethered lipid bilayers on ultra flat gold surfaces. Langmuir 19:5435-5443

20. Vanderkooi J.M., Maniara, G., Green, T.J., Wilson, D.F., 1987, An optical method for measurement of dioxygen concentration based upon quenching of phosphorescence. J. Biol. Chem. 262: 5476-5482

21. Smith, P.E., Brunne, R.M., Mark, A.E., Van Gunsteren, W.F., 1993, Dielectric properties of trypsin inhibitor and lysozym calculated from molecular dynamics simulations, J. Phys. Chem. 97: 2009-2014

22. Robertson, J. W. F., Friedrich, M. G., Kibrom, A., Knoll, W., Naumann, R. L. C., Walz, D., Modeling Ion Transport in Tethered Bilayer Lipid Membranes. 1. Passive Ion Permeation, Biophys. J. submitted

23. Ivashchuk-Kienbaum, Yu., A., 1996, Monitoring of the Membrane Potential in Proteoliposomes with incorporated cytochrome c oxidase using the fluorescent dye indocyanine J. Membrane Biol. 151: 247-259

24. Moody, A. J., Brandt U. and Rich, P.R, 1991,, Single electron reduction of 'slow' and 'fast' cytochrome-c oxidase FEBS Lett., 293:101-105

25. Richter, O.-M.H. and B. Ludwig, B. 2003. Cytochrome c oxidase – structure, function and physiology of a redox-driven molecular machine. Rev Physiol Biochem Pharmacol 147:47-74

26. Jeuken, L.J.C., Jones, A.K., Chapman, St.K., Cecchini, G., Armstrong, F., 2002, Electron-Transfer Mechanisms through Biological Redox Chains in Multicenter Enzymes, J. Am. Chem. Soc, 124: 5702-5713

27. Bard Allen J. and Faulkner, Larry, L. Electrochemical Methods: Fundamentals ands Applications. second edition John Wiley & Sons, New York (2001)

28. Laviron, E., 1979, General expression of the linear potential sweep voltammogram in the case of diffusionless electrochemical systems. J. Electroanal. Chem. 101:19-28

29. Jeuken, L.J.C., McEvoy, J.P., Armstrong, F.A., 2002, Insights into Gated Electron-Transfer Kinetics at the Electrode-Protein Interface: A Square wave Study of the Blue Copper Protein Azurin. J. Phys. Chem. B. 106:2304-2313

30. Svensson-Ek M, Abramson J, Larsson G, Tornroth S; Brzezinski P, Iwata S, 2002, Journal of molecular biology 321: 329-39

31. Hildebrandt, P., Vanhecke F., Buse, G., Soulimane, T., Mauk, A.G., 1993, Resonance Raman Study of the Interactions between Cytochrome c Variants and cytochrome c Oxidase, Biochemistry 32, 10912-10922

Table 1, Electrical parameter values obtained by fitting to the measured data of impedance spectra and thicknesses obtained by fitting to the SPR angle scan plots

	$R_m/\Omega\,cm^2$	$C_m/\mu F\,cm^{-2}$	Layer thickness/nm (SPR)
Ni-NTA layer			2.4
CcO layer before ptBLM formation	$500 \pm 80 \times 10^3$	12.1 ± 2.8	11.1
CcO layer after ptBLM formation	$13 \pm 6 \times 10^6$	7.1 ± 0.5	12.0
ptBLM after cyt c addition	$550 \pm 90 \times 10^3$	7.1 ± 0.5	n.d.

Figure captions

Figure 1. Schematic representation of cytochrome c oxidase (CcO) embedded into a protein-tethered bilayer lipid membrane. The protein is attached to the template stripped gold film on the NTA-Ni^+ complex-modified surface by a his-tag attached to SU I. The lipid bilayer is assembled around the protein by in-situ dialysis of micelles made from detergent-solubilized lipid.

Figure 2. SPR kinetic trace at a constant angle of incidence (55°), binding of CcO is recorded after addition of the detergent-solubilized protein at (a) while the in-situ dialysis is started at (b) by adding detergent solubilized lipid and biobeads. Angle scans of the different layers are shown in the inset.

Figure 3. Impedance spectra, frequency normalized admittance (a) and Bode plots (b), of the Ni-NTA modified surface before (♦) after binding of CcO before (●) and after in-situ dialysis to form the lipid bilayer around the protein (▲). Dotted lines represent experimental data, solid lines show the fitted curves using the equivalent circuits (d) except for the Ni-NTA modified surface where circuit (c) was used.

Figure 4. Impedance spectra of CcO embedded in a ptBLM recorded at a bias potential of + 200 mV vs. NHE, as a function of the concentration of reduced cyt c(a), black (0 M), red ($2.3 \cdot 10^{-4}$ M), green ($5.6 \cdot 10^{-4}$ M), blue ($8.4 \cdot 10^{-4}$ M), magenta ($1.07 \cdot 10^{-3}$ M), cyan ($1.28 \cdot 10^{-3}$ M), orange: $1.6 \cdot 10^{-3}$ M). Spectra were fitted using the equivalent circuit shown in Fig. 3d. Resistances thus obtained were plotted vs. the concentration of cyt c (b). The decrease is considered in terms of proton transfer due to the activation with reduced cyt c.

Figure 5. (A) A series of impedance spectra of CcO embedded in a ptBLM recorded at different bias potentials vs. NHE, at a fixed concentration of $1.8 \cdot 10^{-4}$ M cyt c, black:+400mV, red:+350mV, green:+300mV, yellow:+250mV, pink: +200mV, orange: +150mV, cyan: +100mV, magenta: +50mV, violet: 0mV. (B) Such spectra were recorded for various concentrations of cyt c. Resistivities for the

different concentrations plotted vs. potentials, -▼-: 0 M,-●-: $1.07 \cdot 10^{-4}$ M,-▲-: $1.82 \cdot 10^{-4}$ M ,-■-: $5.07 \cdot 10^{-4}$ M (b).

Figure 6. Cyclic voltammogram of the CcO immobilized in a ptBLM alone (dotted line) with reduced cytochrome c added (1 mM in the bathing solution) under aerobic (solid line) and anaerobic conditions (dashed line), scan rate 50 mV/s.

Figure 7. Schematic representation of the pathway of electrons (red arrows) through the enzyme in the case of a cathodic current flowing through the electrode. Cyt c_{ox} is reduced to form Cyt c_{red} by the electrochemical reduction, as shown by the dotted black arrow (eq. 2 in the text). Electrons travel in the opposite direction from Cyt c_{red} to oxygen catalyzed by the enzyme thereby regenerating cyt c_{ox} (eq. 1).

Figure 8. Schematic representation of the pathway of electrons (red arrows) through the enzyme in the case of an anodic current flowing through the electrode. Electrons are accepted by the heme a_3/Cu_B catalytic center to be transformed from the O to the R state and, after the uptake of oxygen to be transformed to the P and F states (25). Electrons can be taken up by the electrode either from the R state or from the P/F state. The P/F state is favoured in the presence of an excess of cyt c_{red} and oxygen. If electrons are taken up from the electrode by the P/F state, this process is accompanied by the regeneration of (O_2), the product of the electrochemical oxidation, shown by the dotted black arrow, (eq 3 in the text).

Figure 9. Current densities of the peaks of cytochrome c reduction/oxidation as a function of the square root of the scan rate. Cyt c was applied in the reduced (-■-) and oxidized state (-▲-) in the presence (-■-, -▲-) and absence (-●-) of CcO.

Figure 10. Cyclic voltammogram of CcO immobilized in a ptBLM alone (dashed line) with oxidized cytochrome c added (1 mM in the bathing solution) under aerobic (dash-dotted line) and anaerobic conditions (solid line), scan rate 50 mV/s

Figure 11. SERR spectra of cytochrome c_{red} adsorbed on a DTP modified roughened Ag electrode immersed in buffer solution measured at different potentials, spectrum taken at (a) 40 mV, (b) 90 mV , (c) 140 mV, (d) 240 mV, (e) 350 mV, more positive potentials cannot be applied because of irreversible damage to the Ag electrode.

Figure 12. Peak potentials as a function of scan rate (trumpet plots) of cyt c (reduced) adsorbed to CcO with the his-tag attached to subunit I under aerobic conditions, concentration in the bathing solution 1 mM at a temperature of 20°C. An intrinsic rate constant of ET $k_0 = 73.13\ s^{-1}$ and a standard potential of $E^0 = 0.409$ V was determined.

Figure 1

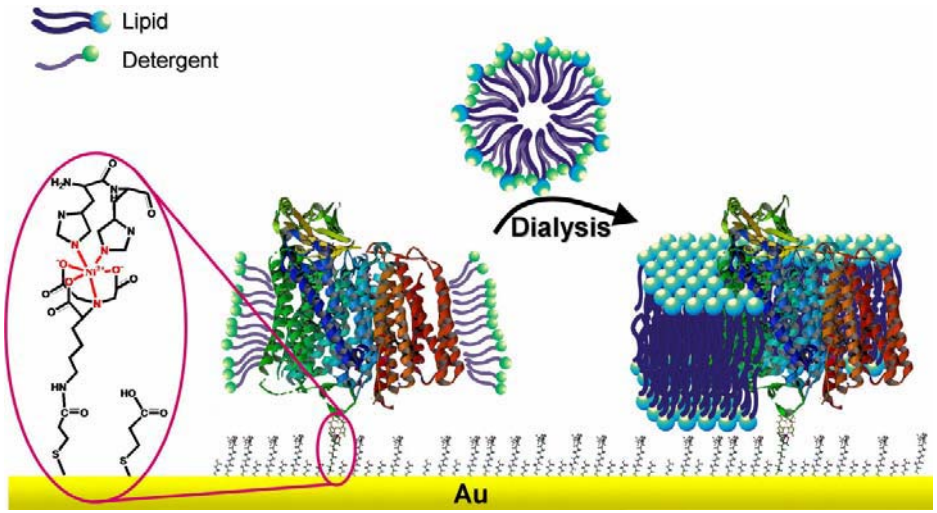

Figure 2

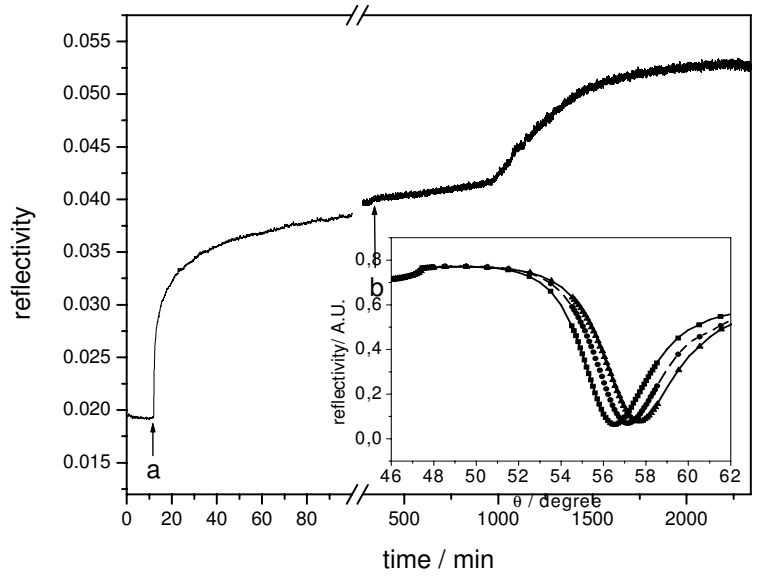

Figure 3

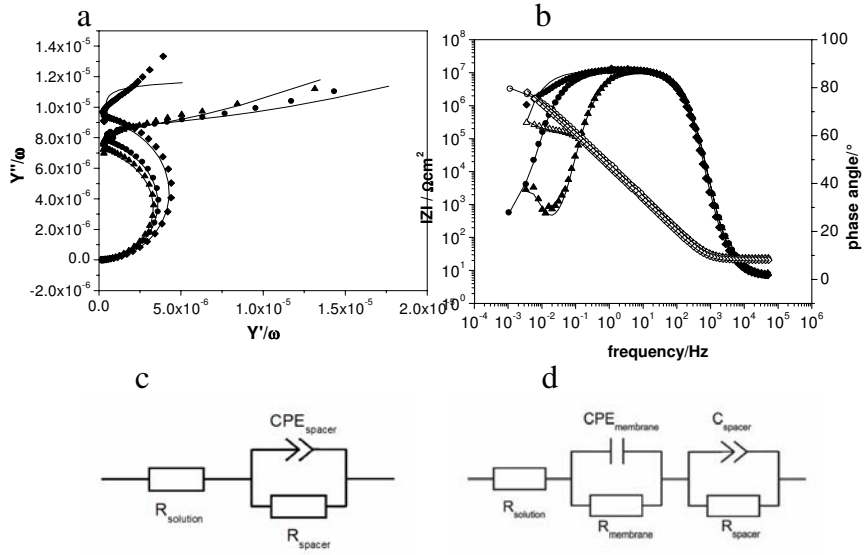

Figure 4

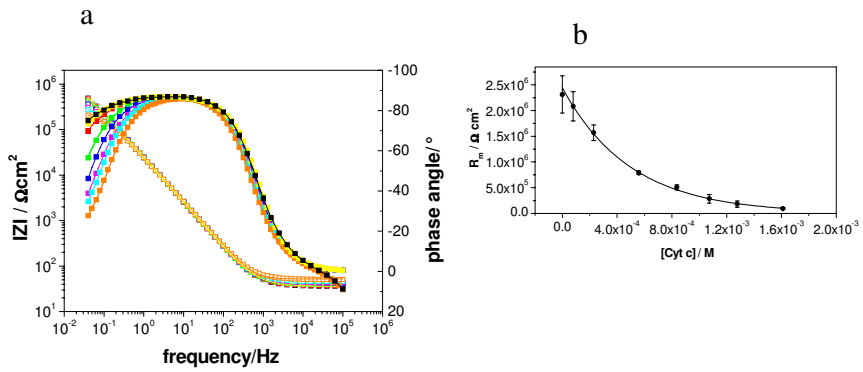

Figure 5

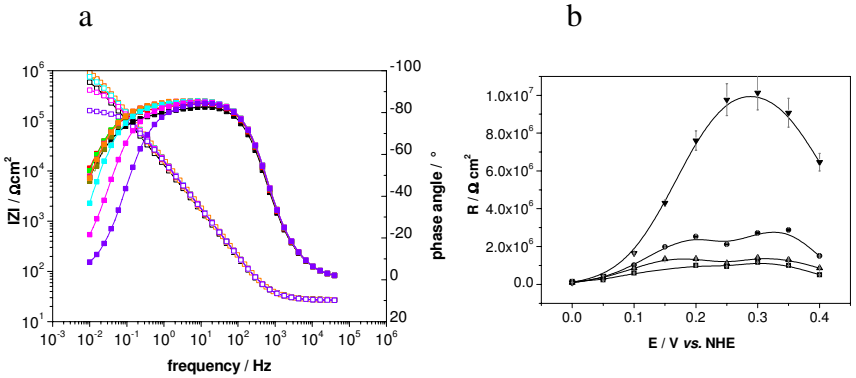

Figure 6

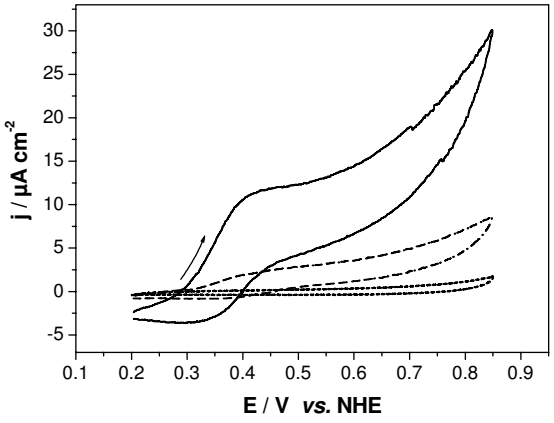

Figure 7

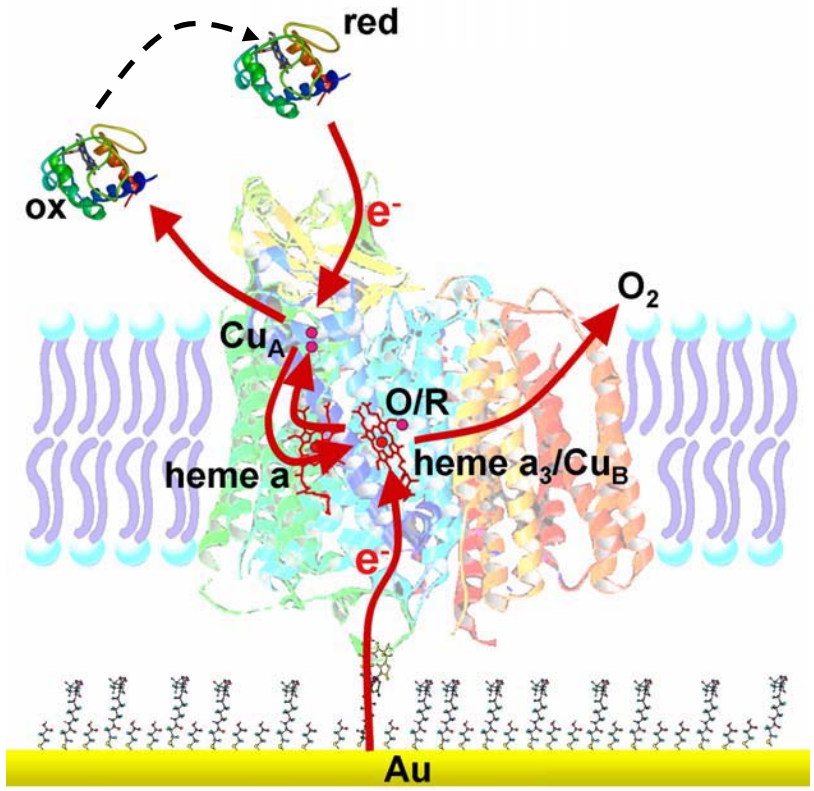

Figure 8

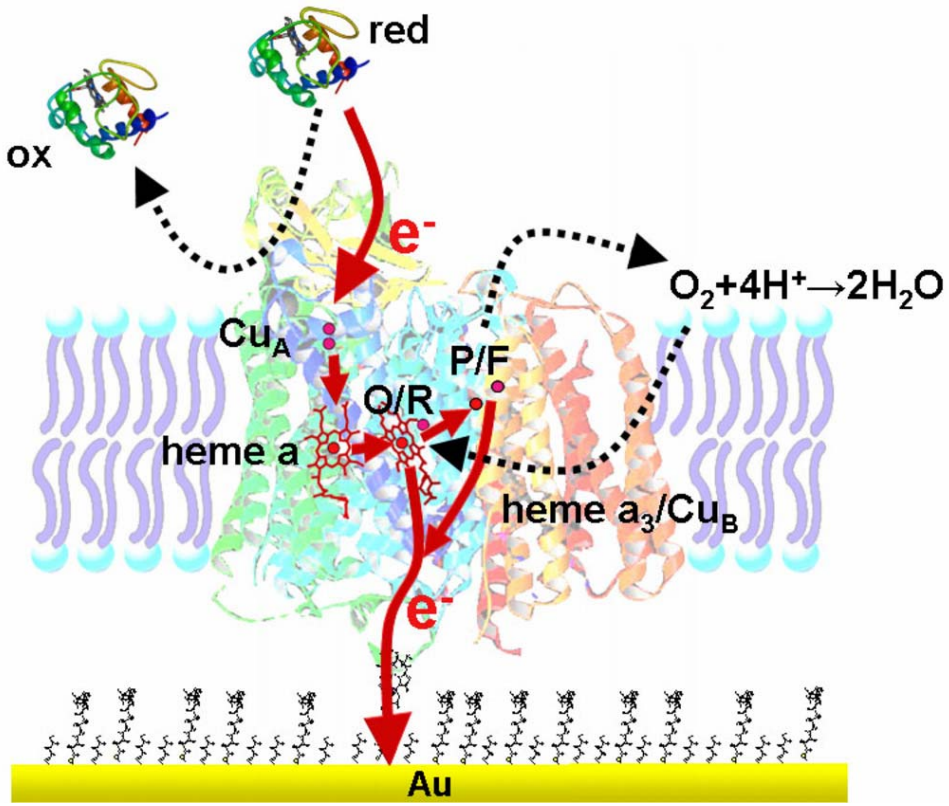

Figure 9

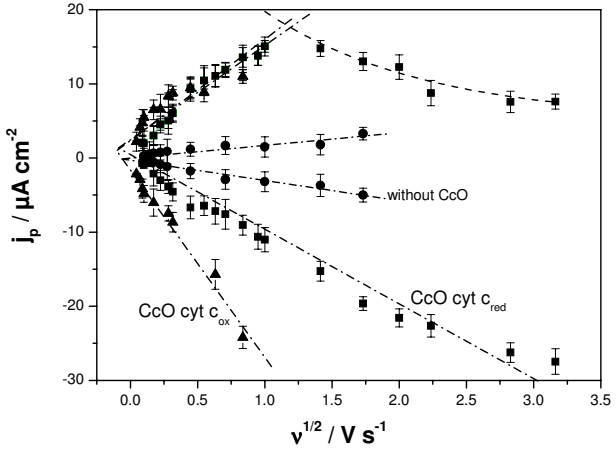

Figure 10

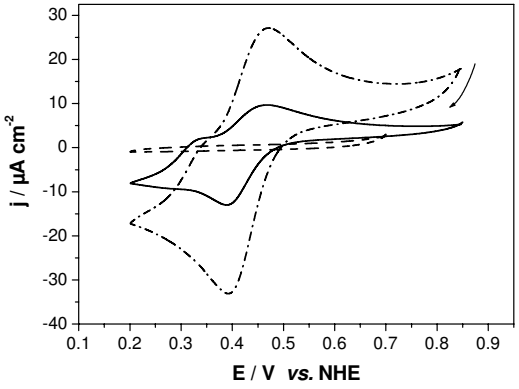

Figure 11

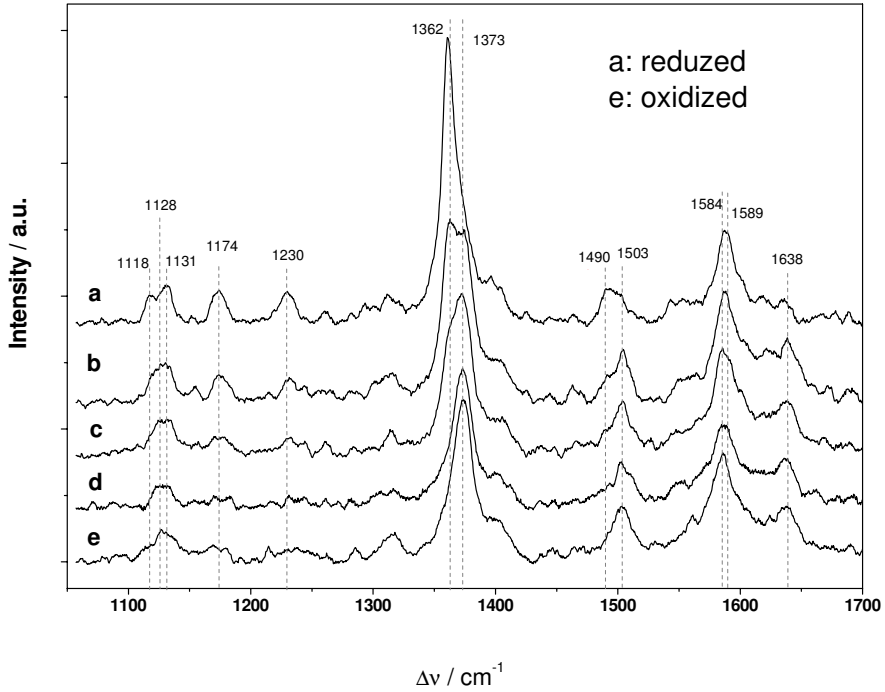

Figure 12

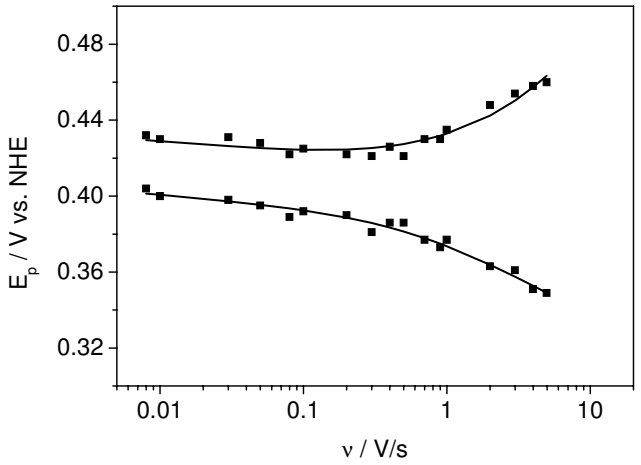

Paper 5

JOURNAL OF BIOLOGICAL CHEMISTRY

Activity of Membrane Proteins Immobilized on Surfaces as a Function of Packing Density

Running Title: **Activity of Membrane Proteins as Function of Packing Density**

Marcel G. Friedrich,*‡ Vinzenz Kirste,* Jiapeng Zhu, † Robert B. Gennis, † Wolfgang Knoll,* and Renate L. C. Naumann*

*Max Planck Institute for Polymer Research, Ackermannweg 10, 55128 Mainz, Germany; †University of Illinois, Department of Biochemistry, 600 South Mathews Street;

‡ Adress correspondence to: Marcel G. Friedrich Ackermannweg 10, 55128 Mainz, Germany; E-mail friedric@mpip-mainz.mpg.de
Marcel G. Friedrich and Vinzenz Kirste contributed equally to this work

SUMMARY **A systematic study of the influence of the packing density of transmembrane proteins on their activity is performed with cytochrome c oxidase (CcO) from *R. sphaeroides* as an example. CcO was genetically engineered with a histine–tag, attached to Subunit II, and then tethered by an interaction with functionalized thiol compounds bound to a gold electrode. The packing density was varied by diluting the functionalized thiol with a non-functionalized thiol that does not bind to the enzyme. After attaching the CcO to the gold surface, a lipid bilayer was formed to incorporate the tethered proteins. The reconstituted protein-lipid bilayer was characterized by surface enhanced infrared reflection absorption spectroscopy, electrochemical impedance spectroscopy, surface plasmon resonance and atomic force microscopy. The activity of the proteins within the reconstituted bilayer was probed by direct electrochemical electron injection, and was shown to be very sensitive to the packing density of protein molecules. At low surface density of CcO, the bilayer did not effectively form and protein aggregates were observed, whereas at very high surface density, very little lipid is able to intrude between the closely packed proteins. In both of these cases, enzyme activity, measured by the efficiency to accept electrons, is low. The activity of the enzyme is preserved in the biomimetic structure, but only at a moderate surface coverage in which a continuous lipid bilayer is present and the proteins are not forced to aggregate. Electrostatic and other interaction forces between protein molecules are held responsible for these effects.**

Received for publication "Staff will complete" and in final form "Staff will complete"

Address reprint requests and inquiries to friedric@mpip-mainz.mpg.de

A central issue of studying proteins confined to surfaces is the preservation of their activity. This is particularly critical for membrane proteins since they require a lipid environment but are still subject to denaturation in the immediate vicinity of surfaces. To address this problem, biomimetic membrane systems have been developed such as hybrid bilayer lipid membranes (1) and tethered bilayer lipid membranes (tBLMs) (2-4). They provide the lipid environment required for the function of the protein but additionally use tethering systems to provide an interstitial space separating the protein from the surface by an aqueous reservoir. One of the most promising systems investigated in this context is the protein-tethered bilayer lipid membrane (ptBLM) (5-7), designed for complex membrane proteins such as the cytochrome c oxidase (CcO) (Fig. 1). It is based on an NTA functionalized surface which, after chelation with Ni^{2+} ions, reversibly binds proteins genetically engineered with histine(his)-tags. A lipid bilayer is then reconstituted *in situ* around the bound proteins. Among the benefits of this strategy, in addition to defining the orientation of the protein with respect to the surface, is the possibility to systematically vary the surface concentration of the protein. One can, therefore, test the possibility that

inter-protein interactions might affect the activity of the enzymes. The distance between single proteins could be an important parameter considering that electrostatic and other interaction forces between molecules could influence charge transfer and other kind of processes involved in protein function. The above mentioned ptBLM system is well designed for this purpose. The surface concentration of proteins can be easily varied by varying the concentration of the chelator (NTA) molecules. Two opposite orientations of the protein were investigated, either with the cytochrome c binding site directed towards the electrode surface (6,7) or pointing away from it (5), simply by engineering the his-tag on the C-terminus of Subunit II or Subunit I, respectively. Indications of the significance the surface concentration as a critical parameter were obtained in previous investigations of the CcO engineered with the his-tag on the C-terminus of Subunit II. In particular, electron transfer initiated by direct electrochemical electron injection into the protein, which can be used as a measure of the protein activity (6,7) was shown to be affected by different packing densities. The aim of the present investigation is a more detailed investigation of this effect.

EXPERIMENTAL PROCEDURES

Di-thio-bis(N-succinimidyl propionate) (DTSP), di-thio-bis(propionic acid) (DTP), *N*-(5-Amino-1-carboxypentyl) iminodiacetic acid (ANTA), dodecyl-β-D-maltoside (DDM), cytochrome c from bovine heart, glucose oxidase and catalase were purchased from Sigma and used as obtained, biobeads from Bio-Rad Laboratories GmbH, Munich, Germany were washed with ethanol and deionised water from a MilliQ water purification system, 1,2-Diphytanoyl-sn-glycero-3-phosphocholine (DiPhyPC) was provided by Avanti Polar Lipids. All other chemicals were of analytical grade.

CcO from *R. sphaeroides* engineered with his-tag on SU II was expressed and purified according to Mitchell and Gennis (8).

Preparation of the samples - Template-stripped gold (TSG) electrodes (9) were used for SPR and electrochemistry measurements, immersed for 120 min in a solution of DTSP and DTP in ratios from 0.2 to 1 (corresponding to 20:80, 40:60, 60:40, 80:20, 100:0 (w/w)) in dry DMSO (total 2mg/ml). After rinsing, the slides were functionalized for 48 h in a 0.15 M solution of ANTA buffered to pH 9.8 by adding 0.5 M KCO_3. Finally, the glass slides were immersed for 30 min in 40 mM $NiSO_4$ in acetate buffer 50 mM, pH 5.5. The excess Ni was removed by thorough rinsing with the Ni^{2+}-free acetate buffer. Immobilisation of the protein to the Ni-chelated NTA surface was performed in a solution of 100 nM CcO in detergent-containing phosphate/DDM buffer (K_2HPO_4 0.1 M, KCl 0.05 M, pH 8, 0.1% DDM) (6,7). Biobeads were added to the lipid-detergent-containing phosphate/DDM buffer, (DiPhyPC 0.05 mg/ml, K_2HPO_4 0.1 M, KCl 0.05 M, pH=8, 0.1% DDM) in order to remove the detergent and to form a lipid bilayer

Electrochemical measurements - Electrochemical measurements were performed using an Autolab instrument (PGSTAT302) equipped with an FRA2-module for impedance measurements, an ECD-module amplifier for low-currents, an ADC750 module for rapid scan measurements, and a SCAN-GEN module for analog potential scanning as well as the frequency response analyzer (FRA) software provided by Eco Chemie, B.V. (Utrecht The Netherlands). Measurements under anaerobic conditions were done in a buffer solution containing K_2HPO_4 0.1M, KCl 0.05M, pH 8, and the oxygen trap consisting of glucose (0.3%w/w), glucose oxidase (75µg/ml) and catalase (12.5µg/ml) (10). This solution was flushed with Ar purged of oxygen by washing through the oxygen trap containing the buffer solution for one or two hours prior to the measurements to assure a completely deoxygenated solution. Impedance spectra were recorded in a frequency range of 50 kHz - 3 mHz with an excitation amplitude of 10 mV. Data were subsequently analyzed by the complex nonlinear fitting algorithm supplied included with the data processing software ZVIEW (Version 2.6, Scribner Associates, Inc.) applied to the equivalent circuits depicted in Fig. 10c and d. The CPEs in the RC circuits (Fig. 10c, d) account for the heterogeneity of the mixed DTP/DTSP-NTA layer.

All electrochemical measurements were taken in a three-electrode configuration with TSG as the working electrode, a $Ag/AgCl,KCl_{sat}$ reference, and a platinum wire as the counter electrode. All electrode potentials are quoted vs. NHE.

Surface Plasmon Resonance Spectroscopy (SPR) - SPR was performed with apparatus using the Kretschmann-configuration with a measuring cell designed for the combination of SPR with electrochemistry. The glass slide (LaSFN9 glass from Hellma Optik, Jena, refractive index n=1.85 at 633 nm) was optically matched to the base of a 90° glass prism (LaSFN9). Monochromatic light from a He/Ne Laser, (Uniphase, San Jose, CA, λ = 632.8 nm) was directed through the prism and collected by a custom made photodiode detector. Recording the change of reflectivity at a fixed angle in the linear regime of the SPR curve as a function of time, shown in Fig. 9, yields the time course of protein binding and reconstitution.

Surface Enhanced Infrared Reflection Absorption Spectroscopy (SEIRAS) - SEIRAS was carried out with a Bruker VERTEX 70 FTIR spectrometer with a resolution of 4 cm^{-1}. The mirror velocity was 60kHz, and 100 scans were taken for each spectrum.

A gold film was formed by chemical deposition onto the surface of the hemispherical silicon ATR crystal (11). The result is a rough gold layer (RMS roughness of about 5nm) as required for an enhancement of the IR absorption of the biomimetic membrane system immobilized on the gold film.

The SEIRAS setup consists of an infrared light source, the hemispherical silicon-crystal, required for total internal reflection and a Teflon cell with buffer solution. The Attenuated Total Reflection (ATR) spectroscopy configuration allows for the excitation of surface plasmons at the rough surface, required a sufficient enhancement of the IR signal.

Atomic force microscopy (AFM) - The AFM measurements were performed with a Scanning Probe Microscope "Multimode Tuna TR" from Veeco, USA. An AFM liquid cell was used and the measurements were carried out in the tapping mode with a silicon nitride cantilever in a triangular shape.

RESULTS

Varying the composition of the CcO monolayer

To modify the concentration of CcO on the surface, the surface concentration of chelating NTA molecules was varied. This was done on the level of the first monolayer consisting of a thiol terminated active ester (DTSP) used for the functionalization with ANTA molecules. The structure of the molecules is given in Fig. 2. DTSP was mixed with DTP in different ratios. DTP is the starting material for the synthesis of DTSP and has a similar structure. However, DTP is terminated by a COOH group which is unable to couple to ANTA. The di-thio-groups split up into two Au-S bonds upon self assembly. DTSP becomes thio-(N)-succinimidyl propionate, (TSP), and DTP is converted to thio- propionic acid (TP). ANTA reacts with TSP resulting in an NTA terminated surface mixed with COOH terminated TP molecules. After chelation with Ni, the NTA group is ready to form a stable complex with the poly-histidine tail of the CcO in order to anchor the enzyme to the surface. The binding and reconstitution of the CcO are illustrated in (Fig. 1).

The composition of the mixed NTA-TP/TP monolayer measured by XPS closely corresponds to the mixing ratio of DTSP/DTP in solution (Fig. 3). A model calculation was carried out based on the simplifying assumption of a Langmuir isotherm for binding. From this calculation a 0.6 mixing ratio of DTSP/DTP yields a Mole ratio of 0.46 on the surface (details of the calculation are given in the appendix). Coupling of ANTA to a monolayer of the same mixing ratio (0.6) of DTSP/DTP, monitored by SEIRAS as a function of time, illustrates that the dilution with DTP leads to a smaller amount of bound ANTA molecules. Fig. 4 shows the actual difference spectra of ANTA molecules, before and after binding. Fig. 5 shows the peak height of the amide I band during the coupling of ANTA to TSP as a function of time (open and closed symbols are for the diluted (TSP/TP) and undiluted (TSP alone) layers, respectively). In any case, ANTA coupling as monitored by SEIRAS, takes up to 24 hours. The time constant of the mixed layer is slightly smaller than that of the undiluted layer (time constants τ = 4.4 vs. 5.7 hrs). Binding of CcO to the diluted NTA layer thus formed (mixing ratio 0.6 in this case) was also monitored by SEIRAS (Fig. 6). The bands at 1658 and 1549 cm^{-1} assigned previously [13] to the amide I, II modes of the protein backbone vibrations of the CcO increase with time. The peak position of the amide I band at 1658 cm^{-1} is characteristic for the predominantly α-helical conformation of the CcO. Bands at 1436 and 1290 cm^{-1} also appear which have been assigned to conformational changes of the Ni-NTA. The peak areas of the amide I and II bands

increase with time (τ = 3.6 min) (Fig. 7, 8) with binding kinetics similar to the undiluted layer (12).

Probing CcO binding and reconstitution by SPR

The immobilization of the protein to the different NTA/Ni-modified gold surface and the formation of the lipid membrane around the CcO molecules by in-situ dialysis was followed by a combination of SPR and electrochemical impedance spectroscopy (EIS) as described earlier (5,7). Reflectivity scans as a function of the angle of incidence (the inset of Fig. 9) were used to determine the optical thickness before (-□-) and after (-○-) protein binding and reconstitution (-∇-). Reflectivity at a fixed angle of incidence, shown in Fig. 9, yields the time course of protein binding and reconstitution. The 0.6 mixing ratio is shown as an example. From this recording, the time course of immobilization was shown to be complete after 40 min, whereas in-situ dialysis taking more than 20 hours was usually done overnight. Quantitative information of the protein surface coverage was not accessible due to the complexity of the mixed protein-detergent layer in a aqueous environment and due to the lack of exact refractive index value of CcO.

Probing CcO binding and reconstitution by EIS

Characteristic changes due to the formation of the layer-by-layer structure, as a function of the DTSP/DTP mixing ratio, were obtained by EIS spectra. Examples of a single set of spectra, before and after binding and reconstitution, are shown in Fig. 10. These data are fitted to the equivalent circuits given in Fig. 10 c and d to yield the resistance and capacitance of the protein and the protein-lipid layer respectively, as a function of mixing ratio. A statistical presentation of the collected data is displayed in Figs. 11 and 12. For a low mixing ratio (0.2), the capacitance of the protein layer is 68 ± 6 μF cm^{-2}, and decreases with increasing mixing ratio, with the largest drop between 0.4 and 0.6, finally reaching 9 ± 1 μF cm^{-2} with a layer made from pure DTSP (Fig. 11). When the bilayer is reconstituted around the protein, the capacitance decreases for all mixing ratios except for the 100% DTSP, where an increase of the capacitance is only observed in some cases. (The error bars represent standard deviations of 7-10 sets of measurements). The resistance of the protein layers is already quite high at all mixing ratios (Fig. 12). This is an indication of a random orientation of the enzymes before reconstitution. They may be more or less tilted with respect to the surface, thereby coming in close contact with each other to form a sealing layer to the bathing solution. This conclusion is based on the observation that the resistance of the protein layer decreases while conducting a series of potential sweeps, which could be due to reorientation and separation of the highly charged proteins. After reconstitution, the resistance increases in all cases, with the most significant change for the 0.6 mixing ratio. To better understand these changes, it has to be considered that the capacitance of a dielectric layer is determined by thickness and dielectric constant of the material. The capacitance (C) of a pure protein monolayer is estimated to be ~6 μFcm^{-2} using $C = \frac{\varepsilon\varepsilon_0 A}{d}$ with A as the area (1 cm^2), d the thickness (5 nm), ε the dielectric constant of the dielectric layer (typically ε = 30) and ε_0 the permittivity of free space. Higher values of 13.1 ± 3.9 to 68 μF cm^{-2} as observed for different mixing ratios are likely due to the large amount of water molecules separating the protein molecules. The dielectric constant of the lipid is much smaller, ε = 2.2, than that of either water (ε = 80) or protein. This explains the decreases of the capacitance upon reconstitution when water and detergent molecules are replaced by lipid bilayer patches. The lowest values reached are 7.3 ± 0.5 μF cm^{-2} for the 60 % mixing ratio. This is in agreement with the estimate of more than 90% coverage of CcO molecules as deduced from the charge transferred by CV measurements due to the direct electron transfer to the CcO (7).

Characterizing CcO monolayers by AFM

Surface layers were exclusively prepared on template stripped gold (TSG) surfaces, due to their low roughness over large surface areas (RMS < 0.2 nm). The roughness hardly changes when mixed NTA layers were prepared on this surface (Fig. 13 a). AFM images of CcO monolayers at mixing ratios varying from 0.001, 0.1, 0.6 to 1 were then recorded (Fig. 13 b-e). Clear differences were obtained between the pure NTA layer and the protein layers, even for the very low mixing ratios 0.001 and 0.1. For the 0.001 ratio, structures with lateral dimensions in the range of 50-80 nm and a height of up to 15 nm are seen. For the 0.1 ratio such structures are even larger, 50-180

nm in the lateral dimension and up to 25 nm high. This is not compatible with dimensions of single enzymes obtained from the X-ray crystallography (4.5 nm × 7.0 nm for the in-plane dimension and 9 nm for the height of CcO from *R. sphaeroides* (13)). These structures indicate the formation of aggregates, possibly due either to non-specific protein binding (not NTA-dependent) or to agglomeration of NTA-tethered proteins due to the flexibility of the immobilized enzymes without the stabilizing environment of a membrane. In the case of the 0.6 mixing ratio, the structures are smaller with 10-20 nm laterally and ~10 nm in height. This is consistent with a monolayer of proteins with the dimensions according to X-ray crystallography. In this case, the arrangement of the enzymes could be stabilized by the high surface coverage. For the NTA layer formed on a 100 % TSP layer, the structures are still smaller, mostly 10 nm in the lateral dimension and < 10 nm in height. This is consistent with the assumption of a very tightly packed monolayer of CcO molecules.

Direct electron transfer (ET) probed by CV

It was shown previously that the activity of a redox-active membrane protein can be probed by direct heterogeneous electron injection from a gold electrode into the redox sites of the protein (6). Direct electron transfer (ET) can be effectively probed by cyclic voltammetry (CV) in combination with spectroscopic methods such as surface-enhanced resonance Raman spectroscopy (SERRS) (6,7). This combination of measurements conclusively demonstrated that electron injection into the primary redox site of CcO gives rise to consecutive ET through all four redox centers within the protein. The direct ET was also shown, under aerobic conditions, to initiate the catalytic turnover of the enzyme as well as proton translocation across the membrane (7). The peak shape of CV signals reflect the kinetics of the ET. For example, the theoretical peak width of a reversible one electron transfer to an absorbed species was estimated to be 90 mV (14). The area of the peak reflects the overall charge transferred during the ET process. Assuming 4 electrons transferred per molecule under anaerobic conditions, the number of active molecules per area can be obtained. CcO incorporated in ptBLMs based on 100 % DTSP monolayers give rise to direct ET, as shown previously (6). However, indications of the significance the surface concentration as a critical parameter were also obtained. In many cases one observes broad and shallow peaks or no peaks at all in the CV. This could indicate a large distribution of ET rate coefficients or alternatively, a strong interaction between the densely packed enzymes, inhibiting electron and other charge transfer pathways. The dependence of the efficiency of the direct ET, as a measure of enzyme activity, on the packing density, determined by the mixing ratio, is illustrated in Fig. 14. The cathodic peaks (baseline corrected and scan rate normalized) are displayed as a function of different mixing ratios. An example of an untreated CV is given in Inset (b) of Fig. 14. For the 0.2 and 1.0 DTSP layers, the peaks are hardly visible, becoming narrower and higher for the 0.4 and 0.8 layers, and reaching an optimum at 0.6. Integration of the peak current yields the charge and, hence, the surface coverage of the redox active CcO molecules. The result is plotted *vs.* the mixing ratio of DTSP/DTP in Inset (c) of Fig. 14. An optimum of ET efficiency was obtained at a mixing ratio of 0.6. This optimum of the mixing ratio therefore represents the standard value for all further mechanistic and kinetic investigations of the immobilized enzymes (7).

DISCUSSION

Figure 1 displays a schematic drawing of the protein-tethered bilayer lipid membrane architecture attached to a mixed TSP/TP monolayer. This Figure illustrates the basic question of this investigation: How can a relatively small dilution factor of the chelator molecules have such significant effects on the ability of the protein to accept electrons by direct ET from the electrode? Large dilution factors (0.001 and 0.1) seem to result in non-specific adsorption of the protein as aggregates, as seen in the AFM. This is consistent with the observation that at these dilution factors, an electrically sealed bilayer is not formed (Fig. 12b). A sufficient amount of chelator molecules (NTA-TSP) must be present to avoid unspecific adsorption and to provide a strict orientation of the enzymes. Even the 0.2 dilution layer does not form a closed layer of protein molecules. This is deduced from the capacitance values obtained by EIS, which indicate a high amount of water after reconstitution even at mixing ratios of up to 0.4. The mixing ratio of 0.6 is the clear optimum for the formation of a lipid bilayer, as far as the electrical properties of the

ptBLM is concerned. According to AFM, with 100% DTSP to maximize enzyme coverage, the enzymes are very tightly packed, such that the interaction between single molecules must be very strong. Lipid molecules can hardly be incorporated in between the protein molecules, which results in more intense inter-molecular forces between enzymes. In the moderately diluted cases, e.g. at a mixing ratio of 0.6, the packing density of the protein is less than when using pure DTSP. Small gaps still appear to be present, as deduced by the impedance and capacitance data. A higher dilution would be desirable, however, the lipid layer does not appear to uniformly span the gaps between proteins so as to form a well sealed ptBLM. Low dilution factors such as the 0.8 and undiluted layer seem to accommodate a few lipids only, as deduced from the small decrease in the capacitance as compared to the more diluted layers. The development of the resistance is in accordance with this interpretation. The undiluted layer, furthermore, does not show full enzyme activity even though a closed layer seems to be formed according to the AFM image.The coverage with protein molecules at the 0.6 mixing ratio is obviously an optimum between higher or lower surface coverage, neither of which permits the formation of an electrically sealed protein/lipid bilayer. This optimum with respect to the electrical properties appears also to be the optimum of the amount of electron accepting molecules on the surface (5.8 pMole/cm^2). Interestingly, this value is consistent with 6 pMole/cm^2 calculated for a densely packed protein monolayer, assuming an ellipsoidal disk of 4.5 nm × 7.0 nm for the in-plane dimension of the protein deduced from the crystal structure of CcO from *R. sphaeroides* (13).

With other dilution factors the amount of electron accepting molecules drops sharply. The undiluted layer, for example, only shows 0.2 pMol/cm^2 of electron accepting molecules even though the AFM image indicates a closed layer. The efficiency to accept electrons appears to require the insertion of lipids to separate the single proteins from each other. Protein flexibility within the reconstituted layer may also be required for optimal efficiency. These considerations lead to the conclusion that charge transfer properties of the enzymes are impaired by electrostatic or other interactions between the single proteins if the surface density of CcO molecules is too high to accommodate the enzymes in their natural conformation within a lipid bilayer. Charge transfer processes inside the protein could well be affected by these interactions, resulting in deleterious effects on the activity of the enzymes.

ACKNOWLEDGEMENT

We acknowledge the assistance of Daniela Mössner, University of Freiburg, for the XPS measurements.

REFERENCES

1. Cullison, J.K., Hawkridge, F.M., Nakashima, N., Yoshikawa, Sh., (1994). A study of Cytochrome c Oxidase in Lipid Bilayer Membranes on Electrode Surfaces. *Langmuir* **10**, 877-882
2. Guidelli, R., G. Aloisi, L. Becucci, A. Dolfi, M. R. Moncelli, and F. T. Buoninsegni. (2001). New directions and challenges in electrochemistry - Bioelectrochemistry at metal/water interfaces. *Journal of Electroanalytical Chemistry* **504(1)**,1-28.
3. Knoll, W., K. Morigaki, R. Naumann, B. Sacca, S. Schiller, and E. K. Sinner. (2004). Functional Tethered Bilayer Lipid Membranes. *Ultrathin Electrochemical Chemo- and Biosensors, Technology and Performance*. Mirsky V. M., editor. Springer-Verlag, Berlin. 239-254.
4. Jeuken, L. J. C. et al., (2006). Redox Enzymes in Tethered Membranes. *JACS* **128**,1711-1716
5. Giess, F., Friedrich, M.G., Heberle, J., Naumann, R.L., Knoll, W., (2004). The protein-tethered lipid bilayer, A novel mimic of the biological membrane. *Biophys. J.* **87**,3213-3220
6. Friedrich, M.G., et al., (2004), Active Site Structure and redox processes of cytochrome c oxidase immobilised in a novel biomimetic lipid membrane. *Chem. Comm.* 2376-2377
7. Friedrich, M.G., Robertson, J.W.F., Walz, D., Knoll, W., and Naumann, R.L.C., (2007). Electronic Wiring of a Multi-Redox Site Membrane Protein in a Biomimetic Surface Architecture. *submitted Biophys. J.*
8. Mitchell, D.M., and Gennis R.B., (1995). Rapid purification of wildtype and mutant cytochrome c oxidase from *Rhodobacter Sphaeroides* by Ni^{2+}-NTA affinity chromatography. *FEBS Letters* **368(1)**,148-150
9. Naumann, R., et al., (2003). Tethered lipid bilayers on ultra flat gold surfaces. *Langmuir,* **19**,5435-5443
10. Vanderkooi J.M., Maniara, G., Green, T.J., Wilson, D.F., (1987). An optical method for measurement of dioxygen concentration based upon quenching of phosphorescence. *JBC* **262**,5476-5482.
11. Miyake, H., Osawa, S. Ye, M., (2002). Electroless deposition of gold thin films on silicon for surface-enhanced infrared spectroelectrochemistry, *Electrochemistry Communications* **4**, 973-977
12. Ataka, K. et al., (2004). Oriented attachment and membrane reconstitution of his-tagged cytochrome c oxidase to a gold electrode, In-situ monitoring by surface enhanced infrared absorption spectroscopy. *JACS* **126**,16199-16206
13. Svensson-Ek, M. et al., (2002). The X-ray Crystal Structures of Wild-type and EQ(I-286) Mutant Cytochrome c Oxidases from Rhodobacter sphaeroides, *J. Mol. Biol.* **321**,329-339
14. Bard Allen J. and Faulkner, Larry, L. *Electrochemical Methods: Fundamentals ands Applications.* second edition John Wiley & Sons, New York (2001)
15. Tanford, C. Physical Chemistry of Macromolecules, John Wiley & Sons, Inc., New York (1963), p. 345

Figure captions

Fig. 1

Schematics of the reconstitution of the protein (cytochrome c oxidase with the his-tag attached to SU II) bound via the Ni-complex to the NTA modified gold surface into a protein-tethered bilayer lipid membrane (ptBLM)

Fig. 2

Upper part: the molecules used for the mixed monolayer: dithiobis (N-succinimidyl propionate) (DTSP), dithiobis (propionic acid) (DTP), the dithio-groups split up into two Au-S bonds upon self assembly, DTP becomes thio (N-succinimidyl propionate), (TSP), DTP becomes thio (propionic acid) (TP) lower part: coupling of N-(5-Amino-1-carboxypentyl) iminodiacetic acid (ANTA) to form the NTA modified (mixed) monolayer of TSP mixed with TP.

Fig. 3

XPS analysis of the surface concentration of the NTA modified (mixed) monolayer of TSP mixed with TP. Mixing ratios in solution are plotted versus the ratio of the elements oxygen and nitrogen vs. sulphur. With ANTA-TP and TP containig 7 oxygens and 2 nitrogens and 2 oxygens and 0 nitrogens per one sulphur, respectively, the parameters for the two graphs were calculated for (Y = A + B * X) and compared with the theoretical values in solution

Oxygen			**Nitrogen**		
parameter	value	deviation	Parameter	value	deviation
A	1.4923	0.17789	A	-0.0588	0.24818
theor.	*2*		*theor.*	*0*	
B	6.2075	0.26818	B	1.973	0.37415
theor.	6		*theor.*	*2*	

Fig. 4

SEIRAS (difference) spectra of the coupling of ANTA to the mixed TSP/TP monolayer

Fig. 5

Peak height of the amide I band as a function of time during coupling of ANTA to the mixed TSP/TP monolayer (open and closed symbols are for the diluted and undiluted layer, respectively).

Fig. 6

Difference spectra of the binding of CcO (100 nMol/L) to the mixed NTA layer at different time intervals.

Fig. 7

Peak area of the peaks at 1658 and 1549 cm^{-1} displayed in Fig. 6, plotted vs. time. The time constant obtained from this plot is 3.6 min.

Fig. 8

3D plot of of the binding of CcO (100 nM) to the mixed NTA layer, bands increase at 1651cm^{-1} (amide I) (a), 1549 (amide II) (b), 1440 (amide II) (c) and 1279 cm^{-1} .

Fig. 9

Kinetic trace of an SPR spectrum recorded during CcO binding (1) and reconstitution (2) at a constant angle of incidence (55°) and transferred into a optical thickness by using the Fresnel equation. The inset shows the reflectivity scans as a function of the angle of incidence before (-□-) and after (-○-) CcO binding and reconstitution (-Δ-), solid lines are the fitted curves.

Fig. 10

Impedance spectra, frequency normalized admittance (a) and Bode plots (b), of the Ni-ANTA modified surface before (1) after binding of CcO before (2) and after reconstitution of the protein (3). Dotted lines represent experimental data, solid lines show the curves fitted to the equivalent circuit (d) except for the Ni-ANTA modified surface which was fitted to the circuit (c).

Fig. 11

Capacitances of the membrane obtained from EIS, before (shaded bars) and after (full bars) in-situ dialysis as a function of the mixing ratio DTSP vs. DTP. The capacitance generally decreases during dialysis. The biggest change is at a ratio of 60 %, at the same time reaching reasonably low values.

Fig. 12

Resistivities of the membrane obtained from EIS, before (shaded bars) and after (full bars) in-situ dialysis as a function of the mixing ratio DTSP vs. DTP. Resistivities generally increase during dialysis. The optimum is at 0.6.

Fig. 13

AFM images (recorded in the tapping mode) and line scans of CcO bound to mixed NTA layers, mixing ratio DTSP/DTP 0.001 (a), 0.1 (b), 0.6 (c) and 1 (d). NTA layer without CcO bound as a reference (e).

Fig. 14

Base line corrected and scan rate normalized reductive peaks from cyclic voltammograms of the direct electron transfer to CcO at different mixing ratios (a) (an example of the full CV is shown in the inset (b), recorded under strictly anaerobic conditions), the surface coverage by active CcO molecules calculated from the integrated area of the current peaks is plotted vs. the mixing ratio (c).

FIGURES

Fig. 1

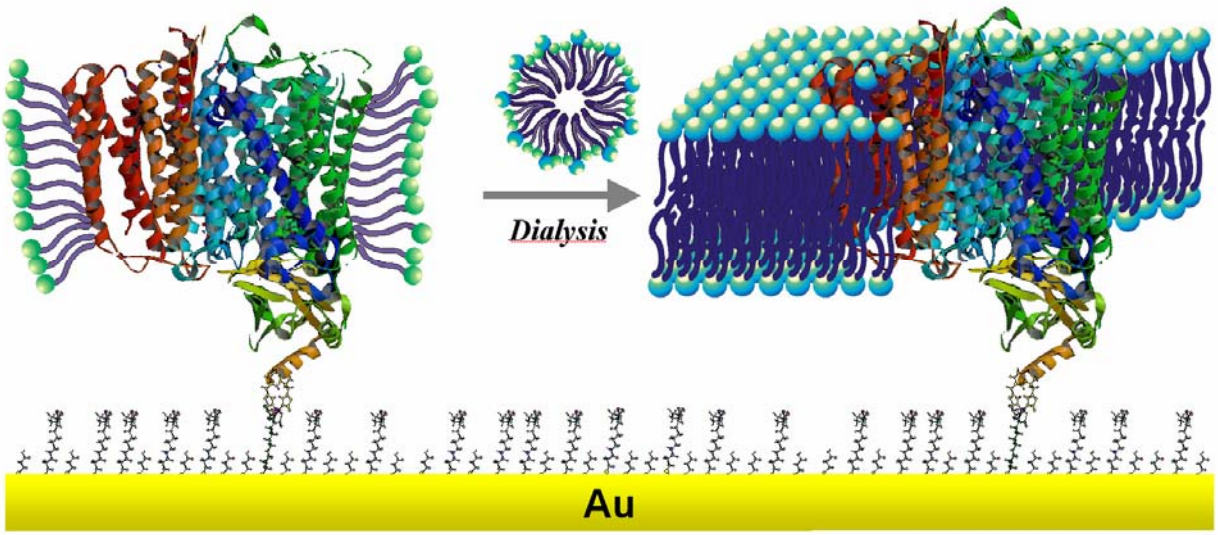

Fig. 2

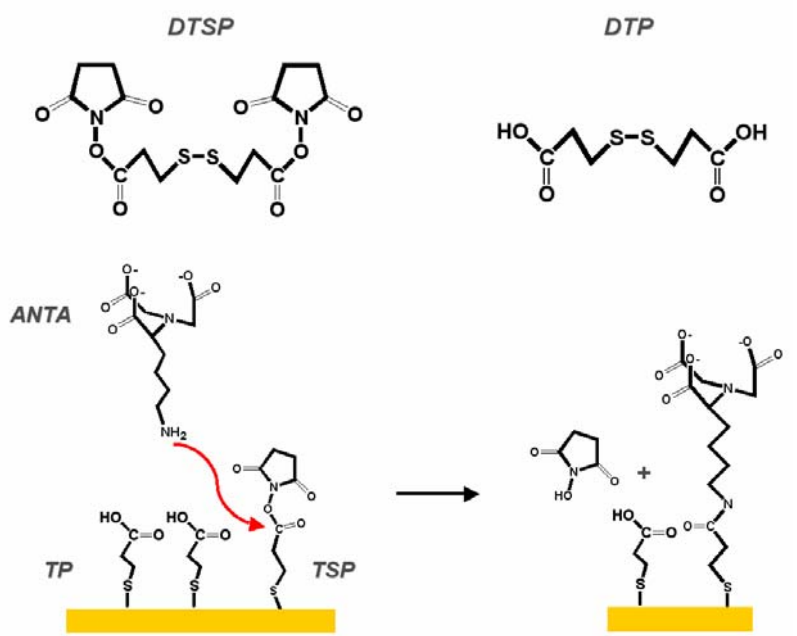
DTSP
DTP
ANTA
TP
TSP

Fig. 3

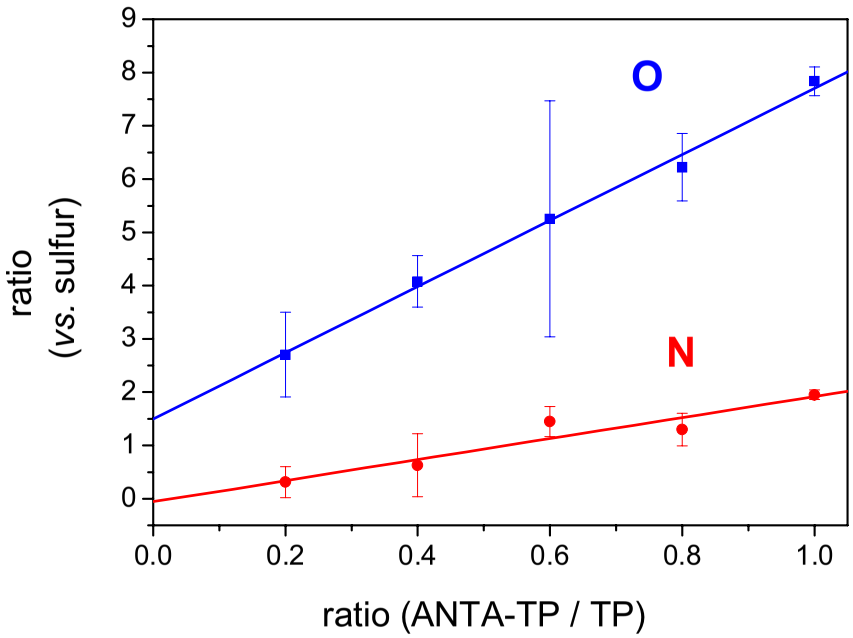
O
N
ratio
(vs. sulfur)
ratio (ANTA-TP / TP)
0
1
2
3
4
5
6
7
8
9
0.0
0.2
0.4
0.6
0.8
1.0

Fig. 4

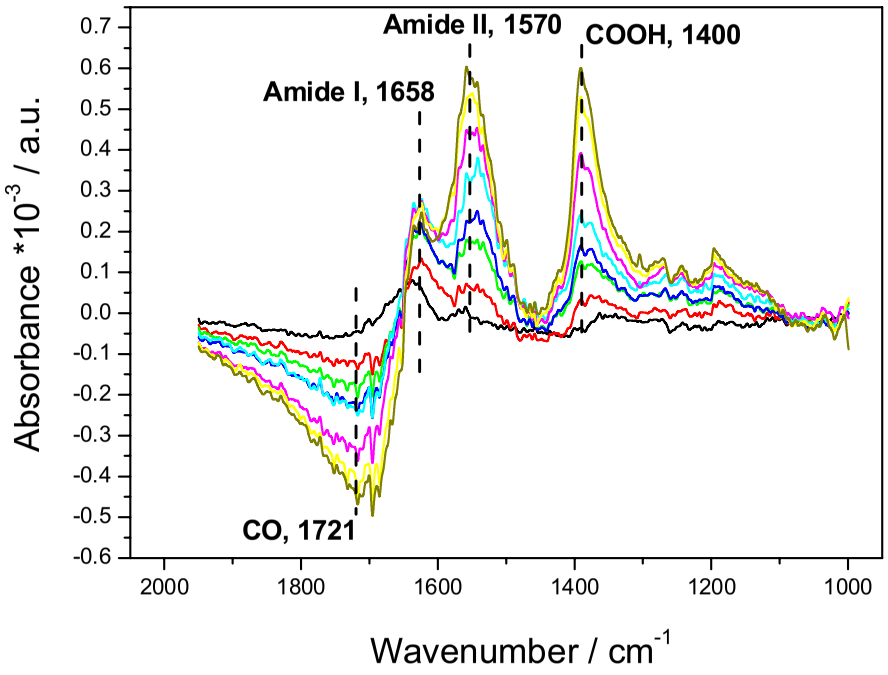
Amide II, 1570
COOH, 1400
Amide I, 1658
CO, 1721
Absorbance *10-3 / a.u.
Wavenumber / cm-1
0.7
0.6
0.5
0.4
0.3
0.2
0.1
0.0
-0.1
-0.2
-0.3
-0.4
-0.5
-0.6
2000
1800
1600
1400
1200
1000

Fig. 5

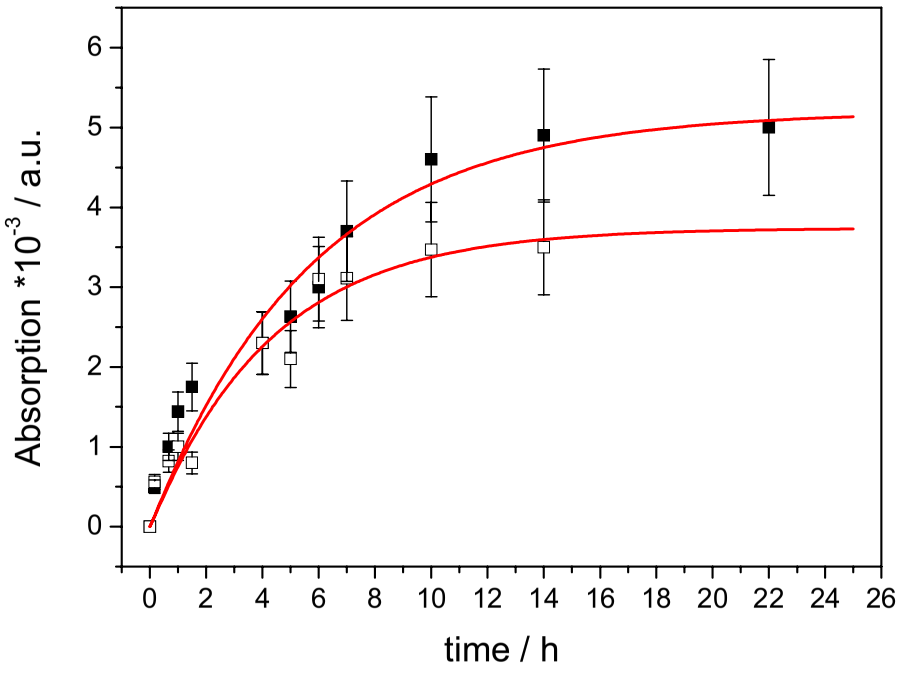
Absorption *10-3 / a.u.
time / h
0
1
2
3
4
5
6
0
2
4
6
8
10
12
14
16
18
20
22
24
26

Fig. 6

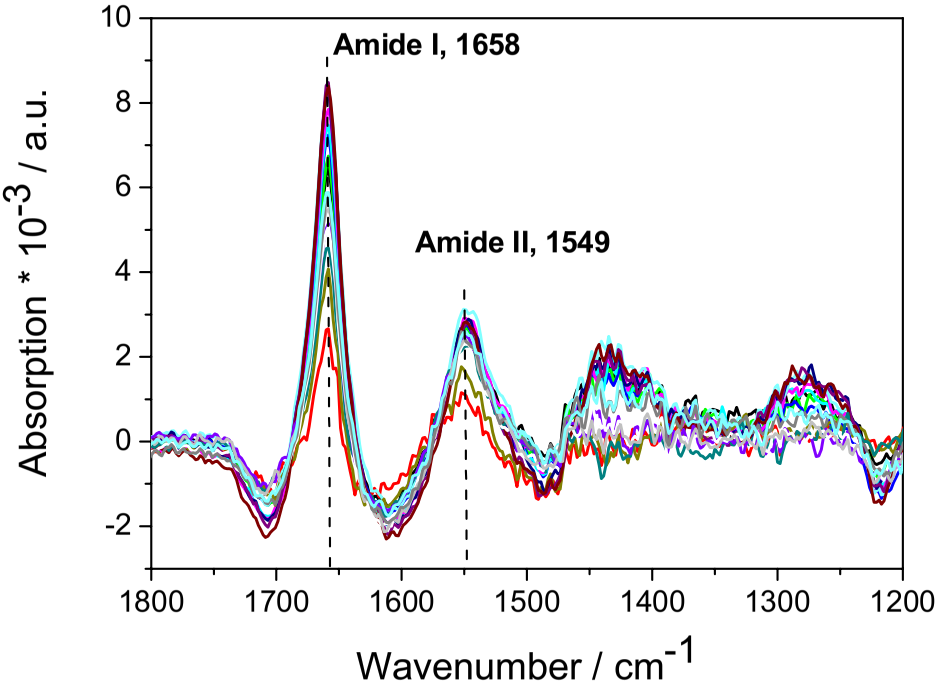
Amide I, 1658
Amide II, 1549
Absorption * 10^-3 / a.u.
Wavenumber / cm^-1
10
8
6
4
2
0
-2
1800
1700
1600
1500
1400
1300
1200

Fig. 7

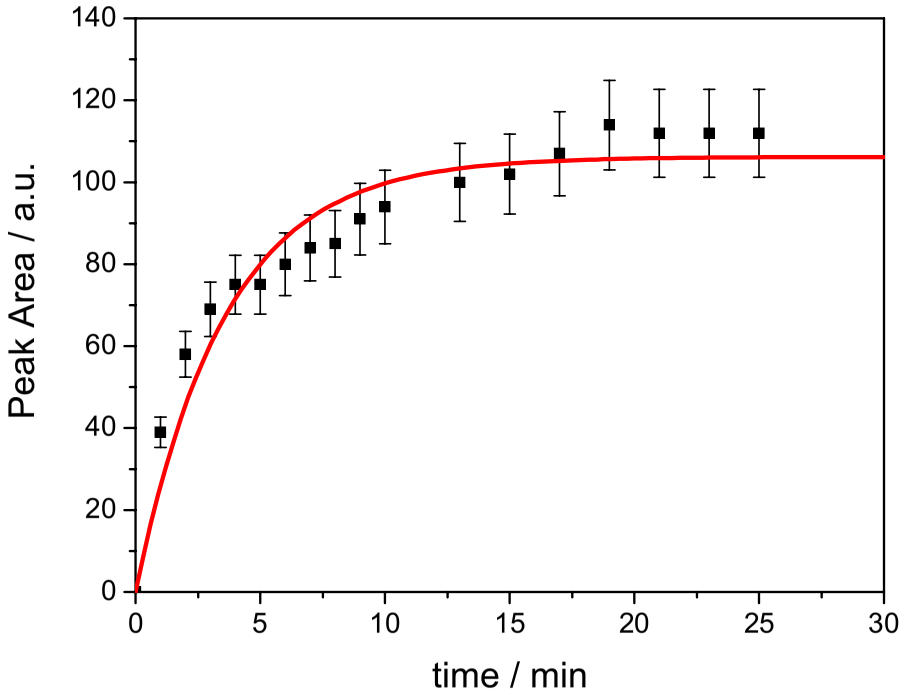
Peak Area / a.u.
time / min
140
120
100
80
60
40
20
0
0
5
10
15
20
25
30

Fig. 8

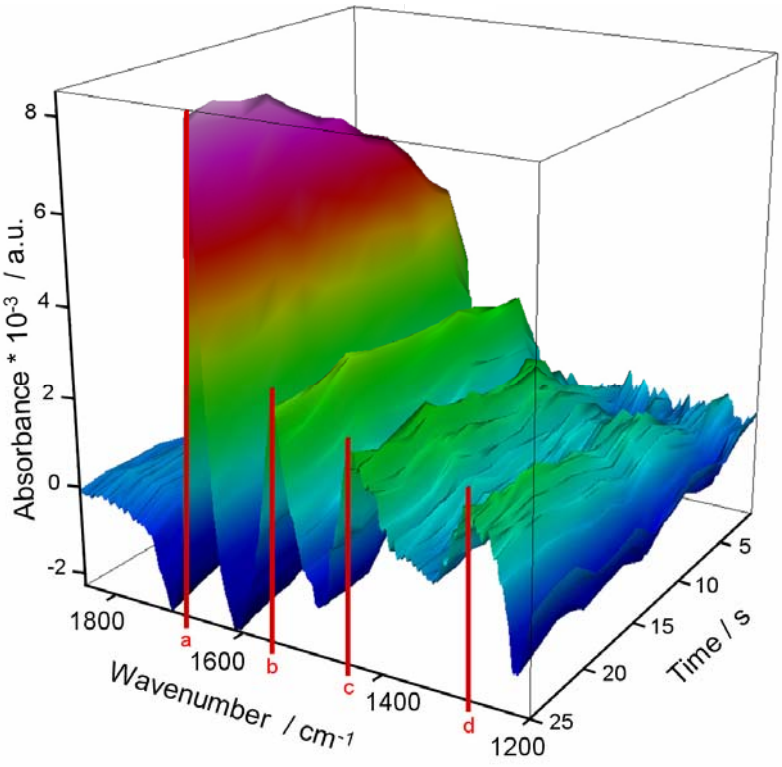
Absorbance * 10-3 / a.u.
8
6
4
2
0
-2
1800
1600
1400
1200
Wavenumber / cm-1
a
b
c
d
5
10
15
20
25
Time / s

Fig. 9

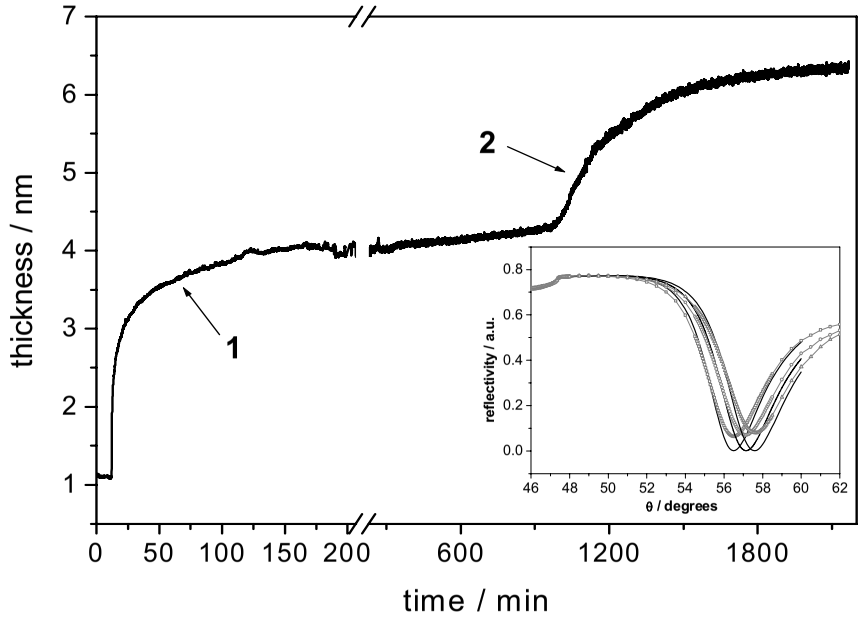
thickness / nm
7
6
5
4
3
2
1
0
50
100
150
200
600
1200
1800
time / min
1
2
reflectivity / a.u.
0.8
0.6
0.4
0.2
0.0
46
48
50
52
54
56
58
60
62
θ / degrees

Fig. 10

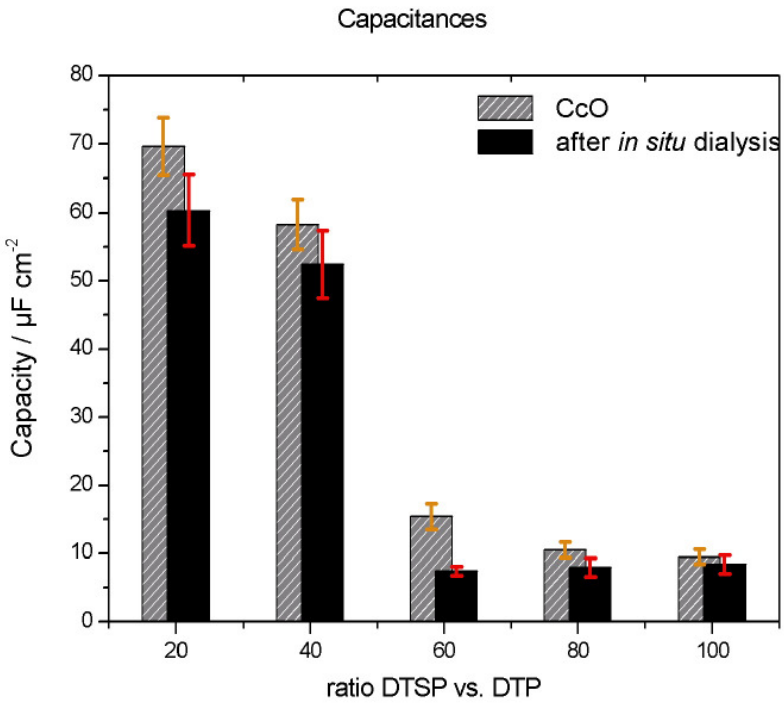
Capacitances
CcO
after *in situ* dialysis
Capacity / µF cm^{-2}
0
10
20
30
40
50
60
70
80
20
40
60
80
100
ratio DTSP vs. DTP

Fig. 11

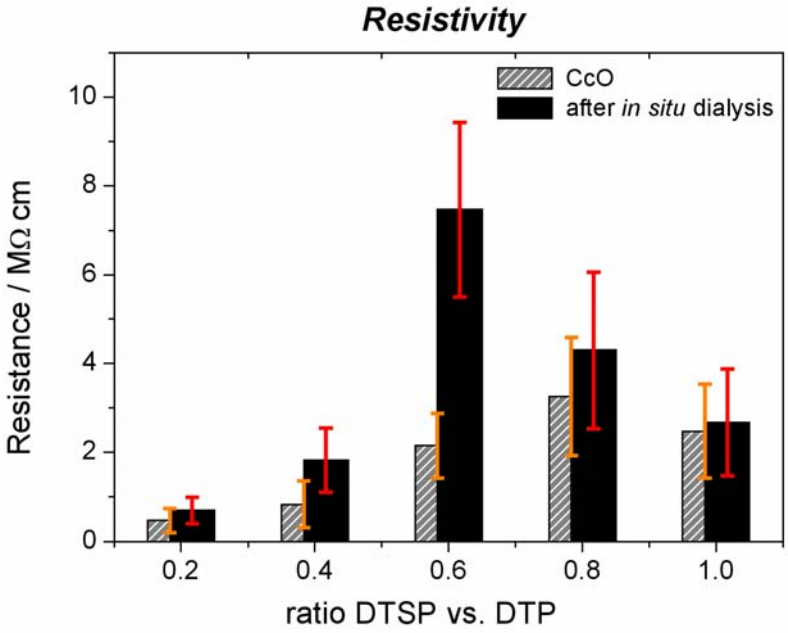
Resistivity
CcO
after *in situ* dialysis
Resistance / MΩ cm
0
2
4
6
8
10
0.2
0.4
0.6
0.8
1.0
ratio DTSP vs. DTP

Fig. 12

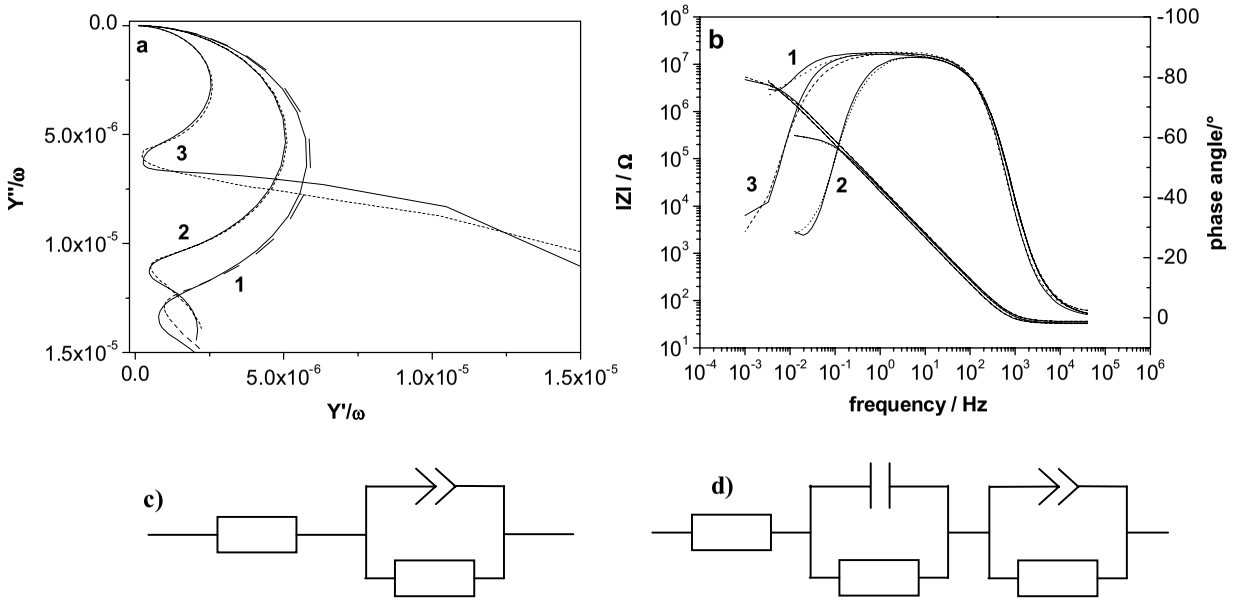
a
b
c)
d)
Y''/ω
Y'/ω
|Z| / Ω
phase angle/°
frequency / Hz
1
2
3

Fig. 13

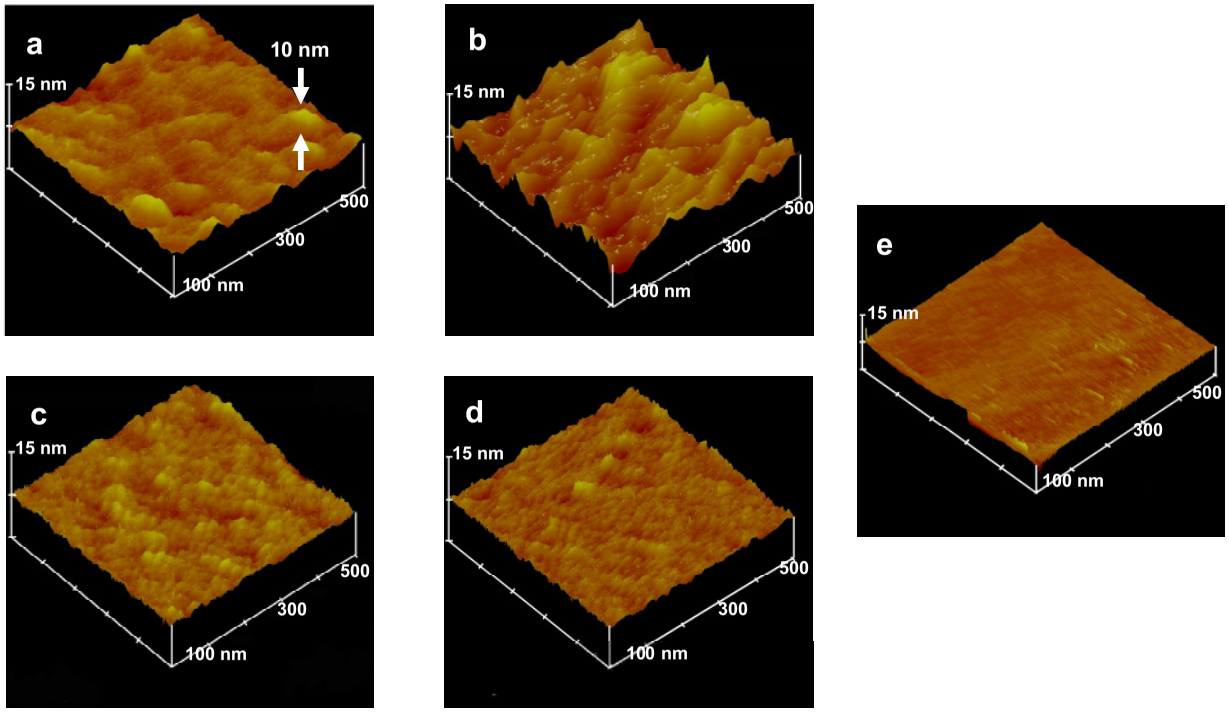
a
b
c
d
e
10 nm
15 nm
100 nm
300
500

Fig. 14

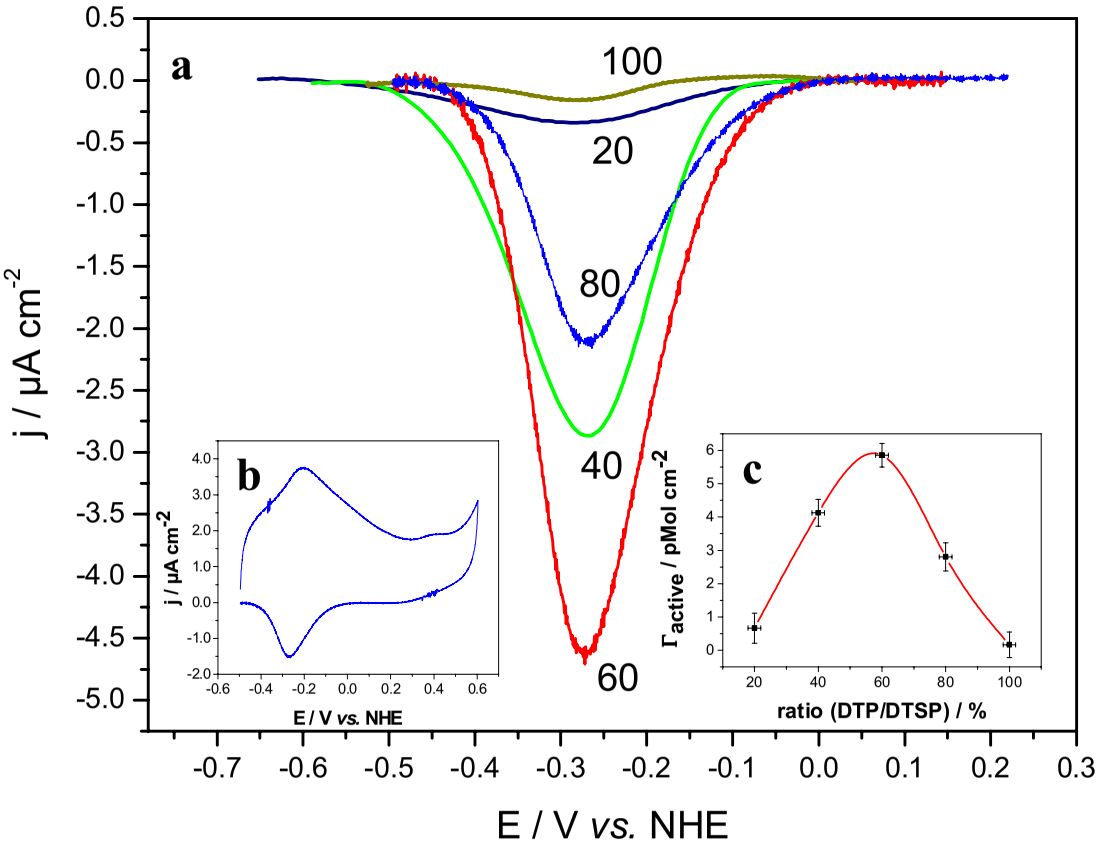
a
100
20
80
40
60
j / µA cm-2
E / V vs. NHE
b
j / µA cm-2
E / V vs. NHE
c
Γactive / pMol cm-2
ratio (DTP/DTSP) / %

Supplemental Information

A model calculation was performed, of the surface concentration of a monolayer of the two species, DTP and DTSP obtained by self assembly from a solution of the composition 60 Mol % DTSP, Mol 40% DTP.

The concentration profile on a surface, where a species with diffusion constant D_0 is adsorbed, is given by equation 1.

$$C_0(x,t) = C_0^* \cdot \mathrm{erf}\left[\frac{x}{2\cdot(D_0 t)^{1/2}}\right] \tag{1}$$

C_0^* is the concentration at t=0 and erf(x) is the Gaussian Error Function $\mathrm{erf}(x) = \int_0^x e^{-x^2} dx$.

The diffusion constant for a molecule with radius of gyration R_G, number of mass elements σ and viscosity η is given by equation 2 (Kirkwood and Riseman).

$$D_0 = \frac{k_B T}{f} \qquad \text{with} \qquad f = \frac{3\pi^{1/2}/8\cdot 6\pi\eta R_G}{1+\frac{1}{2}\left(\frac{\pi}{\sigma}\right)^{1/2}} \tag{2}$$

The values for our experiment are: η(DMSO)= $2*10^{-4}$Ns/m^2, σ(DTSP)=42, σ(DTP)=22, R_G(DTSP)=3Å, R_G(DTP)=1,8Å.

The particles hitting the surface are given by Ficks law for the particle flux. This formula describes the number of particles per area and time.

$$J = D_0 \cdot \left(\frac{\partial C}{\partial x}\right). \tag{3}$$

Integrating equation (3) over time gives the number of particles, which have reached the surface at a certain time t (particles per area):

$$P = \int J dt \tag{4}$$

Insertion of (1) and (2) into (3) and taking the numerical values for the parameters leads to

$$\frac{P_{DTSP}}{P_{DTP}} \approx \frac{4}{7}\frac{C_{0,DTSP}^*}{C_{0,DTP}^*} \tag{5}$$

With the two simple relations $C_{0,DTP}^* = C_0^* \cdot x_{DTP} = C_0^* \cdot (1 - x_{DTSP})$ and

$P_{DTP} = P \cdot y_{DTP} = P \cdot (1 - y_{DTSP})$, where x and y are the ratio of DTSP and DTP at the surface, we finally get:

$$y_{DTSP} \approx \frac{x_{DTSP}}{\frac{7}{4} - \frac{3}{4} \cdot x_{DTSP}} \quad . \tag{6}$$

For a mixing ratio in solution of 60% DTSP and 40% DTP, eq (6) yields 46Mol % DTSP and 54 Mol % DTP on the surface, which corresponds to 64 and 36 % by weight, respectively.

In this model calculation, the saturation of adsorbed species on the surface has not been taken into account. This effect, however, should have an equal influence on the adsorption of both molecules.
The concentration of DTSP and DTP in solution changes only in the range of 0.01% during the absorption process, which can be calculated easily from the absolute initial concentration of 2mg/ml, the area of the gold surface of approx. 15cm², and the volume of solution of approx. 5ml DMSO. Therefore the effect of a concentration change in solution can also be neglected.

Paper 6

Modeling Ion Transport in Tethered Bilayer Lipid Membranes. 1. Passive Ion Permeation

Joseph W.F. Robertson [1,2+], Marcel G. Friedrich [1+], Wolfgang Knoll [1], Renate L.C. Naumann [1,*] and Dieter Walz [3]

[+] J.W.F. Robertson and M.G. Friedrich contributed equally to this publication

1) Max Planck Institute for Polymer Research, Ackermannweg 10, 55128 Mainz, Germany
2) Semiconductor Electronics Division, NIST, Electronics and Electrical Engineering Laboratory, Gaithersburg, Maryland 20899-8120, USA
3) Biozentrum, University of Basel, present address Lerchenstrasse 21, 4059 Basel, Switzerland

Author email addresses:
joseph.robertson@nist.gov
friedric@mpip-mainz.mpg.de
knoll@mpip-mainz.mpg.de
naumannr@mpip-mainz.mpg.de
dieter.walz@unibas.ch

Condensed running title: Modeling Passive Ion Permeation tBLMs

Classification: Biological Sciences, Biophysics, Chemical Sciences, Electrochemistry, Analytical Chemistry

*** Corresponding Author:**

Renate L.C. Naumann

Manuscript information: pages

Word/character counts: counts

Abbreviations footnotes:

Keywords: Ion permeation, WinSpice, MacSpice, tBLM, network modeling, Electrochemical Impedance Spectroscopy

ABSTRACT

Ion transport in tethered bilayer lipid membranes (tBLMs) is simulated, using the integrated Nernst-Planck equation for passive ion transport. Instead of setting up a set of differential equations, the circuit simulation language SPICE (Simulation Program with Integrated Circuit Emphasis) is used to design electric circuits that combine rate equations with processes occurring at the tBLM like charging the membrane or a current through the electrode. Parameters such as concentrations and volumes can then be directly taken into account together with the electric potential. The tBLM is considered to be submersed into a 0.1 M KCl solution and subsequently exposed to different bias potentials. Transients of different parameters, such as the concentration of ions in different compartments and potential drops across different portions of the stratified layer, are calculated as well as impedance spectra as a function of applied bias potentials. Comparison of the simulated spectra with actual measurements revealed that not only passive ion transport itself but also the permeability coefficients seem to be dependent on the membrane potential. It is concluded from this behavior that the mechanism of ion transport across the tBLM seems to follow the transient pore model rather than the solubility-diffusion model.

INTRODUCTION

Tethered bilayer lipid membranes (tBLMs) are well established as a model system of the biological membrane. They have been developed with the prospect to investigate the functionality and kinetics of membrane proteins (1-3). It had been realized that these proteins require an aqueous-like compartment on either side of the lipid bilayer. For this purpose, oligo(ethylene oxide) (4) or other hydrophilic spacer groups had been introduced between the lipid head group and the solid substrate. They provide the space needed to separate the protein from the surface. Moreover, the spacers provide a reservoir for ions mimicking the cytosol. A wide range of channel forming peptides and proteins have been incorporated (5-9) giving the tBLM the hope not only for the development of chemical sensors But also as a platform for fundamental charge transfer studies.

Typically electrochemical impedance spectroscopy (EIS) is used to probe the charge-transport properties of biomimetic membranes. EIS traditionally uses complex nonlinear least squares fitting (10) to calculate parameters from equivalent circuit models based on simple passive circuit elements (e.g. capacitors and resistors). Attempts have been made to interpret these fitted parameters in terms of potential dependent rate equations (11-13). Of particular interest for the development of appropriate models to understand the underlying biophysics of proteins in tBLMs, are the electric field (11) and the concentration gradients (14) within the system which must be thoroughly defined. However, passive elements as for example ohmic resistors have been shown to be inadequate to model the kinetics for the simple K^+ carrier valinomycin (15).

An alternative method for modeling bioelectronic interfaces is a set of partial differential equations to combine potential dependent rate equations (16) with equations describing processes occurring at passive elements, for example the charging of the membrane capacitance or a current through the electrode. Parameters such as concentrations and volumes can then be directly taken into account together with the electric potential and other electric parameters. A convenient method to solve a set of partial differential equations utilizes the circuit simulation language SPICE (Simulation Program with Integrated Circuit Emphasis) (17) which had been introduced earlier to model bioelectrochemical processes across membranes (18,19-23). In this paper, we use the SPICE platform to examine charge transfer processes and interfacial

properties of a tBLM. In order to minimize the complexity of the system, we have restricted this investigation to the passive ion permeation through a bilayer membrane without proteins inserted into it. The results provide a baseline for interfacial ion transport through tBLMs on surfaces.

MATERIALS AND METHODS

Diphytanoylphosphatidyl choline (DphyPC), was supplied from Avanti Polar Lipids, Inc., Alabaster, Al, USA, sodium chloride (SigmaUltra), and potassium chloride were obtained from Sigma-Aldrich. Purified water (>18 MΩ cm) from a Milli-Q (Millipore, Inc) system was used throughout. The synthesis of DPTL was carried out as previously described (24).

Preparation of the template stripped gold (TSG) surface and bilayer.
TSG surfaces were prepared as described previously (25). Briefly, 50 nm thick gold films were deposited by electrothermal evaporation (rate 0.01 nm/sec –0.05 nm/sec, 2×10^{-6} mbar) on silicon wafers. The gold films were then glued with EPO-TEK 353ND-4, (n = 1.5922) to glass slides and cured for 60 min at 150°C. Immediately prior to use the Au/epoxy/glass was separated from the Si wafer and immersed into a 0.2 mg/ml ethanolic DPTL solution for a period of 24 h. After self-assembly, the surfaces were rinsed with copious amounts of ethanol and used immediately.

Vesicles were prepared from extrusion of a solution of 1.5 mg/mL DphyPC in pure water through a 50 nm polycarbonate filters (Avestin inc.). The clear, colorless eluent was diluted to 0.015 mg/mL with 0.1 M KCl and immediately injected into a flow cell containing the DPTL coated surface. Vesicle fusion was followed by surface plasmon resonance spectroscopy and the solution was rinsed with copious amounts of electrolyte when the bilayer formation was complete (25).

Electrochemical measurements
EIS experiments were performed on an EG&G 273 potentiostat/galvanostat equipped with a Solartron 1260 frequency response analyzer. Potential control and data collection were obtained with the Zplot/Zview software package (Scribner Associates, Inc). A three-electrode setup was employed using a Pt wire counter electrode and a Ag|AgCl, 3 M KCl reference electrode. Estimation of the passive element modeling parameters was performed as discussed previously (24).

RESULTS

EIS of a tBLM system
EIS is the single most useful electrochemical technique for examining mechanistic information in a tBLM system. By separating ion transport phenomena into the frequency domain, ion transport processes can be examined with transport components that have distinctly different time scales. Utilizing a wide range of frequencies allows for the non-specific background current to be separated from the ion transport mediated by the protein.

Figure 1 shows EIS traces for tBLMs at several different bias potentials. The impedance was measured from +0.3 V to – 0.4 V. As the potential is stepped negatively, the high frequency impedance, determined essentially by the membrane capacitance, is unchanged (~ 0.6 μF cm^{-2}). At low frequencies, however, the impedance varies systematically. Often tBLM surfaces with incorporated spacer groups (e.g. OEG tethers) show a second time constant resulting from the separation of the τ_{RC} for the spacer and τ_{RC} for the membrane, but this particular surface has an effective membrane resistance too high to see the impedance behavior of the tether (11,26). At the extreme potentials, – 0.3 V and – 0.4 V, O_2 reduction begins to contribute to the low frequency portion of the spectra. However, the faradaic effects for O_2 reduction were ignored for the purposes of the simulations.

To extract further information from these data, they were analyzed with an equivalent circuit consisting of a solution resistance R_{ex} in the reservoir, in series with the membrane, which is modeled by a parallel resistance R_{mem} and capacitance C_{mem}, and a capacitance C_{sr} representing the spacer region (Fig. 1 *inset*). C_{mem} appears to be nearly constant at ~ 0.7 μF cm^{-2} over the entire potential window. R_{mem} shows high background impedance of the membrane on the order of MΩ cm^2. Moreover the resistance peaks at ~0 V, decreasing both at positive and negative potentials. Qualitatively, this behavior can be considered in terms of anions which should be attracted to the electrode surface at positive potentials and cations to be attracted at negative potentials. It is important to note that the position of the maximum is highly sensitive to the individual sample preparation and can vary by as much as 200 mV for any given surface.

SIMULATION PROCEDURES

Ion transport through biological (27) and electrochemical (21,28) interfaces has a significant history of theoretical development, which is directly applicable to tBLM systems. The method used herein for calculating the bioelectrochemical response of ion transport non-specifically through the membrane utilizes the software package SPICE (*MacSPICE* or *WinSPICE*). The advantage of SPICE over simply integrating the equations arising from the various processes involved is the modular construction of the model that allows rapid alterations to the modeled parameters as well as the ability to simulate many different types of experiment (e.g. EIS or transient behavior) (19). A further advantage in the system is real-time access to the multitude variables that arise in a model, such as the ion flux, ion concentrations, and electrical potential profiles, such as the potential drop across the membrane, relative to the potential drop across the tether.

Development of the model circuit
Models that describe passive ion permeation through phospholipid bilayers have been developed on the basis of the solubility-diffusion theory which, however, proved unsatisfactory particularly for small ions such as Na^+ (29). Alternative models were introduced in terms of hydrated transient defects produced by thermal fluctuations of the lipid molecules. This model seems to apply for halide ions when the lipid layer is thin enough (29,30). However, a model of general applicability has so far not been agreed upon. Moreover, permeability coefficients, determined experimentally, vary considerably (29). For the time being, we do not focus on particular mechanisms. Instead, the permeation of K^+ and Cl^- ions is considered in terms of a very general approach, using the integrated Nernst-Planck equation which relates the flux j_i of the ith ion (i.e. the flow per unit membrane area) to the permeability coefficient P_i, the ion concentrations $c_{i,1}$ and $c_{i,2}$ on the two sides of the membrane, and the membrane potential $\Delta\varphi_m$, defined as the difference in electrical potential on both sides of the membrane (for details of the derivation see ref. 19)

$$j_i = P_i \frac{z_i F \Delta\varphi_m}{RT} \frac{c_{i1} \exp\{z_i F \Delta\varphi_m / RT\} - c_{i,2}}{\exp\{z_i F \Delta\varphi_m / RT\} - 1}; \quad \Delta\varphi_m = \varphi_1 - \varphi_2. \tag{1}$$

Here z_i is the charge number of the ion, while R, T, and F have their usual meaning. The electrical current density associated with the ion flux is then given by

$$i_i = z_i F j_i. \quad (2)$$

Strictly speaking, activities should be used in eq. 1, however, for the present purpose it is legitimate to approximate them by concentrations.

In terms of simulations with SPICE it is convenient to comprise the elements modeling the permeation of an ion through the membrane in a so-called subcircuit (19) as shown in Fig. 2. Parameters supplied to the subcircuit as nodes are the concentrations $c_{i,1}$ and $c_{i,2}$ of the ion on both sides of the membrane (c_1 and c_2 in Fig. 2) and the respective potentials φ_1 and φ_2 (phi_1 and phi_2), as well as the permeability coefficient P_i (P), the charge number z_i (z), and the temperature (temp). The non-linear dependent voltage sources at nodes 1, 2, and 3 serve to program eq. 1, and the result obtained as voltage at node 3 is used to generate the ion flux j_i and the current density i_i through the controlled current sources between node pairs c_1, c_2 and phi_1, phi_2, respectively. The source code of the subcircuit is given in the Appendix.

Two such subcircuits, one for each ion, are then inserted into the circuit used to simulate the behavior of the tBLM (Fig. 3). The constant voltage sources at nodes K_ex and Cl_ex define the constant concentrations $c_{K,ex}$ and $c_{Cl,ex}$ for K^+ and Cl^- in the reservoir, respectively, while the capacitors at nodes K_in and Cl_in represent the volume of the sub-membrane space, and the voltages at these nodes then indicate the concentrations $c_{K,in}$ and $c_{Cl,in}$ of the respective ion in this space. The constant voltage sources at nodes P_K, P_Cl and z_K, z_Cl define respectively the permeability coefficient and the charge number for K^+ and Cl^-, while that at node temp defines the temperature. The electrical properties of the tBLM are modeled with the membrane capacitance C_mem, the capacitance of the spacer region C_sr, and the solution resistance R_ex in the reservoir. The voltages at nodes phi_in and phi_ex then represent the electrical potentials φ_{in} and φ_{ex} at the membrane surfaces facing the sub-membrane space and the reservoir, respectively. The voltage source vbias provides the bias potential between the electrode and the reservoir, and in addition the sinusoidal AC voltage if needed. The voltage at node phi_el represents the electrical potential φ_{el} at the electrode/spacer region interface, and the ammeter vi_el between nodes bias and phi_el reports the current density i_{el} flowing through the electrode. Note that all potentials are with respect to a reference point in the reservoir, and that possible surface potentials are neglected.

Assignment of parameter values

To perform simulations, values have to be assigned to the parameters of the elements in the circuit shown in Fig. 3. For the electrical elements $C_{mem} = 0.67$ µF cm^{-2}, $C_{sr} = 5$ µF cm^{-2}, and $R_{ex} = 50$ Ω cm^2 are used. Parameters pertaining to ion permeation are $c_{K,ex} = c_{Cl,ex} = 0.1$ M, and 0.22 nL for the volume of the sub-membrane space, which can be estimated from the length of the spacer. Moreover, $z_K = 1$, $z_{Cl} = -1$, and the temperature is 25°C. The assignment of values to the permeability coefficients P_K and P_{Cl} for K^+ and Cl^- is less straightforward. However, relations between these coefficients and the membrane resistance can be established. According to eq. 1 the flux of the ith ion at equal concentrations on both sides of the membrane, $c_{i,ex} = c_{i,in} = c_i$, is

$$j_i = P_i z_i c_i F \Delta\varphi_m / (RT). \quad (3)$$

Hence the current density due to permeation of K^+ and Cl^- across the membrane at $c_K = c_{Cl} = c_{KCl}$ amounts to (cf. Eq. 2)

$$i = F(z_K j_K + z_{Cl} j_{Cl}) = \Delta\varphi_m [F^2 c_{KCl} (z_K^2 P_K + z_{Cl}^2 P_{Cl})/(RT)] = \Delta\varphi_m / R_{mem}, \quad (4)$$

and can be related to the resistance of the membrane R_{mem} determined under the particular conditions, as shown in eq. 4. A total permeability coefficient can then be defined as

$$P_{tot} = z_K^2 P_K + z_{Cl}^2 P_{Cl} = RT/(F^2 c_{KCl} R_{mem}) \quad (5)$$

and related to R_{mem}. With the ratio of coefficients $p = P_K/P_{Cl}$ we finally obtain

$$P_K = P_{tot} p/(z_K^2 p + z_{Cl}^2) \quad \text{and} \quad P_{Cl} = P_{tot}/(z_K^2 p + z_{Cl}^2) \quad (6)$$

P_K values reported in the literature vary between 10^{-9} cm/s and 10^{-13} cm/s (29). On the other hand, $P_{Cl} = 7.5 \times 10^{-11}$ cm/s and $P_K = 5 \times 10^{-12}$ cm/s was reported for BLMs (31), hence $P_{tot} = 8 \times 10^{-11}$ cm/s and $R_{mem} = 33$ MΩ cm^2 for $c_{KCl} = 0.1$ M (eq. 5) which is too large compared to the value of the membrane resistance obtained by EIS for the tBLM. In the course of the simulations it was found that $P_{tot} = 1.8 \times 10^{-10}$ cm/s ($R_{mem} \approx 14$ MΩ cm^2) is a suitable value. P_K seems to be larger than P_{Cl} because the effect of negative bias potentials on impedance and phase shift at low frequencies is stronger than that of positive bias potentials (see Fig. 1), hence $p = 10$ was chosen.

Impedance spectra from simulations

Spectra were simulated in three steps essentially following the experimental protocol. First the tBLM was formed with no bias potential applied and 0.1 M KCl in the reservoir. In this step the ions partition into the sub-membrane space, which is simulated in a transient analysis with the voltage source vbias disconnected (see Fig. 3), using the initial conditions $c_{K,in} = c_{Cl,in} = \varphi_{in} = 0$. Since $P_K > P_{Cl}$ the flux of K^+ is initially faster than that of Cl^-, hence $c_{K,in}$ rises faster than $c_{Cl,in}$ (Fig. 4A), but also a current across the membrane ensues by which the membrane capacitance is charged and a membrane potential $\Delta\varphi_m = \varphi_{in} - \varphi_{ex}$ is built up (Fig. 4B). However, no potential difference $\Delta\varphi_{sr} = \varphi_{el} - \varphi_{in}$ across the spacer region is formed because the electrode potential φ_{el} is floating. With increasing time $\Delta\varphi_m$ gradually collapses while $c_{K,in}$ and $c_{Cl,in}$ essentially coincide, and the equilibrium state is eventually attained where $c_{K,in} = c_{Cl,in} = 0.1$ M and $\Delta\varphi_m = 0$. Note that after about 12 h $c_{K,in}$, $c_{Cl,in}$, and $\Delta\varphi_m$ have essentially reached their values at equilibrium.

In the second step different bias potentials were applied. Except for a zero bias potential, the ions then repartition and a new equilibrium state is attained. This is again simulated in a transient analysis, but with the voltage source vbias connected and using the initial conditions $c_{K,in} = c_{Cl,in} = 0.1$ M, and $\varphi_{in} = 0$. In a fast process with a relaxation time $\tau = R_{ex} (C_{mem}^{-1} + C_{sr}^{-1})^{-1} \approx 30$ µs (not shown in Fig. 5) C_{mem} and C_{sr} are charged, and the respective potential differences built up are as expected for two capacitors in series, i.e.

$$\Delta\varphi_m = \varphi_{el} C_{sr}/(C_{mem} + C_{sr}) \quad \text{and} \quad \Delta\varphi_{sr} = \varphi_{el} C_{mem}/(C_{mem} + C_{sr}). \quad (7)$$

The altered membrane potential initiates the considerably slower ion permeation, which discharges the membrane capacitance thus causing $|\Delta\varphi_m|$ to decrease. Concomitantly $|\Delta\varphi_{sr}|$ increases since φ_{el} is clamped to the bias potential, so that at equilibrium 97% of the applied potential drops across the spacer region (Fig 5A). The time course of the ion concentrations in

the sub-membrane space is biphasic. As expected, the final values of $c_{K,in}$ are larger and smaller while those for $c_{Cl,in}$ are smaller and larger than those at zero bias potential for positive and negative bias potentials, respectively (Figs. 5A and B). Again, it takes about 12 h for the variables $c_{K,in}$, $c_{Cl,in}$, $\Delta\varphi_m$, and $\Delta\varphi_{sr}$ to reach values close to those at equilibrium.

As a control the simulations in both steps were repeated with different values for P_{tot} and p. This altered the time courses of the variables, but the constant values eventually reached for all variables were always those shown in Figs. 4 and 5, as it should be for true equilibrium states. Moreover, simulations in step 2 were performed with different values for C_{mem} and C_{sr}. Varying C_{mem} at a constant C_{sr} = 5 μF cm^{-2} has very little effect on the time courses of $c_{K,in}$ and $c_{Cl,in}$ yielding essentially the same result as shown in Figs. 5A and B. The potential differences formed in the fast initial phase differ (cf. Eq. 7) but the constant values eventually reached are practically equal to those shown in Fig. 5A. On the other hand, varying C_{sr} at a constant C_{mem} = 0.67 μF cm^{-2} yields similar time courses for $c_{K,in}$ and $c_{Cl,in}$ but with equilibrium values which vary considerably depending on the particular value of C_{sr}. However, the potential differences, starting from the values according to eq. 7, reach values at equilibrium which are close to those shown in Fig. 5A, indicating a potential drop across the spacer region between 99 and 91% of the applied potential for C_{sr} between 2.5 and 20 μF cm^{-2}, respectively.

In the third step EIS was performed. It has been shown previously that the ac analysis implemented in SPICE is not suitable for simulating the spectra (15), hence every single frequency has to be simulated separately in a transient analysis, using the final values of $c_{K,in}$, $c_{Cl,in}$, and φ_{in} from the simulations in the second step as initial conditions. A sinusoidal AC voltage with an amplitude of 10 mV and the given frequency is added to the respective bias potential applied by the voltage source vbias (Fig. 3). The AC voltage elicits oscillations of $c_{K,in}$, $c_{Cl,in}$, $\Delta\varphi_m$, and $\Delta\varphi_{sr}$ whose baselines, except for that of $\Delta\varphi_m$, initially change with time (Fig. 6A and B). When constant baselines are reached the current density i_{el} and the electrode potential φ_{el} (Fig. 6C) are used to calculate the impedance and the phase shift by means of a nonlinear fit program (IGOR), and the spectra thus obtained for different bias potentials are shown in Fig. 7. In the case of zero bias potential both impedance and phase shift agree well with the experimental data (Fig. 1), except for a deviation in phase shift at frequencies larger than 20 kHz whose reason is not yet known. This also confirms that 1.8×10^{-10} cm/s is a proper value for P_{tot}. However, only a slight dependence of the phase shift on the applied bias potential at low frequencies is detectable and even in the wrong direction for positive potentials, while hardly any change in impedance occurs, both in contrast to the experimental data. Choosing p values larger than 10 has hardly any effect, while decreasing p diminishes the existing slight dependence of the phase shift on the bias potential. Hence it is concluded that the decrease in membrane resistance for positive and negative bias potentials and the corresponding differences in phase angle at low frequencies cannot be explained by the different ion concentrations in the sub-membrane space and different but constant permeabilities for K^+ and Cl^-.

The observed behavior of the tBLM is most likely due to a dependence of the permeability on the membrane potential. Such a dependence can arise if ion transport occurs through pores, which result from thermal fluctuations of the lipid molecules. Potential pulse experiments with UO_2^{2+}-modified BLMs have shown that the formation rate constant of pores $k_{p,f}$ is dependent on the membrane potential, i.e. $k_{p,f} \propto \exp[(\Delta\varphi_m/K_s)^2]$, where K_s is a scaling factor (32). The resealing of the pores is a first order process with a rate constant $k_{p,r}$ which appears to be independent of $\Delta\varphi_m$, hence the number of pores at steady state is proportional to $\exp[(\Delta\varphi_m/K_s)^2]$. Since the total permeability of the membrane is proportional to the number of pores

$$P_{tot}(\Delta\varphi_m) = P_{tot}(0)\exp[(\Delta\varphi_m/K_s)^2], \quad (8)$$

where $P_{tot}(0)$ denotes the total permeability coefficient at $\Delta\varphi_m = 0$ arising from the intrinsic steady state number of pores.

Simulations of EIS spectra were performed with P_{tot} in eq. 6 substituted from eq. 8, and with $P_{tot}(0) = 1.8 \times 10^{-10}$ cm/s and $p = 10$ as before. Since the actual values of $k_{p,f}$ and $k_{p,r}$ are not known and eq. 8 pertains to the steady state of pore formation only, a constant value for $\Delta\varphi_m$ is used as an approximation and set equal to the value reached at equilibrium in step 2. With K_s adjusted to 9.3 mV the result shown in Fig. 8 is obtained. The simulated spectra now satisfactorily represent the experimental data, particularly when taken into account that O_2 reduction contributes to the low frequency portion of the experimental spectra at bias potentials of – 0.3 V and – 0.4 V.

CONCLUSIONS

The benefit of SPICE is the possibility to highlight single processes and parameters as a function of different variables. This helps to understand the system such as the tBLM under the influence of various conditions. It can be deduced from the simulations, for example, that the basic process of the equilibration of monovalent ions due to passive ion permation can take quite a long period of time of up to several hours assuming even moderate permeabilities. Passive ion permeation plays a role in all kinds of electrochemical experiments with tethered bilayer membranes.

Another significant result is the distribution of potential differences across the layer structure following the application of different bias potentials. Only in the first rapid phase of ion redisribution, the overall potential drops mainly across the lipid membrane as intuitively expected from the higher restistance of the lipid bilayer as compared to the aqeous-like sub-membrane layer. However, in the course of the accumulation of ions in the vicinity of the electrode, the potential drops to the larger extent across the sub-membrane space, where the potential drop across the sub-membrane space is generated by the charge separation between the electrode and the adjacent layer of accumulated ions.

The parameter directly accessible from EIS spectra is the total permeability of ions across the bilayer of the tBLM. It was shown to be more than one order of magnitude higher ($2 * 10^{-10}$ cm/s) than the ones reported for freely suspended BLMs ($8 * 10^{-11}$ cm/s), however, well within the range of values reported for P_{K+} for all kinds of bilayer membranes.(29,30). A very convenient way to learn about the ratio of permeabilities of anions and cations, for example $p = P_K/P_{Cl,}$ is to carry out EIS spectra as a function of bias potentials. The particular experiment displayed in Fig. 1 could best be modeled with $P_{total} = 1.8\ 10^{-10}$ and a ratio $p = P_K/P_{Cl} = 10$, unusual as compared to BLMs.

This unusual high ratio needs to be reconsidered in terms of another interesting result, namely that a permeability independent from potential does not seem sufficient to describe the potential dependence of EIS spectra. This result is interesting from the mechanistic point of view because a potential dependence of the permeabilities would be in accordance with a pore model of ion permeation. This model predicts an increase of the number of pores with an increase in the membrane potential. The permeability would then no longer be independent of the potential in agreement with the simulations presented in this paper.

Utilizing ion permeability subcircuits within the tBLM network model will provide a more realistic baseline for the further examination of ion transport mechanics from proteinaceous ion channels, ion carriers and ion pumps that can be incorporated into tBLMs.

REFERENCES

1. Guidelli, R., G. Aloisi, L. Becucci, A. Dolfi, M. R. Moncelli, and F. T. Buoninsegni. 2001. New directions and challenges in electrochemistry - Bioelectrochemistry at metal/water interfaces. *Journal of Electroanalytical Chemistry* 504(1):1-28.
2. Knoll, W., K. Morigaki, R. Naumann, B. Sacca, S. Schiller, and E. K. Sinner. 2004. Functional Tethered Bilayer Lipid Membranes. *In* Ultrathin Electrochemical Chemo- and Biosensors, Technology and Performance. Mirsky V. M., editor. Springer-Verlag, Berlin. 239-254.
3. Sinner, E. K., and W. Knoll. 2001. Functional tethered membranes. *Current Opinion in Chemical Biology* 5(6):705-711.
4. Cornell, B. A., V. L. B. Braach-Maksvytis, L. G. King, P. D. J. Osman, B. Raguse, L. Wieczorek, and R. J. Pace. 1997. A biosensor that uses ion-channel switches. *Nature* 387(6633):580-583.
5. Becucci, L., R. Guidelli, C. Peggion, C. Toniolo, and M. R. Moncelli. 2005. Incorporation of channel-forming peptides in a Hg-supported lipid bilayer. *Journal of Electroanalytical Chemistry* 576(1):121-128.
6. He, L. H., J. W. F. Robertson, J. Li, I. Karcher, S. M. Schiller, W. Knoll, and R. Naumann. 2005. Tethered bilayer lipid membranes based on monolayers of thiolipids mixed with a complementary dilution molecule. 1. Incorporation of channel peptides. *Langmuir* 21(25):11666-11672.
7. Glazier, S. A., D. J. Vanderah, A. L. Plant, H. Bayley, G. Valincius, and J. J. Kasianowicz. 2000. Reconstitution of the pore-forming toxin alpha-hemolysin in phospholipid/18-octadecyl-1-thiahexa(ethylene oxide) and phospholipid/n-octadecanethiol supported bilayer membranes. *Langmuir* 16(26):10428-10435.
8. McGillivray, D. J., I. Ignatiev, F. Heinrich, J. W. F. Robertson, D. J. Vanderah, G. Valincius, J. J. Kasianowicz, and M. Lösche. 2007. Functional Reconstitution of Staphylococcus aureus α-Hemolysin iin Tethered Bilayer Lipid Membranes. *Proceedings of the National Academy of Science (USA)* submitted.
9. Valincius, G., D. J. McGillivray, W. Febo-Ayala, D. J. Vanderah, J. J. Kasianowicz, and M. Losche. 2006. Enzyme activity to augment the characterization of tethered bilayer membranes. *Journal of Physical Chemistry B* 110(21):10213-10216.
10. Macdonald, J. R. 2005. *In* Impedance Spectroscopy: Emphasizing Solid Materials and Systems. Barsoukov E., Macdonald J. R., editors. ^{2n}d ed. Wiley, Hoboken, NJ. 188-204.
11. Becucci, L., M. R. Moncelli, R. Naumann, and R. Guidelli. 2005. Potassium ion transport by valinomycin across a Hg-supported lipid bilayer. *Journal of the American Chemical Society* 127(38):13316-13323.
12. Steinem, C., A. Janshoff, H. J. Galla, and M. Sieber. 1997. Impedance analysis of ion transport through gramicidin channels incorporated in solid supported lipid bilayers. *Bioelectrochemistry and Bioenergetics* 42(2):213-220.
13. Vallejo, A. E., and C. A. Gervasi. 2002. Impedance analysis of ion transport through gramicidin channels in supported lipid bilayers. *Bioelectrochemistry* 57(1):1-7.
14. Krishna, G., J. Schulte, B. A. Cornell, R. J. Pace, and P. D. Osman. 2003. Tethered bilayer membranes containing ionic reservoirs: Selectivity and conductance. *Langmuir* 19(6):2294-2305.
15. Naumann, R., D. Walz, S. M. Schiller, and W. Knoll. 2003. Kinetics of valinomycin-mediated K+ ion transport through tethered bilayer lipid membranes. *Journal of Electroanalytical Chemistry* 550:241-252.
16. Nadler, B., Z. Schuss, A. Singer, and R. S. Eisenberg. 2004. Ionic diffusion through confined geometries: from Langevin equations to partial differential equations. *Journal of Physics-Condensed Matter* 16(22):S2153-S2165.
17. Vladimirescu, A. 1994. The SPICE Book. Wiley, New York.
18. Mikulecky, D. C. 1979. A network thermodynamic two-port element to represent the coupled flow of salt and current. *Biophysical Journal* 25:323-340.
19. Walz, D., S. R. Caplan, D. R. L. Scriven, and D. C. Miculecky. 1995. Methods of mathematical modelling. *In* Bioelectrochemistry: Principles and Practice. Caplan S. R., Miller I. R., Milazzo G., editors. Birkhaeuser Verlag, Basel. 49-131.
20. Buck, R. P., and C. Mundt. 1996. Aperiodic equivalent circuit for charge permeable thin-layer cells of symmetric, asymmetric types. *Journal of the Chemical Society-Faraday Transactions* 92(20):3947-3955.
21. Buck, R. P., and C. Mundt. 1996. General aperiodic equivalent circuit for charge permeable thin-layer cells of symmetric or asymmetric types .2. Interfacial kinetics. *Journal of the Chemical Society-Faraday Transactions* 92(24):4987-4992.
22. Coalson, R. D., and M. G. Kurnikova. 2005. Poisson-Nernst-Planck theory approach to the calculation of current through biological ion channels. *Ieee Transactions on Nanobioscience* 4(1):81-93.
23. Horno, J., C. F. González-Fernández, A. Hayas, and F. González-Caballero. 1989. Simulation of concentration polarization in electrokinetic processes by network thermodynamic methods. *Biophysical Journal* 55:527-535.
24. Schiller, S. M., R. Naumann, K. Lovejoy, H. Kunz, and W. Knoll. 2003. Archaea analogue thiolipids for tethered bilayer lipid membranes on ultrasmooth gold surfaces. *Angewandte Chemie-International Edition* 42(2):208-+.
25. Naumann, R., S. M. Schiller, F. Giess, B. Grohe, K. B. Hartman, I. Karcher, I. Koper, J. Lubben, K. Vasilev, and W. Knoll. 2003. Tethered lipid Bilayers on ultraflat gold surfaces. *Langmuir* 19(13):5435-5443.
26. Krishna, G., J. Schulte, B. A. Cornell, R. Pace, L. Wieczorek, and P. D. Osman. 2001. Tethered bilayer membranes containing ionic reservoirs: The interfacial capacitance. *Langmuir* 17(16):4858-4866.
27. Walz, D., and S. R. Caplan. 1995. Nonequilibrium thermodynamics and kinetics. *In* Bioelectrochemistry: Principles and Practice. Caplan S. R., Miller I. R., Milazzo G., editors. Birkhaeuser Verlag, Basel. 1-48.
28. Conway, B. 2005. Impedance Behavior of Electrochemical Supercapacitors and Porous Electrodes. *In* Impedance Spectroscopy: Emphasizing Solid Materials and Systems. Barsoukov E., Macdonald J. R., editors. ^{2n}d ed. Wiley, Hoboken, NJ. 469-497.
29. Paula, S., A. G. Volkov, A. N. VanHoek, T. H. Haines, and D. W. Deamer. 1996. Permeation of protons, potassium ions, and small polar molecules through phospholipid bilayers as a function of membrane thickness. *Biophysical Journal* 70(1):339-348.
30. Paula, S., A. G. Volkov, and D. W. Deamer. 1998. Permeation of halide anions through phospholipid bilayers occurs by the solubility-diffusion mechanism. *Biophysical Journal* 74(1):319-327.
31. Stryer, L. 1981. Biochemistry, 2nd ed. W. H. Freeman & Co., New York. 215.

32. Chizmadzhev, Y. A., J. Teissié, and D. Walz. 2004. Lipid bilayer electropermeabilization. *In* Bioelectrochemistry: Principles and Practice, Vol. 6, Bioelectrochemistry of Membranes. Walz D., Teissié J., Milazzo G., editors. Birkhäuser Verlag, Basel. 173–203.

APPENDIX A: Source code of the subcircuit ionperm

```
.subckt ionperm  c_1  c_2  phi_1  phi_2  Z  P  temp

bzphifrt  1    0     v=96500*v(phi_1,phi_2)*v(Z)/(8.3154889*(v(temp)+273.15))
bexp      2    0     v=exp(v(1))+1e-9
bflux     3    0     v=v(P)*(v(1)+1e-9)*1e-3*(v(c_1)*v(2)-v(c_2))/(v(2)-1)
gflux   c_1  c_2   3  0  1
bcur   phi_1 phi_2  i=96500*v(3)*v(Z)

.ends ionperm
```

Note that the term 1e-9 for bexp and bflux is added in order to avoid the indeterminacy which arises when the membrane potential, i.e. v(phi_1,phi_2), tends to zero. The factor 1e-3 = 10^{-3} L/cm^3 in bflux converts the concentration unit M to mol/cm^3.

FIGURE CAPTIONS

Figure 1: EIS of a tBLM at different bias potentials. The magnitude of the impedance Z (circles) and the phase shift (triangles) are plotted as a function of frequency (Bode plot). DiPhyPC bilayer in 0.1 M KCl solution at bias potentials of +300 mV (green), 0 mV (red), –300 mV (blue), and –400 mV (black).

Figure 2: Subcircuit ionperm used to simulate ion permeation with SPICE. Broken arrows indicate parameters which control programmable voltage and current sources. For further explanation see text.

Figure 3: Circuit used for EIS simulations with SPICE. The element named ionperm represents the subcircuit shown in Fig. 2. For further explanation see text.

Figure 4: Simulation of ion equilibration during formation of the tBLM in 0.1 M KCl solution. (A) Ion concentrations $c_{K,in}$ (black) and $c_{Cl,in}$ (red) in the sub-membrane space, (B) potential differences $\Delta\varphi_m$ (red) and $\Delta\varphi_{sr}$ (black). Note the logarithmic time scale.

Figure 5: Simulation of the re-equilibration of ions when different bias potentials are applied to the pre-equilibrated tBLM. (A) Potential differences $\Delta\varphi_m$ (dotted lines) and $\Delta\varphi_{sr}$ (solid lines), ion concentrations $c_{K,in}$ (B) and $c_{Cl,in}$ (C) in the sub-membrane space for bias potentials of +400 mV (blue), +300 mV (black), –300 mV (green), and –400 mV (red). Note the logarithmic time scale.

Figure 6: Example for the simulated response of ion concentrations (A) and potential differences (B) to a sinusoidal AC voltage. Initially the baselines (broken line) of the some oscillations vary. When constant baselines are reached the current density i_{el} and the electrode potential φ_{el} (C) are analyzed for impedance and phase shift. Bias potential –400mV, AC amplitude 10 mV and frequency 50 mHz.

Figure 7: Bode plot of EIS spectra simulated for different bias potentials with constant ion permeabilities. Color code as in Fig. 1, i.e. +300 mV (green), 0 mV (red), –300 mV (blue), and –400 mV (black). $P_{tot} = 1.8 \times 10^{-10}$ cm/s and $p = 10$.

Figure 8: Bode plot of EIS spectra simulated for different bias potentials but with ion permeabilities which depend on membrane potential. Color code as in Fig. 1, i.e. +300 mV (green), 0 mV (red), –300 mV (blue), and –400 mV (black). Dependence of P_{tot} on $\Delta\varphi_m$ according to eq. 8 with $P_{tot}(0) = 1.8 \times 10^{-10}$ cm/s, $K_s = 9.3$ mV, and $p = 10$.

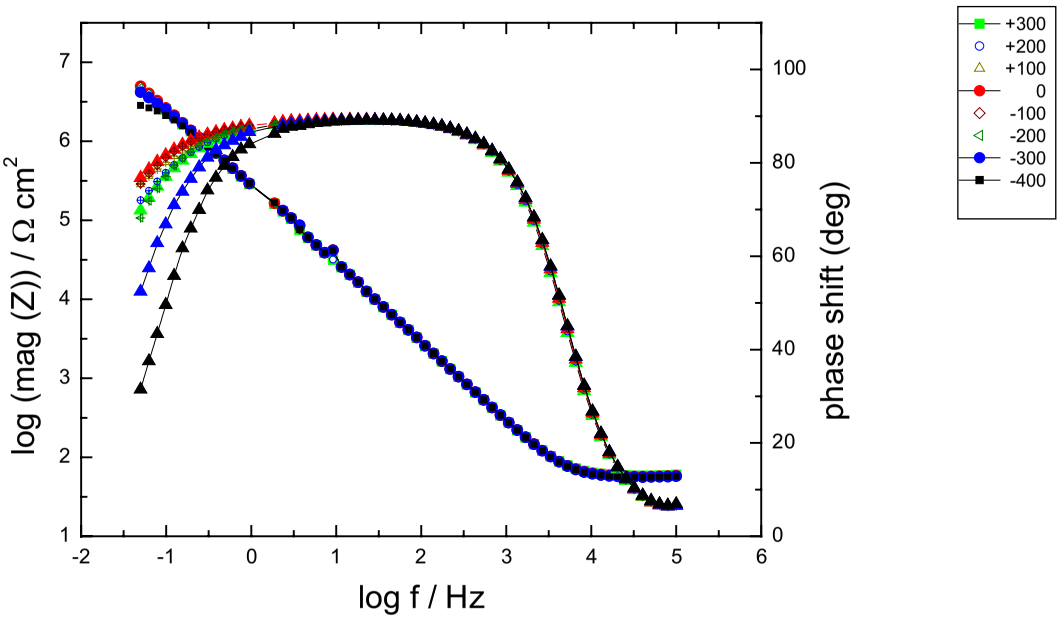
log (mag (Z)) / Ω cm²
phase shift (deg)
log f / Hz
+300
+200
+100
0
-100
-200
-300
-400

Fig. 1

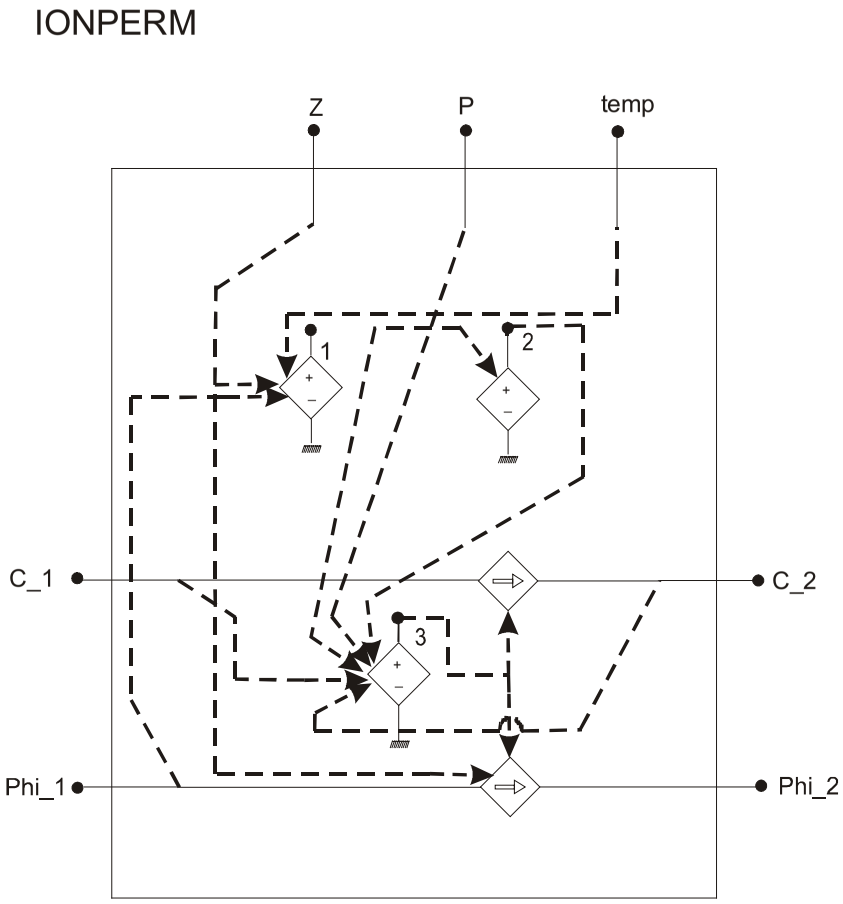
IONPERM
Z
P
temp
1
2
3
C_1
C_2
Phi_1
Phi_2

Fig. 2

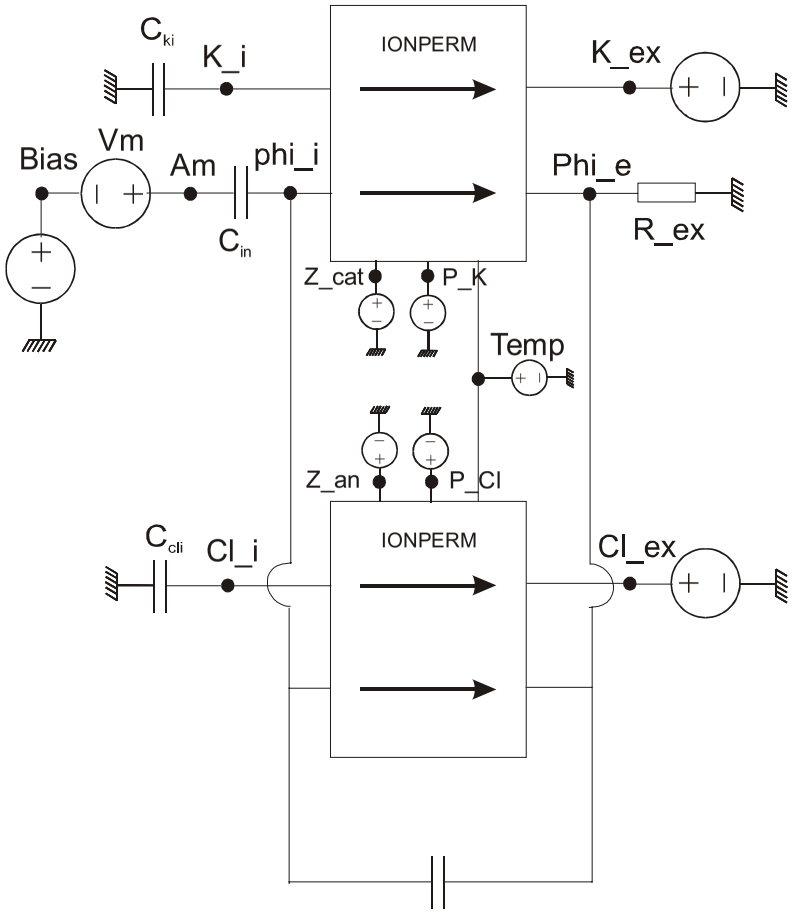
C_ki
K_i
IONPERM
K_ex
Bias
Vm
Am
phi_i
Phi_e
C_in
R_ex
Z_cat
P_K
Temp
Z_an
P_Cl
C_cli
Cl_i
IONPERM
Cl_ex

Fig. 3

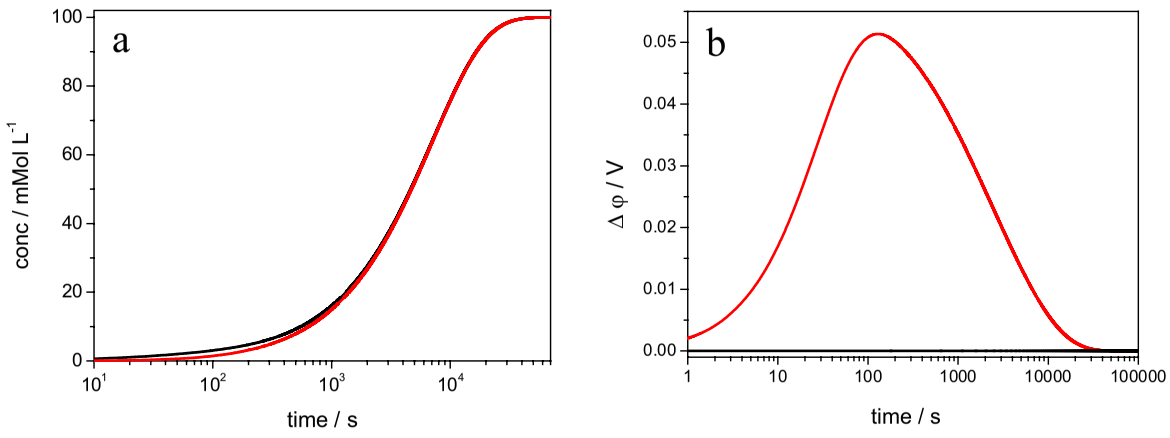
a
conc / mMol L-1
time / s
b
Δ φ / V
time / s

Fig. 4

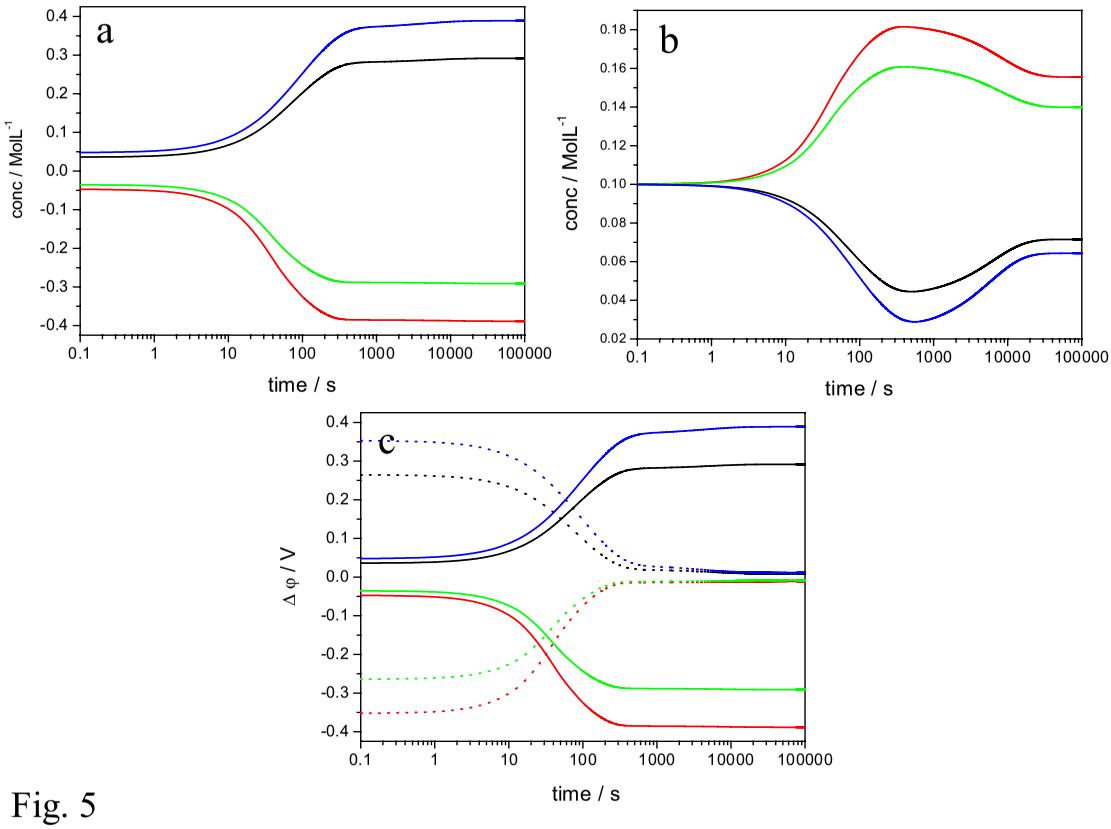
a
b
c
conc / MolL-1
Δ φ / V
time / s

Fig. 5

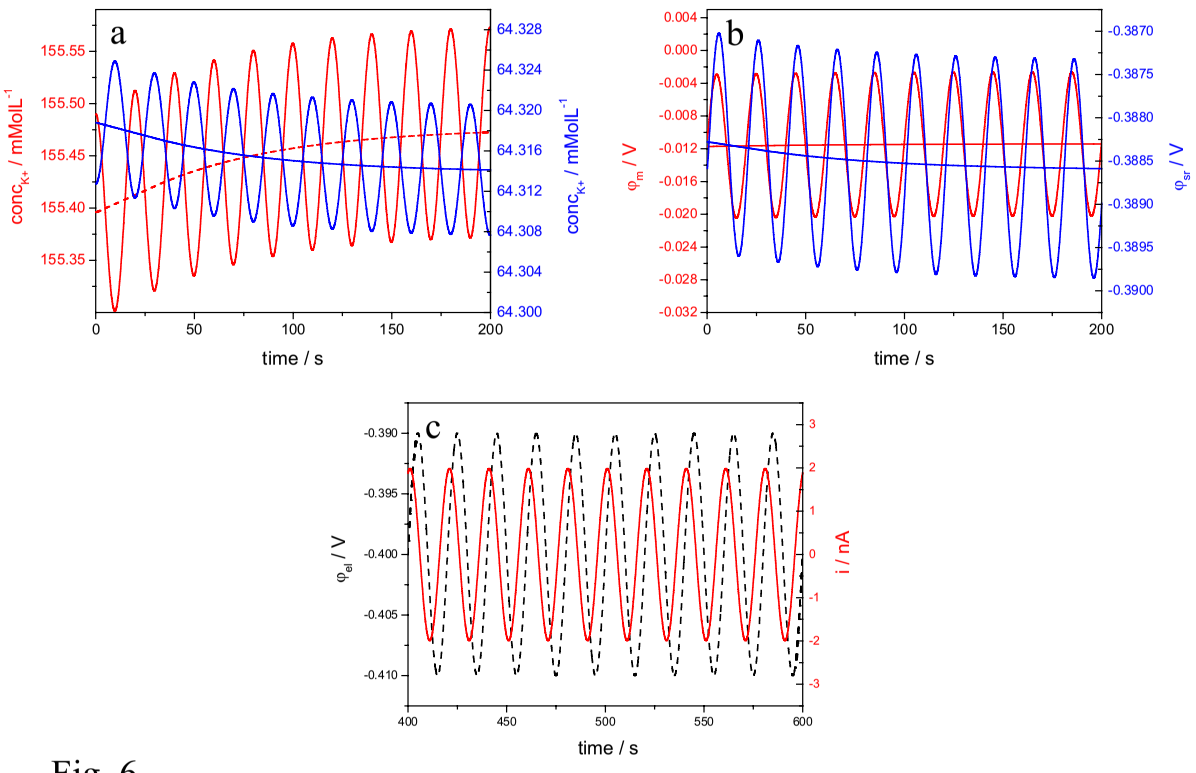
a
b
c
conc_K+ / mMolL-1
φ_m / V
φ_sr / V
φ_el / V
i / nA
time / s

Fig. 6

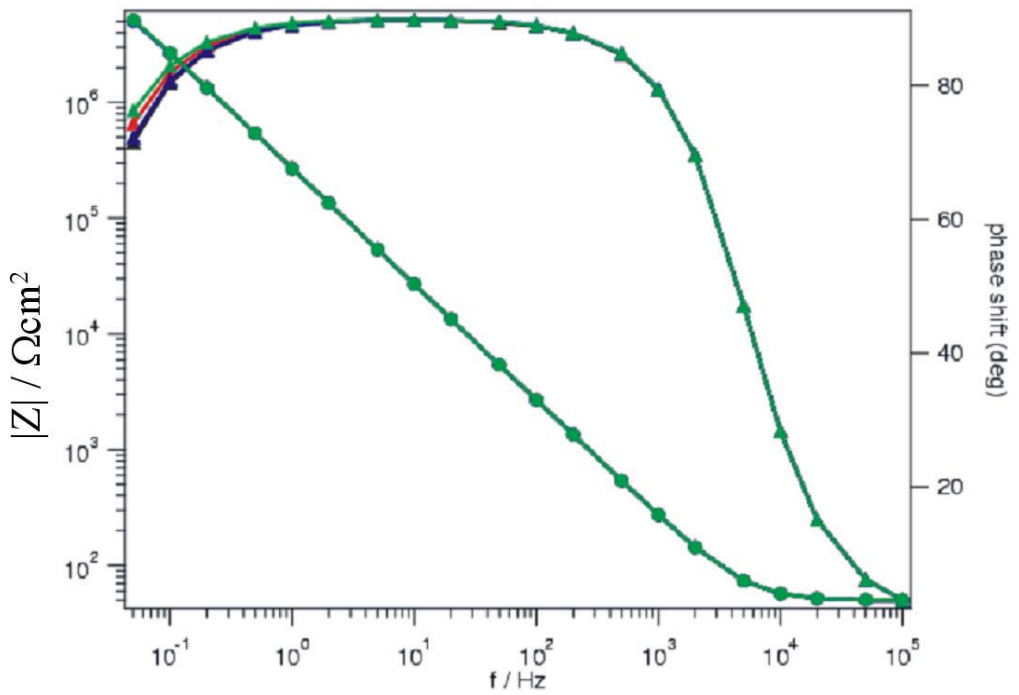

Fig. 7

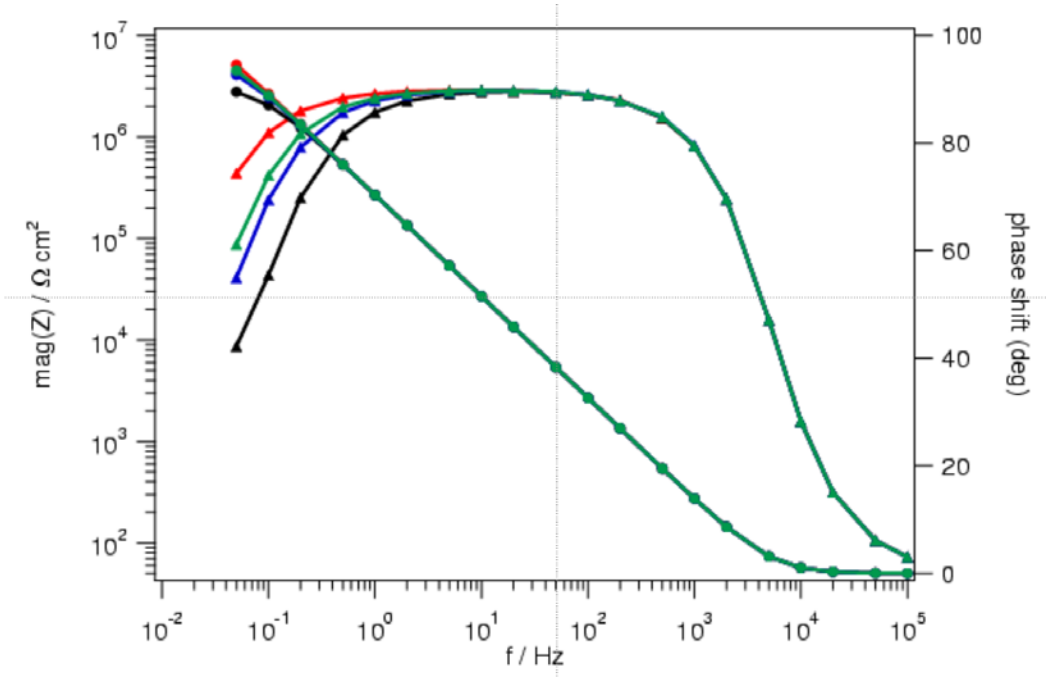

Fig. 8

Paper 7

Time-resolved Surface Enhanced Infrared Reflection Absorption Spectroscopy into electrochemically induced Electron Transfer to Cytochrome c Oxidase

Vinzenz Kirste[1], Marcel G. Friedrich[1], Jiapeng Zhu[2], Robert B. Gennis[2], Wolfgang Knoll[1] and Renate L. C. Naumann[1*]

[1]Max Planck Institute for Polymer Research
Ackermannweg 10
55128 Mainz
Germany

[2]University of Illinois
Department of Biochemistry
600 South Mathews Street
Urbana, IL 61801

[*] correspondence author, email naumannr@mpip-mainz.mpd.de

Introduction

Cytochrome c oxidase (CcO) is the final complex of the respiratory chain. It catalyzes the transformation of the energy of oxygen reduction into a difference of electrochemical potentials of protons across the inner mitochondrial membrane which is then used to generate adenosine triphosphate (ATP). CcO has been the subject of intense research for many years, for a review see ref. 1. Oxygen reduction by NADH was shown to proceed along four redox centers, Cu_A, $heme_a$, heme a_3 and Cu_B, and in an intricate mechanism to be coupled to proton transfer. To elucidate details of this mechanism, FTIR-methods are among the most promising ones (2-4). Methods have been developed, that allow to measure FTIR spectra of monolayers of proteins (5). The surface-enhancement effect of a rough metal surface can be used to perform surface-enhanced FTIR spectra. Subtle changes are isolated by using difference spectroscopy. Monolayers of cyt c (cc) absorbed to self assembled monolayers of thiols were thus measured by Surface-Enhanced Infrared Difference Absorption Spectroscopy (SEIDAS) with a sensitivity and resolution similar to spectroscopy in solution. The redox state of the cc could be controlled by electrochemical electron transfer (ET) to perform spectroelectrochemistry (6). Complex membrane proteins, such as the CcO, require a more elaborate surface architecture. Recently we have developed a method to immobilize the CcO solubilized in detergent (dodecyl-β-D-maltoside, DDM) on a NTA-Ni chelating surface, using the 6-his-tag genetically engineered to the C terminus of the protein. A lipid bilayer is subsequently formed around the CcO, when DDM is replaced by lipids by in-situ dialysis or alternatively by absorption of the detergent by biobeads. The final architecture is referred to as the protein-tethered bilayer lipid membrane (ptBLM) following the term tethered bilayer lipid membrane (tBLM) which indicates a lipid membrane that is separated from the surface by an water-like layer, mimicking the cytosol (8). CcO was immobilized in such architectures in strict orientations either with the cytochrome c binding site (Fig.1) or, in the inverted orientation, with the O_2 reduction side, respectively, directed towards the electrode. For this purpose, CcO of *R. sphaeroides* was used with a His-tag attached to the C-terminus of SU II (9) and CcO of *P. denitrificans* with a His-tag attached to the C-terminus of SU I (10). Biolectronic coupling or direct electrochemical electron transfer could be verified specifically

to the CcO with the cytochrome c binding site directed to the electrode, with an exceptionally high rate coefficient (12). With cc bound to the CcO in the inverted orientation, with the cytochrome c binding site pointing into the bathing solution, electron transfer to cc could be shown to proceed across the protein (11). The layer-by layer formation of the ptBLMs of both orientations were analyzed by different surface-analytical methods, with SEIDAS among them (12). From this it was concluded that FTIR spectroscopy could be sufficiently sensitive to allow for a more detailed analysis of the kinetics of ET processes in these proteins. Surface-Enhanced Infrared Reflection Absorption Spectroscopy (SEIRAS) (10) will be extended into the time domain by applying time–resolved (tr)-SEIRAS to CcO in the orientation with the cytochrome c binding site directed to the electrode. The enzyme can thus be triggered by direct bioelectronic coupling to the electrode. The metal sites themselves are not accessible by IR spectroscopy, however, vibrations of groups in the environment of the Cu and heme centers can be excited which were assigned previously to different redox states (2). ET reactions inside the protein can thus be followed as a function of time.

Principle of tr-SEIRAS triggered by electrochemical potentials

Potentials are applied in a square wave function to the ptBLM on the gold film periodically changing the redox state from the fully oxidized to the fully reduced state. The sudden potential changes at the end of the pulse are used to trigger the FT-IR spectrometer to record a succession of spectra that indicate the kinetics of the redox transition in an exponential function (Fig. 2). These functions are analyzed in terms of a single exponential if the reaction can be considered monomolecular. More complicated reactions require multi-exponentials to fit the data. The frequency of the electrochemical excitation depends on the kinetic parameters of the redox transition to be observed. Slow transitions (in the range of 10 to 100 µs) are followed in the rapid scan mode, whereas the step scan mode is used for rapid transitions (down to µs).

Materials and Methods

Di-thio-bis(N-succinimidyl propionate) (DTSP), di-thio-bis(propionic acid) (DTP), *N*-(5-Amino-1-carboxypentyl) iminodiacetic acid (ANTA), dodecyl-β-D-maltoside (DDM), cytochrome c from bovine heart, glucose oxidase and catalase were purchased from Sigma, biobeads from Bio-Rad Laboratories GmbH, Munich, Germany were washed with ethanol

and deionised water from a MilliQ water purification system (18MΩcm), 1,2-Diphytanoyl-sn-glycero-3-phosphocholine (DPhyPC) was provided by Avanti Polar Lipids. All other chemicals were of analytical grade.

CcO from *R. sphaeroides* engineered with his-tag on SU II was expressed and purified according to Mitchell and Gennis. (13)

Preparation of the samples

Rough gold films chemically deposited (14) on the silicon crystal of the SEIRAS setup were immersed for 120 min in a solution of DTSP and DTP in a ratio of 0.6 in dry DMSO (total 2mg/ml). After rinsing, the crystals were functionalized for 48 h in a 0.15 M solution of ANTA buffered to pH 9.8 by adding 0.5 M KCO_3. Finally, the crystals were immersed for 30 min in 40 mM $NiSO_4$ in acetate buffer 50 mM, pH 5.5. Immobilisation of the protein was performed in a solution of 100 nM CcO in detergent-containing phosphate / DDM buffer (K_2HPO_4 0.1 M, KCl 0.05 M, pH=8, 0.1%DDM) to the Ni-chelated NTA surface. (15) Dialysis was performed by adding biobeads to the lipid-detergent-containing phosphate/DDM buffer (DiPhyPC 0.05 mg/ml).

Electrochemical measurements

Electrochemical measurements were performed using an Autolab instrument (PGSTAT302) equipped with an FRA2-module for impedance measurements, an ECD-module amplifier for low-currents, an ADC750 module for rapid scan measurements, and a SCAN-GEN module for analog potential scanning as well as the frequency response analyzer (FRA) software provided by Eco Chemie, B.V. (Utrecht The Netherlands). Measurements under anaerobic conditions were done in a buffer solution containing K_2HPO_4 0.1M, KCl 0.05 M, pH=8 and the oxygen trap glucose (0.3%w/w), glucose oxidase (75µg/ml) and catalase (12.5µg/ml). (16) This solution was flushed with Ar purged from oxygen by washing through the oxygen trap containing buffer solution for one to two hours prior to the measurements to assure a completely deoxygenated solution. Impedance spectra were recorded in a frequency range of 50 kHz - 3 mHz with an excitation amplitude of 10 mV.

All electrochemical measurements were taken in a three electrode configuration with the gold film as the working electrode, a Ag/AgCl,KCl_{sat} reference, and a platinum wire as the counter electrode. All electrode potentials are quoted vs. NHE.

Surface Enhanced Infrared Reflection Absorption Spectroscopy (SEIRAS)

The spectro-electrochemical cell and the SEIRAS set-up are depicted in Fig. 3 and 4. A fluid cell with a lid, made from Teflon is mounted on top of half-cylinder-shaped silicon prism required for a single reflection in the Attenuated Total reflection Spectroscopy (ATR) mode. The flat surface of the prism is covered with a thin gold film by a chemical deposition technique, providing a nano-particular surface to the gold film with a RMS roughness of 5 nm. (14) Fig. 5 shows AFM images of the chemically deposited film as compared to traditionally evaporated gold.

The IR beam of the FTIR spectrometer (VERTEX 70 FTIR spectrometer from Bruker, Karlsruhe) is coupled into the prism at an incident angle of 60°. The reflected beam is recorded with a photovoltaic MCT (mercury cadmium telluride) detector. Spectra were recorded with 4 cm^{-1} spectral resolution. Spectra were analyzed by the software package OPUS 6 (Bruker, Karlsruhe).

For static measurements the mirror velocity was 60kHz, the phase resolution was 32 cm^{-1}, 100 scans were taken for one spectrum. For each spectrum 100 interferograms are averaged using a Blackmann-Harris 3-Term as the apodisation function.

In the Rapid Scan (RS) mode the mirror velocity was 160kHz, the highest time resolution in this mode was Δt=120ms (measurement time for one sample point spectrum (sps) = 120ms). Taking 64 sps over one redox cycle, measurements with an excitation frequency of 0,13Hz were carried out.

In the Step Scan (SS) mode measurements with a time resolution up to 25µs were carried out. With an excitation frequency of 1kHz, this corresponds to 40sps.
Also spectra with an excitation frequency of 0,5kHz and 2kHz were taken in the SS mode.

The FTIR spectrometer has an air cooled Globar infrared source.

Phase sensitive detection (PSD) was applied to the time resolved spectra, in order to increase the signal to noise (S/N) ratio. PSD works by demodulating the IR signal, which is modulated by the applied periodically changing potential. The basic idea of PSD is to suppress all signals which do not change with a frequency close to the exciting frequency. This results in a discrimination of background signals which do not change with a constant frequency, for example non-protein related peaks, peaks that do not depend on the potential modulation etc.

The method of PSD is described in ref. 18, 19 and 20. The principle is given below.

The periodic response of the system to the exciting modulated signal leads to a periodic response of the time dependent absorbance $A\left(\tilde{\nu},t\right)$.

At a given wavenumber, this time dependent absorbance is multiplied by a sinusoidal function $\sin(k\omega t+\phi_k^{PSD})$ followed by a normalized integration over the modulation period:

$$A_k^{\phi_k^{PSD}}(\tilde{\nu})=\frac{2}{T}\int_0^T A(\tilde{\nu},t)\sin(k\omega t+\phi_k^{PSD})dt \qquad (1)$$

ϕ_k^{PSD} is the operator controlled phase angle. Applying Eq. (1) to all wavenumbers $\tilde{\nu}$ of the spectrum leads to a vector PSD where the absorbance spectra $A\left(\tilde{\nu},t\right)$ and $A_k^{\phi_k^{PSD}}(\tilde{\nu})$ are treated like vectors (vector PSD). $A\left(\tilde{\nu},t\right)$ is the time-resolved absorbance spectrum and $A_k^{\phi_k^{PSD}}(\tilde{\nu})$ is referred to as phase-resolved modulation spectrum or phase-resolved absorbance spectrum associated with the frequency kω
(k=1 corresponds to the fundamental, i.e. to the frequency of excitation ω) and PSD phase setting ϕ_k^{PSD}. For ϕ_k^{PSD}=0° and ϕ_k^{PSD}=90°, $A_k^{\phi_k^{PSD}}(\tilde{\nu})$ is equivalent to the in-phase and out-of-phase components (equation 2).

$$\begin{aligned} A_k^{90°}(\tilde{\nu})&=A_k(\tilde{\nu})\sin[\varphi_k(\tilde{\nu})]=\frac{2}{T}\int_0^T A(\tilde{\nu},t)\cos(k\omega t)dt \quad (k=1,2,...)\\ A_k^{0°}(\tilde{\nu})&=A_k(\tilde{\nu})\cos[\varphi_k(\tilde{\nu})]=\frac{2}{T}\int_0^T A(\tilde{\nu},t)\sin(k\omega t)dt \quad (k=1,2,...)\end{aligned} \qquad (2)$$

In equation 2, $A_k\left(\tilde{\nu}\right)$ is the modulation amplitude of the absorbance and $\varphi_k\left(\tilde{\nu}\right)$ is the corresponding phase lag. $A_k\left(\tilde{\nu}\right)$ can be calculated from $A_k^{90°}(\tilde{\nu})$ and $A_k^{0°}(\tilde{\nu})$ using eq. (3):

$$A_k\left(\tilde{\nu}\right) = \sqrt{A_k^{0°}\left(\tilde{\nu}\right)^2 + A_k^{90°}\left(\tilde{\nu}\right)^2}$$
$$\sin\varphi_k = \frac{A_k^{90°}}{A_k}, \quad \cos\varphi_k = \frac{A_k^{0°}}{A_k} \qquad (3)$$

The purpose of the PSD is the evaluation of the phase-resolved absorbance spectra $A_k^{\varphi_k^{PSD}}(\tilde{\nu})$, if the response of the system is in-phase with the exciting frequency, the process to be investigated has the same time constant. If there is a phase shift, the time constant is slower.

The mathematical procedure of the PSD was implemented in the OPUS software, using a macro from the group of Prof. Fringeli, Vienna.

Results and Discussion

Immobilization of the CcO with the his-tag attached to SU II and reconstitution into a ptBLM was performed as described (15). Layer-by layer formation as followed by SEIRAS was described in ref (17). SEIDA spectra of the immobilization of the CcO are shown in Fig. 6 and 7. The formation of the membrane is shown in Fig. 8. Cyclic voltammetry was performed prior to each tr-SEIRAS experiment, to ensure that the sample was ready to undergo direct ET (15).

Tr SEIRAS measurements were performed in the absence of oxygen, triggered by a periodic change of potentials between +300 and -700 mV. Under these conditions, the enzyme cycles between fully oxidized and fully reduced state. With a sinusoidal excitation of very low frequency, 0.13 Hz, in the RS mode, changes in the spectra in the frequency region 1000 to 1750 cm^{-1} were observed, indicating changes in the redox state particularly of Cu_A, but also of heme a_3 and heme a (fig. 9). In the frequency range 3045-3150 cm^{-1}, a change is observed at

3050 cm^{-1} which can be assigned to the redox transition of Cu_B (inset of Fig. 9). Band assignments, collected in table 1 are taken from ref (2).With the slow changes of the potential, each spectrum displayed in Fig. 9 can be considered to represent a quasi-stationary state at a certain potential. These potentials derived from the sine wave function, are given in the figure caption of Fig. 9. Due to the periodic excitation, each difference spectrum represents the average of the same stationary state attained during repeated multiple turnovers of the enzyme. The fully oxidized state is used as the reference spectrum such that changes in the spectra are due to reduction of the enzyme. The most prominent change is seen in the band at 1647 cm^{-1} which was assigned (1651 cm^{-1}) to the amide I band (α-helix; ν(C=O)vibration of reduced Cu_A). A second band at 1602 cm^{-1} is also attributed to the formation of reduced Cu_A (amide I band, β-sheet; ν(C=O)) with the oxidized state indicated by a band at 1592 cm^{-1}. Other changes referring to the hemes a and a_3 are listed in table 1 together with the other major change attributed to Cu_B at the band at 3050 cm^{-1}. From this result, the periodic reduction and reoxidation of all four redox sites is concluded to occur, initiated by the direct electrochemical electron transfer to Cu_A. This is in full agreement with recently performed combined electrochemical and SERRS measurements (15).

In the above mentioned investigation, Cu_A and heme a were shown to be reduced with rate coefficients of k_S = 4130 ± 390 s^{-1} and k_S = 1650 ± 170 s^{-1}, respectively. tr-SEIRAS measurements were therefore conducted in the step scan mode with a square wave excitation of a frequency of 500 Hz. Phase sensitive detection was used to improve the spectral resolution and the S/N ratio. As a result, time resolved changes of Cu_A and heme a were observed (Fig. 10). The set of data taken at a frequency of 500 Hz was analyzed in terms of the peak height and could be fitted to a single exponential (Fig.11), yielding a rate coefficient of 1980 s^{-1}. This compares reasonably well with the rate coefficient of 4130 s^{-1} found by fast scan cyclic voltammetry.

For an experiment with a modulation frequency of 1 kHz a critical reference experiment was performed under identical conditions, however, using the CcO in the inverted orientation with the cc binding site pointing into the bathing solution. No changes in the spectra could be recorded, strongly supporting the assertion, made earlier, that direct ET does not occur non-specifically to any of the redox centers. Instead, direct ET occurs specifically to Cu_A the binding site of which must be close to the surface. This is shown clearly in the reference spectrum (Fig. 12)

Conclusion

Tr-SEIRAS has been successfully applied to the CcO in the ptBLM. Time resolution down to the µs time scale has been achieved, due to the electrochemical triggering of the ET chain. This time resolution should be sufficient to perform a more detailed kinetic analysis of the enymatic cycle of the CcO.

Table 1

(b) 1800-1000 cm^{-1} Region

1746/1737	heme *a*	ox/red	E, Glu-COOH; ν (C=O); E278 (*28*)
1689	Cu_A	ox	amide I, *β*-sheet; ν (C=O)
1674	heme a_3, complex band	ox	R, Arg-H_5^+; $\nu_{as}(CN_3H_5^+)$; R473 (*28*)/propionate; ν (C=O) (*18*)/formyl (*29*)/amide I, turns; ν (C=O)
1661	heme *a*	red	amide I, α-helix; ν (C=O)/amide I, turns; ν (C=O)
1655	heme a_3	ox	amide I, α -helix; ν (C=O)
1650	Cu_A	red	amide I, α -helix; ν (C=O)
1641	heme a_3	ox	formyl; ν (C=O) (*11*)/amide I, *β* -sheet; ν (C=O)
1630	heme a_3	red	R, Arg-H_5^+; $\nu_s(CN_3H_5^+)$; R473/H, $HisH_2^+$; ν (C=C); H403 (*28*)/formyl (*29*)/amide I, *β*-sheet; ν (C=O)
1618	heme a_3	red	Y, Tyr-OH; ν (CC) ring, *δ*(CH); Y280/W; ν (CC), ν (C=C); W272, W164 (*28*)/vinyl; ν (C-C) (*26*)/amide I, *β*-sheet, ν (C=O)
1603	Cu_A	red	amide I, *β*-sheet; ν (C=O)
1592	Cu_A	ox	H, HisH; ν (C=C); H224, H181/R, Arg-H_5^+; $\nu_{as}(CN_3H_5^+)$; R473/D, Asp-COO^-; $\nu_{as}(COO^-)$; D178 (*28*)
1561	heme a_3	ox	W, Trp-NH; ν (CC), *δ*(CH); W164 (*28*)/propionate (*18*)
1549	heme *a*	red	heme; ν_{38y} (*26*)
1537	heme *a*	ox	propionate (*18*)
1526	heme a_3	red	propionate/heme; ν_{38s} /heme; ν_{38y} (*26*)
1510	Cu_A	red	W, Trp-NH; ν (CN), *δ*(CH), *δ* (NH); W121 (*28*)
1489	Cu_B	red	W; ν (CC), *δ* (CH); W272/H, HisH; ν (C=N), *δ* (CH); H325, H326 (*28*)
1468	Cu_A	ox	W, Trp-NH; *δ* (CH), ν (CC), ν (CN); W121 (*28*)
1431	Cu_A	ox	W, Trp-NH; *δ* (CH), ν (CC), ν (CN); W121/D, Asp-COOH; *δ* (COH); D178/E, Glu-COO $\nu_s(COO^-)$; E218 (*28*)
1420	Cu_A	red	W, Trp-NH; *δ* (NH), ν (CC), *δ* (CH); W121/H, HisH; ν (CN), *δ* (NH), $\delta_s(CH_x)$; H181, H224/D, Asp-COOH; *δ* (COH); D178 (*28*)
1407	Cu_A	red	E, Glu-COO^-; $\nu_s(COO^-)$; E218/D, Asp-COO^-; $\nu_s(COO^-)$; D178/W, Trp-NH; ν (CC), *δ* (NH), *δ* (CH); W121 (*28*)
1389	heme *a*	ox	T; *δ* (COH); *δ* (CH); T50/E; $\gamma_w(CH_2)$; E278 (*28*)/propionate (*18*)
1354	heme a_3	red	W; ν (CC), ν (CN), *δ* (CH); W164, W272/Y; γ_w(CH2); Y280 (*28*)/ A_{1g}, ν_4 (*29*)
1321	Cu_B	red	W; *δ* (CH); W272/Y; *δ* (CH_2) (tail group), ν (CC) *δ* (CH); Y280/T; *δ* (COH), *δ* (CH); T344/D, Asp-COOH; *δ* (COH); D399 (*28*)

(b) 4000-2500 cm^{-1} Region

3092	Cu_B	ox	OH, OH^-; ν (OH); Cu_B OH^- ligand/Y; ν (OH); Y280/H; ν (NH); H326, H325/(CH) alkenes; ν (C=H); H326, H325, H276, W272, Y280
2876	Cu_B	ox	OH, OH^-; ν (OH); Cu_B OH^- ligand/Y; ν (OH); Y280/H; ν (NH); H326, H325/(CH) alkanes; ν (CH); any ligand/H_3O^+; ν_{as}(OH); H^+ x $(H_2O)_n$, *n* = 5 (*31*)

References

1. O.-M. H., Richter, B. Ludwig, *Rev. Physiol. Biochem. Pharmacol.* **147**, 47 (2003)
2. E. A. Gorbikova, K. Vuorilehto, M. Wikström, M. I. Verkhovsky, Biochemistry 2006, 45, 5641-5649, Redox Titration of All Electron Carriers of Cytochrome c Oxidase by Fourier Transform Infrared Spectroscopy
3. J. Behr, H. Michel, W. Mäntele, P. Hellwig, Biochemistry 2000, 39, 1356-1363, Functional Properties of the Heme Propionates in Cytochrome c Oxidase from P. denitrificans. Evidence from FTIR Difference Spectroscopy ansd Site-Directed Mutagenesis

4. P. Hellwig, St. Grzybek, J. Behr, B. Ludwig, H. Michel, W. Mäntele, Biochemistry 1999, 38, 1685-1694, Electrochemical and Ultraviolet/Visible/infrared Spectroscopic Analysis of Heme a and a_3 Redox Reactions in the Cytochrome c Oxidase from P. denitrificans: separation of Heme a and a_3 Contributions and Assignment of Vibrational Modes
5. K. Ataka, J. Heberle, J. Am. Chem. Soc. 2003, 125, 4986-4987, Electrochemicall induced Surface-Enhanced Infrared Difference Absorption (SEIDA) Spectroscopy of a Protein Mo nolayer
6. K. Ataka, J. Heberle, J. Am. Chem. Soc., 2004, 126, 9445-9457, Functional Vibrational Spectroscopy of a Cytochrome c Monolayer: SEIDAS probes the Interaction with Different Surface-Modified Electrodes
7. Giess, F., Friedrich, M.G., Heberle, J., Naumann, R.L., Knoll, W., 2004,The protein-tethered lipid bilayer: A novel mimic of the biological membrane. *Biophys. J.* 87:3213-3220
8. Knoll, W., K. Morigaki, R. Naumann, B. Sacca, S. Schiller, and E. K. Sinner. 2004. Functional Tethered Bilayer Lipid Membranes. *In* Ultrathin Electrochemical Chemo- and Biosensors, Technology and Performance. Mirsky V. M., editor. Springer-Verlag, Berlin. 239-254
9. Friedrich, M.G., et al., 2004, Active Site Structure and redox processes of cytochrome c oxidase immobilised in a novel biomimetic lipid membrane. *Chem. Comm.* 2376-2377
10. Ataka, K. et al., Oriented attachment and membrane reconstitution of his-tagged cytochrome c oxidase to a gold electrode: In-situ monitoring by surface enhanced infrared absorption spectroscopy. *JACS* **126**, 16199-16206 (2004)
11. M. G. Friedrich, M. Plum, et al., JACS
12. M. G. Friedrich, V. Kirste, et al., Biophys. J
13. Mitchell, D.M., and Gennis R.B., 1995. Rapid purification of wildtype and mutant cytochrome c oxidase from *Rhodobacter Sphaeroides* by Ni^{2+}-NTA affinity chromatography. *FEBS Letters* 368(1):148-150

14. Miyake, H., Osawa, S. Ye, M., 2002. Electroless deposition of gold thin films on silicon for surface-enhanced infrared spectroelectrochemistry, *Electrochemistry Communications* 4: 973-977
15. M. G. Friedrich, PNAS
16. Vanderkooi J.M., Maniara, G., Green, T.J., Wilson, D.F. An optical method for measurement of dioxygen concentration based upon quenching of phosphorescence. *JBC* **262**, 5476-5482 (1987).
17. Ataka, K. et al., 2004. Oriented attachment and membrane reconstitution of his-tagged cytochrome c oxidase to a gold electrode: In-situ monitoring by surface enhanced infrared absorption spectroscopy. *JACS,* 126:16199-16206
18. Baurecht, D., Porth, I. A new method of phase sensitive detection in modulation spectroscopy applied to temperature induced folding and unfolding of RNase A. *Vibrational Spectroscopy* **30** (2002) 85-92
19. Fringeli, U. P., Günthard, H. H., Baurecht, D., in: *H. U. Gremlich, B. Yan (Eds.), Infrared and Raman Spectroscopy of Biological Materials, Marcel Dekker, New York, Basel,* Chapter 5 (2000) 143-192
20. Baurecht, D., Fringeli, U. P. Quantitative modulated excitation Fourier transform infrared spectroscopy *Rev. Sci. Instrum.* **72** (2001) 3782

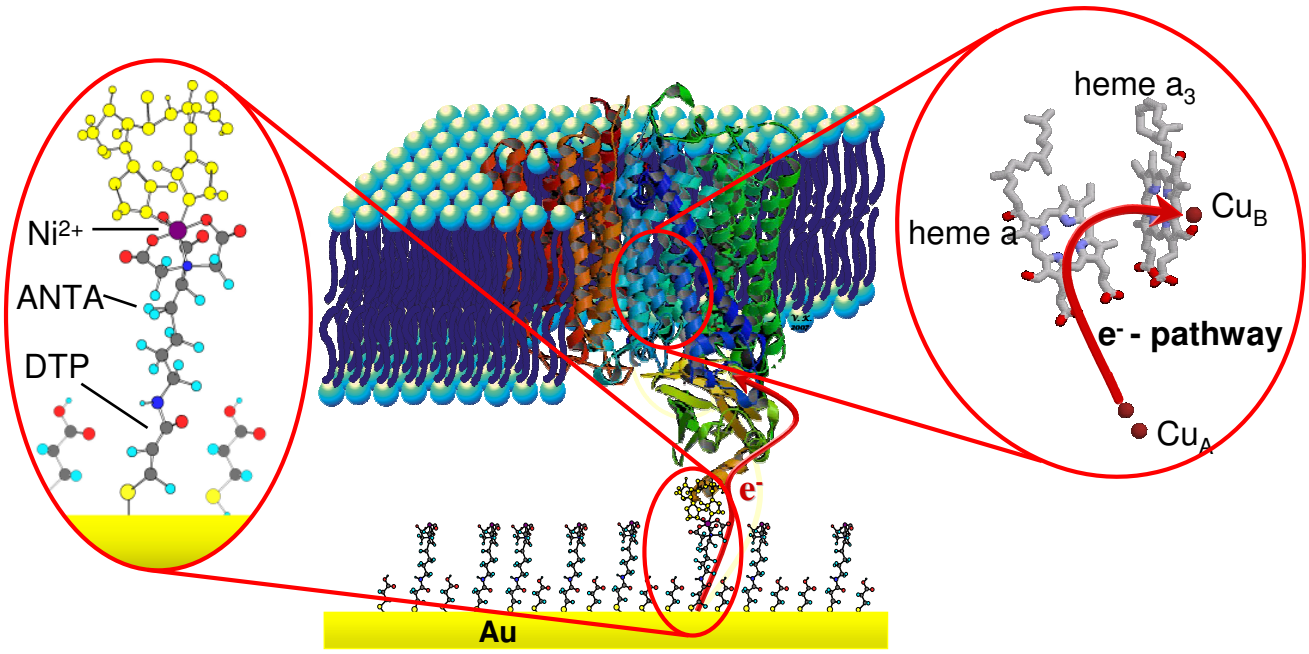

Figure 1: CcO immobilized with the cytochrome c binding site directed towards the gold electrode.
Left zoom: the anchor group
Right zoom: the four redox centers of the protein

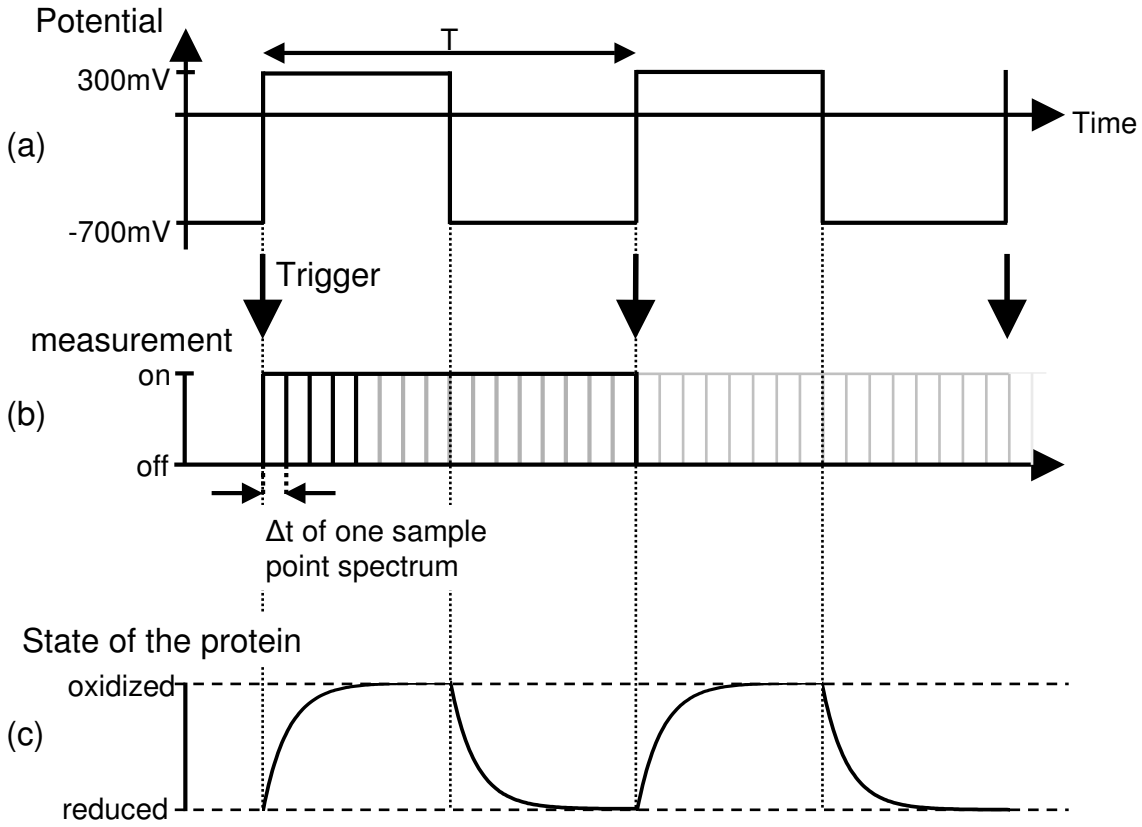

Figure 2: (a) Potentials applied to the ptBLM on the gold film
(b) IR Measurement, triggered by the positive edge of the exciting potential
(c) Corresponding state of the protein during the excitation cycle

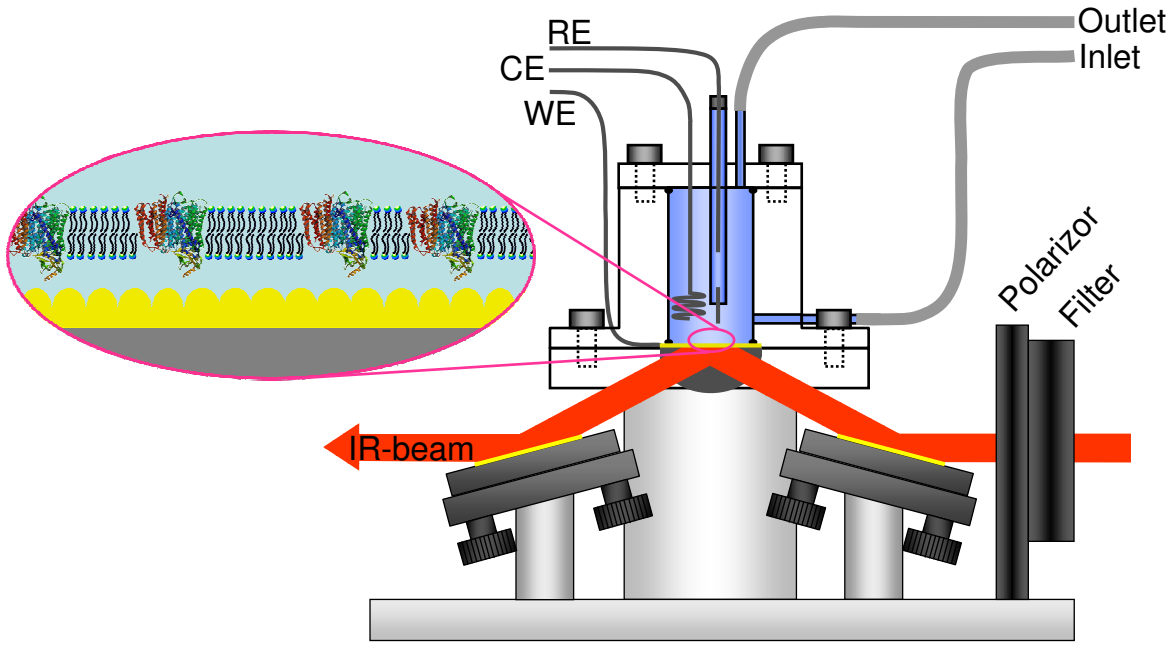

Figure 3: The spectro-electrochemical setup. Details are explained in the text.

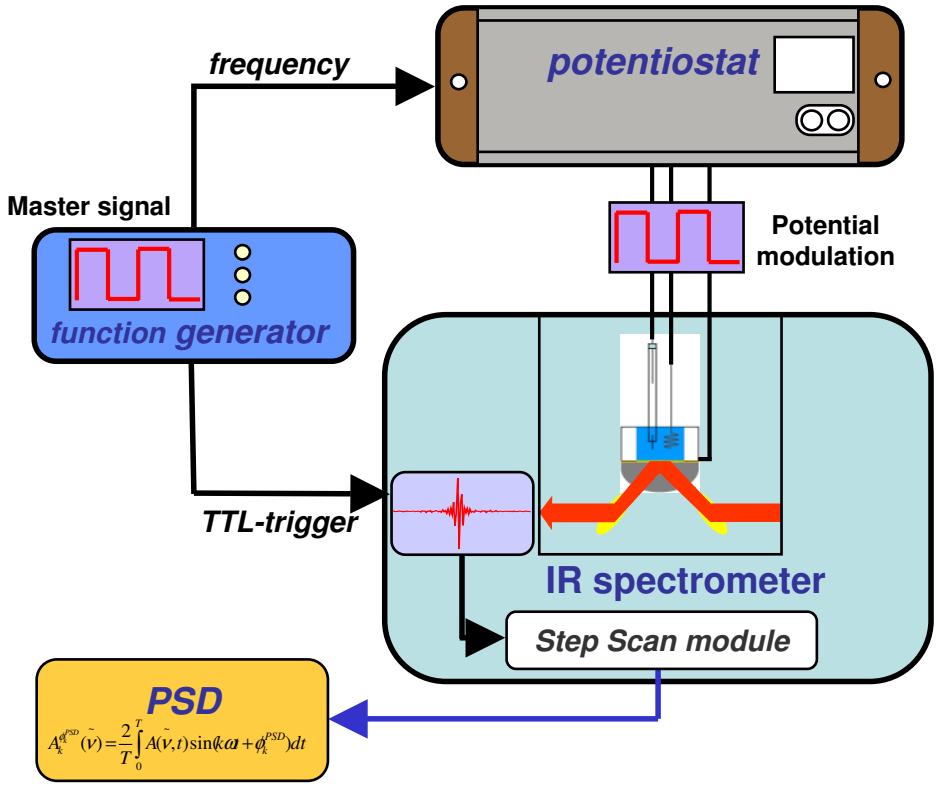

Figure 4: The complete SEIRAS setup. A function generator provides the signal form which is then applied to the ptBLM by the potentiostat. The IR spectrometer is triggered by the same signal of the function generator.
The IR signal is processed in the internal step scan module of the spectrometer.
The phase sensitive detection (PSD) is then applied externally.

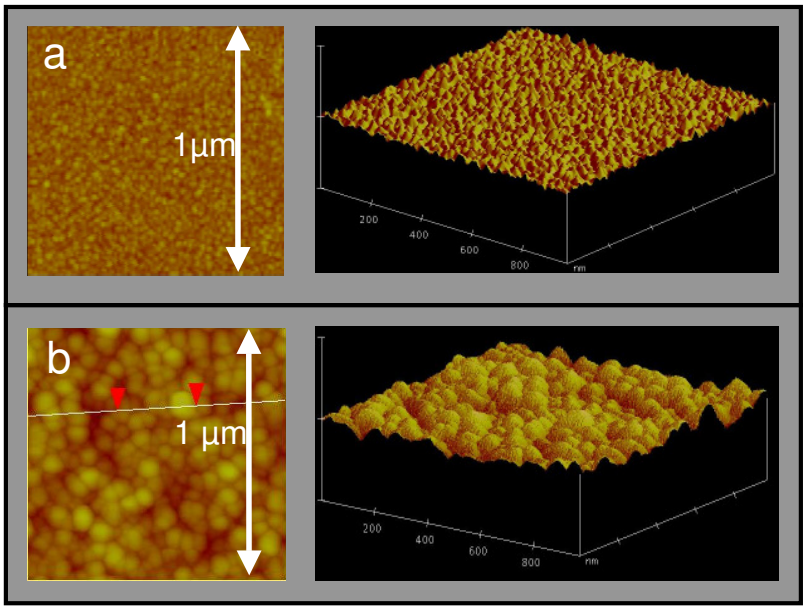

Figure 5: AFM images of an evaporated gold film with a roughness of about 1nm (a) and of the chemically deposited gold film with a roughness of about 5 nm (b). The nano-particular structure of the gold surface is obvious.

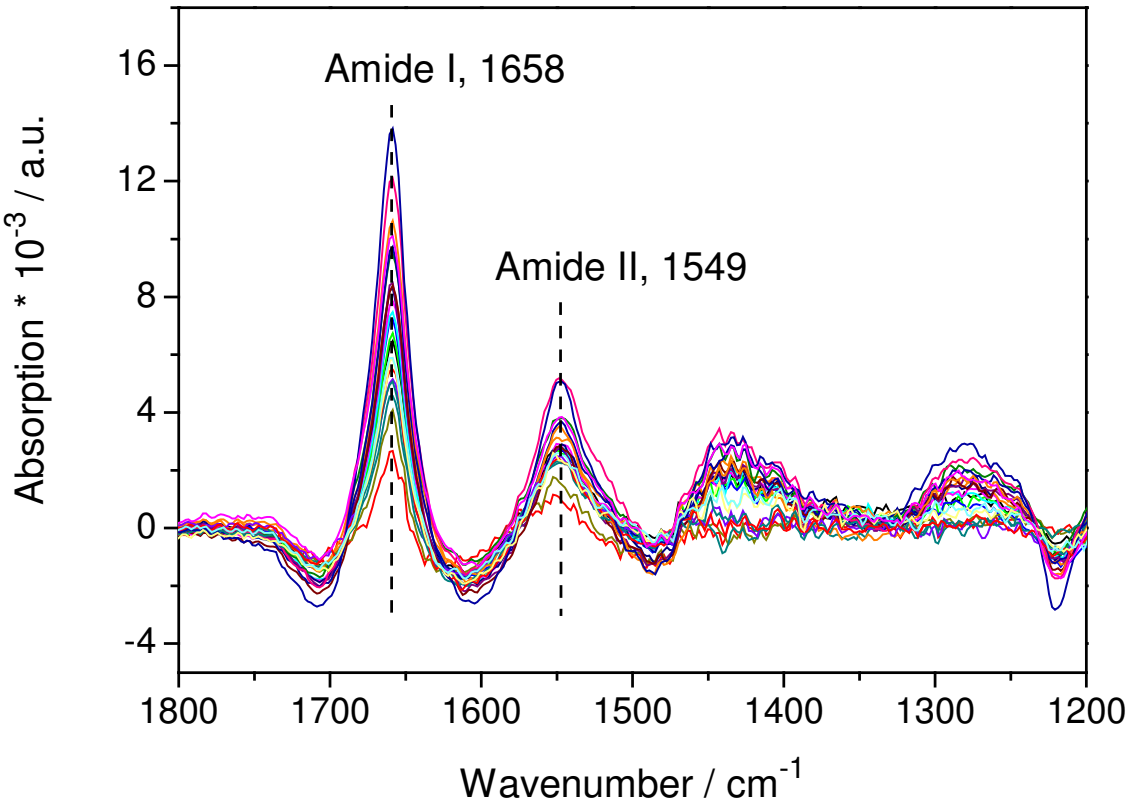

Figure 6: SEIDA spectra of the immobilization of the CcO (Amide I, II region). The bands at 1658 and 1549 cm-1 are assigned to the amide I, II modes of the protein backbone vibrations of the CcO.

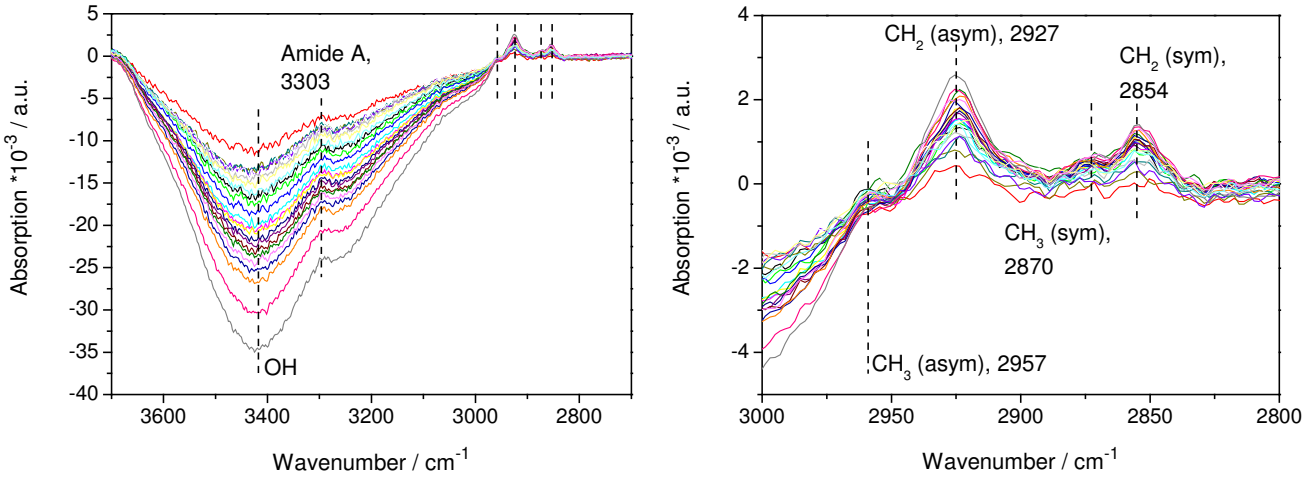

Figure 7: SEIDA spectra of the immobilization of the CcO (Amide A, methyl region).

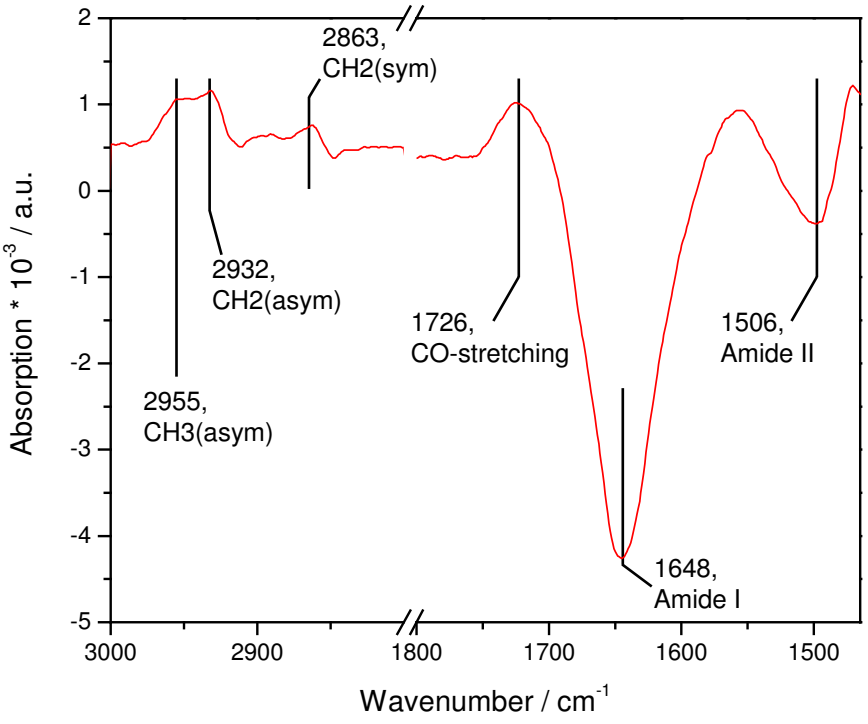

Figure 8: SEIDA spectrum of the reconstituted membrane, 48h after starting dialysis. The increasing methyl bands and the CO-stretching modes show the formation of the membrane, the decreasing Amide I and II bands indicate a ordering (and thus increasing distance) of the protein.

black	287mV
red	199mV
light green	56mV
blue	-79mV
dark green	-273mV
pink	-456mV
orange	-599mV
wine	-687mV

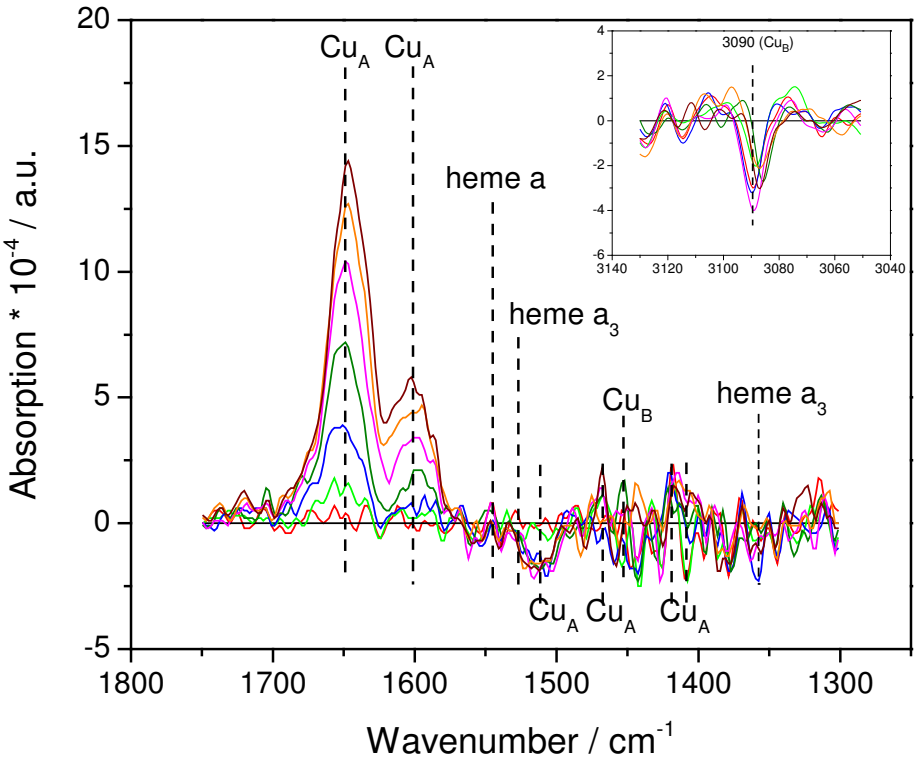

Figure 9: SEIDA spectra at different potentials starting at +287mV (fully oxidized, reference)

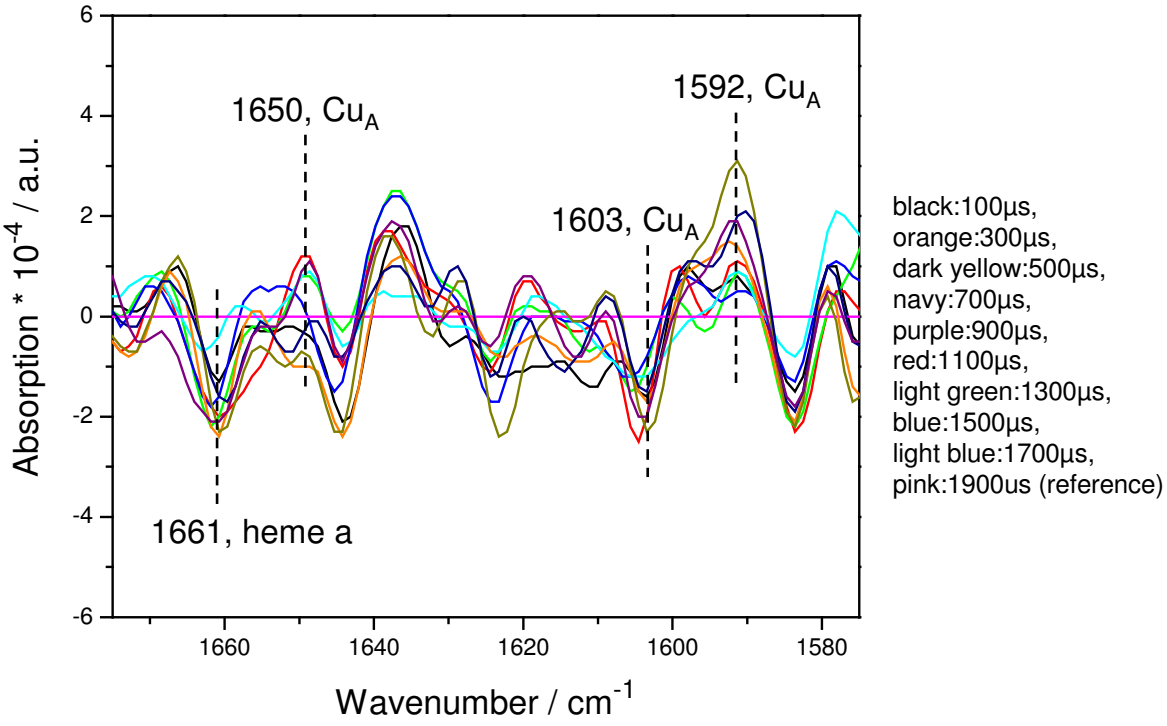

Figure 10: tr-SEIRAS spectra of the CcO with an excitation frequency of 500 Hz.

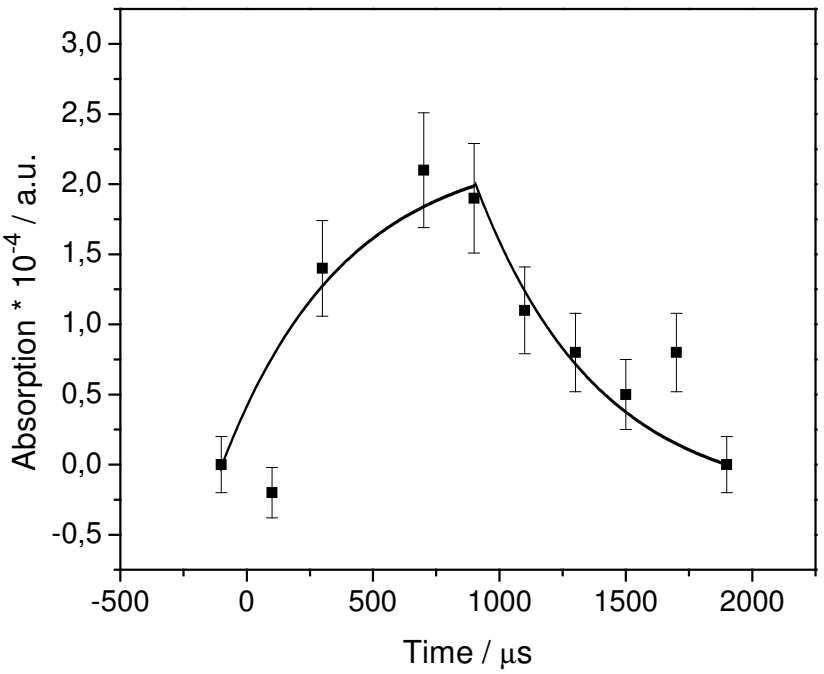

Figure 11: Peak hight of the Cu_A-peak at 1592 cm^{-1} plotted in dependence of time. A monoexponential curve was fitted, the corresponding time constant is $\tau = 1980\ s^{-1}$.

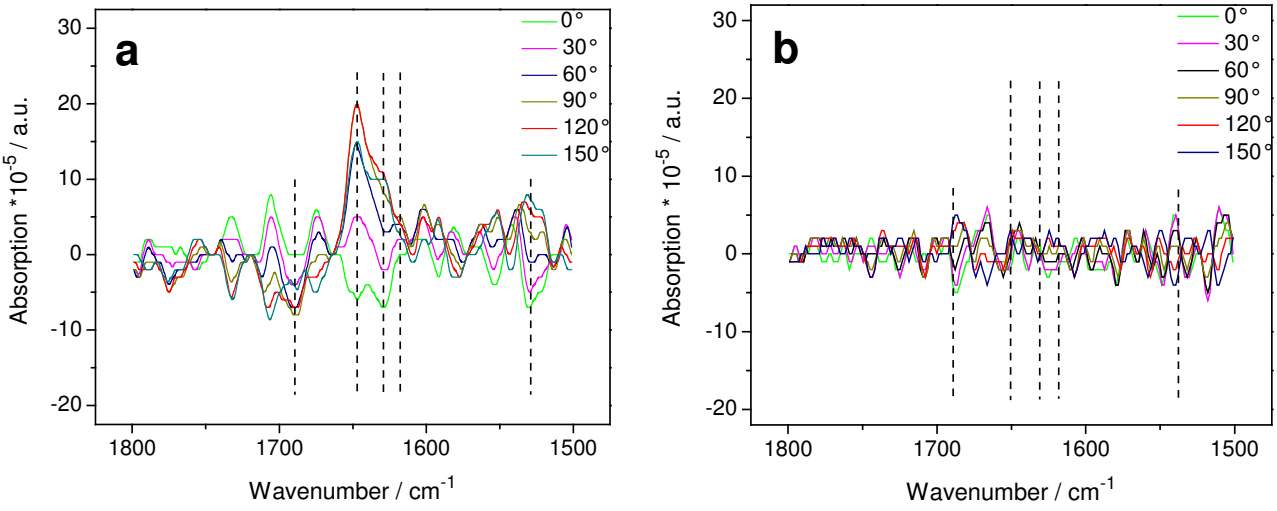

Figure 12: PSD spectra of a 1kHz modulation experiment of CcO (a) with its natural electron entry side directed toward the electrode and (b) directed away from the electrode into the bathing solution. No redox-processes could be observed in the case of the inverted orientation.

Paper 8

In preparation

Orientational Control of Direct Electron Transfer to Cytochrome *c* Oxidase monitored by surface enhanced resonance Raman (SERR) spectroscopy

Marcel G. Friedrich, Wolfgang Knoll and Renate Naumann

Max Planck Institute for Polymer Research
Ackermannweg 10
55128 Mainz
Germany

Introduction

Electrochemical investigation of multi-redox site proteins is a relatively new field of research. Valuable kinetic information has been obtained for water-soluble redox-active enzymes , including their catalytic sites. Bioelectronic coupling of multi-site membrane proteins, however, is still a challenging task. Recently we have verified fast direct ET (in the 100 µs time scale) to CcO, the terminal complex of the respiratory chain, embedded in a ptBLM. This architecture allows direct wiring of the electron acceptor side of the protein, while the wire keeps the protein/membrane assembly at a distance from the electrode, thus effectively avoiding denaturation. A water-like interstitial layer is also provided between the electrode and the membrane, that can serve as a reservoir for ions (Fig. 1).

Electrochemical studies, providing kinetic information, suffer from a lack of structural information, which would be easily available by methods of vibration spectroscopy, such as Raman and FT-IR S. Hence the combination of electrochemistry with these spectroscopic techniques for protein research is extremely valuable, particularly as far as monolayers of proteins on surfaces are concerned. They can be successfully probed by vibration spectroscopy when surface-enhancement techniques are employed, such as those applied in SEIRAS and SERRS. Electrochemical reduction/oxidation of adsorbed soluble proteins such as cyt c has been followed by in-situ SERRS experiments, even on a time resolved basis. Larger more complex proteins were investigated in thin layer cells thus enabling electrochemical control as well as FTIR structural analysis. Redox transitions in these cells take place in the range of seconds and hence are restricted to the investigation of static states of the protein. Fast time resolved step-scan FT-IR and RR studies were performed when the protein was transferred to the reduced state by ligand (CO) photodissociation.

In a preliminary investigation, SERRS had been shown to register the redox state of electrochemically activated CcO embedded in a ptBLM. Spectra of the reduced and oxidized state were recorded with a sensitivity and resolution similar to the one obtained by the protein in solution. This was done with a CcO genetically modified with an his-tag attached to SU II of the protein. In this orientation, the CcO is directed with its electron entry site, CuA;

directed towards the electrode. This mutant was later investigated regarding the rate coefficient of heterogeneous ET (in the ms time range) also in comparison to CcO bearing the his-tag on the opposite side of the CcO. Both mutants, attached to the electrode in opposite orientations, will be investigated in greater detail with respect to direct ET monitored by SERRS.

Materials and Methods

If not otherwise stated, materials and methods were used as described.[11] CcO from *Rhodobacter sphaeroides* with the His-tag engineered to the C-terminus of subunit II was expressed and purified according to Mitchell and Gennis.[43] Roughened silver electrodes,[44] used for SPR and electrochemistry measurements, were immersed for 120 min in a solution of dithiobis (N-succinimidyl propionate) (DTSP) and dithiobis (propionic acid) (DTP) in a 60:40 ratio, in dry DMSO (2mg/ml). After rinsing with DMSO and Ethanol, the electrodes were functionalized for 48 h in a 0.15 M solution of *N*-(5-amino-1-carboxypentyl) iminodiacetic acid (ANTA) buffered to pH 9.8 by adding 0.5 M KCO_3. Finally, the electrodes were immersed for 30 min in 40 mM $NiSO_4$ in acetate buffer (50 mM, pH 5.5). Immobilisation of the protein was performed as previously described.[11] Dialysis was done by adding biobeads (Bio-Rad Laboratories GmbH, Munich, Germany) to the lipid-detergent-containing phosphate / dodecyl β-D- maltoside (DDM) buffer, DiPhyPC 0.05 mg/ml in phosphate/DDM buffer (K_2HPO_4 0.1 M, KCl 0.05 M, pH=8, 0.1%DDM).

Electrochemical measurements were performed using an Autolab instrument (PGSTAT302) equipped with an FRA2-module for impedance measurements, an ECD-module amplifier for low-currents, an ADC750 module for rapid scan measurements and a SCAN-GEN module for analog potential scanning. Measurements under anaerobic conditions were done in a buffer solution containing K_2HPO_4 0.1M, KCl 0.05M, pH=8 and the oxygen trap consisting of glucose (0.3%w/w), glucose oxidase (75µg/ml) and catalase (12.5µg/ml).[45] This solution was flushed with Ar (99.9999% purity grade) purged from oxygen by bubbling through the oxygen trap containing buffer solution for one or two hours prior to the measurements to assure a completely deoxygenated solution. All electrochemical measurements were taken in a three electrode configuration with Ag as the working electrode, a $Ag|AgCl,KCl_{sat}$ reference, and a platinum wire as the counter electrode. All electrode potentials are quoted vs. NHE.

Preparation of the roughened silver electrodes

The electrode tips are first carefully polished using a slurry of alumina of 100 µm grain size. Alumina is removed by placing the tips in a ultra-sonic bath and rinsing the tips with copious amounts of water. SERR active silver surfaces were prepared according to \ref{Hildbrandt_SERRS_alt}, by a sequence of electrochemical reduction and oxidation steps in a 0.1 M KCl solution.

Surface Enhanced Resonance Raman Spectroscopy (SERRS) Setup

The setup to perform SERRS measurements is depicted in Fig. 2. Surface enhanced resonance Raman (SERR) spectra were collected using a confocal Raman microscope (LabRam, HR800, HORIBA Jobin Yvon) equipped with a liquid nitrogen cooled back-illuminated CCD camera optimized for near ultra-violet light. The laser beam from a Kr^+ laser (Innova 90C, Coherent, λ_{exc} = 413 nm, I_{Laser} = 30 mW) , was directed through a pre-monochromator (LaserspecIII, Spectrolab Research Laboratory, Newbury England) in order to remove the background radiation consisting of plasma lines produced by the laser medium. The laser beam is then directed through an objective focusing the laser beam onto a quartz crystal of an acoustic optical modulator (AOM) (A.A. MT200/A0,5\@400nm01/24091, A.A. opto-éléctronique, St. Remy, France). The modulator can be used to perform time resolved measurements by a controlled direction of the light through pinholes, triggered by an external master signal.
The AOM was mounted on a stage free to move in x,y,z- direction as well as to change angular positions in order to efficiently couple the laser beam onto the quartz crystal to achieve an optimum of intensity of (in) the 1st order of the diffracted light. The AOM is operated by a wave generator (Mod.200.B26 N-01, RF_{out} = 2W/+24V, A.A. opto-éléctronique, St. Remy, France), providing a radio frequency waveform. The AOM can be triggered by a TTL (master-) signal provided by a function generator. The laser beam is further directed (by an optical pathway consisting of) through a mirror system into a microscope (Olympus BX41) and through a long-distance water immersion objective (Olympus LUMPLFL, 100 XW, WD=1.5, BFOBJ), specialized for near-infrared, onto the surface of the sample. The stage of the Microscope was modified to hold a sample holder for the measuring cell, free to move in z and in x direction directed by an micrometer screw, allowing to focus the laser beam on the surface and to direct the laser beam to different positions on the sample surface. The backscattered light is collected by the same objective,

and guided through a notchfilter (413 nm), and a series of optical elements (pinhols and slits), designed to filter out the laser line and to cut off stray light to alternatively a 600 line/mm grating (in order to obtain a coarse spectra) or a 1800 line/mm grating to obtain the final spectra. The light is then processed by a liquid-N_2 cooled back-illuminated CCD camera. Before recording the spectra, the spectrograph was adjusted (aligned) to the line (band) at (522 cm^{-1}) of the Si spectrum.

Measuring cell:

The Raman measurements were performed in a custom-made spectroelectrochemical cell using an upside-down RDE (rotating disc electrode) with a roughened silver surface (diameter 10 mm) inserted into a Teflon mantle. The measuring cell was combined with the microscope of the Raman spectroscopy setup decribed above. The cell is sealed to ambient air by a lid provided with inlets for the counter, reference (Ag|AgCl,KCl_{sat}) electrodes, an inlet for deoxygenation as well as for the microscope objective. An inner Teflon trough was fixed to the RDE rotating in-line with the electrode. The cell was flushed with Ar, purged from oxygen by washing through the oxygen trap containing buffer solution (see above). In order to prevent photo-reduction or photo-degradation of the enzyme, the electrode was rotated with 15 Hz or 900 rpm while the laser intensity on the sample surface was kept lower than 100 μW, by the insertion of different grey filters at the entrance to the microscope. In order to prevent the surface from running dry by the centrifugal force, a “wave-breaker” was fixed to the microscope objective, guiding the water back to the surface. SERR spectra of several independent measurements and different samples were averaged in order to improve the signal to noise ratio.

Electric contact of the silver working electrode of the spectroelectrochemical cell to the Autolab instrument was established by an sliding contact. , Potentials were applied by a three-electrode configuration. Potentials generated by the Autolab can be triggered by a function generator in order to be able to perform time resolved measurements.

Results

Immobilization of the CcO on the roughened silver electrodes was done as described for the gold electrodes used for electrochemistry and SEIRAS measurements. CcO with the his-tag attached to SU II was used and reconstituted into a ptBLM as described earlier (15). Layer-by layer formation was followed by electrochemical impedance spectroscopy. Cyclic voltammograms (CVs) were recorded under strictly anaerobic conditions in order to ensure that the sample was prepared to undergo direct electron transfer (ET). The significance of the lipid bilayer as a necessary precondition for this process had been emphasized before in the case of gold electrodes. The same holds for silver electrodes used in the present investigation. Direct ET had been shown to take place but only with the CcO immobilized with the cyt c binding site oriented towards the electrode. In this orientation, Cu_A, the first of the four electron acceptors effectively wired to the electrode via the Ni-his-tag. It should be noted that the potential window is considerably smaller for the Ag compared to the Au electrodes, particularly on the direction of positive potentials. Potentials larger than +200 mV must not be applied to the Ag electrode.

SERR spectra recorded in an anaerobic atmosphere taken at increasingly negative potentials ranging from (-150 mV) (-350 mV) are shown in Fig. (3D-gesamt). The most significant difference is the gradual change of the bands from 1358 cm^{-1} to 1370 cm^{-1} which originate from the ν_4 modes of both hemes in the oxidized state (-150 mVand), reduced (-350 mV), respectively (*12,21*). Furthermore, conjugated vinyl and formyl substituents of the type-a hemes of CcO give rise to resonance Raman-active stretching modes between 1610 and 1680 cm^{-1}. For example, a small change is observed due to the weakly bound formyl substituent of heme a_3, from 1663 cm^{-1} in the oxidised state to 1671 cm^{-1} in the reduced state, while the formyl group remains in a hydrophobic environment. A further characteristic marker for the reduced heme a is the intense and well-separated band at 1517 cm^{-1} (ν_{11}), not present in the oxidized state. Redox induced changes of the C=O side group of heme a_3 can be observed by a larger frequency downshift from 1646 to 1610 cm^{-1}, which reflects a substantial redox-linked change of the stronger hydrogen bond interactions of this substituent with Gln471 and Arg52 (*12,21*). Both porphyrin modes (ν_4 and ν_{11}) and the formyl stretching modes allow monitoring of the oxidation states of the individual hemes of the immobilized CcO. The bands at 1477 and 1490 cm^{-1} result from the mode ν_3 of a ferric, hexa- (6cHS) and pentacoordinated (5cHS) high-spin (HS) heme a_3, respectively or at 1500 (ν_3) and 1585 cm^{-1} (ν_2) a ferric hexacoordinated low-spin (6cLS) heme (*12, 21, 23*). This finding shows a potential-dependent structural rearrangement in the environment of the catalytic center and bridging ligand, which is partially dissociated from the heme a_3. Band assignments taken from different references quoted in the text, are collected in Table 1. It should be mentioned that Cu centers are not visible because of a selective resonance enhancement of the heme structure. Redox changes of

both Cu_A and Cu_B as a function of applied potentials have been shown by SEIRAS. Moreover, electrons arriving at Cu_A are transferred to the catalytic center of heme a_3 / Cu_B (*1,2*). It thus follows from the Raman spectra that electrons taken up by Cu_A are transferred to both heme a and a_3. As a consequence, a gradual transition of the redox state as well as the coordination and spin state of both heme centers occurs in the potential range between -150 mV and -350 mV. This is in agreement with electrochemical measurements where a number of four electrons were shown to be transferred in the reduction and oxidation steps.

Next, the CcO was immobilized and reconstituted into a ptBLM with the his-tag attached to SU I. In this inverted orientation, no indication of direct ET to CcO is found by electrochemical measurements. Accordingly, no indication of reduction can be seen in the SERR spectra taken in the potential range between +200 mV and –1100 mV showing that the enzyme remains in the oxidized state (Fig…..) A functional impairment of the enzyme can be excluded since redox centers can be reduced chemically by adding dithionite (Fig….). Moreoever, the characteristic marker band region (1300-1750 cm^{-1}) is very sensitive to the integrity of the heme structure and its protein environment and the immobilized CcO can be activated by reduced cytochrome c

Conclusion

ET to CcO immobilized in a ptBLM had been claimed to occur directly across the entire distance of at least of 4 nm to heme a_3 independently from the orientation of the protein. We cannot confirm this result. We conclude from our experiments, that direct ET to the CcO was accomplished via Cu_A as the first electron acceptor, followed by ET to heme a and a_3, but only in the orientation with Cu_A directed towards the electrode. A discrimination between heme a and a_3 was not possible by SERR spectra which is not surprising in view of the redox potentials which are very similar. The assumption of Cu_A as the first electron acceptor is in agreement with the ET to CcO to be relatively fast (k_0 > 4000 s^{-1}) as compared to water soluble (k_0 between 100 s^{-1} to 1600 s^{-1}) or electrostatically absorbed proteins such as cyt c (k_0 = 20 s^{-1}). The fast ET is explained in terms of an effective wiring via the Ni-his-tag, where the Ni^{+}/Ni^{++} pair acts as a transient redox acceptor and the stretch of 6 histidines as a partially conjugated π-electron system. This conclusion is strongly supported by static and tr-SEIRAS measurements. Cu_A was shown to be the first electron acceptor followed by the hemes, but only in the orientation mentioned above. This is confirmed by both SERR and SEIRA experiments using the inverted orientation. Heme a_3 in this case, is directed towards the electrode connected via the Ni-his-tag wire. Definitely no direct ET can be observed, even at potentials as low as – 1V, both on gold and silver electrodes. This had been confirmed by electrochemical experiments using CcO in this orientation. Direct ET to CcO was not observed , unless cyt c was adsorbed to the cyt c binding site, directed towards the bathing solution. A conformational transition to a state exhibiting an open heme pocket in the hemes a and a_3 within the CCO was postulated as a consequence of cyt c binding. This could open the way from heme a_3 all the way to the his-tag and further on to the electrode, mediated by cyt c.

Table 1:

Raman vibrational modes of Cytochrome c Oxidase ***(Rhodobacter sphaeroides)***							
Oxidized (cm^{-1})				***Reduced*** (cm^{-1})			
heme a		***heme a_3***		***heme a***		***heme a_3***	
1370 (*)	ν_4	1370 (*)	ν_4	1358 (*)	ν_4	1358 (*)	ν_4
1467	ν_{28}						
		1477/78	ν_3 (6cHS)				
		1490	ν_3 (5cHS)	1466	ν_{28}	1473.6	ν_3
1500	ν_3			1490	ν_3		
				1517	ν_{11}		
1528	ν_{38y}						
		1507/10	ν_{38y}				
		1558/54	ν_{38x}				
1570	ν_{38x}						
bzw. A center frequency 1528	ν_{38}	1532	ν_{38}				
		1520	ν_{11}				
1541	ν_{11a}						
1563	ν_{38x}	1569/70	ν_2				
1585	ν_2	1577	ν_{37}	1537	ν_{38y}	(1531)	ν_{38y}
1603	ν_{37}	1610	ν_{10}	1568	ν_{38x}	1564	ν_{38x}
1622(+)	$\nu_{C=C}$	1621(+)	$\nu_{C=C}$	1586	ν_2	1581	ν_2
1635	ν_{10}			1610	$\nu_{C=O}$	1605	ν_{10}
1646	$\nu_{C=O}$			1614	ν_{10}	1620	$\nu_{C=C}$
		1669-71	$\nu_{C=O}$	1625	$\nu_{C=C}$	1663	$\nu_{C=O}$

* originates from modes of both heme a and a_3
\+ not distinguishable

$\nu_{C=C}$ = vinyl stretching mode
$\nu_{C=O}$ = formyl stretching mode

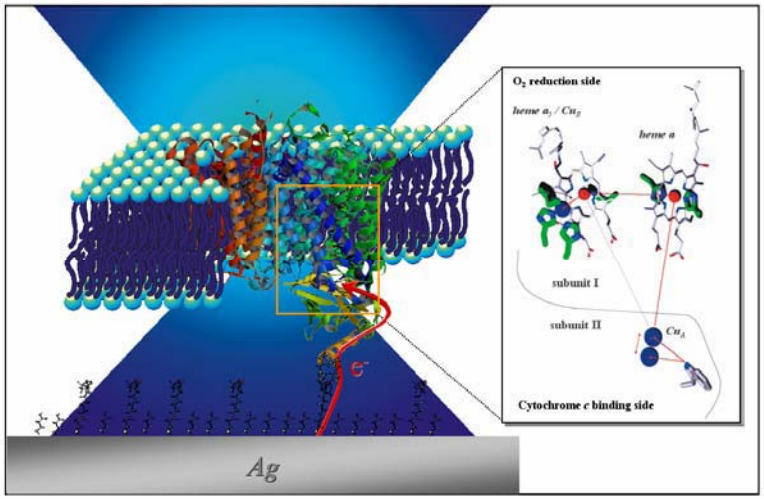

Figure 1: Scheme of the immobilized cytochrome c oxidase, embedded in a ptBLM architecture. The Enzyme is directed with its natural electron entry side towards the electrode, thus allowing for a direct electron injection into the active sites of the enzyme (inset).

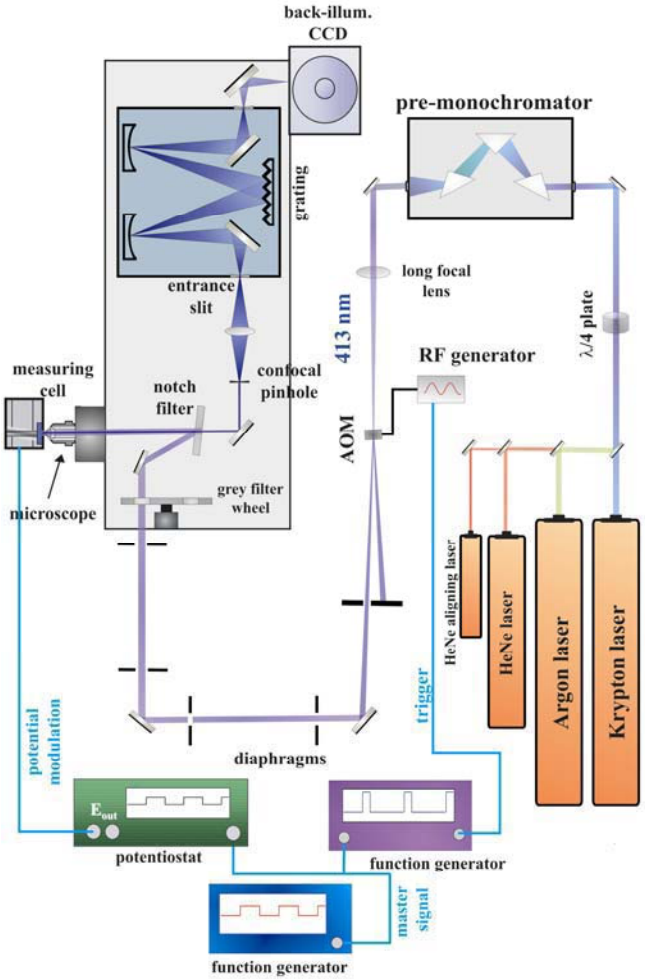

Figure 2: Schema of the home-build SERRS setup for time-resolved measurements.

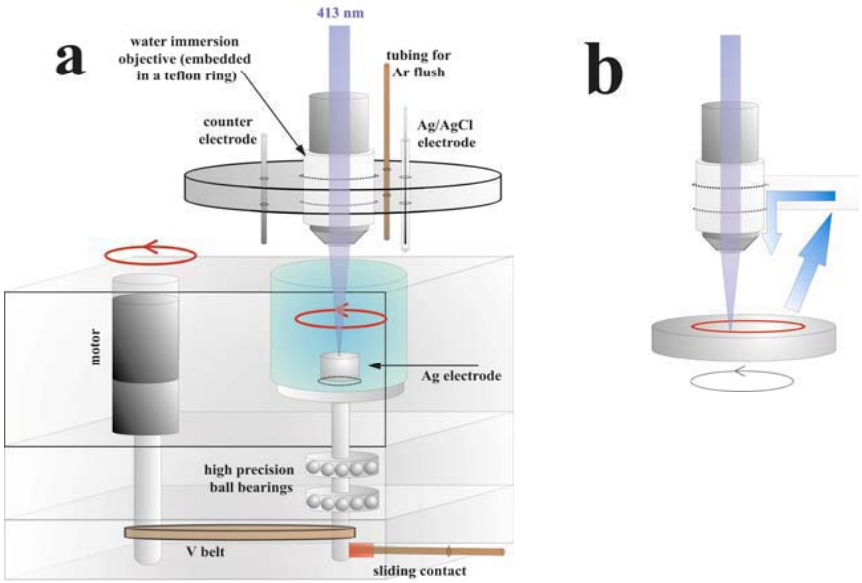

Figure 3: Spectroelectrochemical cell for potential controlled SERRS measurements on protein monolayer.

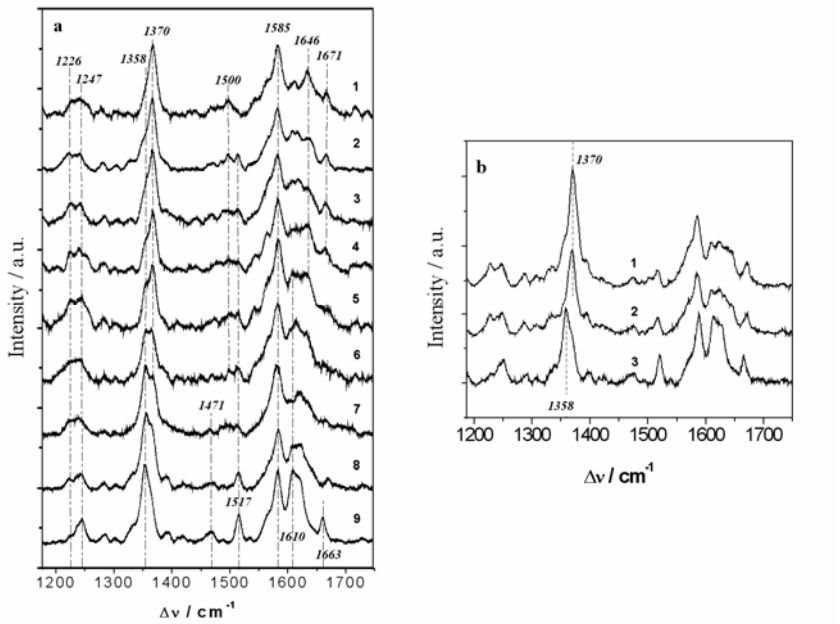

Figure 4: SERR spectra of CcO at different potentials applied across the biomimetic protein-membrane architecture immersed in buffer solution. (a) with the his-tag on SU II at -150 mV (1), -175 mV (2), -200 mV (3), -225 mV (4), -250 mV (5), -275 mV (6), -300 mV (7), -325 mV (8) and -350 mV (9). (b) with the his-tag on SU I, spectrum taken at +200 mV (1), -1100 mV (2) and after chemical reduction with dithionite (3).

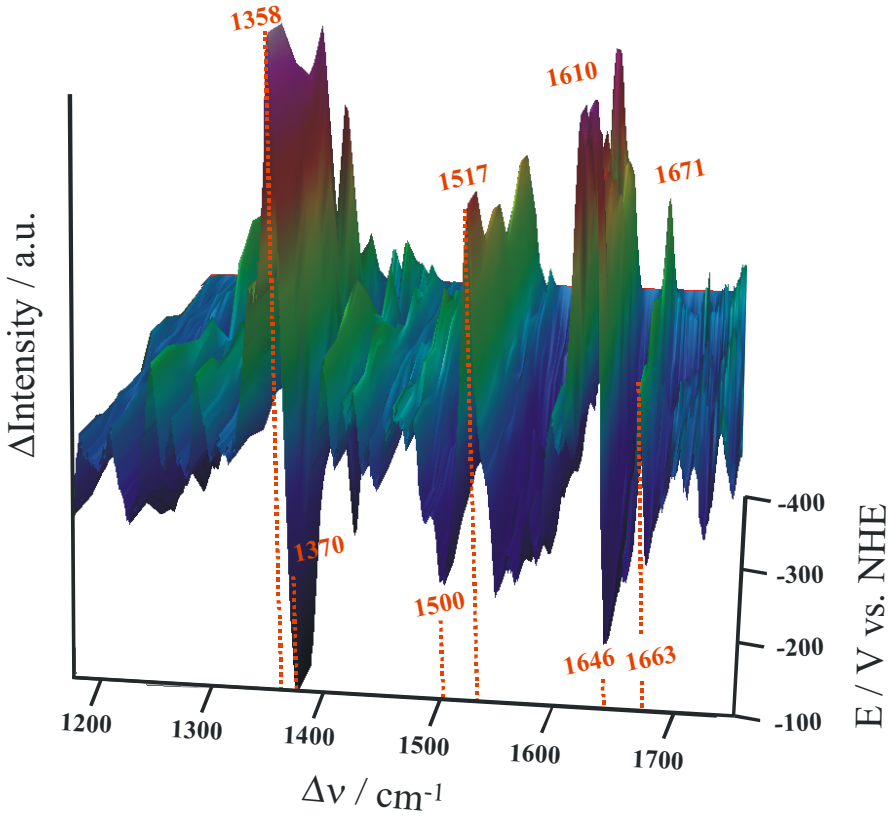

Figure 5: Difference spectra (with CcO in the oxidized form as the reference) showing the transition of the SERR spectra of CcO from the oxidized (-100 mV) to the reduced state (-400 mV). The 3D representation shows clearly three regions, 1350- 1370 cm^{-1}, 1500- 1520 cm^{-1} and 1600- 1620 cm^{-1}, with significant changes.

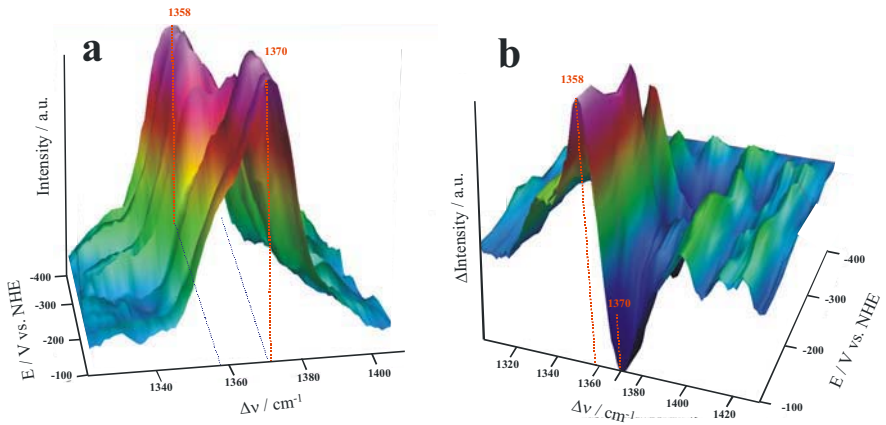

Figure 6: (a) Transition of the redox-sensitive ν_4 modes of both hemes [1358 cm^{-1} (reduced) and 1370 cm^{-1} (oxidized)].
(b) Difference spectra of the same spectral region.

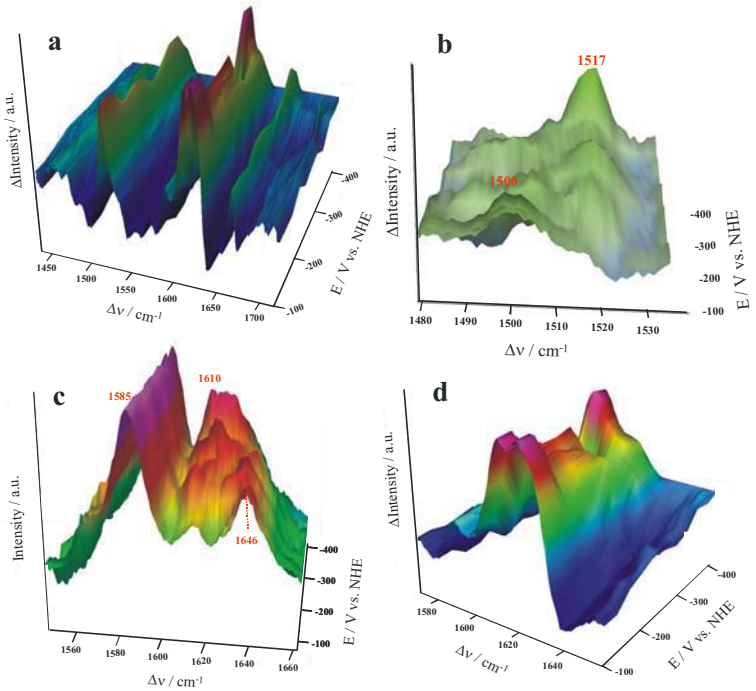

Figure 7: (a) Difference spectra of the high frequency region 1450 - 1700 cm^{-1} (b) Expansion of the region between 1480 and 1530 , showing the transition of the ν_{11} (1517 cm^{-1}) mode of reduced heme a (not present in the oxidized form) and the ν_3 mode (1500 cm^{-1}) of the reduced heme a_3. (c) Absolute and (d) difference spectra of the heme and fromyl stretching region between 1580 and 1650 cm^{-1}.

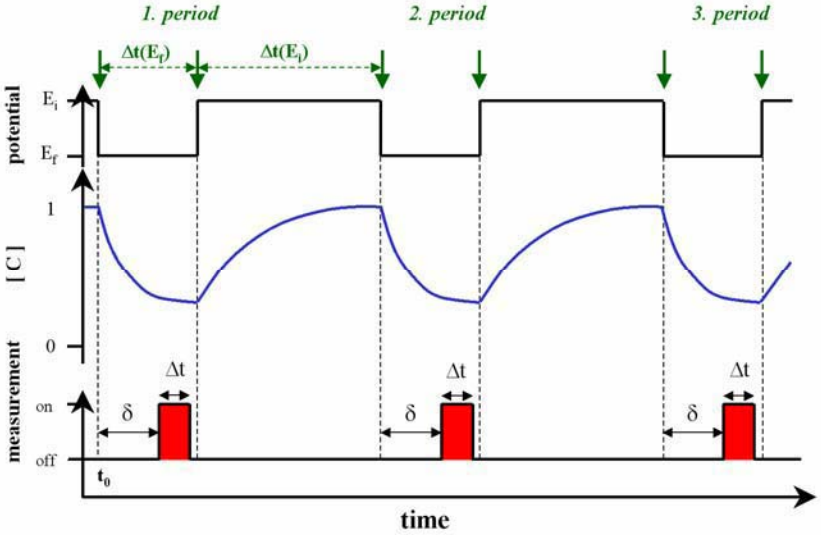

Figure 8: Principle of potential modulated time-resolved SERRS measurements.